Unraveling the Potential and Complex Interplay of Endolysosomal Proteins TRPML1, TPC2, and Rab7a: Implications for Cancer and Neurodegenerative Disorders

Carla Abrahamian

München

2023

Aus dem Walther-Straub-Institut für Pharmakologie und Toxikologie
Institut der Ludwig-Maximilians-Universität München
Vorstand: Prof. Dr. med. Thomas Gudermann

Unraveling the Potential and Complex Interplay of Endolysosomal Proteins TRPML1, TPC2, and Rab7a: Implications for Cancer and Neurodegenerative Disorders

Dissertation
zum Erwerb des Doktorgrades der Naturwissenschaften
an der Medizinischen Fakultät der
Ludwig-Maximilians-Universität München

vorgelegt von

Carla Abrahamian

aus Damaskus, Syrien

2023

Mit Genehmigung der Medizinischen Fakultät
der Universität München

Betreuer: Prof. Dr. Dr. Christian Michael Grimm

Zweitgutachter: Prof. Dr. Stylianos Michalakis

Dekan: Prof. Dr. med. Thomas Gudermann

Tag der mündlichen Prüfung: 18. März 2024

Affidavit

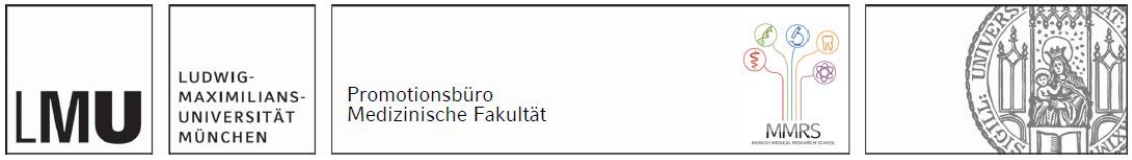

Affidavit

Abrahamian, Carla

_____

Surname, first name

_____

Street

_____

Zip code, town, country

I hereby declare, that the submitted thesis entitled:

Unraveling the Potential and Complex Interplay of Endolysosomal Proteins TRPML1, TPC2, and Rab7a: Implications for Cancer and Neurogenerative Disorders

is my own work. I have only used the sources indicated and have not made unauthorised use of services of a third party. Where the work of others has been quoted or reproduced, the source is always given.

I further declare that the dissertation presented here has not been submitted in the same or similar form to any other institution for the purpose of obtaining an academic degree.

München, 08.04.2024

_____

place, date

Carla Abrahamian

_____

Signature doctoral candidate

This thesis is dedicated to the extraordinary and resilient women who shaped my life: Yerado, Arpy, Armine, and Zella

Table of Content

List of Abbreviations

1,10-PT	1,10-phenanthroline
ANXA1	Annexin A1 encoding gene
AP	Autophagosome
ARF	ADP ribosylation factor
ATP	Adenosine triphosphate
BC	Breast cancer
bHLH-ZIP	Basic helix-loop-helix leucine zipper
BP	Binding protein
BRAF	V-raf murine sarcoma viral oncogene homolog B1
BRCA1	Breast cancer gene 1
BRCA2	Breast cancer gene 2
C-terminus	Carboxy-terminus
Cas9	CRISPR-associated protein 9
CD	Cluster of differentiation
CDKN2A	Cyclin dependent kinase inhibitor 2a
CHX	Cycloheximide
CLN3	Ceroid-lipofuscinosis, neuronal, 3
Co-IP	Co-immunoprecipitation
CREB	cAMP-response element binding protein
CRISPR	Clustered regularly interspaced short palindromic repeats
DCT	Dopachrome tautomerase
DI	Domain I
DII	Domain II
dKO	Double knockout
DMSO	Dimethyl sulfoxide
EE	Early endosome
ER	Endoplasmic reticulum
ERK	Extracellular signal-regulated kinase
FDR	False discovery rate
FRET	Fluorescence resonance energy transfer
FYCO1	Fyve and coiled-coil domain autophagy adaptor 1
G-protein	Guanine nucleotide-binding protein
GAP	GTPase-activating protein
GDP	Guanosine diphosphate
GEF	Guanine nucleotide exchange factor
GFP	Green fluorescent protein
GoF	Gain of Function
GSK3β	Glycogen synthase kinase 3 beta
GTPase	Guanosine triphosphatase
HN1L	Hematological and neurological expressed 1-like protein
iPSC	Induced pluripotent stem cell
JPT2	Jupiter microtubule-associated homolog 2
KD	Knockdown
KO	Knockout
LAMP	Lysosome-associated membrane glycoprotein
LAMP1	Lysosomal-associated membrane protein 1
LE	Late endosome
LIMP	Lysosomal integral membrane protein
LRRK2	Leucin-rich repeat kinase 2
LSD	Lysosomal storage disease
Lsm	Sm-like protein
Lsm12	Sm-like protein 12
LTS	Lysosomal-targeting sequence

LY	Lysosome
MAPK	Mitogen-activated protein kinases
MC1R	Melanocortin 1 receptor
MC1R	Melanocortin 1 receptor
MCOLN1	Transient receptor potential mucolipin 1 encoding gene
MCOLN2	Transient receptor potential mucolipin 2 encoding gene
MCOLN3	Transient receptor potential mucolipin 3 encoding gene
MITF	Microphthalmia-associated transcription factor
MLIV	Mucolipidosis type IV
mRNA	Messenger RNA
mTOR	Mechanistic target of rapamycin
mTORC1	Mechanistic target of rapamycin complex 1
MVBs	Multivesicular bodies
MYC	Master Regulator of Cell Cycle Entry and Proliferative Metabolism
N-terminus	Amino-terminus
NAADP	Nicotinic acid adenine dinucleotide phosphate
NAADP-BP	NAADP binding protein
NPC1	Niemann-pick c1
NRAS	Neuroblastoma RAS viral oncogene homolog
OE	Overexpression
P2X4	P2X purinoreceptor 4
PD	Parkinson's disease
$PI(3,5)P_2$	Phosphatidylinositol 3,5-bisphosphate
$PI(4,5)P_2$	Phosphatidylinositol 4,5-bisphosphate
PI3P	Phosphatidylinositol 3-phosphate
PIKfyve	Phosphatidylinositol kinase FYVE finger-containing enzyme
PM	Plasma membrane
PMEL	Pigment cell-specific protein
PRKN	Parkin
PTEN	Phosphatase and tensin homolog
Rab	Ras-associated binding
Rab11	Ras-related protein-11a
Rab22a	Ras-related protein Rab-22A
Rab27a	Ras-related protein 27a
Rab5	Ras-related protein-5a
Rab7a	Ras-related protein-7a
Rab7b	Ras-related protein-7b
Rab9	Ras-related protein-9a
Rac1	Ras-related C3 botulinum toxin substrate 1
Ran	Ras-related nuclear protein
Ras	Rat sarcoma
RE	Recycling endosome
RGS4	Regulator of G protein signaling 4
Rho	Ras homologous
RTK	Receptor tyrosine kinase
siRNA	Small interfering RNA
SLC7A5	Solute carrier transporter 7a5
SNARE	Soluble N-ethylmaleimide-sensitive factor activating protein receptor
SNP	Single nucleotide polymorphism
SOX10	Sry-box transcription factor 10
SURF4	Surfeit locus protein 4
TFEB	Transcription factor EB
TGN	Trans-Golgi network
TMED10	Transmembrane p24 trafficking protein 10
TMEM163	Transmembrane protein 163
TMEM165	Transmembrane protein 165
TMEM185A	Transmembrane protein 185A
TMI	Transmembrane I

TMII	Transmembrane II
TNBC	Triple-negative breast cancer
TPC	Two-pore channel
TPC1	Two-pore channel 1
TPC2	Two-pore channel 2
TPCN1	Two-pore channel 1 encoding gene
TPCN2	Two-pore channel 2 encoding gene
TPEN	N,N,N,N-Tetrakis(2-pyridylmethyl)-ethylenediamine
TRP	Transient receptor potential
TRPA1	Transient receptor potential ankyrin 1
TRPC	Transient receptor potential canonical
TRPM	Transient receptor potential melastatin
TRPML	Transient receptor potential mucolipin
TRPML1	Transient receptor potential mucolipin 1
TRPML2	Transient receptor potential mucolipin 2
TRPML3	Transient receptor potential mucolipin 3
TRPP	Transient receptor potential vanilloid 1
TYR	Tyrosinase
TYRP1	Tyrosinase related protein 1
UV	Ultraviolet
UVA	Ultraviolet A
UVB	Ultraviolet B
V-ATPase	Vacuolar-type H^+-atpase
VDAC	Voltage-dependent anion channel 1
VGIC	Voltage-gated ion channel
VPS34	Phosphatidylinositol 3-kinase VPS34
WT	Wild-type
β-Catenin	Catenin beta-1

List of Publications

This thesis is based on the following publications found in the main text and submitted manuscripts and review articles found in the appendix.

*these authors contributed equally to this work

In the Main Text:

Paper I:

Netcharoensirisuk, P.*, **Abrahamian, C.***, Tang, R.*, Chen, C. C., Rosato, A. S., Beyers, W., Chao, Y. K., Filippini, A., Di Pietro, S., Bartel, K., Biel, M., Vollmar, A. M., Umehara, K., De-Eknamkul, W.*, & Grimm, C.* (2021). Flavonoids increase melanin production and reduce proliferation, migration and invasion of melanoma cells by blocking endolysosomal/melanosomal TPC2. *Scientific reports*, *11*(1), 8515. https://doi.org/10.1038/s41598-021-88196-6

Paper II:

Yuan, Y., Jaślan, D., Rahman, T., Bolsover, S. R., Arige, V., Wagner, L. E., 2nd, **Abrahamian, C.**, Tang, R., Keller, M., Hartmann, J., Rosato, A. S., Weiden, E. M., Bracher, F., Yule, D. I., Grimm, C.*, & Patel, S.* (2022). Segregated cation flux by TPC2 biases Ca^{2+} signaling through lysosomes. *Nature communications*, *13*(1), 4481. https://doi.org/10.1038/s41467-022-31959-0

Paper III:

Scotto Rosato, A*, Krogsaeter, E. K.*, Jaślan, D., **Abrahamian, C.**, Montefusco, S., Soldati, C., Spix, B., Pizzo, M. T., Grieco, G., Böck, J., Wyatt, A., Wünkhaus, D., Passon, M., Stieglitz, M., Keller, M., Hermey, G., Markmann, S., Gruber-Schoffnegger, D., Cotman, S., Johannes, L., Crusius, D., Boehm, U., Wahl-Schott, C., Biel, M., Bracher, F., De Leonibus, E., Polishchuk E., Medina, D.L.*, Paquet, D.*, Grimm, C. * (2022). TPC2 rescues lysosomal storage in mucolipidosis type IV, Niemann-Pick type C1, and Batten disease. *EMBO molecular medicine*, *14*(9), e15377. https://doi.org/10.15252/emmm.202115377

Paper IV:

Rühl, P., Rosato, A. S., Urban, N., Gerndt, S., Tang, R., **Abrahamian, C.**, Leser, C., Sheng, J., Jha, A., Vollmer, G., Schaefer, M., Bracher, F., & Grimm, C. (2021). Estradiol analogs attenuate autophagy, cell migration and invasion by direct and selective inhibition of TRPML1, independent of estrogen receptors. *Scientific reports*, *11*(1), 8313. https://doi.org/10.1038/s41598-021-87817-4

In the appendix:

Paper V:

Abrahamian, C.*, Tang, R.*, Deutsch, R.*, Ouologuem, L, Blenniger, J., Weiden, E.-M., Kudrina, V., Rilling, J., Feldmann, C., Stepanov, Y., Scotto Rosato, A., Calvo, G., Soengas, M., Fröhlich, T., Gudermann, T., Biel, M., Wahl-Schott, C., Chen, C.-C., Bartel, K.*, Grimm, C.* (2023) Rab7a is a direct effector of the intracellular Ca^{2+} channel TPC2 regulating melanoma progression through modulation of the Wnt signaling pathway. *Cell Reports. Manuscript in submission.*

Paper VI:

Frey, N., Ouloguem, L., Siow, W. X., Stöckl, J., Blenniger, J., **Abrahamian, C.**, Grimm, C., Bartel., K. (2023). Endolysosomal TRPML1 channel regulates cancer cell-migration by facilitating the intracellular trafficking of E-cadherin and β1-integrin. *Journal of Biological Chemistry. Manuscript in submission*

Paper VII (review):

Abrahamian, C., & Grimm, C. (2021). Endolysosomal Cation Channels and MITF in Melanocytes and Melanoma. *Biomolecules*, *11*(7), 1021. https://doi.org/10.3390/biom11071021

Paper VIII (review):

Spix, B.*, Chao, Y. K.*, **Abrahamian, C.***, Chen, C. C., & Grimm, C. (2020). TRPML Cation Channels in Inflammation and Immunity. *Frontiers in immunology*, *11*, 225. https://doi.org/10.3389/fimmu.2020.00225

List of Figures

All figures were created using Biorender.com. Figure 4 is adapted from the following templates “Life Cycle of Rab27: A Monomeric GTPase That Regulates Vesicular Trafficking”, created by Elena De Vita and “Wnt Signaling Pathway Activation and Inhibition”.

Summary (English)

The endolysosomal network comprises distinct interconnected membrane-bound organelles, namely early endosomes (EEs), recycling endosomes (REs), multivesicular bodies (MVBs), late endosomes (LEs), and lysosomes (LYs)[1]. Within eukaryotic cells, LYs serve as primary degradative centers, housing a variety of enzymes that function optimally at their acidic pH and are capable of degrading proteins, lipids, and carbohydrates[2]. Lysosomal function and physiology are regulated by resident proteins and ion channels that facilitate ion movement across the endolysosomal membrane. The transient receptor potential mucolipin channel 1 (TRPML1) and two-pore channel 2 (TPC2) are chief cation channels found in LEs and LYs and share several characteristics. These channels are permeable to calcium (Ca^{2+}) and sodium (Na^{+}) and govern cargo trafficking, vesicle fusion, and membrane dynamics in the endolysosomal system. Additionally, both TRPML1 and TPC2 interact with the mammalian target of rapamycin complex 1 (mTORC1), are involved in lysosomal exocytosis and autophagy, and are activated by phosphatidylinositol 3,5-bisphosphate ($PI(3,5)P_2$). Dysfunctions or mutations in endolysosomal ion channels have been associated with various channelopathies, encompassing autoimmune disorders, fatty liver disease, neurodegenerative diseases, lung disease, metabolic disorders, and cancer[3, 4]. A prominent group of disorders directly related to lysosomal pathophysiology is known as lysosomal storage diseases (LSDs). Mucolipidosis type IV (MLIV), the autosomal recessive LSD, arises from mutations in the gene encoding TRPML1 (*MCOLN1*). Typically, MLIV manifests in childhood with neurodegenerative symptoms accompanied by visual and motor impairments[5-7]. MLIV patients often exhibit an accumulation of lipid products and increased aggregates, such as p62/ Sequestosome 1 (SQSTM1), within intracellular organelles.

In Scotto Rosato et al., 2022, we aimed to rescue LSD phenotypes by activating TPC2 using the selective agonist TPC2-A1-P. We utilized different models, including induced pluripotent stem cell (iPSC)-derived neurons, patient fibroblasts, and in vivo MLIV mice. Interestingly, stimulation of MLIV cells with TPC2-A1-P reduced lipid and cholesterol accumulation, reversed the autophagy blockade, and restored cellular ultrastructure. Additionally, MLIV mice treated with TPC2-A1-P ameliorated central nervous system defects and exhibited improved motor performance compared to mice treated with DMSO vehicle control[8].

Besides LSDs, a study has revealed an intriguing connection between TRPML1 and triple-negative breast cancer (TNBC)[9]. TNBC is known for its aggressive nature, characterized by the absence of estrogen receptor (ER), progesterone receptor (PR), and human epidermal growth factor receptor 2 (HER2) amplification[10]. TRPML1 showed an upregulated expression in TNBCs, and its silencing inhibited the growth of these cancer cells by regulating the activity of mTORC1[9]. For this purpose, we extended our work to investigate the proposed role of TRPML1 in TNBC. In Rühl et al., 2021, we successfully developed the first isoform-selective and potent antagonist for TRPML1, namely the steroid 17β-estradiol methyl ether (EDME). To decipher its mechanism of action, we treated the MDA-MB-231 TNBC cell line with EDME and generated a CRISPR/Cas9 TRPML1 knockout (KO) within the same cell line. The results were compelling, showing that both TRPML1 KO and EDME treatment reduced cell migration and invasion compared to the control. The TRPML1 KO line provided further evidence of the on-target effects of EDME[11]. These findings offer valuable insight into the potential of temporarily modulating TRPML1 activity to suppress the growth and migration of aggressive TNBC.

Nevertheless, despite key similarities, TRPML1 and TPC2 also possess distinct properties. Notably, TPC2 can also be activated by the Ca^{2+}-mobilizing second messenger nicotinic acid adenine dinucleotide phosphate (NAADP), rendering the ion selectivity of TPC2, a highly debatable topic. A previous study in our laboratory demonstrated the agonist-dependent activation of TPC2 using small molecule activators, TPC2-A1-P (used in Scotto Rosato et al., 2022) mimicking $PI(3,5)P_2$ activation, and TPC2-A1-N mimicking NAADP activation[12]. Intrigued by the agonist-mediated switch of TPC2 between non-selective selective Ca^{2+} and selective Na^+ states, we further investigated the simultaneous application of these compounds on TPC2 behavior in Yuan et al., 2022. To explore this aim, we tested the co-application of TPC2-A1-P and TPC2-A1-N using Ca^{2+} imaging via genetically encoded Ca^{2+} indicator GCaMP6 and electrophysiology patch clamp recordings. Our preliminary investigations aimed at testing various cell lines for the expression of TPC2 (data published in Abrahamian et al., 2021, appendix). The melanoma cell line, SK-MEL-5, showed high expression for TPC2 but not the TPC1 isoform on a transcript level and was selected for further investigation. Indeed, in wild-type (WT) SK-MEL-5 cells, robust Ca^{2+} responses were evoked that were twice as high as those observed in Hela cells. A TPC2 KO was created in this line to be used as a control for different experiments. As expected, TPC2-deficient SK-MEL-5 cells showed significantly reduced Ca^{2+} evoked responses. The simultaneous activation of TPC2 by TPC2-A1-P and TPC2-A1-N resulted in increased Ca^{2+} permeability and flux in WT cells; however, Na^+ flux remained unaltered[13]. Our study provides novel insight into the complex interaction of TPC2 with its ligands, demonstrating its preference for potentiating Ca^{2+} permeability over Na^+ in response to signaling cues. This versatile behavior has profound implications on cellular function and physiology, particularly of significance when targeting TPC2 in disease models.

In a pathological context, we expanded our gene expression analysis of endolysosomal cation channels and Rab proteins across various cancer types. We observed the highest expression for *MCOLN1*, *TPCN2*, and *RAB7A* particularly in comparison to other lysosomal genes tested, including *MCOLN2*, *MCOLN3*, *TPCN1*, and *RAB7B*. Intriguingly, these genes (*MCOLN1*, *TPCN2*, and *RAB7A*) showed the most significant enrichment in melanoma and a hepatocellular carcinoma line, surpassing other cancer types like cervical adenocarcinoma, ovarian cancer, colon adenocarcinoma, lung adenocarcinoma, and pancreatic ductal adenocarcinoma, among others. Consequently, melanoma, a highly aggressive type of skin cancer originating from melanocytes, was our primary focus of investigation. Identified risk factors for melanoma include excessive exposure to ultraviolet (UV) radiation, family history, fair hair, skin, and eye color[14]. In particular, we focused on exploring the role of TPC2 in melanoma, given its substantial expression in this type of cancer, localization to mature melanosomes, as well as its pivotal role in pigmentation[15]. Gain of function (GoF) mutations (G734E and M484L) in human TPC2 have been associated with reduced melanin production and blond hair[16]. In accordance with this finding, our study focused on pigmented in vitro melanoma lines, MNT-1 (human) and B16F10 (mouse). Remarkably, the genetic ablation of TPC2 in MNT-1 demonstrated an increased melanin content and a larger but less acidic melanosome lumen. Besides, Naringenin, a natural flavonoid, has been found to block TPC2 activity. To expand on this discovery, we performed a screening of novel flavonoids derived from *Dalbergia parviflora*, which could potentially be more potent than Naringenin. Among the tested compounds, two were prominent hits: MT-8 (O-methylated isoflavone) and UM-9 (tri-O-methylated isoflavan). We validated these compounds using electrophysiology patch clamp experiments, which demonstrated their ability to inhibit TPC2 at a much lower concentration compared to Naringenin. In addition, both MT-8 and UM-9 showed the highest melanin generation in MNT-1 and B16F10 cells, indicating their potential as effective TPC2 antagonists. Accordingly, we sought to elucidate the physiological

significance of TPC2 in regulating melanoma phenotypes in these pigmented lines using our hit compounds and the knockout model. Our experiments focused on assessing the impact of TPC2 on melanoma cell behavior, revealing substantial reductions in cell proliferation, migration, and invasion in the TPC2-deficient melanoma cells compared to their WT counterpart. We examined the downstream signaling cascades influenced by the endolysosomal machinery. Exceptionally, the melanoma oncogene, MITF, demonstrated a significant reduction on a protein level in the TPC2 KO MNT-1 cells compared to the WT cells. Further analysis using the protein stability cycloheximide chase experiments revealed that this downregulation was attributed to the proteasomal degradation of MITF. To confirm this observation, we treated the TPC2-deficient cells with the proteasomal inhibitor MG-132, which ameliorated MITF expression to levels comparable to WT cells. Moreover, we explored the signaling pathways known to regulate MITF and melanoma growth, including MAPK, cAMP, canonical Wnt, and Akt pathways. Our result demonstrated an inverse increase in GSK3β levels in TPC2 KO MNT-1 cells compared to WT, solidifying the role of GSK3β in melanoma as the negative regulator of MITF, promoting its proteasomal degradation[17].

Intriguingly, a proteomic analysis of the TPC2 interactome unveiled Rab7 as an interaction partner of TPC2[18]. Rab7a, a small guanosine triphosphatase (GTPase), serves as a lysosomal marker and plays critical roles in the trafficking and degradation of molecules, fusion of late endosomes and autophagosomes, and lysosomal biogenesis[19]. Nevertheless, the functional impact of Rab7a on TPC2 channel activity and the consequent pathophysiological relevance of this interaction remains unclear. In our study (Abrahamian et al., 2023, appendix), we first reproduced the co-immunoprecipitation (Co-IP) data from Lin-Moshier et al., 2014[18] and further performed fluorescence resonance energy transfer (FRET) experiments, confirming the physical interaction between Rab7a and TPC2. Moreover, utilizing endolysosomal patch-clamp and Ca^{2+} imaging techniques, we demonstrated that Rab7a strongly enhances the activity of TPC2, establishing the functional interaction between these two lysosomal proteins. To explore the potential implications in melanoma, we generated different knockout models using CRISPR/Cas9, employed selective small molecule antagonists and agonists, and performed siRNA knockdown (KD) and overexpression (OE) studies in a range of melanoma lines with different mutational backgrounds. Interestingly, we observed significantly diminished melanoma cell proliferation, migration, and invasion in most MITF-dependent melanoma lines upon KO or KD of Rab7a or TPC2. However, most MITF-independent lines exhibited no alternations in melanoma phenotypes upon Rab7a or TPC2 depletion. Furthermore, we identified a positive correlation between the transcript levels of Rab7a and TPC2 in these melanoma lines, as well as a positive correlation between the protein expression of Rab7a with MITF and GSK3β. Consistent with the data obtained from the MITF-dependent pigmented MNT-1 line, the loss or pharmacological inhibition of Rab7a or TPC2 decreased the protein expression of MITF and β-Catenin, while GSK3β protein levels were increased. These findings corroborate the proposed model of the connection between the Wnt/β-Catenin pathway, MITF, and the endolysosomal machinery in melanoma[20]. In addition, we performed different rescue experiments in the Rab7a and TPC2 knockout lines. Our results demonstrated that the OE of Rab7a only partially alleviated the phenotype of TPC2 KO, whereas TPC2 OE effectively rescued the Rab7a KO phenotype. Based on these findings, we identified Rab7a as a melanoma oncogene and an effector of TPC2, highlighting their potential as targets for therapeutic interventions in melanoma.

Overall, our findings advance our understanding of the therapeutic potential and interplay of lysosomal proteins in the context of neurodegenerative disorders and cancer, with a particular focus on breast cancer and melanoma. Through different works, we demonstrated that mutations,

alterations in expression, or dysregulated activity of TRPML1 or TPC2 could result in detrimental effects on cellular functions and associated signaling cascades. Consequently, the investigation of endolysosomal cation channels and proteins and the generation of novel selective small molecule agonists and antagonists targeting these channels can offer valuable insights into the molecular mechanism underlying disease heterogeneity, shed light on the variations in disease manifestation, and uncovers novel opportunities for drug repurposing.

Summary (Deutsch)

Das endolysosomale Netzwerk umfasst verschiedene miteinander verbundene membranbegrenzte Organellen, frühe Endosomen (EEs), Recycling-Endosomen (REs), multivesikuläre Körper (MVBs), späte Endosomen (LEs) und Lysosomen (LYs)[1]. Innerhalb eukaryotischer Zellen dienen LYs als primäre abbauende Zentren, in denen eine Vielzahl von Enzymen vorhanden ist, die bei ihrem sauren pH-Wert optimal funktionieren und Proteine, Lipide und Kohlenhydrate abbauen können[2]. Die Funktion und Physiologie der Lysosomen werden durch residente Proteine und Ionenkanäle reguliert, die die Ionenbewegungen über die endolysosomale Membran vermitteln. Von den in LEs und LYs vorkommenden Kationenkanälen sind der „transient receptor potential mucolipin Kanal 1“ (TRPML1) und der „two-pore channel 2“ (TPC2) die wichtigsten und teilen dabei mehrere Eigenschaften. Diese beiden Kanäle sind permeabel für Calcium (Ca^{2+}) und Natrium (Na^{+}) und kontrollieren den zellulären Transport, die Fusion von Vesikeln und die Membrandynamik im endolysosomalen System. Darüber hinaus interagieren sowohl TRPML1 als auch TPC2 mit mTORC1, sind an der lysosomalen Exozytose und Autophagie beteiligt und werden durch Phosphatidylinositol 3,5-bisphosphate ($PI(3,5)P_2$) aktiviert. Dysfunktionen oder Mutationen in endolysosomalen Ionenkanälen wurden mit verschiedenen Kanalopathien in Verbindung gebracht, darunter Autoimmunerkrankungen, Fettlebererkrankungen, neurodegenerative Erkrankungen, Lungenerkrankungen, Stoffwechselerkrankungen und Krebs[3, 4]. Die Erkrankungen, die direkt mit der lysosomalen Pathophysiologie zusammenhängen, sind als lysosomale Speicherkrankheiten (LSDs) bekannt. Die Mukolipidose Typ IV (MLIV), eine autosomal rezessive LSD, entsteht durch Mutationen im Gen, das TRPML1 (*MCOLN1*) kodiert. Typischerweise äußert sich die MLIV im Kindesalter mit neurodegenerativen Symptomen, begleitet von Seh- und motorischen Beeinträchtigungen[6, 7]. Bei MLIV-Patienten kommt es häufig zu einer Ansammlung von Lipidprodukten und erhöhten Ablagerungen, wie z.B. von p62/Sequestosome 1 (SQSTM1), innerhalb intrazellulärer Organellen.

In Scotto Rosato et al., 2022, hatten wir das Ziel, die LSD-Phänotypen durch Aktivierung von TPC2 mit dem selektiven Agonisten TPC2-A1-P zu korrigieren. Dazu nutzten wir verschiedene Modelle, darunter aus induzierten pluripotenten Stammzellen (iPSCs) abgeleitete Neuronen, Patienten-Fibroblasten und in vivo MLIV-Mäuse. Die Stimulation von MLIV-Zellen mit TPC2-A1-P reduzierte die Anreicherung von Lipiden und Cholesterin, kehrte die Autophagie-Blockade um und stellte die zelluläre Ultrastruktur wieder her. In vivo zeigten MLIV-Mäuse, die mit TPC2-A1-P behandelt wurden, eine Verminderung der Defekte im zentralen Nervensystem und eine verbesserte motorische Leistung im Vergleich zu den mit DMSO-Kontrolle behandelten MLIV-Mäusen[21].

Neben den LSDs wurde in einer Studie eine interessante Verbindung zwischen TRPML1 und dem „triple-negativen Brustkrebs“ (TNBC) aufgedeckt[22]. TNBC ist bekannt für seine aggressive Natur und ist durch das Fehlen der Estrogenrezeptoren (ER), Progesteronrezeptoren (PR) und der Amplifikation des humanen epidermalen Wachstumsfaktorrezeptors 2 (HER2) gekennzeichnet[10]. TRPML1 zeigte eine erhöhte Expression in TNBCs, und sein Ausschalten hemmte das Wachstum dieser Krebszellen durch die Regulation der Aktivität des mTORC1-Komplexes[9]. Aus diesem Grund erweiterten wir unsere Arbeit, um die Rolle von TRPML1 im TNBC zu untersuchen. In Rühl et al., 2021, entwickelten wir erfolgreich den ersten isoformselektiven und potenten Antagonisten für TRPML1, das Steroid 17β-Estradiolmethylether (EDME). Um seinen Wirkungsmechanismus zu entschlüsseln, behandelten wir die MDA-MB-231 TNBC-Zelllinie mit EDME und erzeugten einen CRISPR/Cas9 TRPML1-Knockout (KO) innerhalb derselben Zelllinie. Die Ergebnisse waren überzeugend und zeigten, dass sowohl der TRPML1-KO als auch die EDME-Behandlung die

Zellmigration und -invasion im Vergleich zur Kontrolle reduzierten. Die TRPML1-KO-Zelllinie lieferte weitere Beweise für die gezielten Effekte von EDME[11]. Diese Ergebnisse bieten wertvolle Einblicke in das Potenzial einer vorübergehenden Hemmung von TRPML1 zur Unterdrückung der aggressiven TNBC-Migration und des Wachstums.

Trotz wesentlicher Ähnlichkeiten besitzen TRPML1 und TPC2 auch unterschiedliche Eigenschaften. Beachtenswert ist, dass TPC2 auch durch den Ca^{2+}-mobilisierenden Second Messenger Nicotinsäure Adenin-Dinukleotid-Phosphat (NAADP) aktiviert werden kann, wodurch die Ionenselektivität von TPC2 zu einem stark umstrittenen Thema wird. Eine frühere Studie in unserem Labor zeigte die agonistabhängige Aktivierung von TPC2 mittels kleiner Molekül-Aktivatoren, TPC2-A1-P (verwendet in Scotto Rosato et al., 2022), welches die $PI(3,5)P_2$-Aktivierung imitieren, und TPC2-A1-N, welches die NAADP-Aktivierung nachahmen[12]. Angesichts des agonistvermittelten Wechsels von TPC2 zwischen nichtselektivem, selektivem Ca^{2+} und selektivem Na^+ Zustand untersuchten wir die gleichzeitige Anwendung dieser Verbindungen auf das Verhalten von TPC2 in Yuan et al., 2022. Um dieses Ziel zu erforschen, testeten wir die Kombination von TPC2-A1-P und TPC2-A1-N mittels Ca^{2+}-Imaging unter Verwendung des genetisch codierten Ca^{2+}-Indikators GCaMP6s und elektrophysiologischen Patch-Clamp-Messungen. Unsere vorläufigen Untersuchungen zielten darauf ab, verschiedene Zelllinien auf die Expression von TPC2 zu testen (Daten veröffentlicht in Abrahamian et al., 2021, Anhang). Die Melanomzelllinie SK-MEL-5 zeigte eine hohe Expression von TPC2, jedoch nicht der TPC1-Isoform auf Transkriptebene, und wurde für weitere Untersuchungen ausgewählt. Tatsächlich zeigten die Wildtyp (WT)-SK-MEL-5-Zellen robuste Ca^{2+}-Reaktionen, die doppelt so hoch waren wie die in Hela-Zellen beobachteten. Ein TPC2-Knockout wurde in dieser Linie erstellt, um ihn als Kontrolle für verschiedene Experimente zu verwenden, und wie erwartet zeigten TPC2-defiziente SK-MEL-5-Zellen signifikant reduzierte Ca^{2+}-induzierte Reaktionen. Die gleichzeitige Aktivierung von TPC2 durch TPC2-A1-P und TPC2-A1-N führte zu einer erhöhten Ca^{2+}-Permeabilität und zu einem erhöhten Ca^{2+}-Fluss; jedoch blieb der Na^+-Fluss unverändert[13]. Unsere Studie bietet einen neuen Einblick in die komplexe Interaktion von TPC2 mit seinen Liganden und zeigt seine Präferenz für die Steigerung der Ca^{2+}-Permeabilität im Vergleich zu Na^+ als Reaktion auf Signalgebung. Dieses vielseitige Verhalten hat tiefgreifende Auswirkungen auf die zelluläre Funktion und Physiologie, insbesondere bei der gezielten Bekämpfung von TPC2 in Krankheitsmodellen.

Im pathologischen Kontext erweiterten wir unsere Genexpressionsanalyse der endolysosomalen Kationenkanäle und Rab-Proteine über verschiedene Krebstypen hinweg. Bemerkenswerterweise beobachteten wir die höchste Expression im Falle von MCOLN1, TPCN2 und RAB7A im Vergleich zu anderen getesteten lysosomalen Genen, darunter MCOLN2, MCOLN3, TPCN1 und RAB7B. Interessanterweise zeigten diese Gene die signifikanteste Anreicherung in Melanom-Zelllinien und einer Hepatokarzinom-Zelllinie, die unter anderem andere Krebstypen wie Zervixadenokarzinom, Ovarialkrebs, Dickdarmadenokarzinom, Lungenadenokarzinom und Pankreasgangadenokarzinom übertrafen. Folglich war das Melanom, ein hoch aggressiver und von Melanozyten abstammender Hautkrebstyp, unser Hauptuntersuchungsziel. Identifizierte Risikofaktoren für Melanome umfassen übermäßige UV-Strahlenexposition, familiäre Vorgeschichte, und helle Haar-, Haut- und Augenfarbe[14]. Insbesondere konzentrierten wir uns darauf, die Rolle von TPC2 in Melanomen zu erforschen, da es in Melanomen stark exprimiert wird und sich in reifen Melanosomen befindet und eine wichtige Rolle bei der Pigmentierung spielt[15]. „Gain-of-Function“ (GoF)-Mutationen (G734E und M484L) in menschlichem TPC2 wurden mit reduzierter Melaninproduktion und blondem Haar in Verbindung gebracht[23]. In Übereinstimmung mit dieser Erkenntnis konzentrierte sich unsere Studie

auf pigmentierte *in-vitro*-Melanomzelllinien, MNT-1 (human) und B16F10 (Maus). Bemerkenswerterweise führte die genetische Ablation von TPC2 in MNT-1 Zellen zu einem erhöhten Melaningehalt und zu einem größeren, aber weniger sauren Melanosomenlumen. Dementsprechend wollten wir die physiologische Bedeutung von TPC2 bei der Regulierung von Melanom-Phänotypen in diesen pigmentierten Linien aufklären. Unsere Experimente konzentrierten sich darauf, die Auswirkungen von TPC2 auf das Verhalten von Melanomzellen zu bewerten und zeigten signifikant verringerte Zellproliferation, Migration und Invasion in den TPC2-defizienten MNT-1-Zellen im Vergleich zu ihren Wildtyp-Gegenstücken. Darüber hinaus untersuchten wir die durch die endolysosomale Maschinerie beeinflussten nachgeschalteten Signalwege. Bemerkenswerterweise war das Melanom-Onkogen MITF auf Proteinebene in den TPC2 KO MNT-1-Zellen signifikant reduziert im Vergleich zu den WT-Zellen. Weitere Analysen mittels „Proteinstabilitäts-Cycloheximid-Chase-Experimenten“ zeigten, dass diese Herunterregulierung auf den proteasomalen Abbau von MITF zurückzuführen war. Zur Bestätigung dieser Beobachtung behandelten wir die TPC2-defizienten Zellen mit dem proteasomalen Inhibitor MG-132, der die MITF-Expression auf ein ähnliches Niveau wie bei Wildtypzellen wiederherstellte. Darüber hinaus untersuchten wir die Signalwege, die MITF und das Wachstum von Melanomen regulieren,einschließlich der MAPK-, cAMP-, kanonischen Wnt- und Akt-Signalwege. Unser Ergebnis zeigte eine umgekehrte Zunahme der GSK3β-Spiegel in TPC2 KO MNT-1-Zellen im Vergleich zu WT und bestätigte damit die Rolle von GSK3β in Melanomen als negativer Regulator von MITF, der seinen proteasomalen Abbau fördert[17]. Interessanterweise enthüllte eine proteomische Analyse des TPC2-Interaktoms Rab7 als Interaktionspartner von TPC2[18]. Rab7a, eine kleine Guanosin-Triphosphatase (GTPase), fungiert als lysosomaler Marker und spielt eine entscheidende Rolle beim Transport und Abbau von Molekülen, der Fusion von späten Endosomen und Autophagosomen sowie der lysosomalen Biogenese[19]. Dennoch bleibt der funktionelle Einfluss von Rab7a auf die Aktivität von TPC2 und die daraus resultierende pathophysiologische Bedeutung dieser Interaktion unklar. In unserer Studie (Abrahamian et al., 2023, Anhang) haben wir zunächst die Co-Immunpräzipitationsdaten von Lin-Moshier et al., 2014 reproduziert und Fluoreszenz-Resonanz-Energie-Transfer-Experimente (FRET) durchgeführt, um die physische Interaktion zwischen Rab7a und TPC2 zu bestätigen. Darüber hinaus haben wir endolysosomale Patch-Clamp- und Ca^{2+}-Bildgebungstechniken verwendet, um zu zeigen, dass Rab7a die Aktivität von TPC2 stark verstärkt und somit die funktionelle Interaktion zwischen diesen beiden lysosomalen Proteinen etabliert. Um die potenziellen Auswirkungen auf Melanome zu untersuchen, haben wir verschiedene Knockout-Modelle mit CRISPR/Cas9 generiert, selektive kleine Molekülantagonisten und -agonisten verwendet sowie siRNA-Knockdown- (KD) und Überexpressionsstudien (OE) in einer Reihe von Melanomzelllinien mit unterschiedlichen Mutationshintergründen durchgeführt. Interessanterweise haben wir in den meisten MITF-abhängigen Melanomzelllinien eine signifikant verringerte Zellproliferation, Migration und Invasion beobachtet, wenn Rab7a oder TPC2 ausgeschaltet oder herunterreguliert wurden. Die meisten MITF-unabhängigen Linien zeigten jedoch keine Veränderungen im Melanom-Phänotyp nach der Depletion von Rab7a oder TPC2. Darüber hinaus haben wir eine positive Korrelation zwischen den Transkriptniveaus von Rab7a und TPC2 in diesen Melanomzelllinien sowie eine positive Korrelation zwischen der Proteinexpression von Rab7a mit MITF und GSK3β festgestellt. Konsistent mit den Daten aus der MITF-abhängigen, pigmentierten MNT-1-Linie verringerte der Verlust oder die pharmakologische Hemmung von Rab7a oder TPC2 die Expression von MITF und β-Catenin, während die Expression von GSK3β erhöht war. Diese Ergebnisse unterstützen das vorgeschlagene Modell der Verbindung zwischen dem Wnt/β-Catenin-Signalweg, MITF und der endolysosomalen Maschinerie in Melanomen[20]. Zudem führten wir

verschiedene Rettungsexperimente in den Rab7a- und TPC2-Knockout-Linien durch. Unsere Ergebnisse zeigten, dass die Überexpression von Rab7a nur teilweise den Phänotyp von TPC2 KO verbesserte, während die Überexpression von TPC2 den Phänotyp von Rab7a KO effektiv rettete. Basierend auf diesen Erkenntnissen haben wir Rab7a als Melanom-Onkogen und Effektor von TPC2 identifiziert und ihre potenzielle Bedeutung als Ziel für therapeutische Eingriffe in Melanomen hervorgehoben.

Insgesamt tragen unsere Ergebnisse dazu bei, unser Verständnis für das therapeutische Potenzial und das Zusammenspiel von lysosomalen Proteinen im Zusammenhang mit neurodegenerativen Erkrankungen und Krebs zu verbessern, wobei ein besonderer Schwerpunkt auf Brustkrebs und Melanom liegt. Durch verschiedene Untersuchungen haben wir gezeigt, dass Mutationen, Veränderungen in der Expression oder eine gestörte Aktivität von TRPML1 oder TPC2 schädliche Auswirkungen auf zelluläre Funktionen und damit verbundene Signalwege haben können. Daher kann die Untersuchung von endolysosomalen Kationenkanälen und Proteinen und die Entwicklung neuer selektiver kleiner Molekülagonisten und -antagonisten, die auf diese Kanäle abzielen, wertvolle Einblicke in den molekularen Mechanismus der Krankheitsheterogenität bieten, die Variationen in der Krankheitsmanifestation beleuchten und neue Möglichkeiten für die Wiederverwendung von Medikamenten aufdecken.

Introduction

1. The Endolysosomal System:

The endolysosomal system represents a sophisticated network of membrane-bound and highly dynamic intracellular compartments within eukaryotic cells. It is classified into early endosomes (EEs), recycling endosomes (REs), late endosomes (LEs)/multivesicular bodies (MVBs), and lysosomes (LYs). These organelles and vesicles orchestrate the trafficking of proteins and lipids, meticulous sorting of cargoes, taking up extracellular material from cells via endocytosis, neutralizing pathogens through phagocytosis, promoting proteostasis and homeostasis through autophagy and as well as degradation of damaged organelles and molecules, controlling metabolism, and ultimately functioning as intracellular signaling hubs[24-26]. Each endosomal compartment fulfills convoluted roles within cells by virtue of their distinguished morphology, composition, pH, resident ion channels, and molecular signature by marker proteins (i.e., Rab GTPase, CD molecules, LAMP, and LIMP proteins) (**Fig. 1**)[27, 28].

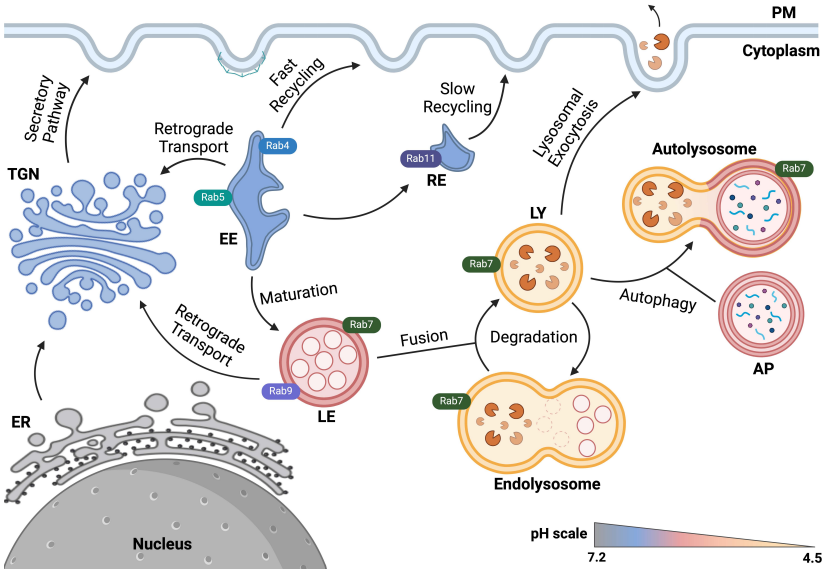

Figure 1. The Endolysosomal System. A schematic representation of the endolysosomal system illustrating the maturation from EEs to LEs to endolysosomes and LYs. The color gradient depicts the progressive drop in pH, transitioning from grey (neutral) to yellow (acidic). The diagram highlights various trafficking routes, including retrograde transport, secretory pathway, fast and slow recycling, as well as essential processes such as degradation, lysosomal exocytosis, and autophagy. Each organelle is marked by its corresponding Rab GTPase.

1.1. Endosomes:

EEs serve as the initial entry points and primary sorting stations for internalized endocytic cargos. These tubulovesicular compartments harbor a slightly acidic intraluminal pH of ~6.2 and are marked by Rab5. Rab proteins are a superfamily of small GTPases that act as molecular determinants and coordinators of endolysosomal organelles[29]; they are described in more detail later. EEs sort incoming cargoes and determine their itineraries to be either degraded via transport to LEs/LYs or recycled back directly or indirectly to the plasma membrane (PM). Thus, EEs are aptly described as sorting endosomes[30, 31]. As the name implies, REs are organelles with a luminal pH of ~6.2[32, 33] that regulate the intracellular endocytic recycling pathway, which is essential for the reuse of molecules, maintenance of receptors on the cell surface[34], and remodeling constituents of the PM[35]. The regulation of rapid and direct recycling is controlled by Rab4, while slow and indirect recycling is dependent on Rab11[34, 36] through the regulation of the Cysteine 12 residue of the G-protein inhibitor, RGS4[37]. This culminates in an extensive and highly dynamic tubulation of the REs visible using live cell imaging[34]. Moving along the endocytic pathway, maturation from EEs to LEs necessitates morphological changes, the loss of EE-associated Rab5, and the gain of Rab7. LEs originate from the early endosomal vacuolar domains[38] and are pre-lysosomal endocytic compartments[39] with an

acidic luminal pH of ~5.0–6.0[33]. LEs are spherically shaped, encompassing closely packed intraluminal vesicles lacking tubules, and are interchangeably referred to as multivesicular bodies (MVBs). LEs are predominantly located in juxtanuclear regions and tend to accumulate near the microtubule organizing center[39]. They regulate incoming cargo from the endocytic and autophagic pathways and outgoing cargo to the lysosome, trans-Golgi network (TGN), and PM[38]. The degradative route concludes with the movement of LEs to the perinuclear region, accompanied by acidification, changes in morphology, and alterations in the concentration of ions in the lumen (i.e., Ca^{2+}, K^{+}, Cl^{-}, Na^{+})[26]. This enables the fusion of LEs with each other and with LYs either through the transient kiss-and-run pathway or direct fusions, which are events that can be applied to several biological processes, including intracellular trafficking and synaptic transmission[40, 41]. Alternatively, cargo molecules can be transported to the TGN from EEs, REs, or LEs, steering towards secretory pathways and away from the degradative fate in lysosomes (**Fig. 1**). Retrograde trafficking from endosomes to the TGN is a house-keeping process that relies on the coordinated action of SNARE complexes, clathrin, Rab GTPases, and tethering trafficking from LEs to the TGN, whereas Rab22a and PIKfyve coordinate transport from EEs to the TGN[42, 43].

1.2. Lysosomes:

Through the action of the ATP-driven proton pump, vacuolar-type H^{+}-ATPase (V-ATPase), protons are transported across the lysosomal membrane, creating an acidic environment suitable for proteolysis and digestion of components within the lysosome lumen[44, 45]. Lysosomes are acidic (pH~4.5-5.0) membrane-enclosed organelles found in nearly all types of eukaryotic cells, with the exception of erythrocytes[46]. These organelles were initially discovered by Christian de Duve and colleagues in 1955[47], for which they were awarded the Nobel Prize in Physiology and Medicine in 1974[48]. LYs are categorized into endolysosomes and classical dense lysosomes (**Fig. 1**). Endolysosomes are hybrid organelles formed as a result of the fusion between LEs and LYs. In endolysosomes, macromolecules and other proteins are actively degraded; however, these organelles are transient and mature into classical dense lysosomes. In contrast, classical dense LYs are more stable and are responsible for storing and recycling cellular components[38, 49]. The abundance (50-3000 per cell), size (0.1-1 µM), distribution, and position of lysosomes can vary depending on the cell type[50], metabolic state and nutrient availability[45], accumulation of non-degraded material[51], and in response to extracellular and intracellular stimuli[52]. These parameters are suggestive of cellular physiology and pathophysiology[53]. Two classes of proteins are crucial for lysosomal function: integral membrane proteins and soluble acid hydrolases[54], around 25 and 60 of which have been found so far in the mammalian LY, respectively[55]. The hydrolytic enzymes present in LYs, e.g., proteases, phosphatases, lipases, sulphatases, nucleases, peptidases, and glycosidases, enable the degradation of macromolecules such as proteins, carbohydrates, lipids, and nucleic acids, thus accrediting lysosomes as the chief

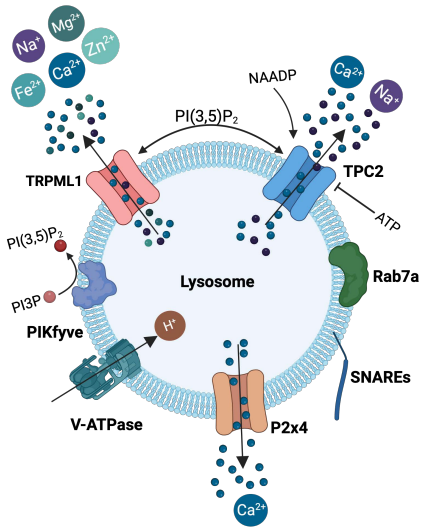

Figure 2. The Lysosome. An illustration of the lysosome showcasing various components and their functions. The depiction includes ion channels with their ion permeabilities, e.g., TRPML1 and TPC2, P2X4 receptor, also Rab7a and SNARE proteins, and the V-ATPase. Additionally, PIKfyve is shown to generate $PI(3,5)P_2$ from PI3P.

digestive system of the cell[51]. These enzymes are activated solely at the acidic pH within the LYs but inactivated at the neutral pH of the cytosol. This protects the cell from uncontrolled digestion of material within the cytoplasm, where lysosomal enzymes could be released, and the lysosomal membrane could be broken down[56]. Although LYs have been long regarded as "incinerators of cells"[57] or "suicide bags"[58], emerging evidence demonstrates that their role extends beyond their degradative capacity. LYs are involved in intracellular signal transduction, immunity, plasma membrane repair, gene regulation, apoptosis, energy metabolism, and maintenance of cellular homeostasis[57, 59, 60]. Consequently, lysosomal dysfunction is linked to a wide range of pathologies, notably lysosomal storage diseases (LSDs)[61, 62], neurodegenerative diseases[63, 64], lung disease[65], autoimmune and metabolic disorders[66, 67], and various types of cancer[4, 9, 11, 17, 68-70].

2. Ion Channels:

The lysosomal lumen contains abundant ions, including Ca^{2+}, Na^{+}, Fe^{2+}, Cl^{-}, Zn^{2+}, K^{+}, and H^{+}, each serving specialized physiological roles. The concentration of these ions is cell-type-specific: i.e., $[Ca^{2+}]_{LY}$=0.50 mM which is 5000-fold higher than the cytosolic concentration (~100 nM); $[Na^{+}]_{LY}$=2-140 mM and $[Na^{+}]_{cytosol}$=12 mM, constituting the most abundant ion within LYs; $[Cl^{-}]_{LY}$=80 mM and $[Cl^{-}]_{cytosol}$=15 mM; $[K^{+}]_{LY}$=2-50 mM and $[K^{+}]_{cytosol}$=150 mM, $[H^{+}]_{LY}$=0.025 mM and $[H^{+}]_{cytosol}$=12 mM, 500-fold higher than cytosolic H^{+}[45, 71, 72]. The influx of these ions across the lysosomal membrane is controlled by a distinct group of transporters and ion channels. At least one or multiple ion channels govern the movement of each type of ion[73, 74]. Among the prominent endolysosomal ion channels are the transient receptor potential mucolipin channels (TRPMLs) and two-pore channels (TPCs). These cation channels are paramount for the primary function of LYs and the maintenance of ion homeostasis. Consequently, in the past decade, they have emerged as potential drug targets for a plethora of diseases[3, 75] (**Fig. 2**).

2.1. Mucolipins:

TRP channels are a superfamily of non-selective cation channels, classified into six subfamilies in mammals: TRPML (mucolipin), TRPM (melastatin), TRPC (canonical), TRPP (polycystin), TRPA (ankyrin), and TRPV (vanilloid)[76]. In 2021, the Nobel Prize in Physiology or Medicine was awarded to Patapoutian and Julius in recognition of their significant contributions to the TRP channel field, particularly for their work on TRPV1 and molecular basis of proprioception, touch, and temperature sensing in the nervous system[77]. In mammals, three evolutionarily conserved isoforms are found for mucolipins: TRPML1, 2, and 3, encoded by *MCOLN1*, *2*, and *3* genes, respectively. These isoforms exhibit around 75% of amino acid sequence similarity[78] and comprise six transmembrane domains with cytoplasmic carboxy (C)- and amino (N)-terminal tails. The domains 5 and 6 form the pore-region[78-80], and the selectivity of mucolipins for cations is attributed to the aspartate and glutamate residues found within this region[81] (**Fig. 3.A.**). Although TRPMLs differ in tissue distribution, localization within the endolysosomal system, and function[82], all members are regulated by luminal pH and activated by binding to $PI(3,5)P_2$, a phosphoinositide specific to endolysosomes[83]. This dissertation focuses on the human TRPML1 isoform.

2.1.1. TRPML1:

TRPML1, the founding and most characterized member of the mucolipin family, predominantly localizes to LEs and LYs[78]. It is ubiquitously expressed across mammalian cells and mediates lysosomal Ca^{2+} release into the cytosol[84]. TRPML1-mediated Ca^{2+} release is paramount for the proper function of these organelles and execution of an array of membrane trafficking pathways, i.e., signal transduction, regulation of fission and fusion events, autophagy, lysosomal formation and

exocytosis[85]. Given its critical cellular functions, numerous regulatory mechanisms are in place to tightly control the activity of TRPML1 in subcellular compartments. For instance, during lysosomal exocytosis, TRPML1 exhibits low activity on the plasma membrane while demonstrating high activity within LYs. Its activity is dually regulated by Ca^{2+} and pH, as evidenced by the investigation of the TRPML1 V432P gain-of-function (GoF) mutation, which keeps the channel constitutively open[86]. The kinase PIKFyve phosphorylates phosphatidylinositol 3-phosphate (PI3P) to $PI(3,5)P_2$, the latter activating TRPML1. In addition, TRPML1 can be activated by increased levels of endogenous mitochondrial reactive oxygen species or exogenous oxidants, inducing Ca^{2+} release from lysosomes[87]. In contrast, its activity is inhibited by mTORC1, sphingomyelins, and $PI(4,5)P_2$[88]. Moreover, various synthetic small-molecule agonists and antagonists for TRPML1 have been developed and validated using techniques such as Ca^{2+} imaging and endolysosomal patch clamp. These compounds exhibit varying selectivity for mucolipins. Examples of TRPML1 agonists include MLSA1, MLSA5[89], MK6-83[90], and ML1-SA1(EVP-169)[65]; and inhibitors: ML-SI1, ML-SI3[65, 91], EDME, Pru-10, and Pru-12[11].

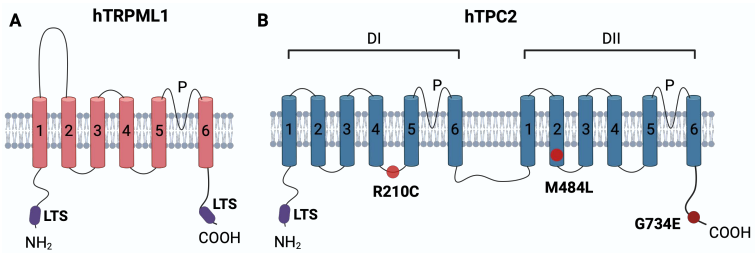

Figure 3. Simplified Structures of TRPML1 and TPC2. The lysosomal-targeting sequence (LTS) is marked in purple. **A**. hTRPML1 consists of 6 transmembrane domains and the pore region is formed between domains 5 and 6. **B**. hTPC2 has two repeating domains, DI and DII, each comprising 6 transmembrane domains. Like TRPML1, TPC2 has a pore region between domains 5 and 6. Mutations in TPC2 that are associated with pigmentation defects are illustrated in shades of red.

2.1.2. TRPML1-mediated Autophagy and Lysosomal Exocytosis:

Autophagy is a ubiquitous catabolic machinery present in all eukaryotes[92] and is dependent on the endolysosomal system[93]. It is involved in recycling cytoplasmic content (i.e., dysfunctional or damaged organelles, protein aggregates, and intracellular pathogens) and maintaining genomic stability and cellular homeostasis[94]. This process is initiated by the de novo formation of double-membrane vacuoles, termed autophagosomes (APs), which sequester organelles and macromolecules to be degraded. These APs subsequently fuse with lysosomes, forming autolysosomes, where the cellular content is degraded and can be reused by the cell for biosynthesis and energy metabolism[95] (**Fig. 1**). Autophagy acts as a tumor suppressor protective machinery during the early stages of tumor initiation by eliminating damaged proteins. In contrast to advanced stages of cancer progression, autophagy acts as a pro-metastatic mechanism, supporting the survival and growth of cancer cells[96, 97]. TRPML1 has been established as a core player in signaling events regulating autophagy. Under cellular nutrient-rich conditions, mTORC1 phosphorylates TFEB on the lysosomal surface at serine residues S142 and S211. This phosphorylation leads to the sequestration and inactivation of TFEB in the cytoplasm via its interaction with 14-3-3 proteins. Conversely, during physical exercise and starvation, TRPML1 releases Ca^{2+} from LYs, which activates calcineurin. Calcineurin then binds and de-phosphorylates TFEB, allowing its nuclear translocation. Simultaneously, mTORC1 activity is suppressed under these conditions. Therefore, TRPML1-mediated Ca^{2+} release results in both the de-phosphorylation of TFEB via calcineurin activation and reduced levels of TFEB phosphorylation via mTORC1 suppression. As a result, TRPML1 is involved in modulating sustained autophagy, particularly during prolonged starvation conditions through TFEB activation[98]. Mutations in the *MCOLN1* in humans are directly accountable for the autosomal lysosomal storage disorder, Mucolipidosis type IV (MLIV)[90]. In the MLIV patient fibroblasts, the blockade of the autophagic mechanism is responsible for the proteinopathy due to

impaired fusion between APs and LYs and abnormal accumulation of autophagosomes, P62/SQSTM1 aggregates, ubiquitin proteins, and other waste products. Beyond autophagy pathway regulation, both TRPML1 and TRPML3 are involved in modulating lysosomal exocytosis[7], a Ca^{2+}-regulated process in which LYs fuse with the PM, releasing their content into the extracellular space. This program is essential for PM repair, secretion of inflammatory cytokines, and cellular clearance[99]. The increase in intracellular [Ca^{2+}] is a key driver of lysosomal exocytosis, as demonstrated in studies using Xenopus oocytes[100]. While the constitutively active form of TRPML1 has been shown to undergo uncontrolled lysosomal exocytosis[101], significantly reduced lysosomal exocytosis has been observed in MLIV patient cells[100].

2.2. Two-Pore Channels:

Two-pore channels (TPCs) are non-selective cation channels belonging to the voltage-gated ion channel (VGIC) superfamily. The animal TPC subfamily comprises three isoforms: TPC1, TPC2, and TPC3. In mice and humans, only TPC1 and TPC2 are found, encoded by *TPCN1* and *TPCN2* genes, respectively[102]. These channels are named after their unique structure, which consists of two repeating shaker-like domains (DI and DII), each comprising six transmembrane segments (6-TMI and 6-TMII) that form six membrane-spanning regions (S1-S6). The transmembrane domains of each subunit are connected by a cytoplasmic linker, forming an ion-conducing pore between S5-S6[103] (**Fig. 3.B.**). TPCs exhibit high sequence similarities in the filter region[104] (i.e., 27% in mice)[105] and share common interaction partners (i.e., 35.8% of identified proteins)[106]. Both TPC1 and TPC2 are inhibited by ATP via mTOR and activated by the second messenger NAADP and the phosphoinositide $PI(3,5)P_2$. However, these isoforms differ significantly in their ion selectivity, localization, function, and activation mode. TPC1 is activated through a voltage-dependent mechanism, inhibited by luminal Ca^{2+} and phosphorylation, and predominantly localizes to EEs and REs. In contrast, TPC2 is activated in a voltage-independent manner, regulated by cytosolic and lysosomal Mg^{2+}, and primarily found in LEs and LYs[12, 107, 108]. Similar to TRPML1, many small-molecule agonists and antagonists with varying toxicities and selectivity for TPC2 were synthesized. Notably, the agonists TPC2-A1-P and TPC2-A1-N[12] and antagonists Naringenin[109], Ned-19[110], SG005, SG094[111], MT-8, and UM-9[17]. This dissertation centers on the human TPC2 isoform.

2.2.1. TPC2 and Pigmentation:

Two-pore channel 2 is a cation channel permeable to Na^+ and Ca^{2+} ions and is ubiquitously expressed in LYs, LEs, melanocytes, and melanosome-limiting membranes (**Fig. 2 and 4**). Melanosomes are specialized lysosomal-related intracellular organelles found in melanocytes, responsible for the synthesis and deposition of melanin pigments, which determine the pigmentation of mammalian skin and hair[112, 113]. Dysregulation in the process of melanogenesis underlies visual defects and pigmentation-related disorders (i.e., Charcot-Marie-Tooth disease type 4J, albinism, Tietz syndrome, neurofibromatosis type 1, Cantu syndrome, different types of Xeroderma Pigmentosum) and multiple types of cancer, prominently melanoma and intraocular melanoma[114]. Over the past decade, accumulating evidence deciphered the pivotal role of TPC2 in regulating hair and skin pigmentation. A genome-wide association study in 2008 on Icelandic and Dutch populations identified single nucleotide polymorphisms (SNPs) associated with human pigmentation. The identified polymorphic variants were rs3829241 and rs35264875, corresponding to G734E and M484L mutations in *TPCN2*, respectively. These two mutations in TPC2 were linked to the shift in hair color from brown to blond in individuals[115]. Subsequent functional characterization using endolysosomal patch clamp recordings in overexpressed HEK cells confirmed that both G734E and M484L variants were GoF mutations of TPC2. However, these mutations play different functional

roles due to their distinct locations within the TPC2 protein (i.e., G734E in the C-terminus and M484L in TMII of DII). Further phenotypic and genotyping analyses were performed using fibroblasts isolated from 120 individuals of the German population, either wild-type (WT) or carriers of these mutations. The results corroborated the earlier study, with approximately 80% of WT donors having brown color and around 72% of blond-haired test subjects being homozygous E (position 734) and homozygous L (position 484)[16, 116]. In 2023, a de novo mutation, R210C, in *TPNC2* was identified in a 7-year-old individual presenting with hair and skin hypopigmentation. Likewise, this R210C mutation was characterized as a GoF mutation of TPC2 using electrophysiology patch clamp and in vivo mice studies[117] (**Fig 3.B**.). Mechanistically, TPC2 modulates pigmentation by regulating melanosome size and pH[113], increasing acidity and melanosome membrane potential[118], hence, contributing to the decreased activity of the enzyme tyrosinase (TYR).

2.2.2. Ion Selectivity of TPC2:

Activating ligands and ion selectivity of TPCs have been a debatable topic for over a decade. Initial studies reported that mammalian TPC2 is activated by NAADP, a water-soluble calcium-mobilizing second messenger, releasing Ca^{2+} from LYs. However, other groups challenged this view and proposed that TPCs, similar to TRPMLs, are directly activated by the endogenous $PI(3,5)P_2$, mainly localized to LYs and endosomes. NAADP was found to elicit Ca^{2+} release, whereas activated $PI(3,5)P_2$ predominantly evokes Na^+ release[13, 119]. For instance, Wang et al., 2012 performed endolysosomal patch-clamp experiments and could not record NAADP-mediated currents, even at high concentrations [1 µM], thus limiting the scope of TPC2 activation by $PI(3,5)P_2$[120]. However, it is worth noting that the isolation of enlarged lysosomes necessary for these measurements may arguably result in the loss of vital accessory proteins, such as NAADP binding proteins (NAADP-BP)[12, 18], which could impact the observed results. In 2021, independent research groups identified NAADP-BPs that activate TPCs, i.e., JPT2/HN1L and Lsm12. JPT2/HN1L specifically activates Ryanodine receptor 1 and TPC1, while Lsm12 acts as a receptor for NAADP and regulates both TPC1 and TPC2 activation[121-123]. It seems that research is still in the infancy of understanding TPC activation, particularly unfolding the molecular mechanism and physiological consequences for activating specific ion channels mediated by NAADP-BPs[124]. A finding by Gerndt et al., 2021 was a breakthrough in the field, as the first lipophilic isoform-selective agonists for TPC2 were developed, which helped reconcile the conflicting reports. These structurally unrelated small molecule activators, known as TPC2-A1-P and TPC2-A1-N, mirrored the endogenous stimuli of TPC2, $PI(3,5)P_2$ and NAADP, respectively. Activation of TPC2 by TPC2-A1-P favored Na^+ permeability over Ca^{2+}, promoting lysosomal exocytosis. While higher calcium permeability was observed using TPC2-A1-N, alkalinizing the lysosomal lumen and arresting vesicular motility[12]. In sum, the ion selectivity of TPC2 was shown to be agonist-dependent, mediating different ion fluxes with distinct physiological relevance.

3. Lysosome-associated Rab Proteins:

The Ras superfamily of GTPases encompasses over 150 monomeric proteins in humans, with sizes ranging from 20-30 kDa. This superfamily is subdivided into five structurally or functionally related families of proteins: Ras, Rab, Rho, Ran, and Arf[125, 126]. While Ras is the original member of the superfamily, Rab proteins constitute the largest branch[127, 128]. Rab GTPases are conserved from yeast to mammals, and their number differs across species[129, 130] In humans, at least sixty different Rab proteins have been identified[19, 131, 132]. Rabs, similar to other GTPases, act as binary molecular switches, shuttling between inactive GDP-bound and active GTP-bound states, localized to the cytosol and membrane, respectively[133, 134]. These proteins serve as organelle-specific markers that

regulate various steps of organelle maturation and transport along the endocytic pathway and confer functionality and identity to these compartments[132, 135]. By assuming their active state on membranes, specific downstream effector molecules are recruited to membrane sites, enabling their role as regulators of membrane trafficking, such as vesicle formation, budding and transport, cargo sorting, and membrane fusion[129, 132]. A “Rab Cascade” describes the fine collaboration between two Rab GTPases, where one GTP-bound Rab activates the succeeding Rab in the cascade by recruiting a specific Guanine nucleotide exchange factor (GEF). This leads to a loop of Rab conversions throughout the endolysosomal system[136-138]. An antagonistic Rab GAP (GTPase-activating protein) cascade model proposes that the activation of a Rab protein is possible through the inactivation of its precursor Rab, facilitated by recruiting GAP[136, 139]. During endosome maturation, e.g., Rab7 is recruited to LEs accompanied by the loss of Rab5 on EEs, a process known as Rab5-to-Rab7 switch[140-143].

3.1. Rab7:

Rab7, also known as Ypt7p in yeasts, is one of the most crucial and extensively investigated Rab proteins in humans. It is a ubiquitously expressed protein and a guardian of essentially every event occurring between EEs to LYs[144]. By the recruitment of effector proteins, Rab7 controls the maturation of endosomes, cargo sorting, fusion of LEs and LYs, vesicle trafficking from LEs to LYs, biogenesis of LYs and perinuclear lysosomal compartment, fusion of LYs and APs, followed by degradation of macromolecules sequestered in APs[135, 145, 146]. Furthermore, Rab7 is responsible for overseeing the speed and direction of endosomal transport with dynein and kinesin[147, 148], regulating actin dynamics in interaction with Rac1[149] and its newly identified effector Armus[150, 151], a Rab-GAP. It also directs the movement of LEs and APs along microtubules via its effector FYCO1[152]. In 2000, Pereira-Leal and Seabra comprehensively analyzed the mammalian Rab family, elucidating the primary structure and sequence conservation patterns. Their study highlighted the highly conserved RabSF regions and RabF motifs across different species. The authors categorized animal and fungi Rabs into “Rab functional groups” according to their shared ancestry, sequence identity, and localization. Notably, they highlighted that the two human Rab7 proteins, Rab7a and Rab7b, cannot be considered isoforms as they differ in the two motifs mentioned, and their sequence is limited to 50% similarity[127, 153]. Co-localization studies using confocal microscopy have revealed that Rab7a localizes predominantly to LEs and LYs, while Rab7b to LEs and the TGN. The discrepancy in localization implies divergent functional roles in endolysosomal trafficking, where Rab7a governs the transport from EEs to LEs and from LEs to LYs, while Rab7b from endosomes to the TGN[131, 146, 154, 155]. Dysfunctions of Rab7 are associated with a number of pathologies, mainly melanoma[156, 157], and the autosomal dominant neurodegenerative disease known as Charcot-Marie-Tooth type 2B (CMT2B)[158-160]. A pan GTPase inhibitor known as CID-1067700 has been shown to competitively block Rab7, and it has been used in both in vitro and in vivo experiments[161, 162]. This dissertation will be discussing Rab7a, henceforward interchangeably referred to as Rab7.

4. Endolysosomal System-associated Pathologies:

Precision medicine has been a paradigm shift for ameliorating diagnosis and tailoring treatment options for patients aiming to provide cost-effective therapies with maximized efficiency and minimized adverse effects[163, 164]. The quest for novel molecular targets facilitated by high-throughput screenings, proteomics, next-generation sequencing, bioinformatics, genomic, and cell biology tools witnessed considerable knowledge into the lysosomes and interconnection with disease dysregulations[8, 17, 165]. LYs regulate digestion and clearance of damaged organelles and macromolecules delivered via phagocytosis, endocytosis, and autophagy[166, 167]. The proper

functioning of LYs relies on endolysosomal ion channels that release lysosomal Ca^{2+}, while their refilling is controlled by the endoplasmic reticulum (ER)[80,168]. Mutations in TRP channels, TPCs, or alterations in Ca^{2+}-binding proteins are ascribed to dysregulated Ca^{2+} homeostasis and intracellular signaling, resulting in abnormal cell proliferation, death, and migration. Ultimately, LYs, along with their resident ion channels and proteins, govern cellular fate, metabolism, and behavior[169]. Mutations in these cation channels or aberrations of lysosomal function or structure have detrimental effects on cells and underlie a range of fatal channelopathies, particularly cancer and neurodegenerative disorders[80, 102, 169-172].

4.1. Melanoma:

Melanoma is the most lethal and least prevalent type of skin cancer, originating from the malignant transformation of melanocytes, the pigment cells derived from the neural crest. It can develop either de novo in healthy skin or near/in precursor lesions, such as dysplastic or acquired nevi, and is evaluated through the collection of a skin biopsy of the suspected area. However, melanoma is often misdiagnosed or remains undiagnosed until advanced stages. Patients diagnosed with metastatic stage IV have a five-year relative survival rate of 10%, compared to 97% at stage 0. The etiology of melanoma is attributed to factors such as high ultraviolet radiation (UVA and UVB) radiation exposure, socioeconomic status, genetics (mutations in *CDKN2A, NRAS, BRAF,* and *MITF*), as well as specific characteristics like skin, eye, and hair color. Pigmentation traits are considered photoprotective[173], i.e., individuals with blond or red hair, fair skin, and light eye color are at a significantly higher risk of developing melanoma[14, 112, 174]. The pigment melanin is produced by melanocytes within specialized organelles known as melanosomes. The regulation of the pigmentary system is reliant on various pigmentation genes, such as *TYR*, *MITF*, *MC1R*, *TYRP1*, *MC1R*, and *DCT*[175, 176], as well as pH, and ion homeostasis[177]. Melanosomes undergo segregation and maturation from endolysosomal vesicles. In melanocytes, stage I melanosomes are spherically shaped and correspond to the vacuolar domains of EEs, containing amyloid fibrils and the pigment cell-specific protein (PMEL). Melanosomes at stage II are elongated and physiologically distinct from endosomal organelles. During this stage, intraluminal fibril formation is completed, resulting in the formation of a melanosomal matrix. Stage III melanosomes are characterized by melanin production, which settles on the thickened and darkened fibrils. Melanin deposition is concluded in the final stage, IV, concealing internal structures[178-180]. Rab7 governs early and intermediate-stage melanosomes, while mature and active melanosomes are associated with Rab27a[180, 181]. Interestingly, gene set enrichment analysis of gene ontology gene sets, followed by functional and histological studies in distinct cancer types, revealed the highest enrichment of lysosomal and vacuolar gene sets in melanoma, exceeding the enrichment in pigmentation-relevant sets, with the false discovery rate (FDR)<$1.0x10^{-8}$ and FDR<$3.04x10^{-5}$, respectively[157, 182]. The lysosomal genes of interest for this dissertation: *RAB7A*, *MCOLN1*, and *TPCN2*, have all been proposed as vital players in regulating melanoma growth and invasion by several independent research groups[109, 157, 183, 184]. Possibly, the most obvious and prominent link between the endolysosomal machinery and melanoma involves the microphthalmia-associated transcription factor (MITF), a melanoma oncogene. By binding to the CLEAR element, MITF induces the transcription of autophagosomal and lysosomal genes in melanoma and melanocytes, independent of TFEB. Hence, this basic helix-loop-helix leucine zipper (bHLH-ZIP) transcription factor regulates melanocyte development and melanogenesis. The M-MITF isoform is the most predominant and is amplified in approximately 20% of metastatic melanomas[185-187]. Ploper et al., 2015 deciphered a positive feedback loop involving the activation of the canonical Wnt cascade and inhibiting the destruction complex, including the kinase

Glycogen Synthase Kinase 3 Beta (GSK3β). This leads to stabilizing β-catenin and MITF, accumulating in the nucleus and activating lysosomal genes. This was demonstrated in vitro in the C32 melanoma line, where the induction of MITF by tetracycline ultimately resulted in the expansion of MVBs/LEs, in turn significantly increasing the number of Rab7-positive vesicles and transcription of *MCOLN1* and other lysosomal genes. In contrast, Wnt pathway inactivation led to GSK3β-mediated phosphorylation of β-Catenin and MITF on multiple residues on its C-terminus (S409, S405, S401, and S397), destabilizing MITF and causing its proteasomal degradation[20, 112] (**Fig. 4**).

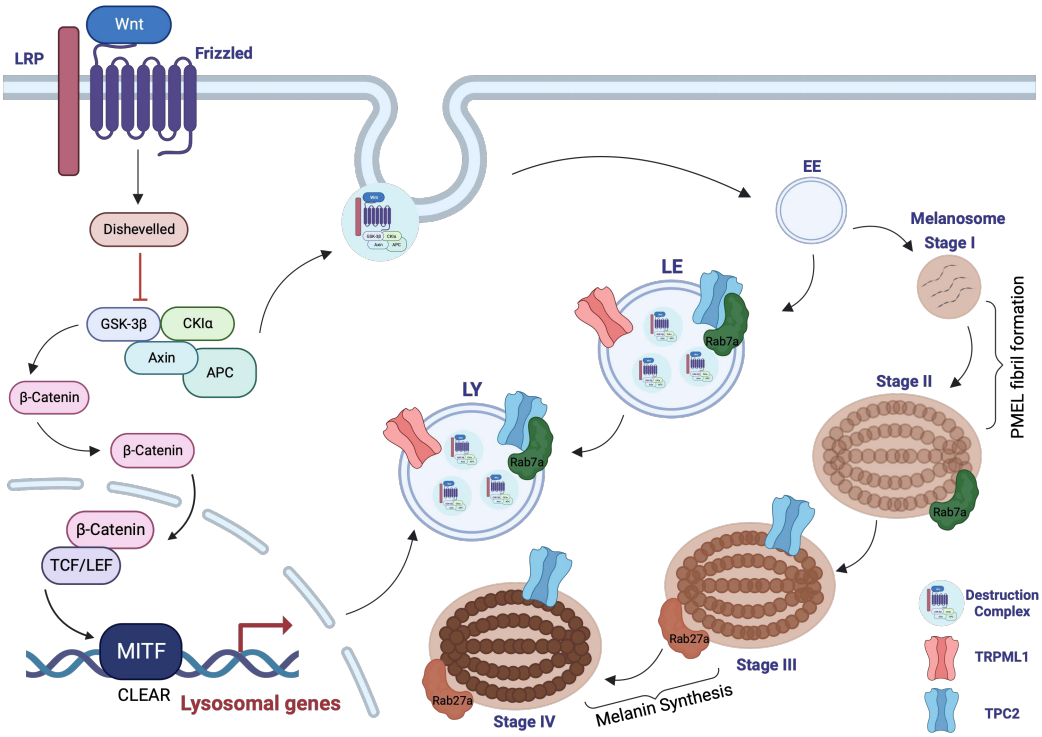

Figure 4. The Connection between the Endolysosomal System, Melanogenesis and Canonical Wnt Pathway in Melanoma. The left-hand side depicts the activation of the Wnt pathway in melanoma, where the destruction complex is inhibited and sequestered into the LEs/MVBs. This leads to the stabilization of the unphosphorylated β-Catenin and MITF, initiating a positive feedback loop. MITF induces LEs/MVBs, further sequestering the destruction complex. The transcriptional activity of MITF promotes the expression of pigmentation-related genes (i.e., *PMEL*, *TYRP1*, and *TYR*), ultimately activating melanogenesis. On the right-hand side, the four stages of melanosome formation and maturation are shown. The localization of TRPML1 (red), TPC2 (blue), Rab7a (green), and Rab27a (brown) is illustrated.

4.1.1. The Role of TRPML1, Rab7a, and TPC2 in Melanoma:

TRPML1 plays a contradicting role in melanoma. An initial report by Kasitinon et al., 2019 demonstrated that the loss of TRPML1 in melanoma displayed impaired proliferation and reduced melanoma tumor growth in vitro and in vivo, sparing normal melanocytes. The author revealed that metastatic melanoma cells lacking TRPML1 upregulated the MAPK pathway (ERK phosphorylation) and mTORC1 signaling, allowing them to overcome proteotoxic stress. The effects were rescued through the inhibition of mTORC1[183]. In contrast, a study by Du et al., 2021 demonstrated the upregulation of TRPML1 in the two melanoma cell lines, MeWo and M12, compared to an immortalized line of human melanocytes. The authors claimed that activating TRPML1 in these cell lines by agonists ML-SA8 or MLSA5 triggered cell death while suppressing TRPML1 via ML-SI4 or ML-SI3 had no significant effect. The observed cell death was proposed to be non-apoptotic, Zn^{2+}-dependent effects that are regulated by the mitochondria, investigated using zinc chelators such as 1,10-PT and TPEN[188]. Interestingly, Alonso-Curbelo et al., 2014 demonstrated the role of Rab7 GTPase in melanoma. The authors deemed Rab7a a melanoma oncogene, exhibiting the highest enrichment among tested lysosomal gene sets. Downregulation of Rab7a resulted in reduced cell

survival and proliferation, as confirmed through analysis using keratinocytes, fibroblasts, melanocytes, and other cancer types as control. Silencing of Rab7a in melanoma cells was accompanied by increased F-actin, stress fibers, scattering and decreased cell-cell contacts. Examination of the Rab7 promoter revealed that the oncogene MYC and the neural crest stem cell biomarker SOX10 act as upstream modulators for the transcription of Rab7a in melanoma cells. Nevertheless, it should be noted that neither of these inducers (MYC and SOX10) is reliant on endolysosomal trafficking pathways[157]. As for the functional TRPML1 relative, TPC2, studies have demonstrated that blocking TPC2 with Ned-19 or Naringenin leads to the inhibition of cancer cell viability and proliferation in the B16 cells, both in vitro and in vivo. Furthermore, there is evidence that TPC2 plays a role in VEGF-evoked angiogenesis, a critical process in tumor metastasis and vascularization[109, 189]. Given the explicit contribution of TPC2 to pigmentation, further investigations into its role in melanoma are imperative. Notably, all three identified GoF mutations ($TPC2^{M484L}$, $TPC2^{G734E}$, $TPC2^{R210C}$) have been associated with hypopigmentation phenotypes[16, 115, 116] (**Fig. 3.B.**). Moreover, the TPC2-depleted MNT-1 melanoma cell line has exhibited increased melanin generation, entailing the mechanistic role of TPC2 in modulating melanoma growth and predisposition[113].

4.2. Breast Cancer:

Breast cancer (BC) is the most frequent type of cancer and the leading cause of cancer-related deaths among women globally and in Germany[190, 191]. While BC in males is rare and accounts for less than 1% of all BC diagnoses worldwide, it is vital to consider sex differences when evaluating the toxicity and efficacy of chemotherapy[192, 193]. Notably, there has been a significant increase in the male-to-female ratio for incidence rates of both common and childhood cancers globally, despite the shorter life span in males[193]. BC development is primarily attributed to acquired genetic alterations and DNA damage caused by lifestyle risk factors, age, certain oral contraceptives (reversible effect), and menopausal hormone therapy[194]. Family history and inherited mutations in tumor suppressor genes such as *BRCA1* and *BRCA2* also elevate the risk of BC in male and female carriers[195]. The most common subtype of BC is invasive ductal cancer, accounting for up to 70% of BC diagnoses[194], while triple-negative breast cancer (TNBC) is the most aggressive form, found in approximately 20% of patients[9]. TNBC earns the designation for the lack of HER2 amplification, ER and PR expression[196], and it is associated with metastasis to the lung and brain, limited treatment options, and poor prognosis[197]. It has been illustrated that TRPML1 transcript levels were higher in three TNBC lines than in normal epithelial cells or another type of breast cancer line positive for all three receptors. In addition, silencing TRPML1 in TNBCs resulted in reduced viability and invasion in vitro and decreased tumor growth in vivo. The authors also demonstrated a downregulation of mTORC1 activity and lysosomal exocytosis of ATP in TRPML1-deficient TNBC cells[9]. Moreover, studies performed using the orthotopic BC line, 4T1, siRNA KD, or pharmacological inhibition of TPC2 using tetrandrine or Ned-19 reduced proliferation rates[198], decreased adhesive or migratory capacity in vitro[68], and diminished lung metastasis in vivo. In the TNBC MDA-MB-468 line, silencing of TPC2 led to reduced vimentin expression, a mesenchymal marker, while no effects were observed for the KD of the TPC1 isoform[199].

4.3. Neurodegenerative disorders and MLIV:

Lysosomes degrade extracellular material through phagocytosis and endocytosis and break down endogenous material through autophagy[45, 57]. In addition to their recycling functions, LYs are involved in immunoregulation, including antigen presentation on major histocompatibility complex molecules, the release of pro-inflammatory mediators, and activation of toll-like receptors[60, 200].

Consequently, mutations in lysosomal membrane proteins or enzymes that impair lysosomal function give rise to a group of rare metabolic disorders known as lysosomal storage diseases (LSDs). Currently, more than 70 LSDs have been identified, including Gaucher disease (most prevalent), Niemann-Pick disorders, Farby disease, Pompe disease, and mucolipidoses, with the likelihood of unveiling further related disorders in the future[201-203]. One specific LSD is mucolipidosis type IV (MLIV), an autosomal recessive neurodegenerative disorder caused by mutations in the *MCOLN1* gene located on chromosome 19p13[90, 204]. The first patient with MLIV was diagnosed 50 years ago[205], and to date, over 15 different mutations in *MCOLN1* have been described[206]. The most common mutation observed in patients is a splicing variation (transition from A→G) at the 3′ sites of intron 3[6, 207]. MLIV is typically diagnosed in infancy, and patients often present with motor delays, ophthalmic impairments due to retinal degradation and corneal opacification, and achlorhydria as a result of hampered secretion of gastric acid[206, 208, 209]. These mutations lead to defective endolysosomal trafficking, lysosomal exocytosis, and autophagy, resulting in the abnormal accumulation of phospholipids, mucopolysaccharides, carbohydrates, gangliosides, and heavy metals (e.g., Zn^{2+} and Fe^{2+}) in different cell types of MLIV patients[90, 206, 210, 211]. Unfortunately, treatment options for MLIV thus far are limited to symptomatic management of neurological, motor, or visual impairments[211, 212]. As MLIV is a life-limiting condition and patients have a shortened lifespan, no direct link has been found yet between MLIV and cancer predisposition[204, 212]. Interestingly, Parkinson's disease, another neurodegenerative disorder linked to the endolysosomal machinery (specifically to TPC2[102, 213] and Rab7[214]), shows positive correlations with melanoma. The higher risk of melanoma development in PD patients has been well-documented. This is attributed to systemic pigmentation and melanin metabolism, immunodeficiency, and shared genetic factors (e.g., *MC1R*, *PTEN*, *PRKN*, and *LRRK2*). This intriguing association between melanoma and PD raises questions about the potential underlying mechanism and the role of endolysosomal proteins in mediating common pathways[215, 216].

5. TRPML1 and TPC2: Converging and Diverging Functionalities and Interactions:

TRPML1 and TPC2 are endolysosomal cation channels predominantly found in late endosomes and lysosomes. TPC2 is additionally localized to melanosomal membranes. Both ion channels are activated by $PI(3,5)P_2$ and are permeable for Ca^{2+} and Na^{+}; however, TRPML1 is additionally permeable to Zn^{2+}, Fe^{2+}, K^{+}, and Mg^{2+}, which could confer distinct cellular features[188, 217, 218]. Moreover, electrophysiology patch-clamp recordings revealed that TRPML1 currents were ATP-insensitive[219]. In contrast, evident inhibition of TPC2 by ATP was demonstrated[220], further corroborated by diminished ATP sensitivity observed in the TPC2 GoF G734E mutation[16]. Contrary to the well-elucidated role of TRPML1 in autophagy, the precise involvement of TPC2 in the autophagic machinery is still debatable and remains enigmatic. Although an interaction between TPC2 and mTOR has been reported, conflicting data have emerged from different research groups, suggesting a dualistic role for TPC2, i.e., that it could function as both a negative and a positive regulator of autophagy. However, existing studies have primarily relied on OE models or NAADP activation of TPC2, hindering our comprehensive understanding of its mechanism[221-224]. In line with the autophagy findings, the induction of Ca^{2+}-dependent lysosomal exocytosis by TRPML1 has been well-established[81]. In comparison, the role of TPC2 in lysosomal exocytosis remained undefined until the utilization of structurally distinct small molecule activators of TPC2. TPC2-A1-N, mimicking NAADP, had no impact on lysosomal exocytosis. In contrast, TPC2-A1-P, mimicking $PI(3,5)P_2$ activation, induced lysosomal exocytosis in a concentration- and time-dependent manner,

suggesting an agonist-selective differential effect of TPC2 on lysosomal exocytosis and cellular physiology[12]. In humans, TRPML1 and TPC2 are expressed ubiquitously in all cells; however, their expression levels vary across different cell and cancer types[112, 217, 225, 226]. Proteomics and Co-IP studies have identified the interactomes of TRPML1 and TPC2, revealing several shared interaction partners, including TMED10, VDAC1, SURF4, and SLC7A5, essential for trafficking, proteostasis, and homeostasis. Other interaction partners are unique to TRPML1, such as TMEM185A and TMEM163, while TPC2 interacts with proteins such as TMEM165 and ANXA1[18, 106, 227]. Notably, a direct protein-protein interaction has been demonstrated between Rab7a and TPC2[18]. Nevertheless, an interaction between TRPML1 and Rab7a has not been elucidated[18, 106]. Moreover, co-localization studies in dendritic cells have reported an interaction between Rab7b and TRPML1. The interaction between Rab7a and TPC2 is particularly intriguing as Rab7a is primarily localized to LEs and LYs and is a crucial regulator of autophagy, lysosomal positioning and biogenesis. In addition, similar to TRPML1 and TPC2, Rab7a is crucial for intracellular trafficking[228-230], cholesterol transport[7, 21, 231, 232], and regulation of cancer hallmarks[68, 111, 157, 182, 183] (**Fig. 5**). Hence, the characterization of TRPML1 and TPC2, along with their respective overlapping or unique functionalities, holds great potential for developing effective treatments for cancer and neurodegenerative disorders. Despite their differences in ion permeability, interaction partners, and cellular mechanism, it is paramount to acknowledge that the seemingly conflicting effects observed in disease contexts could be influenced by cell line or type dependencies. This poses a significant challenge, particularly in oncological investigation due to cancer cell heterogeneity[7]. Therefore, this emphasizes the urgency of performing experiments within the same conditions and utilizing models such as gene editing tools in the same cell line to facilitate precise comparisons. Additionally, given the overlapping role of TRPML1 and TPC2, it is of utmost importance to investigate the activation of one channel in the absence of the others to assess potential rescue effects in cancer or lysosomal storage disorders. Furthermore, exploring the impact of interaction partners, such as Rab7a, on the function and channel activity of TPC2, and investigating their physiological relevance in pathological conditions, is crucial to tailoring treatments and uncovering associated signaling cascades.

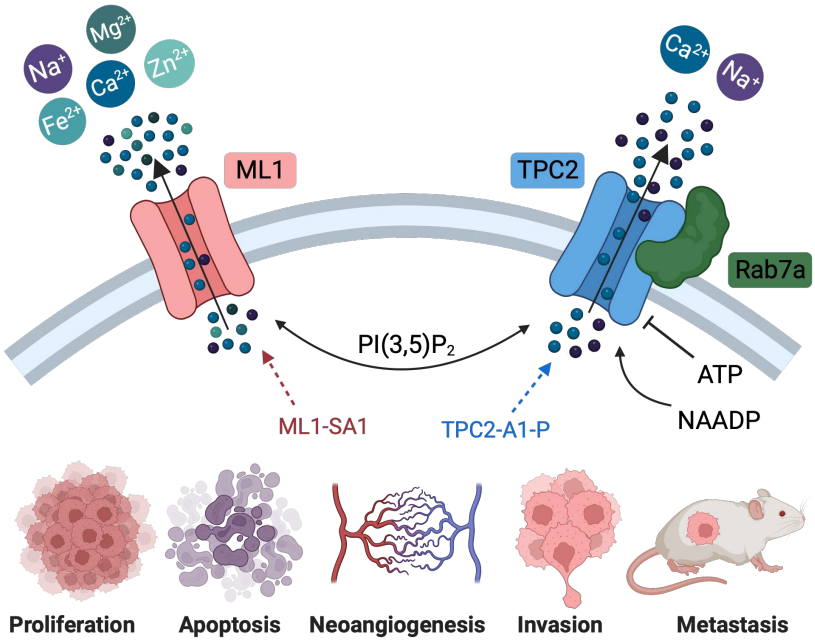

Figure 5. Impact of endolysosomal proteins on cancer hallmarks. A graphical representation of the proposed role of the endolysosomal proteins TRPML1, TPC2, and Rab7a in the context of cancer. The unique ion permeabilities of TRPML1 and TPC2 are showcased, along with key selective small molecule agonists for each channel. Additionally, endogenous activators and blockers are illustrated.

Publications: Short Summaries and Contributions

Paper I: Summary and Contributions

Flavonoids increase melanin production and reduce proliferation, migration and invasion of melanoma cells by blocking endolysosomal/melanosomal TPC2

Ponsawan Netcharoensirisuk*, **Carla Abrahamian***, Rachel Tang*,
Cheng-Chang Chen, Anna Scotto Rosato, Wyatt Beyers, Yu-Kai Chao, Antonio Filippini, Santiago Di Pietro, Karin Bartel, Martin Biel, Angelika M. Vollmar, Kaoru Umehara, Wanchai De-Eknamkul, & Christian Grimm

Two-pore channel 2 (TPC2) is a ubiquitously expressed endolysosomal cation channel, residing primarily in late endosomes, lysosomes, and mature melanosomes - lysosomal-related organelles[20, 225]. TPC2 plays essential roles in intracellular trafficking and transport[68], VEGF-induced neoangiogenesis[184], and energy metabolism[111] in cancer cells. A genome-wide association study identified two single nucleotide polymorphisms in human TPC2 associated with pigmentation characteristics[115]. In 2017, our laboratory employed the specialized endolysosomal patch clamp technique to investigate $TPC2^{G734E}$ and $TPC2^{M484L}$ variants and observed a heightened channel activity. Subsequently, this study (Chao et al., 2017) confirmed their link to the shift from brown to blond hair color through genotypic analysis of donor fibroblasts[16, 116]. Based on these intriguing findings connecting TPC2 to pigmentation, we sought to delve into its potential role in melanoma, the deadliest subtype of skin cancer. Notably, skin pigmentation in malignant melanoma serves as an ultraviolet absorbent, conferring photoprotective and antioxidant properties against UV radiation-induced damage. For the in vitro analysis, we utilized a knockout model and pharmacological inhibition of TPC2 in the pigmented melanoma lines, MNT-1 and B16F10, to corroborate our findings. Previous electrophysiology recordings had proposed the natural flavonoid, Naringenin, as a blocker of TPC2 activity. Building on this study, a collaboration was initiated between our laboratory and the research group led by Prof. Dr. Wanchai De-Eknamkul at Chulalongkorn University in Thailand. Within this group, Dr. Ponsawan Netcharoensirisuk isolated 44 flavonoid compounds from *Dalbergia parviflora*, a plant native to Southeast Asia, and evaluated their impact on melanin generation and tyrosinase activity in the melanoma lines. Among the candidates tested, two compounds, namely the O-methylated isoflavone (MT-8) and the tri-O-methylated isoflavan (UM-9), exhibited the most robust melanin production. The treatment of MNT-1 cells with either MT-8 or UM-9 resulted in a concentration-dependent increase in melanin production, akin to the effects observed with TPC2 knockout in the respective cell line. These findings were further validated by electrophysiology experiments in HEK293 cells that stably overexpress human TPC2, carried out by Prof. Dr. Cheng-Chang Chen, Dr. Yu-Kai Chao, and Rachel Tang. Their experiments demonstrated that both MT-8 and UM-9 had significant inhibitory effects on hTPC2, with the IC_{50} values for MT-8 at 2.6±0.3 µM and UM-9 at 9.5±2.8 µM, much lower than that of Naringenin at 74± 9 µM. Besides the experiments mentioned, I executed and designed all other experiments found in the main text and described in detail below, followed by the necessary statistical analysis and the making of figures. Additionally, I took part in drafting and revising the manuscript through the different stages of submission and revision. Specifically, to gain physiological insights, I performed different assays to compare the tumor phenotype in MNT-1 WT and TPC2 KO cells and in treatment with the selected compounds. Intriguingly, I observed a significant reduction in proliferation, migration, and invasion in the TPC2 KO MNT-1 cells compared to the WT, monitoring the effects over a span of 96 hours. Furthermore, I treated the cells with the compounds, and I observed a similar substantial decrease in these cancer hallmarks for MT-8 at 45 µM and UM-9 at 10 µM, a significantly lower concentration than that of Naringenin (100 µM) required for similar effects. Crucially, when I treated the TPC2 KO cells with the compounds at the same concentrations, there were no observable effects compared to the vehicle control, affirming the TPC2-dependent nature of these effects. To decipher the mechanism behind the observed anti-tumorigenic effects of TPC2, I investigated the expression of the melanoma oncogene, microphthalmia-associated transcription factor (MITF), which plays a crucial role in melanocyte function and differentiation. Additionally, I explored the regulation of tyrosinase, the rate-limiting enzyme responsible for melanin production. Interestingly, the genetic ablation of TPC2 led to reduced protein levels of MITF and an increase in tyrosinase activity in melanoma cells, in line with data by Dr. Netcharoensirisuk. To validate the expression of MITF and increase the reliability and accuracy of our data, three different antibodies for MITF were used. Remarkably, the genetic ablation of TPC2 resulted in reduced protein levels of MITF and increased tyrosinase activity in melanoma.

Moreover, to understand the mechanism underlying the reduction of MITF in the TPC2 KO cells, I carried out cycloheximide (CHX) chase assays. CHX is a compound that inhibits translation elongation, thereby blocking cytoplasmic protein synthesis. The results showed that MITF degraded more rapidly in the TPC2 KO cells compared to the WT upon CHX treatment. To further investigate whether this degradation of MITF in TPC2 KO cells depends on proteasomal activity, I treated the cells with the proteasomal inhibitor, MG-132. Interestingly, I observed that MG-132 treatment rescued MITF protein levels in the TPC2 KO cells, bringing them to levels comparable to WT cells. MITF is regulated post-transcriptionally by various signaling cascades. Therefore, to gain a comprehensive understanding of its association with TPC2, I performed western blot and qPCR experiments to assess several signaling pathways, including phosphorylation of ERK, AKT, and CREB, and total levels of GSK3β and β-catenin. Among these pathways, the canonical Wnt pathway showed significant changes, with a notable increase in GSK3β protein levels observed in TPC2 KO compared to WT cells. This finding supports the hypothesis of a positive feedback loop between MITF, the canonical Wnt pathway, and the endolysosomal machinery in melanoma. Essentially, MITF is stabilized through Wnt/GSK3β, promoting the biosynthesis of late endosomes and multivesicular bodies, which, in turn, potentiates further Wnt signaling. Our results underscore the dual benefits of inhibiting TPC2 in melanoma. Firstly, it reduces the MITF-driven melanoma progression by increasing GSK3β-mediated MITF degradation. Secondly, it directly interferes with tyrosinase activity, leading to the synthesis of UV-blocking melanin in melanosomes. Overall, our study highlights the potential of TPC2 as a clinical melanoma marker and holds promise for improved management, facilitating early intervention, and tailored therapeutic strategies to enhance patient outcomes.

Paper I

www.nature.com/scientificreports

scientific reports

Check for updates

OPEN

Flavonoids increase melanin production and reduce proliferation, migration and invasion of melanoma cells by blocking endolysosomal/melanosomal TPC2

Ponsawan Netcharoensirisuk[1,2,7], Carla Abrahamian[1,7], Rachel Tang[1,7], Cheng-Chang Chen[3], Anna Scotto Rosato[1], Wyatt Beyers[4], Yu-Kai Chao[1], Antonio Filippini[5], Santiago Di Pietro[4], Karin Bartel[3], Martin Biel[3], Angelika M. Vollmar[3], Kaoru Umehara[6], Wanchai De-Eknamkul[2]✉ & Christian Grimm[1]✉

Two-pore channel 2 (TPC2) resides in endolysosomal membranes but also in lysosome-related organelles such as the melanin producing melanosomes. Gain-of-function polymorphisms in hTPC2 are associated with decreased melanin production and blond hair color. Vice versa genetic ablation of TPC2 increases melanin production. We show here an inverse correlation between melanin production and melanoma proliferation, migration, and invasion due to the dual activity of TPC2 in endolysosomes and melanosomes. Our results are supported by both genetic ablation and pharmacological inhibition of TPC2. Mechanistically, our data show that loss/block of TPC2 results in reduced protein levels of MITF, a major regulator of melanoma progression, but an increased activity of the melanin-generating enzyme tyrosinase. TPC2 inhibition thus provides a twofold benefit in melanoma prevention and treatment by increasing, through interference with tyrosinase activity, the synthesis of UV blocking melanin in melanosomes and by decreasing MITF-driven melanoma progression by increased GSK3β-mediated MITF degradation.

Wile many cancer incidences are falling, the incidence rate of malignant melanoma is rising at a rate of 3–7% in most European countries versus 2.6% in the US, and is expected to further rise. There are about 100.000 new cases per year in Europe and the US, each, with approximately 22.000 deaths per year in Europe and 7.000 in the US[1,2]. Statistics in the US indicate that melanoma is more than 20 times more common in whites than in African Americans. When discovered early, melanoma can be surgically removed and patients have a high chance of being cured. However, when metastases have already formed, the prognosis is generally very poor, going along with a strongly decreased life expectancy. Patients then survive only 6–9 months on average after diagnosis, highlighting the importance of early diagnosis but also the need for new effective melanoma treatments. Melanocytes produce melanin in their melanosomes and most melanoma cells also still make melanin. Hence, most melanoma tumors appear black or brown while some do not make melanin anymore and can then appear pink, tan, or even white. Individuals with a higher ratio of yellow pheomelanin to brown eumelanin in their skin and hair, i.e. blondes

[1]Walther Straub Institute of Pharmacology and Toxicology, Faculty of Medicine, Ludwig-Maximilians-University, Munich, Germany. [2]Department of Biochemistry and Microbiology/Pharmacognosy, Faculty of Pharmaceutical Sciences, Chulalongkorn University, Bangkok, Thailand. [3]Department of Pharmacy, Center for Drug Research, Ludwig-Maximilians-University, Munich, Germany. [4]Department of Biochemistry and Molecular Biology, Colorado State University, Fort Collins, CO, USA. [5]Department of Anatomy, Histology, Forensic Medicine and Orthopedics, Unit of Histology and Medical Embryology, Sapienza University of Rome, 00161 Rome, Italy. [6]Yokohama University of Pharmacy, Yokohama, Japan. [7]These authors contributed equally: Ponsawan Netcharoensirisuk, Carla Abrahamian and Rachel Tang. ✉email: Wanchai.D@chula.ac.th; christian.grimm@med.uni-muenchen.de

and redheads have a greater risk for melanoma than black or brown haired individuals (by a factor of 2–4). The pheomelanin/eumelanin ratio accounts for some of this risk[3].

Ambrosio et al. (2016) have recently shown that knockout of two-pore channel TPC2 in human MNT-1 melanoma cells elicits a strong increase in pigment content and that this effect can be reversed by transient overexpression of TPC2-GFP[4]. Vice versa, Sulem et al. (2008) have shown that certain TPC2 polymorphisms, rs35264875 (encoding TPC2M484L) and rs3829241 (encoding TPC2G734E) are associated with reduced pigmentation and a higher probability for blond hair in humans[5]. Chao et al. (2017) investigated the functional effects of these variations on the channel properties using endolysosomal patch-clamp electrophysiology and found that both polymorphisms are gain-of-function (GOF) variants[6]. Furthermore, it has been shown recently that pharmacological or siRNA mediated inhibition of TPC2 abrogates migration of cancer cells and the formation of metastases[7]. However, a more detailed mechanistic understanding of how TPC2 activity and expression in melanosomes on the one hand and endolysosomes on the other hand affect melanoma cells is lacking. Here, we used MNT-1 human melanoma cells to assess the effect of genetic ablation or pharmacological inhibition of TPC2 on proliferation, migration, and invasion as well as melanin production. Surprisingly, we found that melanoma cell proliferation, migration, and invasion are inversely correlated with TPC2-dependent melanin production as loss of TPC2 increases melanin content but decreases proliferation/migration/invasion. This is possible due to independent mechanisms: via regulation of MITF (microphthalmia-associated transcription factor) protein levels through interference with endolysosomal activity of TPC2 and endolysosomal GSK3β degradation on the one hand and on the other hand via MITF-independent regulation of tyrosinase activity by TPC2 in melanosomes. Similar effects were found with novel, flavonoid based inhibitors of TPC2, corroborating a new treatment option for melanoma using TPC2 as a pharmacological target. Flavonoids, previously proposed anti-cancer agents thus emerge as direct inhibitors of TPC2 and the higher risk for blond haired individuals or individuals with light pigmentation to develop melanoma may be directly correlated to TPC2 activity and GOF variation.

Results

Human TPC2$^{-/-}$ melanoma cells show reduced proliferation, migration, and invasion but increased melanin production and tyrosinase activity. Genetic ablation or inhibition of TPC2 has been demonstrated before to affect cancer cell migration and the formation of metastases[7,8] as well as neoangiogenesis[9]. We show here that knockout of TPC2 in MNT-1 human melanoma cells results in significant decrease in melanoma cell proliferation, migration, and invasion (Fig. 1a–f). Ambrosio et al. (2016) have recently reported that TPC2 knockout elicits a strong increase in pigment content in MNT-1 cells[4]. Consistently, siRNA-mediated knockdown of TPC2 was also found to cause a substantial increase in melanin content in MNT-1 cells and primary human melanocytes[4]. We recapitulated these findings and confirmed the strong increase in melanin production in TPC2$^{-/-}$ cells (Fig. 1g,h). We further found a significant increase in the activity of tyrosinase, which is the key enzyme responsible for efficient melanin production with a pH optimum at 6.8 (Fig. 1i). At the same time, we also found increased protein levels of tyrosinase in TPC2$^{-/-}$ MNT-1 cells while transcript levels were unchanged (Fig. S1a-d and S1g). In contrast to tyrosinase, expression levels of other proteins involved in melanogenesis or regulated by MITF such as Dct (dopachrome tautomerase, TYRP2), Rab27a, or PMEL (premelanosome potein) were unchanged (Fig. S1c-f).

Flavonoids from a Southeast Asian plant extract affect melanin production in melanoma cells. In an unbiased approach to identify compounds that affect melanin production in melanoma cells, we screened several plant extracts in B16F10 mouse melanoma cells. An extract prepared from *Dalbergia parviflora* (*D. parviflora*), also called Akar Laka which is mainly found in lowland tropical areas, in particular in Myanmar, Thailand, Malaysia, Indonesia, and the Philippines showed the strongest effect alongside *Kaempferia parviflora* (*K. parviflora*), also called Thai ginseng or Thai black ginger, a native plant of Thailand (Fig. 2a). Subsequently, 44 different flavonoid compounds were isolated from *D. parviflora* (Fig. S2) and tested for their effects on melanin production in B16F10 mouse melanoma cells (Fig. 2b; Fig. S3a and 3b). Among the top five hits with the strongest effect on melanin generation were MT-8, an O-methylated isoflavone, also called pratensein, and UM-9, a tri-O-methylated isoflavan, also called duartin. Based on the results obtained in the melanin content assay, the following chemical features were identified to be optimal for the isoflavone group (e.g. MT-8): Aryl ring A should be dihydroxy-substituted at positions 5 (-OH) and 7 (-OH), and the aromatic ring B should be methoxy-substituted at position 4′. For the isoflavan group (e.g. UM-9), ring A should be one hydroxy-substituted at position 7 and one methoxy-substituted at position 8, with ring B being dimethoxy-substituted at positions 4′ and 2′ (or 3′). Subsequently, the screening was replicated in human melanoma cells (MNT-1), where UM-9 and MT-8 were again found to be among the top five hits (Fig. 2c). The effects of UM-9 and MT-8 were found to be concentration and time dependent. The most prominent effects were seen at day 3–4 when using a concentration of 10–20 µM in B16F10 cells (Fig. 2d,e; Fig. S3c-f). Similar optimal concentrations were found for MNT-1 cells (Fig. S3g-h).

Flavonoids block TPC2 activity in endolysosomal patch-clamp experiments. The flavonoid naringenin (NAR) has been shown before to block TPC2[10]. We therefore tested NAR and other candidate blockers including MT-8 and UM-9 in endolysosomal patch clamp experiments to assess their activity on hTPC2 inhibition following activation with the endogenous endolysosomal membrane phosphoinositide $PI(3,5)P_2$. In these experiments, using hTPC2 stably overexpressed in HEK293 cells, *D. parviflora* extract, MT-8 and UM-9 were found to exhibit strong inhibitory effects on hTPC2 (Fig. 3a–c,h). In contrast, KM-4 which showed very weak effects on pigmentation, showed also very weak inhibitor activity on hTPC2 (Fig. 3d). TR-9 and TR-12 which showed variable effects on melanin generation also proved to be less efficacious inhibitors of hTPC2 (Fig. 3e–f,h).

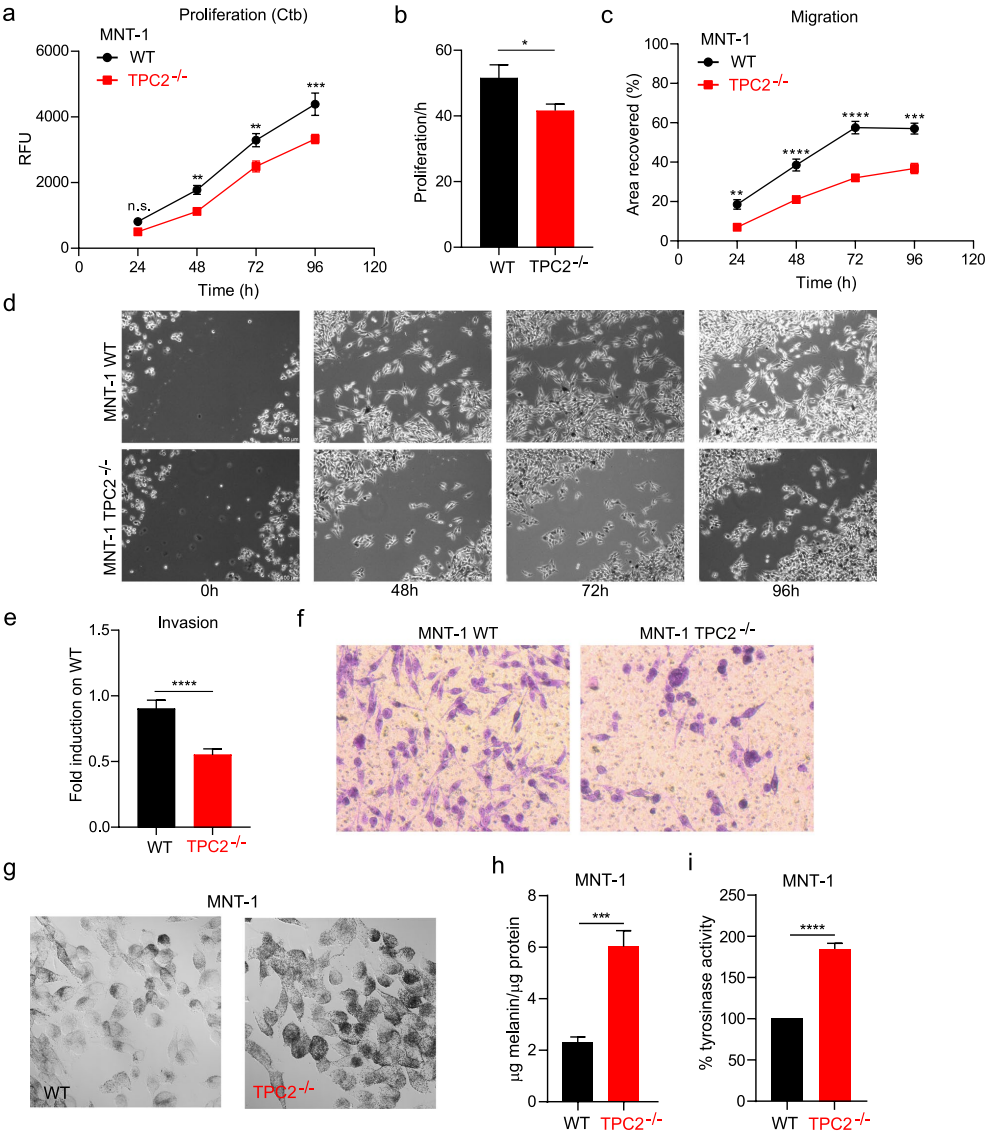

Figure 1. Proliferation, migration, and invasion in WT and TPC2$^{-/-}$ MNT-1 cells. Proliferation was assessed using the CellTiter-Blue (Ctb) assay for the different time-points subtracted from the 0 h value reading of cells. Viable, metabolically active cells undergo a reduction reaction of resazurin to resorufin, while non-viable cells do not. Migration was assessed using the wound healing scratch assay, and invasion using transwell chambers in MNT-1 melanoma cells. (**a**) Genetic ablation of TPC2 in MNT-1 cells shows significant reduction of proliferation over 96 h. (**b**) Rate of proliferation per hour shows significant reduction in TPC2$^{-/-}$ cells. (**c**) Migration in TPC2$^{-/-}$ cells is significantly slower compared to WT MNT-1 cells, monitored for 24, 48, 72, and 96 h. (**d**) Representative images of wound healing monitored in WT and TPC2$^{-/-}$ cells at different time-points. (**e**) and (**f**), MNT-1 TPC2$^{-/-}$ are significantly less invasive than WT cells after 24 h. Statistical analysis (**e**) and representative Figures of WT and TPC2$^{-/-}$ MNT-1 cells are shown (**f**). Cells were allowed to migrate into transwell chambers for 24 h. (**g**) Laser scanning microscope images visualizing the differences between WT and TPC2$^{-/-}$ MNT1 cells in melanin content. (**h**) Quantification of melanin content in WT and TPC2$^{-/-}$ MNT1 cells normalized to total protein content. (**i**) Tyrosinase activity was determined by the rate of dopachrome formation. The activity was expressed as percentage of WT cells. Statistical significance was determined by either two-way ANOVA followed by Bonferroni multiple comparisons test (**a**, **c**) or Student's t-test (**b**, **e**, **h**, **i**). Shown are mean values ± SEM, (n = 3, each). *P < 0.05, **P < 0.01, ***P < 0.001, ****P < 0.0001.

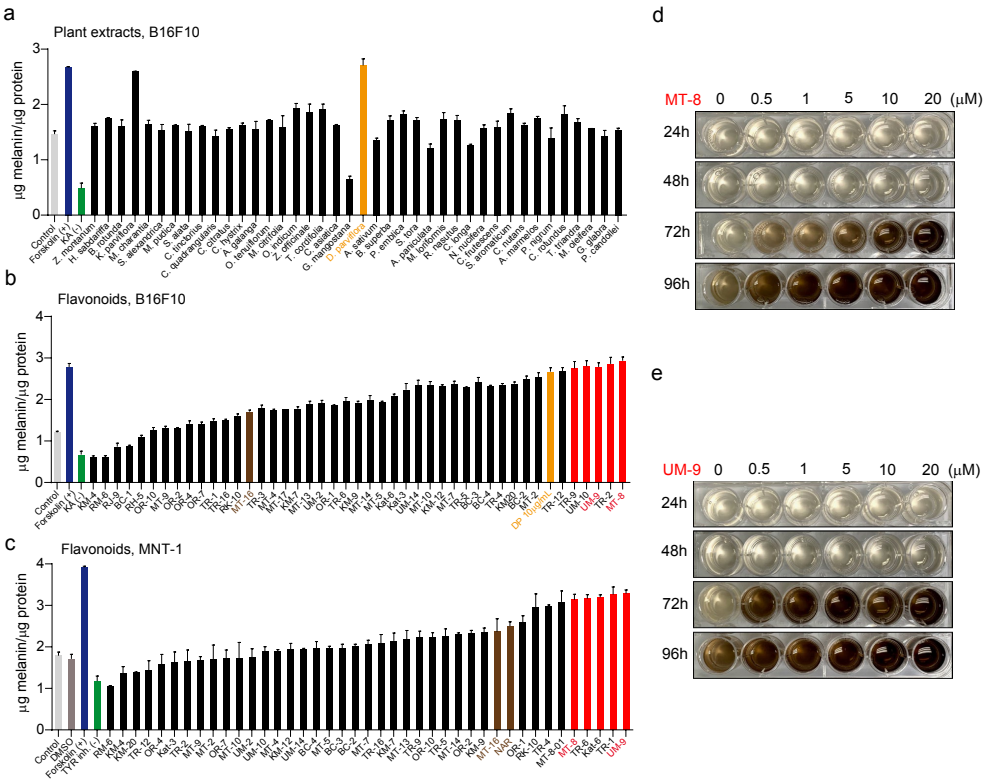

Figure 2. Flavonoid compound screening in B16F10 and MNT-1 cells using effect on melanin content as read-out. (**a**) Effect of different plant extracts including D. parviflora extract on the melanin content of B16F10 cells. Forskolin was used as positive control. KA (Kojic acid = 5-Hydroxy-2-(hydroxymethyl)-4H-pyran-4-one) was used as negative control. Data are shown as mean values ± SD (n = 3, each). (**b**) Effect of different flavonoids on the melanin content of B16F10. Forskolin was used as positive control. KA was used as negative control. MT-16 = NAR = naringenin was shown before to block TPCs. The data are shown in the sequence of ascending effect. Top five hits are highlighted in red and *D. parviflora* (DP) extract is highlighted in yellow. Data are shown as mean values ± SD (n = 3, each). (**c**) Effect of different flavonoids on the melanin content of MNT-1 cells. Forskolin was used as positive control. 4-Butyl-resorcinol (TYR inh.) was used as negative control. The data are shown in the sequence of ascending effect. Top five hits are highlighted in red. In both B16F10 and MNT-1 cells the compounds UM-9 and MT-8 were consistently found to be among the top 5 hits. MT-16 and commercially available NAR (cat. #67604-48-2; Sigma) are highlighted in brown. Data are shown as mean values ± SD (n = 3, each). In all experiments the following concentrations of the compounds were used: Forskolin (10 µM), TYR inh. (10 µM), KA (10 µM), flavonoids (20 µM). In a-c mean values ± SEM are shown, (n = 3, each). (**d**) and (**e**) Examples of experiments showing the time and concentration dependent effects of MT-8 (**d**) and UM-9 (**e**) on melanin content in B16F10 cells. For quantification see Fig. S2c-f.

NAR (MT-16), which had a comparably strong effect in human MNT-1 cells (weaker in mouse B16F10 cells) on pigmentation, was confirmed as an inhibitor of hTPC2 (Fig. 3g–h). IC_{50} values indicate however that NAR is less potent than UM-9 and MT-8 (IC_{50} (NAR) = 74 ± 9 µM; IC_{50} (MT-8) = 2.6 ± 0.3 µM; IC_{50} (UM-9) = 9.5 ± 2.8 µM) (Fig. 3i–k). NAR was also less potent in increasing the relative melanin content (Fig. S3i). In contrast to TPC2, the endolysosomal cation channel hTRPML1, stably overexpressed in HEK293 cells, was not blocked by flavonoids but instead by the previously reported TRPML blocker ML-SI3[11] (Fig. 3l–m).

TPC2-inhibiting flavonoids increase melanin production and tyrosinase activity in human melanoma cells in a TPC2-dependent manner. Next, we further assessed the effect of the TPC2 inhibitors MT-8 and UM-9 on melanin generation and tyrosinase activity in MNT-1 WT versus $TPC2^{-/-}$ cells. Forskolin[12] and the tyrosinase inhibitor 4-Butyl-resorcinol (TYR inh.)[13] were used as positive and negative controls, respec-

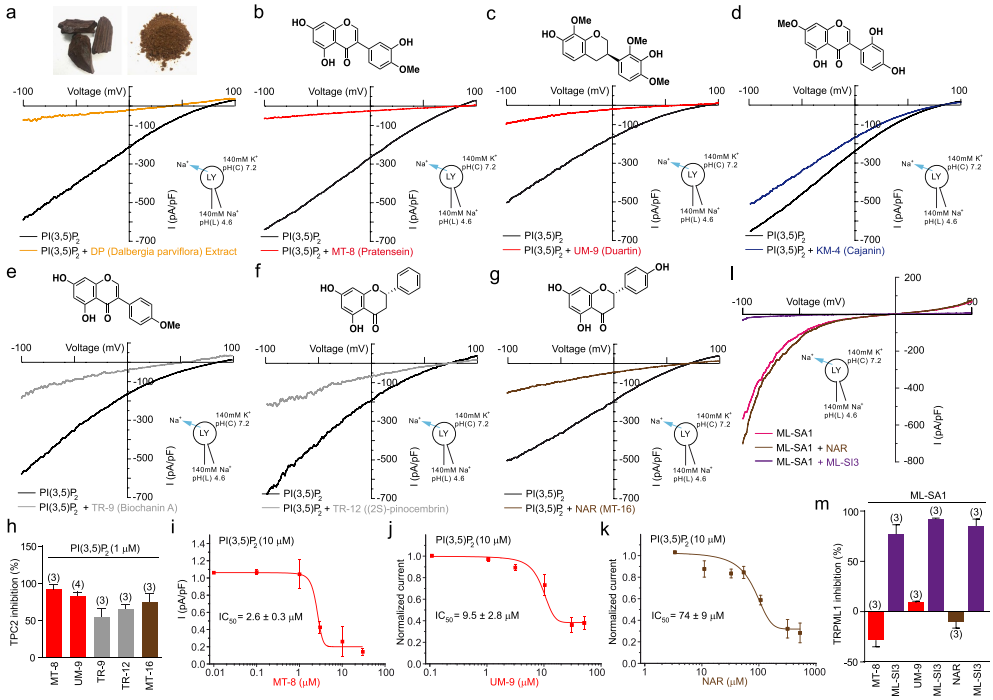

Figure 3. Flavonoids as inhibitors of TPC2 channel activity. (**a**) Heartwood and extract from *D. parviflora* (upper panel), and endolysosomal patch-clamp measurement demonstrating effect of the extract (10 µg/ml) to block TPC2 stimulated by $PI(3,5)P_2$ (1 µM). Shown is a representative $PI(3,5)P_2$-evoked current from enlarged endolysosomes isolated from HEK293 cells stably expressing human TPC2 (hTPC2). Recordings were carried out using standard bath and pipette solutions and applying ramp protocols (− 100 mV to + 100 mV over 500 ms) every 5 s at a holding potential of -60 mV. (**b**–**g**) Similar recordings as shown in a using different flavonoids (10 µM, each) to block TPC2. Structures of the respective test compounds are shown on top of the I–V traces. (**h**) Shown are average current densities (mean ± SEM) at − 100 mV of experiments as shown in **b**–**g**. (**i**–**k**) Effect-response relationships of MT-8, UM-9, and NAR using 10 µM $PI(3,5)P_2$ for activation. (**l**–**m**) Data showing no blocking effect of MT-8 or NAR on TRPML1 (activation with 10 µM ML-SA1). As a positive control TRPML blocker ML-SI3 was used.

tively. $TPC2^{-/-}$ cells were used to assess specificity of the compound effects. MT-8 significantly increased melanin production and tyrosinase activity in WT MNT-1 cells while no significant increase was found in $TPC2^{-/-}$ MNT-1 cells, suggesting effects were TPC2-dependent (Fig. 4a–d). UM-9 also significantly increased melanin production and tyrosinase activity in WT MNT-1 cells while no significant increase was found in $TPC2^{-/-}$ MNT-1 cells, suggesting effects were again TPC2-dependent (Fig. 4e–h). Vice versa, activation with the novel lipophilic small molecule agonist TPC2-A1-P[14] resulted in the opposite effect, reducing melanin production similar to TYR inhibitor with no effect in $TPC2^{-/-}$ MNT-1 cells (Fig. 4i,j). NAR was also confirmed, like MT-8 and UM-9 to increase melanin production in a TPC2 dependent manner (Fig. 4i,j).

TPC2-inhibiting flavonoids reduce melanoma cell proliferation, migration, and invasion in a TPC2-dependent manner. An anti-cancer potential of flavonoids has long been claimed[15–17]. Proposed anticancer mechanisms for flavonoids are inhibition of proliferation, inflammation, invasion, metastasis, and activation of apoptosis[15]. We first tested the effect of vehicle (DMSO) on WT and $TPC2^{-/-}$ MNT-1 cell proliferation (Fig. 5a) and confirmed highly significant assay windows between WT and $TPC2^{-/-}$ MNT-1 cells at 48 and 72 h after treatment. Next, we assessed whether the effect of flavonoids, in particular of the hit compounds MT-8 and UM-9 as well as NAR on melanoma cell proliferation was mediated by TPC2. We found that MT-8 and UM-9 reduced proliferation of MNT-1 WT cells efficiently to the levels of $TPC2^{-/-}$ MNT-1 cells while application of the compounds on $TPC2^{-/-}$ MNT-1 cells showed no significant effect, indicating on-target activity of MT-8 and UM-9 (Fig. 5b–i). Likewise, NAR reduced proliferation in a TPC2-dependent manner but dose–response measurements revealed significant effects for NAR only at concentrations of > 80 µM (Fig. 5g) which is in agreement with the high IC_{50} measured in TPC2 inhibition experiments. Next, we assessed the effect of the compounds

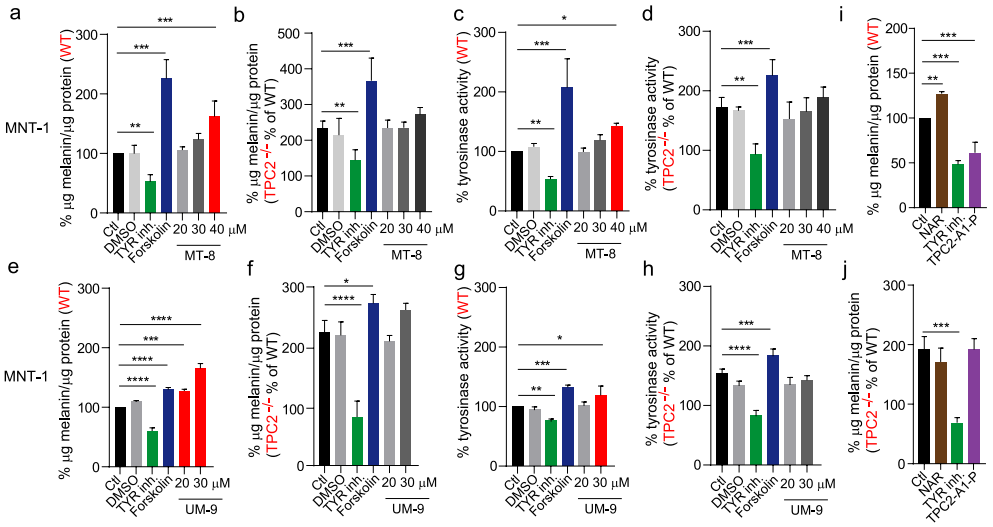

Figure 4. Melanin production and tyrosinase activity in flavonoid treated WT and TPC2$^{-/-}$ MNT-1 cells. (**a**) and (**b**) Melanin content in WT and TPC2$^{-/-}$ MNT1 cells after treatment with different concentrations of MT-8 (20, 30 and 40 µM) or DMSO, and with tyrosinase inhibitor (10 µM) and forskolin (10 µM) as negative and positive controls, respectively. (**c**) and (**d**) Tyrosinase activity in WT versus TPC2$^{-/-}$ MNT1 cells after treatment with MT-8 in different concentrations. (**e**) and (**f**) Melanin content in WT and TPC2$^{-/-}$ MNT1 cells after treatment with different concentrations of UM-9 (20 and 30 µM) or DMSO, and with tyrosinase inhibitor (10 µM) or forskolin (10 µM) as negative and positive controls. (**g**) and (**h**) Tyrosinase activity in WT versus TPC2$^{-/-}$ MNT1 cells after treatment with UM-9 in different concentrations. (**i**) and (**j**) Melanin content in WT and TPC2$^{-/-}$ MNT-1 cells after treatment with naringenin (NAR; 50 µM), tyrosinase inhibitor (10 µM), or TPC2-A1-P (TPC2 activator; 50 µM). Statistical significance was determined by one-way ANOVA followed by Dunnett 's multiple comparisons test. Shown are mean values ± SEM, (n = 3, each). *P < 0.05, **P < 0.01, ***P < 0.001, ****P < 0.0001.

and DMSO control on migration of WT and TPC2$^{-/-}$ MNT-1 cells. We confirmed the highly significant assay windows between WT and TPC2$^{-/-}$ MNT-1 cells for migration at different time points (Fig. 5j–k). Application of MT-8, UM-9, and NAR reduced the migration efficiency of MNT-1 WT cells to TPC2$^{-/-}$ values (Fig. 5l–m) while addition of the compounds to TPC2$^{-/-}$ MNT-1 cells did not significantly reduce migration efficiency any further (Fig. 5l–m), again corroborating on-target effects of the compounds. Likewise, we assessed the effect of the compounds and DMSO control on invasion of WT and TPC2$^{-/-}$ MNT-1 cells (Fig. 5n–p). Application of MT-8, UM-9, and NAR reduced the invasion efficiency of MNT-1 WT cells to TPC2$^{-/-}$ values while addition of the compounds to TPC2$^{-/-}$ MNT-1 cells did not significantly reduce invasion efficiency any further (Fig. 5n–p).

MITF protein levels are reduced in TPC2 knockout melanoma cells while GSKβ levels are increased. MITF is a major regulator of melanoma proliferation and progression, and mutations in MITF are associated with Tietz albinism-deafness syndrome, Waardenburg syndrome type 2A, and melanoma development[18,19]. Several pathways are involved in the regulation of MITF such as the RAS/RAF/MEK/ERK pathway, the PI3K/AKT, and the Wnt/GSK3β/β-Catenin signalling pathways[20]. Melanin formation is also triggered by melanocyte-stimulating hormone (MSH), a peptide hormone encoded by the *proopiomelancortin* gene (POMC). MSH binding to MC1R results in the induction of MITF via CREB (cAMP response element-binding protein)[20]. We performed Western blot experiments to assess protein levels of MITF and several key proteins involved in the regulation of MITF expression. We found that in TPC2$^{-/-}$ MNT-1 cells MITF protein levels were strongly decreased compared to WT cells. We confirmed this result by using three different antibodies against MITF (Fig. 6a,b and Fig. S4). We next assessed the expression levels of CREB, ERK, Akt, and GSK3β (Fig. 6c–j, Fig. S4, and Fig. 7). While ERK, Akt, and CREB showed no significant differences, the expression of GSK3β was significantly increased. GSK3β is a negative regulator of MITF expression and can target MITF for proteasomal degradation. Activation of Wnt signalling can prevent this process by increasing the endolysosomal destruction of GSK3β[21]. An increased level of GSK3β suggests reduced degradation of the GSK3β containing destruction complexes in endolysosomes, resulting in increased GSK3β-dependent MITF degradation.

To further corroborate this hypothesis we assessed the MITF protein stability in WT and TPC2$^{-/-}$ MNT-1 cells by using cycloheximide (CHX). CHX is an inhibitor of protein synthesis and can be used to determine the longevity of proteins[22]. In Western blot experiments we found an increased sensitivity of TPC2$^{-/-}$ compared

to WT MNT-1 cells to CHX treatment, resulting in a faster and significantly stronger degradation of MITF in TPC2$^{-/-}$ MNT-1 cells (Fig. 6k–l and Fig. S4). To demonstrate that the differences in degradation of MITF were dependent on proteasomal activity we used the proteasome inhibitor MG-132. MG-132 was found to reestablish WT MITF levels within 5 h after treatment to TPC2$^{-/-}$ MNT-1 cells (Fig. 6m–n), indicative of proteasomal degradation causing the reduction in MITF levels.

Discussion

We show here a TPC2-dependent inverse correlation between melanin generation and melanoma proliferation, migration, and invasion by using both genetic and pharmacological approaches. While genetic ablation or pharmacological inhibition increase melanin production in a TPC2-dependent manner, proliferation, migration, and invasion of melanoma cells are reduced. We further found that the flavonoids MT-8 (pratensein) and UM-9 (duartin) efficiently reduce melanoma cell proliferation, migration, and invasion in a TPC2-dependent manner, thus providing a molecular rationale for previously suggested anti-cancer effects of flavonoids[15–17]. Besides MT-8 and UM-9, the related compound MT-16 which corresponds to NAR was confirmed as a TPC2 inhibitor. NAR had been demonstrated before to impair VEGF-induced vessel formation[9,10] in a TPC2 dependent manner. Flavonoids thus emerge as anti-cancer drugs acting through the endolysosomal/melanosomal cation channel TPC2.

Melanin content and the development of melanoma have previously been suggested to be correlated[12] and it is well established that melanin is one of the major protective factors against UV radiation mediated DNA damage that results in melanoma development. TPC2 now emerges as a critical regulator of both melanin generation and melanoma proliferation, migration, and invasion in human melanoma cells due to its dual functions in melanosomes and endolysosomes.

Through regulation of genes related to invasiveness, migration and metastasis MITF can promote melanoma progression[19]. We found here that knockout of TPC2 results in a strong decrease in MITF protein abundance, suggesting that the reduction in MITF levels is likely causative for the observed reduced effects on proliferation/migration/invasion in TPC2$^{-/-}$ MNT-1 cells. Wnt signalling is known to stabilize MITF protein levels in melanoma cells. Ploper et al. (2015) have shown that Wnt signalling can also regulate MITF at the protein degradation level, underscoring the importance of misregulated endolysosomal biogenesis and trafficking in Wnt signalling and cancer[21]. Wnt inhibits GSK3β and promotes sequestration of destruction complexes containing GSK3β into endosomes and MVBs, thus stabilizing MITF protein levels (Fig. 7). In the absence of Wnt and Wnt signalling GSK3β phosphorylates MITF, targeting MITF for proteasomal degradation. In TPC2$^{-/-}$ cells endolysosomal trafficking and degradation are impacted as shown before for, e.g. LDL, EGF/EGFR, or PDGFR trafficking and degradation[23–25], suggesting a possible impact on the sequestration and degradation of the destruction complex containing GSK3β. Consequently, we found increased GSK3β protein levels and an increased proteasomal degradation of MITF. Of note, flavonoids have been reported before to affect MITF expression through interference with Wnt signalling. Thus, e.g. Syed et al. (2011) showed that human melanoma cell growth inhibition by flavonoids was associated with disruption of Wnt signalling and decreased MITF levels[26]. Such data further support a connection between flavonoids, TPC2, Wnt signalling and MITF expression.

A role of TPC2 and TPC2 variation in melanoma development is also supported by genome-wide association studies. Thus, Kosiniak-Kamysz et al. (2014) examined 33 candidate polymorphisms located in 11 pigmentation genes and the vitamin D receptor (VDR) gene in a population of 130 cutaneous melanoma patients and 707 healthy controls[27]. In the final multivariate analysis with genetic interactions included and after adjustment for age and skin colour, five epistatic effects remained significant, i.e. interactions between MC1R and TYR, SLC45A2 and VDR, HERC2 and VDR, OCA2 and TPC2. The identified TPC2 variant rs3829241 ($P = 0.007$) is one (TPC2^{G734E}) of the two variants shown to be GOF variants[6] and to be associated with blond hair color in humans[5].

Taken together, our data provide strong evidence not only for a role of TPC2 in cancer proliferation, migration, and invasion in general but specifically a twofold role for TPC2 in melanoma development by affecting on the one hand MITF protein abundance and on the other hand melanin production independently of MITF through direct interference with tyrosinase activity in melanosomes. Thus, melanoma cell proliferation, migration, and invasion are inversely correlated with TPC2-dependent melanin production as reduction of TPC2 expression increases melanin content but decreases proliferation/migration/invasion. This is possible due to independent mechanisms: via regulation of MITF protein levels through interference with endolysosomal activity of TPC2 and endolysosomal GSK3β degradation on the one hand and on the other hand via regulation of tyrosinase activity in melanosomes which likewise express TPC2[28]. In a very recent study, D'Amore et al. (2020) have also investigated the role of TPC2, but in a model of human amelanotic melanoma: CHL1. In CHL1 cells, TPC2 was surprisingly found to increase the metastatic traits of this amelanotic melanoma cell line by a mechanism involving store-operated calcium entry and the Hippo signalling pathway that negatively regulates YAP/TAZ activity. Clearly, these differences between amelanotic melanoma cells (CHL1) on the one hand and highly pigmented melanoma cells (MNT-1) but also a range of other cancer cells (e.g., HUH7, T24, 4T1)[7] on the other hand regarding TPC2 need to be further elucidated in future studies.

Materials and methods

Endolysosomal patch-clamp experiments. Endolysosomal patch-clamp experiments were performed as previously described[6,14,23,25,29,30]. In brief, for whole-LE/LY manual patch-clamp recordings, cells were treated with 1 μM vacuolin (HEK293 cells: overnight) in an incubator at 37 °C with 5% CO_2. Compound was washed out before patch-clamp experimentation. Currents were recorded using an EPC-10 patch-clamp amplifier (HEKA, Lambrecht, Germany) and PatchMaster acquisition software (HEKA). Data were digitized at 40 kHz and filtered at 2.8 kHz. Fast and slow capacitive transients were cancelled by the compensation circuit of the

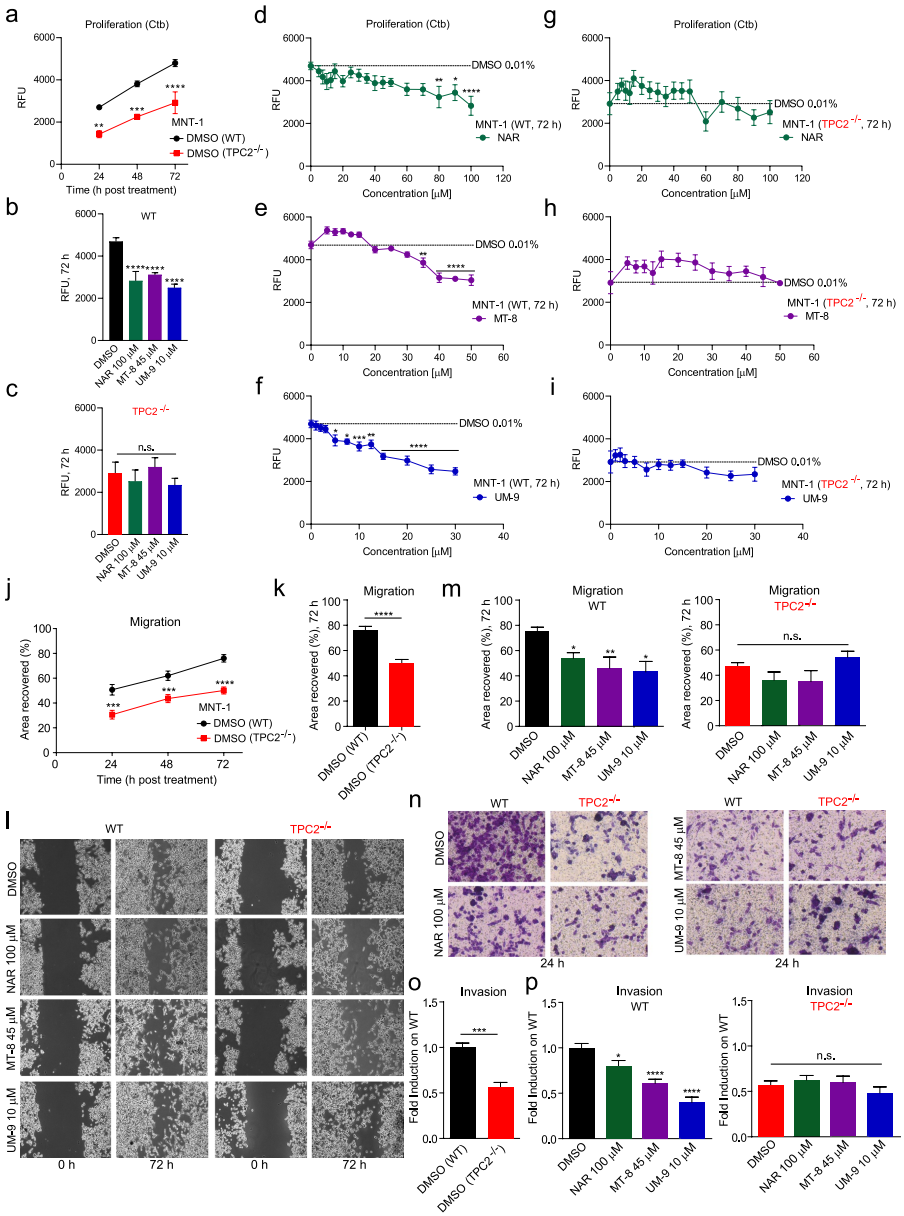
a
Proliferation (Ctb)
RFU
Time (h post treatment)
MNT-1
DMSO (WT)
DMSO (TPC2-/-)
b
WT
RFU, 72 h
DMSO
NAR 100 µM
MT-8 45 µM
UM-9 10 µM
c
TPC2-/-
n.s.
d
Proliferation (Ctb)
DMSO 0.01%
MNT-1 (WT, 72 h)
NAR
Concentration [µM]
e
MNT-1 (WT, 72 h)
MT-8
f
MNT-1 (WT, 72 h)
UM-9
g
Proliferation (Ctb)
MNT-1 (TPC2-/-, 72 h)
NAR
h
MNT-1 (TPC2-/-, 72 h)
MT-8
i
MNT-1 (TPC2-/-, 72 h)
UM-9
j
Migration
Area recovered (%)
MNT-1
DMSO (WT)
DMSO (TPC2-/-)
k
Migration
Area recovered (%), 72 h
m
Migration
WT
TPC2-/-
n.s.
l
WT
TPC2-/-
DMSO
NAR 100 µM
MT-8 45 µM
UM-9 10 µM
0 h
72 h
n
24 h
o
Invasion
Fold Induction on WT
p
Invasion
WT
TPC2-/-

◂**Figure 5.** Proliferation, migration, and invasion in flavonoid treated WT and TPC2$^{-/-}$ MNT-1 cells. (**a**) Proliferation of WT and TPC2$^{-/-}$ MNT-1 cells after treatment with DMSO control for 24, 48, and 72 h. (**b**) Anti-proliferative effect of UM-9 (10 μM), MT-8 (45 μM), and NAR (100 μM) on MNT-1 WT cells compared to DMSO control 72 h post treatment. (**c**) Application of the flavonoids as above to TPC2$^{-/-}$ MNT-1 cells shows no significant difference as compared to vehicle control on proliferation at 72 h post treatment. (**d**–**i**) Effect of NAR, MT-8, or UM-9 treatment for 72 h in MNT-1 WT (d-f) and TPC2$^{-/-}$ (**g**–**i**) MNT-1 cells. Statistical significance was determined by two-way ANOVA followed by Bonferroni multiple comparison test relative to DMSO control (100 μM). (**j**) MNT-1 WT and TPC2$^{-/-}$ cells treated with DMSO show significant difference in migration at 24, 48, and 72 h post treatment. (**k**) Wound closure of DMSO treated WT vs TPC2$^{-/-}$ MNT-1 cells at 72 h post treatment. (**l**) Wound closure process pictured at 0 and 72 h post treatment in MNT-1 WT and TPC2$^{-/-}$ cells treated with flavonoids or DMSO control. (**m**) MNT-1 WT (left) and TPC2$^{-/-}$ (right) cells treated with 100 μM of NAR, 45 μM of MT-8, and 10 μM of UM-9 show significantly slower migration rates upon 72 h treatment compared to DMSO control (100 μM). (**n**) Invasion pictured at 24 h post treatment in MNT-1 WT and TPC2$^{-/-}$ cells treated with flavonoids or DMSO control. (**o**) MNT-1 WT and TPC2$^{-/-}$ cells treated with DMSO show significant difference in invasion at 24 h post treatment. (**p**) MNT-1 WT (left) and TPC2$^{-/-}$ (right) cells treated with 100 μM of NAR, 45 μM of MT-8, and 10 μM of UM-9 show significantly slower invasion rates 24 h post treatment compared to DMSO control (100 μM). Statistical significance was determined by either two-way ANOVA followed by Bonferroni multiple comparison test (**j**), Student's t-test (**k**, **o**), or one-way ANOVA followed by Bonferroni multiple comparison test (**m**, **p**). Shown are mean values ± SEM, (n = 3, each). *P < 0.05, **P < 0.01, ***P < 0.001, ****P < 0.0001.

EPC-10 amplifier. All recordings were obtained at room temperature and were analyzed using PatchMaster acquisition software (HEKA) and OriginPro 6.1 (OriginLab). Recording glass pipettes were polished and had a resistance of 4–8 MΩ. For all experiments, salt-agar bridges were used to connect the reference Ag–AgCl wire to the bath solution to minimize voltage offsets. Liquid junction potential was corrected. For the application of small molecules, compounds were added directly to the patched endolysosomes to either evoke or inhibit the current. The cytoplasmic solution was completely exchanged by cytoplasmic solution containing compound. The current amplitudes at −100 mV were extracted from individual ramp current recordings. Unless otherwise stated, cytoplasmic solution contained 140 mM K-MSA, 5 mM KOH, 4 mM NaCl, 0.39 mM $CaCl_2$, 1 mM EGTA and 10 mM HEPES (pH was adjusted with KOH to 7.2). Luminal solution contained 140 mM Na-MSA, 5 mM K-MSA, 2 mM Ca-MSA 2 mM, 1 mM $CaCl_2$, 10 mM HEPES and 10 mM MES (pH was adjusted with methanesulfonic acid to 4.6). In all experiments, 500-ms voltage ramps from − 100 to + 100 mV were applied every 5 s. All statistical analysis was completed using OriginPro9.0 and GraphPadPrism software.

Cell culture. HEK293 cells stably expressing hTPC2-YFP or hTRPML1-YFP were used for patch-clamp experiments. Cells were maintained in DMEM supplemented with 10% FBS, 100 U penicillin/mL, and 100 μg streptomycin/mL. Cells were plated on glass cover slips 24–48 h before experimentation. Cells were transiently transfected with Turbofect (Fermentas) according to the manufacturer's protocols and used, e.g. for confocal imaging or patch-clamp experiments 24–48 h after transfection. Cells were treated with compounds at 37 °C and 5% CO_2. MNT-1 WT and TPC2$^{-/-}$ KO cell lines were grown in high glucose DMEM, supplemented with 20% FBS, 10% AIM-V, 1% sodium pyruvate (Thermo Fisher), and 1% penicillin–streptomycin (Sigma-Aldrich). B16F10 cells were grown in high glucose DMEM, supplemented with 10% FBS (Thermo Fisher), 1% L-glutamin, and 1% penicillin–streptomycin (Sigma-Aldrich). Cell lines were maintained at 37 °C in a 5% CO_2 incubator.

Melanin screening in B16F10 mouse melanoma cells. Melanin content determination was performed as described previously with some modifications[31]. In brief, B16F10 cells at density of 5×10^3 cells/well in 96-well plate were cultured and incubated with various plant extracts or flavonoids at a concentration of 20 μg/ml or 20 μM, respectively, for 4–5 days. Melanin content was measured using a microplate reader (Anthros, Durham, NC, USA) and calculated based on the OD ratio between treated and untreated cells.

Melanin content and tyrosinase activity assays. MNT-1 WT and TPC2$^{-/-}$ KO cell lines were grown as described in the cell culture section. After reaching 80–90% confluency, cells were subcultured (every 2–3 days). Forskolin (Sigma-Aldrich Cas Nr. 66,575,299) was used as positive control and 4-Butyl-resorcinol (TYR-inh., Sigma-Aldrich, Cas Nr.18979-61-8) as negative control. For experiments, cells were plated in 6-well plates with 200,000 cells per well. Cells were incubated for 72 h at 37 °C and 5% CO_2. After removing cell culture media, cells were washed in DPBS twice, then cells were collected using a cell scraper. Cells were centrifuged at 3000 rpm for 5 min. Pellets were lysed with RIPA buffer, supplemented with 1% protease inhibitor cocktail (Sigma-Aldrich) and 1% phosphatase inhibitor (Sigma-Aldrich) at 4 °C (on ice) for 45 min. Cells were centrifuged at 12.000 rpm for 15 min (4 °C), supernatant was subsequently removed and protein content determined using a protein dye reagent assay (Bio-Rad; protein standard curve (BSA) 0, 1, 3, 5, 8, 10, 12, 15 μg/mL). Cell pellets were dissolved in 250 μL 1 N NaOH/10% DMSO and incubated at 80 °C for 2 h. After centrifugation at 12.000 rpm for 10 min, supernatants were removed to a 96-well plate. Absorbance was measured (in triplicates, each) at 405 nm using a microplate reader (Tecan, Infinite M200 PRO). Melanin content was normalized to total protein content.

To measure tyrosinase activity 100 μg protein from the supernatant after RIPA lysis were transferred into a 96-well plate and 50 μL of 15 mM L-DOPA (Sigma) were added (total volume was adjusted to 100 μL using PBS, pH 6.8 (adjusted with 1 N HCl)). After 30 min incubation at 37 °C, dopachrome formation was determined by

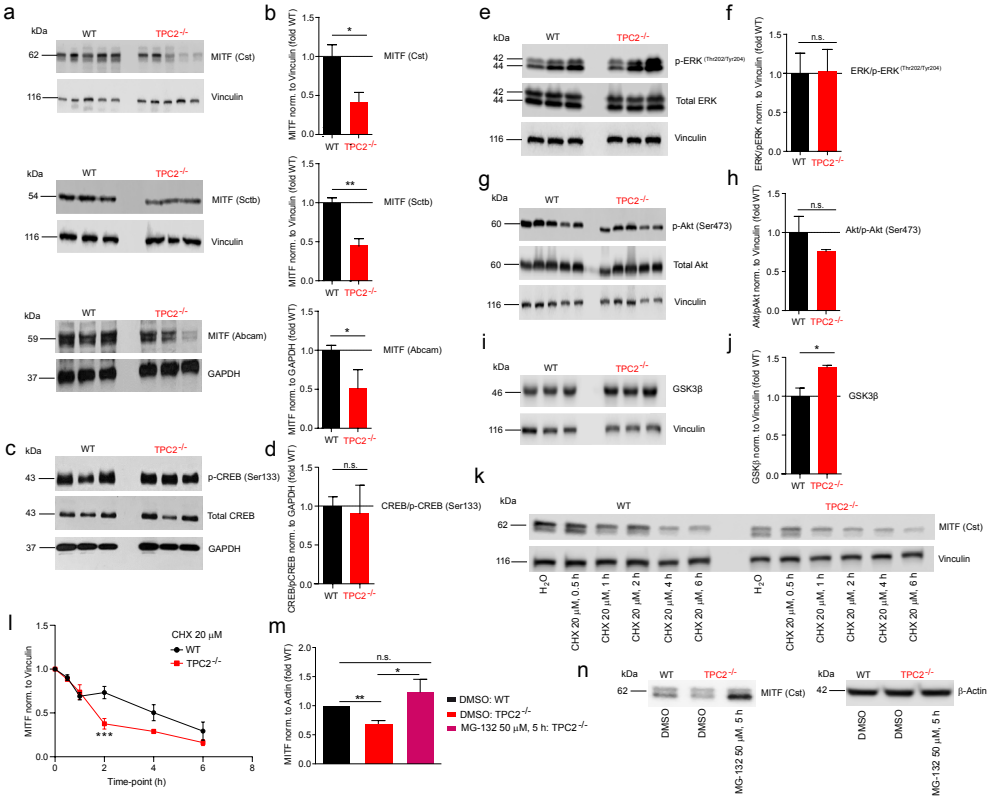

Figure 6. Effect of TPC2 knockout on MITF expression and expression of MITF regulator proteins using Western blot analysis and effect of protein synthesis and proteasome inhibition on MITF expression in WT and TPC2$^{-/-}$ MNT-1 cells. Western blot experiments were performed with WT and TPC2$^{-/-}$ MNT-1 cells as described in the Methods section. (**a**) and (**b**) WB experiments (**a**) and statistical analysis (**b**) showing MITF expression levels in WT and TPC2$^{-/-}$ cells detected using three different anti-MITF antibodies (Cst = Cell Signaling Technology, Sctb = Santa Cruz Biotechnology). (**c**–**j**) WB experiments (**c**, **e**, **g**, **i**) and statistical analyses (**d**, **f**, **h**, **j**) showing expression levels of CREB/pCREB, ERK/pERK, Akt/pAkt and GSK3β in WT and TPC2$^{-/-}$ cells detected using antibodies as described in the Methods section. Statistical significance was determined by Student's t-test. Shown are mean values ± SEM, (n = 3, each). *P < 0.05, **P < 0.01. (**k**–**l**) WB experiments (**k**) and statistical analysis (**l**) showing the effect of cycloheximide (CHX) on MITF degradation in WT and TPC2$^{-/-}$ MNT-1 cells. Statistical significance was determined by two-way ANOVA followed by Bonferroni multiple comparison test. Shown are mean values ± SEM, (n = 3, each). ***P < 0.001. (**m**) and (**n**) Rescue effect of the proteasome inhibitor MG-132 on MITF expression in TPC2$^{-/-}$ MNT-1 cells. Statistical significance was determined by Student's t-test. Shown are mean values ± SEM, (n = 3, each). *P < 0.05, **P < 0.01.

measuring the absorbance at 475 nm using a microplate reader (Tecan, Infinite M200 PRO). Tyrosinase activity (%) was calculated as follows: OD475 (sample) × 100 / OD475 (control).

Cell proliferation assay. Cell proliferation assay was performed in 96-well, flat-bottom microtiter plates (Sarstedt), in triplicates, and at a 5×10^3 cell density per well. Cells were seeded overnight, including cells measured as day zero control. Proliferation rate was assessed by incubation with CellTiter-Blue (Ctb, Promega, Mannheim, Germany) reagent for 3 h. Fluorescence was measured using a microplate reader at 560Ex/600Em (Tecan, Infinite M200 PRO).

Wound healing/migration assay. Wound healing assay was performed using 12-well plates (Sarstedt) at a density of 120,000 cells/well. Cells were incubated overnight, and a scratch was performed using a yellow pipet tip. Pictures were taken at 0, 24, 48, and 72 h with an inverted microscope (Leica DM IL LED) and using a

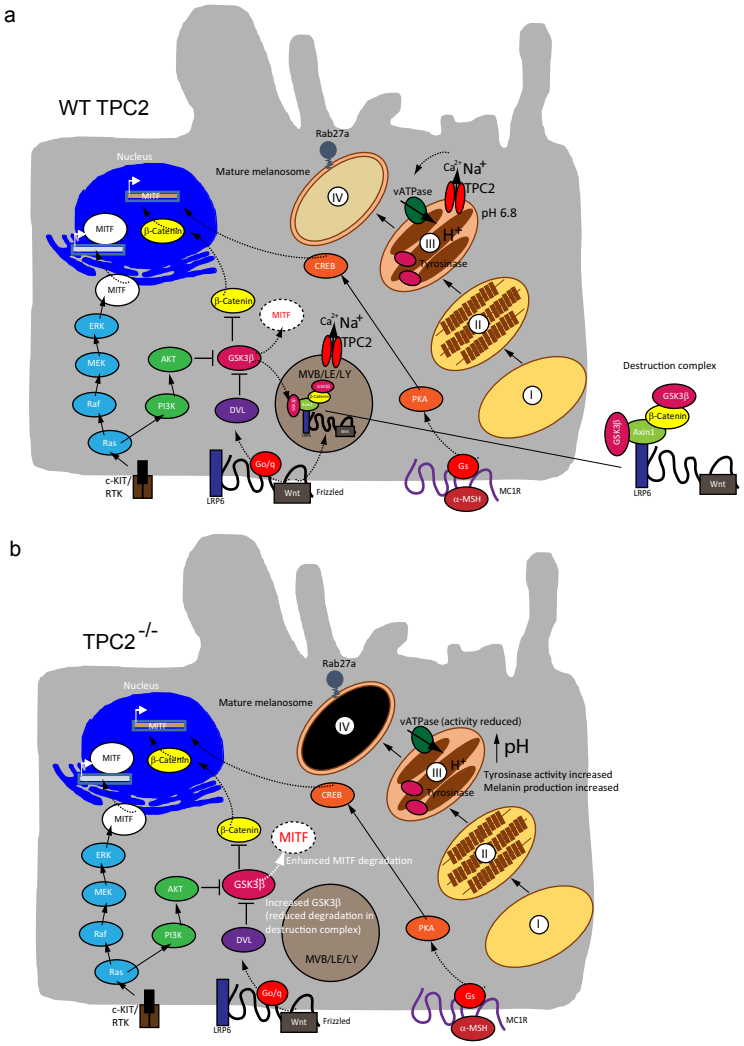

Figure 7. MITF signalling pathways and proposed effects in TPC2 knockout melanoma cells. (**a**) and (**b**) Cartoons showing MITF signalling pathways in WT (**a**) and TPC2$^{-/-}$ cells (**b**). Several pathways regulate MITF expression: RAS/RAF/MEK/ERK, PI3K/AKT, Wnt/GSK3β/β-Catenin, and MSH/CREB signalling pathways. GSK3β is a negative regulator of MITF expression and promotes proteasomal degradation of MITF. GSK3β degradation in endolysosomes is enhanced by Wnt signalling. Tyrosinase activity depends on melanosomal pH and is regulated by TPC2 activity in melanosomes. Loss-of-function of TPC2 in endolysosomes and melanosomes results in increased GSK3β and decreased MITF protein levels as well as increased tyrosinase activity and melanin content.

microscope camera (Leica DFC 3000 G). The wounded cell area was quantified using ImageJ 1.52a software and was subtracted from 0 h values.

Invasion assay. Transwell chambers in 24-well permeable support plates (Corning, #3421) were coated with Corning Matrigel basement membrane matrix (Corning, #354234) for 1.5 h. A total of 3×10^4 MNT-1 cells were seeded on top of the chambers in serum-free medium, and direct stimulation with compounds was per-

formed. The lower compartment contained the chemotactic gradient, medium with 10% FBS. Cells were allowed to migrate for 24 h, and were then fixed and stained with crystal violet containing methanol. Non-invaded cells were removed with Q-tips and pictures were taken of the bottom side of the membrane using an inverted microscope (Olympus CKX41) and an Olympus SC50 camera (Olympus). The number of invaded cells was quantified using ImageJ 1.52a software.

Western blotting. Western blot experiments were performed as described previously[32]. Briefly, cells were washed twice with 1 × PBS and pellets were collected. Total cell lysates were obtained by solubilizing in TRIS HCl 10 mM pH 8.0 and 0.2% SDS supplemented with protease and phosphatase inhibitors (Sigma). Protein concentrations were quantified via Bradford assay. Proteins were separated via a 10% sodium dodecyl sulphate polyacrylamide gel electrophoresis (SDS-PAGE; BioRad) and transferred to polyvinylidene difluoride (PVDF; BioRad) membranes. Membranes were blocked with 5% bovine serum albumin (Sigma) or milk diluted in Tris Buffered Saline supplemented with 0.5% Tween-20 (TBS-T) for 1 h at room temperature (RT), then incubated with primary antibody at 4 °C overnight. Then, membranes were washed with TBS-T and incubated with horseradish peroxidase (HRP) conjugated anti-mouse or anti-rabbit secondary antibody (Cell Signaling Technology) at RT for 1 h. Membranes were then washed and developed by incubation with Immobilon Crescendo Western HRP substrate (Merck) and by using an Odyssey imaging system (LI-COR Biosciences). Quantification was carried out using unsaturated images on ImageJ 1.52a software. The blots were cropped prior to hybridisation with antibodies against vinculin, GAPDH, or actin. The following antibodies were used: Phospho-p44/42 MAPK (Erk1/2) (Thr202/Tyr204) (Cell Signaling Technology, 1:1000, cat. #9106), p44/42 MAPK (Erk1/2) (Thr202/Tyr204) (Cell Signaling Technology, 1:1000, cat. #9102), Phospho-Akt (Ser473) (Cell Signaling Technology, 1:1000, cat. #4058), Akt (Cell Signaling Technology, 1:1000, cat. #9272), MITF (Santa Cruz Biotechnology, 1:1000, cat. #Sc-71588), MITF (Cell Signaling Technology, 1:1000, cat. #97800), MITF (Abcam, 1:1000, cat. #ab12039), GSK-3β (Cell Signaling Technology, 1:1000, cat. #9832), CREB and pCREB (Cell Signaling Technology, 1:1000, cat. #9197S and #9198S), ß-Actin (Santa Cruz Biotechnology, 1:1000, cat. #Sc-47778), Vinculin (Cell Signaling Technology, 1:1000, cat. #4650), GAPDH (Cell Signaling Technology, 1:1000, cat. #5174S), Anti-Mouse (Cell Signaling Technology, 1:10,000, cat. #7076), and Anti-Rabbit (Cell Signaling Technology, 1:10,000, cat. #7074).

RNA isolation and quantitative PCR. Total RNA was isolated from the cells using the RNeasy Mini Kit (Qiagen). Reverse Transcription was performed using the Revert First Strand cDNA Synthesis Kit (Thermo Fisher). Real-time quantitative Reverse Transcription PCR (qPCR) was performed in triplicates for each sample using the LightCycler 480 SYBR Green I Master and using the LightCycler 480 II machine (Roche Life Science), following the recommended parameters. HPRT was used as the housekeeping gene. The following human primer sets were used: Tyrosinase primers set A: fw: 5′-GTCTGTAGCCGATTGGAGGA -3′; rev: 5′- TGGGGT TCTGGATTTGTCAT -3′. Tyrosinase primers set B: fw: 5′-TGACAG TATTTTTGAGCAGTGG -3′; rev: 5′-GGTGCATTGGCTTCTGGATA-3′.

Plant material. Commercially available heartwood of *Dalbergia parviflora* was purchased from "Chao Krom Poe" herbal medicine dispensary in Bangkok in 2004. The samples were identified as wild *Dalbergia parviflora* at Princess Sirindhorn Wildlife Sanctuary, known as "Pa Phru To Daeng" which is a peat swamp forest in Mueang Narathiwat, Tak Bai, Su-ngai Kolok, and Su-ngai Padi districts of Narathiwat Province in Southern Thailand (06° 04′ 33.8″ N, 101° 57′ 49.3″ E). Data collection in the area was carried out with the authorization and guidelines of the National Research Council of Thailand (NRCT), and complied with the IUCN Policy Statement on Research Involving Species at Risk of Extinction and the Convention (1989) and the Convention on International Trade in Endangered Species of Wild Fauns and Flora (CITES, 1975). The plant was identified by Dr. Chawalit Niyomdham of the Forest Herbarium, National Park, Wildlife and Plant Conservation Department, Bangkok, Thailand. Its voucher specimen (number 68143)[33,34] was deposited at The Forest Herbarium, Bangkok, Thailand.

Extraction and isolation of flavonoids. The dried heartwood of *D. parviflora* (2 kg) was extracted three times with MeOH (3 × 20 L) at room temperature. The extracts were combined and concentrated under reduced pressure at 60 °C to yield 910 g of a viscous mass. A part of this concentrated extract (150 g) was chromatographed on a silica gel column (12 × 40 cm) and fractionated using chloroform-MeOH (98:2, 96:4, 94:6, 90:10, 15 L each). Fractions of 500 mL were collected and pooled by TLC analysis to yield a total of 26 combined fractions. Purification of these fractions as reported previously[33,34] gave various flavonoid compounds as summarized in Fig. S1. Purification of fraction 14 (8.9 g) using HPLC on a Develosil- Lop-ODS column (5 × 100 cm, flow rate, 45 mL/min with detection at 205 nm), with MeCN-H_2O (30:70) as the eluent gave MT-8 (pratensein) (715 mg) (t_R = 220 min). Purification of fraction 6 (3.1 g) using HPLC on a Develosil-Lop-ODS column (5 × 100 cm, flow rate: 45 mL/min with detection at 205 nm), with MeCN-H_2O (32:68) as the eluent, gave UM-9 (duartin) (39 mg) (t_R = 240 min). Both compounds were identified by comparison of their spectroscopic data with published values[35,36].

NMR analytical data. NMR spectra were measured on an JEOL alpha 400 (^{1}H-NMR: 400 MHz, ^{13}C-NMR: 100.4 MHz) spectrometer[33,34]. NMR-Spectra were measured in deuterated solvents and chemical shifts are reported in δ (ppm) relative to the internal standard tetramethylsilane (TMS) or the solvent peak at 35 °C, respectively. *J* values are given in hertz. Multiplicities are abbreviated as follows: s = singlet, d = doublet, t = triplet, q = quartet, m = multiplet. Signal assignments were carried out based on ^{1}H, ^{13}C, HMBC, HMQC

and COSY spectra. Inverse-detected heteronuclear correlations were measured using HMQC (optimized for $^{1}J_{C\text{-}H}$ = 145 Hz) and HMBC (optimized for $^{3}J_{C\text{-}H}$ = 8 Hz) pulse sequences with a pulsed field gradient. FABMS spectra were obtained on a JEOL JMS-700 using a *m*-nitrobenzyl alcohol matrix. Optical rotation was measured on a JASCO DIP-360 digital polarimeter. Column chromatography (CC) was performed with powdered silica gel (Kieselgel 60, 230–400 mesh, Merck KGaA, Darmstadt, Germany) and styrene–divinylbenzene (Diaion HP-20, 250–800 µm particle size, Mitsubishi Chemical Co., Ltd.). Precoated glass plates of silica gel (Kieselgel 60, F254, Merck Co., Ltd., Japan) and RP-18 (F254S, Merck KGaA) were used for TLC analysis. The TLC spots were visualized under UV light at a wavelength of 254 nm and sprayed with dilute H_2SO_4, followed by heating. HPLC separation was mainly performed with a JASCO model 887-PU pump, and isolates were detected by an 875-UV variable-wavelength detector. Reversed-phase columns for preparative separations (Develosil Lop ODS column, 10—20 µm, 5 × 50 × 2 cm; Nomura Chemical Co. Ltd., Aichi, Japan; flow rate 45 mL/min with detection at 205 nm) and semi-preparative separations (Capcell Pak ODS, 5 µm, 2 × 25 cm, Shiseido Fine Chemiacls Co. Ltd, Tokyo, Japan; flow rate 9 mL/min with detection at 205 nm) were used. MT-8 (pratensein): Amorphous powder; ^{1}H-NMR (400 MHz, $(CD_3)_2CO$) δ (ppm) = 13.03 (s, 1H, 5-H), 8.18 (s, 1H, 2-H), 7.13 (d, *J* = 2 Hz, 1H, 2′-H), 7.04 (dd, *J* = 9, 2 Hz, 1H, 6′-H), 6.99 (d, *J* = 9 Hz, 1H, 5′-H), 6.41 (d, *J* = 2 Hz, 1H, 8-H), 6.28 (d, *J* = 2 Hz, 1H, 6-H), 3.87 (s, 3H, 4′-OCH_3). ^{13}C-NMR (100.4 MHz, $(CD_3)_2CO$) δ (ppm) = 181.6 (C-4), 165.0 (C-7), 164.0 (C-5), 159.1 (C-9), 154.5 (C-2), 165.0 (C-7), 148.6 (C-4′), 147.3 (C-3′), 125.0 (C-1′), 121.3 (C-6′), 124.0 (C-3), 112.3 (C-5′), 106.3 (C-10), 99.9 (C-6), 94.5 (C-8), 56.4 (C-4′ OCH_3). FABMS *m/z* 323 [MNa] + (calcd for $C_{16}H_{12}O_6Na$). UM-9 (duartin): morphous powder; ^{1}H-NMR (400 MHz, $(CD_3)_2CO$) δ (ppm) = 6.70 (d, *J* = 9 Hz, 1H, 5′-H), 6.65 (d, *J* = 9 Hz, 1H, 6′-H), 6.64 (d, *J* = 9 Hz, 1H, 5-H), 6.40 (d, *J* = 9 Hz, 1H, 6-H), 4.29 (ddd, *J* = 10, 3, 2 Hz, 1H, 2 eq-H), 3.96 (t, *J* = 10 Hz, 1H, 2ax-H), 3.47 (dddd, *J* = 11, 10, 5, 3 Hz, 1H, 3-H), 2.91 (dd, *J* = 16, 11 Hz, 1H, 4ax-H), 3.47 (ddd, *J* = 16, 5, 2 Hz, 1H, 4 eq-H), 3.87 (s, 3H, 2′-OCH_3) , 3.81 (s, 3H, 4′-OCH_3) , 3.77 (s, 3H, 8-OCH_3). C-NMR (100.4 MHz, $(CD_3)_2CO$) δ (ppm) = 149.4 (C-7), 148.5 (C-9), 148.3 (C-4′), 146.5 (C-2′), 140.2 (C-3′), 136.6 (C-8), 128.0 (C-1′), 124.5 (C-6), 117.2 (C-6′), 115.4 (C-10), 108.4 (C-6), 107.9 (C-5′), 70.8 (C-2), 32.5 (C-2), 32.1 (C-3), 60.7 (C-8 OCH_3), 60.5 (C-2′ OCH_3), 56.4 (C-4′ OCH_3). $[\alpha]_D$ + 15.4° (*c* 1.0, $CHCl_3$). FABMS *m/z* 355 [MNa] + (calcd for $C_{18}H_{20}O_6Na$).

Statistical analysis

Details of statistical analyses and n values are provided in the "Materials and Methods" or the Figures or Figure legends. Statistical analyses were carried out using Origin 8 and GraphPad Prism 8. All error bars are depicted as mean ± SEM. Statistical significance is denoted on Figures as outlined in the legends.

Data availability

All data generated or analyzed during this study are included in this published article and its additional files.

Received: 15 October 2020; Accepted: 7 April 2021
Published online: 19 April 2021

References

1. Siegel, R. L., Miller, K. D. & Jemal, A. Cancer statistics, 2020. *CA Cancer J. Clin.* **70**(1), 7–30 (2020).
2. Krensel, M., Schäfer, I. & Augustin, M. Cost-of-illness of melanoma in Europe: A modelling approach. *J. Eur. Acad. Dermatol. Venereol.* **33**(Suppl 2), 34–45 (2019).
3. Premi S, Wallisch S, Mano CM, Weiner AB, Bacchiocchi A, Wakamatsu K, et al. Photochemistry. Chemiexcitation of melanin derivatives induces DNA photoproducts long after UV exposure. Science. 2015;347(6224):842–7.
4. Ambrosio, A. L., Boyle, J. A., Aradi, A. E., Christian, K. A. & Di Pietro, S. M. TPC2 controls pigmentation by regulating melanosome pH and size. *Proc. Natl. Acad. Sci. USA* **113**(20), 5622–5627 (2016).
5. Sulem, P. *et al.* Two newly identified genetic determinants of pigmentation in Europeans. *Nat. Genet.* **40**(7), 835–837 (2008).
6. Chao, Y. K. *et al.* TPC2 polymorphisms associated with a hair pigmentation phenotype in humans result in gain of channel function by independent mechanisms. *Proc. Natl. Acad. Sci. USA* **114**(41), E8595–E8602 (2017).
7. Nguyen, O. N. *et al.* Two-pore channel function is crucial for the migration of invasive cancer cells. *Cancer Res.* **77**(6), 1427–1438 (2017).
8. Parrington, J., Lear, P. & Hachem, A. Calcium signals regulated by NAADP and two-pore channels-their role in development, differentiation and cancer. *Int. J. Dev. Biol.* **59**(7–9), 341–355 (2015).
9. Favia, A. *et al.* VEGF-induced neoangiogenesis is mediated by NAADP and two-pore channel-2-dependent Ca2+ signaling. *Proc. Natl. Acad. Sci. USA* **111**(44), E4706–E4715 (2014).
10. Pafumi, I. *et al.* Naringenin impairs two-pore channel 2 activity and inhibits VEGF-induced angiogenesis. *Sci. Rep.* **7**(1), 5121 (2017).
11. Wang, W. *et al.* Up-regulation of lysosomal TRPML1 channels is essential for lysosomal adaptation to nutrient starvation. *Proc. Natl. Acad. Sci. USA* **112**(11), E1373–E1381 (2015).
12. D'Orazio, J. A. *et al.* Topical drug rescue strategy and skin protection based on the role of Mc1r in UV-induced tanning. *Nature* **443**(7109), 340–344 (2006).
13. Kolbe, L. *et al.* 4-n-butylresorcinol, a highly effective tyrosinase inhibitor for the topical treatment of hyperpigmentation. *J. Eur. Acad. Dermatol. Venereol.* **27**(Suppl 1), 19–23 (2013).
14. Gerndt S, Chen CC, Chao YK, Yuan Y, Burgstaller S, Scotto Rosato A, et al. Agonist-mediated switching of ion selectivity in TPC2 differentially promotes lysosomal function. Elife. 2020;9.
15. Romagnolo, D. F. & Selmin, O. I. Flavonoids and cancer prevention: a review of the evidence. *J. Nutr. Gerontol. Geriatr.* **31**(3), 206–238 (2012).
16. Batra P, Sharma AK. Anti-cancer potential of flavonoids: recent trends and future perspectives. 3 Biotech. 2013;3(6):439–59.
17. Abotaleb M, Samuel SM, Varghese E, Varghese S, Kubatka P, Liskova A, et al. Flavonoids in Cancer and Apoptosis. Cancers (Basel). 2018;11(1).
18. Yokoyama, S. *et al.* A novel recurrent mutation in MITF predisposes to familial and sporadic melanoma. *Nature* **480**(7375), 99–103 (2011).

19. Garraway, L. A. *et al.* Integrative genomic analyses identify MITF as a lineage survival oncogene amplified in malignant melanoma. *Nature* **436**(7047), 117–122 (2005).
20. Hocker, T. L., Singh, M. K. & Tsao, H. Melanoma genetics and therapeutic approaches in the 21st century: Moving from the benchside to the bedside. *J. Invest. Dermatol.* **128**(11), 2575–2595 (2008).
21. Ploper, D. *et al.* MITF drives endolysosomal biogenesis and potentiates Wnt signaling in melanoma cells. *Proc. Natl. Acad. Sci. USA.* **112**(5), E420–E429 (2015).
22. Kao SH, Wang WL, Chen CY, Chang YL, Wu YY, Wang YT, et al. Analysis of Protein Stability by the Cycloheximide Chase Assay. Bio Protoc. 2015;5(1).
23. Grimm, C. *et al.* High susceptibility to fatty liver disease in two-pore channel 2-deficient mice. *Nat. Commun.* **5**, 4699 (2014).
24. Ruas, M. *et al.* TPC1 has two variant isoforms, and their removal has different effects on endolysosomal functions compared to loss of TPC2. *Mol. Cell Biol.* **34**(21), 3981–3992 (2014).
25. Sakurai Y, Kolokoltsov AA, Chen CC, Tidwell MW, Bauta WE, Klugbauer N, et al. Ebola virus. Two-pore channels control Ebola virus host cell entry and are drug targets for disease treatment. Science. 2015;347(6225):995–8.
26. Syed, D. N. *et al.* Inhibition of human melanoma cell growth by the dietary flavonoid fisetin is associated with disruption of Wnt/β-catenin signaling and decreased Mitf levels. *J. Invest. Dermatol.* **131**(6), 1291–1299 (2011).
27. Kosiniak-Kamysz, A. *et al.* Increased risk of developing cutaneous malignant melanoma is associated with variation in pigmentation genes and VDR, and may involve epistatic effects. *Melanoma Res.* **24**(4), 388–396 (2014).
28. Bellono, N. W., Escobar, I. E. & Oancea, E. A melanosomal two-pore sodium channel regulates pigmentation. *Sci. Rep.* **6**, 26570 (2016).
29. Chen, C. C. *et al.* Small molecules for early endosome-specific patch clamping. *Cell Chem. Biol.* **24**(7), 907-916.e4 (2017).
30. Chen, C. C. *et al.* Patch-clamp technique to characterize ion channels in enlarged individual endolysosomes. *Nat. Protoc.* **12**(8), 1639–1658 (2017).
31. An, S. M., Lee, S. I., Choi, S. W., Moon, S. W. & Boo, Y. C. p-Coumaric acid, a constituent of Sasa quelpaertensis Nakai, inhibits cellular melanogenesis stimulated by alpha-melanocyte stimulating hormone. *Br. J. Dermatol.* **159**(2), 292–299 (2008).
32. Scotto Rosato A, Montefusco S, Soldati C, Di Paola S, Capuozzo A, Monfregola J Polishchuk E, Amabile A, Grimm C, Lombardo A, De Matteis MA, Ballabio A, Medina DL. TRPML1 links lysosomal calcium to autophagosome biogenesis through the activation of the CaMKKβ/VPS34 pathway. Nature Commun. 2019;10:5630.
33. Umehara, K. *et al.* Estrogenic constituents of the heartwood of Dalbergia parviflora. *Phytochemistry* **69**(2), 546–552 (2008).
34. Umehara, K. *et al.* Flavonoids from the heartwood of the Thai medicinal plant Dalbergia parviflora and their effects on estrogenic-responsive human breast cancer cells. *J. Nat. Prod.* **72**(12), 2163 (2009).
35. Matsuura S, Tanaka T, linuma, Tanaka, Himuro N, et al. Constituents of useful plants. I.X. Constituents of Arachis hypogaea L. Yakugaku Zasshi 1983;103:907–1000.
36. Ollis WD, Suthernland, IO, Alves, HM, Gottlieb. O. R.Duartin, an isolflavan from Macherium opacum. Phytochemistry 1978;17:1401–1403.

Acknowledgements

This work was supported, in part, by funding of the German Research Foundation (SFB/TRR152 TP04 to C.G., DFG grant GR-4315/2-1 to C.G., DAAD Project 57453751 to C.G., TRF Project 4.E.CU/59/E.1 to W.D., Chulalongkorn University Natural Product Biotechnology Research Unit GRU 6205633003-1 to W.D., and NIH grant GM-125619 to S.D.P.

Author contributions

P.N., C.A., R.T., C.-C.C., A.S.R., W.B., and Y.-K.C. performed experiments and analysed data. S.D.P, A.F. and K.U. provided reagents and material. C.G and W.D. wrote the manuscript and provided funding. K.B., M.B., and A.M.V. edited the manuscript. All of the authors discussed the results and commented on the manuscript.

Funding

Open Access funding enabled and organized by Projekt DEAL.

Competing interests

The authors declare no competing interests.

Additional information

Supplementary Information The online version contains supplementary material available at https://doi.org/10.1038/s41598-021-88196-6.

Correspondence and requests for materials should be addressed to W.D.-E. or C.G.

Reprints and permissions information is available at www.nature.com/reprints.

Publisher's note Springer Nature remains neutral with regard to jurisdictional claims in published maps and institutional affiliations.

Supplementary Information

Flavonoids increase melanin production and reduce proliferation, migration and invasion of melanoma cells by blocking endolysosomal/melanosomal TPC2

Ponsawan Netcharoensirisuk[1,2#], Carla Abrahamian[1#], Rachel Tang[1#], Cheng-Chang Chen[3], Anna Scotto Rosato[1], Wyatt Beyers[4], Yu-Kai Chao[1], Antonio Filippini[5], Santiago Di Pietro[4], Karin Bartel[3], Martin Biel[3], Angelika M. Vollmar[3], Kaoru Umehara[6], Wanchai De-Eknamkul[2*], Christian Grimm[1*]

Fig. S1. Western blots of tyrosinase, Dct (dopachrome tautomerase, TYRP2), Rab27a, and PMEL (premelanosome protein) in WT and TPC2$^{-/-}$ MNT-1 cells. Western blot experiments were performed with WT and TPC2$^{-/-}$ MNT-1 cells as described in the Methods section. (a-f) Representative WB experiments (a, c, e) and statistical analysis (b, d, f) showing tyrosinase, Dct and PMEL expression levels in WT and TPC2$^{-/-}$ cells detected using the following primary and secondary antibodies: Mouse anti tyrosinase (Cat No. SC20035, Santa Cruz Biotechnology, 1:500 or 1:1000), rabbit anti Dct (Abcam Cat No. ab74073, 1:2000), mouse anti Rab27a (Cat No. SC81914, Santa Cruz Biotechnology, 1:1000), mouse anti pmel17 (Cat No. SC377325, Santa Cruz Biotechnology, 1:1000), rabbit anti GAPDH (Cat No. 2118S, Cell Signaling Technology, 1:1000), and mouse anti ß-Actin (Protein Tech, 1:40000, Cat No. 66009-1-Ig). Secondary antibodies: anti-rabbit IgG HRP-Linked (Cat No. 7074S, Cell Signaling Technology, 1:1000), anti-mouse IgG HRP-Linked (Cat No. 7076S, Cell Signaling Technology, 1:1000), and anti-mouse (Sigma, 1:10000, cat. # GENA931). (g) qRT-PCR results using primer sets A and B as described in the Methods section to determine tyrosinase transcript levels in WT and TPC2-/- MNT-1 cells. Statistical significance was determined by Student's t-test. Shown are mean values ± SEM, (n = 3, each). *P<0.05, ***P<0.001.

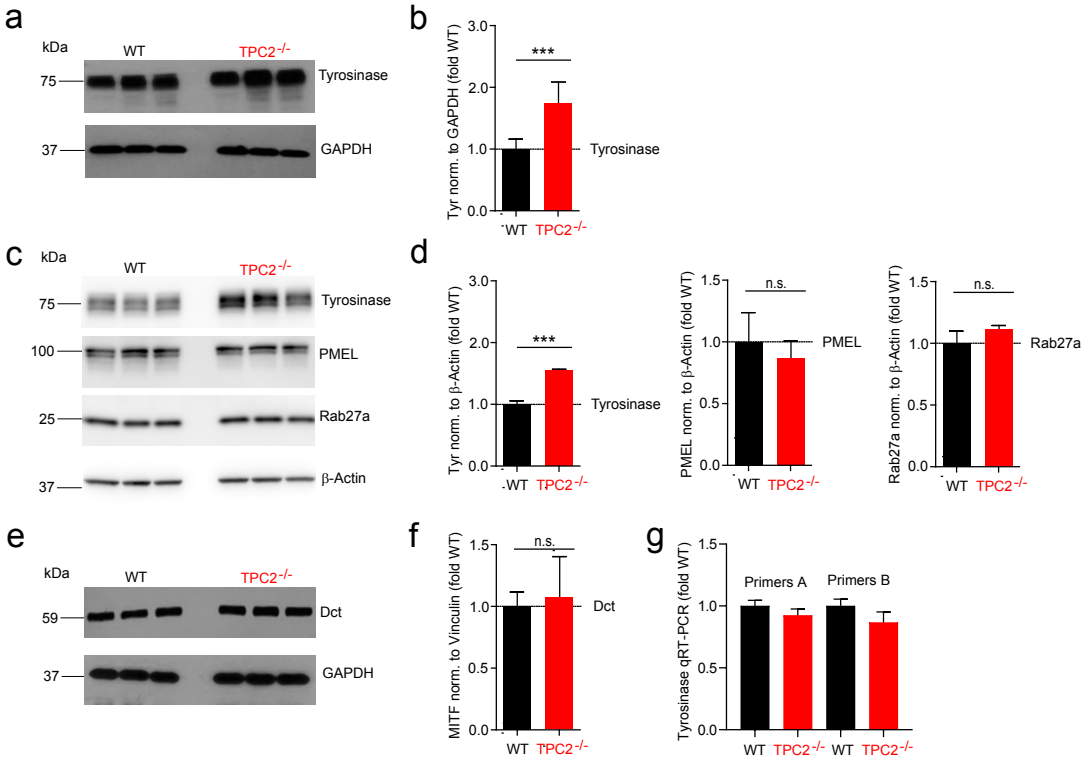

Fig. S2. Chemical structures of isolated flavonoids. All flavonoids used in the melanin content screens in B16F10 mouse melanoma and human MNT-1 melanoma cells are shown.

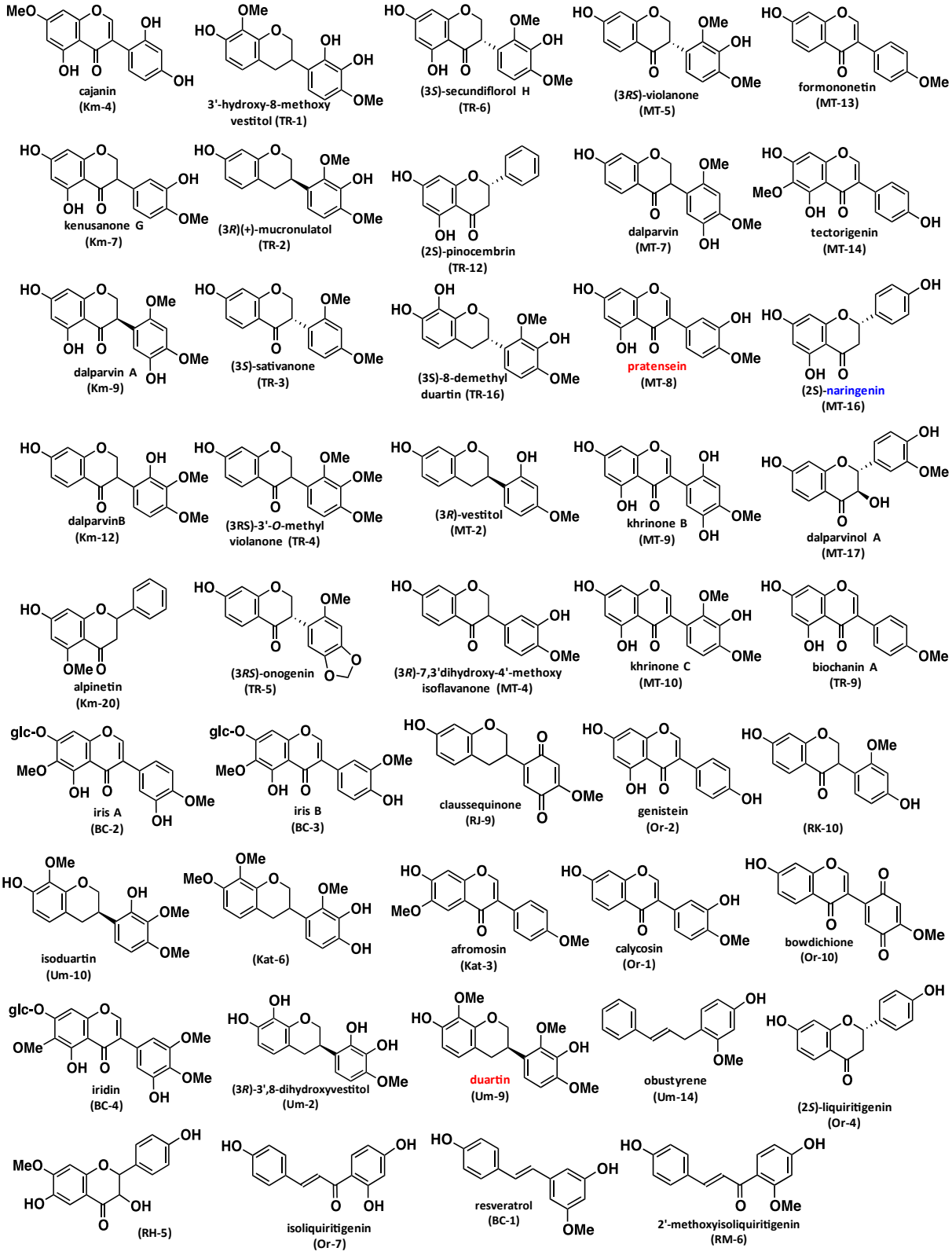
cajanin (Km-4)
3'-hydroxy-8-methoxy vestitol (TR-1)
(3S)-secundiflorol H (TR-6)
(3RS)-violanone (MT-5)
formononetin (MT-13)
kenusanone G (Km-7)
(3R)(+)-mucronulatol (TR-2)
(2S)-pinocembrin (TR-12)
dalparvin (MT-7)
tectorigenin (MT-14)
dalparvin A (Km-9)
(3S)-sativanone (TR-3)
(3S)-8-demethyl duartin (TR-16)
pratensein (MT-8)
(2S)-naringenin (MT-16)
dalparvinB (Km-12)
(3RS)-3'-O-methyl violanone (TR-4)
(3R)-vestitol (MT-2)
khrinone B (MT-9)
dalparvinol A (MT-17)
alpinetin (Km-20)
(3RS)-onogenin (TR-5)
(3R)-7,3'dihydroxy-4'-methoxy isoflavanone (MT-4)
khrinone C (MT-10)
biochanin A (TR-9)
iris A (BC-2)
iris B (BC-3)
claussequinone (RJ-9)
genistein (Or-2)
(RK-10)
isoduartin (Um-10)
(Kat-6)
afromosin (Kat-3)
calycosin (Or-1)
bowdichione (Or-10)
iridin (BC-4)
(3R)-3',8-dihydroxyvestitol (Um-2)
duartin (Um-9)
obustyrene (Um-14)
(2S)-liquiritigenin (Or-4)
(RH-5)
isoliquiritigenin (Or-7)
resveratrol (BC-1)
2'-methoxyisoliquiritigenin (RM-6)

Fig S3. Concentration and time dependent effects of flavonoids on melanin content and tyrosinase activity in B16F10 cells. (a) and (b) Examples of experiments as quantified in Figure 1b. Cells were cultured in 96 well plates for 4-5 days until melanin content was assessed using a microplate reader at 405 nm. (c) and (d) Quantification of the time and concentration dependent effects of MT-8 on tyrosinase activity (c) and melanin content (d). (e) and (f) Quantification of the time and concentration dependent effects of UM-9 on tyrosinase activity (e) and melanin content (f). (g-i) Melanin content in WT and TPC2$^{-/-}$ MNT1 cells after treatment with different concentrations of MT-8, UM-9, and NAR. Statistical significance was determined by two-way ANOVA followed by Bonferroni multiple comparisons test. Shown are mean values ± SEM, (n = 3, each). *P<0.05, **P<0.01, ***P<0.001.

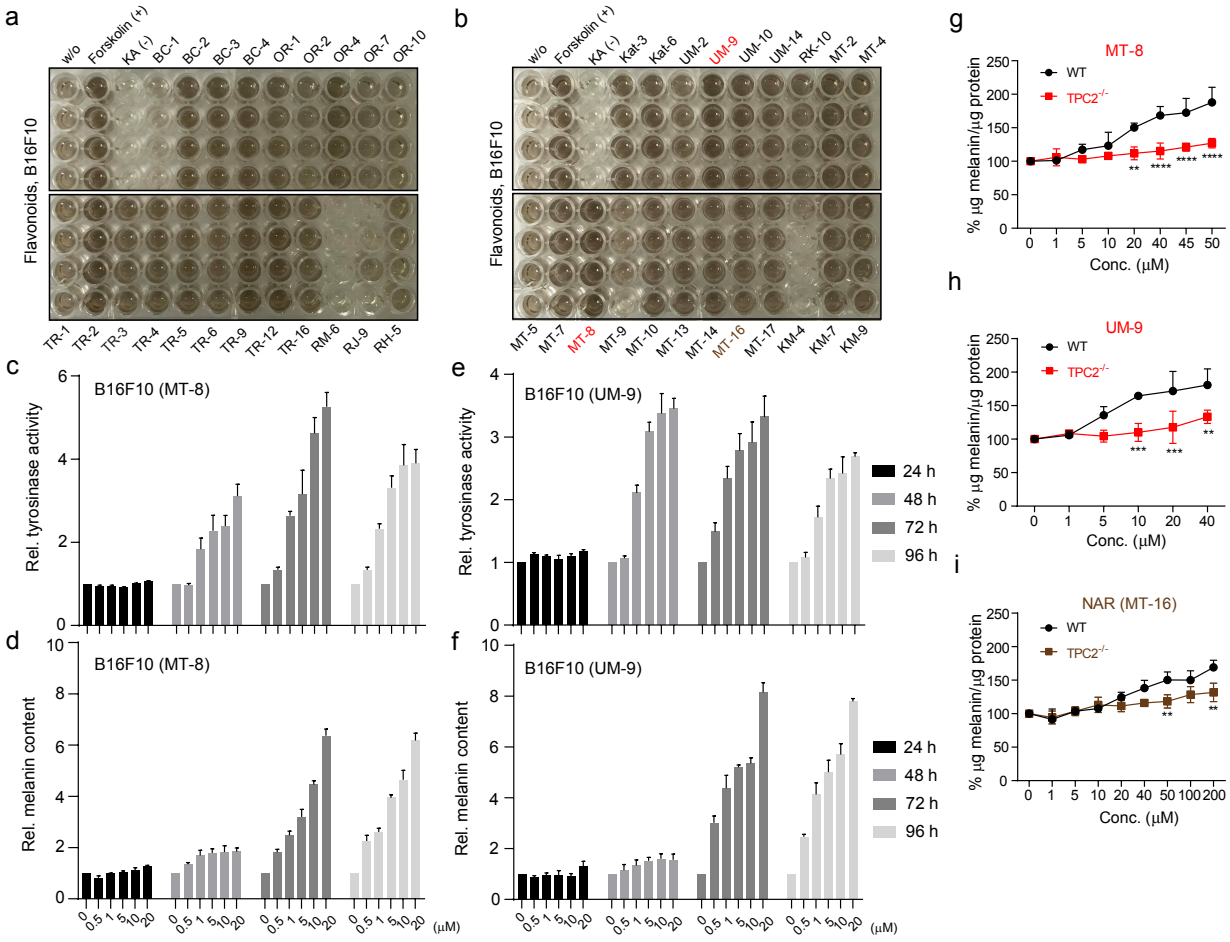

Figure S4. Whole western blots of proteins as shown in Figure 6 and Figure S1.

Fig.6a upper panel

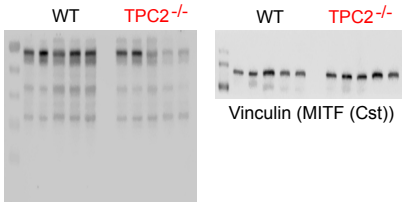

Fig.6a middle panel

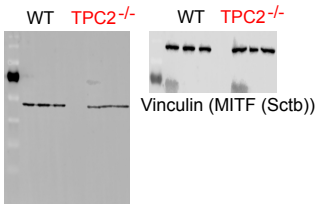

Fig.6a lower panel

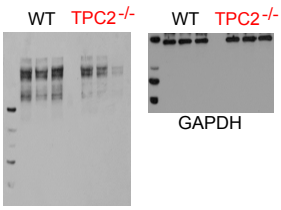

Fig.6c

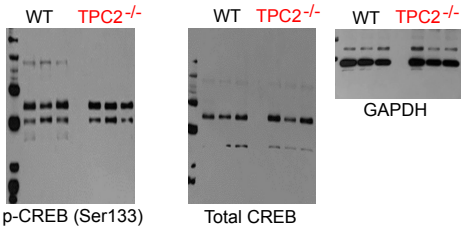

Fig.6e

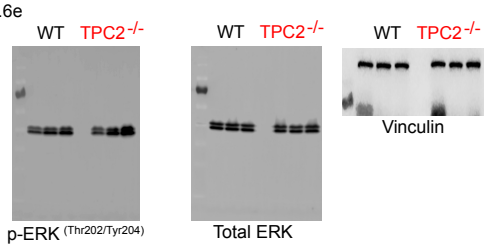

Fig.6g

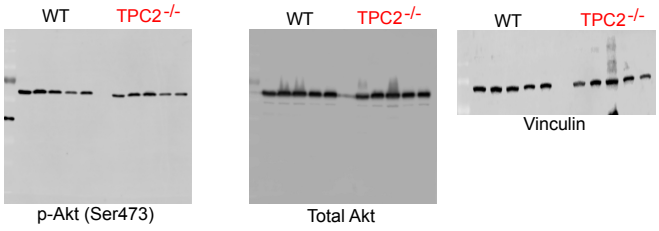

Fig.6i

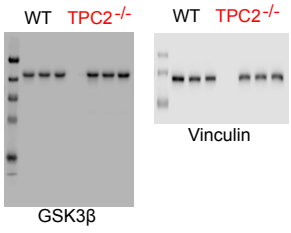

Fig.6k

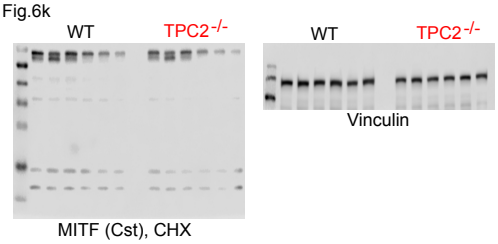

Fig.6n

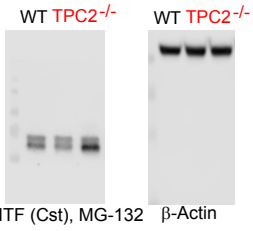

Suppl. Fig.S1a

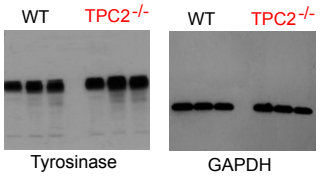

Suppl. Fig.S1e

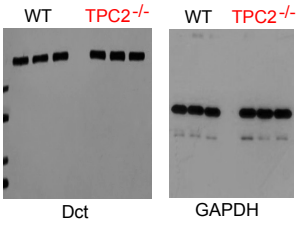

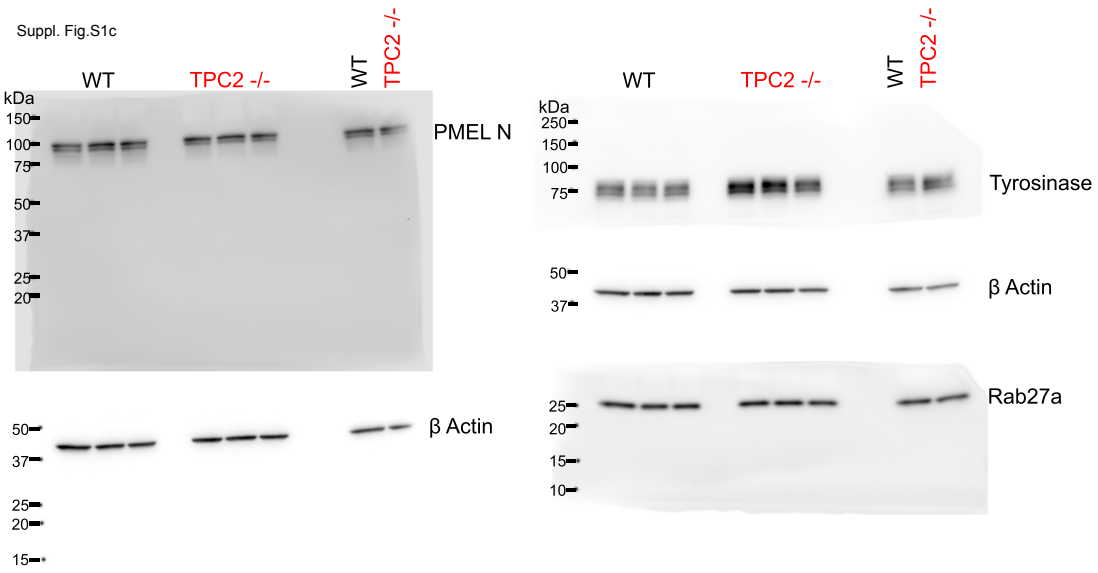
Suppl. Fig.S1c
WT
TPC2 -/-
WT
TPC2 -/-
kDa
150
100
75
50
37
25
20
PMEL N
50
37
25
20
15
β Actin
WT
TPC2 -/-
WT
TPC2 -/-
kDa
250
150
100
75
Tyrosinase
50
37
β Actin
25
20
15
10
Rab27a

Paper II: Summary and Contributions

Segregated cation flux by TPC2 biases Ca^{2+} signaling through lysosomes

Yu Yuan, Dawid Jaślan, Taufiq Rahman, Stephen R. Bolsover, Vikas Arige, Larry E. Wagner II, **Carla Abrahamian**, Rachel Tang, Marco Keller, Jonas Hartmann, Anna S. Rosato, Eva-Maria Weiden, Franz Bracher, David I. Yule, Christian Grimm*, & Sandip Patel*

TPC2 has drawn attention as a potential target in neurodegenerative disorders and cancer[21, 102]. However, its activation mechanisms have been a subject of debate, leading to intriguing discoveries in recent years. In animals, TPC2 has been described both as a Na^+ channel stimulated by the phosphoinositide, $PI(3,5)P_2$ and as a Ca^{2+}-permeable channel activated by the calcium-mobilizing messenger, NAADP. In 2020, our laboratory provided significant insights into the ion selectivity of TPC2 (Gerndt et al., 2020) by synthesizing novel lipophilic TPC2 agonists, with TPC2-A1-N favoring increased Ca^{2+} permeability mimicking activation by NAADP, and TPC2-A1-P promoting greater Na^+-selectivity akin to $PI(3,5)P_2$. This work challenged the notion of a fixed selectivity by demonstrating the agonist-dependent ion selectivity of TPC2 and the distinct effects on lysosomal activity induced by the agonists, proposing that TPC2 can mediate different cellular responses through specific ion fluxes[12]. Our study sought to investigate the co-application of TPC2-A1-N and TPC2-A1-P. The co-simulation with the two agonists evoked a remarkably potentiated Ca^{2+} response compared to TPC2-A1-N or TPC2-A1-P alone, as shown in our Ca^{2+} imaging experiments. To confirm this effect, whole-cell and endolysosomal patch clamp experiments were conducted under bi-ionic conditions, with Na^+ in the bath solution and Ca^{2+} in the pipet solution. Significantly larger inward Ca^{2+} currents were induced with the co-application or sequential application of either compound, compared to their individual application, with no effect on the outward Na^+ currents. This was corroborated by the co-application of endogenous ligands $PI(3,5)P_2$ and NAADP, indicating that TPC2 exhibits selective modification of its Ca^{2+} permeability upon co-stimulation. These findings suggest the potential of $PI(3,5)P_2$ to function as a Ca^{2+}-mobilizing messenger when NAADP is present. Our results provide clear evidence that upon co-activation with the agonists TPC2-A1-N or TPC2-A1-P, the Na^+ permeability of TPC2 remains independently regulated. In contrast, its Ca^{2+} permeability is selectively enhanced, leading to robust global Ca^{2+} signals in various cell types. To support these findings, I performed a gene expression profiling in different cell lines and identified the SK-MEL-5 cell line with one of the highest TPC2 expressions. Indeed, upon co-activation of TPC2-A1-N or TPC2-A1-P, the initially evoked Ca^{2+} signals in the SK-MEL-5 cell line were twice that of Hela cells. To assess the on-target effects, I generated a CRISPR/Cas9 KO of TPC2 in this cell line. The process involved several steps, including guide RNA design, cloning, transfection, clonal expansion, validation, and testing off-target effects. While the creation of a full channel knockout posted an initial challenge, targeting the early Exon 3 was successful. Indeed, the KO cells exhibited diminished currents and Ca^{2+} responses to the agonist combinations. In sum, our study sheds new light on the intricate interplay of TPC2 with its ligands, revealing its favorability and selectivity to enhance Ca^{2+} permeability rather than Na^+ to adapt to specific signaling cues. This multifaceted behavior has significant consequences on cellular responses, particularly in lysosomal activity. Understanding the dynamic nature of TPC2 opens up exciting possibilities for developing targeted therapies aimed at regulating its function in various diseases.

Paper II

nature communications

Article

https://doi.org/10.1038/s41467-022-31959-0

Segregated cation flux by TPC2 biases Ca^{2+} signaling through lysosomes

Received: 14 February 2022

Accepted: 12 July 2022

Published online: 02 August 2022

Check for updates

Yu Yuan[1], Dawid Jaślan[2], Taufiq Rahman[3], Stephen R. Bolsover[1], Vikas Arige[4], Larry E. Wagner II[4], Carla Abrahamian[2], Rachel Tang[2], Marco Keller[5], Jonas Hartmann[1], Anna S. Rosato[2], Eva-Maria Weiden[2], Franz Bracher[5], David I. Yule[4], Christian Grimm[2] ✉ & Sandip Patel[1] ✉

Two-pore channels are endo-lysosomal cation channels with malleable selectivity filters that drive endocytic ion flux and membrane traffic. Here we show that TPC2 can differentially regulate its cation permeability when co-activated by its endogenous ligands, NAADP and $PI(3,5)P_2$. Whereas NAADP rendered the channel Ca^{2+}-permeable and $PI(3,5)P_2$ rendered the channel Na^+-selective, a combination of the two increased Ca^{2+} but not Na^+ flux. Mechanistically, this was due to an increase in Ca^{2+} permeability independent of changes in ion selectivity. Functionally, we show that cell permeable NAADP and $PI(3,5)P_2$ mimetics synergistically activate native TPC2 channels in live cells, globalizing cytosolic Ca^{2+} signals and regulating lysosomal pH and motility. Our data reveal that flux of different ions through the same pore can be independently controlled and identify TPC2 as a likely coincidence detector that optimizes lysosomal Ca^{2+} signaling.

Sensing signals and coordinating the ensuing outputs is vital for maintaining cell and tissue homeostasis. To this end, cells possess a battery of ion channels on both the plasmalemma and in organelles that open in response to specific cues. It is clear now that the lysosome, traditionally viewed as the cell's recycling center, is a signaling organelle endowed with a number of ion channels linked to diseases[1–3]. Understanding how these channels are regulated is vital to understand cell function and dysfunction.

Two-pore channels (TPCs) are a class of evolutionarily ancient, ubiquitously expressed ion channels that localize to lysosomes and other acidic organelles in animal cells[4–6]. Here, they regulate a diverse range of processes including both vesicular[7] and non-vesicular[8] membrane traffic. They are fast emerging as drug targets in disorders such as viral infection[9,10] and cancer[11]. But despite such considerable patho-physiological importance, their activation mechanisms are ill-defined. On the one hand, they are described as Ca^{2+}-permeable channels activated by NAADP[12–16]. NAADP is a water soluble Ca^{2+} mobilizing messenger that triggers Ca^{2+} release primarily from acidic organelles to regulate numerous Ca^{2+}-dependent outputs[17,18]. But on the other hand, TPCs are described as Na^+ channels activated by $PI(3,5)P_2$[19–21]. $PI(3,5)P_2$ is a minor, endo-lysosomal-enriched phosphoinositide produced by the PIKfyve complex that regulates organelle size, autophagy and endocytic membrane traffic[22,23].

Our recent work showed that the ion selectivity of TPC2 is not fixed, as is generally assumed for ion channels, but rather agonist-dependent[24]. This unique property reconciles contradictory findings relating to gating and ionic permeability of TPC2. Discovery of lipophilic TPC2 agonists revealed that one of these molecules rendered the channel more Ca^{2+}-permeable mimicking the effect of NAADP whereas the other rendered the channel more Na^+-selective mimicking the effect of $PI(3,5)P_2$[24]. These agonists also revealed distinct effects on lysosomal activity in cells introducing a paradigm whereby the same ion channel can mediate unique cellular outputs through distinct ion fluxes. This raises the question of how TPC2 behaves under physiological conditions when it is simultaneously exposed to conflicting endogenous cues.

[1]Department of Cell and Developmental Biology, University College London, London, UK. [2]Walther Straub Institute of Pharmacology and Toxicology, Faculty of Medicine, Ludwig-Maximilians University, Munich, Germany. [3]Department of Pharmacology, University of Cambridge, Cambridge, UK. [4]Department of Pharmacology and Physiology, University of Rochester, Rochester, NY, USA. [5]Department of Pharmacy—Center for Drug Research, Ludwig-Maximilians University, Munich, Germany. ✉e-mail: christian.grimm@med.uni-muenchen.de; patel.s@ucl.ac.uk

Our results show that the Ca^{2+} but not Na^+ permeability of TPC2 is selectively enhanced when the channel is co-activated by its ligands. Ca^{2+} and Na^+ flux by TPC2 can therefore be independently controlled. Such regulation translates into robust global Ca^{2+} signals in a number of cell types but not in TPC2 knockout cells, impacting lysosomal activity in a synergistic way. We suggest TPC2 as a functional coincidence detector that tunes its ionic behavior on demand to suit signaling needs.

Results

TPC2 agonists synergistically activate TPC2

NAADP and $PI(3,5)P_2$ have dramatically different effects on TPC2 rendering the channel either more Ca^{2+}-permeable or more Na^+-selective[24]. What happens when the channel is co-activated (Fig. 1a)? To answer this, we first used cells expressing the genetically-encoded Ca^{2+} indicator GCaMP6s fused to the cytosolic C-terminus of TPC2 to record release of Ca^{2+} into the cytosol. Stimulation of these cells with the cell-permeable NAADP mimetic TPC2-A1-N evoked a readily recordable Ca^{2+} response whereas the $PI(3,5)P_2$ mimetic TPC2-A1-P induced only a minor one (Fig. 1b). Surprisingly, co-addition of the agonists evoked a markedly potentiated Ca^{2+} response (Fig. 1b–d). This effect was dependent on TPC2 containing a functional pore because little Ca^{2+} release could be detected in parallel experiments using cells expressing a 'pore-dead' mutant, $TPC2^{L265P}$ (Fig. 1e, f) which substantially reduces (>10-fold) but does not eliminate conductance[25].

Because release of lysosomal Ca^{2+} results in secondary release from the ER[26], we also examined the effects of co-stimulating TPC2 in cells stably expressing TPC2 targeted to the plasma membrane ($TPC2^{L11A/L12A}$). In this format, TPC2 behaves as an influx channel uncoupled from ER Ca^{2+} release[25]. Figure 1g, h compares Ca^{2+} signals in response to TPC2-A1-N and TPC2-A1-P alone and in combination in cells loaded with the Ca^{2+}-indicator Fura-2. This analysis revealed that the TPC2-A1-P response was characteristically delayed. Strikingly, when the agonists were co-applied to cells, the Ca^{2+} signals were markedly accelerated (Fig. 1g). These data were quantified by measuring the initial rate of Ca^{2+} influx. As summarized in Fig. 1h, there was little influx in response to TPC2-A1-P whereas that of the combination was ~4-fold increased relative to TPC2-A1-N. We also performed experiments with $TPC2^{L11A/L12A}$-expressing cells loaded with the low affinity Ca^{2+} indicator Fura-2 FF (Fig. 1i, j). With this dye, there was little detectable influx over the first 5 min when cells were stimulated with TPC2-A1-N or TPC2-A1-P (Fig. 1i) in accord with its higher K_d for Ca^{2+} (5.5 μM) relative to Fura-2 (0.14 μM). But there was substantial influx in response to the agonist combination (Fig. 1i, j) thereby again revealing marked synergism.

To further characterize the effect of the agonist combination, we performed sequential additions. We stimulated $TPC2^{L11A/L12A}$ with TPC2-A1-N after TPC2-A1-P to mimic receptor-mediated signaling events where NAADP levels demonstrably rise[27]. As shown in Fig. 1k, TPC2-A1-N induced robust Ca^{2+} influx. This signal was significantly faster than the combination applied simultaneously (Fig. 1l). Similar results were obtained when the order was reversed. In these experiments, we used Fura-FF to prevent confounding issues of elevated baselines (due to TPC2-A1-N-mediated Ca^{2+} influx) in the quantification of subsequent entry. Under these conditions, TPC2-A1-P again markedly increased Ca^{2+} influx following TPC2-A1-N stimulation over and above that of the combination applied simultaneously (Fig. 1m, n).

Figure 1o shows the results of automated plate reading where the effect of systematically increasing the concentration of TPC2-A1-P on the Ca^{2+} responses to increasing concentrations of TPC2-A1-N was performed. This analysis summarized in Fig. 1p reveals that synergism is concentration-dependent and saturable.

Because the binding site for TPC2-A1-P likely overlaps with that of $PI(3,5)P_2$[24], we compared agonist combination responses in cells transiently expressing a 'lipid-dead' mutant, $TPC2^{K204}$. As shown in Fig. 1q–r, Ca^{2+} influx was significantly reduced by the mutation.

In sum, multiple lines of evidence indicate that TPC2 agonists directly activate Ca^{2+} flux through TPC2 in a synergistic way.

Cation permeability of TPC2 is independently regulated

To further probe the properties of co-activated TPC2, we examined the effects of the agonists on Na^+ fluxes. To do this, we measured cytosolic Na^+ using the ratiometric Na^+ indicator SBFI in cells stably expressing $TPC2^{L11A/L12A}$. As shown in Fig. 2a, b, TPC2-A1-N and TPC2-A1-P (both at 30 μM) induced Na^+ signals. These signals were reduced upon replacement of extracellular Na^+ with NMDG (Supplementary Fig. 1a–d) and in cells transiently expressing pore-dead TPC2 at the cell surface (Supplementary Fig. 1e–h) consistent with TPC2-mediated Na^+ influx. Figure 2c, d compares the Na^+ and Ca^{2+} signals evoked by each agonist. The kinetics and the amplitude of the Na^+ signals evoked by TPC2-A1-N and TPC2-A1-P were similar and thus in marked contrast to the Ca^{2+} signals where TPC2-A1-N evoked a more rapid response (Fig. 2c). The absolute rates of Na^+ and Ca^{2+} influx were therefore more similar for TPC2-A1-N than TPC2-A1-P (Fig. 2d). Strikingly, co-addition of the agonists did not affect the Na^+ signals at two different combinations (Fig. 2a, b).

The differential effects of the agonist combination on Ca^{2+} and Na^+ influx raised the intriguing possibility that TPC2 selectively alters its Ca^{2+} permeability upon co-stimulation. To test this directly, we performed macro-patch recording of agonist-evoked currents from cells stably expressing $TPC2^{L11A/L12A}$ under bi-ionic conditions using Ca^{2+} in the pipette solution (extracellular/luminal face of TPC2) and Na^+ in the bath (cytosolic face of TPC2). As shown in Fig. 2e, TPC2-A1-N induced an inward Ca^{2+} current and an outward Na^+ current. So too did TPC2-A1-P but the Ca^{2+} current was negligible (Fig. 2e, f). Stimulation of $TPC2^{L11A/L12A}$ with TPC2-A1-N after TPC2-A1-P induced a significant increase in Ca^{2+} current relative to TPC2-A1-N alone (Fig. 2e, f) consistent with enhanced Ca^{2+} signals (Fig. 1). But it had little effect on the Na^+ current (Fig. 2e, f). Essentially similar results were obtained when the order of the additions was reversed (Fig. 2e, f). Thus, stimulation of $TPC2^{L11A/L12A}$ with TPC2-A1-P after TPC2-A1-N induced a larger Ca^{2+} current but the Na^+ current was unchanged and smaller than TPC2-A1-P alone (Fig. 2f).

We compared the actions of the synthetic agonists with their endogenous counterparts. As shown in Fig. 2e–h, NAADP induced Ca^{2+} and Na^+ currents similar to TPC2-A1-N (hit rate 6/10 patches). Like TPC2-A1-P, $PI(3,5)P_2$ induced Na^+ currents only (Fig. 2e–h). Addition of NAADP after $PI(3,5)P_2$ or $PI(3,5)P_2$ after NAADP resulted in a Ca^{2+} current ~ 2-fold larger than NAADP alone (Fig. 2h). Na^+ currents in the presence of the combination were not different to $PI(3,5)P_2$ alone (Fig. 2h) again suggesting differential regulation of Na^+ and Ca^{2+} currents by the agonist combination.

Cell surface targeted TPC2 may not faithfully recapitulate the properties of TPC2 in its native environment. We therefore also analyzed TPC2 currents from enlarged lysosomes using vacuolar patch clamp in cells stably expressing TPC2. As shown in Fig. 2i, j, simultaneous addition of TPC2-A1-N and TPC2-A1-P induced a larger Ca^{2+} current than TPC2-A1-N alone. Similar results were obtained when the effects of NAADP and $PI(3,5)P_2$ were compared with NAADP alone (hit rate 8/12 patches; Fig. 2k–l). In marked contrast, the Na^+ currents induced by the synthetic or natural agonist combination were comparable to currents induced respectively by TPC2-A1-P or $PI(3,5)P_2$ alone (Fig. 2j, l).

To understand this selective potentiation, we analyzed reversal potentials (E_{rev}) to infer the relative permeability of TPC2 to Ca^{2+} and Na^+ upon agonist stimulation (Fig. 2m, n). E_{rev} for currents mediated by $TPC2^{L11A/L12A}$ in response to TPC2-A1-N and NAADP were similar (~ −10 mV) but more positive than TPC2-A1-P and $PI(3,5)P_2$ (~−70 mV) (Fig. 2m). These values correspond to P_{Ca}/P_{Na} values of ~0.6 and ~0.04, respectively. Similar values were obtained for TPC2 expressed in lysosomes (Fig. 2n). These data confirm that both cell surface and lysosomally-targeted TPC2 toggles its ion selectivity between a relatively non-selective state to a more Na^+-selective one.

https://doi.org/10.1038/s41467-022-31959-0

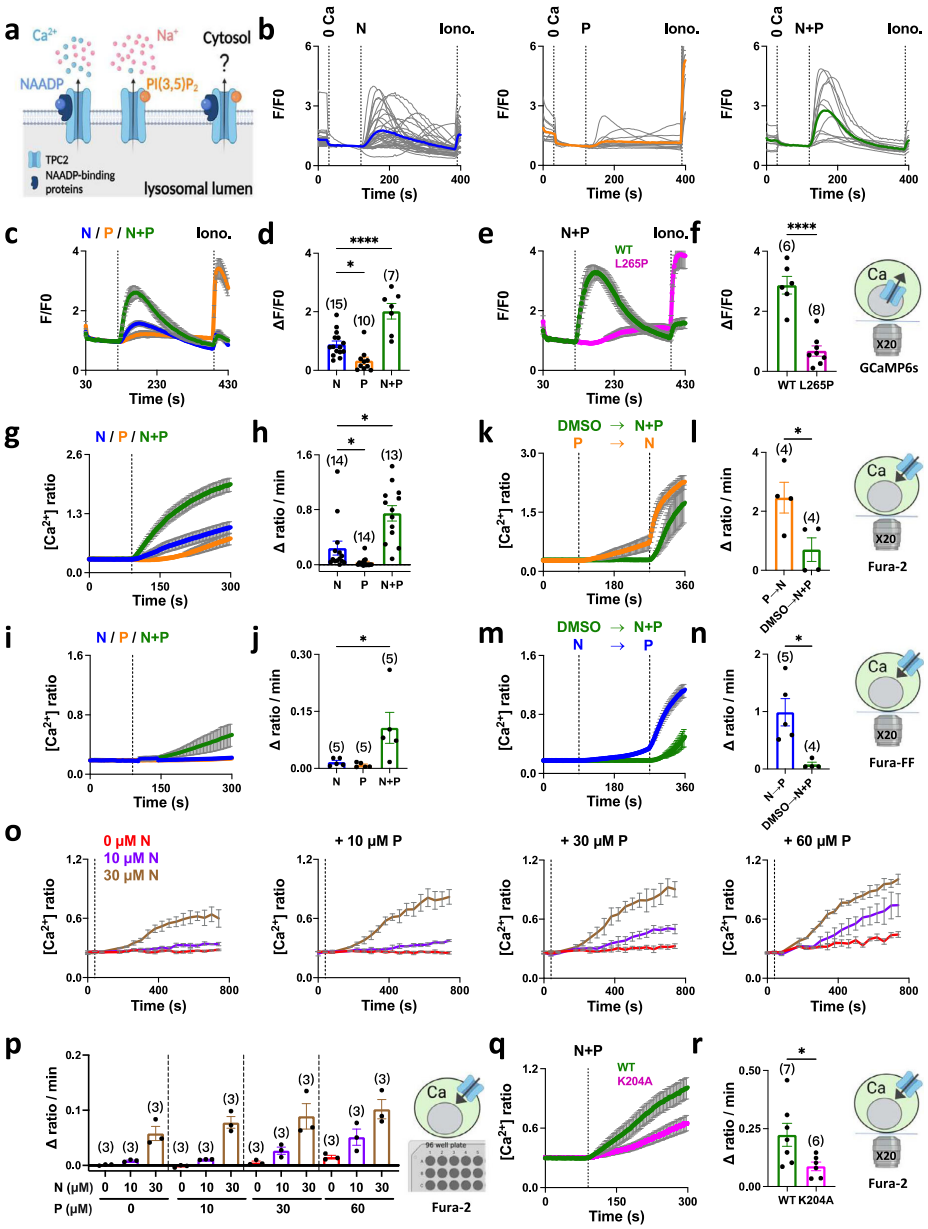

E_{rev} increased when $TPC2^{L11A/L12A}$ was challenged with TPC2-A1-N after TPC2-A1-P or with NAADP after $PI(3,5)P_2$ (Fig. 2m) consistent with the increased Ca^{2+}-current (Fig. 2f, h). However, in both stimulation scenarios, the E_{rev} for the combinations did not reach that for the singletons and instead was intermediate (Fig. 2m). These measured values (~−30–45 mV) corresponded to a P_{Ca}/P_{Na} of ~0.2–0.3 i.e. a moderately Na^+-selective state. These data indicate that a change in ion selectivity cannot account for the increased Ca^{2+} current obtained in the presence of both agonists. This was even more apparent when the order of stimulations was reversed. Thus, activation of $TPC2^{L11A/L12A}$ with TPC2-A1-P after TPC2-A1-N failed to affect E_{rev} (Fig. 2m) despite a doubling of the Ca^{2+} current (Fig. 2f). Notably, E_{rev} for $PI(3,5)P_2$ after NAADP did change adopting an intermediate value similar to NAADP after $PI(3,5)P_2$ (Fig. 2m). These

Fig. 1 | TPC2 agonists synergistically activate TPC2. a Differential effects of TPC2 activators on cation flux. **b**–**d** Effect of TPC2-A1-N (N; 30 μM), TPC2-A1-P (P; 60 μM) or a combination of the two (N+P) on Ca^{2+} levels of individual HeLa cells transiently transfected with TPC2 fused to GCaMP6s. Each trace in **b** is the fluorescence response of a single cell imaged from a typical field of view. The thicker trace is the average of the population. External Ca^{2+} was removed (0 Ca) prior to stimulation and ionomycin (iono., 2 μM) added at the end of the experiment. **c** pooled time-course data expressed as mean ± s.e.m. from 7 to 15 experiments. **d** peak change in signal from multiple experiments where each point represents the mean response of all cells from an independent experiment. *$p = 0.01$, ****$p < 0.0001$ (One-way ANOVA followed by Dunnett's post hoc test). **e**, **f** Effect of the TPC2-A1-N (30 μM) and TPC2-A1-P (60 μM) combination on Ca^{2+} levels of wild type (WT) or pore-dead TPC2 (L265P) fused to GCaMP6s. Pooled data expressed as mean ± s.e.m. from 6 to 8 experiments (**e**) and the peak change in signal from multiple experiments (**f**). ****$p < 0.0001$ (Unpaired t-test, two-tailed). **g**–**j** Effect of TPC2-A1-N (30 μM), TPC2-A1-P (60 μM) or a combination of the two on Ca^{2+} levels of HEK cells stably expressing $TPC2^{L11A/L12A}$. Cells were loaded with Fura-2 (**g**, **h**) or Fura-FF (**i**, **j**). Data are expressed as time-courses (mean ± s.e.m. from 5 to 14 experiments; **g**, **i**) and the rate of Ca^{2+} entry (**h**, **j**). *$p < 0.05$ (Kruskal-Wallis test followed by Dunn's post hoc test) (**h**); *$p = 0.03$ (Mann-Whitney test, two-tailed) (**j**). **k**–**n** Effect of sequential agonist additions on Ca^{2+} levels in HEK cells stably expressing $TPC2^{L11A/L12A}$. In **k**, Fura-2-loaded cells were stimulated with TPC2-A1-N (30 μM) after TPC2-A1-P (60 μM) and the response (mean ± sem from 4 experiments) compared that when the agonists were added simultaneously. In **m**, Fura-FF-loaded cells were stimulated with TPC2-A1-P (60 μM) after TPC2-A1-N (30 μM) (mean ± sem from 4 to 5 experiments). Pooled data quantifying the rate of Ca^{2+} entry are shown in **l** and **n**. *$p = 0.04$ (Unpaired t-test, two-tailed) (**l**); *$p = 0.01$ (Unpaired t-test, two-tailed) (**n**). **o**–**p** Effect of increasing concentrations of TPC2 agonists on Ca^{2+} levels in Fura-2-loaded HEK cells stably expressing $TPC2^{L11A/L12A}$. Cells were stimulated with 10 and 30 μM TPC2-A1-N in the presence of 10, 30 and 60 μM TPC2-A1-P using an automated plate reader. Data are expressed as mean ± s.e.m. from 3 experiments (**o**) and the rate of Ca^{2+} entry (**p**). **q**–**r** Effect of the TPC2-A1-N (10 μM) and TPC2-A1-P combination (30 μM) on Ca^{2+} levels of Fura-2-loaded HeLa cells transiently expressing cell surface TPC2 ($TPC2^{L11A/L12A}$) or a lipid-dead mutant ($TPC2^{L11A/L12A/K204A}$). Pooled data expressed as mean ± sem from 6 to 7 experiments (**q**) and the rate of Ca^{2+} entry (**r**). *$p = 0.04$ (Unpaired t-test, two-tailed). Source data are provided as a Source Data file.

data reveal a 'dominant' effect of TPC2-A1-N on ion selectivity distinguishing it from NAADP.

Essentially, similar results were found for TPC2 recorded from lysosomes. Thus, E_{rev} for the synthetic agonist combination was not different to TPC2-A1-N alone (Fig. 2n). And E_{rev} for the natural agonist combination was intermediate between NAADP and $PI(3,5)P_2$ (Fig. 2n).

Taken together, these data show that upon co-stimulation, TPC2 alters its permeability to Ca^{2+} but not Na^+ independent of changes in ion selection.

Co-activation of native TPC2 evokes global Ca^{2+} signals

In the next series of experiments, we examined the consequences of activating endogenous TPC2 on cellular Ca^{2+} signals. As shown in Fig. 3a, TPC2-A1-N induced a detectable Ca^{2+} response in single Fura-2 labelled HeLa cells. But the response was sluggish and modest in amplitude relative to responses in cells overexpressing TPC2 (Fig. 1b). TPC2-A1-P however had little detectable effect (Fig. 3a). Co-addition of the agonists induced robust Ca^{2+} responses (Fig. 3a, b), consistent with the synergistic activation of recombinant TPC2. The effect was particularly pronounced when the cells were simulated with TPC2-A1-P prior to TPC2-A1-N (Fig. 3c, d).

To establish specificity, we took three approaches. First, we examined the effects of inactive chemical analogues of TPC2-A1-N and TPC2-A1-P as negative controls (Fig. 3e). In the TPC2-A1-N analogue SGA-10, two chlorine residues at one of the benzenoid rings were replaced by hydrogen atoms (Fig. 3e)[24]. As shown in Fig. 3f, g, SGA-10 failed to evoke Ca^{2+} signals in HeLa cells consistent with a selective effect of the parent compound on TPC2. When combined with TPC2-A1-P, there was a small increase in the Ca^{2+} signal. In the TPC2-A1-P analogue SGA-153, the cyclohexylmethyl residue at the pyrrole nitrogen was replaced by an isopropyl residue (Fig. 3e)[24]. Like TPC2-A1-P, SGA-153 had little effect on cytosolic Ca^{2+} levels (Fig. 3f, g). But in contrast to TPC2-A1-P, SGA-153 only moderately potentiated the response to TPC2-A1-N (Fig. 3f, g), again attesting to specificity. In the second approach, we examined the effect of pore-dead TPC2 on agonist-evoked Ca^{2+} signals. Expression of $TPC2^{L265P}$ significantly reduced the response to the agonist combination compared to cells expressing LAMP1 (Fig. 3h, i) or untransfected cells (Fig. 3k–l). These results (summarized in Fig. 3j and m) are consistent with the pore mutant acting in a dominant-negative manner[28]. Third, we used CRISPR-Cas9 to knockout TPC2. For these experiments, we targeted TPC2 in SK-MEL-5 cells which express high levels of TPC2[29]. TPC2 depletion reduced TPC2 transcript levels by >90% (Fig. 3n) and reduced agonist-evoked currents (Supplementary Fig. 2). In control cells, the TPC2-A1-N and TPC2-A1-P combination again evoked robust Ca^{2+} signals (Fig. 3o). The initial rate of rise of these signals (Fig. 3o) was ~2-fold faster than those evoked in HeLa cells (Fig. 3a). Upon TPC2 targeting, the response to the agonist combination was substantially reduced (Fig. 3o). Similar inhibitory effects of TPC2 depletion were observed using a fixed concentration of TPC2-A1-N and increasing concentrations of TPC2-A1-P (Fig. 3p).

Taken together, these chemical, molecular and genetic analyses indicate that co-activation of endogenous TPC2 synergistically activate Ca^{2+} fluxes.

Co-activation of TPC2 regulates lysosomal function

In the final set of experiments, we examined the functional impact of TPC2 co-activation. Lysosomes have long been thought to generate local Ca^{2+} signals during NAADP-mediated signaling events that 'trigger' Ca^{2+} release from the neighboring ER resulting in global Ca^{2+} signals[30]. These events, however, have been difficult to resolve. To investigate this putative coupling event, we first examined the effects of TPC2-A1-P on a sub threshold concentration of TPC2-A1-N which alone fail to evoke detectable Ca^{2+} signals. As shown in Fig. 4a, TPC2-A1-N (10 μM) was without effect on cytosolic Ca^{2+} levels in both HeLa cells and SK-MEL-5 cells. However, co-activation with TPC2-A1-P resulted in robust signals particularly in SK-MEL-5 cells (Fig. 4a) but less so in TPC2 KO cells (Fig. 3p). We also examined the effects of TPC2 agonists in primary pancreatic acinar cells (Supplementary Fig. 3). These cells were the first mammalian cells in which the effects of NAADP were characterized[31]. As shown in Fig. 4b, c, at a low concentration (20 μM) neither TPC2-A1-N nor TPC2-A1-P alone affected cytosolic Ca^{2+} levels. But again, the combination elicited a robust response.

To further examine the local-global transition, we used high resolution TIRF microscopy to define the spatio-temporal nature of the Ca^{2+} signals mediated by TPC2. These experiments were performed in HEK-293 cells in which local IP_3-mediated Ca^{2+} signaling events have been extensively characterized[32,33]. As shown in Fig. 4d–f and Supplementary Movie 1, TPC2-A1-N evoked highly localized Ca^{2+} signals somewhat reminiscent of fundamental Ca^{2+} signals evoked by IP_3 receptors termed 'puffs'. We therefore refer to these events as 'tuffs', reflecting their origin (TPC2), their form (puff-like) and lack of ease to capture (tough; homophone). Tuffs were also resolved in response to TPC2-A1-P but these events were less frequent (Fig. 4e, Supplementary Movie 2). Co-activation of TPC2 substantially increased tuff frequency without affecting tuff amplitude (Fig. 4e, f, Supplementary Movie 3). Tuffs evoked by these means were also kinetically similar to those evoked by TPC2-A1-N and TPC2-A1-P alone, with comparable rise and fall times (Supplementary Fig. 4). However, there was a significant increase in the number of

https://doi.org/10.1038/s41467-022-31959-0

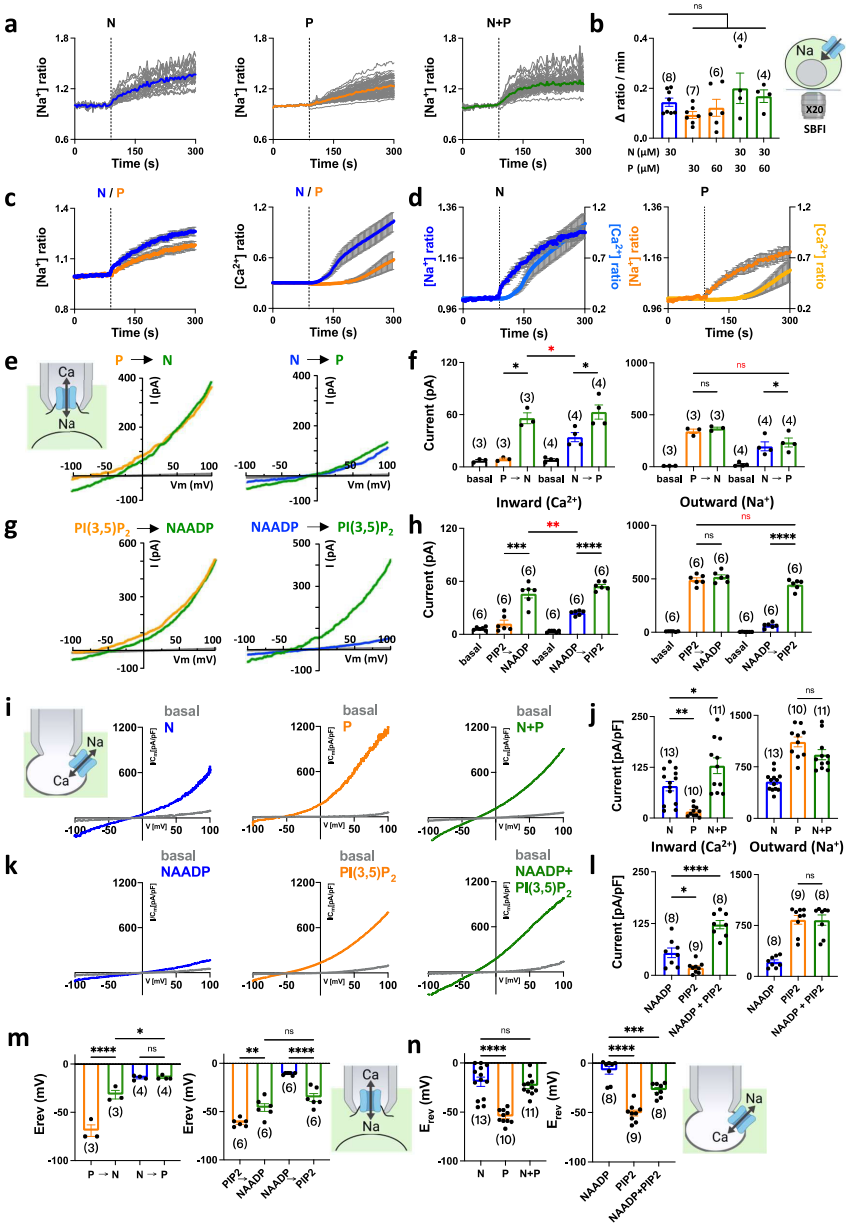

sites from which tuffs originated when TPC2 was co-activated by its ligands (Fig. 4f).

The pH of lysosomes is key to their degradative function and under acute control by NAADP and direct TPC2 activation[24,34–36]. We therefore examined the consequences of the agonist combinations on lysosomal pH. pH was measured ratiometrically with endocytosed fluorescein dextran. TPC2-A1-N increased lysosomal pH in SK-MEL-5 cells whereas TPC2-A1-P did not (Fig. 4g). Similar results were obtained in HeLa cells (Fig. 4h, Supplementary Movie 4). As shown in Fig. 4i, j, lysosomal pH responses upon co-activation of TPC2 were substantially larger in both cell types. This was particularly striking at low concentrations of TPC2-A1-N which alone induced small pH responses (summarized in Fig. 4j). Attempts to compare pH responses in TPC2 knockout SK-MEL-5 cells were confounded by differential uptake,

Fig. 2 | Cation permeability of TPC2 is independently regulated. a Effect of TPC2-A1-N (N; 30 μM), TPC2-A1-P (P; 30 μM) or a combination of the two (N+P) on Na^+ levels of individual SBFI-loaded HEK cells stably expressing $TPC2^{L11A/L12A}$. Each trace is the normalised fluorescence ratio response of a single cell imaged from a typical field of view. The thicker trace is the average of the population. **b** Pooled data (mean ± sem) quantifying the rate of Na^+ influx from 4-8 experiments in response to the indicated concentration of agonists. n.s. not significant (One-way ANOVA followed by Dunnett's post hoc test). **c**, **d** Comparison of TPC2-A1-N and TPC2-A1-P responses on cytosolic Na^+ and Ca^{2+} in $TPC2^{L11A/L12A}$-expressing cells loaded with SBFI and Fura-2, respectively. Data are mean ± sem from 4 to 10 experiments. **e**–**h** Effect of sequential agonist additions on currents from HEK cells stably expressing $TPC2^{L11A/L12A}$ under bi-ionic conditions. Macropatches were stimulated with 10 μM TPC2-A1-N and 10 μM TPC2-A1-P (**e**) or 1 μM $PI(3,5)P_2$ and 100 nM NAADP (**g**) in the indicated order. Pooled data (mean ± sem) quantifying the inward Ca^{2+} currents at −100 mV and outward Na^+ currents at +100 mV from 3 to 6 experiments before (basal) and after agonist addition are shown in **f** and **h**. $^*p < 0.05$, $^{***}p = 0.0003$, $^{****}p < 0.0001$, n.s. not significant (Paired t-test, two-tailed); $^*p = 0.04$, $^{**}p = 0.002$, n.s. not significant (Unpaired t-test, two-tailed, in red). **i**–**l** Effect of agonist additions on currents from HEK cells stably expressing TPC2 in lysosomes under bi-ionic conditions. Cells were stimulated with 10 μM TPC2-A1-P or 10 μM TPC2-A1-N (**i**) or 1 μM $PI(3,5)P_2$ and 100 nM NAADP (**k**) either alone or in combination. Pooled data (mean ± sem) quantifying the inward Ca^{2+} currents at −60 mV or outward Na^+ currents at +100 mV from 8 to 13 experiments in response to the agonists are shown in **j** and **l**, respectively. $^*p = 0.02$, $^{**}p = 0.005$ (One-way ANOVA followed by Dunnett's post hoc test) (**j**); $^*p = 0.02$, $^{****}p < 0.0001$ (One-way ANOVA followed by Dunnett's post hoc test) (**l**); n.s. not significant (Unpaired t-test, two-tailed, **j** and **l**). **m**, **n** Effect of TPC2 agonists on reversal potentials. Pooled data (mean ± sem from 3 to 13 experiments) quantifying the effect of TPC2 agonists on E_{rev} in HEK cells stably expressing $TPC2^{L11A/L12A}$ at the cell surface (**m**) or TPC2 in lysosomes (**n**). Values were derived from the bi-ionic experiments described in **e**–**l**. $^*p = 0.01$, $^{**}p = 0.007$, $^{****}p < 0.0001$, n.s. not significant (One-way ANOVA followed by Tukey's post hoc test) (**m**); $^{***}p = 0.0005$, $^{****}p < 0.0001$, n.s. not significant (One-way ANOVA followed by Dunnett's post hoc test) (**n**). Source data are provided as a Source Data file.

distribution and baseline stability of fluorescein dextran (Supplementary Fig. 5).

Lysosomes are dynamic organelles that interact with the cytoskeleton[37]. The consequences of native TPC2 activation on lysosome motility was therefore also examined. As shown in Fig. 4k, TPC2-A1-N but not TPC2-A1-P reduced lysosome motility in HeLa cells (Supplementary Movie 4). To quantify motility, we computed the mean of pixel-wise absolute differences in lysosome labelling from timelapses between each time point and the next. The resulting profiles revealed that lysosome motility was slowed by TPC2-A1-N in a time-dependent manner (Fig. 4l). As with the pH responses (Fig. 4i, j), there was clear synergism between the agonists such that the agonist combination caused a larger change in motility than either of the agonists alone (Fig. 4l–m). And again, marked synergism was apparent upon near-threshold stimulation with TPC2-A1-N (Fig. 4l–m). Similar regulation of lysosome dynamics by TPC2 was evident in SK-MEL-5 cells (Fig. 4m).

In sum, co-activation of TPC2 globalizes lysosomal-derived Ca^{2+} signals, regulating lysosomal pH and motility.

Discussion

TPC2 functions as a Ca^{2+}-permeable, non-selective cation channel when activated by the Ca^{2+} mobilizing messenger NAADP and as a Na^+-selective channel when activated by the phosphoinositide $PI(3,5)P_2$. Here we show that despite radically different effects of TPC2 agonists on channel behavior, they work synergistically to selectively control Ca^{2+} flux and lysosome activity (Fig. 4n).

Whereas Ca^{2+} fluxes and currents through TPC2 upon co-activation were dramatically enhanced, Na^+ flux and currents were largely unaltered (Figs. 1–2). Such a selective effect is remarkable considering that both ions share the same permeation pathway. Mechanistically, our previous work revealed that the ion selectivity of TPC2 is agonist-dependent allowing TPC2 to toggle between a selective (Na^+) and a non-selective (Ca^{2+}-permeable) state[24]. But increased Ca^{2+} currents through TPC2 reported here could not be explained in full by changes in ion selectivity because fully liganded TPCs had either the same or lower relative permeabilities to Ca^{2+} versus Na^+ compared to TPC2 activated by NAADP (or its mimetic) alone. We speculate that the ensemble current as well as ion selectivity of TPC2 can be independently regulated by its ligands, the interplay of which will dictate net flux from the lysosome. In our experiments, NAADP was a less consistent activator of TPC2 compared to the other activators (Fig. 2). This likely reflects its indirect mechanism of action through NAADP-binding proteins[15,16,38] which may differentially dissociate.

Functionally, we show that co-activation of endogenous TPC2 regulates several lysosomal activities (Fig. 4). Beyond their pH-dependent role in degradation, it is clear now that lysosomes are dynamic Ca^{2+} stores serving the cell in both 'local' mode to regulate membrane traffic and 'global' mode during signaling[39]. We succeeded in resolving tuffs, local TPC2-dependent Ca^{2+} signals (Fig. 4d–f). Intriguingly tuffs evoked by TPC2-A1-P although much less frequent than those evoked by TPC2-A1-N were indistinguishable in terms of their amplitudes and kinetics (Fig. 4e, f; Supplementary Fig. 4). We therefore predict that the unitary Ca^{2+} conductance of TPC2 is agonist-independent and that the differing Ca^{2+} permeabilities are due to changes in open probability. Of note, we found that the number of tuff sites increased when TPC2 was co-activated. These data indicate heterogeneity in agonist sensitivity of individual lysosomes and point to the existence of a population of normally 'silent' TPC2 channels. Thus, enhanced Ca^{2+} signaling upon TPC2 co-activation likely results in changes at both the molecular and organellar level.

Direct measurements of cellular NAADP show that it is a second messenger; its levels are low in resting cells but rise rapidly in response to a number of Ca^{2+} mobilizing stimuli[27] often transiently[40]. $PI(3,5)P_2$ is a low abundance phosphoinositide[23]. We mimicked signaling scenarios in an intact cell setting through sequential additions of TPC-A1-P and TPC2-A1-N (Figs. 1k–l, 3c, d). The resulting Ca^{2+} changes were robust and global in nature. $PI(3,5)P_2$ levels are also under environmental control e.g. hypertonic shock in yeast[41]. And again, sequential activation of TPC2 by TPC2-A1-P after TPC2-A1-N revealed robust Ca^{2+} responses (Fig. 1m, n). One implication of this is that $PI(3,5)P_2$ can (somewhat radically) be thought of as a Ca^{2+} mobilizing messenger in the presence of NAADP despite signaling through Na^+ in its absence. But how widespread agonist-evoked production of $PI(3,5)P_2$ in mammalian cells remains unclear. We therefore favour a model where $PI(3,5)P_2$ sets the Ca^{2+} signaling capability of NAADP consistent with previous work showing NAADP-mediated Ca^{2+} signals are stimulated upon overexpression of PIKfyve and inhibited by PIKfyve inhibitors[42]. Regardless, TPC2 can be viewed as a coincidence detector able to tune its behavior depending on the relative levels of its activators. Although Ca^{2+} signals evoked by activation of endogenous TPC2 were attenuated by inactive TPC2 analogues, dominant negative TPC2 and TPC2 knock-out (Fig. 3), they were not abolished raising the possibility of some off-target effects of the agonist combination.

Beyond Ca^{2+}, we found that both the acidity and motility of lysosomes were regulated by native TPC2 channels in an agonist-selective and synergistic way (Fig. 4g–m). The increase in pH might reflect permeability of TPC2 to H^+[24] and/or increases in luminal H^+ buffering capacity coupled to cation release. Interestingly, TPC2 knockout also appeared to destabilise lysosomal pH in our hands (Supplementary Fig. 5) adding to the debate surrounding the role of TPC2 in regulating

https://doi.org/10.1038/s41467-022-31959-0

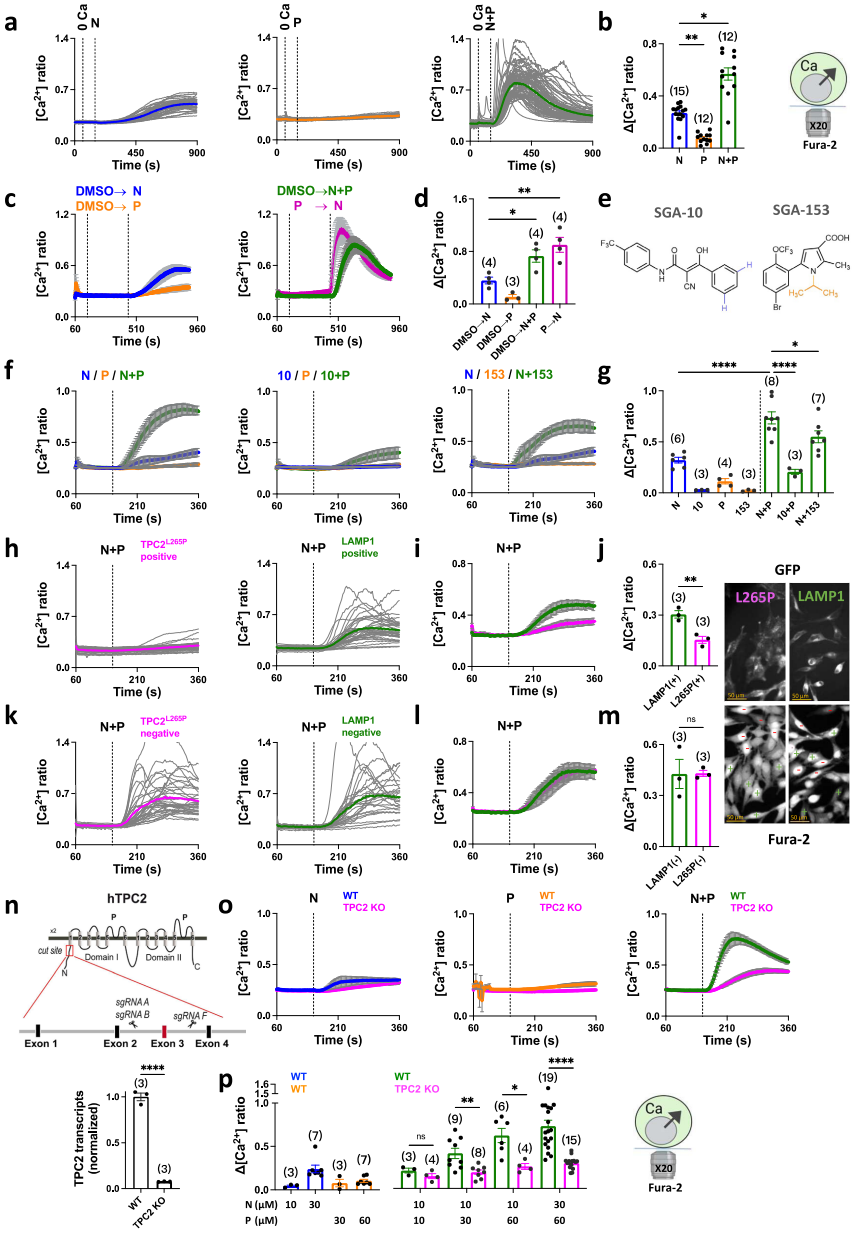

pH[7,20]. We speculate that the decrease in lysosome movement upon TPC2 activation facilitates inter-organellar communication with the ER, much like that reported for mitochondria during ER-mitochondria Ca^{2+} transfer[43]. With Na^+ fluxes unperturbed, Na^+-dependent functions of TPCs e.g., regulating membrane potential[20] or osmotic balance[44] likely remain intact during activation. In this way, segregated fluxes through TPC2 selectively facilitate lysosomal Ca^{2+} signaling.

Methods

Cells

HeLa cells, HEK-293 cells (wild type[32] or stably expressing human $TPC2^{L11I/L12A}$-mRFP[45] or TPC2-YFP[46]) and SK-MEL-5 cells (wild type or TPC2 knockout) were maintained in Dulbecco's Modified Eagle Medium (DMEM), supplemented with 10% (v/v) Fetal Bovine Serum (FBS), 100 μg/mL streptomycin and 100 units/mL penicillin

Fig. 3 | Co-activation of endogenous TPC2 evokes global Ca^{2+} signals. a, **b** Effect of TPC2-A1-N (N; 30 μM), TPC2-A1-P (P; 60 μM) or a combination of the two (N+P). on Ca^{2+} levels of individual naïve (untransfected) HeLa cells loaded with Fura-2. Each trace is the fluorescence ratio response of a single cell imaged from a typical field of view (**a**). The thicker trace is the average of the population. External Ca^{2+} was removed (0 Ca) prior to stimulation. Pooled data (mean ± sem) quantifying the peak change in ratio from 12 to 15 experiments where each point represents the mean response of all cells from an independent experiment, are shown in **b**. $^{*}p = 0.02$, $^{**}p = 0.004$ (Kruskal-Wallis test followed by Dunn's post hoc test). **c**, **d** Effect of the agonist combination on Ca^{2+} levels where the agonists were added simultaneously (N+P) or when TPC2-A1-N was added after TPC2-A1-P (P > N) **c**. Data are mean ± sem from 3 to 4 independent experiments. Pooled data quantifying the peak change in ratio is shown in **d**. $^{*}p = 0.03$, $^{**}p = 0.004$ (One-way ANOVA followed by Dunnett's post hoc test). **e** Structures of the inactive TPC2-A1-N analogue, SGA-10 and the inactive TPC2-A1-P analogue, SGA-153. **f**, **g** Effect of SGA-10 (10; 30 μM) and SGA-153 (153, 60 μM) on Ca^{2+} levels. Cells were co-stimulated with TPC2-A1-N or TPC2-A1-P as indicated. Pooled data (mean ± sem from 3 to 8 experiments) quantifying the peak change in ratio is shown in **g**. $^{*}p = 0.04$, $^{****}p < 0.0001$ (One-way ANOVA followed by Dunnett's post hoc test). **h**–**m** Effect of $TPC2^{L265P}$-GFP or LAMP1-GFP on Ca^{2+} responses to TPC2-A1-N (30 μM) and TPC2-A1-P (60 μM). Cells were transiently transfected and segregated according to whether they were GFP-positive or -negative. Results are shown as responses of individual cells from a typical field of view (**h**, **k**) or as mean ± sem from 3 experiments (**i**, **l**). Pooled data quantifying the peak change in ratio are shown in **j** and **m**. Epifluorescence images of GFP and Fura-2 (380 nm excitation) from a typical field of view showing transfected (+) and non-transfected (−) cells. $^{**}p = 0.008$, n.s. not significant (Unpaired t-test, two-tailed). **n** CRISPR targeting strategy for knockout of TPC2 in SK-MEL-5 cells (top) and qPCR validation (bottom) presented as mean ± sem from 3 experiments. $^{****}p < 0.0001$ (Unpaired t-test, two-tailed). **o**, **p** Effect of TPC2-A1-N (10 μM or 30 μM) and/or TPC2-A1-P (30 μM or 60 μM) on cytosolic Ca^{2+} in wild-type (WT) and TPC2 knockout (KO) SK-MEL-5 cells (**o**). Dare are mean ± s.e.m from 3 to 19 experiments. Pooled data quantifying the peak change in ratio in response to the indicated agonist concentration are shown in **p**. $^{*}p = 0.01$, $^{**}p = 0.005$, n.s. not significant (Unpaired t-test, two-tailed); $^{****}p < 0.0001$ (Mann-Whitney test, two-tailed). Source data are provided as a Source Data file.

(all from Invitrogen) at 37 °C in a humidified atmosphere with 5% CO_2. These lines are not commonly misidentified. Cells were passaged with trypsin. Cells were plated onto coverslips coated with poly-L-lysine (20–100 μg/mL, Sigma) for epifluorescence imaging and electrophysiology or with poly-D-lysine (100 μg/mL, Sigma) for TIRF imaging. For vacuolar patch clamp measurements, cells were treated with apilimod (1 μM) for 14 h to 18 h to enlarge endo-lysosomal organelles. For plate reading, cells were plated onto opaque-walled 96 well microplates (Corning).

Pancreatic acinar cells were obtained from male, 8–12 weeks old C57BL/6 J mice (Jackson Laboratories) housed at 22 ± 1 °C, with humidity not less than 30% on a 12 h light and dark cycle following CO_2 asphyxiation and cervical dislocation according to The University of Rochester's University Committee on Animal Resource (Protocol UCAR-2001-214E). Pancreata were enzymatically digested with type II collagenase (Sigma) in oxygenated DMEM (Invitrogen) with 0.1% bovine serum albumin (BSA) and 1 mg/mL soybean trypsin inhibitor for 30 min at 37 °C and 70 RPM in a shaking water bath. Cells were gently triturated to break up acinar clumps. Acini were then filtered through nylon mesh with a pore size of 100 μm, centrifuged at 75 × *g* through 4% BSA in DMEM, and resuspended in DMEM with 1% BSA.

Chemicals

TPC2-A1-N, TPC2-A1-P, SGA-10, and SGA-153 were synthesized as described previously[24]. For some experiments, TPC2-A1-N and TPC2-A1-P were purchased from MedChem Express.

Plasmids

Plasmids used were TPC2-GCaMP6s[24], $TPC2^{L265P}$-GCaMP6s[24], LAMP1-GFP[47], $TPC2^{L265P}$-GFP[25], $TPC2^{L11A/L12A}$-GFP[25], $TPC2^{L11A/L12A/K204A}$-GFP[24] and $TPC2^{L11A/L12A/L265P}$-GFP[24]. HeLa cells were transiently transfected with plasmids 18-26 hrs prior to imaging, using lipofectamine™ 2000 (from Invitrogen) according to the manufacturer's instructions.

TPC2 knockout

TPC2 knockout was created in the SK-MEL-5 melanoma cell line. Exon 3 in *TPCN2* was targeted, by designing guide RNAs in Intron 2/3 and Intron 3/4 (Supplementary Fig. 2). This strategy led to a frameshift mutation, rendering nonsense protein translations of TPC2 and reduced agonist-evoked vacuolar currents (Supplementary Fig. 2). Protocols were as previously described for targeting the *MCOLN1* gene in[48] and will be described in full elsewhere.

Single cell epifluorescence microscopy

Cytosolic Ca^{2+}, cytosolic Na^{+} and lysosomal pH were measured at the single cell level using fluorescent probes.

For HeLa cells, HEK-293 cells stably expressing human $TPC2^{L11/L12A}$ and SK-MEL-5 cells, cytosolic Ca^{2+} was measured using the genetically-encoded Ca^{2+} indicator GCaMP6s fused to the C-terminus of TPC2 or the fluorescent dyes, Fura-2 (from Biotium) and Fura-FF (from Cayman Chemical). Ca^{2+} imaging experiments were performed at room temperature in HEPES-buffered saline (HBS1) containing 10 mM NaHEPES, 1.25 mM KH_2PO_4, 2 mM $MgSO_4$, 3 mM KCl, 156 mM NaCl, 2 mM $CaCl_2$ and 10 mM glucose (pH 7.4; all from Sigma-Aldrich). For dye loading, cells were incubated with Fura-2 AM or Fura-FF AM (2.5 μM) and 0.005% (v/v) pluronic acid (from Invitrogen) for 1 h in HBS. Where indicated, some experiments were performed in nominally Ca^{2+}-free HBS where $CaCl_2$ was omitted and the cells were stimulated with ionomycin (Ca^{2+} salt, Cayman Chemical) toward the end of recording period.

For pancreatic acinar cells, cytosolic Ca^{2+} was measured using Fura-2. Ca^{2+} imaging experiments were performed at room temperature in HEPES-buffered saline (HBS2) containing 137 mM NaCl, 0.56 mM $MgCl_2$, 4.7 mM KCl, 1 mM Na_2HPO_4, 10 mM HEPES, 5.5 mM glucose, and 1.26 mM $CaCl_2$ (pH 7.4). Cells were incubated with Fura-2-AM (5 μM; Thermofisher) in HBS2 supplemented with 1% BSA for 30 min. Fura-2 loaded cells were adhered to a Cell-Tak (Corning)-coated glass coverslip in a Warner perfusion chamber and perfused with HBS2.

Cytosolic Na^{+} in HEK cells stably expressing $TPC2^{L11/L12A}$ was measured using the fluorescent Na^{+} indicator SBFI. Na^{+} imaging experiments were performed at room temperature in HBS. Cells were incubated with SBFI AM (5 μM) and 0.005% (v/v) pluronic acid (both from Invitrogen) for 1 h in HBS. Where indicated, some experiments were performed in low Na^{+} HBS where NaCl was replaced by NMDG (Sigma).

Lysosomal pH in HeLa and SK-MEL-5 cells was measured using fluorescein in HBS at room temperature. Cells were loaded with fluorescein-dextran (0.1 mg/mL; MW 10,000; from Invitrogen) by endocytosis overnight in culture followed by up to 10 hrs chasing period in dextran-free culture medium.

After transfection and/or dye loading, cells were washed in HBS and were subsequently mounted in a 1 mL imaging chamber (Biosciences Tools) for microscopy. Epifluorescence images were acquired every 3 s. For Fura-2, Fura-FF, SBFI and some GCaMP6s measurements, images were captured with a cooled coupled device camera (TILL photonics) attached to an Olympus IX71 inverted fluorescence microscope fitted with a monochromatic light source under the control of TillVision 4.0 software. Fura-2, Fura-FF, and SBFI were excited at 340/380 nm and emitted fluorescence was captured using a 440 nm long-pass filter at 20× magnification. GCaMP6s was excited at 470 nm and emitted fluorescence was captured using a 515 nm long-pass filter with a 40× objective.

https://doi.org/10.1038/s41467-022-31959-0

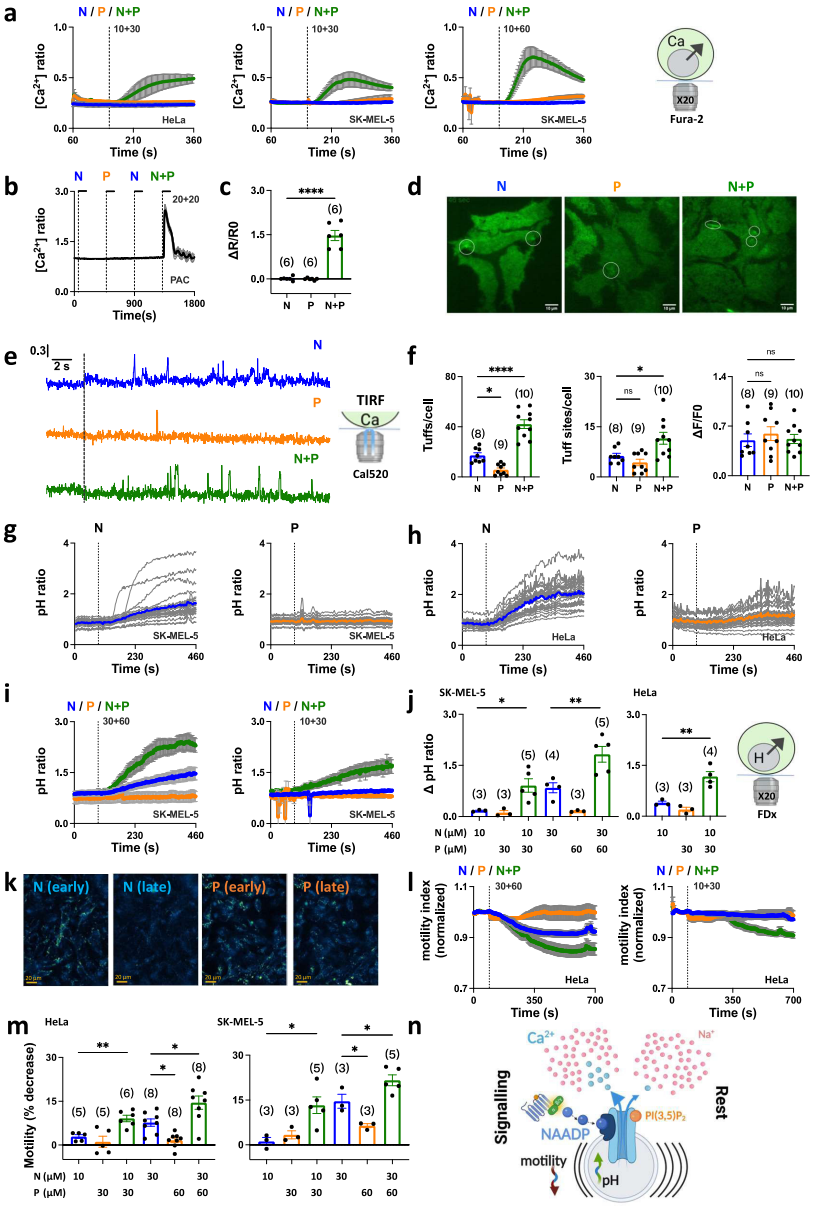

For fluorescein measurements and other GCaMP6s measurements, images were captured using a Megapixel monochrome cooled coupled device camera attached to an Olympus IX73 inverted fluorescence microscope fitted with a CoolLED multiple wavelength LED source under the control of MetaFluor 7.10.3.279 software. Fluorescein was excited at 490 nm/405 nm and emitted fluorescence was captured using a 510 nm long-pass filter at 20× or 40× magnification. GCaMP6s was excited at 470 nm and emitted fluorescence was captured using a 510 nm long-pass filter with a 20× objective.

For Fura-2 measurements in pancreatic acinar cells, imaging was performed using an inverted Olympus IX-71 microscope through a 40× oil immersion objective lens (N.A. = 1.35). Cells were excited alternately with UV at wavelengths of 340 and 380 nm using a monochromator-based illumination system (TILL Photonics), and the emission at

Fig. 4 | Co-activation of TPC2 regulates lysosomal function. a Effect of subthreshold concentration of TPC2-A1-N (10 μM), the indicated concentration of TPC2-A1-P or a combination on Ca^{2+} levels of individual HeLa or SK-MEL-5 cells loaded with Fura-2. Data are presented as mean ± sem from 3 to 9 experiments. **b**, **c** Effect of subthreshold concentration of TPC2-A1-N (20 μM), TPC2-A1-P (20 μM) or a combination of the two on Ca^{2+} levels of individual primary mouse pancreatic acinar cells loaded with Fura-2 **b**. Each trace is the normalized fluorescence ratio response of a single cell imaged from a typical field of view. The thicker trace is the average of the population. Pooled data (mean ± sem) quantifying the peak change in ratio from 6 experiments are shown in **c**. $^{****}p < 0.0001$ (Unpaired t-test, two-tailed). **d**–**f** Effect of TPC2-A1-N (30 μM), TPC2-A1-P (30 μM) or a combination of the two on subcellular Ca^{2+} levels of individual HEK cells loaded with Cal-520. Typical TIRF images with elementary events highlighted by circles are shown in **d**. Representative time courses of fluorescence changes from the centre of single tuff sites (1 × 1 μm) in response to the indicated agent. **e** Pooled data (mean ± sem) quantifying the number of events and sites detected per cell, and the peak response from 8 to 10 experiments are shown in **f**. $^{*}p < 0.05$, $^{****}p < 0.0001$, n.s. not significant (One-way ANOVA followed by Dunnett's post hoc test). **g**, **h** Effect of TPC2-A1-N (30 μM) and TPC2-A1-P (60 μM) on lysosomal pH of individual SK-MEL-5 (**g**) or HeLa (**h**) cells loaded with fluorescein-dextran (FDx). Each trace is the fluorescence ratio response of a single cell imaged from a typical field of view. The thicker trace is the average of the population. **i, j**, Effect of the indicated combinations of TPC2-A1-N and TPC2-A1-P on lysosomal pH of SK-MEL-5 cells **i**. Data are presented as mean ± sem from 3 to 5 experiments. Pooled data quantifying the peak change in ratio from multiple experiments using the indicated cell type and agonist combination are shown in **j**. $^{*}p = 0.02$, $^{**}p < 0.01$ (One-way ANOVA followed by Dunnett's post hoc test). **k**–**m** Effect of TPC2-A1-N and TPC2-A1-P on lysosomal motility. Images show maximum projections of motility calculated from differences in pixel-wise intensity on a frame-by-frame basis over an early (120–240 s) and late (570–690 s) period following addition of TPC2-A1-N (30 μM) or TPC2-A1-P (60 μM) to HeLa cells **k**. Intense signals represent large changes over time equating to more lysosome movement. Full time-courses presented as mean ± sem from 3 to 8 experiments in response to the indicated agonist combination are shown in **l**. Pooled data quantifying motility at 700 s from multiple experiments using the indicated cell type and agonist combination **m**. $^{*}p < 0.05$, $^{**}p = 0.008$ (One-way ANOVA followed by Dunnett's post hoc test). **n** Model showing that NAADP and $PI(3,5)P_2$ work in a synergistic manner to selectively optimize Ca^{2+} signalling from lysosomes to regulate lysosomal pH and motility leaving Na^+ signals unperturbed. Source data are provided as a Source Data file.

510 nm was captured using a Sensicam QE camera under the control of TillVision 4.0 software.

Population-based cytosolic Ca^{2+} measurements

Cytosolic Ca^{2+} in populations of HEK stably expressing $TPC2^{L11/L12A}$ was measured using Fura-2 and a fluorescence plate reader (Clariostar, BMG Labtech) under the control of Mars 3.42 R3 software. Cells were incubated with Fura-2 AM (2.5 μM) and 0.005% (v/v) pluronic acid (from Invitrogen) for 1 h in HBS. A single measurement comprised 16 flashes at 335 nm and 380 nm (each at 8 nm bandpass) while recording fluorescence at 520 nm (90 nm bandpass). Measurements were repeated on an individual well at 40 s intervals with 15 wells being recorded in parallel using "plate mode". Defined volumes of TPCA1-N and TPCA1-P, each at 210 μM, were added simultaneously through two independent injector needles to achieve the indicated final concentrations. Background fluorescence was measured from wells containing cells that were incubated with HBS without Fura-2.

Subcellular cytosolic Ca^{2+} measurements

Elementary cytosolic Ca^{2+} signals in wild-type HEK-293 cells were measured using Cal-520 and TIRF microscopy. Prior to imaging, the cells were washed three times with HBS2. The cells were subsequently incubated with Cal520-AM (5 μM; AAT Bioquest #21130) and ci-IP_3/PM (0.5 μM, Tocris #6210) in HBS2 supplemented with 0.01% BSA in dark at room temperature. After 1-h incubation, the cells were washed three times with HBS2 and incubated in HBS2 containing EGTA-AM (5 μM, Invitrogen #E1219). After 45 min incubation, the media was replaced with fresh HBS2 and incubated for additional 30 min at room temperature to allow for de-esterification of loaded reagents[49].

Following loading, the coverslip was mounted in a chamber and imaged using an Olympus IX83 inverted total internal reflection fluorescence (TIRF) microscopee equipped with an oil-immersion PLAPO OTIRFM 60× objective lens/1.45 numerical aperture. The cells were illuminated using a 488 nm laser to excite Cal-520 and the emitted fluorescence was collected through a band-pass filter by a Hamamatsu ORCA-Fusion CMOS camera. The angle of the excitation beam was adjusted to achieve TIRF with a penetration depth of ~140 nm. Images were captured from a field of view by directly streaming into RAM. TIRF images were captured using 2 × 2-pixel binning (216 nm/pixel) from equal field of views for HEK-293 cells at a rate of ~50 frames per second. Agonists were applied directly to the imaging chamber.

After visualizing images with the cellSens [Ver.2.3] life science imaging software (Olympus), images were exported as vsi files as described in[50] The vsi files were converted to tif files using ImageJ 1.53f51and further processed using FLIKA (Ver 1), a Python programming-based tool for image processing[51]. From each recording, 200 frames (~4 s) before agonist addition were averaged to obtain a ratio image stack (F/F0) and standard deviation for each pixel for recording up to 30 s following photolysis. The image stack was Gaussian-filtered, and pixels that exceeded a critical value (0.8 for our analysis) were located. The 'Detect-puffs' plug-in was utilized to detect the number of clusters, number of events, amplitudes and durations of localized Ca^{2+} signals from equal areas across different conditions from individual cells. All the events identified automatically by the algorithm were manually confirmed before further analysis[32,52].

Cell surface patch-clamp measurements

Currents were recorded in the inside-out configuration from macropatches excised from the plasma membrane of HEK-293 cells stably expressing $TPC2^{L11/L12A}$. Data were acquired using an AxoPatch 200 B amplifier (Molecular Devices) and pClamp10.2 suite (Molecular Devices). Records were filtered at 2 kHz and digitized at 10 kHz using Digidata 1440 A (Molecular Devices). ClampFit 10.2 was used for offline analysis of data. Currents were evoked by voltage ramps from −100 mV to +100 mV over 400 ms repeated at 5 s intervals from a holding potential of 0 mV.

Patch-pipettes were pulled from thick-walled, filamented borosilicate glass capillaries (Sutter Instrument) using Narishige PC-10 vertical puller, fire polished using a Narishige MF-830 microforge (Digitimer Ltd.). The pipette (luminal) solution contained (in mM): 105 $CaCl_2$, 5 HEPES, 5 MES (pH adjusted to 4.6 using MSA). The bath (cytosolic) solution contained (mM): 160 NaCl and 5 HEPES (pH adjusted to 7.2 using NaOH). Pipettes had a resistance of 1–3 MΩ when filled with the pipette solution. Liquid junction potentials were estimated using pClamp 10 and corrected as described previously[53].

TPC2-A1-N, TPC2-A1-P, $PI(3,5)P_2$ (diC8 form; Echelon Biosciences), and NAADP (Tocris) were applied to the bath solution of excised macropatches via an 8-channel pressurized perfusion system controlled by ValveLink 8.2 controller (AutoMate Scientific). All electrophysiological recordings were made at room temperature (21–23 °C).

The permeability ratio (P_{Ca}/P_{Na}) was calculated from the reversal potential according to[54]:

$$\frac{P_{Ca}}{P_{Na}} = \frac{\gamma_{Na}}{\gamma_{Ca}} * \frac{[Na]_i}{4[Ca]_o} * \exp^{(E_{rev}\frac{F}{RT})} * (\exp^{(E_{rev}\frac{F}{RT})} + 1)$$

where P_{Ca} = Ca^{2+} permeability; P_{Na} = Na^+ permeability; γ_{Ca} = Ca^{2+} activity coefficient (0.52); γ_{Na}= Na^+ activity coefficient (0.75); $[Ca]_o$ =

concentration of Ca^{2+} in the lumen; $[Na]_i$ = concentration of Na^+ in the cytosol; E_{rev} = reversal potential; F—Faraday's constant, R—gas constant; T—absolute temperature.

Vacuolar patch-clamp measurements

Currents were recorded in the whole-vacuole configuration from enlarged lysosomes manually excised from HEK-293 cells stably expressing TPC2 as described in ref. 55. Data were acquired, digitized (40 kHz) and filtered (2.9 kHz) using an EPC-10 amplifier and PatchMaster software v2x90.4 (both HEKA, Lambrecht, Germany). During each recording, fast and slow capacitive transients were cancelled by amplifier compensation circuit. Currents were evoked by voltage ramps from −100 mV to +100 mV repeated at 5 s intervals from a holding potential of 0 mV and normalized to organelle size.

Patch pipettes were pulled from borosilicate glass and polished to resistances in the range of 8–11 MΩ. Liquid junction potential was corrected as described[55]. Pipette and bath solutions were the same composition as those for the macropatch recordings.

TPC2-A1-N, TPC2-A1-P, $PI(3,5)P_2$ (diC8 form; Echelon Biosciences) and NAADP (Bio-Techne) were applied by complete exchange of the cytoplasmic solution. All compounds were freshly diluted before experimentation.

Lysosomal motility measurements

Lysosome motility was calculated from the images acquired for pH measurements. Cell-free areas were discarded by computing local standard deviations across the image and thresholding the result. Changes in intensity at 490 nm over time were normalized by dividing images by their mean intensity at each time point. Motility was quantified as the mean of pixel-wise absolute differences in normalized intensity between each time point and the next (3 s intervals). To attain robustness to artifacts such as a local loss of poorly attached cells upon agonist addition, images were split into 25 (5 × 5) equally sized chunks and those with cell coverage <1/3 anywhere along time course were removed. Motility was quantified in each remaining chunk independently and the resulting measures were combined by taking the median. A 1d median filter was applied to the resulting motility time profiles. Motility measures were normalized to the baseline prior to agonist addition.

Statistics

Parametric tests were performed using a paired t-test, unpaired t-test or one-way ANOVA. Non-parametric tests were performed using Kruskal-Wallis or Mann-Whitney analysis, respectively. All data were analyzed using Prism 9 (GraphPad Software). $^*p < 0.05$ $^{**}p < 0.01$ $^{***}p < 0.001$ $^{****}p < 0.0001$.

All cartoons from Figs. 1–4 and Supplementary Fig. 2 and 5 were created with BioRender.

Reporting summary

Further information on research design is available in the Nature Research Reporting Summary linked to this article.

Data availability

The source data underlying Figs. 1d, f, h, l, j, n, p, r, 2b, f, h, j, l, m, n, 3b, d, g, j, m, n, p, 4c, f, j, m, Supplementary Figs. 1b, d, f, h, 3b, 4, 5b are provided as a Source Data file. Source data are provided with this paper.

References

1. Settembre, C., Fraldi, A., Medina, D. L. & Ballabio, A. Signals from the lysosome: a control centre for cellular clearance and energy metabolism. *Nat. Rev. Mol. Cell Biol.* **14**, 283–296 (2013).
2. Xu, H. & Ren, D. Lysosomal physiology. *Annu. Rev. Physiol.* **77**, 57–80 (2015).
3. Platt, F. M. Sphingolipid lysosomal storage disorders. *Nature* **510**, 68–75 (2014).
4. Rahman, T. et al. Two-pore channels provide insight into the evolution of voltage-gated Ca^{2+} and Na^+ channels. *Sci. Signal.* **7**, ra109 (2014).
5. Patel, S. Function and dysfunction of two-pore channels. *Sci. Signal* **8**, re7 (2015).
6. Jaślan, D., Böck, J., Krogsaeter, E. & Grimm, C. Evolutionary aspects of TRPMLs and TPCs. *Int. J. Mol. Sci.* **21**, 4181 (2020).
7. Grimm, C. et al. High susceptibility to fatty liver disease in two-pore channel 2-deficient mice. *Nat. Commun.* **5**, 4699 (2014).
8. Kilpatrick, B. S. et al. An endosomal NAADP-sensitive two-pore Ca^{2+} channel regulates ER-endosome membrane contact sites to control growth factor signaling. *Cell Rep.* **18**, 1636–1645 (2017).
9. Sakurai, Y. et al. Two-pore channels control Ebola virus host cell entry and are drug targets for disease treatment. *Science* **347**, 995–998 (2015).
10. Gunaratne, G. S., Yang, Y., Li, F., Walseth, T. F. & Marchant, J. S. NAADP-dependent Ca(2+) signaling regulates Middle East respiratory syndrome-coronavirus pseudovirus translocation through the endolysosomal system. *Cell Calcium* **75**, 30–41 (2018).
11. Müller, M. et al. Gene editing and synthetically accessible inhibitors reveal role for TPC2 in HCC cell proliferation and tumor growth. *Cell Chem. Biol.* **28**, 1119–1131.e27 (2021).
12. Calcraft, P. J. et al. NAADP mobilizes calcium from acidic organelles through two-pore channels. *Nature* **459**, 596–600 (2009).
13. Zong, X. et al. The two-pore channel TPCN2 mediates NAADP-dependent Ca^{2+}-release from lysosomal stores. *Pflug. Arch.* **458**, 891–899 (2009).
14. Brailoiu, E. et al. Essential requirement for two-pore channel 1 in NAADP-mediated calcium signaling. *J. Cell Biol.* **186**, 201–209 (2009).
15. Gunaratne, G. S. et al. Essential requirement for JPT2 in NAADP-evoked Ca(2+) signaling. *Sci. Signaling* **14**, eabd5605 (2021).
16. Zhang, J., Guan, X., Shah, K. & Yan, J. Lsm12 is an NAADP receptor and a two-pore channel regulatory protein required for calcium mobilization from acidic organelles. *Nat. Commun.* **12**, 4739 (2021).
17. Lee, H. C. NAADP-mediated calcium signaling. *J. Biol. Chem.* **280**, 33693–33696 (2005).
18. Galione, A. A primer of NAADP-mediated Ca signalling: from sea urchin eggs to mammalian cells. *Cell Calcium* **58**, 27–47 (2015).
19. Wang, X. et al. TPC proteins are phosphoinositide-activated sodium-selective ion channels in endosomes and lysosomes. *Cell* **151**, 372–383 (2012).
20. Cang, C. et al. mTOR regulates lysosomal ATP-sensitive two-pore Na(+) channels to adapt to metabolic state. *Cell* **152**, 778–790 (2013).
21. Cang, C., Bekele, B. & Ren, D. The voltage-gated sodium channel TPC1 confers endolysosomal excitability. *Nat. Chem. Biol.* **10**, 463–469 (2014).
22. Jin, N., Lang, M. J. & Weisman, L. S. Phosphatidylinositol 3,5-bisphosphate: regulation of cellular events in space and time. *Biochem. Soc. Trans.* **44**, 177–184 (2016).
23. Hasegawa, J., Strunk, B. S. & Weisman, L. S. PI5P and PI(3,5)P(2): minor, but essential phosphoinositides. *Cell Struct. Funct.* **42**, 49–60 (2017).

24. Gerndt, S. et al. Agonist-mediated switching of ion selectivity in TPC2 differentially promotes lysosomal function. *Elife* **9**, e54712 (2020).
25. Brailoiu, E. et al. An NAADP-gated two-pore channel targeted to the plasma membrane uncouples triggering from amplifying Ca^{2+} signals, The. *J. Biol. Chem.* **285**, 38511–38516 (2010).
26. Yuan, Y. et al. The lysosomotrope GPN mobilises Ca(2+) from acidic organelles. *J. Cell Sci.* **134**, jcs256578 (2021).
27. Galione, A. et al. NAADP as an intracellular messenger regulating lysosomal calcium-release channels. *Biochem. Soc. Trans.* **38**, 1424–1431 (2010).
28. Penny, C. J. & Patel, S. Poring over two-pore channel pore mutants. *Messenger (Los. Angel)* **4**, 46–52 (2015).
29. Abrahamian, C. & Grimm, C. Endolysosomal cation channels and MITF in melanocytes and melanoma. *Biomolecules* **11**, 1021 (2021).
30. Patel, S., Churchill, G. C. & Galione, A. Coordination of Ca^{2+} signalling by NAADP. *Trends Biochem. Sci.* **26**, 482–489 (2001).
31. Cancela, J. M., Churchill, G. C. & Galione, A. Coordination of agonist-induced Ca^{2+}-signalling patterns by NAADP in pancreatic acinar cells. *Nature* **398**, 74–76 (1999).
32. Lock, J. T., Alzayady, K. J., Yule, D. I. & Parker, I. All three IP(3) receptor isoforms generate Ca(2+) puffs that display similar characteristics. *Sci. Signal.* **11**, eaau0344 (2018).
33. Lock, J. T. & Parker, I. IP(3) mediated global Ca(2+) signals arise through two temporally and spatially distinct modes of Ca(2+) release. *Elife* **9**, e55008 (2020).
34. Morgan, A. J. & Galione, A. NAADP induces pH changes in the lumen of acidic Ca^{2+} stores. *Biochem. J.* **402**, 301–310 (2007).
35. Morgan, A. J. & Galione, A. Fertilization and nicotinic acid adenine dinucleotide phosphate induce pH changes in acidic Ca(2+) stores in sea urchin eggs. *J. Biol. Chem.* **282**, 37730–37737 (2007).
36. Cosker, F. et al. The ecto-enzyme CD38 is a nicotinic acid adenine dinucleotide phosphate (NAADP) synthase that couples receptor activation to Ca^{2+} mobilization from lysosomes in pancreatic acinar cells. *J. Biol. Chem.* **285**, 38251–38259 (2010).
37. Oyarzún, J. E. et al. Lysosome motility and distribution: relevance in health and disease. *Biochim. Biophys. Acta Mol. Basis Dis.* **1865**, 1076–1087 (2019).
38. Roggenkamp, H. G. et al. HN1L/JPT2: a signaling protein that connects NAADP generation to Ca(2+) microdomain formation. *Sci. Signaling* **14**, eabd5647 (2021).
39. Patel, S. & Kilpatrick, B. S. Two-pore channels and disease. *Biochim. et. Biophys. Acta Mol. Cell Res.* **1865**, 1678–1686 (2018).
40. Yamasaki, M. et al. Role of NAADP and cADPR in the induction and maintenance of agonist-evoked Ca^{2+} Spiking in mouse pancreatic acinar cells. *Curr. Biol.* **15**, 874–878 (2005).
41. Dove, S. K. et al. Osmotic stress activates phosphatidylinositol-3,5-bisphosphate synthesis. *Nature* **390**, 187–192 (1997).
42. Jha, A., Ahuja, M., Patel, S., Brailoiu, E. & Muallem, S. Convergent regulation of the lysosomal two-pore channel-2 by Mg^{2+}, NAADP, $PI(3,5)P_2$ and multiple protein kinases. *EMBO J.* **33**, 501–511 (2014).
43. Yi, M., Weaver, D. & Hajnóczky, G. Control of mitochondrial motility and distribution by the calcium signal: a homeostatic circuit. *J. Cell Biol.* **167**, 661–72. (2004).
44. Freeman, S. A. et al. Lipid-gated monovalent ion fluxes regulate endocytic traffic and support immune surveillance. *Science* **367**, 301–305 (2020).
45. Gerndt, S., Krogsaeter, E., Patel, S., Bracher, F. & Grimm, C. Discovery of lipophilic two-pore channel agonists. *FEBS J.* **287**, 5284–5293 (2020).
46. Chao, Y. K. et al. TPC2 polymorphisms associated with a hair pigmentation phenotype in humans result in gain of channel function by independent mechanisms. *Proc. Natl Acad. Sci. USA* **114**, E8595–e8602 (2017).
47. Falcon-Perez, J. M., Nazarian, R., Sabatti, C. & Dell'Angelica, E. C. Distribution and dynamics of Lamp1-containing endocytic organelles in fibroblasts deficient in BLOC-3. *J. Cell Sci.* **118**, 5243–5255 (2005).
48. Rühl, P. et al. Estradiol analogs attenuate autophagy, cell migration and invasion by direct and selective inhibition of TRPML1, independent of estrogen receptors. *Sci. Rep.* **11**, 8313 (2021).
49. Lock, J. T., Ellefsen, K. L., Settle, B., Parker, I. & Smith, I. F. Imaging local Ca^{2+} signals in cultured mammalian cells. *J. Vis. Exp.* 52516 (2015).
50. Arige, V., Emrich, S. M., Yoast, R. E., Trebak, M. & Yule, D. I. A protocol for detecting elemental calcium signals (Ca(2+) puffs) in mammalian cells using total internal reflection fluorescence microscopy. *STAR Protoc.* **2**, 100618 (2021).
51. Ellefsen, K. L., Settle, B., Parker, I. & Smith, I. F. An algorithm for automated detection, localization and measurement of local calcium signals from camera-based imaging. *Cell Calcium* **56**, 147–56. (2014).
52. Arige, V. et al. CREB regulates the expression of type 1 inositol 1,4,5-trisphosphate receptors. *J. Cell Sci.* **134**, jcs258875 (2021).
53. Barry, P. H. JPCalc, a software package for calculating liquid junction potential corrections in patch-clamp, intracellular, epithelial and bilayer measurements and for correcting junction potential measurements. *J. Neurosci. Methods* **51**, 107–16. (1994).
54. Fatt, P. & Ginsborg, B. L. The ionic requirements for the production of action potentials in crustacean muscle fibres. *J. Physiol.* **142**, 516–543 (1958).
55. Chen, C. C. et al. Patch-clamp technique to characterize ion channels in enlarged individual endolysosomes. *Nat. Protoc.* **12**, 1639–1658 (2017).

Acknowledgements

We thank Cheng-Chang Chen (National University of Taiwan) for pilot electrophysiological work. This work was supported by BBSRC grants BB/T015853/1 (to S.P.) and BB/W01551X/1 (to T.R. and S.P.), DFG grants GR4315/4-1, GR4315/2-2, and SFB/TRR152 P04 (to C.G.), DFG grant BR1034/7-1 (to F.B.) and NIH grant DE014756 from the NIDCR (to D.I.Y.). J.H. was partially supported by an MRC grant to Roberto Mayor (MRC, 558941) and is an EMBO long-term postdoctoral fellow (EMBO, ALTF 1284-2020).

Author contributions

Y.Y. designed, performed, and analysed all the imaging experiments unless otherwise stated and collated and re-analysed all additional data. D.J. performed and analysed the vacuolar patch clamp experiments. T.R. performed and analysed the cell surface patch clamp experiments. S.R.B. performed and analysed the population-based cytosolic Ca^{2+} measurements. V.A. performed and analysed the subcellular cytosolic Ca^{2+} measurements. LEW performed and analysed the single cell cytosolic Ca^{2+} measurements using pancreatic acinar cells. C.A. created the TPC2 knockout cells. C.A. and R.T. validated the TPC2 knockout cells. M.K. synthesized the TPC2 agonists. J.H. analysed lysosome motility. A.S.R. and E.-M.W. performed pilot assays. T.R., F.B., D.I.Y., C.G., and S.P. designed experiments and provided funding. S.P. coordinated research and wrote the manuscript with Y.Y. All of the authors discussed the results and commented on the manuscript.

Competing interests

The authors declare no competing interests.

Additional information

Supplementary information The online version contains supplementary material available at https://doi.org/10.1038/s41467-022-31959-0.

Correspondence and requests for materials should be addressed to Christian Grimm or Sandip Patel.

Peer review information *Nature Communications* thanks Haoxing Xu and the other, anonymous, reviewer(s) for their contribution to the peer review of this work.

Supplementary information

Segregated cation flux by TPC2 biases Ca^{2+} signaling through lysosomes.

Yu Yuan[1], Dawid Jaślan[2], Taufiq Rahman[3], Stephen R. Bolsover[1], Vikas Arige[4], Larry E. Wagner II[4], Carla Abrahamian[2], Rachel Tang[2], Marco Keller[5], Jonas Hartmann[1], Anna S. Rosato[2], Eva-Maria Weiden[2], Franz Bracher[5], David I. Yule[4], Christian Grimm[2,*] and Sandip Patel[1,*]

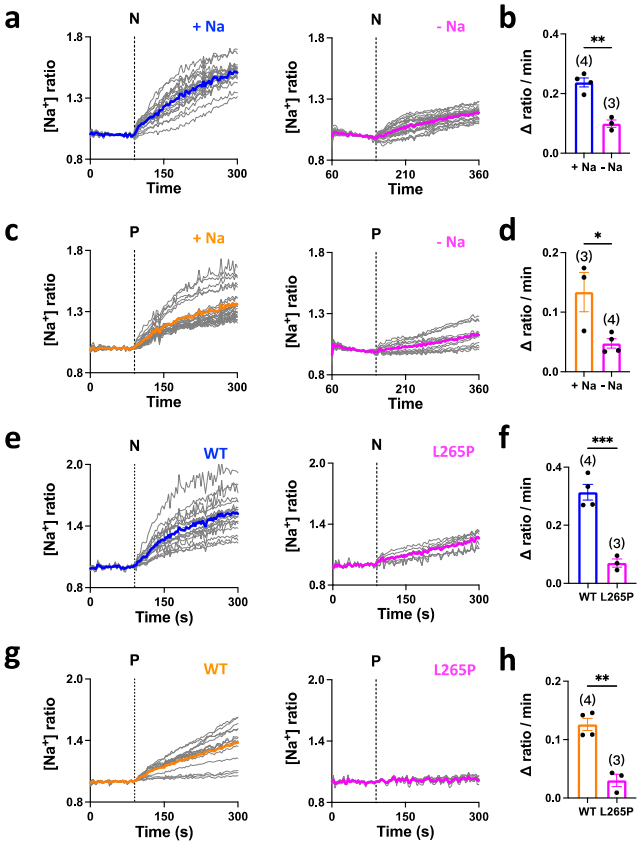

Supplementary Figure 1. Cell surface TPC2 mediates Na^+ influx.

a – d, Effect of TPC2-A1-N (30 μM, **a**) and TPC2-A1-P (30 μM, **c**) on Na^+ levels of individual SBFI-loaded HEK cells stably expressing $TPC2^{L11A/L12A}$. Experiments were performed in HBS ($+Na^+$) or HBS in which NaCl was replaced with NMDG ($-Na^+$). Each trace is the normalized fluorescence ratio response of a single cell imaged from a typical field of view. The thicker trace is the average of the population. Pooled data (mean ± s.e.m. from 3-4 experiments) quantifying the rate of Na^+ influx from multiple experiments is shown in **b** and **d**. *P=0.03, **P=0.001 (Unpaired t-test, two-tailed).

e – h, Effect of TPC2-A1-N (30 μM, **e**) and TPC2-A1-P (30 μM, **g**) on Na^+ levels of individual SBFI-loaded HeLa cells transiently expressing $TPC2^{L11A/L12A}$ or pore-dead $TPC2^{L11A/L12A/L265P}$. Experiments were performed in HBS. Each trace is the normalized fluorescence ratio response of a single cell imaged from a typical field of view. The thicker trace is the average of the population. Pooled data (mean ± s.e.m. from 3-4 experiments) quantifying the rate of Na^+ influx from multiple experiments are shown in **f** and **h**. **P=0.001, ***P=0.0008 (Unpaired t-test, two-tailed).

Source data are provided as a Source Data file.

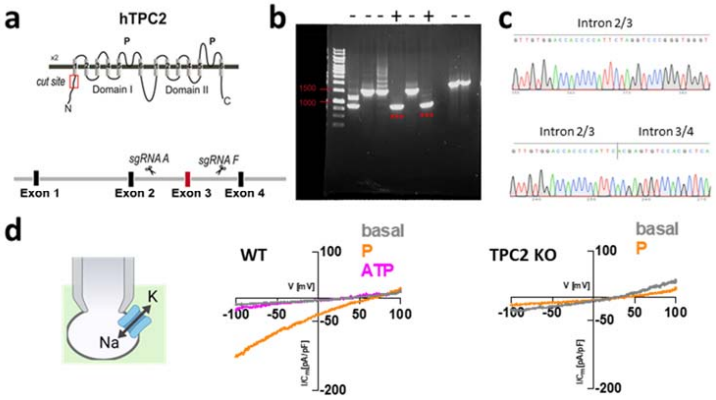

Supplementary Figure 2. Validation of TPC2 knockout cells.

a, CRISPR targeting strategy for knockout of TPC2 in SK-MEL-5 cells.

b, Genomic PCR analysis of independent clonal lines resulting in the identification of two positives that yielded products consistent with knockout (***). Expected sizes of the products were 1521 bp (wild type) and 831 bp (knockout).

c, Genomic sequencing wildtype (WT) and TPC2 knockout (KO) cells used in this study.

d, Effect of TPC2-A1-P (10 µM) and ATP (1 mM) on lysosomal currents recorded from wildtype and TPC2 knockout cells.

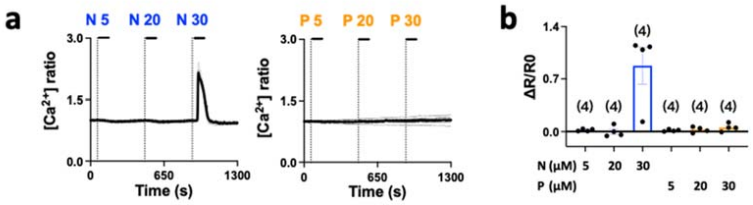

Supplementary Figure 3. Activation of native TPC2 evokes agonist-selective changes in Ca^{2+}.

a, Effect of increasing concentrations of TPC2-A1-N and TPC2-A1-P on Ca^{2+} levels of individual primary mouse pancreatic acinar cells loaded with Fura-2. Each trace is the normalized fluorescence ratio response of a single cell imaged from a typical field of view. The thicker trace is the average of the population.

b, Pooled data (mean ± s.e.m. from 4 experiments) quantifying the peak change in normalized ratio from multiple experiments.

Source data are provided as a Source Data file.

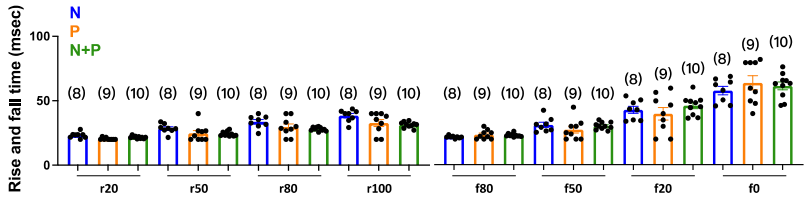

Supplementary Figure 4. Elementary TPC2-mediated Ca^{2+} signals are kinetically similar.
Pooled data (mean ± s.e.m. from 8-10 experiments) showing the mean rise (r) and fall (f) times of tuffs recorded from individual HEK cells loaded with Cal-520. Data were calculated to the indicated normalized intensity level for an individual event.
Source data are provided as a Source Data file.

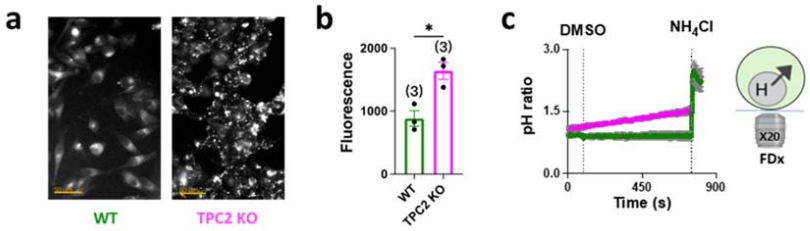

Supplementary Figure 5. TPC2 knockout confounds fluorescein dextran comparisons.
a, Representative epifluorescence images of wild-type and TPC2 knockout cells labelled with fluorescein dextran (excitation = 405 nm).
b, Pooled data (mean ± s.e.m. from 3 experiments) quantifying basal fluorescein dextran fluorescence. *P=0.01 (Unpaired t-test, two-tailed).
c, Ratiometric fluorescein dextran measurements in wild type and TPC2 knockout cells (mean ± s.e.m. from 3 experiments) stimulated with DMSO (0.1 %v/v) and NH_4Cl (5 mM).
Source data are provided as a Source Data file.

Paper III: Summary and Contributions

TPC2 rescues lysosomal storage in mucolipidosis type IV, Niemann-Pick type C1, and Batten disease

Anna Scotto Rosato*, Einar K Krogsaeter*, Dawid Jaślan, **Carla Abrahamian**, Sandro Montefusco, Chiara Soldati, Barbara Spix, Marina Teresa Pizzo, Giuseppina Grieco, Julia Böck, Amanda Wyatt, Daniela Wünkhaus, Marcel Passon, Marc Steiglitz, Marco Keller, Guido Hermey, Sandra Markmann, Doris Gruber-Schoffnegger, Susan Cotman, Ludger Johannes, Dennis Crusius, Ulrich Boehm, Christian Wahl-Schott, Martin Biel, Franz Bracher, Elvira De Leonibus, Elena Polishchuk, Diego Medina*, Dominik Paquet*, & Christian Grimm*

TRPML1, also known as Mucolipin 1, is a cation channel encoded by the *MCOLN1* gene found in late endosomes and lysosomes. Its role in maintaining lysosomal function and regulating lysosomal calcium signaling is critical for various cellular processes, including lysosomal exocytosis, autophagy, membrane trafficking, and repair. Mutations in *MCOLN1* lead to Mucolipidosis type IV (MLIV), a rare lysosomal storage disorder (LSD) characterized by motor delays and neurodegeneration[90, 172]. In MLIV, lysosomal Ca^{2+} release and function are impaired, resulting in defective lysosomal exocytosis and autophagy. Consequently, various substances like lipids and cholesterol accumulate within lysosomes[75, 100]. In addition, dysregulated lysosomal Ca^{2+} homeostasis has also been observed in other LSDs, such as Niemann-Pick type C1 (NPC1) caused by mutations in the *NPC1* gene and Batten disease caused by mutations in the *CLN3* gene, featuring similar phenotypes as MLIV. Unlike NPC1 and CLN3, TRPML1 presents a druggable target, and its activation has shown potential for ameliorating LSD defects. However, as certain LSDs, including MLIV, exhibit no TRPML1 activity, novel approaches are needed to rescue the disease phenotypes[90, 233-235]. Our study aimed to explore TPC2, a cation channel closely related to TRPML, localized to LYs and LEs, as a potential therapeutic target for rescuing certain LSD defects. TPC2 shares similarities with TRPML1, including its involvement in lysosomal Ca^{2+} release, intracellular trafficking, and activation by $PI(3,5)P_2$[172]. We hypothesized that activation of TPC2 could help reverse disease phenotypes. Hence, we utilized the selective TPC2-A1-P compound, previously shown to be a potent activator of TPC2 activity, mimicking $PI(3,5)P_2$ activation. For preliminary experiments, I generated a TPC2 knockout model in control fibroblasts. Moreover, we used human fibroblasts derived from MLIV and NPC1 patients and treated them with TPC2-A1-P or overexpressed (OE) TPC2 GoF mutation. Remarkably, TPC2-A1-P treatment or OE significantly diminished lipid lactosylceramide and intracellular cholesterol accumulation typically observed in patient cells. The simultaneous TPC2 activation and OE effect in MLIV cells was even more substantial. Treating MLIV and NPC1 fibroblasts with TPC2-A1-P under nutrient-starvation conditions led to the reversal of autophagy blockade and clearance of p62 accumulation. Subsequent electron microscopy experiments revealed the changes in endolysosomal morphology in MLIV and NPC1 fibroblasts. Interestingly, the activation of TPC2 by TPC2-A1-P restored the cellular ultrastructure. As LSD patients typically exhibit neurodegenerative symptoms, we investigated the expression of TPC2 in the central nervous system of humans and mice. We created a TPC2-GFP reporter mouse model, which revealed that TPC2 is expressed in neurons, microglia, and astrocytes. We then utilized a novel gene-edited MLIV induced pluripotent stem cells (iPSCs), which also showed the expression of relevant genes. Similar to MLIV fibroblasts, iPSC-derived TRPML1 KO neurons displayed ultrastructural and autophagy impairments compared to control cells. However, these effects were alleviated by TPC2-A1-P stimulation. Using viability assays, I tested the toxicity of TPC2-A1-P on fibroblasts and iPSCs, excluding any toxic effects even at concentrations as high as 100 µM. Furthermore, to corroborate our in vitro findings, we employed an in vivo MLIV mouse model. I administered the TPC2-A1-P compound daily through the intraperitoneal route at a dose of 20 mg/kg and used appropriate vehicle control injections for MLIV and WT mice around two months old. As MLIV mice often display motor delays, I assisted in carrying out motor performance experiments using the accelerating RotaRod tasks. Intriguingly, MLIV mice treated with TPC2-A1-P showed significant improvements in motor defects. Our experimental findings demonstrate the potential therapeutic significance of transient TPC2 activation using TPC2-A1-P in mitigating the pathogenic effects of MLIV and NPC1, offering a promising avenue for developing targeted therapies for lysosomal storage diseases. Further research and exploration of TPC2 as a therapeutic target offers hope for developing effective treatments for these rare disorders.

Paper III

Article

TRANSPARENT PROCESS OPEN ACCESS

EMBO Molecular Medicine

TPC2 rescues lysosomal storage in mucolipidosis type IV, Niemann–Pick type C1, and Batten disease

Anna Scotto Rosato[1,†], Einar K Krogsaeter[1,†], Dawid Jaślan[1], Carla Abrahamian[1], Sandro Montefusco[2], Chiara Soldati[2], Barbara Spix[1], Maria Teresa Pizzo[2], Giuseppina Grieco[2], Julia Böck[1], Amanda Wyatt[3], Daniela Wünkhaus[4], Marcel Passon[1], Marc Stieglitz[5], Marco Keller[5], Guido Hermey[6], Sandra Markmann[4], Doris Gruber-Schoffnegger[4], Susan Cotman[7], Ludger Johannes[8], Dennis Crusius[9], Ulrich Boehm[3], Christian Wahl-Schott[10], Martin Biel[5], Franz Bracher[5], Elvira De Leonibus[2,11], Elena Polishchuk[2], Diego L Medina[2,12,*], Dominik Paquet[9,13,**] & Christian Grimm[1,***]

Abstract

Lysosomes are cell organelles that degrade macromolecules to recycle their components. If lysosomal degradative function is impaired, e.g., due to mutations in lysosomal enzymes or membrane proteins, lysosomal storage diseases (LSDs) can develop. LSDs manifest often with neurodegenerative symptoms, typically starting in early childhood, and going along with a strongly reduced life expectancy and quality of life. We show here that small molecule activation of the Ca^{2+}-permeable endolysosomal two-pore channel 2 (TPC2) results in an amelioration of cellular phenotypes associated with LSDs such as cholesterol or lipofuscin accumulation, or the formation of abnormal vacuoles seen by electron microscopy. Rescue effects by TPC2 activation, which promotes lysosomal exocytosis and autophagy, were assessed in mucolipidosis type IV (MLIV), Niemann–Pick type C1, and Batten disease patient fibroblasts, and in neurons derived from newly generated isogenic human iPSC models for MLIV and Batten disease. For *in vivo* proof of concept, we tested TPC2 activation in the MLIV mouse model. In sum, our data suggest that TPC2 is a promising target for the treatment of different types of LSDs, both *in vitro* and *in-vivo*.

Keywords Batten; MLIV; NPC1; TPC2; TRPML
Subject Categories Genetics, Gene Therapy & Genetic Disease; Organelles; Pharmacology & Drug Discovery
DOI 10.15252/emmm.202115377 | Received 3 November 2021 | Revised 14 July 2022 | Accepted 15 July 2022 | Published online 5 August 2022
EMBO Mol Med (2022) 14: e15377

Introduction

Lysosomal Ca^{2+} release is of significant physiological relevance. Lysosomal Ca^{2+} regulates several cellular processes, e.g., autophagy (Medina *et al*, 2015), membrane trafficking (Dong *et al*, 2010; Ruas *et al*, 2010; Cao *et al*, 2015), exocytosis (Samie *et al*, 2013; Davis *et al*, 2020), nutrient adaptation (Cang *et al*, 2013), membrane repair (Cheng *et al*, 2014), and cell migration (Bretou *et al*, 2017). Disruption of lysosomal Ca^{2+} content or Ca^{2+} release is associated with several diseases, particularly neurodegenerative lysosomal storage diseases (Kiselyov *et al*, 2010; Lloyd-Evans & Platt, 2011; Feng & Yang, 2016). Mucolipidosis type IV (MLIV) constitutes the most direct link between defective lysosomal Ca^{2+} release and neurodegeneration, caused

1 Faculty of Medicine, Walther Straub Institute of Pharmacology and Toxicology, Ludwig-Maximilians-Universität, Munich, Germany
2 Telethon Institute of Genetics and Medicine, Naples, Italy
3 Experimental Pharmacology, Center for Molecular Signaling (PZMS), Saarland University School of Medicine, Homburg, Germany
4 Evotec AG, Hamburg, Germany
5 Department of Pharmacy, Center for Drug Research, Ludwig-Maximilians-Universität, Munich, Germany
6 Center for Molecular Neurobiology Hamburg (ZMNH), Institute of Molecular and Cellular Cognition, UKE, Hamburg, Germany
7 Department of Neurology, Center for Genomic Medicine, Massachusetts General Hospital, Harvard Medical School, Boston, MA, USA
8 Cellular and Chemical Biology Department, Institut Curie, U1143 INSERM, UMR3666 CNRS, PSL Research University, Paris, France
9 Institute for Stroke and Dementia Research (ISD), Ludwig-Maximilians-University (LMU) Hospital, Munich, Germany
10 Institute for Neurophysiology, Hannover Medical School, Hannover, Germany
11 Institute of Biochemistry and Cell Biology (IBBC), CNR, Rome, Italy
12 Medical Genetics Unit, Department of Medical and Translational Science, Federico II University, Naples, Italy
13 Munich Cluster for Systems Neurology (SyNergy), Ludwig-Maximilians-University (LMU), Munich, Germany
*Corresponding author. Tel: +39 08119230698; E-mail: medina@tigem.it
**Corresponding author. Tel: +49 89440046123; E-mail: dominik.paquet@med.uni-muenchen.de
***Corresponding author. Tel: +49 89218073811; E-mail: christian.grimm@med.uni-muenchen.de
†These authors contributed equally to this work

by dysfunction of the lysosomal cation channel TRPML1 (also called MCOLN1) (Slaugenhaupt, 2002; Feng & Yang, 2016). TRPML1 signaling or TRPML1-mediated Ca^{2+} release is similarly impaired in other LSDs such as Niemann–Pick type C1 (NPC1) (Shen *et al*, 2012), Niemann–Pick type A (NPA; also called infantile neurovisceral form of acid sphingomyelinase (SMPD1) deficiency) (Zhong *et al*, 2016), and Fabry disease (Zhong *et al*, 2016). Pharmacological and genetic activation of TRPML1 ameliorates NPC1-associated lactosylceramide (LacCer) trafficking defects and cholesterol accumulation (Shen *et al*, 2012), while activation of the lysosomal big conductance Ca^{2+}-activated potassium (BK) channel TRPML1 dependently rescues aberrant lysosomal storage in NPA and Fabry disease (Zhong *et al*, 2016). Furthermore, loss of FIG 4 (polyphosphoinositide phosphatase) and PYKfyve (FYVE finger-containing phosphoinositide kinase), which are both involved in the synthesis of the endogenous TRPML/two-pore channel (TPC) agonist $PI(3,5)P_2$ (phosphatidylinositol 3,5-bisphosphate), is associated with neurological or neurodegenerative disease phenotypes (Chow *et al*, 2007; Zhang *et al*, 2007; Zou *et al*, 2015), and TRPML1 activation in FIG $4^{-/-}$ cells rescues lysosomal storage phenotypes (Zou *et al*, 2015).

While activation of TRPML1 in LSDs is gaining traction, effects of activating the related two-pore channel 2 (TPC2 or TPCN2) remain unexplored. TPC2 shares several features with TRPML1: both channels are permeable for Ca^{2+} and Na^+ (Calcraft *et al*, 2009; Zong *et al*, 2009; Wang *et al*, 2012; Gerndt *et al*, 2020), reside in endolysosomal membranes (Pryor *et al*, 2006; Calcraft *et al*, 2009; Kim *et al*, 2009; Ruas *et al*, 2010), are activated by $PI(3,5)P_2$ (Dong *et al*, 2010; Wang *et al*, 2012; Gerndt *et al*, 2020), are widely expressed in the CNS (Bae *et al*, 2014; Pereira *et al*, 2017; Foster *et al*, 2018; Minckley *et al*, 2019), cause trafficking defects when lost (Dong *et al*, 2010; Shen *et al*, 2012; Chen *et al*, 2014; Grimm *et al*, 2014; Nguyen *et al*, 2017), interact with mTOR/TFEB/autophagy pathways (Medina *et al*, 2011; Cang *et al*, 2013; Medina *et al*, 2015; Wang *et al*, 2015; Li *et al*, 2016; Ogunbayo *et al*, 2018; Scotto Rosato *et al*, 2019), and promote lysosomal exocytosis (Medina *et al*, 2011; Samie *et al*, 2013; Gerndt *et al*, 2020).

We therefore hypothesized that TPC2 activation may modulate lysosomal Ca^{2+} signaling to rescue LSD phenotypes, particularly in LSDs where TRPML1 is impacted. In our study, we focused on MLIV and NPC1 on the one hand, LSDs that both have been shown before to be connected to disrupted lysosomal Ca^{2+} signaling and TRPML1 dysfunction (Shen *et al*, 2012). On the other hand, we focused on juvenile neuronal ceroid lipofuscinosis (JNCL) or Batten disease, caused by mutations in CLN3, an LSD which shows prominent retinal and neurodegenerative phenotypes with gradual vision loss and progressive cognitive decline as observed in MLIV, and with a similar age-dependent disease onset and evidence for disturbed lysosomal Ca^{2+} homeostasis (Chandrachud *et al*, 2015). By analyzing disease hallmarks in patient fibroblasts, novel CRISPR/Cas9-engineered iPSCs/iPSC-derived neurons, and the MLIV mouse upon treatment with a TPC2 small molecule agonist, TPC2-A1-P, we demonstrate that TPC2 activation ameliorates the phenotypes of these LSDs both *in vitro* and *in vivo*.

Results

TPC2 activation modulates LSD phenotypes in human patient fibroblasts

Based on the concept that disrupted endolysosomal Ca^{2+} homeostasis constitutes a major pathomechanism underlying LSDs as evidenced by MLIV, we assessed the effect of our recently published $PI(3,5)P_2$-mimetic TPC2 agonist, TPC2-A1-P (Gerndt *et al*, 2020), releasing both Ca^{2+} and Na^+, on the phenotypes of the above-mentioned LSDs. For NPC1 and MLIV, lactosylceramide (LacCer) and cholesterol trafficking defects are reported (Shen *et al*, 2012; Chen *et al*, 2014). Hence, we started our study by assessing these defects in fibroblasts from NPC1 and MLIV patients compared to control (CTR) fibroblasts. The lipid LacCer is internalized clathrin independently and targeted to the Golgi apparatus in CTR cells, whereas in several LSD fibroblasts including NPC1 and MLIV it accumulates in late endosomes and lysosomes. Accordingly, we observed significant endolysosomal accumulation of LacCer in NPC1 and MLIV, and a range of other LSDs compared to CTR, but not for JNCL ($CLN3^{\Delta 1.02kb/\Delta 1.02kb}$) and Gaucher, as reported previously (Vitner *et al*, 2010), demonstrating reproducibility of the assay (Fig 1A). We next assessed the effect of TPC2 activation in MLIV and NPC1 versus CTR fibroblasts. In MLIV fibroblasts, carrying the most common patient variation ($MCOLN1^{IVS3\text{-}2A>G/Ex1\text{-}7del}$; GM02048) TPC2 activation by TPC2-A1-P significantly reduced lysosomal accumulation of LacCer (Mander's coefficient) and the number of LacCer puncta per area after incubation overnight (16 h) (Fig 1B and C), while in NPC1 cells ($NPC1^{P237S/I1061T}$; GM03123), significant rescue was seen after 48 h incubation (Fig 1D and E). To assess maximal rescue effects, we tested overexpression of a gain-of-function variant of TPC2 ($TPC2^{M484L/G734E}$; Chao *et al*, 2017) with and without TPC2-A1-P activation in MLIV fibroblasts (Fig 1F and G). Both TPC2 overexpression alone and overexpression in combination with TPC2-A1-P significantly reduced lysosomal accumulation of LacCer in MLIV cells, with a stronger effect seen in the combination. To exclude any potential toxic effects of TPC2-A1-P on fibroblasts, cell viability assays were performed (Fig EV1A). Commercially available drugs reported to activate TPC2 were examined alongside TPC2-A1-P (Zhang *et al*, 2019). In these tests, TPC2-A1-P showed no toxicity up to the maximal test concentration (100 μM; Fig EV1B). By using the Ca^{2+} chelator BAPTA-AM, we could further demonstrate that reduction in free intracellular Ca^{2+} induces a similar LacCer trafficking defect in CTR as in MLIV or NPC1 cells (Fig 1H and I), suggesting a relevant role of Ca^{2+} in the process. Furthermore, TPC2-A1-P rescued the lysosomal LacCer accumulation in mock, but not in siTPC2-treated NPC1 fibroblasts, corroborating the on-target effect of TPC2-A1-P (Fig 1J and K). LacCer trafficking is also affected by intracellular cholesterol levels (Pryor *et al*, 2006; Vitner *et al*, 2010; Shen *et al*, 2012; Chen *et al*, 2014). Cholesterol reduction reportedly restores proper LacCer trafficking to Golgi, whereas cholesterol overload redirects LacCer to endolysosomal compartments (Puri *et al*, 1999). We therefore next assessed endolysosomal cholesterol accumulation, which has been reported for both MLIV and NPC1 (Shen *et al*, 2012; Chen *et al*, 2014; Grimm *et al*, 2014). Altered cellular cholesterol homeostasis can conveniently be visualized using the polyene antibiotic filipin. While we could not detect cholesterol storage in JNCL cells, we

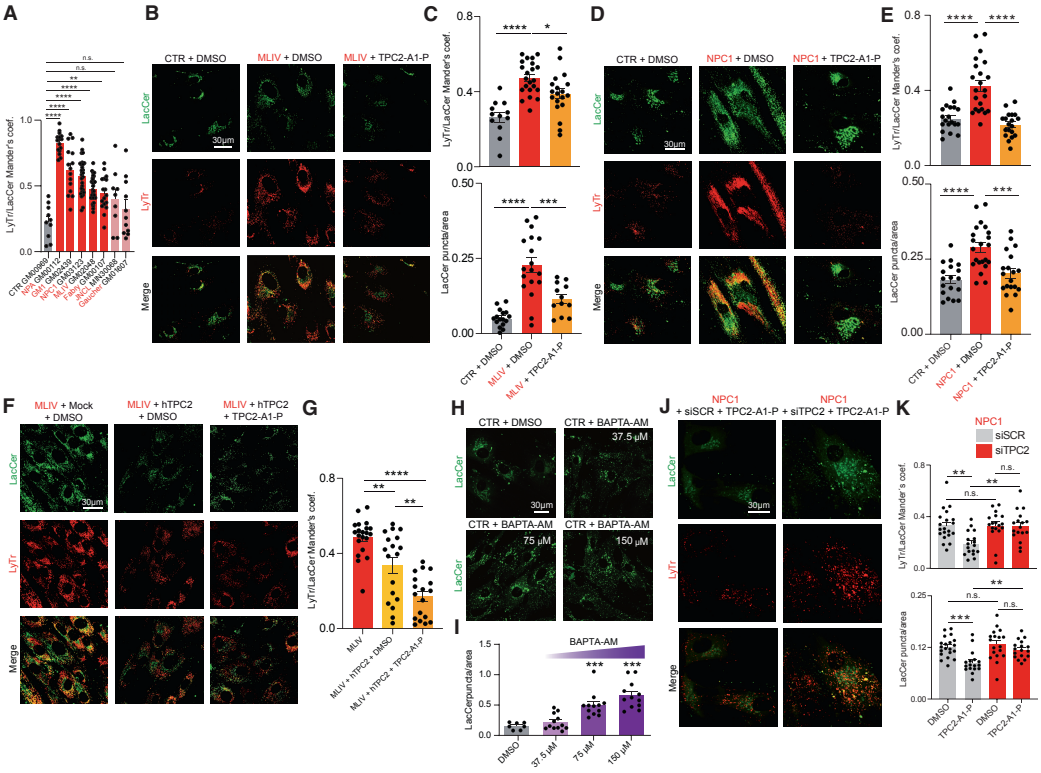

Figure 1. TPC2 agonist effect on lactosylceramide trafficking.

A Colocalization of LacCer and LysoTracker (LyTr) in different CTR and LSD patient fibroblasts. Mander's coefficients were calculated using the Fiji JACoP plugin.

B, C Confocal images (B) and statistical analysis (C) showing colocalization of LacCer and LyTr in human CTR and MLIV fibroblasts, treated with TPC2-A1-P (30 μM, 16 h).

D, E Confocal images (D) and statistical analysis (E) showing colocalization of LacCer and LyTr in human CTR and NPC1 fibroblasts, treated with TPC2-A1-P (30 μM, 48 h).

F, G Confocal images and statistical analysis showing LacCer/LyTr colocalization in MLIV patient fibroblasts which were moc -electroporated and treated with DMSO or electroporated with a gain-of-function hTPC2(M484L/G734E):mCherry TOPO 3.1 vector and treated with either DMSO or TPC2-A1-P (30 μM, 16 h).

H, I Ca^{2+} chelation (BAPTA-AM) dose dependently impairs LacCer trafficking in CTR fibroblasts.

J, K Confocal images (J) and statistical analysis (K) of NPC1 patient fibroblasts treated with 50 nM mock siRNA (siSCR) or siRNA targeting TPCN2 (siTPC2) for 72 h. Cells were then treated with DMSO or TPC2-A1-P (30 μM).

Data information: Shown are mean values ± SEM. $n > 3$ technical and biological replicates for each tested condition (each dot represents an imaged frame containing several cells); one-way ANOVA, *post hoc* Bonferroni's (A, C, E, G, I) or Tukey's (K) multiple comparisons test. *p-value < 0.05; **p-value < 0.01; ***p-value < 0.001; ****p-value < 0.0001.

could confirm that NPC1 and MLIV fibroblasts strongly accumulate cholesterol (Fig 2A and B). In both NPC1 and MLIV cells, accumulated cholesterol was efficiently reduced upon TPC2 activation with TPC2-A1-P (Fig 2C and D). While in MLIV cells, significant effects were seen already after 24 h treatment, again in NPC1 cells only after 48 h effects were significant (Fig EV2A and B). In a further set of experiments, we tested $TPC2^{M484L/G734E}$ overexpression with and without TPC2-A1-P activation, finding that only overexpression in combination with the agonist significantly reduced intracellular cholesterol (Fig 2E–G). Using BAPTA-AM, we could again demonstrate, in analogy to LacCer, that chelation of Ca^{2+} results in cholesterol accumulation (Fig EV2C and D), confirming free intracellular Ca^{2+} to play a role in the process. BAPTA-AM was also shown to blunt the effect of TPC2-A1-P (Fig EV2E and F). We further silenced TPC2 expression in healthy human fibroblasts, which resulted in cholesterol accumulation in siTPC2, but not in mock-treated cells (Fig 2H and I), in accordance with previous observations in murine TPC2 knockout fibroblasts (Grimm *et al*, 2014). Furthermore, TPC2-

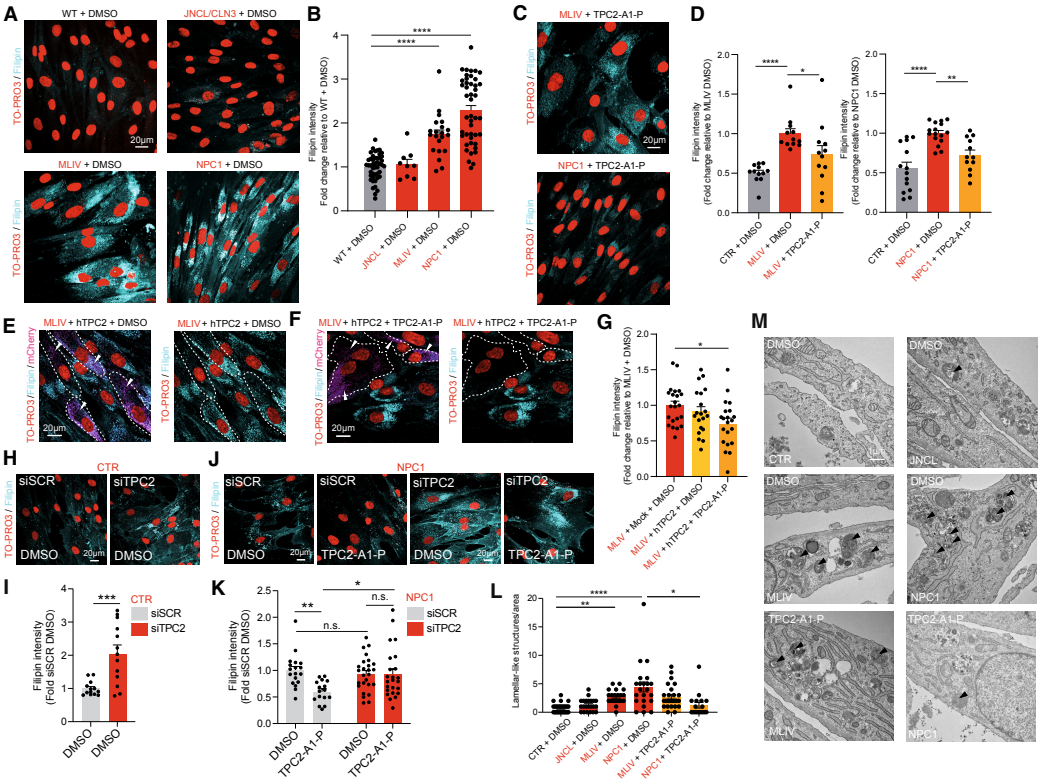

Figure 2. TPC2 agonist effect on cholesterol accumulation and ultrastructural changes.

A, B Confocal images (A) and statistical analysis (B) of cholesterol accumulation in human CTR, MLIV, JNCL, and NPC1 fibroblasts. Cholesterol accumulation was evident for NPC1 and MLIV fibroblasts but not for JNCL fibroblasts. The images show filipin staining to visualize cholesterol accumulation and TO-PRO3 as nuclear staining.

C, D TPC2-A1-P (30 μM, 48 h) rescued NPC1 and MLIV cholesterol accumulation.

E–G Confocal images (E-F) and statistical analysis (G) of MLIV patient fibroblasts mock electroporated and treated with DMSO or electroporated with a gain-of-function hTPC2(M484L/G734E):mCherry TOPO 3.1 vector (white arrowheads) and treated with either DMSO or TPC2-A1-P (30 μM, 48 h).

H–K Confocal images (H-I) and statistical analysis (J-K) of human CTR and NPC1 patient fibroblasts treated with 50 nM mock siRNA (siSCR) or siRNA targeting TPCN2 (siTPC2) for 72 h. Cells were then treated with DMSO or TPC2-A1-P (30 μM).

L, M Statistics (L) and electron microscopy images (M) of human CTR, MLIV, JNCL, and NPC1 fibroblasts. The effect of the treatment with TPC2 agonist (30 μM, 48 h) was examined in NPC1 and MLIV cells.

Data information: Shown are mean values ± SEM. $n > 3$ technical and biological replicates for each tested condition (each dot represents an imaged frame containing several cells); one-way ANOVA, *post hoc* Bonferroni's multiple comparisons test (B, D, E, L), or two-tailed Student's *t*-test (J and K). *p-value < 0.05; **p-value < 0.01; ***p-value < 0.001; ****p-value < 0.0001.

A1-P rescued the cholesterol accumulation in mock-treated, but not in siTPC2-treated NPC1 fibroblasts, corroborating the on-target effect of TPC2-A1-P (Fig 2J and K). Efficacy of the siRNAs was validated using qRT-PCR (Fig EV2G). We next used electron microscopy (EM) to assess ultrastructural changes following compound treatment. Gross alterations in endolysosomal morphology have previously been reported in MLIV and NPC1 fibroblasts (Garver *et al*, 2000; Vergarajauregui *et al*, 2008). We found an abundance of lysosomes with aberrant/lamellar structures in NPC1 and to a lesser extent in MLIV cells, but observed no changes in lysosomal morphology in JNCL fibroblasts (Fig 2L and M). NPC1 fibroblasts showed a stronger difference from CTR than MLIV fibroblasts and only for the former we found TPC2-A1-P treatment to significantly restore ultrastructural morphology (Fig 2L and M). While neither ultrastructural changes nor changes in LacCer trafficking or cholesterol accumulation were detectable in JNCL cells, JNCL patient fibroblasts are known to accumulate lipofuscin—appearing as an autofluorescent green-to-yellow pigment under ultraviolet light (Mole *et al*, 2020). We used the cell

cycle blocker mitomycin C to exacerbate the progressive storage of lipofuscin within lysosomal compartments in JNCL fibroblasts (Fig 3A–C). Treatment with TPC2-A1-P rescued this autofluorescence, decreasing it to CTR levels (Fig 3A–C). Furthermore, we used fluorescently labeled Shiga toxin (STX) to visualize globotriaosylceramide (Gb3) accumulation, a recently reported (Soldati *et al*, 2021) phenotype in JNCL cells, and found that TPC2-A1-P rescued Gb3 accumulation significantly (Fig 3D and E). In conclusion, activating TPC2 with TPC2-A1-P restores various LSD phenotypes in patient-derived fibroblasts.

Generation of human isogenic iPSC models of MLIV and JNCL using CRISPR/Cas9

To extrapolate our patient fibroblast data to human neurons with isogenic controls, we used CRISPR/Cas9 to generate iPSCs expressing either the most common MLIV-causing mutation $MCOLN1^{IVS3\text{-}2A>G}$ (Bargal *et al*, 2001) or the JNCL-causing mutation $CLN3^{D416G}$. In addition, we generated a knockout model for CLN3 ($CLN3^{\Delta Ex4\text{–}7}$) (Fig 4A and B). To identify a suitable JNCL point mutant candidate, we performed a systematic analysis of the subcellular localization of

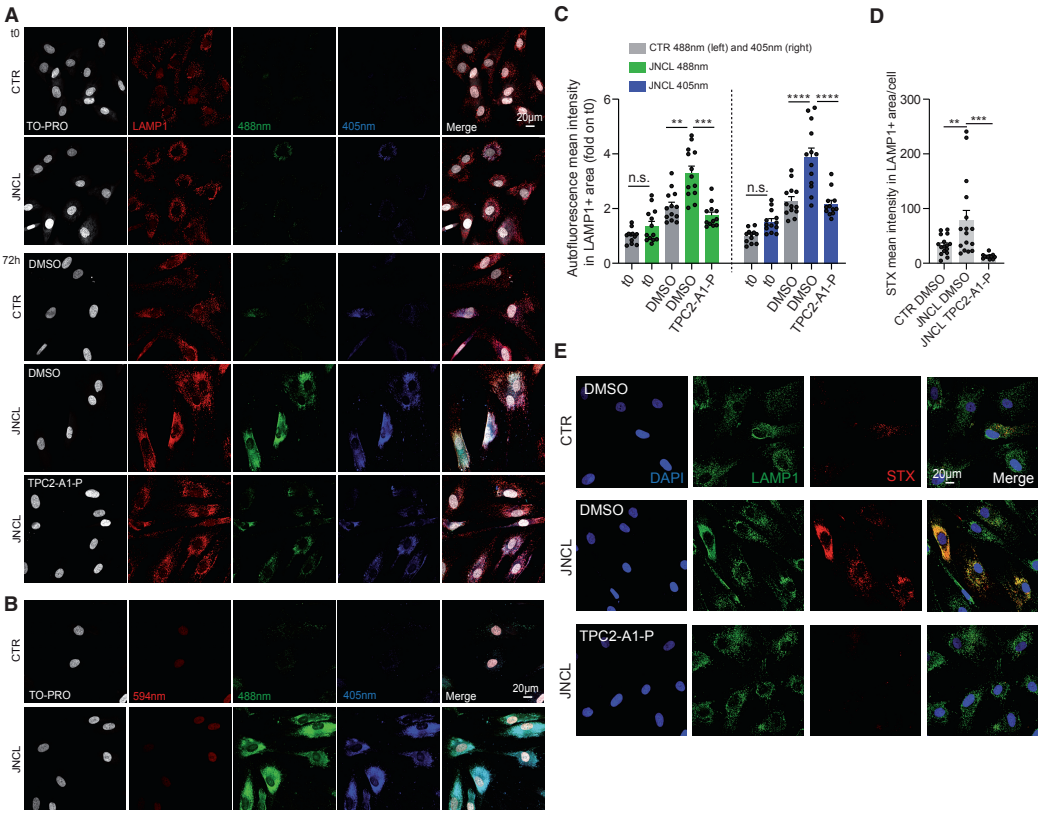

Figure 3. TPC2 agonist effect on lipofuscin and Gb3 accumulation.

A Confocal images of CTR and JNCL fibroblasts. Images show LAMP1 staining and autofluorescence at 405 and 488 nm excitation wavelength, respectively, corresponding to the lipofuscin autofluorescence spectrum. Cells were treated with DMSO or TPC2-A1-P (30 µM) following cell cycle arrest (2 h mitomycin C treatment).

B Confocal images showing no autofluorescence signal at 594 nm excitation wavelength (used for LAMP1 staining).

C Mean autofluorescence intensity in $LAMP1^{+}$ area.

D, E Confocal images of Gb3 accumulation stained with Shiga toxin (STX) in CTR and JNCL fibroblasts. Cells were treated with DMSO or TPC2-A1-P (30 µM) after cell cycle arrest.

Data information: Shown are mean values ± SEM. $n > 3$ technical and biological replicates for each tested condition (each dot represents an imaged frame containing several cells); one-way ANOVA, *post hoc* Bonferroni's multiple comparisons test. **p-value < 0.01; ***p-value < 0.001; ****p-value < 0.0001.

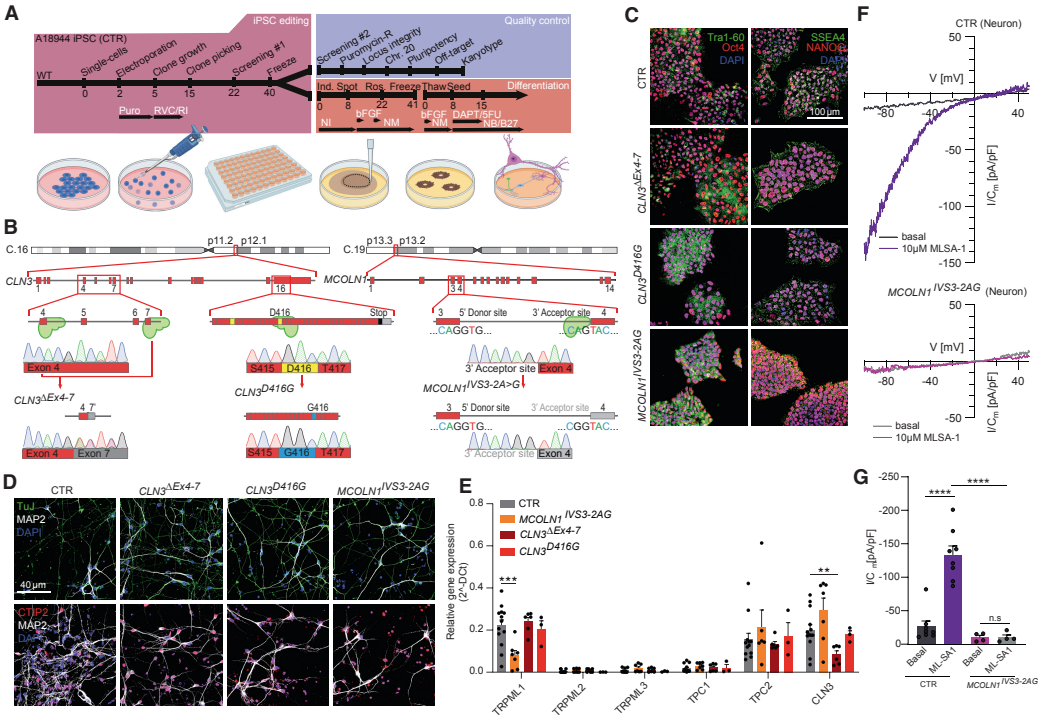

Figure 4. Generation, differentiation, and characterization of lysosomal storage disease iPSCs.

A, B Timeline of gene editing, quality control, and differentiation. The A18944 iPSC line (CTR) was used for gene editing. iPSCs were electroporated with a plasmid carrying spCas9, target gRNAs, and repair template. Target sites are shown in (B).

C Immunofluorescence images of pluripotency markers Tra1-60, Oct4, SSEA4, and NANOG demonstrate pluripotency of CTR and gene-edited iPSCs.

D Edited iPSCs were differentiated into cortical neurons expressing the neuronal markers TuJ and MAP2, and the cortical neuron transcription factor CTIP2.

E Using RT-qPCR, we assessed the expression of lysosomal storage disease genes (TRPML1 for MLIV and CLN3 for JNCL) and drug targets (TRPMLs and TPCs).

F, G iPSC-derived neurons were treated with apilimod to enlarge lysosomes, and TRPML1 responsiveness was assessed. ML-SA1 (10 µM)-elicited TRPML1 currents were observed in CTR lysosomes but not in MLIV neurons, indicative of abrogated TRPML1 function.

Data information: Shown are mean values ± SEM. $n > 3$ technical and biological replicates for each tested condition (each dot represents a single measurement from distinct neuronal differentiations); Gaussian distribution assumed; one-way ANOVA, followed by Tukey *post hoc* test. **p-value < 0.01; ****p-value < 0.0001.

disease-causing CLN3 point mutations and correlated them with reported clinical phenotypes (Fig EV3A–E). Based on this analysis, we chose CLN3^{D416G}, which shows significant reduction in endolysosomal localization compared to its WT counterpart but not complete mislocalization. Clinically, CLN3^{D416G} causes the classical, severe JNCL phenotype, marked by retinitis pigmentosa and progressive neurodegeneration (Kousi *et al*, 2012). The mutations were engineered into WT A18944 iPSCs (CTR) using CRISPR/Cas9-mediated gene editing (Fig 4A and B) (Weisheit *et al*, 2020). Active gRNAs (Brinkman *et al*, 2014) were transfected alongside spCas9 and repair template. Since the cut sites overlapped with introduced mutations, our approaches did not require blocking mutations to prevent re-editing, yielding several homozygously edited clones (Paquet *et al*, 2016; Kwart *et al*, 2017). Established iPSC clones were deeply quality controlled to exclude undesired on-target effects by qgPCR and SNP genotyping (Weisheit *et al*, 2020, 2021), integration of editing components by confirming puromycin sensitivity, chromosomal abnormalities by performing molecular karyotyping, and off-target effects by sequencing the top off-target sites determined by two distinct algorithms (CFD/MIT) (Fig EV4A–E). Maintenance of pluripotency in edited lines was confirmed by staining for pluripotency markers Tra1-60, Oct4, SSEA4, and NANOG (Fig 4C).

Effect of TPC2 activation in neurons derived from human LSD iPSCs

JNCL and MLIV are both marked by primary neuronal dysfunction as evidenced by neuronal monocultures developing pathological characteristics such as autophagic defects, ultrastructural abnormalities, and expansion of the lysosomal compartment (Curcio-Morelli

et al, 2010; Lojewski *et al*, 2014; Kinarivala *et al*, 2020). We therefore employed our established protocol to differentiate iPSCs into cortical neurons (Paquet *et al*, 2016) (Fig 4D) and assessed whether these neurons express genes relevant for disease (TRPML1 for MLIV and CLN3 for JNCL) and treatment (TRPML1 and TPC2). Transcripts of TRPML1, TPC2, and CLN3 were readily detectable in the cortical neurons, while the endolysosomal cation channels TRPML2, TRPML3, and TPC1 were largely undetectable (Fig 4E). Measuring TRPML1-dependent currents using the endolysosomal patch-clamp technique (Chen *et al*, 2017), showed absence and presence in MCOLN1$^{IVS3\text{-}2A>G}$ mutant and CTR neurons, respectively (Fig 4F and G). Phenotypically, we assessed these neurons by analyzing lysosomal cathepsin B (CtsB) activity, LysoTracker (LyTr) staining, and ultrastructures by electron microscopy. To exclude any potential toxic effects of TPC2-A1-P on iPSC-derived neurons again, cell viability assays were performed (Fig EV1C). Increased CtsB activity is linked to cell death in MLIV (Colletti *et al*, 2012) and, conversely, decreased CtsB activity has been reported in CLN3 disease (Metcalf *et al*, 2008). We applied fluorescence recovery after photobleaching (FRAP) as established by Metcalf *et al* (2008), finding MCOLN1$^{IVS3\text{-}2A>G}$ neurons to exhibit significantly increased CtsB activity, while JNCL (CLN3^{D416G} and CLN3$^{\Delta Ex4\text{–}7}$) neurons either exhibited slightly reduced or unchanged CtsB activity compared to CTR. TPC2-A1-P treatment significantly decreased CtsB activity in iPSC-derived MCOLN1$^{IVS3\text{-}2A>G}$ neurons (Fig 5A and B). We next assessed the protein levels of intracellular CtsB by western blot analysis, finding increased CtsB levels in MCOLN1$^{IVS3\text{-}2A>G}$ compared to CTR neurons, rescued by TPC2-A1-P treatment (Fig 5C and D). We further assessed acidic compartments by LyTr (LysoTracker) staining. The lysosomal compartment appeared expanded in MCOLN1$^{IVS3\text{-}2A>G}$ and JNCL neurons compared to CTR, which was ameliorated upon TPC2-A1-P treatment (Fig 5E–G). We continued with electron microscopy analyses of MCOLN1$^{IVS3\text{-}2A>G}$ and JNCL neuronal progenitor cells to assess their ultrastructure. Lysosomal inclusion bodies were readily detected in DMSO-treated MCOLN1$^{IVS3\text{-}2A>G}$ neuronal progenitor cells (NPC), and their number was significantly decreased upon TPC2-A1-P treatment. Ultrastructural analyses in JNCL cells on the other hand revealed no significant change in inclusion body density, remaining further unchanged upon TPC2 activation or DMSO treatment (Fig 5H and I). However, the Cristae numbers per mitochondrial area were significantly reduced in CLN3$^{\Delta Ex4\text{–}7}$ compared to CTR NPC, and TPC2-A1-P treatment significantly increased these numbers again (Fig 5H and I).

Lysosomal exocytosis and autophagy as potential rescue mechanisms

We next examined the effect of TPC2-A1-P on lysosomal exocytosis in LSD cells as potential mechanism, underlying the observed rescue effects. Using LAMP1 translocation to the plasma membrane as readout, we found that TPC2-A1-P has a similar effect on lysosomal exocytosis in CTR as well as in MLIV, NPC1, and JNCL patient fibroblasts, demonstrating an intact TPC2-mediated exocytosis capability in the diseased cells (Fig 6A–D). As positive controls, the TRPML1 agonist ML-SA1 and ionomycin were used. We next assessed the effect of TPC2-A1-P on autophagy. Again, as positive control, ML-SA1 was used. TPC2-A1-P increased starvation-mediated autophagy in CTR fibroblasts (Fig 6E–G) in a TPC2-dependent manner as demonstrated by siRNA experiments (Fig EV4F and G) and recovered impaired autophagic flux in NPC1 and MLIV fibroblasts (Fig 6F and G). Likewise, in iPSC-derived cortical neurons, TPC2-A1-P increased starvation-mediated autophagy in CTR and MCOLN1$^{IVS3\text{-}2A>G}$ (MLIV) neurons (Fig 6H). The autophagic flux blockade in NPC1 and MLIV fibroblasts also leads to P62/Sequestosome 1 (SQSTM1) accumulation (Vergarajauregui *et al*, 2008; Elrick *et al*, 2012; Sarkar *et al*, 2013). While starvation alone does not sufficiently clear P62 accumulation, we found that treatment with TPC2-A1-P under starvation conditions alleviates the autophagic flux blockade in MLIV and NPC1 fibroblasts, clearing the accumulated P62 (Figs 6I and J, and EV4H–K).

TPC2 expression in brain assessed by RT-qPCR and by analyzing a novel reporter mouse model

To investigate the *in vivo* efficacy of TPC2-A1-P, we made use of the MLIV mouse model (Venugopal *et al*, 2007; Grishchuk *et al*, 2014, 2015; Walker & Montell, 2016). One essential prerequisite for TPC2 as a drug target for neurodegenerative LSDs is expression in various cell types of the CNS. To assess Tpc2 expression in the brain, we generated a TPC2 reporter mouse model (*Tpcn2*$^{IRES\text{-}Cre/eR26\text{-}\tau GFP}$) (Figs 7A and EV5A and B) (Wyatt *et al*, 2017). The labeling of TPC2-positive cells via expression of τGFP is dependent on the expression of Cre recombinase under control of the TPC2 promotor. Focusing on the hippocampus and cerebellum, two vulnerable brain regions in LSD-associated neurodegeneration (Frei *et al*, 1998; Prasad *et al*, 2000; Greene *et al*, 2001; Pontikis *et al*, 2004; Walkley & Suzuki, 2004; Grishchuk *et al*, 2014, 2015), we observed the most distinct Tpc2 expression pattern in neuronal fibers extending toward the hippocampal CA3 pyramidal layer. Furthermore, throughout the hippocampus, Tpc2^{+} pyramidal neurons and processes were readily observed (Fig 7B). Tpc2 was also expressed in hippocampal and cerebellar astrocytes, microglia, and mural cells (CD13^{+}) (Fig 7B). To quantify channel expression, we analyzed Tpc2 transcript levels in the mouse brain, finding Tpc2 transcripts in cortex, hippocampus, cerebellum, and other brain regions (Fig 7C). We also assessed TPC2 transcription in the human brain (Fig 7D). The highest TPC2 expression was observed in hippocampus, cerebellum, corpus callosum, nucleus accumbens, and paracentral and postcentral gyrus (Fig 7D). We further quantified cell-type-specific expression in hippocampus, cerebellum, and corpus callosum using the reporter mouse model (Fig 7E). In conclusion, TPC2 is expressed in all relevant cell types and regions of the brain to treat the lysosomal storage diseases under investigation here (Fig 7F).

Pharmacokinetics and *in vivo* testing of TPC2-A1-P in the MLIV mouse model

To determine blood–brain barrier permeability and clearance of TPC2-A1-P, we injected CTR (WT) mice with the compound and measured its levels in plasma and brain by LC–MS/MS. Following its injection, TPC2-A1-P decayed rapidly both in plasma and brain, being undetectable after 240 min (Fig 8A). We determined the elimination rate constants in the plasma and brain, fitting a two-phase decay model to plasma elimination, and a one-phase decay model in the brain (Fig 8B). We extrapolated these results

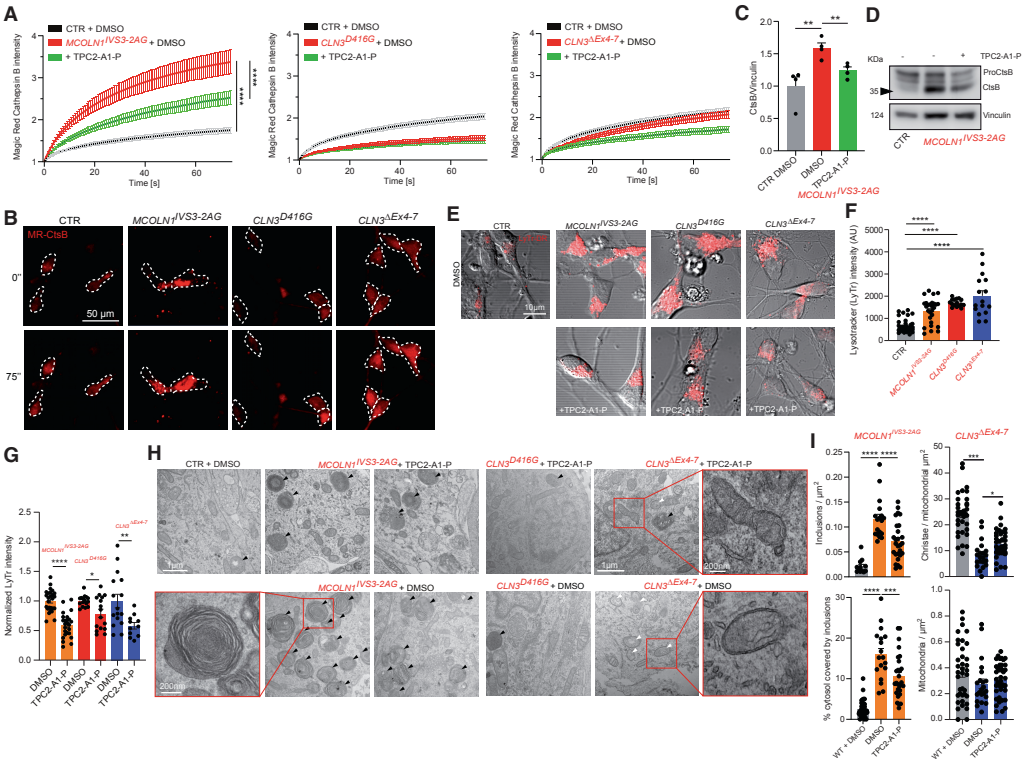

Figure 5. Effect of TPC2-A1-P on human neuronal LSD phenotypes.

Cortical neurons were differentiated from iPSCs, generating lysosomal storage disease neurons and isogenic controls.

A, B Lysosomal proteolysis was measured following pre-treatment with DMSO/TPC2-A1-P, using the magic red (MR) cathepsin B substrate, and performing FRAP measurements to assess the proteolysis rate. MCOLN1$^{IVS3\text{-}2A>G}$ (MLIV) neurons showed increased proteolysis, while CLN3^{D416G} and CLN3$^{\Delta Ex4-7}$ neurons (JNCL) exhibited either significantly lower or slightly reduced proteolysis rates, respectively.

C, D Western blot analysis of cathepsin B (CtsB) in CTR and MCOLN1$^{IVS3\text{-}2A>G}$ neurons treated with TPC2-A1-P (30 μM) or DMSO.

E–G Cortical neurons were treated with compounds and acidic compartments stained with LysoTracker (LyTr). The endolysosomal expansion was observed in MCOLN1$^{IVS3\text{-}2A>G}$, CLN3^{D416G}, and CLN3$^{\Delta Ex4-7}$ neurons, which was ameliorated by TPC2-A1-P (30 μM) treatment.

H, I Electron microscopy analysis of neuronal rosettes (neuronal progenitor cells, NPC) treated with DMSO or TPC2-A1-P. TPC2-A1-P treatment significantly decreased the number of inclusion bodies (black arrowheads) in MCOLN1$^{IVS3\text{-}2A>G}$. CLN3^{D416G} and CLN3$^{\Delta Ex4-7}$ lacked an appropriate assay window and showed no significant accumulation of inclusion bodies. However, CLN3$^{\Delta Ex4-7}$ NPC showed significantly more mitochondria with aberrant cristae numbers (white arrowheads), a phenotype which was rescued by TPC2-A1-P (30 μM) treatment.

Data information: Shown are mean values ± SEM. $n > 3$ technical and biological replicates for each tested condition (each dot represents an imaged frame containing several cells, obtained from at least three distinct neuronal differentiations); one-way ANOVA, *post hoc* Tukey's multiple comparisons test, or two-tailed Student's *t*-test (C). ***p*-value < 0.01; ****p*-value < 0.001; *****p*-value < 0.0001.

to predict that an injection of 20 mg/kg TPC2-A1-P would yield a therapeutic dose for ca. 20 min upon injection (estimated C_0 between 30 and 60 μM and above 10 μM for ca. 20 min; Fig 8C). Due to its rapid clearance, we opted for a daily intraperitoneal treatment regimen. After 3 months of daily injections, mice were sacrificed, and brains were collected for histology. Previous reports demonstrated gliosis in both human patients (Folkerth *et al*, 1995) and the MLIV mouse model (Grishchuk *et al*, 2014; DeRosa *et al*, 2021). We assessed gliosis in cerebellum and hippocampus of the MLIV mouse model, observing prominent astrogliosis in the cerebellar arbor vitae (av) and granular (gr) cell layer, and mild microgliosis of the cerebellar arbor vitae, while no significant differences were seen in hippocampus (Fig 8D). Mice injected with TPC2-A1-P were found to show significant amelioration of the astrogliosis phenotype in the cerebellar av (Fig 8D and E). Furthermore, P62/SQSTM1 aggregates were shown previously to accumulate in the central nervous system of the MLIV mouse model, suggesting an impairment in protein degradation (Micsenyi

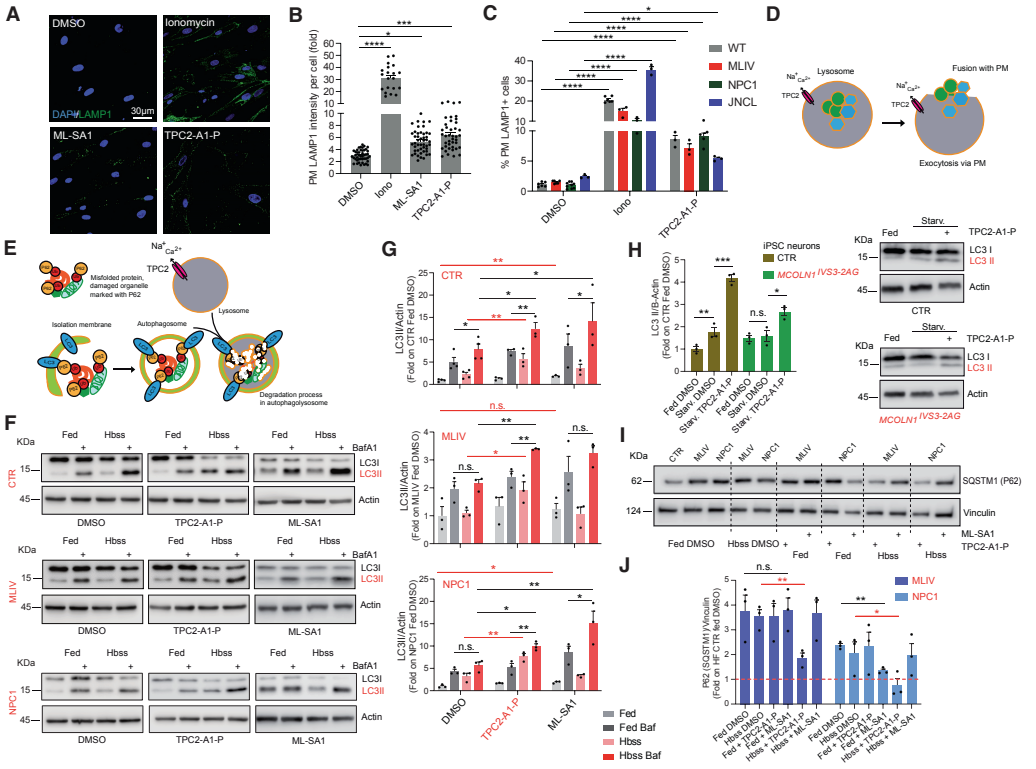

Figure 6. Effect of TPC2-A1-P on lysosomal exocytosis and autophagy.

A Confocal images of plasma membrane (PM) LAMP1 immunofluorescence in CTR fibroblasts. LAMP1 on the PM is expressed as fold change relative to DMSO-treated cells.

B Statistical analysis of lysosomal exocytosis data as shown in (A).

C Lysosomal exocytosis in CTR, MLIV, NPC1, and JNCL human fibroblasts. PM-localized LAMP1 was measured by flow cytometry, expressed as percent of CTR DMSO-treated cells. Ionomycin in (A–C) (4 μM; 10 min treatment) was used as a positive control. TPC2-A1-P and ML-SA1 (30 μM, each; 90 min treatment in A–C).

D Cartoon showing lysosomal exocytosis. Statistics (B, C): Shown are mean values ± SEM. $n > 3$ for each tested condition (in (B), each dot represents an imaged frame containing several cells, and in (C) each dot is the mean FITC intensity value expressed as a percentage obtained from at least 1×10^4 events); two-way ANOVA, *post hoc* Dunnett's (B), or Tukey's (C) multiple comparisons test; *p-value < 0.05; ***p-value < 0.001; ****p-value < 0.0001.

E Cartoon showing the roles of LC3 and P62 in the autophagic pathway.

F, G Immunoblot analysis of endogenous LC3 (LC3I-II) following TPC2-A1-P or ML-SA1 (30 μM, each) treatment, alone or with BafA1, under fed (complete media), or starvation (HBSS) conditions in CTR, MLIV, and NPC1 patient fibroblasts. Graphs show densitometry of LC3II bands normalized to actin.

H Immunoblot analysis of endogenous LC3 (LC3I-II) following TPC2-A1-P (30 μM) or DMSO treatment, under fed (complete neurobasal/B27), or starvation (DMEM/F12 free) conditions in CTR and MLIV iPSC-derived cortical neurons. Graphs show densitometry of LC3II bands normalized to actin.

I, J Immunoblot and statistical analysis of endogenous SQSTM1 (P62) upon TPC2-A1-P or ML-SA1 (30 μM, each) treatment, under fed (complete media), or starvation (HBSS) conditions in CTR, MLIV, and NPC1 patient fibroblasts.

Data information: In (G, H, J) shown are mean values ± SD. $n = 3$ lysates per condition pooled from three independent experiments; two-tailed Student's t-test.
*p-value < 0.05; **p-value < 0.01; ***p-value < 0.001.

et al, 2009). Indeed, we observed a massive accumulation of P62/SQSTM1 inclusions in the MLIV mouse cerebellar granular cell layer and in the hippocampus compared to CTR (WT). Treatment with TPC2-A1-P significantly reduced the number of P62/SQSTM1 aggregates (Fig 8F–I). Finally, we tested TPC2-A1-P- versus vehicle-treated mice on motor performance on the accelerating rotarod tasks (Walker & Montell, 2016), demonstrating a significant rescue effect of TPC2-A1-P over vehicle treatment in MLIV mice (Fig 8J). In contrast to rotarod, no significant differences between CTR and MLIV mice were found in horizontal exploratory activity in the open-field test (Fig EV5C). Altogether, these data suggest that TPC2 activation is able to restore central

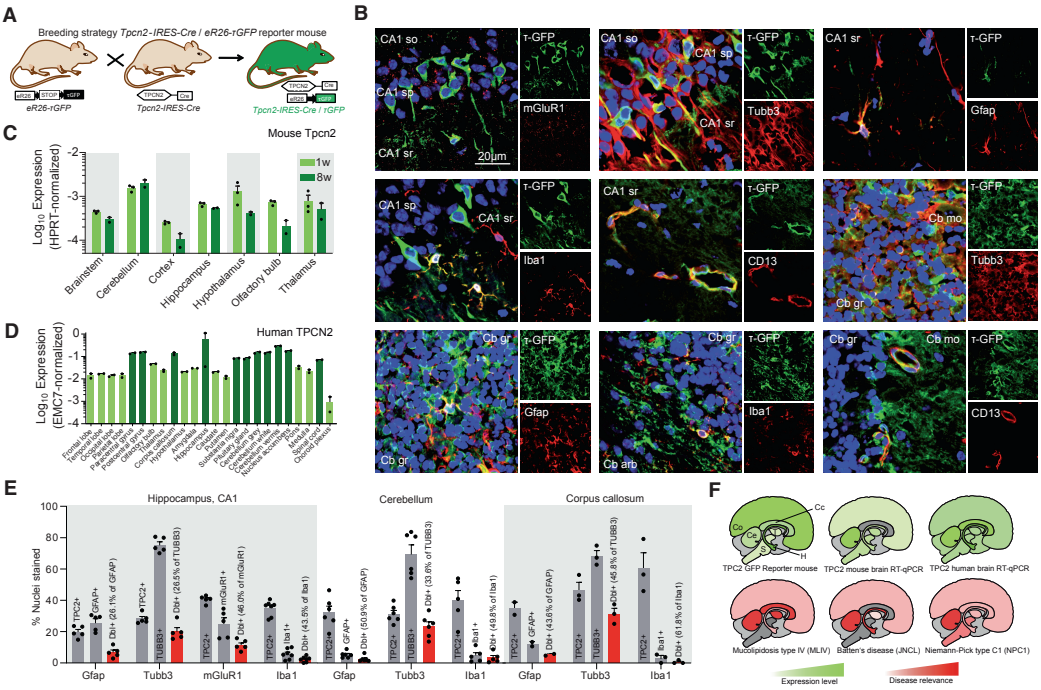

Figure 7. Expression of TPC2 in human and mouse brains.

The TPC2 reporter mouse *Tpcn2*$^{IRES\text{-}Cre/eR26\text{-}tGFP}$ was generated as previously described (Wen *et al*, 2011; Wyatt *et al*, 2017).

A–B Both neurons and glia were found to express Tpc2 in the corpus callosum, the hippocampus, and the cerebellum (so, stratum oriens; sp, stratum pyramidale; sr, stratum radiatum; mo, molecular layer; gr, granular layer). Subpopulations of astrocytes (Gfap) and microglia (Iba1) express Tpc2 (E).

C One week (1w)- or 8-week (8w)-old mouse brains were dissected, and brain Tpc2 transcript was mapped.

D A cDNA array was used to map TPC2 transcripts in the human brain.

E Quantification of astrocytes(Gfap), microglia (Iba1) and neurons in different brain areas and percentage of cells coexpressing Tpc2 and the respective marker (Dbl = double labeled).

F Tpc2 expression in the Tpc2 reporter mouse, mouse brain, and human brain is summarized as cartoons, finding highest expression in cerebellum and hippocampus (top panels). Affected brain regions in the lysosomal storage diseases MLIV, JNCL, and NPC1 based on patient and mouse data are color-coded.

nervous system defects and the decline in motor performance in the MLIV mouse model.

Discussion

Boosting lysosomal trafficking, autophagy, and exocytosis shows a promising therapeutic strategy to improve lysosomal function in several diseases (Medina *et al*, 2011; Bae *et al*, 2014; Grimm *et al*, 2014; Medina *et al*, 2015; García-Rúa *et al*, 2016; Zhong *et al*, 2016; Grimm *et al*, 2017; Bonam *et al*, 2019; Tsunemi *et al*, 2019). Here, we assessed the effect of TPC2 activation on LSD phenotypes in human fibroblasts and isogenic iPSC-based neuronal models. We show that TPC2 activation with TPC2-A1-P rescues storage phenotypes in MLIV, NPC1, and JNCL cells. Our *in vivo* results further indicate that TPC2-A1-P restores central nervous system defects, including astrogliosis and accumulation of P62/SQSTM1 inclusions in MLIV mice (Folkerth *et al*, 1995; Grishchuk *et al*, 2014; DeRosa *et al*, 2021), as well as improves their motor performance (rotarod). Endolysosomes depend on the activity of their channels and transporters, dysfunction of which often severely affects organelle function and underlies neurodegenerative disease pathology. TRPML1 and TPC2 are the primary lysosomal Ca^{2+} release channels, mediating the Ca^{2+} efflux that so often is impaired in neurodegeneration (e.g., NPC1, MLIV, Fabry, and Alzheimer's disease (Feng & Yang, 2016)). TRPML1 function is directly affected in MLIV (Chen *et al*, 2014), while in NPC1 and other LSDs, TRPML1 activity is reduced, e.g., by accumulating sphingomyelin (Shen *et al*, 2012). In addition, lysosomal pH is often increased in LSDs, affecting the activity of not only many lysosomal enzymes but also TRPML1 (Dong *et al*, 2010). While TRPML1 activity is pH dependent, decreasing with increasing pH,

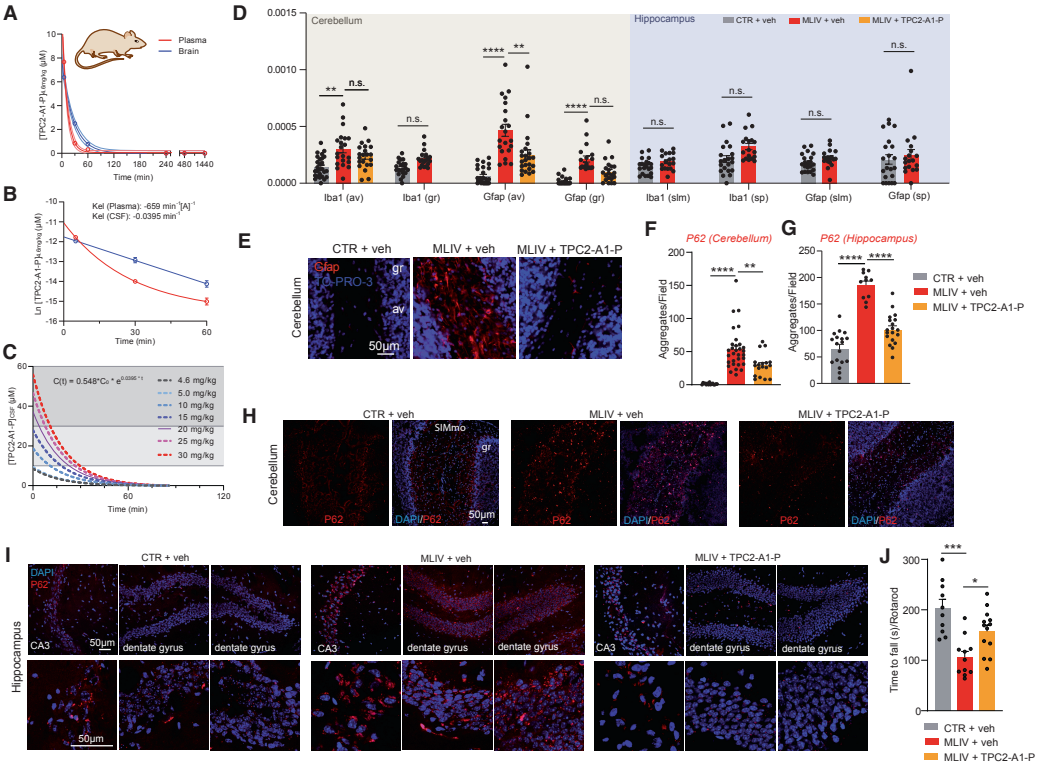

Figure 8. TPC2-A1-P pharmacokinetics and *in vivo* rescue effects in MLIV mice.

A TPC2-A1-P was injected intravenously, and mice were sacrificed at the indicated time. TPC2-A1-P was measured in plasma and brain by LC–MS/MS. TPC2-A1-P was rapidly eliminated, being undetectable by 240 min.

B Elimination rate constants were determined using a semi-log plot. A two-phase decay model could fit the obtained data points in plasma, while a one-phase decay model fits the data in the brain.

C Brain [TPC2-A1-P] was simulated for various injected doses. 20 mg/kg TPC2-A1-P was chosen to avoid off-target activity while providing a therapeutic dose for > 20 min.

D, E From 2 months of age, MLIV mice were injected daily with TPC2-A1-P i.p. and sacrificed after 13 weeks; av, arbor vitae; gr, granular cell layer; slm, stratum lacunosum moleculare; and sp, stratum pyramidale. Mild microgliosis (Iba1) was observed only in the cerebellar av, while astrogliosis (Gfap) was observed in the cerebellar av and gr layers in MLIV mice. TPC2-A1-P ameliorated MLIV-associated cerebellar astrogliosis.

F, G Plots showing mean numbers of P62 aggregates per section (cerebellum (F) and hippocampus (G)).

H, I Confocal images of endogenous P62/SQSTM1 inclusion in CTR and MLIV mouse cerebellar coronal (H) and hippocampal (I) sections.

J Results of the rotarod experiments using MLIV mice treated with vehicle or TPC2-A1-P, respectively, compared to vehicle-treated WT littermates (CTR).

Data information: Shown in (D) are mean cell densities for the indicated marker ± SEM; shown in (F, G) and (J) are mean values ± SEM (each dot represents an imaged frame containing several cells, >3 frames per condition (F, G) or single animals (J)); two-way ANOVA, *post hoc* Bonferroni's (D), Dunnett's (F, G), or Tukey's (J) multiple comparisons test. *$p < 0.05$; **$p < 0.01$; ***p-value < 0.001; ****$p < 0.0001$. The following mouse numbers per condition were used: CTR+DMSO, $n = 6$; MLIV + DMSO, $n = 3$; MLIV + TPC2-A1-P, $n = 4$ (D–I); CTR+veh, $n = 10$; MLIV + veh, $n = 11$; MLIV + TPC2-A1-P, $n = 13$ (J).

TPC2 activation by $PI(3,5)P_2$ is pH independent (Wang *et al*, 2012), which may be an advantage when targeting TPC2. Our results provide an incentive to further investigate the potential benefit of TPC2 activation in various LSDs. Besides LSDs, TRPML1/TPC2 activation may also have relevance for adult-onset neurodegenerative disease therapy. Indeed, stimulation of lysosomal exocytosis via TRPML1 has recently been shown to clear α-synuclein accumulation in Parkinson's disease dopaminergic neurons (Tsunemi *et al*, 2019), while another study demonstrated that activation of TRPML1 cleared amyloid-beta (Aβ), which accumulates by unknown mechanisms in the lysosomal and autophagic compartments of neurons in the HIV-infected brain

(Bae *et al*, 2014). These examples encourage further investigation of targeting TRPML1/TPC2 also in adult-onset neurodegenerative disease therapy.

Materials and Methods

Human fibroblast cell culture and electroporation

The following human fibroblast cells isolated from healthy/diseased individuals were investigated: CTR (control) (GM00969), MLIV (GM02048/MCOLN1$^{IVS3\text{-}2A>G/Ex1\text{-}7del}$), NPC1 (NPC1$^{P237S/I1061T}$; GM03123), NPA (SMPD1$^{L302P/L302P}$; GM00112), Gangliosidosis (GLB1$^{R201C/R201C}$; GM02439), Gaucher (GBA$^{N370S/V394L}$; GM01607), and Fabry (GLA$^{W162+IVS4\text{-}16A>G+IVS6\text{-}22C>T}$; GM00107) from Coriell, and JNCL fibroblasts (CLN3$^{\Delta1.02kb/\Delta1.02kb}$; MIN30068). The cells were grown in DMEM (supplemented with 1 g/l glucose, pyruvate, GlutaMAX, 15% FBS, and 1% P/S) and kept at 37°C with 5% CO_2. Cells were electroporated using the Neon system (Invitrogen) with 100 µl tips according to the manufacturer's instructions, electroporating 10^6 cells at a time with 5 µg plasmid using 2 × 20 ms 1,400 V pulses. Following electroporation, 30,000 cells were seeded for cell biological assays into ibiTreat-coated eight-well chambers (ibidi) or onto poly-L-lysine-coated 12 mm glass coverslips.

Lactosylceramide (LacCer) trafficking assay

Human fibroblasts were cultured in ibiTreat eight-well chambers (ibidi) for live-cell imaging overnight prior to treatments. Cells were treated with 30 µM agonist in DMSO (to a final DMSO concentration of 0,3%) overnight or up to 48 h, and the lactosylceramide trafficking assay was subsequently initiated: Cells were washed once with PBS, and 25 µM LacCer (BODIPY FL C5-Lactosylceramide, Invitrogen) pulsed in serum-free culture medium for 1 h at 37°C. Cells were washed twice with PBS and chased with complete DMEM (including 15% FBS and the indicated agonists) for 2 h at 37°C. LyTr-DR (LysoTracker-Deep Red; diluted 1:10,000, Invitrogen) was added 1,5 h into the chase time to visualize acidic organelles. The cells were subsequently washed three times with PBS, before adding a complete phenol-red-free medium for imaging. The cells were transferred to a pre-heated 37°C incubation chamber mounted onto a Zeiss Confocal microscope (LSM 880) and imaged using a 63 X water objective at 488 nm (LacCer) and 633 nm (LyTr) excitation wavelength, respectively. For data quantification, the Fiji software was used alongside the JACoP plugin for colocalization quantification, calculating the Mander's coefficient for LyTr-DR overlapping LacCer. LacCer density calculations were performed using Harmony High-Content Imaging and Analysis Software (PerkinElmer).

Filipin unesterified cholesterol storage assay

Human fibroblasts were cultured in 24-well chambers on poly-L-lysine-coated coverslips overnight prior to treatments. Cells were treated with 30 µM agonist in DMSO (to a final DMSO concentration of 0.3%) for 48 h, and the filipin staining was initiated: Cells were washed twice with ice-cold PBS, and fixed in 4% PFA for 30 min. Fixed cells were again washed with cold PBS, and unesterified cholesterol was visualized by filipin staining (PBS with 0.05 mg/mL filipin, Sigma-Aldrich, and 10% FBS) for 2 h at room temperature in a dark humid chamber. Cells were subsequently washed with ice-cold PBS twice, and nuclei stained using TO-PRO-3 (1:500, Invitrogen). Cells were washed twice and mounted on microscope slides overnight for imaging. Images were captured using a Zeiss Confocal Microscope (LSM 880), using a 40X oil objective, at 405 nm (filipin), 560 nm (mCherry), and 633 nm (TO-PRO-3). For data quantification, we calculated average filipin intensity per cell using Harmony High-Content Imaging and Analysis Software (PerkinElmer).

Mitomycin C treatment and JNCL autofluorescence analysis

Human fibroblasts (CTR and JNCL) were treated for 2 h with 30 µM mitomycin C (Millipore) to induce cell cycle arrest. Cells were seeded onto a glass coverslip (2,5 x 10^4) overnight. After 16 h, t0 cells were fixed with PFA 4% or treated for 72 h with DMSO, TPC2-A1-P, or ML-SA1 (30 µM). After 72 h, cells were fixed with 4% PFA. PFA was quenched for 10 min with 50 mM NaCl in DPBS 1X. Cells were then blocked and permeabilized in blocking buffer (0.05% Saponin, 1%BSA, and 50 mM NaCl) for 20 min. LAMP1 antibody exposure was performed overnight (1:800, SantaCruz). Cells were then incubated with Alexa Fluor 594-conjugated secondary antibody (Thermo Fisher) for 1 h at room temperature. Nuclei were stained using To-Pro (Thermo Fisher, 1:500 in PBS 1X) for 20 min. Confocal images were acquired using an LSM 880 microscope (Zeiss) with 40X magnification. Autofluorence mean intensities at 488 nm and 405 nm excitation in the LAMP1+ area were calculated using unsaturated images on ImageJ 1.52a software.

Lysosomal exocytosis experiments and isolation and culture of primary macrophages

Lysosomal exocytosis experiments were performed as described previously (Gerndt *et al*, 2020). Further details are provided in the Appendix Supplementary Methods.

Autophagy assays

Human CTR, MLIV, and NPC1 fibroblasts (5 × 10^4) were seeded in 12-well plate overnight. Treatment was performed for 180 min in complete media or HBSS 10 mM Hepes (Thermo Fisher) with DMSO or TPC2-A1-P (30 µM) or ML-SA1 (30 µM). To determine the amplitude of the autophagic flux, a cotreatment with 100 nM of the vacuolar ATPase inhibitor Bafilomycin A1 (Millipore) was performed. Samples were then prepared for western blot analysis. For western blot analysis, antibodies were used as indicated in the Appendix Supplementary Methods.

Site-directed mutagenesis and colocalization analysis using confocal microscopy

All human CLN3 mutants were generated from WT cDNA templates using QuikChange Site-Directed Mutagenesis Kit (Stratagene), following manufacturer's instructions. Further details are provided in the Appendix Supplementary Methods.

Generation and quality control of lysosomal storage disease iPS cells

The protocol for generating homozygous knock-in mutations in induced pluripotent stem cells (iPSCs) has previously been extensively described (Paquet *et al*, 2016). All details are provided in the Appendix Supplementary Methods.

Differentiation and staining of lysosomal storage disease iPSC-derived cortical neurons and staining

Cortical neurons were obtained as previously described (Paquet *et al*, 2016). All details are provided in the Appendix Supplementary Methods.

Real-time quantitative PCR analysis

In order to assess the expression levels of the target channels and disease genes, we used real-time quantitative PCR (RT-qPCR). Further details are provided in the Appendix Supplementary Methods.

LysoTracker (LyTr) staining

iPSC-derived neurons were terminally matured in glass-bottom, poly-ornithine/laminin-coated eight-well chambers (ibidi) as previously described, using DAPT and 5-FU for 7 days, and kept in culture for another week before imaging. iPSC-derived neurons were treated with 0.3% DMSO or 30 μM TPC2-A1-P for 48 h prior to live-cell imaging. LyTr-DR was added at a dilution factor of 1:10,000 to the culture medium 30 min prior to confocal microscopy. The cells were transferred to a pre-heated 37°C incubation chamber mounted onto a Zeiss Confocal microscope (LSM 880) and imaged using a 63 X water objective and an excitation wavelength of 633 nm (LyTr). Quantification of captured images was performed using the Fiji software. A mask was generated around the neuronal cell bodies, and the mean intensity was recorded.

Magic Red Cathepsin B activity measurements

We used fluorescence recovery after photobleaching (FRAP) approach previously utilized for assessing proteolysis upon CLN3 knockdown (Metcalf *et al*, 2008) to assess proteolysis in iPSC-derived neurons. Further details are provided in the Appendix Supplementary Methods.

Endolysosomal patch-clamp experiments

Endolysosomal patch-clamp experiments were performed as described previously (Chen *et al*, 2017). Further details are provided in the Appendix Supplementary Methods.

Generation of the TPC2 reporter mouse line

Mice harboring the Tpcn2$^{IRES\text{-}Cre}$ locus were bred with ROSA26-floxed stop-τGFP mice, giving rise to mice constitutively expressing τGFP under the control of the TPC2 promoter. Further details are provided in the Appendix Supplementary Methods.

The paper explained

Problem
Batten disease (JNCL), mucolipidosis type IV (MLIV), and Niemann–Pick type C1 (NPC1) are fatal neurodegenerative rare lysosomal storage diseases. There is currently no curative therapy available for either of these diseases.

Results
We show here that treatment with a PI(3,5)P_2-mimetic small molecule agonist of the endolysosomal cation channel TPC2, TPC2-A1-P, ameliorates cellular disease phenotypes in patient fibroblasts and iPSC-derived neuronal models of MLIV, NPC1, and JNCL as well as disease phenotypes in the mouse model of MLIV *in vivo*.

Impact
Our data suggest that activation of TPC2 has the potential to serve as a novel approach to treat different lysosomal storage disorders, in particular those going along with a disturbed endolysosomal Ca^{2+} homeostasis.

Pharmacokinetic study of TPC2-A1-P in C57Bl/6N mice

The purpose of this study was to determine the pharmacokinetic characteristics of TPC2-A1-P in C57Bl/6N mice following single intravenous (IV) dosing. Study design, animal selection, handling, and treatment were all in accordance with the Enamine PK study protocols and conducted by the animal laboratory personnel at Enamine/Bienta. All details of the study are provided in the Appendix Supplementary Methods.

Electron microscopy experiments

Electron microscopy experiments were performed as recently described (Polishchuk *et al*, 2019). Details are provided in the Appendix Supplementary Methods.

Cell viability assay

Cell viability assays were performed using CellTiter-Blue reagent according to the manufacturer's protocol. Further details are provided in the Appendix Supplementary Methods.

Rotarod and open field

Rotarod and open-field experiments were performed as recently described (Giordano *et al*, 2018; De Risi *et al*, 2021). Details are provided in the Appendix Supplementary Methods.

Statistics

Detailed information about statistics is provided in every figure legend.

Data availability

This study includes no data deposited in external repositories.

Expanded View for this article is available online.

Acknowledgments
We thank Dr. Herman van der Putten (NCL Foundation Hamburg, Germany) for fruitful discussions. This work was supported, in part, by funding of the German Research Foundation (DFG GR4315/4-1 and project number 239283807, SFB/TRR152 projects P04 to C.G., P06 to C.W.-S., P12 to M.B. B, and Z02 to U.B.), Germany's Excellence Strategy within the framework of the Munich Cluster for Systems Neurology (EXC2145 SyNergy ID 390857198) to D.P., Vascular Dementia Research Foundation to D.P., the University of Pennsylvania Orphan Disease Center and the Mucolipidosis IV Foundation Grant MDBR-17-120-ML4 to C.G, and an NCL Foundation Grant to D.P. and C.G. Open Access funding enabled and organized by Projekt DEAL.

Author contributions
Anna Scotto Rosato: Data curation; formal analysis; methodology. **Einar K Krogsaeter:** Data curation; formal analysis. **Dawid Jaślan:** Data curation; formal analysis; methodology. **Carla Abrahamian:** Data curation; formal analysis. **Sandro Montefusco:** Formal analysis; investigation. **Chiara Soldati:** Methodology. **Barbara Spix:** Data curation; formal analysis. **Mariateresa Pizzo:** Data curation; investigation. **Giuseppina Grieco:** Formal analysis; methodology. **Julia Böck:** Data curation; formal analysis. **Amanda Wyatt:** Data curation; methodology. **Daniela Wünkhaus:** Methodology. **Marcel Passon:** Data curation. **Marc Stieglitz:** Data curation. **Marco Keller:** Methodology. **Guido Hermey:** Resources. **Sandra Markmann:** Methodology. **Doris Gruber-Schoffnegger:** Methodology. **Susan Cotman:** Resources. **Ludger Johannes:** Methodology. **Dennis Crusius:** Methodology. **Ulrich Boehm:** Funding acquisition; methodology. **Christian Wahl-Schott:** Resources; funding acquisition. **Martin Biel:** Resources; funding acquisition. **Franz Bracher:** Conceptualization; resources; supervision; funding acquisition. **Elvira De Leonibus:** Data curation; formal analysis; supervision; investigation. **Elena Polishchuk:** Data curation; formal analysis; methodology. **Diego L Medina:** Funding acquisition. **Dominik Paquet:** Conceptualization; resources; supervision; funding acquisition; methodology; project administration; writing – review and editing. **Christian Grimm:** Conceptualization; resources; supervision; funding acquisition; validation; visualization; methodology; writing – original draft; project administration.

In addition to the CRediT author contributions listed above, the contributions in detail are:

E.K., A.S.R., D.J., S.M., C.A., J.B., C.S., B.S., D.W., M.P., and M.S. collected and analyzed data. A.W. and U.B. designed and generated the TPC2 reporter mouse model (*Tpcn2*$^{IRES\text{-}Cre/eR26\text{-}rtGFP}$). M.K. synthesized and quality-controlled TPC2-A1-P. G.H. provided the HeLa CLN3$^{-/-}$ cells. C.G., C.W-S., and M.B. provided funding for the generation of the TPC2 reporter mouse. S.C. provided CLN3 patient fibroblasts. S.M. (Evotec) and D.G.S. (Evotec) commented on the manuscript and discussed results. F.B. provided funding and designed chemical syntheses. E.P. and D.M. designed and funded the Shiga toxin (STX) and electron microscopy studies. E.D.L., M.T.P., G.G., and S.M. designed or performed behavioral tests. STX was provided by L.J. D.P. and C.G. designed and funded the study, and collected and analyzed data. C.G. wrote the manuscript. All of the authors discussed the results and commented on the manuscript.

Disclosure and competing interests statement
The authors declare that they have no conflict of interest.

For more information
https://www.ncl-stiftung.de/
http://ml4.org/
https://beyondbatten.org/
https://www.curebatten.org/
https://www.omim.org/entry/252650
https://omim.org/entry/204200
https://www.omim.org/entry/257220
https://lmu-munich.wixsite.com/lysolabmunich
https://twitter.com/lysolabmunich
https://www.en.wsi.med.uni-muenchen.de/personen/professors/grimm/index.html
https://www.linkedin.com/in/prof-dr-dr-christian-grimm-7097795/

References

Bae M, Patel N, Xu H, Lee M, Tominaga-Yamanaka K, Nath A, Geiger J, Gorospe M, Mattson MP, Haughey NJ (2014) Activation of TRPML1 clears intraneuronal A-beta in preclinical models of HIV infection. *J Neurosci* 34: 11485 – 11503

Bargal R, Avidan N, Olender T, Ben AE, Zeigler M, Raas-Rothschild A, Frumkin A, Ben-Yoseph O, Friedlender Y, Lancet D *et al* (2001) Mucolipidosis type IV: novel MCOLN1 mutations in Jewish and Non-Jewish patients and the frequency of the disease in the Ashkenazi Jewish population. *Hum Mutat* 17: 397 – 402

Bonam SR, Wang F, Muller S (2019) Lysosomes as a therapeutic target. *Nat Rev Drug Discov* 18: 923 – 948

Bretou M, Sáez PJ, Sanséau D, Maurin M, Lankar D, Chabaud M, Spampanato C, Malbec O, Barbier L, Muallem S *et al* (2017) Lysosome signaling controls the migration of dendritic cells. *Sci Immunol* 2: eaak9573

Brinkman EK, Chen T, Amendola M, Van Steensel B (2014) Easy quantitative assessment of genome editing by sequence trace decomposition. *Nucleic Acids Res* 42: 1 – 8

Calcraft PJ, Ruas M, Pan Z, Cheng X, Arredouani A, Hao X, Tang J, Rietdorf K, Teboul L, Chuang KT *et al* (2009) NAADP mobilizes calcium from acidic organelles through two-pore channels. *Nature* 459: 596 – 600

Cang C, Zhou Y, Navarro B, Seo YJ, Aranda K, Shi L, Battaglia-Hsu S, Nissim I, Clapham DE, Ren D (2013) mTOR regulates lysosomal ATP-sensitive two-pore Na+ channels to adapt to metabolic state. *Cell* 152: 778 – 790

Cao Q, Zhong XZ, Zou Y, Zhang Z, Toro L, Dong X-P (2015) BK channels alleviate lysosomal storage diseases by providing positive feedback regulation of lysosomal Ca^{2+} release. *Dev Cell* 33: 427 – 441

Chandrachud U, Walker MW, Simas AM, Heetveld S, Petcherski A, Klein M, Oh H, Wolf P, Zhao WN, Norton S *et al* (2015) Unbiased cell-based screening in a neuronal cell model of batten disease highlights an interaction between Ca^{2+} homeostasis, autophagy, and CLN3 protein function. *J Biol Chem* 290: 14361 – 14380

Chao YK, Schludi V, Chen CC, Butz E, Nguyen ONP, Müller M, Krüger J, Kammerbauer C, Ben-Johny M, Vollmar AM *et al* (2017) TPC2 polymorphisms associated with a hair pigmentation phenotype in humans result in gain of channel function by independent mechanisms. *Proc Natl Acad Sci U S A* 114: E8595 – E8602

Chen C-C, Keller M, Hess M, Schiffmann R, Urban N, Wolfgardt A, Schaefer M, Bracher F, Biel M, Wahl-Schott C *et al* (2014) A small molecule restores function to TRPML1 mutant isoforms responsible for mucolipidosis type IV. *Nat Commun* 5: 4681 – 4691

Chen C-C, Cang C, Fenske S, Butz E, Chao Y-K, Biel M, Ren D, Wahl-Schott C, Grimm C (2017) Patch-clamp technique to characterize ion channels in enlarged individual endolysosomes. *Nat Protoc* 12: 1639 – 1658

Cheng X, Zhang X, Gao Q, Samie MA, Azar M, Tsang WL, Dong L, Sahoo N, Li X, Zhuo Y *et al* (2014) The intracellular Ca2+ channel MCOLN1 is required for sarcolemma repair to prevent muscular dystrophy. *Nat Med* 20: 1187 – 1192

Chow CY, Zhang Y, Dowling JJ, Jin N, Adamska M, Shiga K, Szigeti K, Shy ME, Li J, Zhang X *et al* (2007) Mutation of FIG 4 causes neurodegeneration in the pale tremor mouse and patients with CMT4J. *Nature* 448: 68 – 72

Colletti GA, Miedel MT, Quinn J, Andharia N, Weisz OA, Kiselyov K (2012) Loss of lysosomal ion channel transient receptor potential channel mucolipin-1 (TRPML1) leads to cathepsin B-dependent apoptosis. *J Biol Chem* 287: 8082 – 8091

Curcio-Morelli C, Charles FA, Micsenyi MC, Cao Y, Venugopal B, Browning MF, Dobrenis K, Cotman SL, Walkley SU, Slaugenhaupt SA (2010) Macroautophagy is defective in mucolipin-1-deficient mouse neurons. *Neurobiol Dis* 40: 370 – 377

Davis LC, Morgan AJ, Galione A (2020) NAADP-regulated two-pore channels drive phagocytosis through endo-lysosomal Ca2+ nanodomains, calcineurin and dynamin. *EMBO J* 39: e104058

De Risi M, Tufano M, Alvino FG, Ferraro MG, Torromino G, Gigante Y, Monfregola J, Marrocco E, Pulcrano S, Tunisi L *et al* (2021) Altered heparan sulfate metabolism during development triggers dopamine-dependent autistic-behaviours in models of lysosomal storage disorders. *Nat Commun* 12: 3495

DeRosa S, Salani M, Smith S, Sangster M, Miller-Browne V, Wassmer S, Xiao R, Vandenberghe L, Slaugenhaupt S, Misko A *et al* (2021) MCOLN1 gene therapy corrects neurologic dysfunction in the mouse model of mucolipidosis IV. *Hum Mol Genet* 30: 908 – 922

Dong X-P, Shen D, Wang X, Dawson T, Li X, Zhang Q, Cheng X, Zhang Y, Weisman LS, Delling M *et al* (2010) PI(3,5)P2 controls membrane trafficking by direct activation of mucolipin Ca2+ release channels in the endolysosome. *Nat Commun* 1: 38

Elrick MJ, Yu T, Chung C, Lieberman AP (2012) Impaired proteolysis underlies autophagic dysfunction in Niemann-Pick type C disease. *Hum Mol Genet* 21: 4876 – 4887

Feng X, Yang J (2016) Lysosomal calcium in neurodegeneration. *Messenger* 5: 56 – 66

Folkerth RD, Alroy J, Lomakina I, Skutelsky E, Raghavan SS, Kolodny EH (1995) Mucolipidosis type IV: morphology and histochemistry of an autopsy case. *J Neuropathol Exp Neurol* 54: 154 – 164

Foster WJ, Taylor HBC, Padamsey Z, Jeans AF, Galione A, Emptage NJ (2018) Hippocampal mGluR1-dependent long-term potentiation requires NAADP-mediated acidic store Ca2+ signaling. *Sci Signal* 11: eaat9093

Frei KP, Patronas NJ, Crutchfield KE, Altarescu G, Schiffmann R (1998) Mucolipidosis type IV: characteristic MRI findings. *Neurology* 51: 565 – 569

García-Rúa V, Feijóo-Bandín S, Rodríguez-Penas D, Mosquera-Leal A, Abu-Assi E, Beiras A, María Seoane L, Lear P, Parrington J, Portolés M *et al* (2016) Endolysosomal two-pore channels regulate autophagy in cardiomyocytes. *J Physiol* 594: 3061 – 3077

Garver WS, Heidenreich RA, Erickson RP, Thomas MA, Wilson JM (2000) Localization of the murine niemann-pick C1 protein to two distinct intracellular compartments. *J Lipid Res* 41: 673 – 687

Gerndt S, Chen C-CC, Chao Y-KK, Yuan Y, Rosato AS, Krogsaeter E, Urban N, Nam O, Nguyen P, Miller MT *et al* (2020) Agonist-mediated switching of ion selectivity in TPC2 differentially promotes lysosomal function. *Elife* 9: e54712

Giordano N, Iemolo A, Mancini M, Cacace F, De Risi M, Latagliata EC, Ghiglieri V, Bellenchi GC, Puglisi-Allegra S, Calabresi P *et al* (2018) Motor learning and metaplasticity in striatal neurons: relevance for Parkinson's disease. *Brain* 141: 505 – 520

Greene NDE, Lythgoe MF, Thomas DL, Nussbaum RL, Bernard DJ, Mitchison HM (2001) High resolution MRI reveals global changes in brains of Cln3 mutant mice. *Eur J Paediatr Neurol* 5: 103 – 107

Grimm C, Holdt LM, Chen C-C, Hassan S, Muller C, Jors S, Cuny H, Kissing S, Schroder B, Butz E *et al* (2014) High susceptibility to fatty liver disease in two-pore channel 2-deficient mice. *Nat Commun* 5: 4699 – 4712

Grimm C, Butz E, Chen CC, Wahl-schott C, Biel M (2017) From mucolipidosis type IV to Ebola: TRPML and two-pore channels at the crossroads of endo-lysosomal trafficking and disease. *Cell Calcium* 67: 148 – 155

Grishchuk Y, Sri S, Rudinskiy N, Ma W, Stember KG, Cottle MW, Sapp E, Difiglia M, Muzikansky A, Betensky RA *et al* (2014) Behavioral deficits, early gliosis, dysmyelination and synaptic dysfunction in a mouse model of mucolipidosis IV. *Acta Neuropathol Commun* 2: 133

Grishchuk Y, Pena KA, Coblentz J, King VE, Humphrey DM, Wang SL, Kiselyov KI, Slaugenhaupt SA (2015) Impaired myelination and reduced brain ferric iron in the mouse model of mucolipidosis IV. *Dis Model Mech* 8: 1591 – 1601

Kim HJ, Soyombo AA, Tjon-Kon-Sang S, So I, Muallem S (2009) The Ca2+ channel TRPML3 regulates membrane trafficking and autophagy. *Traffic* 10: 1157 – 1167

Kinarivala N, Morsy A, Patel R, Carmona AV, Sajib MS, Raut S, Mikelis CM, Al-Ahmad A, Trippier PC (2020) An iPSC-derived neuron model of CLN3 disease facilitates small molecule phenotypic screening. *ACS Pharmacol Transl Sci* 3: 931 – 947

Kiselyov K, Yamaguchi S, Lyons CW, Muallem S (2010) Aberrant Ca2+ handling in lysosomal storage disorders. *Cell Calcium* 47: 103 – 111

Kousi M, Lehesjoki AE, Mole SE (2012) Update of the mutation spectrum and clinical correlations of over 360 mutations in eight genes that underlie the neuronal ceroid lipofuscinoses. *Hum Mutat* 33: 42 – 63

Kwart D, Paquet D, Teo S, Tessier-Lavigne M (2017) Precise and efficient scarless genome editing in stem cells using CORRECT. *Nat Protoc* 12: 329 – 334

Li RJ, Xu J, Fu C, Zhang J, Zheng YG, Jia H, Liu JO (2016) Regulation of mTORC1 by lysosomal calcium and calmodulin. *Elife* 5: e19360

Lloyd-Evans E, Platt FM (2011) Lysosomal Ca2+ homeostasis: role in pathogenesis of lysosomal storage diseases. *Cell Calcium* 50: 200 – 205

Lojewski X, Staropoli JF, Biswas-legrand S, Simas AM, Haliw L, Selig MK, Coppel SH, Goss KA, Petcherski A, Chandrachud U *et al* (2014) Human iPSC models of neuronal ceroid lipofuscinosis capture distinct effects of TPP1 and CLN3 mutations on the endocytic pathway. *Hum Mol Genet* 23: 2005 – 2022

Medina DL, Fraldi A, Bouche V, Annunziata F, Mansueto G, Spampanato C, Puri C, Pignata A, Martina JA, Sardiello M *et al* (2011) Transcriptional activation of lysosomal exocytosis promotes cellular clearance. *Dev Cell* 21: 421 – 430

Medina DL, Di Paola S, Peluso I, Armani A, De Stefani D, Venditti R, Montefusco S, Scotto-Rosato A, Prezioso C, Forrester A *et al* (2015) Lysosomal calcium signalling regulates autophagy through calcineurin and TFEB. *Nat Cell Biol* 17: 288 – 299

Metcalf DJ, Calvi AA, Seaman MNJ, Mitchison HM, Cutler DF (2008) Loss of the batten disease gene CLN3 prevents exit from the TGN of the mannose 6-phosphate receptor. *Traffic* 9: 1905 – 1914

Micsenyi MC, Dobrenis K, Stephney G, Pickel J, Vanier MT, Slaugenhaupt SA, Walkley SU (2009) Neuropathology of the Mcoln1−/− knockout mouse model of mucolipidosis type IV. *J Neuropathol Exp Neurol* 68: 125 – 135

Minckley TF, Zhang C, Fudge DH, Dischler AM, Lejeune KD, Xu H (2019) Sub-nanomolar sensitive GZnP3 reveals TRPML1-mediated neuronal Zn^{2+} signals. *Nat Commun* 10: 4806

Mole SE, Schulz A, Haltia M (2020) Rosenberg's molecular and genetic basis of neurological and psychiatric disease. In *Rosenberg's molecular and genetic basis of neurological and psychiatric disease*, RN Rosenberg, JM Pascual (eds), pp 53–71. Amsterdam: Elseiver

Nguyen ONP, Grimm C, Schneider LS, Chao Y-K, Atzberger C, Bartel K, Watermann A, Ulrich M, Mayr D, Wahl-Schott C *et al* (2017) Two-pore channel function is crucial for the migration of invasive cancer cells. *Cancer Res* 77: 1427–1438

Ogunbayo OA, Duan J, Xiong J, Wang Q, Feng X, Ma J, Zhu MX, Evans AM (2018) MTORC1 controls lysosomal Ca2+release through the two-pore channel TPC2. *Sci Signal* 11: 1–6

Paquet D, Kwart D, Chen A, Sproul A, Jacob S, Teo S, Olsen KM, Gregg A, Noggle S, Tessier-Lavigne M (2016) Efficient introduction of specific homozygous and heterozygous mutations using CRISPR/Cas9. *Nature* 533: 125–129

Pereira GJS, Antonioli M, Hirata H, Ureshino RP, Nascimento AR, Bincoletto C, Vescovo T, Piacentini M, Fimia GM, Smaili SS (2017) Glutamate induces autophagy via the two-pore channels in neural cells. *Oncotarget* 8: 12730–12740

Polishchuk EV, Merolla A, Lichtmannegger J, Romano A, Indrieri A, Ilyechova EY, Concilli M, De CR, Crispino R, Mariniello M *et al* (2019) Activation of autophagy, observed in liver tissues from patients with wilson disease and from ATP7B-deficient animals, protects hepatocytes from copper-induced apoptosis. *Gastroenterology* 156: 1173–1189

Pontikis CC, Cella CV, Parihar N, Lim MJ, Rezaie P, Pearce DA, Cooper JD (2004) Late onset neurodegeneration in the $Cln3^{-/-}$ mouse model of juvenile neuronal ceroid lipofuscinosis is preceded by low level glial activation. *Brain Res* 1023: 231–242

Prasad A, Fischer WA, Maue RA, Henderson LP (2000) Regional and developmental expression of the Npc1 mRNA in the mouse brain. *J Neurochem* 75: 1250–1257

Pryor PR, Reimann F, Gribble FM, Luzio JP (2006) Mucolipin-1 is a lysosomal membrane protein required for intracellular lactosylceramide traffic. *Traffic* 7: 1388–1398

Puri V, Watanabe R, Dominguez M, Sun X, Wheatley CL, Marks DL, Pagano RE (1999) Cholesterol modulates membrane traffic along the endocytic pathway in sphingolipid-storage diseases. *Nat Cell Biol* 1: 386–388

Ruas M, Rietdorf K, Arredouani A, Davis LC, Lloyd-Evans E, Koegel H, Funnell TM, Morgan AJ, Ward JA, Watanabe K *et al* (2010) Purified TPC isoforms form NAADP receptors with distinct roles for Ca^{2+} signaling and endolysosomal trafficking. *Curr Biol* 20: 703–709

Samie M, Wang X, Zhang X, Goschka A, Li X, Cheng X, Gregg E, Azar M, Zhuo Y, Garrity AG *et al* (2013) A TRP channel in the lysosome regulates large particle phagocytosis via focal exocytosis. *Dev Cell* 26: 511–524

Sarkar S, Carroll B, Buganim Y, Maetzel D, Ng AHM, Cassady J, Cohen M, Chakraborty S, Wang H, Spooner E *et al* (2013) Impaired autophagy in the lipid storage disorder Niemann-Pick type C1 disease. *Cell Rep* 5: 1302–1315

Scotto Rosato A, Montefusco S, Soldati C, Di Paola S, Capuozzo A, Monfregola J, Polishchuk E, Amabile A, Grimm C, Lombardo A *et al* (2019) TRPML1 links lysosomal calcium to autophagosome biogenesis through the activation of the CaMKKb/VPS34 pathway. *Nat Commun* 10: 5630

Shen D, Wang X, Li X, Zhang X, Yao Z, Dong X, Yu T, Lieberman AP, Showalter HD, Xu H (2012) Lipid storage disorders block lysosomal trafficking by inhibiting TRP channel and calcium release. *Nat Commun* 3: 731–751

Slaugenhaupt S (2002) The molecular basis of mucolipidosis type IV. *Curr Mol Med* 2: 445–450

Soldati C, Lopez-fabuel I, Wanderlingh LG, Garcia-macia M, Monfregola J, Esposito A, Napolitano G, Guevara-ferrer M, Rosato AS, Krogsaeter EK *et al* (2021) Repurposing of tamoxifen ameliorates CLN3 and CLN7 disease phenotype. *EMBO Mol Med* 13: e13742

Tsunemi T, Perez-Rosello T, Ishiguro Y, Yoroisaka A, Jeon S, Hamada K, Suresh MKV, Wong YC, Xie Z, Akamatsu W *et al* (2019) Increased lysosomal exocytosis induced by lysosomal Ca^{2+} channel agonists protects human dopaminergic neurons from α-synuclein toxicity. *J Neurosci* 39: 5760–5772

Venugopal B, Browning MF, Curcio-Morelli C, Varro A, Michaud N, Nanthakumar N, Walkley SU, Pickel J, Slaugenhaupt SA (2007) Neurologic, gastric, and opthalmologic pathologies in a murine model of mucolipidosis type IV. *Am J Hum Genet* 81: 1070–1083

Vergarajauregui S, Connelly PS, Daniels MP, Puertollano R (2008) Autophagic dysfunction in mucolipidosis type IV patients. *Hum Mol Genet* 17: 2723–2737

Vitner EB, Platt FM, Futerman AH (2010) Common and uncommon pathogenic cascades in lysosomal storage diseases. *J Biol Chem* 285: 20423–20427

Walker MT, Montell C (2016) Suppression of the motor deficit in a mucolipidosis type IV mouse model by bone marrow transplantation. *Hum Mol Genet* 25: 2752–2761

Walkley SU, Suzuki K (2004) Consequences of NPC1 and NPC2 loss of function in mammalian neurons. *Biochim Biophys Acta* 1685: 48–62

Wang X, Zhang X, Dong X, Samie M, Li X, Clapham DE, Ren D, Xu H (2012) TPC proteins are phosphoinositide-activated sodium-selective ion channels in endosomes and lysosomes. *Cell* 151: 372–383

Wang W, Gao Q, Yang M, Zhang X, Yu L, Lawas M, Li X, Bryant-Genevier M, Southall NT, Marugan J *et al* (2015) Up-regulation of lysosomal TRPML1 channels is essential for lysosomal adaptation to nutrient starvation. *Proc Natl Acad Sci U S A* 112: E1373–E1381

Weisheit I, Kroeger JA, Malik R, Klimmt J, Crusius D, Dannert A, Dichgans M, Paquet D (2020) Detection of deleterious on-target effects after HDR-mediated CRISPR editing. *Cell Rep* 31: 107689

Weisheit I, Kroeger JA, Malik R, Wefers B, Wurst W, Dichgans M, Paquet D, Lichtner P (2021) Simple and reliable detection of CRISPR-induced on-target effects by qgPCR and SNP genotyping. *Nat Protoc* 16: 1714–1739

Wen S, Go IN, Mai O, Schauer C, Leinders-zufall T, Boehm U (2011) Genetic identification of GnRH receptor neurons: a new model for studying neural circuits underlying reproductive physiology in the mouse brain. *Endocrinology* 152: 1515–1526

Wyatt A, Wartenberg P, Candlish M, Krasteva-christ G, Flockerzi V, Boehm U (2017) Genetic strategies to analyze primary TRP channel-expressing cells in mice. *Cell Calcium* 67: 91–104

Zhang Y, Zolov SN, Chow CY, Slutsky SG, Richardson SC, Piper RC, Yang B, Nau JJ, Westrick RJ, Morrison SJ *et al* (2007) Loss of Vac14, a regulator of the signaling lipid phosphatidylinositol 3,5-bisphosphate, results in neurodegeneration in mice. *Proc Natl Acad Sci U S A* 104: 17518–17523

Zhang X, Chen W, Li P, Calvo R, Southall N, Hu X, Bryant-genevier M, Feng X, Geng Q, Gao C *et al* (2019) Agonist-specific voltage-dependent gating of lysosomal two-pore Na^{+} channels. *Elife* 8: e51423

Zhong XZ, Sun X, Cao Q, Dong G, Schiffmann R, Dong XP (2016) BK channel agonist represents a potential therapeutic approach for lysosomal storage diseases. *Sci Rep* 6: 1–11

Zong X, Schieder M, Cuny H, Fenske S, Gruner C, Rötzer K, Griesbeck O, Harz H, Biel M, Wahl-Schott C (2009) The two-pore channel TPCN2 mediates

NAADP-dependent Ca(2+)-release from lysosomal stores. *Pflugers Arch* 458: 891 – 899

Zou J, Hu B, Arpag XS, Yan Q, Hamilton A, Zeng Y, Vanoye CG (2015) Reactivation of lysosomal Ca^{2+} efflux rescues abnormal lysosomal storage in FIG 4-deficient cells. *J Neurosci* 35: 6801 – 6812

Expanded View Figures

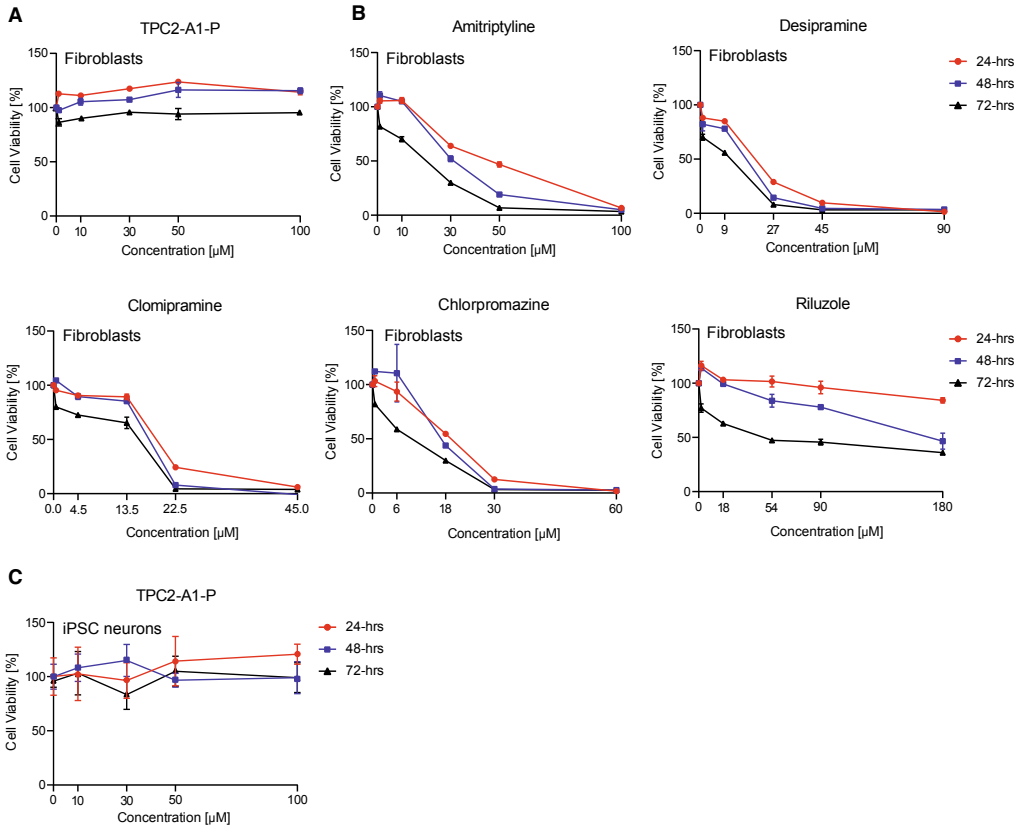

Figure EV1. Effect of TPC2-A1-P and various drugs reported to activate TPC2 on cell viability.

A–C Cell viability assay for TPC2-A1-P and other compounds reported to activate TPC2 (Zhang *et al*, 2019) on human patient fibroblasts (A, B) and iPSC-derived neurons (C). Cells were incubated for 24, 48, and 72 h with increasing compound concentrations, and cell viability was assessed with CellTiter-Blue according to the manufacturer's protocol. Data are presented as mean ± SEM. $n > 3$ for each tested condition.

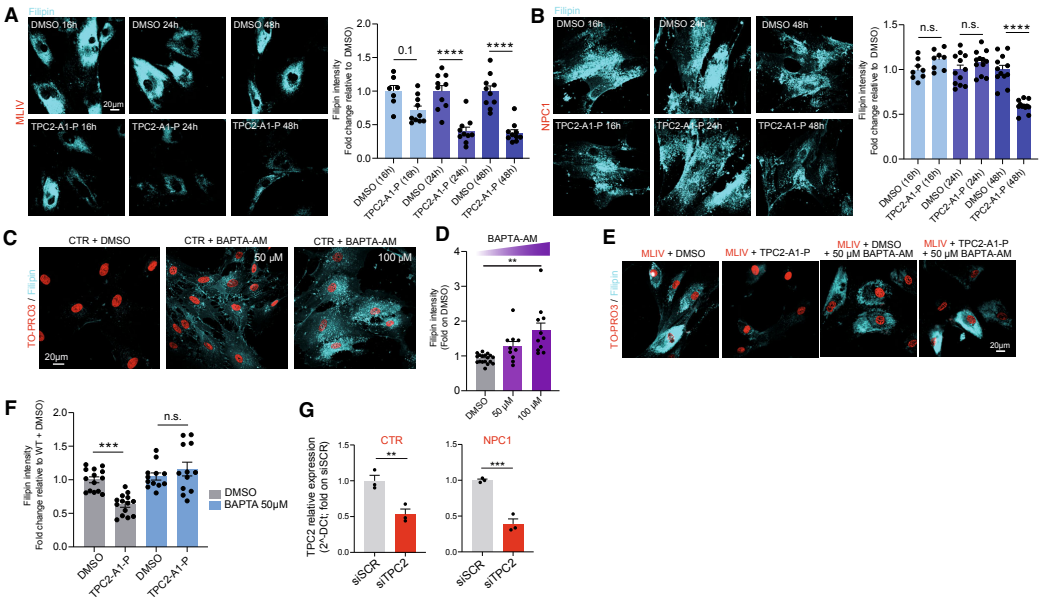

Figure EV2. Time course of filipin rescue and effect of BAPTA-AM in human fibroblasts.

A, B Time course of filipin rescue (treatment with either DMSO or 30 μM TPC2-A1-P) in human MLIV and NPC1 fibroblasts (16–48 h).

C, D Ca^{2+} chelation (BAPTA-AM) dose dependently causes cholesterol accumulation in CTR fibroblasts.

E, F Ca^{2+} chelation (BAPTA-AM) blunts the effect of TPC2-A1-P (48 h treatment) when added for the last 3 h.

G RT-qPCR showing TPCN2 knockdown efficiency in human CTR and NPC1 fibroblasts.

Data information: Shown are mean values ± SEM. $n > 3$ technical and biological replicates for each tested condition (each dot represents an imaged frame containing several cells or three independent qPCR experiments, respectively); one-way (A, B) or two-way (F) ANOVA, *post hoc* Tukey's multiple comparisons test, or two-tailed Student's *t*-test (D, G). ***p*-value < 0.01; ****p*-value < 0.001; *****p*-value < 0.0001.

Figure EV3. Colocalization of GFP-CLN3 and Batten disease-causing missense mutants with endolysosomal markers (LAMP1 for LE/LY, Rab5 for EE, and Rab11 for RE) and MitoTracker-DR.

A–D Confocal images of CLN3 KO HeLa cells cotransfected with either GFP-CLN3 CTR (WT) or GFP-CLN3 missense mutant variants (as indicated) and endolysosomal markers: LAMP1-RFP, Rab5-RFP, or Rab11-DsRed. Six mutants (B), $CLN3^{S131R}$, $CLN3^{C134R}$, $CLN3^{A158P}$, $CLN3^{G165E}$, $CLN3^{L170P}$, and $CLN3^{V330I}$, appeared strongly mislocalized to the cytosol. When present in patients (usually heterozygously, alongside the more prevalent $CLN3^{\Delta 1.02kb}$ variant), these variants reportedly result in a variety of clinical phenotypes, including classic JNCL, cone-rod dystrophy, autophagic vacuolar myopathy, or retinitis pigmentosa (RP). A further six mutants (C), $CLN3^{L101P}$, $CLN3^{G189W}$, $CLN3^{I285V}$, $CLN3^{E295K}$, $CLN3^{R334C}$, and $CLN3^{Q352H}$ showed no significant difference in colocalization with LAMP1, Rab5, or Rab11 compared to CTR CLN3. For these, clinical phenotypes have not been described, incompletely characterized, or described as protracted Batten disease or RP. The remaining nine mutations (D), $CLN3^{G187A}$, $CLN3^{G189R}$, $CLN3^{G192E}$, $CLN3^{V290L}$, $CLN3^{L306H}$, $CLN3^{V330F}$, $CLN3^{R334H}$, $CLN3^{R405W}$, and $CLN3^{D416G}$ showed significantly reduced lysosomal localization (LAMP1), while retaining endosomal localization. $CLN3^{D416G}$ also showed a significant decrease in Rab11 (recycling endosome) colocalization compared to CLN3 CTR. Rab5 (early endosome) colocalization was altered in four of these nine mutants, including $CLN3^{D416G}$. Due to its consistent reduction in colocalization with all endolysosomal markers, $CLN3^{D416G}$ was chosen as a candidate for iPSC generation (with classic, more severe clinical JNCL phenotype).

E Quantification of experiments as shown in A-D. Shown are the respective Mander's correlation coefficients (MCC) for automated colocalization analysis (JACoP/Fiji) of GFP-CLN3 CTR and missense mutants with LAMP1-RFP, Rab5-RFP, Rab11-DsRed, or MitoTracker-DR (negative control).

Data information: Data are presented as mean ± SD. $n > 3$ technical and biological replicates for each tested condition; one-way ANOVA Dunnett's multiple comparisons test. **p*-value < 0.1; ***p*-value < 0.01; ****p*-value < 0.001; *****p*-value < 0.0001.

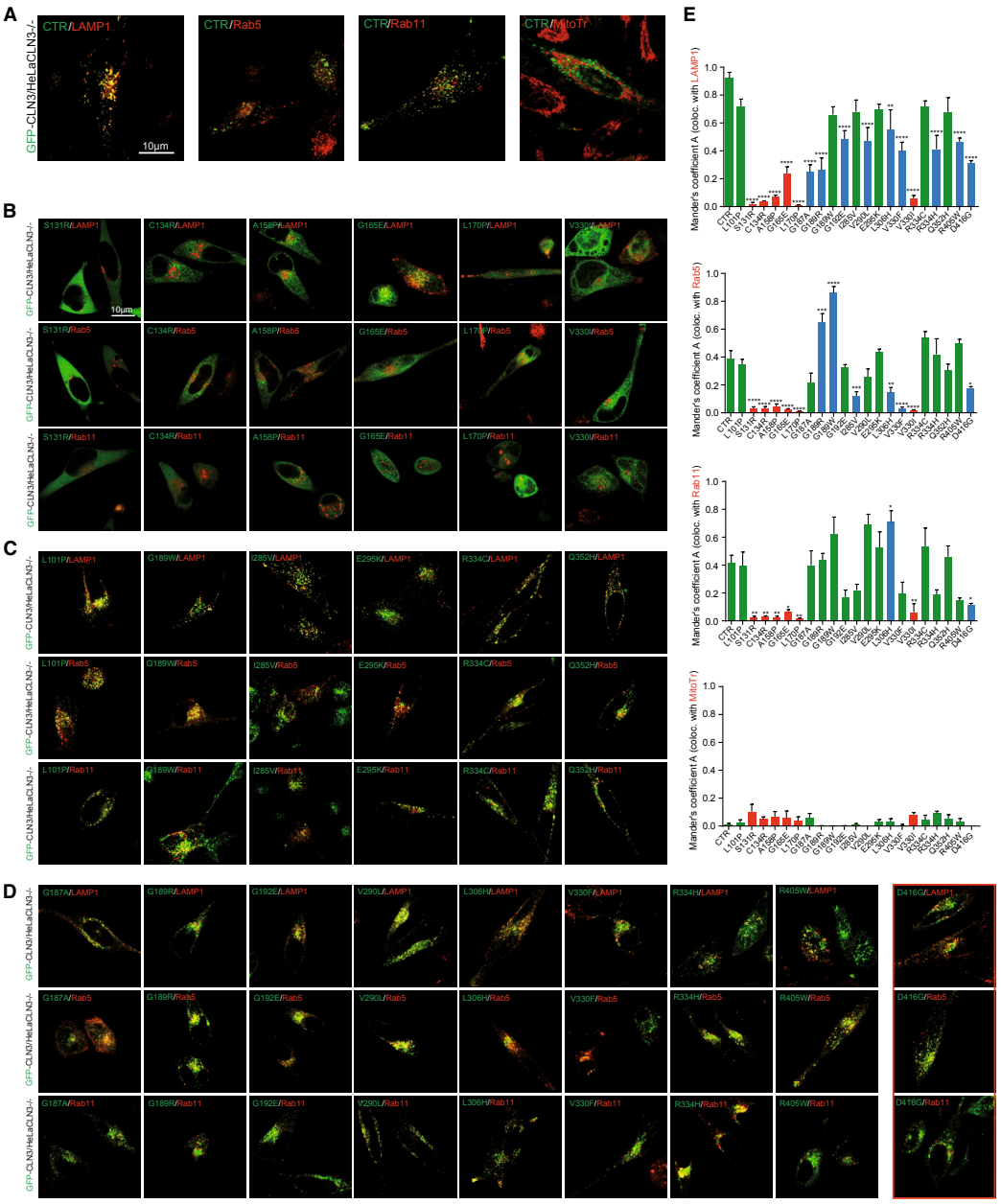

Figure EV3.

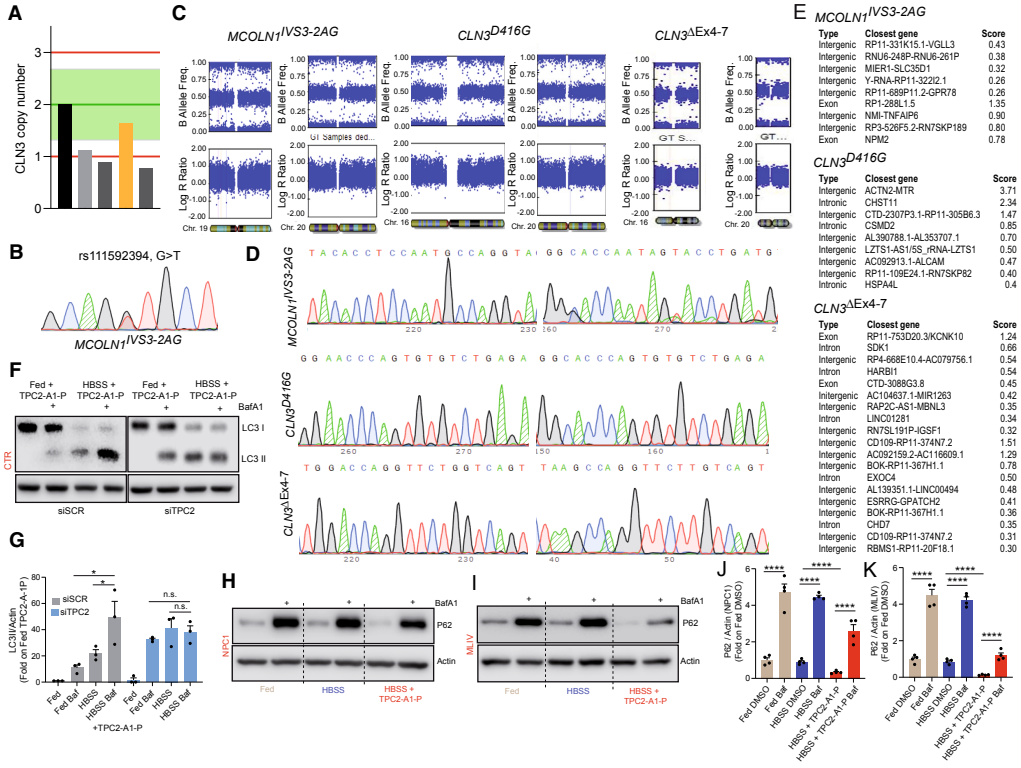

Figure EV4. Quality control of novel MLIV and CLN3 iPSC lines and autophagy (LC3 and P62) experiments.

A Four CLN3^{D416G} iPSC clones were screened for locus copy numbers by qgPCR in comparison to the unedited parent line (black bar) to rule out undesired on-target editing. The clone showing two CLN3 copies was selected (yellow bar).

B A heterozygous, silent SNP was found alongside the MLIV$^{IVS3-2A>G}$ edit, confirming the presence of both edited alleles and ruling out large indels due to on-target effects.

C Molecular karyotyping did not reveal any detectable aberrations in the selected cell lines at the targeted locus or chromosome 20, which is frequently altered in edited iPSCs.

D The most likely off-target sites of the gRNAs used for each edit were predicted by CFD and MIT algorithms and sequenced, revealing no off-target editing in the selected CLN3 and MLIV clones. The most likely off-target sites for each clone are depicted.

E Tabular summary of sequenced off-target sites.

F, G Effect of HBSS + TPC2-A1-P on LC3 in siSCR or siTPC2--treated human CTR fibroblasts.

H–K Effect of TPC2-A1-P on P62 accumulation with and without bafilomycin A1 treatment in human NPC1 and MLIV fibroblasts.

Data information: Shown are mean values ± SEM. $n > 3$ technical and biological replicates for each tested condition (each dot in (F), (H), and (I) represent three independent western blot experiments, respectively); two-tailed Student's *t*-test (G, J, K). *$p < 0.05$; ****p-value < 0.0001.

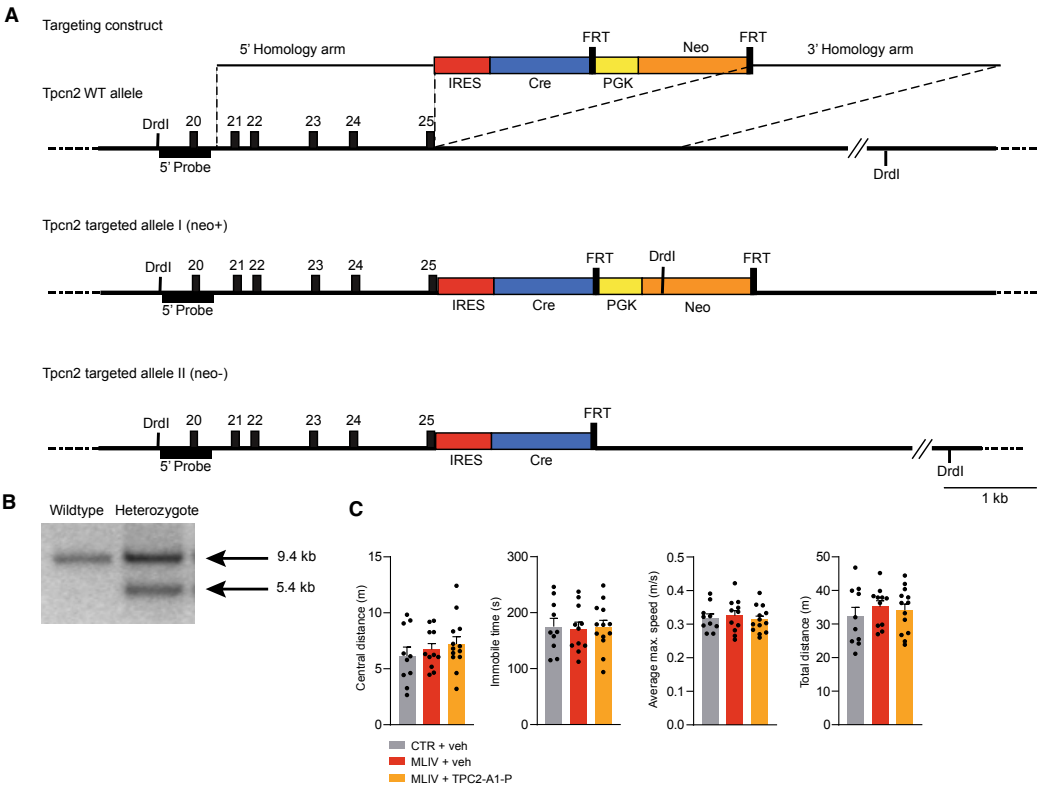

Figure EV5. Targeting strategy for TPC2 reporter mouse model and supplementary behavioral data (MLIV mouse model).

A Targeting strategy used to express Cre recombinase under the control of the Tpcn2 promoter. The targeting vector contains an IRES-Cre-FRT-PGK-NEO-FRT cassette in which a phosphoglycerate kinase promoter drives neomycin resistance (Pgk-neo). This cassette is incorporated by homologous recombination in embryonic stem cells subsequent to the stop codon in exon 25.

B Southern blot of embryonic stem cell DNA cut with DrdI, demonstrating correct targeting of the Tpcn2-IRES-Cre knock-in allele.

C Results of the open-field test using MLIV mice treated with vehicle or TPC2-A1-P, respectively, compared to vehicle-treated WT littermates (CTR). No differences between CTR and MLIV mice were observed.

Appendix Supplementary Methods

TPC2 rescues lysosomal storage in mucolipidosis type IV, Niemann-Pick type C1 and Batten disease

Anna Scotto Rosato*[1], Einar Krogsaeter*[1], Dawid Jaślan[1], Carla Abrahamian[1], Sandro Montefusco[2], Chiara Soldati[2], Barbara Spix[1], Maria Teresa Pizzo[2], Giuseppina Grieco[2], Julia Böck[1], Amanda Wyatt[3], Daniela Wünkhaus[4], Marcel Passon[1], Marc Stieglitz[5], Marco Keller[5], Guido Hermey[6], Sandra Markmann[4], Doris Gruber-Schoffnegger[4], Susan Cotman[7], Ludger Johannes[8], Dennis Crusius[9], Ulrich Boehm[3], Christian Wahl-Schott[10], Martin Biel[5], Franz Bracher[5], Elvira De Leonibus[2,11], Elena Polishchuk[2], Diego L. Medina[2,12#], Dominik Paquet[9,13#], Christian Grimm[1#]

Suppl. materials and methods

Maintenance of iPSCs
iPSC experiments were performed in accordance with all relevant guidelines and regulations. Female iPSC line A18944 was purchased from ThermoFisher (#A18945). iPSCs were grown in Essential 8 Flex Medium (ThermoFisher, #A2858501) on VTN-coated (ThermoFisher, #A14700) cell culture plates at 37°C with 5% CO_2 and split as small clumps twice a week after a 5 min incubation in PBS/EDTA.

Generation of lysosomal storage disease iPS cells
Design and preparation of editing reagents and quality control of edited iPSCs was performed as described previously (Kwart *et al*, 2017; Weisheit *et al*, 2020, 2021). To generate knock-in patient mutant iPS cells for JNCL ($CLN3^{D416G}$) and MLIV ($MCOLN1^{IVS3\text{-}2A>G}$), we used CRISPOR (Concordet & Haeussler, 2018) to identify suitable gRNAs mediating efficient and specific homozygous knock-in editing events. gRNAs were cloned into the BsmBI cloning site of the MLM3636 vector (gift from Keith Joung, Addgene plasmid #43860; http://n2t.net/addgene:48360; RRID: Addgene_43860), and their editing efficiencies assessed by transfecting into HEK293 cells alongside a Cas9-GFP-encoding plasmid using the X-tremeGENE 9 DNA Transfection Reagent (Merck), and genomic DNA isolated using the NucleoSpin Tissue Kit (Macherey Nagel) after 48 h of culture. The edited sites were amplified by PCR and purified using the NucleoSpin Gel and PCR Clean-up Kit (Macherey Nagel) before they were sequenced by Sanger sequencing (Eurofins Genomics). Sequence traces were analyzed by sequence-trace decomposition using TIDE (Brinkman *et al*, 2014), and active gRNAs identified. We identified the following gRNAs to generate lysosomal storage disease iPS cells (5'→3', edited base in bold, PAM sequence follows hyphen): $CLN3^{D416G}$ (ACCTGCATCTCTGA**C**ACACT-GGG), and $MLIV^{IVS3\text{-}2A>G}$ cells (GCAGGCAACGCCAGGTACTGGGG). The primers used to sequence the edited sites were (5'→3'): $CLN3^{D416G}$ (AGTGCCTCA ACCTGGTGTTC, CCATGGATAAAATCGGCATT) and $MLIV^{IVS3\text{-}2A>G}$ (CGCAGCCTACACGCGGGAGCA, GCTCCCAA CAGTGAAGCCTC). Repair templates were designed as the mutated nucleotide flanked by 50 base-pairs and ordered as Ultramer DNA Oligonucleotides (IDT). The human female episomal iPSC line A18944 (ThermoFisher) was quality controlled for suitability for differentiations and to rule out common chromosomal abnormalities. For gene editing in iPSCs, the cells were split into single cells using Accutase (ThermoFisher) onto Geltrex (ThermoFisher)-coated vessels, and supplemented with rock inhibitors (Y27632, Selleckchem). Two days later, the cells were dissociated into single cells, and 2 million cells electroporated by 2x20 ms, 65V pulses using the ECM830 system (BTX) with 30 µg (pSpCas9(BB)-2A-Puro (PX459) V2.0 (gift from Feng Zhang; Addgene plasmid #62988; http://n2t.net/addgene:62988; RRID: Addgene_62988 (Ran *et al*, 2013) 5 mg MLM3636-sgRNA, and 30 µg repair template. Cells were seeded onto Geltrex (ThermoFisher)-coated 10 cm cell culture dishes and cultured in StemFlex medium (ThermoFisher). From days 2-5, electroporated cells were selected for by Puromycin (350 ng/µL; VWR) treatment (Steyer *et al*, 2018), before the cells were allowed to recuperate without Puromycin from day 5 onwards, with supplementation of rock inhibitors and RevitaCell Supplement (ThermoFisher) depending on density and colony formation. Colonies were picked individually into 96-well plates and analyzed for presence of desired mutations. This was done by lysis and gDNA extraction, PCR amplification of the edited site, and restriction fragment length polymorphism (RFLP) analysis. $MLIV^{IVS3\text{-}2A>G}$-edited sites were amplified with the primers previously used for sequencing the edited site, while $CLN3^{D416G}$ was screened for using primers permitting RFLP analysis of the edited site (GTGATGAGCACCGGGAGTTTACAATGGCGG, GGAGCACAGTTCATGGAGGG). RFLP analysis was next performed using MwoI to screen for $CLN3^{D416G}$ and KpnI to screen for $MCOLN1^{IVS3\text{-}2A>G}$ (all enzymes from NEB). PCR products showing presence of the desired restriction site were sequenced by Sanger sequencing using the aforementioned primer pairs, and homozygously edited clones selected for expansion.

Quality control of edited iPSCs
Quality controls included confirming edited sequencing traces of propagated clones, assessing puromycin tolerance to exclude Cas9 vector integration, ensuring absence of undesired on-target (Weisheit *et al*, 2020) editing events and partial chromosome 20 triplications assessed by quantitative genomic PCR (qgPCR),

sequencing the top 5 predicted CFD and MIT off-target sites, staining for pluripotency markers by immunocytochemistry, and molecular karyotyping to interrogate chromosomal abnormalities (Weisheit *et al*, 2021). Puromycin tolerance was assessed upon performing a single-cell split of iPSCs onto Geltrex-coated 6-well wells, and treating the iPSCs with Puromycin (350 ng/µL; VWR) for 3 days. Selected clones died within the three days of Puromycin treatment. Adverse on-target editing events and chromosome 20 triplications were assessed as previously described (Amps *et al*, 2011; Weisheit *et al*, 2020). In short, genomic DNA was isolated using the NucleoSpin Tissue Kit (Macherey Nagel), and subsequently analyzed by qgPCR. The human TERT TaqMan Copy Number Reference Assay (ThermoFisher 4403316) was used as an internal control, and the BCL2L1 copy number probed using the primer set (GGTGGTTGACTTTCTCTCCTAC, TCTCCGAT TCAGTCCCTTCT), and the probe 56-FAM/TGTGGAAGA/ZEN/GAACAGGACTGA GGC/3IABkFQ for detection. To assess on-target editing effects, the same reference probe was used as for chromosome 20 qgPCR, alongside primer/probes targeting the edited site: For $CLN3^{D416G}$, the copy number of the edited site was assessed with the following primer set for amplification (GCATCTACCTCGT CTTCCTGA, CTCCCCAAGTGGGAGACAAT), and the probe 56-FAM/TTGCCTCTGCATGACTTCCTCTGC/3IA BkFQ for detection. For the $MLIV^{IVS3-2A>G}$ locus integrity assessment, on-target editing was not assessed by qgPCR, due to the presence of a silent, heterozygous SNP within the same sequencing trace as the edited base (rs111592394, G>T), present in the wild-type A18944 iPSCs. Presence of the heterozygous SNP alongside the edited base upon Sanger sequencing thereby indicated the presence of two edited chromosomes, ruling out larger chromosomal deletions and ensuring integrity of the edited locus. Using the same genomic DNA, we also performed fingerprinting analysis to confirm the shared lineage of the edited cells and their wild-type counterparts. This was done by PCR analysis of the D1S80 locus using the following primer combination: GTCTTGTTGGAGATGCACGTGCCCCTTGC, GAAACTGGCCTCCAAACACTGCCCGCCG. The detailed protocol has previously been described (Weisheit *et al*, 2021). The top 5 predicted off-target sites (by CFD and MIT algorithms) were also amplified and Sanger sequenced, finding no off-target editing events in the edited cells. For staining for pluripotency markers, iPSC colonies were with anti-SSEA4 (ab16287, 1:500), rabbit anti-NANOG (D73G4, 1:500), mouse anti-Tra160 (MAB4360, 1:500), and rabbit anti-Oct4 (S090023, 1:500) as described earlier (Paquet et al. 2016). Selected clones showed uniform expression of all interrogated pluripotency markers. Finally, molecular karyotyping analysis was performed by isolating genomic DNA using the NucleoSpin Tissue Kit (Macherey Nagel), and analyzing it using an Illumina BeadArray scanned with an Illumina iScan. Samples with call rates below 95% were excluded, and only SNPs with a GenTrain score above 0.7 included for analysis (Weisheit *et al*, 2021). The clones used for differentiations and further experiments passed all of the aforementioned quality control checkpoints.

Differentiation and staining of lysosomal storage disease iPSC-derived cortical neurons

iPSC-derived human cortical neurons were differentiated as previously described (Paquet *et al*, 2016) with modifications. WT and gene-edited A18944 iPSCs were expanded for neuronal inductions in Essential 8 Flex medium and split into single-cells using Accutase for 8 min at 37ºC at day in vitro 0 (DIV0). Upon dissociation, F12 medium was added to neutralize Accutase, cells were triturated, counted, and centrifuged (1000 rpm, 4 min). Cells were resuspended in neuronal induction (NI) medium, consisting of neuronal maintenance (NM) medium (50% Neurobasal, 50% DMEM/F12, 0.1 mg/mL penicillin-streptomycin, 0.5X B27 supplement, 0.5X N-2 supplement, 2 mM GlutaMAX, 0.1 mM non-essential amino acids, 5 µL insulin, 0.1 mM β-mercaptoethanol), SB431542 (10 µM; Selleckchem), LDN193189 (250 nM; Selleckchem) and Rock Inhibitor (RI) Y27632 (10 µM; Selleckchem) and plated at 1 million cells per of a Geltrex-coated 12-well plate. Cells were subsequently fed daily by complete NI medium exchange without RI. At DIV8, cells were split into single cells using Accutase for 10 min at 37ºC before the Accutase was neutralized with F12 medium. The cells were triturated, counted, and centrifuged (1000 rpm, 4 min). Cells were resuspended in NI medium supplemented with RI at 30 million cells/mL, and 350 µL droplets were plated onto dried, crystallized poly-L-ornithine (Sigma-Aldrich)/laminin-coated 6-well plate wells. Cells were allowed to attach for 1 hour before the wells were filled with NI/RI. Media replaced daily with NI. At DIV11, culture medium was changed to NM. At days DIV11 and DIV12, NM was supplemented with bFGF (100 ng/mL; StemCell Technologies). Two days prior to neural rosette isolation, NM was again supplemented with bFGF to boost the expansion of neural rosettes. Upon appearance of neural rosettes (around DIV23), cells were incubated for 1 h in STEMdiff neural rosette

selection reagent (NRSR; StemCell Technologies) at 37ºC. NRSR was replaced with NM, and rosettes manually isolated while excluding the edges of the spots, containing non-rosette cells. Rosettes were collected, triturated into smaller clumps, and centrifuged (1000 rpm, 4 min), before they were resuspended in NM supplemented with bFGF at a ratio of 3:2. The rosettes were seeded on fresh poly-L-ornithine/laminin-coated 6-well plates, and the medium replaced with NM+bFGF the following day. The rosettes were fed daily with NM, and at around DIV32 split with Accutase for 4 min, neutralized with NM, centrifuged (1000 rpm, 4 min), and resuspended in NM for seeding into new poly-L-ornithine/laminin-coated 6-well plates at a ratio of 1:3. At DIV42, neural rosettes were either frozen in NM supplemented with bFGF and 10% DMSO for long-term storage or split for terminal differentiation into mature cortical neurons.

For terminal maturation, the neural rosettes were split into single cells using Accutase for 10 min, Accutase neutralized using NM, triturated, centrifuged (1000 rpm, 4 min), resuspended in Neurobasal medium supplemented with B27, penicillin/streptomycin, and glutamine (from here on termed NB/B27), filtered through 40 µm strainers, and counted. NB/B27 medium was added to seed 400,000 cells/12 mm coverslip, or 200,000 cells/Ibidi 8-well plate well. Coverslips and Ibidi 8-well plate wells were freshly coated with poly-L-ornithine/laminin prior to neuronal seeding. NB/B27 medium was replaced as half feeds every 2-3 days. The cells were supplemented with the γ-secretase inhibitor DAPT for the first 7 days after plating to augment neuronal maturation, and with 5-fluorouracil (5-FU) for days 2-7 to prevent expansion of contaminating, proliferating cells (predominantly NPCs and astrocyte precursors). At day 7 after seeding, culture vessels were agitated to dislodge cell debris, and the medium completely replaced with NB/B27 without DAPT or 5-FU. From 7 days after plating onward, the neurons were kept in NB/B27 medium without DAPT or 5-FU until experiments were performed. Unless otherwise stated, reagents used for cortical neuron differentiation were obtained from ThermoFisher.

Following a week after terminal differentiation, the cortical neurons were stained for the neuronal markers β3-Tubulin/TuJ1, MAP2, and CTIP2. Neurons were fixed with 4% PFA in PBS for 30 min, washed twice with PBS, and blocked for 1 hour with blocking buffer (PBS with 3% donkey serum, 0.1% Triton X100, and 0.02% w/v sodium azide). Following blocking, cells were stained overnight at 4°C with the following antibodies: chicken anti-MAP2 (ab5392; 1:1000), mouse anti-Tuj1 (MMS-435P; 1:500) and rat anti-CTIP2 (ab18465; 1:200). The following day, cells were washed three times with PBS and stained with secondary antibodies for 2 h at room temperature. The following secondary antibodies were used: Donkey anti-mouse Alexa488 (A32766; 1:500), goat anti-rat Alexa555 (A21434; 1:500), and goat anti-chicken Alexa647 (A32933; 1:500). Cells were washed once with PBS, stained with DAPI for 20 min (ThermoFisher, 1:50,000 in PBS), and washed three times with PBS before being mounted on microscope slides for confocal imaging. Images were captured using a Zeiss Confocal microscope (Zeiss LSM880) equipped with a 40X oil objective, exciting at 405 nm (DAPI), 488 nm (Alexa488-conjugated 2° antibodies), 561 nm (Alexa568-conjugated 2° antibodies), and 633 nm (Alexa647-conjugated 2° antibodies).

Pharmacokinetic study of TPC2-A1-P in C57Bl/6N mice

Levels of the compound were determined by LC-MS/MS in blood plasma and brain samples over time after a single dose. The following reagents and consumables were used: DMSO Chromasolv Plus, HPLC grade, ≥99.7% (Sigma-Aldrich, USA; Cat #34869), Acetonitrile Chromasolv, gradient grade, for HPLC, ≥99.9% (Sigma-Aldrich, USA; Cat #34851), Methanol Chromasolv Plus, for HPLC, ≥99.9% (Sigma-Aldrich, USA; Cat 34860), Polyethylene glycol (PEG400) (AppliChem, Germany, Lot# 2S008911, CAS#25322-68-3), Blood collection microtubes, EDTA K2/K3, Purple, 0.5ml (Jiangxi, China, Code # NLD907), 2,2,2-Tribromoethanol 97% (Sigma-Aldrich; Cat # T48402), Compound IS-2015 was used as internal standard (IS), DMSO-PEG400-physiological saline (20%:50%:30%, v/v) was used as formulation vehicle. TPC2-A1-P was dissolved in DMSO and vortexed for 2 min. PEG400 was next added and the mixture was vortexed for 1 min. Next, saline was added and vortexed for 1 min, resulting in a clear solution. The batch of the working formulation was prepared 1 h prior to the in vivo study. The following equipment was used for compound detection: Gradient HPLC system (Shimadzu, Japan), MS/MS detector API 3000 PE with TurboIonSpray Electrospray module (PE Sciex, Canada), VWR Membrane Nitrogen Generators N2-04-L1466, nitrogen purity 99%+ (VWR, USA). Male C57Bl/6N mice aged 10 weeks were used in this study. The animals were randomly assigned to the treatment groups and fasted for 4 h before dosing. Six time points (5, 30, 60, 240, 480 and 1440 min) were set

for this pharmacokinetic study. Each time-point treatment group included 4 animals. There was also one vehicle dosed animal. Mice were injected i.p. with 2,2,2-tribromoethanol at the dose of 150 mg/kg prior to drawing the blood. Blood collection was performed from the orbital sinus in microtainers containing K2EDTA. Animals were next sacrificed by cervical dislocation after the blood samples collection. All samples were immediately processed, flash-frozen and stored at -70°C until subsequent analysis. Plasma samples (50 µl) were mixed with 200 µl of internal standard (IS) solution. After mixing by pipetting and centrifuging (4 min, 6000 rpm), 1 µl of each supernatant was injected into the LC-MS/MS system. A solution of compound IS-2015 (400 ng/ml in acetonitrile-methanol mixture, 1:1, v/v) was used as IS for quantification of TPC2-A1-P in plasma samples. Brain samples (weight 200 mg ± 1 mg) were dispersed in 800 µl of IS400(80) using zirconium oxide beads (115 mg ± 5 mg) in The Bullet Blender homogenizer for 30 seconds at speed 8. Samples were centrifuged (4 min, 14,000 rpm), and 1 µl of each supernatant injected into LC-MS/MS system. A solution of compound IS-2015 (400 ng/ml in water-methanol mixture, 1:4, v/v) was used as an internal standard (IS400(80)) for quantification of TPC2-A1-P in brain samples. Analyses of plasma and brain samples were conducted by the bioanalytical laboratory personnel at Enamine/Bienta. The concentrations of each compound in the blood plasma and brain were determined using high performance liquid chromatography/tandem mass spectrometry (HPLC-MSMS). The Shimadzu HPLC system consisted of controller Prominence CBM20A2, isocratic pumps LC-10ADvp, an autosampler Prominence SIL-20AC, a sub-controller FCV-14AH, and a degasser DGU-14A. Mass spectrometric analysis was performed using an API 3000 (triple-quadrupole) instrument from AB Sciex (Canada) with an electro-spray (ESI) interface. The data acquisition and system control was performed using Analyst 1.5.2 software (AB Sciex, Canada). Calibration standards for quantification of compound in plasma samples: TPC2-A1-P was dissolved in DMSO at concentration of 2 mg/ml (stock solution). A series of calibration standards was prepared by serial dilution of stock solution with blank mouse plasma to a final concentration ranging from 20 to 20,000 ng/ml. Standard plasma samples (50 µl) were mixed with IS (200 µl). After mixing by pipetting and centrifuging for 4 min at 6000 rpm, 1 µl of each supernatant was injected into LC-MS/MS system. The TPC2-A1-P stock solution (see description above) was consecutively diluted with IS400(80) to get a series of calibration solutions with final concentrations ranging from 5 to 2000 ng/ml. The calibration curve was constructed using blank mouse brain samples. To obtain calibration standards, blank brain samples were homogenized in 800 µl of corresponding calibration solution using zirconium oxide beads (115 mg ± 5 mg) in The Bullet Blender® homogenizer (30 seconds, speed 8). After that, the samples were centrifuged for 4 min at 14000 rpm, and 1 µl of each supernatant was injected into LC-MS/MS system. The regression analysis of TPC2-A1-P was performed by plotting the peak area ratio (y) against the compound concentration in calibration standards (x, ng/ml or ng/g). The validity of the calibration curves (relationship between peak area ratio and compound concentration) was ensured by the correlation coefficients (R) calculated for the quadratic regression. The concentrations of TPC2-A1-P in plasma and brain samples below the lower limit of quantitation (Plasma LLOQ – 20 ng/ml; Brain LLOQ – 20 ng/g) were designated as zero. The pharmacokinetic data analysis was performed using non-compartmental, bolus injection or extravascular input analysis models in WinNonlin 5.2 (PharSight).

Site-directed mutagenesis and colocalization analysis using confocal microscopy

All human CLN3 mutants were generated from WT cDNA templates using QuikChange Site-Directed Mutagenesis Kit (Stratagene) and verified by sequencing both strands entirely. For site-directed mutagenesis of CLN3 mutants L101P, S131R, C134R, A158P, G165E, L170P, I285V, L306H, V330F and V330I, the KAPA HiFi Hotstart Ready Mix (Roche) was used and the already mentioned plasmid pcDNA6.2/N-EmGFP-DEST with hCLN3 as a template and (10 ng of plasmid DNA in a 25 µl reaction) and primers that had been obtained from Eurofins Genomics (see Table S2 for primer sequences). PCR was done with a Mastercycler® nexus gradient (Eppendorf) PCR conditions were set to an initial denaturing step at 95°C for 3 min, followed by 16 cycles containing of a denaturing step at 98°C for 20 sec, an annealing step at 68°C for 1 min, and an elongation step at 72°C for 7 min, followed by an additional elongation step at 72°C for 7 min. After PCR amplification, the mix was digested for 2 h at 37°C with FastDigest DpnI and 100 µl of XL1Blue E. coli cells (Agilent) were transformed with 5 µl of the digested mix by incubating them for 20 min on ice, heat-shocking them for 40 sec at 37°C, incubating them another 2 min on ice, pre-culturing them for 1 h at 37 °C in a shaker at 200 rpm after addition of 900 µl LB(+) medium, and plating 250 µl of pre-culture on an ampicillin-

containing agar plate. After colony growth, colonies were cultured for 16 h at 37°C at 200 rpm in a shaker and plasmid DNA was isolated with a CompactPrep Plasmid Mini Kit. Isolated plasmid DNA was sequenced to check for successful mutagenesis. Mutants G187A, G189R, G189W, V290L, E295K, R334C, R334H, Q352H, R405W and D416G have been generated using the QuikChange Site-Directed Mutagenesis Kit (Stratagene). Sequencing of plasmid DNA was done by Eurofins Genomics. In case of successful clonation, a Midi preparation of the respective plasmid DNA was done using the CompactPrep Plasmid Midi Kit. DNA concentration was measured with a NanoDrop™ 2000c spectrophotometer. All CLN3 WT and mutant isoforms were N-terminally tagged GFP versions. For functional studies constructs were transiently expressed in $CLN3^{-/-}$ HeLa cells with the use of Turbofect (ThermoFisher) and analysed 24-48 h after transfection using a confocal microscope (Zeiss LSM 880). Colocalization analysis was done with the JACoP plugin of FiJi. For each cell, a region of interest (ROI) was selected and the channels were separated. For MCC (Mander's correlation coefficient) values, fixed thresholds were set for each transfected plasmid (GFP-CLN3: 92, LAMP1-RFP: 86, Rab5-RFP: 84, Rab11-DsRed: 77, MitoTracker-DR: 122).

Endolysosomal patch-clamp experiments

For whole-LE/LY manual patch-clamp recordings, cells were treated with apilimod (neurons). Compounds were washed out before patch-clamp experimentation. Unless otherwise stated, the cytoplasmic solution contained 140 mM K-MSA, 5 mM KOH, 4 mM NaCl, 0.39 mM $CaCl_2$, 1 mM EGTA and 20 mM HEPES (pH was adjusted with KOH to 7.2) and luminal solution contained 140 mM Na-MSA, 5 mM K-MSA, 2 mM Ca-MSA, 1 mM $CaCl_2$, 10 mM HEPES and 10 mM MES (pH was adjusted with NaOH to 4.6) were used. For the application of small molecule agonists (ML-SA1, ML1-SA1 (EVP169)), cytoplasmic solution was completely exchanged by cytoplasmic solution containing agonist. Intact endolysosomes were manually isolated as described before (Chen *et al*, 2017). Currents were recorded using an EPC-10 patch-clamp amplifier (HEKA, Lambrecht, Germany) and PatchMaster acquisition software (HEKA). Data were digitized at 40 kHz and filtered at low-pass filter frequency of 2.9 kHz. Recording glass pipettes were polished and had a resistance in range of 8-11 MΩ. Fast and slow capacitive transients were cancelled by the compensation circuit of the EPC-10 amplifier. Mean capacitance value for LE/LY of fibroblasts was 0.5 ± 0.1 (SEM; n=4). In all experiments, 500-ms voltage ramps from -100 to +100 mV were applied every 5 s, holding potential was kept at 0 mV. The current amplitudes at -100 mV were extracted from individual ramp current recordings. Offline analysis was performed with the software Origin8 (OriginLab Corp., Northampton, MA, USA).

Knockdown of TPC2 (siRNA)

Human fibroblasts have been electroporated using Neon Transfection System with 50nM of siRNA targeting a control sequence (ON-TARGETplus Non-targeting Pool, D-001810-10-05) and siRNA targeting TPCN2 ON-TARGET plus human TPCN2 (219931) siRNA SMARTpool, L-006508-00-0005). Cells were incubated with siRNA for 72h. Knockdown efficiency have been estimated by using Real-time quantitative PCR.

Real-time quantitative PCR analysis

To assess expression levels of the target channels and disease genes, we used real-time quantitative PCR (RT-qPCR). RNA was isolated from iPSC-derived neurons at day 10 after terminal maturation using the RNeasy Mini Kit (Qiagen), following manufacturer's instructions. RNA was immediately synthesized into cDNA and stored at -80ºC. cDNA was synthetized using the RevertAid First Strand cDNA Synthesis Kit (ThermoFisher), using 50 ng RNA as template for cDNA synthesis. cDNA synthesis was primed using a 1:1 combination of random hexamers and oligo(dT) primers, and cDNA synthesis initiated by a 5-minute incubation at 25ºC followed by a 60-minute incubation at 42ºC. The reaction was terminated by heating at 70ºC for 5 min, the cDNA diluted 1:7 with nuclease-free water, and frozen at -20ºC for storage. For RT-qPCR of cDNA isolated from iPSC-derived neurons, we employed the SYBR Green system (ThermoFisher) and the LightCycler 480 Instrument (Roche). Alternatively, for the prepared Human Brain cDNA Array (OriGene), we used the SYBR Green system and a CFX96 instrument (Biorad) to accommodate the pre-aliquoted cDNA plate. The primer pairs used for human samples were as follows (5'→3'): TRPML1 (TCTTCCAGCACGGAGACAAC, GCCACATGAACCCCACAAAC), TRPML2 (AACGGTGTTTCCTGTTCCGA, GCCATTGCATTTCTGA CGGTTA), TRPML3 (TGCTTCTGTGGATGGATCG, GAGACCATGTTCAGAGAACG), TPC1 (TCCCA

AAGCGCTGAGATTAC, TCTGGTTTGAGCTCCCTTTC), TPC2 (GTACCCCTCTTGTGTGGACG, GGC CCTGACAGTGACAACTT), CLN3 (GGTTCTCGTCAGTGGGATTT, CTGATGAGATGCTAGCGAA GAC), EMC7 (Eisenberg & Levanon, 2013; Artyukhov *et al*, 2017) (AAAGGAGGTAGTCAGGCCGT, GTTGCTTCACACGGTTTTCCA). For detecting mouse transcripts from biopsies, sample preparation and detection was performed as previously described, but transcripts detected with the following primers: TPC2 (TAAAGTACCGCTCCATCTACCA, GCAGACGTTCGAG TAATACCAG), HPRT (Hruz *et al*, 2011) (GCTCGAGATGTCATGAAGGAGAT, AAAGAACTTATAG CCCCCCTTGA). For iPSCs we opted for EMC7 as our preferred housekeeping gene due to consistent expression throughout neuronal differentiation (Eisenberg & Levanon, 2013; Artyukhov *et al*, 2017; Burke *et al*, 2020)

Magic Red Cathepsin B activity measurements

Lysosomal protease activity was measured using the Magic Red Cathepsin B Kit (AbD Serotec), which utilizes a cathepsin B target sequence (RR), fused by amide bonds to the fluorophore cresyl violet and quenching its fluorescence. Proteolytic cleavage of the quenching target sequence thus increases the cresyl violet fluorescence, which can be detected by confocal imaging. We used a fluorescence recovery after photobleaching (FRAP) approach previously utilized for assessing proteolysis upon CLN3 knockdown (Metcalf *et al*, 2008) to assess proteolysis in iPSC-derived neurons. The Magic Red Cathepsin B Kit was prepared according to manufacturer's instructions and the iPSC-derived neurons loaded for 60 min at 37ºC before imaging with a Zeiss LSM880 confocal microscope, equipped with a 37°C incubation unit and a 63X water immersion objective. FRAP bleaching was performed using 514 nm, 561 nm, and 633 nm lasers targeted towards the most intensely labelled area of the neuronal soma at 100% intensity for 200 iterations (85 s). The pinhole was kept wide (4.70 AU) to image throughout several focal planes, avoiding focal plane shifts or vesicular movement in the z-direction to influence the signal. Next, fluorescence recovery was measured upon excitation with a DPSS 561 nm laser, recording images every 75 ms for 75 seconds. Fluorescence recovery within photobleached regions was finally quantified relative to the initial fluorescence after photobleaching. For compound treatment of iPSC-derived neurons, compounds were administered 48 h prior to loading Magic Red Cathepsin B.

Lysosomal exocytosis experiments

Human fibroblasts (2 x 10^4) were seeded on 8-well plates (Ibidi) and cultured overnight. Cells were washed once with Minimum Essential Media (MEM) supplemented with 10 mM HEPES and then treated with TPC2-A1-P (30 μM) or ML-SA1 (30 μM) for 90 min. Ionomycin (4 μM for 10 min) and ML-SA1 were used as positive controls. Following treatment, cells were incubated with an anti-LAMP1 antibody (1:200, SantaCruz) in MEM supplemented with 10 mM HEPES and 1% BSA for 20 min on ice. Cells were then fixed with 2.6% PFA (ThermoFisher) for 20 min and incubated with Alexa Fluor 488 conjugated secondary antibody (ThermoFisher) for 1 h in PBS containing 1% BSA. Nuclei were stained with DAPI. Confocal images were acquired using an LSM 880 microscope (Zeiss) with 40X magnification. Plasma membrane LAMP1 mean intensity was calculated using unsaturated images on ImageJ 1.52a software. For the flow cytometry assay human fibroblasts (wild type, MLIV, NPC1 and JNCL) (15 x 10^4) were seeded overnight in a 6 well plate. Cells were washed once with Minimum Essential Media (MEM) supplemented with 10 mM HEPES and then treated with TPC2-A1-P (30 μM) for 90 min. Ionomycin (4 μM for 10 min) was used as positive control. Following treatment, cells were collected in falcon tubes and incubated on rotation with an anti-LAMP1 antibody (1:200, SantaCruz) in MEM supplemented with 10 mM HEPES and 1% BSA for 20 min at 4°C. Cells were then fixed with 2.6% PFA (ThermoFisher) for 20 min and incubated with Alexa Fluor 488 conjugated secondary antibody (ThermoFisher) for 1 h in PBS containing 1% BSA. Samples were then resuspended in DPBS 1 X and before FACS analysis cells were filtered with a pre-separation filter with a cut off of 20/30 μm. The instrument used was BD FACS Aria III.

Construction of the TPC2-IRES-Cre targeting vector (to generate a TPC2 reporter mouse line) and gene targeting

The final targeting construct is comprised of a 5' TPC2 homology arm, an IRES-Cre-FRT-pgk-Neo-FRT cassette and a 3' TPC2 homology arm. The 2665-bp 3' homology arm containing sequence downstream of the

final exon of Tpcn2 (exon 25) was amplified by polymerase chain reaction (PCR) from genomic R1 mouse embryonic stem (ES) cell DNA. The fragment was then subcloned into pKO-DTA using a 5' AscI site and a BamHI site localized at the 3'end, which were incorporated within the primer sequences. In a similar manner, the 2332-bp 5' homology arm containing the stop codon of TPC2 was generated and also cloned into the vector using XhoI and AscI sites. PCR amplification of both homology arms was undertaken using the high-fidelity PfuUltra II DNA polymerase to minimize PCR-induced mutations, and any nucleotides that differed from the database sequence upon sequence analysis were verified by independent PCR amplification and sequencing. Finally, the IRES-Cre-FRT-pgk-Neo-FRT cassette was cloned into the AscI site found at the junction of the 2 homology arms. The completed targeting construct was then further verified by a complete sequence analysis and restriction mapping. Following verification of the integrity of the targeting construct, plasmid DNA was linearized using the NotI enzyme and then electroporated into R1 ES cells at the FARAH Mammalian Transgenics Platform, University of Liege. Following electroporation, correctly targeted clones were identified by Southern blot analysis and these were then used to generate mice following standard protocols (injection of ES cells [129/Sv] into blastocysts [C57BL/6], implantation of injected blastocysts into foster mothers, backcross of male chimeras with C57BL6 females). F1 animals resulting from backcrosses were then crossed with FLP-deleter mice, which contain a ubiquitously expressed FLP recombinase gene, to facilitate removal of the FRT-flanked neomycin selection cassette.

Generation and analysis (by immunohistochemistry) of the TPC2 reporter mouse line

Mice harboring the Tpcn2$^{IRES\text{-}Cre}$ locus were bred with ROSA26-floxed-stop-τGFP mice, giving rise to mice constitutively expressing τGFP under control of the TPC2 promoter. The Tpcn2$^{IRES\text{-}Cre}$ mouse serves the purpose of expressing Cre recombinase cDNA under control of the TPC2 promoter, without affecting protein function (Mountford & Smith, 1995). The latter mouse harbors a transgene insertion on the *ROSA26* locus, consisting of a loxP-flanked (floxed) polyadenylation termination sequence followed by cDNA of the microtubule-associated protein tau (τ), conjugated to GFP. Without co-expression of Cre recombinase, the transgene is silenced by virtue of the floxed transcriptional termination signal. However, TPC2 promoter-driven Cre recombinase expression excises the termination signal, facilitating constitutive τGFP expression (see Fig. 8A) (Wyatt *et al*, 2017). The fusion of GFP to τ furthermore permits GFP distribution throughout neurites, enabling identification of expressing neurons (Wen *et al*, 2011; Iwata *et al*, 2019). At 11 weeks of age, the mice were anaesthetized upon intraperitoneal injection of ketamine and xylazine, and a needle inserted into the left ventricle. A small incision was made in the right atrium for liquid to leave the body. The circulation was first flushed with PBS before 4% PFA was injected into the mouse. Organs were removed and separately post-fixated in 4% PFA for 6 h at 4°C. PFA was next aspirated, and the organs stored overnight in 18% sucrose solution at 4°C. Organs were next embedded in OCT medium, first for 4 h at room temperature, then in embedding molds in isobutane beakers surrounded by ethanol and dry ice. Frozen embedding molds were stored at -80°C until slicing. For slicing, embedding molds were thawed to -16°C, and sliced into 14 µm thick slices. Slices were stored at -80°C until further use. For immunohistochemistry, slices were thawed to room temperature for 15 min, and washed three times with PBS. The slices were next blocked for 1 hour (10% normal donkey serum, 3% bovine serum albumin, 0.3% Triton X-100), and primary antibody staining solutions added at 4°C overnight. The following primary antibodies and dilution factors in PBS were used: chicken anti-GFP (Invitrogen, A10262; 1:1000), rabbit anti-β3 tubulin (Abcam, ab18207; 1:500), rat anti-CD13 (Abcam, ab33489; 1:200), rabbit anti-Iba1 (WAKO, 019-19741; 1:100), Cy3-conjugated mouse anti-GFAP (Sigma Aldrich, C9205; 1:500), and rabbit anti-mGluR1 (Alomone, AGC-006; 1:100). Slices were washed three times with PBS, and next stained with secondary antibodies for 2 h at room temperature. The following secondary antibodies and dilution factor in PBS were used: anti-chicken Alexa488 (Invitrogen, A11039; 1:500), anti-rabbit Cy3 (Jackson Dianova, 711-165-152; 1:500), and anti-rat Cy3 (Jackson Dianova, 112-165-143; 1:500). Samples were washed once with PBS, stained with DAPI for 30 min, washed three times with PBS, and mounted for imaging using a Zeiss LSM880 confocal microscope, equipped with a 40X oil immersion objective.

Autophagy assays
For western blot analysis, the following antibodies were used: β-Actin (Santa Cruz SC 47778, 1:4000), LC3 (Novus NB100-2220, 1:1000) P62/SQSMT1 (BD 610833, 1:1000), Vinculin (Cell Signaling Technology, 1:1000, cat. #4650). Total cell lysate was prepared by solubilization in TRIS HCl 10 mM pH 8.0 and 0.2% SDS supplemented with protein and phosphatases inhibitor (Sigma). Protein concentration was determined by the Bradford method (Biorad). After SDS-polyacrylamide gel electrophoresis (PAGE) and immunoblotting, the protein recognized by the specific antibody were visualized by chemiluminescence methods (Luminata Crescendo Western HRP substrate, Millipore) using peroxidase-conjugated anti-rabbit or anti-mouse secondary antibodies (Cell Signaling Technology). Membranes were developed using an Odyssey imaging system (LI-COR Biosciences). Quantification was carried out using unsaturated images on ImageJ 1.52a software.

Electron microscopy experiments
Human fibroblasts or neuronal stem cells were seeded in 6-well plates and treated with 30 µM TPC2-A1-P or DMSO for 48h. The cells were fixed with 1% glutaraldehyde for 30 min at room temperature, then washed with 1X PBS and post-fixed as previously described (Polishchuk *et al*, 2019). After dehydration, the specimens were embedded in epoxy resin and polymerized at 60 °C for 72 h. Thin 60 nm sections were cut using a Leica EM UC7 microtome. EM images were acquired from thin sections using a FEI Tecnai-12 electron microscope equipped with a VELETTA CCD digital camera (FEI, Eindhoven, NL). Each EM experiment was repeated three times and 20 fields of view were analyzed for each sample. Double-blind analysis of the samples was performed: number of inclusions (fingerprint-like structures/area), % cytosol covered by inclusions (area of inclusion/cell area), and mitochondria numbers/ area as well as mitochondria cristae numbers/area.

In vivo experiments in MLIV mice
Animals were used under animal protocols approved by the government (Regierung von Oberbayern, ROB-55.2-2532.Vet_02-17-170) and University of Munich (LMU) Institutional Animal Care Guidelines or in accordance with the guidelines and policies of the European Communities Council, approved by the Italian Ministry of Health. Mice were housed in individually ventilated cages in rooms maintained at constant temperature (20-24°C) and humidity (45-65%) with a 12 hour light cycle. Animals were allowed food and water ad libitum.
Experiments were performed with previously described MLIV (*Mcoln1*^{tm1Sasl}, i.e. *Mcoln1*$^{\Delta Ex3\text{-}5}$) mice and littermate controls (Venugopal *et al*, 2007). Mice were genotyped as initially described using gDNA extracted from ear clips (Venugopal *et al*, 2007). The injection solutions were prepared in pre-warmed PBS in a sterile laminar flow hood. 4-week old mice were injected with either vehicle (PBS with 10% DMSO and 10% PEG-400) or vehicle plus 20 mg/kg TPC2-A1-P i.p. every day for 13 weeks using a 25G needle. The appearance and body weight of injected mice was scored on a weekly basis. No gross scoring differences were observed between vehicle and TPC2-A1-P-injected mice until the experimental endpoint. Following the course of injections, mice were euthanized as previously described for the TPC2 reporter mouse, and brains retrieved for immunohistochemistry.
Furthermore, male and female WT (n = 10, 5 males and 5 females) and MLIV (n = 24, 13 males and 11 females) 9-week old mice, after receiving i.p. injections every day (either vehicle or TPC2-A1-P as described above) for one week, were subjected to the open field test (day1) and to the Rotarod test (day 2). In the open field test mice were left free to explore a Plexiglas arena (35 × 47 × 60 cm) for 15 min. The distance travelled (m), the maximum speed (m/s), the immobility time (s) and the distance (m) travelled in the center of the arena (central distance) were recorded using a video camera (PANASONIC WV-BP330) and automatically scored through a video-tracking system (ANY-MAZE, Stoelting, USA). The accelerating rotarod test was applied using a commercial apparatus (Ugo Basile) consisting of a rod suspended horizontally at a height of 14 cm from the floor. The rod (5 cm in diameter) was accelerated from 4 rpm to 40 rpm in 300 s and the latency to fall from the rod was measured; animals were left to run on the maximum speed for additional 300 s. The tests were repeated four times (with an intertrial interval of 30 min) and the average latency to fall was calculated. Sex x group effects were tested using a two-way ANOVA (with sex and groups, as between factors); as no sex x groups interaction was observed for any of the measures, values between the two sexes were averaged.

Cell viability assay
Human patient fibroblasts (HF) were seeded at a cell density of 3.000 cells per well, while iPSC-derived neurons were seeded at a density of 2.000 cells per well in 96-well plates (Sarstedt). Both, HF and iPSC-derived neurons were treated the following day with different concentrations of TPC2-A1P and HF also with other reported TPC2 agonists (Zhang et al, 2019), and monitored over 24-, 48-, 72-h. DMSO was used as vehicle control and full medium as blank. Cell viability using CellTiter-Blue reagent was measured according to the manufacturer's protocol. The compounds amitriptyline (#PHR1384), chlorpromazine (#C0982) clomipramine (#C7291) and desipramine (#D3900) were ordered from Sigma Aldrich and riluzole (#0768) was ordered from Tocris. The analysis was performed with GraphPad Prism 9.1.

Immunohistochemistry on mouse brain
Brain preparation and embedding in OCT was performed as described above for the TPC2 reporter mouse. Frozen embedding molds were stored at -80°C until slicing. For slicing, embedding molds were thawed to -16°C, and sliced into 40 µm thick slices. Slices were stored at -80°C until further use. For immunohistochemistry, slices were thawed to room temperature for 30 min, and washed three times with PBS. For staining glial markers, immunohistochemistry was performed as previously described for the TPC2 reporter mouse. For P62 immunohistochemistry, the slices were blocked for 1 hour with blocking buffer (3% BSA, 5% FBS, 0.1% Triton X-100 in PBS1X) and anti P62/SQSTM1 primary antibody was added o/n at 4°C in the same blocking buffer (1:500, GP62-C Progen). Slices were washed three times with PBS, and next stained with secondary antibodies for 1h at room temperature (1:400, A-11074 ThermoFisher). Samples were washed once with PBS, stained with DAPI for 15 min, washed three times with PBS, and mounted for imaging using a Zeiss LSM880 confocal microscope, equipped with a 10X objective, zoom 0.6.

Suppl. references

Amps K, Andrews PW, Anyfantis G, Armstrong L, Avery S, Baharvand H, Baker J, Baker D, Munoz MB, Beil S, *et al* (2011) Screening ethnically diverse human embryonic stem cells identifies a chromosome 20 minimal amplicon conferring growth advantage. *Nat Biotechnol* 29: 1132–1144

Artyukhov AS, Dashinimaev EB, Tsvetkov VO, Bolshakov AP, Konovalova E V., Kolbaev SN, Vorotelyak EA & Vasiliev A V. (2017) New genes for accurate normalization of qRT-PCR results in study of iPS and iPS-derived cells. *Gene* 626: 234–240

Brinkman EK, Chen T, Amendola M & Van Steensel B (2014) Easy quantitative assessment of genome editing by sequence trace decomposition. *Nucleic Acids Res* 42: 1–8

Burke EE, Chenoweth JG, Shin JH, Collado-Torres L, Kim SK, Micali N, Wang Y, Colantuoni C, Straub RE, Hoeppner DJ, *et al* (2020) Dissecting transcriptomic signatures of neuronal differentiation and maturation using iPSCs. *Nat Commun* 11: 1–14

Chen C-C, Cang C, Fenske S, Butz E, Chao Y-K, Biel M, Ren D, Wahl-Schott C & Grimm C (2017) Patch-clamp technique to characterize ion channels in enlarged individual endolysosomes. *Nat Protoc* 12: 1639–1658

Concordet JP & Haeussler M (2018) CRISPOR: Intuitive guide selection for CRISPR/Cas9 genome editing experiments and screens. *Nucleic Acids Res* 46: W242–W245

Eisenberg E & Levanon EY (2013) Human housekeeping genes, revisited. *Trends Genet* 29: 569–574

Hruz T, Wyss M, Docquier M, Pfaffl MW, Masanetz S, Borghi L, Verbrugghe P, Kalaydjieva L, Bleuler S, Laule O, *et al* (2011) RefGenes: Identification of reliable and condition specific reference genes for RT-qPCR data normalization. *BMC Genomics* 12: 156

Iwata M, Watanabe S, Yamane A, Miyasaka T & Misonou H (2019) Regulatory mechanisms for the axonal localization of tau protein in neurons. *Mol Biol Cell* 30: 2441–2457

Kwart D, Paquet D, Teo S & Tessier-Lavigne M (2017) Precise and efficient scarless genome editing in stem cells using CORRECT. *Nat Protoc* 12: 329–334

Metcalf DJ, Calvi AA, Seaman MNJ, Mitchison HM & Cutler DF (2008) Loss of the batten disease gene CLN3 prevents exit from the TGN of the mannose 6-phosphate receptor. *Traffic* 9: 1905–1914

Mountford PS & Smith AG (1995) Internal ribosome entry sites and dicistronic RNAs in mammalian transgenesis. *Trends Genet* 11: 179–184

Paquet D, Kwart D, Chen A, Sproul A, Jacob S, Teo S, Olsen KM, Gregg A, Noggle S & Tessier-Lavigne M (2016) Efficient introduction of specific homozygous and heterozygous mutations using CRISPR/Cas9. *Nature* 533: 125–129

Polishchuk E V, Merolla A, Lichtmannegger J, Romano A, Indrieri A, Ilyechova EY, Concilli M, Cegli R De, Crispino R, Mariniello M, *et al* (2019) Activation of Autophagy, Observed in Liver Tissues From Patients With Wilson Disease and From ATP7B-Deficient Animals, Protects Hepatocytes From Copper-Induced Apoptosis. *Gastroenterology* 156: 1173–1189

Ran FA, Hsu PD, Wright J, Agarwala V, Scott DA & Zhang F (2013) Genome engineering using the CRISPR-Cas9 system. *Nat Protoc* 8: 2281–2308

Steyer B, Bu Q, Cory E, Jiang K, Duong S, Sinha D, Steltzer S, Gamm D, Chang Q & Saha K (2018) Scarless Genome Editing of Human Pluripotent Stem Cells via Transient Puromycin Selection. *Stem Cell Reports* 10: 642–654

Venugopal B, Browning MF, Curcio-Morelli C, Varro A, Michaud N, Nanthakumar N, Walkley SU, Pickel J & Slaugenhaupt SA (2007) Neurologic, Gastric, and Opthalmologic Pathologies in a Murine Model of Mucolipidosis Type IV. *Am J Hum Genet* 81: 1070–1083

Weisheit I, Kroeger JA, Malik R, Klimmt J, Crusius D, Dannert A, Dichgans M & Paquet D (2020) Detection of Deleterious On-Target Effects after HDR-Mediated CRISPR Editing. *Cell Rep* 31: 107689

Weisheit I, Kroeger JA, Malik R, Wefers B, Wurst W, Dichgans M, Paquet D & Lichtner P (2021) Simple and reliable detection of CRISPR-induced on-target effects by qgPCR and SNP genotyping. *Nat Protoc* 16: 1714–1739

Wen S, Go IN, Mai O, Schauer C, Leinders-zufall T & Boehm U (2011) Genetic Identification of GnRH Receptor Neurons : A New Model for Studying Neural Circuits Underlying Reproductive Physiology in the Mouse Brain. 152: 1515–1526

Wyatt A, Wartenberg P, Candlish M, Krasteva-christ G, Flockerzi V & Boehm U (2017) Genetic strategies to analyze primary TRP channel-expressing cells in mice. *Cell Calcium* 67: 91–104

Zhang X, Chen W, Li P, Calvo R, Southall N, Hu X, Bryant-genevier M, Feng X, Geng Q, Gao C, *et al* (2019) Agonist-specific voltage-dependent gating of lysosomal two-pore Na+ channels. *Elife* 8: e51423

Paper IV: Summary and Contributions

Estradiol analogs attenuate autophagy, cell migration and invasion by direct and selective inhibition of TRPML1, independent of estrogen receptors

Philipp Rühl, Anna Scotto Rosato, Nicole Urban, Susanne Gerndt, Rachel Tang, **Carla Abrahamian**, Charlotte Leser, Jiansong Sheng, Archana Jha, Günter Vollmer, Michael Schaefer, Franz Bracher, & Christian Grimm

The founding member of the mucolipin subfamily of TRP channels, TRPML1, plays a vital role in maintaining lysosomal ionic balance and controlling autophagy by regulating the activity of TFEB. TRPML1 and TFEB prevent excessive autophagy during prolonged starvation by contributing to mTORC1 reactivation[81, 98, 236, 237]. Mutations in TRPML1 lead to lysosomal trafficking defects, neurodegeneration, and lysosomal storage diseases, with MLIV being the most notable example[90]. In recent years, interest in the role of TRPML1 and other endolysosomal cation channels in cancer has grown, although conflicting data exist across different cancer types[183, 188]. A study by Xu et al., 2019 reported the upregulation of TRPML1 in the aggressive triple-negative breast cancer (TNBC) subtype. The authors demonstrated that the knockdown of TRPML1 suppressed TNBC proliferation, growth, and invasion by regulating mTORC1 activity. Despite the clinical burden of TNBC, effective therapies remain elusive. Current research has identified mTORC1 as a potential target for treatment; however, drugs aimed at this pathway have been unsuccessful in impeding TNBC progression due to the essential role of mTORC1 in various cell types and functions. Hence, the development of TRPML1 antagonists holds promise for breast cancer therapy[9]. Nevertheless, existing TRPML1 channel blockers lack mucolipin isoform selectivity and may simultaneously suppress two or more channels. To identify potential TRPML1 inhibitors, we conducted a compound screening, testing a total of 2430 compounds. Among them, the steroid 17β-estradiol methyl ether (EDME) displayed selective inhibitory effects on TRPML1, sparing TRPML3 and exhibiting the lowest IC_{50} values for TRPML1. We further subjected EDME to comprehensive counter-screening against numerous other members of the TRP superfamily and compared its performance to available pharmacological steroidal compounds. The validation was carried out using whole-cell and endolysosomal patch clamp experiments and single-cell Ca^{2+} imaging using Fura-2. EDME emerged as a potent and selective TRPML1 blocker. To evaluate its functional impact, we performed TFEB shift and autophagy assays using human fibroblasts. Treating the cells with EDME, along with two of its analogs, PRU-10 and PRU-12, produced comparable effects to MLIV patient fibroblasts, inhibiting autophagy and TFEB translocation to the nucleus. To examine its estrogen receptor-independent effects and implications in oncology, I focused on the poorly differentiated and highly invasive TNBC line, MDA-MB-231. My qPCR experiments revealed the expression in the WT cell line, showing the highest expression of TRPML1 compared to TRPML2 and TRPML3. To test the effects of EDME and compare them with TRPML1 KO, I generated TRPML1 KOs in the MDA-MB-231 using different strategies and guide RNA combinations and performed necessary validation screenings. Subsequently, I tested the invasiveness and migratory capacities of MDA-MB-231 WT, TRPML1 KOs, and TRPML1 cells treated with varying concentrations of EDME. Strikingly, EDME-treated cells exhibited reduced migration and invasion similar to TRPML1 KO, suggesting its potential as an effective TRPML1 inhibitor of TNBC. To ensure the specificity and on-target effects of EDME, I treated the TRPML1 KO cells with the compound, which did not show any significant effects, confirming its selective action. Overall, our study successfully identified 17β-estradiol methyl ether (EDME) as a potent and selective inhibitor of TRPML1, an endolysosomal cation channel. EDME showed promising effects in inhibiting autophagy and TFEB translocation, both vital processes regulated by TRPML1. Importantly, EDME exhibited potential as an effective TRPML1 inhibitor in aggressive TNBCs, reducing migration and invasion. These findings offer promising prospects for developing targeted therapies aimed at transiently modulating TRPML1 function in TNBC function and other cancers.

Paper IV

www.nature.com/scientificreports

scientific reports

Check for updates

OPEN

Estradiol analogs attenuate autophagy, cell migration and invasion by direct and selective inhibition of TRPML1, independent of estrogen receptors

Philipp Rühl[1,7], Anna Scotto Rosato[2,7], Nicole Urban[3,7], Susanne Gerndt[1], Rachel Tang[2], Carla Abrahamian[2], Charlotte Leser[1], Jiansong Sheng[4], Archana Jha[5], Günter Vollmer[6], Michael Schaefer[3]✉, Franz Bracher[1]✉ & Christian Grimm[2]✉

The cation channel TRPML1 is an important regulator of lysosomal function and autophagy. Loss of TRPML1 is associated with neurodegeneration and lysosomal storage disease, while temporary inhibition of this ion channel has been proposed to be beneficial in cancer therapy. Currently available TRPML1 channel inhibitors are not TRPML isoform selective and block at least two of the three human isoforms. We have now identified the first highly potent and isoform-selective TRPML1 antagonist, the steroid 17β-estradiol methyl ether (EDME). Two analogs of EDME, PRU-10 and PRU-12, characterized by their reduced activity at the estrogen receptor, have been identified through systematic chemical modification of the lead structure. EDME and its analogs, besides being promising new small molecule tool compounds for the investigation of TRPML1, selectively affect key features of TRPML1 function: autophagy induction and transcription factor EB (TFEB) translocation. In addition, they act as inhibitors of triple-negative breast cancer cell migration and invasion.

TRPML1 is a lysosomal cation channel of the transient receptor potential (TRP) superfamily permeable for Ca^{2+}, Na^{+}, Fe^{2+}, Zn^{2+}, and other cations. TRPML1 is involved in a number of physiological processes and human diseases. Loss or mutation of TRPML1 causes the neurodegenerative lysosomal storage disorder mucolipidosis type IV[1]; vice versa activation of TRPML1 clears intraneuronal Aβ in preclinical models of HIV infection[2] and protects human dopaminergic neurons from α-synuclein toxicity through increased lysosomal exocytosis[3]. TRPML1 is also essential for sarcolemma repair to prevent muscular dystrophy[4], and small molecule activation of TRPML1 ameliorates Duchenne muscular dystrophy[5]. TRPML1 further plays a role in gastric acid secretion and may represent a therapeutic target for chronic Helicobacter pylori infection[6–8]. TRPML1 also acts as ROS (reactive oxygen species) sensor in lysosomes[9], it regulates autophagy through calcineurin and transcription factor EB (TFEB)[10] or in a TFEB-independent manner[11,12], it regulates lysosomal motility and lysosomal positioning[13], and it plays a role in osteoclastogenesis and bone remodeling[14]. Furthermore, TRPML1 has functions in the immune system, e.g. it controls the migration of dendritic cells[15] and it plays a role in the education process of natural killer (NK) cells[16]. Finally, HRAS-driven cancer cells, i.e. cells containing mutations in HRAS, a small GTPase of the Ras superfamily, are vulnerable to TRPML1 inhibition[17]. Loss of TRPML1 impairs the growth of melanoma[18] and reduces cell proliferation, cell viability and tumor growth in the MDA-MB-231 breast cancer cell line, a highly aggressive, invasive and poorly differentiated triple-negative breast cancer (TNBC) cell line lacking estrogen and progesterone receptor expression as well as HER2 (human epidermal growth factor receptor 2) amplification[18].

[1]Department of Pharmacy – Center for Drug Research, Ludwig-Maximilians University, Munich, Germany. [2]Walther Straub Institute of Pharmacology and Toxicology, Faculty of Medicine, Ludwig-Maximilians University, Munich, Germany. [3]Rudolf-Boehm-Institute for Pharmacology and Toxicology, University of Leipzig, Leipzig, Germany. [4]CiPA LAB, LLC, Gaitherburg, MD, USA. [5]Casma Therapeutics Inc, Cambridge, MA, USA. [6]Institute of Zoology, Molecular Cell Physiology and Endocrinology, University of Dresden, Dresden, Germany. [7]These authors contributed equally: Philipp Rühl, Anna Scotto Rosato, and Nicole Urban. ✉email: Michael.Schaefer@medizin.uni-leipzig.de; franz.bracher@cup.uni-muenchen.de; christian.grimm@med.uni-muenchen.de

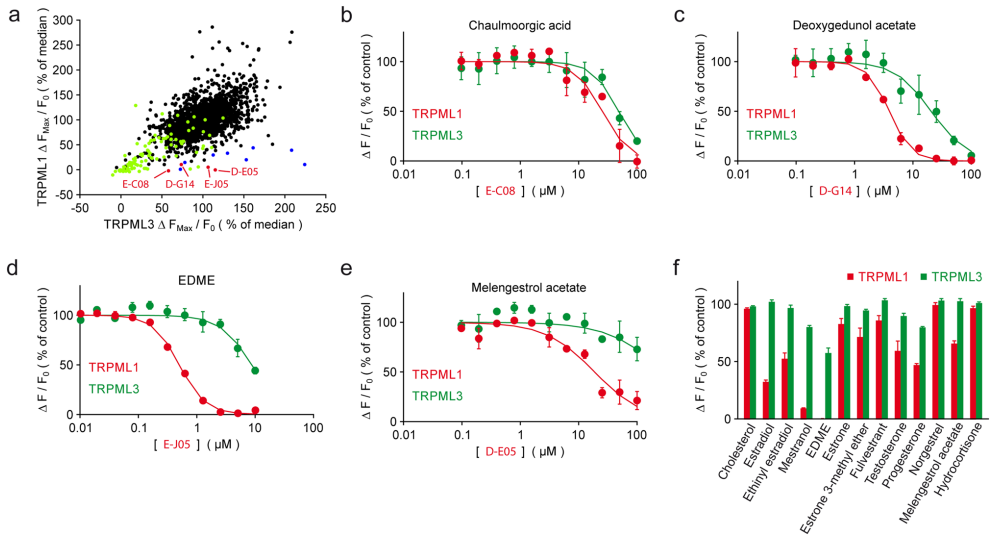

Figure 1. Compound screening and hit validation. (**a**) Dot plot showing the inhibitory effects of 2430 bioactive compounds (20 μM) on fluo4-loaded HEK293 cell lines stably expressing hTRPML1ΔNC-YFP and hTRPML3-YFP after activation of the cells with 5 μM ML-SA1. Peak fluorescence intensities after stimulation were normalized to the median response in the respective screening plate. Black dots indicate compounds with no discernible effect on either TRPML1 or TRPML3. Green dots represent fluorescent compounds that were not further considered. Blue dots are notoriously positive hits previously identified in several other screened targets. Red dots indicate TRPML1-selective hits. (**b**–**e**) Representative concentration–response curves of the 4 specific hits in (A) for TRPML1 (red dots and lines) and TRPML3 (green dots and lines). (**f**) Effect of retested and pharmacologically relevant steroids on TRPML1 and TRPML3 at a concentration of 12.5 μM, which in the case of EDME completely blocks TRPML1. Shown is the inhibition of Fluo-4 fluorescence responses to stimulation with 5 μM ML-SA1 and normalization to an untreated control. Aggregated data sets from 3 to 5 independent experiments, each performed in duplicates, are displayed (means ± SEM).

In recent years several TRPML channel activators have been developed by different groups, e.g. SF-22, MK6-83, ML-SA1, or ML-SA5[5,19–21]. In addition, TRPML isoform-selective agonists have been discovered recently such as a TRPML2-selective agonist, ML2-SA1[22] or TRPML3-selective agonists, SN-2 and EVP-21[20,22]. TRPML1-selective agonists are currently not available, neither are TRPML1-selective antagonists. Only inhibitors without isoform-selectivity, e.g. ML-SI1 and ML-SI3 have been described so far[23,24]. TRPML channel isoforms can occur not only in the same cell type, e.g. in certain types of macrophages and other immune cells, but also in the same type of organelle, e.g. in early endosomes (EE), late endosomes (LE), or lysosomes (LY). In particular, TRPML1, 2, and 3 in LE/LY and TRPML2 and 3 in EE. Isoform-selective agonists and antagonists are therefore highly desired as chemical tools to decipher channel functions in endogenously expressing cell systems and organelles with TRPML isoform-heterogeneity; and therapeutically to exclude potential side effects mediated by inhibition or activation of the other TRPML isoforms. We have screened a library of 2430 drug-like small molecule compounds, the majority of which from the Spectrum Collection compound library (MS Discoveries; 2000 compounds) containing numerous FDA-approved drugs, to identify TRPML isoform-selective inhibitors. In the following we describe the first highly potent and subtype-selective antagonist of TRPML1, 17β-estradiol methyl ether (EDME), which we further modified chemically to improve its characteristics. Thus, analogs of EDME were generated with reduced estrogen receptor alpha (ERα) activity. Functionally, we found that EDME and its analogs inhibit autophagy and translocation of TFEB, a master regulator of autophagy and lysosomal biogenesis, to the nucleus by direct and selective inhibition of TRPML1. In human estrogen receptor negative (ER-) breast cancer cells (MDA-MB-231) EDME was found to reduce migration and invasion, corroborating the efficacy of these compounds to interfere with cancer hallmarks in a TRPML1-dependent but estrogen receptor independent manner.

Results

Identification of EDME as selective TRPML1 antagonist. Initially, 2430 compounds were tested on hTRPML1ΔNC-YFP, a plasma membrane variant of wild-type TRPML1 lacking N- and C-terminal lysosomal targeting sequences as reported previously[22], and hTRPML3-YFP, both stably expressed in HEK293 cells. TRPML1 and TRPML3 were activated with 5 μM ML-SA1, respectively (Fig. 1a), a concentration which

showed no effect in the parental control cell line. Four TRPML1 selective hit compounds [the synthetic gestagen melengestrol acetate (D-E05; MGA), 17β-estradiol methyl ether (E-J05; EDME), the natural triterpene deoxygedunol acetate (D-G14; DGA), and the fatty acid derivative chaulmoorgic acid (E-C08)] were initially identified and subsequently retested by performing concentration–response measurements (Fig. 1b–e, S1). MGA and EDME were thus confirmed as highly TRPML1-selective with IC_{50} values of 18.6 µM (MGA) and 0.5 µM (EDME). EDME showed the lowest IC_{50} for TRPML1. Subsequently, other pharmacologically relevant steroidal compounds were tested. Of those, estradiol, ethinylestradiol, and mestranol which is the 3-methyl ether of ethinylestradiol also showed stronger inhibitory effects on TRPML1 than on TRPML3 with mestranol showing the strongest effect. However, none of these reached the TRPML1-inhibitory activity of EDME. Other steroid hormones like progesterone and testosterone showed much weaker inhibitory effects compared to EDME or mestranol while cholesterol, hydrocortisone, estrone, estrone 3-methyl ether, norgestrel, and fulvestrant, the latter one used to treat hormone receptor positive metastatic breast cancer, had no effect on either TRPML1 or TRPML3 (Figs. 1f, S1). TRPML channels belong to the superfamily of transient receptor potential (TRP) channels. Those are the channels TRPMLs are most closely related with. Hence, we have counter screened EDME against a plethora of other members of the TRP superfamily, namely TRPC3, 4, 5, 6, and 7 of the canonical or classical TRP subfamily, members of the melastatin subfamily, TRPM2, 3, and 8 as well as members of the vanilloid subfamily, TRPV1, 2, 3, and 4. We further repeated testing against TRPML2 and TRPML3 as well as the functionally related endolysosomal two-pore cation channel TPC2. Channels were activated with previously reported activation concentrations of known ligands, respectively (Fig. 2a). While no meaningful IC_{50}s were obtained for EDME for most channels including TPC2, activated by either TPC2-A1-P or TPC2-A1-N as reported recently[25], the following IC_{50}s were determined for TRPML1, 2 and 3: 0.6 µM, 5.9 µM, and 19.5 µM (Table S1). To further corroborate these data we performed whole-cell patch-clamp experiments with EDME using stable cell lines expressing either the plasma membrane variant $hTRPML1^{L15/16A,\ L577/578A}$, hTRPML2, or hTRPML3. While no block for TRPML3 was found, TRPML2 was blocked with an IC_{50} of 3.8 µM. The IC_{50} measured for TRPML1 was 0.22 µM (Fig. 2b,d). For comparison, we also tested the recently described TRPML inhibitor ML-SI3 which blocked TRPML1 with an IC_{50} of 4.7 µM and TRPML2 with an IC_{50} of 1.7 µM, suggesting that ML-SI3 has an almost threefold stronger effect on TRPML2 compared to TRPML1 and is > 20-fold weaker on TRPML1 than EDME (Fig. 2c,e). Next, we confirmed the inhibitory effect of EDME in endolysosomal patch-clamp experiments by isolating vacuolin-enlarged endo-lysosomes from hTRPML1 WT expressing HEK293 cells (Fig. 2f–h). Finally, we used TRPML1 endogenously expressing murine alveolar macrophages to confirm inhibition of TRPML1 activation by EDME (Fig. 2i).

Systematic modification of EDME. Initial structure–activity relationships (SAR) were detected by analyzing the structures of the screening hits and other steroidal compounds tested in either the random screening or the consecutive experiments. From these data it was evident that natural and synthetic steroids lacking an aromatic ring A (typical for estrogens) have virtually no (cholesterol, phytosterols, glucocorticoids, mineralocorticoids, antiestrogens, antiandrogens, 5α-reductase inhibitors) or only weak TRPML1-inhibitory activity (some androgens and gestagens) (Fig. 1f). In the class of gestagens progesterone and melengestrol acetate (MGA) had shown modest TRPML1 inhibition (IC_{50} = 12 µM and 19 µM, respectively). Further, stilbene-type synthetic estrogens and plant phytoestrogens were inactive in the primary screen. In the class of estrogens, the native hormone 17β-estradiol was significantly weaker (IC_{50} = 5.3 µM) than EDME. Likewise, the synthetic 17-ethinyl derivative ethinylestradiol was only weakly active. Modification of 17β-estradiol at 3-OH with an ionic residue (estradiol-3-sulfate sodium salt) eliminated TRPML1-inhibitory activity. Only mestranol, a congener of EDME bearing an additional ethinyl group at C-17, showed considerable activity. From these structures of mainly weakly active or inactive steroidal and related compounds it was evident that there is a very steep structure–activity relationship: only estrane-type compounds are promising and variations at ring D are most likely critical; the most obvious position for further modifications was position 3 at the aromatic ring A. Therefore we synthesized 10 modified versions of EDME, most of which have in common a replacement of the methoxy group at C-3 with a lipophilic residue. One single variation was performed on ring D by conversion of alfatradiol, the 17α epimer of physiological 17β-estradiol, into its 3-methoxy derivative PRU-2 by simple O-methylation[26]. A couple of ethers of 17β-estradiol were obtained by various etherification protocols: known O-alkyl derivatives like ethyl ether PRU-5[27], isopropyl ether PRU-6[28], and allyl ether PRU-7[29] were obtained under standard Williamson conditions. Since for these trivial alkyl ethers undesired oxidative O-dealkylation by CYP enzymes to give free 17β-estradiol cannot be excluded[25], we prepared two estradiol ethers with presumably high metabolic stability. Difluoromethyl ether PRU-4[30] was obtained from 17β-estradiol using Zafrani's diethyl (bromodifluoromethyl)phosphonate reagent[31], and phenyl ether PRU-8 was prepared by O-phenylation with benzyne generated from 2-(trimethylsilyl)phenyl trifluoromethanesulfonate with fluoride ions[32]. In order to obtain lipophilic 17β-estradiol analogs without a C,O-bond at C-3, for which metabolism into the parent hormone should be fully excluded, we converted the phenolic group into the O-triflate to give the useful building block PRU-9[33]. Suzuki–Miyaura cross-coupling of PRU-9 with phenylboronic acid gave the 3-phenylestrane PRU-11, Stille cross-coupling with tributyl(vinyl)tin under Pd(II) catalysis[34] the 3-vinylestrane PRU-10. Methyl ketone PRU-12[34] was obtained via Stille cross-coupling of PRU-9 with tributyl(1-ethoxyvinyl)tin, followed by aqueous hydrolysis of the formed enol ether (Scheme S1). These EDME analogs were tested for TRPML1 inhibition in single cell Fura-2 calcium imaging experiments at a concentration of 10 µM (Figs. 3a–l and S2). Surprisingly, in these experiments all compounds showed strong efficacy in blocking TRPML1 with the exception of 17α-epimer PRU-2. In a next series of experiments, we performed concentration–response measurements with 17β-estradiol (E2), EDME and the 10 analogs. For analysis of subtype selectivity, we further tested all compounds on TRPML1, 2, and 3 as well as the related endolysosomal cation channel TPC2 (Fig. 4a–l). Again, 17α-epimer PRU-2 showed only poor activity,

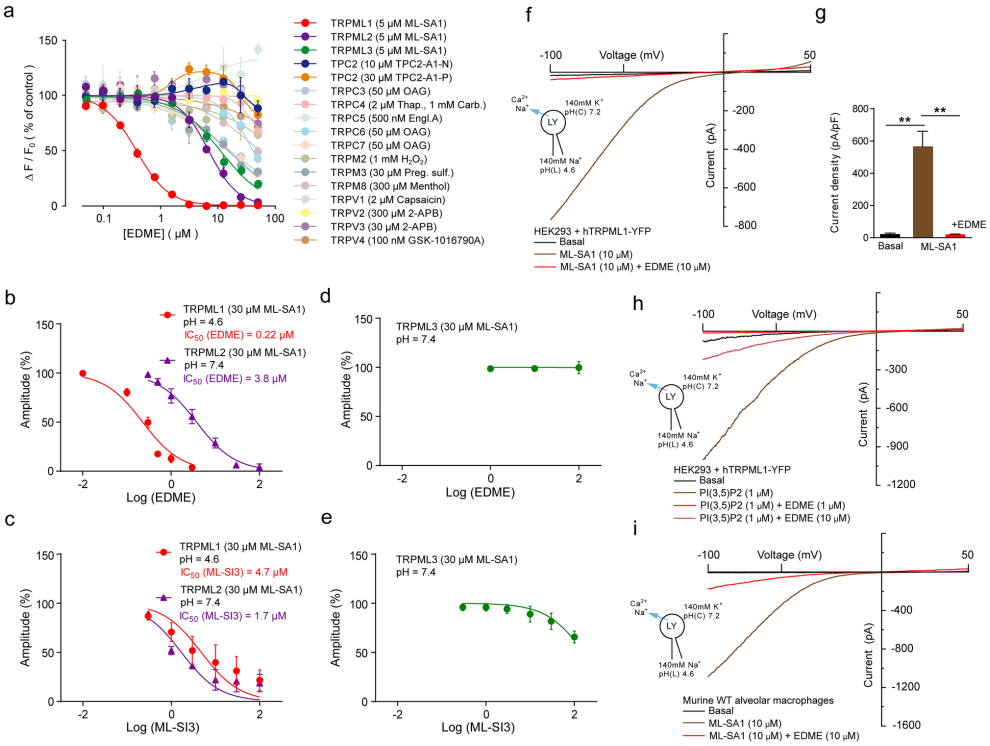

Figure 2. EDME is a potent and selective blocker of TRPML1. (**a**) Representative concentration-effect relationships for Ca^{2+} increases (Fluo-4) in response to different concentrations of EDME on HEK293 cells stably expressing different TRP channels including hTRPML1ΔNC, 2, 3, or TPC2, respectively. Corresponding activators for each TRP channel are listed in parentheses. (**b**–**e**) Concentration-effect relationships obtained from whole-cell patch-clamp measurements showing effect of EDME (**b**, **d**) and the previously described non-selective TRPML blocker ML-SI3 (**c**, **e**) on hTRPML1L15/16A, L577/578A (pH 4.6; n = 6, each), hTRPML2 (pH 7.4; n = 4, each), and hTRPML3 (pH 7.4; n = 3, each) in the presence of 30 µM ML-SA1. Current recording was done with WinWCP5.2.7 (University of Strathclyde, UK) software, and analysis was done with the help of a customized Igor pro program (WaveMetrics). (**f**) Endolysosomal patch-clamp experiment showing effect of EDME on WT hTRPML1 after activation with ML-SA1 (10 µM). (**g**) Statistical analysis for experiments as shown in (**f**) (luminal pH 4.6; n = 3, each). P-values were calculated by one-way ANOVA followed by Tukey's post hoc test. **p-value < 0.01. (**h**) Endolysosomal patch-clamp experiment showing effect of EDME on WT hTRPML1 after activation with the endogenous ligand $PI(3,5)P_2$ (1 µM). (**i**) Endolysosomal patch-clamp experiment showing effect of EDME (10 µM) on TRPML1 endogenously expressed in mouse alveolar macrophages after activation with ML-SA1 (10 µM). All endolysosomal patch-clamp experiments were analyzed using PatchMaster acquisition software (https://www.heka.com/) and OriginPro 6.1 (https://www.originlab.com/). All statistical analysis was done using GraphPadPrism software (https://www.graphpad.com/scientific-software/prism/).

whereas all other EDME analogues with a 17β hydroxyl group were identified as potent inhibitors of TRPML1 with IC_{50} values below 1 µM (Table S1). PRU-8, PRU-9, PRU-10, and PRU-12 showed a further improved selectivity profile compared to EDME (Fig. 4h–j,l).

Effect of EDME and analogs at estrogen receptor alpha. To assess the effect of EDME and its synthetic analogs at ERα, we performed a yeast estrogen receptor assay used to determine the relative transactivation activity of the human ERα in response to test substances as previously described[35]. Briefly, Saccharomyces cerevisiae stably transfected with a human ERα construct and an estrogen responsive element fused to the reporter gene lacZ encoding for β-galactosidase were treated with the test substances. We found that PRU-2, PRU-10 and PRU-12 had relatively low efficacy at ERα while EDME and the other analogs had comparably strong effects (Fig. 5). PRU-2, the 17α-epimer of EDME, showed the desired low efficacy at ERα, but since it had a much higher

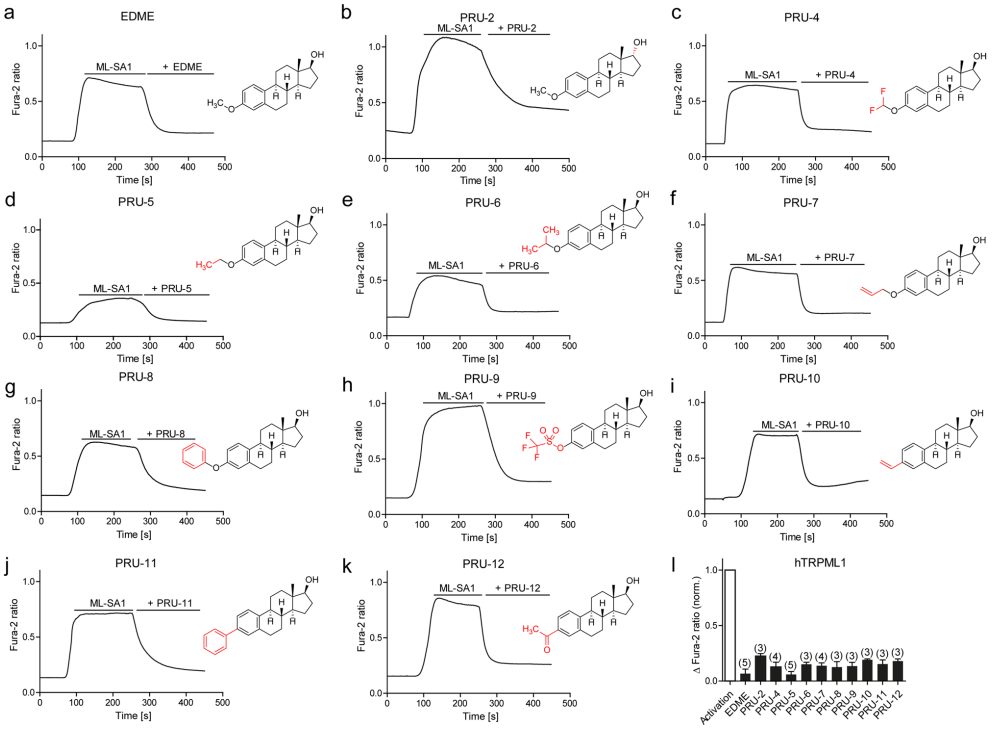

Figure 3. EDME and analogs in Fura-2 single cell calcium imaging experiments. (**a**–**k**) Representative Fura-2 calcium signals recorded from HEK293 cells stably expressing hTRPML1ΔNC-YFP. Cells were stimulated with ML-SA1 (10 µM), then treated with EDME and analogs (10 µM, each). Characteristic structural motifs of the EDME analogs are highlighted in red in the structures. (**l**) Statistical analysis of the maximal change in Fura-2 ratio (mean ± SEM) with the number of independent experiments in parentheses (with 5–12 cells in each experiment). Data were normalized to the maximal effect of the agonist ML-SA1.

IC_{50} (14 µM) for TRPML1 compared to EDME this compound was not further considered. PRU-8 showed a very good selectivity profile for TRPMLs, but unfortunately a strong effect at ERα, whereas PRU-10 and PRU-12 showed both a low ERα activity and a good TRPML isoform selectivity profile. In the following experiments, we therefore focused on EDME, PRU-10, and PRU-12.

Effect of EDME and selected analogs on autophagy and TFEB translocation. TRPML1 plays a major role in autophagy and starvation-stimulated TFEB nuclear translocation[10,11]. Indeed, cells from Mucolipidosis type IV (MLIV) patients show a delayed fusion of autophagosomes with late endosomes/lysosomes and alterations in TFEB shuttling[10,36,37]. In order to evaluate the efficacy of the novel compounds on TRPML1 functions we tested their effects on TFEB dephosphorylation and autophagic flux. As previously demonstrated for other, non-selective inhibitors, treatment with EDME reduced TFEB molecular downshift induced by nutrient starvation (Figs. 6a,b and S3). In order to evaluate lysosome-dependent degradation of autophagic material, we treated cells with EDME, PRU-10, and PRU-12 in combination with bafilomycin A1, a potent V-ATPase inhibitor[38]. Cells treated with TRPML1 inhibitors behaved similarly to MLIV patient fibroblasts which lack functional TRPML1 (Figs. 6c and S3). No increase in LC3 compared to vehicle (DMSO) was found, suggesting an impairment in the induction of autophagy upon starvation (Figs. 6d–f and S3). EDME and PRU-12 had the strongest effects, showing efficacy at as low as 1 µM. For PRU-10 a higher effective concentration was needed (3 µM). Estradiol showed effects when a concentration of 10 µM was applied. Concentrations of 10 nM or 1 µM showed no effect (Figs. 6g–h and S3). Taken together, these results demonstrate functional efficacy of EDME and analogs in blocking endogenous TRPML1 activity in intact cells, establishing them as suitable tools for cellular assays.

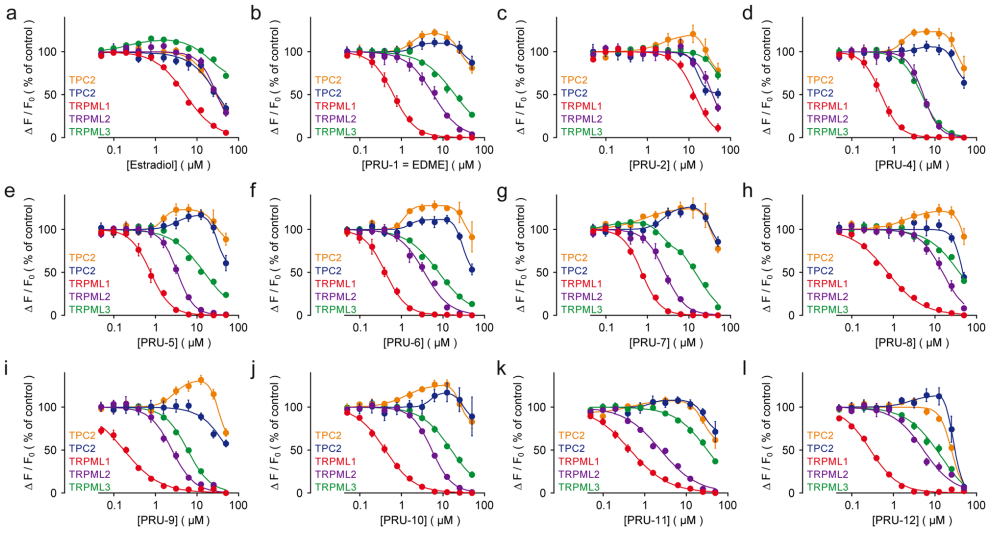

Figure 4. Estradiol, EDME and analogs in Fluo-4 calcium imaging experiments. (**a**–**l**) Concentration-effect relationships for Ca^{2+} increases (Fluo-4) in response to different concentrations of EDME, estradiol and analogs on HEK293 cells stably expressing hTRPML1ΔNC-YFP, hTRPML2-YFP, hTRPML3-YFP or hTPC2L11A/L12A-RFP[22,24]. Cells were activated with ML-SA1 (5 μM) for TRPMLs or TPC2-A1-N (10 μM; blue) and TPC2-A1-P (30 μM; orange) for hTPC2. Data are calculated from 3 to 5 independent experiments, each, and represented as means ± SEM. IC_{50} values are presented in Table S1.

Effect of EDME and selected analogs on breast cancer cell migration and invasion. The MDA-MB-231 human breast cancer cell line is one of the most commonly used breast cancer cell lines in medical research. MDA-MB-231 is a highly aggressive, invasive and poorly differentiated triple-negative breast cancer (TNBC) cell line. It lacks estrogen and progesterone receptor expression as well as HER2 (human epidermal growth factor receptor 2) amplification. Knockdown of TRPML1 has been reported before to result in reduced migration and invasion of MDA-MB-231 cells[35]. We used EDME to show reduction in migration and invasion, and we generated TRPML1 KO cell lines using CRISPR/Cas9 to confirm involvement of TRPML1 and on-target effect of EDME. At the same time the lack of estrogen receptor was used to confirm estrogen receptor independent efficacy of EDME. Two TRPML1 KO cell lines (KO1 and KO2) were generated and loss of TRPML1 was confirmed by qRT-PCR and by endolysosomal patch-clamp experimentation (Fig. 7a–d). As shown before in overexpressing HEK293 cells and in endogenously expressing alveolar macrophages, EDME inhibits TRPML1 activation with ML-SA1. Both KO cell lines showed complete lack of activation by ML-SA1, suggesting absence of TRPML1 but also TRPML2 and TRPML3, which would likewise be activated by the non-selective TRPML-agonist ML-SA1. This was further confirmed by qRT-PCR analysis (Fig. 7e). We next assessed the effect of EDME on migration and invasion of MDA-MB-231 cells. Invasion was found to be significantly reduced after application of EDME at various concentrations (Fig. 7f–h). Effects were comparable to those seen in MDA-MB-231 TRPML1 KO cells (KO1 and KO2). Importantly, the effect was not further reduced in KO cells, indicating on-target activity of EDME (Fig. 7f,g). Like invasion migration was also reduced significantly after application of EDME at various concentrations (Fig. 7i,j). In sum these experiments confirmed estrogen receptor independent and TRPML1-mediated activity of EDME.

Discussion

We describe here the first in-class TRPML1-selective inhibitors, which are blocking endogenously expressing TRPML1 and efficiently interfere with major functional activities of TRPML1, autophagy regulation and TFEB translocation to the nucleus. Autophagy is a vital process, involved in various diseases such as neurodegenerative, metabolic and infectious diseases as well as cancer. Both reduced and increased autophagy can impact disease. Autophagy is regulated by many factors including glucose, growth factors, amino acids, or starvation and energy status. The elimination of unwanted protein aggregates and damaged organelles is essential to avoid cell damage, e.g. damage to neurons and other brain cells, resulting eventually in a neurodegenerative processes. Pharmacological activation of autophagy processes has been propagated for the treatment of metabolic diseases such as obesity (activation of liver autophagy) or neurodegenerative diseases caused by the accumulation of inclusions or aggregates of different proteins as in the case of Parkinson's, Huntington's, or Alzheimer's disease to enhance clearance and to prevent cell death. In cancer, autophagy seems to function as a tumor suppressor

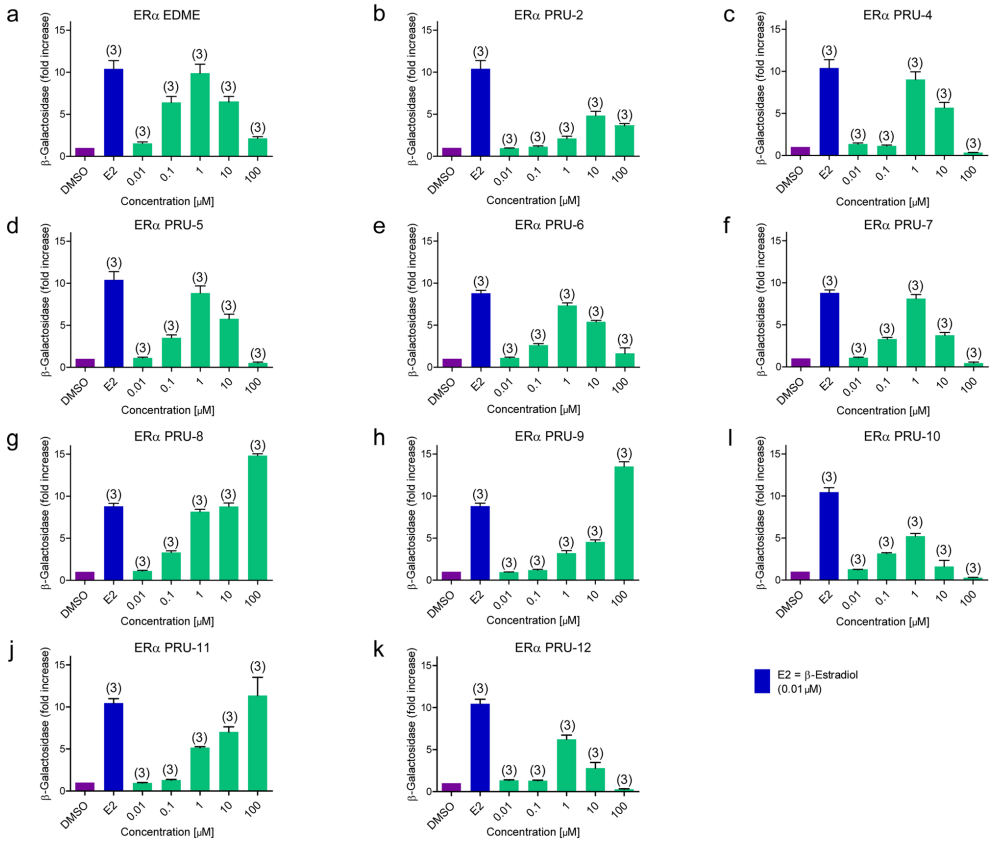

Figure 5. Activity at ERα of EDME and analogs. (**a**–**k**) Shown are effects of EDME and analogs at the estrogen receptor alpha (ERα) in *Saccharomyces cerevisiae* stably transfected with ERα, with the number of independent experiments in parentheses. The weakest effects at ERα were found for PRU-2, PRU-10, and PRU-12.

that prevents tumor initiation but also as a pro-survival factor helping tumor cells to endure metabolic stress and to avoid cell death triggered by chemotherapeutics[39]. Despite this diametrically opposed role autophagy might play in cancer, several inhibitors of the autophagic machinery are in preclinical development[40]. TFEB is a master regulator of autophagy by promoting expression of genes involved in autophagy, it also regulates lysosomal biogenesis, lysosomal exocytosis, lysosomal positioning and energy metabolism. Lysosomal Ca^{2+} release through TRPML1 activates calcineurin, which binds and dephosphorylates TFEB, thus promoting its nuclear translocation[10] while phosphorylated TFEB remains inactive in the cytosol. Here, we demonstrate efficacy of the estradiol-derived TRPML1 antagonist EDME and analogs, which were rationally designed based on a profound SAR analysis of numerous tested steroidal compounds, on autophagy and TFEB translocation as well as breast cancer cell migration and invasion. To confirm that these effects were estrogen receptor independent we used the estrogen receptor negative MDA-MB-231 human breast cancer cell line. In sum, we identified novel potent and selective inhibitors for TRPML1, which effectively block autophagy and TFEB translocation as well as migration and invasion of TRPML1 endogenously expressing cells. Despite some activity of EDME at ERα, the experiments in ER negative MDA-MB-231 breast cancer cells demonstrate estrogen receptor independent effects of EDME similar to effects seen in TRPML1 KO MDA-MB-231 cells. Furthermore, we have generated the EDME analogs PRU-10 and PRU-12, which show comparable TRPML isoform selectivity but further reduced efficacy at ERα.

Materials and methods

Compound screening and generation of concentration response curves. To identify inhibitors of TRPML1 and TRPML3, the Spectrum Collection compound library (MS Discoveries; 2000 compounds) and additional 430 bioactive compounds were screened. To this end, fluorometric Ca^{2+} influx assays were performed

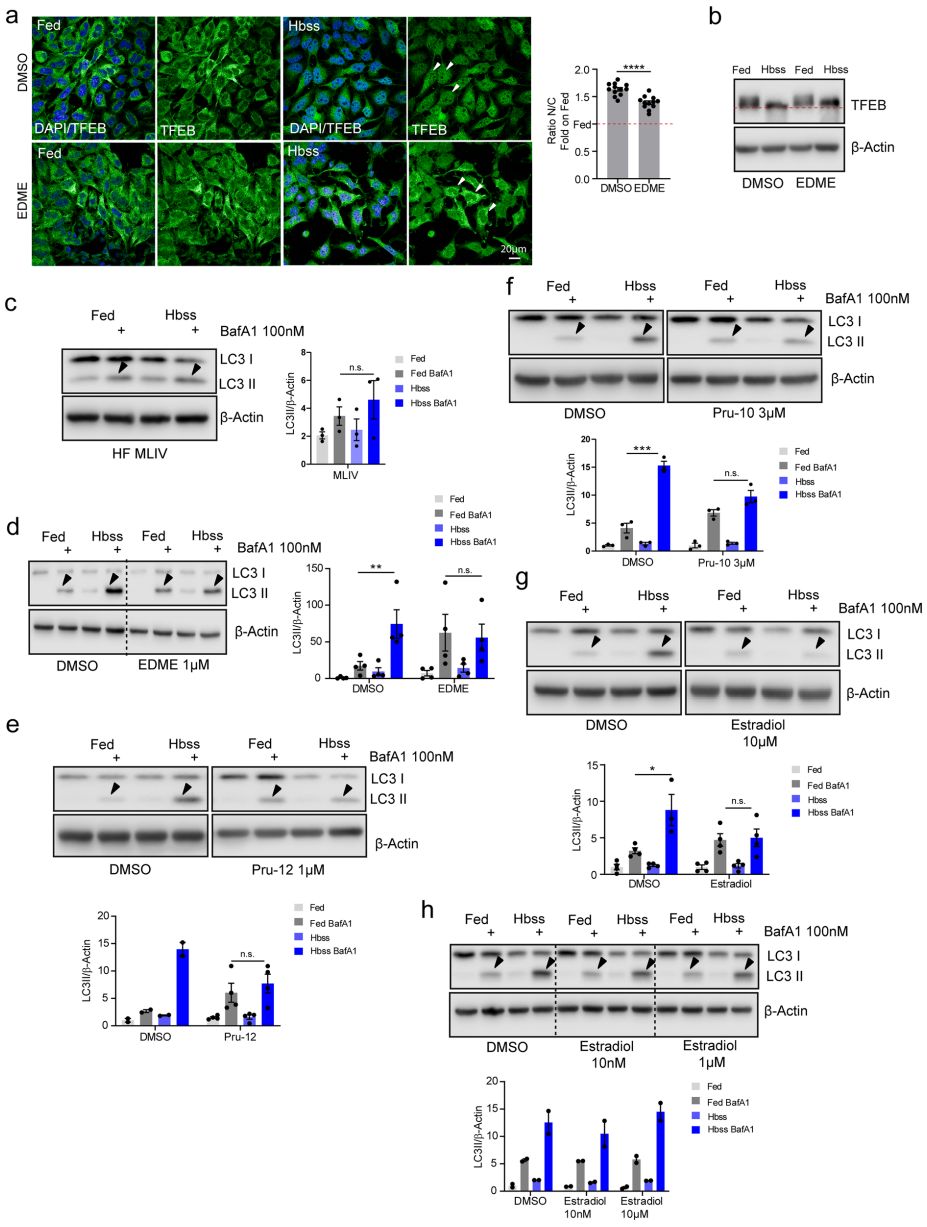
a
Fed
Hbss
DMSO
EDME
DAPI/TFEB
TFEB
20μm
Ratio N/C
Fold on Fed
DMSO EDME
b
Fed Hbss Fed Hbss
TFEB
β-Actin
DMSO EDME
c
Fed Hbss
BafA1 100nM
LC3 I
LC3 II
β-Actin
HF MLIV
LC3II/β-Actin
n.s.
Fed
Fed BafA1
Hbss
Hbss BafA1
MLIV
d
Fed Hbss Fed Hbss
BafA1 100nM
DMSO
EDME 1μM
**
n.s.
DMSO
EDME
e
Fed Hbss Fed Hbss
BafA1 100nM
DMSO
Pru-12 1μM
Pru-12
f
Fed Hbss Fed Hbss
BafA1 100nM
DMSO
Pru-10 3μM
***
n.s.
Pru-10 3μM
g
Fed Hbss Fed Hbss
BafA1 100nM
DMSO
Estradiol
10μM
*
n.s.
Estradiol
h
Fed Hbss Fed Hbss Fed Hbss
BafA1 100nM
DMSO
Estradiol
10nM
Estradiol
1μM
Estradiol
10μM

◂**Figure 6.** Effect of EDME and selected analogs on autophagy and TFEB nuclear translocation. (**a**) Representative confocal images of endogenous TFEB in HeLa cells treated with DMSO and EDME (1 μM) in complete media (Fed) or Hbss (nutrient starved media). The plot represents the TFEB nuclear to cytosol ratio and values are expressed as fold induction on Fed. Values are means ± SEM of n = 300 cells per condition, pooled from two independent experiments. (**b**) Representative image of immunoblot analysis of endogenous TFEB in human fibroblasts treated with DMSO and EDME (1 μM) in Fed and Hbss. The red dashed line highlights TFEB molecular downshift. (**c**) Representative image of immunoblot analysis of endogenous LC3 in MLIV patients' fibroblasts treated with Fed and Hbss alone or in the presence of BafA1 (bafilomycin A1). Plot shows the densitometry of LC3II band normalized to actin. The data in the graphs are mean values ± SEM, n = 3 lysates per condition pooled from 3 independent experiments. (**d**–**h**) Representative image of immunoblot analysis of endogenous LC3 in human fibroblasts wild type treated with DMSO, EDME 1 μM, PRU-12 1 μM, PRU-10 3 μM and estradiol (10 μM, 1 μM, and 10 nM) in Fed and Hbss alone or in the presence of BafA1. Plot shows the densitometry of LC3II band normalized to actin. The data in the graphs are mean values ± SEM, n = 2–4 lysates per condition pooled from 2 to 4 independent experiments. P-values were calculated by two-tailed Student's t-test. *p-value < 0.05; **p-value < 0.01. All statistical analysis was done using GraphPadPrism software (https://www.graphpad.com/scientific-software/prism/).

by using the calcium dye Fluo-4/AM (Invitrogen, Thermo Fisher Scientific, Waltham, MA, USA) and a custom-made fluorescence imaging plate reader built into a robotic liquid handling station (Freedom Evo 150, Tecan, Männedorf, Switzerland). All measurements were done in a HEPES buffered solution (HBS), containing 132 mM NaCl, 6 mM KCl, 1 mM $MgCl_2$, 1 mM $CaCl_2$, 5.5 mM D-glucose, 10 mM HEPES, pH 7.4. Screening compounds dissolved in DMSO (10 mM) were prediluted in 150 mM NaCl, 20 mM HEPES, pH 7.4, to a concentration of 200 μM. For primary screens, HEK293 stably expressing plasma membrane-targeted TRPML1 or TRPML3 were trypsinized and resuspended in cell culture medium supplemented with 4 μM Fluo-4/AM. After incubation at 37 °C for 30 min, the cell suspension was briefly centrifuged resuspended in HBS, and dispensed into black pigmented, clear-bottom 384-well microwell plates (Greiner μClear, Frickenhausen, Germany). Plates were placed into the FLIPR and fluorescence signals (excitation 470 nm, emission 515 nm) were recorded with a Zyla 5.5 camera (Andor, Belfast, UK) and the μManager software like previously described[41]. In a first video, compound libraries were successively added to the cells with the Tecan 96-tip multichannel arm to a final concentration of 20 μM to map unspecific effects like autofluorescence or toxicity. In a second step the agonist ML-SA1 was pipetted in each well and fluorescence signals were recorded for 10 min. Analyses were done by calculating fluorescence intensities for each well and background areas with ImageJ (National Institutes of Health, Bethesda, MD, USA). Finally, the background was subtracted and the fluorescence intensities were normalized to initial intensities (F/F0). Concentration response curves were generated by the same procedure but compounds were manually prediluted in 96-well plates containing HBS, now supplemented with 0.1% bovine serum albumin. Here data was fitted to a four-parameter Hill equation to obtain Imin, Imax, IC_{50}), and the Hill coefficient n.

Synthesis of compounds. EDME analogs were prepared starting from commercially available 17β-estradiol (E2) and 17α-estradiol (alfatradiol) as described in detail in the Supporting Information. All compounds were fully characterized by ^{1}H- and ^{13}C-NMR, IR and HRMS data.

Whole-cell patch-clamp experiments. For whole-cell patch-clamp experiments tetracycline-inducible hTRPML1L15/16A, L577/578A, hTRPML2 and TRPML3 HEK293 cell lines were used, generated by ICAGEN Inc. using the FLP-in-Tet-On system. Experiments were performed as described previously[20,42]. In brief, cells were cultured on coverslips (Fisherbrand, Fisher Scientific) in complete DMEM medium with 10% FBS (Thermo Fisher). HEK293 cells expressing the desired channel protein were patch-clamped after overnight induction with tetracycline (1 μg/mL). Patch-clamp pipettes were pulled from glass capillaries (Sutter Instrument) using a micropipette puller (P-87; Sutter Instrument) and had a resistance of 3–5 MΩ when filled with the pipette solution. The pipette solution contained (mM) 122 Cs-methanosulfonate, 4 NaCl, 10 EGTA, 2 Na-ATP, 2 $MgCl_2$ and 20 HEPES, pH 7.2 (with CsOH). The standard bath solution contained (mM) 153 NaCl, 5 KCl, 2 $CaCl_2$, 1 $MgCl_2$, 20 HEPES and 10 Glucose (pH 7.4 with NaOH). The low pH bath solution contained (mM) 150 Na-Gluconate, 5 KCl, 2 $CaCl_2$, 1 $MgCl_2$, 10 glucose, 10 HEPES and 10 MES (pH 4.6). Whole-cell currents were recorded using a Multiclamp 700B amplifier (Molecular Devices) with low-pass filtering at 3 kHz. The currents were digitized at a sampling frequency of 10 kHz using BNC-2110 and PCI-6221 with NI-DAQmx (National Instruments) and stored directly to a hard drive. Current recording was done with WinWCP5.2.7 (University of Strathclyde, UK) software, and analysis was done with the help of a customized Igor pro program (WaveMetrics). The current was recorded by 1 s rapid alterations of membrane potential (RAMP) from − 100 to + 100 mV from a holding potential of 0 mV. RAMPs were spaced at 4-s intervals. The current recorded at − 100 mV was used for current measurement. Concentration–response curves were fitted by using the model where X is the concentration and Y is the normalized response Y = 100/(1 + 10^(X-LogIC50)).

Endolysosomal patch-clamp experiments. For whole-LE/LY manual patch-clamp recordings, cells were treated with 1 μM vacuolin-1 (> 2 h) at 37 °C and 5% CO_2 and experiments performed as described previously[19,25]. Compound was washed out before patch-clamp experimentation. Currents were recorded using an EPC-10 patch-clamp amplifier (HEKA, Lambrecht, Germany) and PatchMaster acquisition software (https://www.heka.com/). Data were digitized at 40 kHz and filtered at 2.8 kHz. Fast and slow capacitive transients were cancelled by the compensation circuit of the EPC-10 amplifier. All recordings were obtained at room tem-

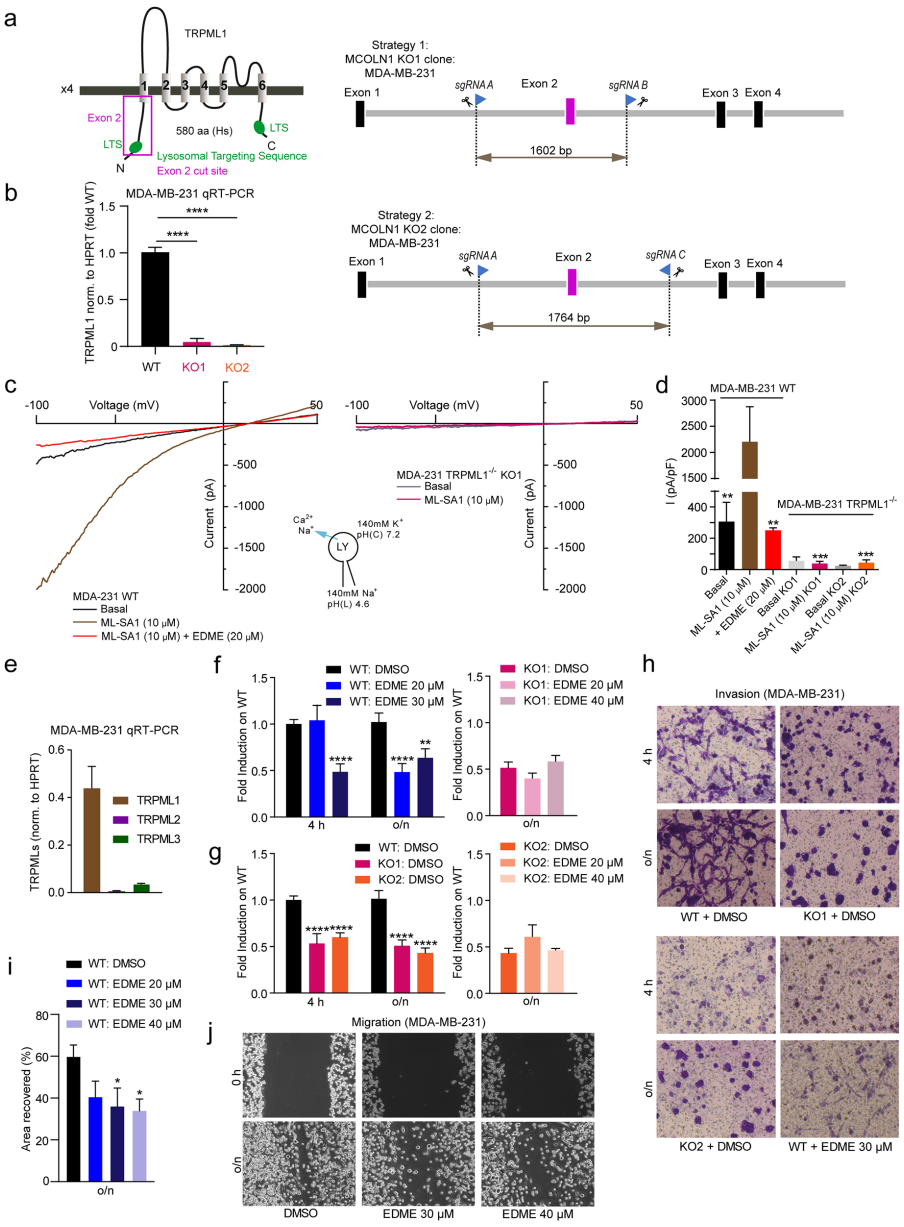
a
TRPML1
x4
Exon 2
LTS
580 aa (Hs)
LTS
C
N
Lysosomal Targeting Sequence
Exon 2 cut site
Strategy 1:
MCOLN1 KO1 clone:
MDA-MB-231
Exon 1
sgRNA A
Exon 2
sgRNA B
Exon 3 Exon 4
1602 bp
b
MDA-MB-231 qRT-PCR
TRPML1 norm. to HPRT (fold WT)
WT
KO1
KO2
Strategy 2:
MCOLN1 KO2 clone:
MDA-MB-231
sgRNA C
1764 bp
c
Voltage (mV)
Current (pA)
MDA-231 WT
Basal
ML-SA1 (10 μM)
ML-SA1 (10 μM) + EDME (20 μM)
MDA-231 TRPML1-/- KO1
140mM K+
pH(C) 7.2
140mM Na+
pH(L) 4.6
LY
d
MDA-MB-231 WT
MDA-MB-231 TRPML1-/-
I (pA/pF)
Basal
ML-SA1 (10 μM)
ML-SA1 (10 μM) + EDME (20 μM)
Basal KO1
ML-SA1 (10 μM) KO1
Basal KO2
ML-SA1 (10 μM) KO2
e
MDA-MB-231 qRT-PCR
TRPMLs (norm. to HPRT)
TRPML1
TRPML2
TRPML3
f
WT: DMSO
WT: EDME 20 μM
WT: EDME 30 μM
KO1: DMSO
KO1: EDME 20 μM
KO1: EDME 40 μM
Fold Induction on WT
4 h
o/n
g
KO2: DMSO
KO2: EDME 20 μM
KO2: EDME 40 μM
h
Invasion (MDA-MB-231)
4 h
o/n
WT + DMSO
KO1 + DMSO
KO2 + DMSO
WT + EDME 30 μM
i
WT: EDME 40 μM
Area recovered (%)
j
Migration (MDA-MB-231)
0 h
DMSO
EDME 30 μM
EDME 40 μM

◂**Figure 7.** Effect of EDME on ER- breast cancer (MDA-MB-231) cell migration and invasion. (**a**) Genetic ablation of human MCOLN1 (TRPML1) in MDA-MB-231 cells was created by using two CRISPR/Cas9 strategies targeting Exon 2, resulting in KO1 and KO2. For further details see Methods section. Validation was performed by endolysosomal patch-clamp experimentation and by quantitative PCR analysis. (**b**) qRT-PCR results showing expression levels of TRPML1 in WT, KO1, and KO2 MDA-MB-231 cell lines. (**c**) Representative current densities measured from vacuolin-enlarged endo-lysosomes isolated from WT and KO1 MDA-MB-231 cells. (**d**) Statistical analysis for experiments as shown in c (n = 3, each). (**e**) qRT-PCR results showing expression levels of TRPML1, 2, and 3 in WT MDA-MB-231 cells. (**f**–**g**) Invasion assay using transwell chambers. Statistical analysis of experiments as presented in (**h**) (n = 3, each). Statistical significance was determined by two-way ANOVA followed by Bonferroni multiple comparison test. **p-value < 0.01; ***p-value < 0.0001. (**h**) Shown are representative images for WT MDA-MB-231 cells and the two TRPML1$^{-/-}$ MDA-MB-231 cell lines KO1 and KO2 at 4 h and after o/n treatment, treated with either DMSO (control vehicle) or EDME at different concentrations. (**i**, **j**) Migration/wound healing scratch assay experiments. Shown in i is the statistical analysis of experiments as presented in (**j**) at various concentrations of EDME compared to DMSO (n = 3, each). Statistical significance was determined by one-way ANOVA followed by Bonferroni multiple comparison test. *p-value < 0.05. Shown in j are representative images for WT MDA-MB-231 cells at 0 h and after o/n incubation post scratch, treated with either the control vehicle (DMSO) or EDME at different concentrations. All statistical analysis was done using GraphPadPrism software (https://www.graphpad.com/scientific-software/prism/).

perature and were analyzed using PatchMaster acquisition software (https://www.heka.com/) and OriginPro 6.1 (https://www.originlab.com/). Recording glass pipettes were polished and had a resistance of 4–8 MΩ. For all experiments, salt-agar bridges were used to connect the reference Ag–AgCl wire to the bath solution to minimize voltage offsets. Liquid junction potential was corrected. For the application of the small molecule inhibitors/flavonoids, cytoplasmic solution was completely exchanged by cytoplasmic solution containing compound. The current amplitudes at − 100 mV were extracted from individual ramp current recordings. Unless otherwise stated, cytoplasmic solution contained 140 mM K-MSA, 5 mM KOH, 4 mM NaCl, 0.39 mM $CaCl_2$, 1 mM EGTA and 10 mM HEPES (pH was adjusted with KOH to 7.2). Luminal solution contained 140 mM Na-MSA, 5 mM K-MSA, 2 mM Ca-MSA, 1 mM $CaCl_2$, 10 mM HEPES and 10 mM MES (pH was adjusted with methanesulfonic acid to 4.6). In all experiments, 500-ms voltage ramps from -100 to + 100 mV were applied every 5 s. All statistical analysis was done using GraphPadPrism software.

Transfection, cell culture and calcium imaging. Single cell Ca^{2+} imaging experiments were performed using Fura-2 as previously described[42]. HEK293 cells stably expressing hTRPML1ΔNC-YFP, hTRPML2-YFP, hTPPML3-YFP or hTPC2L11A/L12A-RFP (22, 24) were cultured at 37 °C with 5% of CO_2 in Dulbecco's modified Eagle medium (Thermo Fisher), supplemented with 10% fetal bovine serum, 100 U/mL penicillin, and 0.1 mg/mL streptomycin. Cells were plated onto poly-L-lysine (sigma)-coated glass coverslips and grown for 2–3 days. For Ca^{2+} imaging experiments cells were loaded for 1 h at room temperature with Fura-2 AM (4.0 µM) and 0.005% (v/v) pluronic acid (both from Thermo Fisher) in HEPES-buffered solution (HBS) comprising 138 mM NaCl, 6 mM KCl, 2 mM $MgCl_2$, 2 mM $CaCl_2$, 10 mM HEPES, and 5.5 mM D-glucose (adjusted to pH 7.4 with NaOH). After loading, cells were washed with HBS and mounted in an imaging chamber. All recordings were performed in HBS. Ca^{2+} imaging was performed using a Leica DMi8 live cell microscope. Fura-2 was excited at 340 nm/380 nm. Emitted fluorescence was captured using 515 nm long-pass filter. Compounds were pre diluted in DMSO and stored as 10 mM stock solutions at − 20 °C, not exceeding three months. Working solutions were prepared directly before using by dilution with HBS.

For endolysosomal patch-clamp experiments murine alveolar macrophages were prepared and cultured as described recently[22,25]. The human TRPML2-YFP stable cell line was generated as described previously[42].

MDA-MB-231 cell culture and genetic ablation of human MCOLN1 (TRPML1). MDA-MB-231 cells were grown in high glucose DMEM, supplemented with 10% FBS (Thermo Fisher), and 1% penicillin–streptomycin (Sigma-Aldrich). Cell lines were maintained at 37 °C in a 5% CO_2 incubator. The following guide RNAs (Metabion) were designed to target Exon 2 of the human MCOLN1 gene using CRISPOR software (http://crispor.tefor.net/): sgRNA A: 5′-GGGTCCCAGCTACTAACTAC-3′; sgRNA B: 5′-GTGCAGCCATTGGGTCAACA-3′; sgRNA C: 5′-GAAAAGGGACCCAATTGTCC-3′. Approximately 3 × 105 MDA-MB-231 cells were seeded in 6-well plates (Sarstedt). The cells were co-transfected with two combinations of sgRNAs: A + B and A + C, using Lipofectamine 3000 (Themo Fisher) reagent, according to the manufacturer's instructions. Antibiotic selection with Puromycin and Blasticidin (Gibco) was carried out for 72 h, followed by single cell dilution and clonal expansion of cells in collagen-coated 96-well plates (Sarstedt). The clones were screened and validated through several methods: first, gDNA isolation (PureLink Genomic DNA Mini Kit, Thermo Fisher), PCR (Q5 High-Fidelity DNA Polymerase, NEB) and agarose gel electrophoresis; second, isolation of RNA (Rneasy Mini Kit, Qiagen), cDNA synthesis (RevertAid First Strand cDNA synthesis kit, Thermo Fisher) and qPCR (LightCycler 480 SYBR Green I Master, Roche Life Science); third, measuring TRPML1 channel activity via the endolysosomal patch clamp technique. The strategy insured the genetic knockout of Exon 2 of human MCOLN1, its first transmembrane domain, the lysosomal targeting sequence (LTS), and a pre-mature stop codon creating a frameshift mutation.

Estrogen receptor assay. The yeast estrogen receptor assay (YES-assay) was provided by Dr. J.P. Sumpter (Brunel University, Uxbridge, UK; Routledge & Sumpter, 1996) and was used to determine the relative trans-

activation activity of the human ERα in response to test substances as previously described[35]. Briefly, *Saccharomyces cerevisiae* stably transfected with a human ERα construct and an estrogen responsive element fused to the reporter gene lacZ encoding for β-galactosidase were treated with the test substances for 48 h. The β-galactosidase enzymatic activity was measured in a colorimetric assay using the substrate chlorophenol red β-D-galactopyranoside (Roche Diagnostics, Mannheim Germany). Formation of chlorophenol red was measured at 540 nm. For the test, all compounds were diluted in DMSO. 17β-estradiol (10 nM; Sigma, Deisenhofen, Germany) served as positive control and DMSO was used as vehicle control. All compounds, were dose dependently tested in a concentration range of 0.01–100 µM, using technical quadruplicates and biological triplicates.

Autophagy assays and TFEB shift. 5 × 104 wild-type human fibroblasts were seeded in a 12-well plate and treated overnight with DMSO or different TRPML1 inhibitors (EDME, PRU-10, PRU-12). The day after, cells were treated for 3 h in full media (Fed) or HBSS supplemented with 10 mM HEPES (nutrient starved) in presence of DMSO or different TRPML1 inhibitors (EDME, PRU-10, PRU-12). For autophagic flux experiments, cells were co-treated with 100 nM of bafilomycin A1 (Sigma).

Total cell lysates were prepared using TRIS HCl 10 mM pH 8.0 and 0.2% SDS supplemented with protein and phosphatase inhibitors (Sigma). Protein concentration was determined using the Bradford method. After SDS–polyacrylamide gel electrophoresis (PAGE) and immunoblotting, the protein recognized by the specific antibody was visualized by chemiluminescence methods (Luminata Crescendo Western HRP substrate, Millipore) using HRP-conjugated anti-rabbit or anti-mouse secondary antibodies (Cell Signalling). Images were acquired using Li-Cor Odyssey Fc Imaging System and densitometric quantification of unsaturated images was performed using ImageJ software (NIH). Uncropped and unprocessed western blot scans are provided as Fig. S1. The following primary antibodies were used: LC3 (Novus Cat. No. NB100-2220, 1:1000 in 5% milk), TFEB (Cell Signaling Cat. No. 4240, 1:1000 in 5% BSA) and β-actin (Santa Cruz Cat. No. Sc-47778, 1: 1000 in 5% BSA).

Wound healing/migration and invasion assays. Wound healing assay was performed using 12-well plates (Sarstedt) at full confluency. Cells were incubated overnight (serum-free), and a scratch was performed using a yellow pipet tip. Pictures were taken at 0 h and after over night (o/n) incubation using an inverted microscope (Leica DM IL LED) and using a microscope camera (Leica DFC 3000 G). The wounded cell area was quantified using ImageJ 1.52a software and was subtracted from 0 h values.

For invasion measurements transwell chambers in 24-well permeable support plates (Corning, #3421) were coated with Corning Matrigel basement membrane matrix (Corning, #354234) for 1.5 h. A total of 4 × 104 MDA-MB-231 WT and TRPML1 KO cells were seeded on top of the chambers in serum-free medium, and direct stimulation with EDME was performed. The lower compartment contained the chemotactic gradient, medium with 10% FBS. Cells were allowed to migrate for 4 h and o/n, and were then fixed and stained with crystal violet containing methanol. Non-invaded cells were removed with Q-tips and pictures were taken of the bottom side of the membrane using an inverted microscope (Olympus CKX41) and an Olympus SC50 camera (Olympus). The number of invaded cells was quantified using ImageJ 1.52a software.

RNA isolation and quantitative PCR. Total RNA was isolated from cells using the RNeasy Mini Kit (Qiagen). Reverse Transcription was performed using the Revert First Strand cDNA Synthesis Kit (Thermo Fisher). Real-time quantitative Reverse Transcription PCR (qPCR) was performed in triplicates for each sample using LightCycler 480 SYBR Green I Master and using the LightCycler 480 II machine (Roche Life Science), following the recommended parameters. HPRT was used as the housekeeping gene. The following human primer sets were used: HPRT; fw: 5′-TGGCGTCGTGATTAGTGATG-3′, rev: 5′-AACACCCTTTCCAAATCCTCA-3′; MCOLN1: fw: 5′-TCTTCCAGCACGGAGACAAC-3′, rev: 5′-GCCACATGAACCCCACAAAC-3′; MCOLN2: fw: 5′-AACGGTGTTTCCTGTTCCGA-3′, rev: 5′-GCCATTGCATTTCTGACG GTTA-3′; MCOLN3: fw: 5′-TGCTTCTGTGGATGGATCG-3′, rev: 5′-GAGACCATGTTC AGAGAACG-3′; TPCN1: fw: 5′-TCCCAA AGCGCTGAGATTAC-3′, rev: 5′-TCTGGTTTGAG CTCCCTTTC-3′; TPCN2: fw: 5′-GTACCCCTCTTGTGT GGACG-3′, rev: 5′-GGCCCTGACA GTGACAACTT-3′.

TFEB immunofluorescence. 3.5 × 104 HeLa cells were seeded in a 24-well plate and treated overnight with DMSO or EDME 1 µM. The day after, cells were treated for 3 h in full media (Fed) or HBSS supplemented with 10 mM HEPES (nutrient starved) in presence of DMSO or EDME 1 µM. Cells were fixed in PFA 4% 10′ and permeabilized 7′ with PBS 1X and 0.02% Triton-X. TFEB antibody (Cell Signaling Cat. No. 4240, 1:100 overnight) and Goat anti-Rabbit IgG (H + L) Secondary Antibody, Alexa Fluor 488 (ThermoFisher, 1:400 45′) were applied in blocking buffer saponin (1% BSA, 0.05% saponin and 50 mM NH4Cl in PBS1X). Samples were examined under a Zeiss LSM 880 confocal microscope. Optical sections were obtained under a 40 × immersion objective at a definition of 1024 × 1024 pixels (average of 8 scans), adjusting the pinhole diameter to 1 Airy unit for each emission channel to have all the intensity values between 1 and 254 (linear range). TFEB nuclear and cytoplasmic intensity was measured on unsaturated images using ImageJ software (NIH). The value reported is a ratio value resulting from the average intensity of nuclear TFEB fluorescence divided by the cytosolic intensity of TFEB fluorescence.

Statistical analysis. Details of statistical analyses and n values are provided in the Materials and Methods or the Figures or Figure legends. Statistical analyses were carried out using GraphPadPrism software (https://www.graphpad.com/scientific-software/prism/). All error bars are depicted as mean ± SEM. Statistical significance is denoted on Figures as outlined in the legends.

Data availability

All data generated or analyzed during this study are included in this published article and its additional files.

Received: 27 August 2020; Accepted: 5 April 2021
Published online: 15 April 2021

References

1. Bargal, R. *et al.* Identification of the gene causing mucolipidosis type IV. *Nat. Genet.* **26**, 118–123 (2000).
2. Bae, M. *et al.* Activation of TRPML1 clears intraneuronal Abeta in preclinical models of HIV infection. *J. Neurosci.* **34**, 11485–11503 (2014).
3. Tsunemi, T. *et al.* Increased lysosomal exocytosis induced by lysosomal Ca(2+) channel agonists protects human dopaminergic neurons from alpha-synuclein toxicity. *J. Neurosci.* **39**, 5760–5772 (2019).
4. Cheng, X. *et al.* The intracellular Ca(2)(+) channel MCOLN1 is required for sarcolemma repair to prevent muscular dystrophy. *Nat. Med.* **20**, 1187–1192 (2014).
5. Yu, L. *et al.* Small-molecule activation of lysosomal TRP channels ameliorates Duchenne muscular dystrophy in mouse models. *Sci. Adv.* **6**, e2736 (2020).
6. Capurro, M. I. *et al.* VacA generates a protective intracellular reservoir for Helicobacter pylori that is eliminated by activation of the lysosomal calcium channel TRPML1. *Nat. Microbiol.* **4**, 1411–1423 (2019).
7. Chandra, M. *et al.* A role for the Ca^{2+} channel TRPML1 in gastric acid secretion, based on analysis of knockout mice. *Gastroenterology* **140**, 857–867 (2011).
8. Sahoo, N. *et al.* Gastric acid secretion from parietal cells is mediated by a Ca^{2+} efflux channel in the tubulovesicle. *Dev. Cell.* **41**, 262-273.e6 (2017).
9. Zhang, X. *et al.* MCOLN1 is a ROS sensor in lysosomes that regulates autophagy. *Nat. Commun.* **7**, 12109 (2016).
10. Medina, D. L. *et al.* Lysosomal calcium signalling regulates autophagy through calcineurin and TFEB. *Nat. Cell Biol.* **17**, 288–299 (2015).
11. Scotto Rosato, A. *et al.* TRPML1 links lysosomal calcium to autophagosome biogenesis through the activation of the CaMKKbeta/VPS34 pathway. *Nat. Commun.* **10**, 5630 (2019).
12. Zhang, X. *et al.* Rapamycin directly activates lysosomal mucolipin TRP channels independent of mTOR. *PLoS Biol.* **17**, e3000252 (2019).
13. Li, X. *et al.* A molecular mechanism to regulate lysosome motility for lysosome positioning and tubulation. *Nat. Cell. Biol.* **18**, 404–417 (2016).
14. Erkhembaatar, M. *et al.* Lysosomal Ca(2+) signaling is essential for osteoclastogenesis and bone remodeling. *J. Bone Miner. Res.* **32**, 385–396 (2017).
15. Bretou, M. *et al.* Lysosome signaling controls the migration of dendritic cells. *Sci. Immunol.* **2**, 9573 (2017).
16. Goodridge, J. P. *et al.* Remodeling of secretory lysosomes during education tunes functional potential in NK cells. *Nat. Commun.* **10**, 514 (2019).
17. Jung, J. *et al.* HRAS-driven cancer cells are vulnerable to TRPML1 inhibition. *EMBO Rep.* **20**, e47953 (2019).
18. Kasitinon, S. Y. *et al.* TRPML1 promotes protein homeostasis in melanoma cells by negatively regulating MAPK and mTORC1 signaling. *Cell Rep.* **28**, 2293–2305 (2019).
19. Chen, C. C. *et al.* A small molecule restores function to TRPML1 mutant isoforms responsible for mucolipidosis type IV. *Nat. Commun.* **5**, 4681 (2014).
20. Grimm, C. *et al.* Small molecule activators of TRPML3. *Chem. Biol.* **17**, 135–148 (2010).
21. Shen, D. *et al.* Lipid storage disorders block lysosomal trafficking by inhibiting a TRP channel and lysosomal calcium release. *Nat. Commun.* **3**, 731 (2012).
22. Plesch, E. *et al.* Selective agonist of TRPML2 reveals direct role in chemokine release from innate immune cells. *Elife* **7**, e39720 (2018).
23. Wang, W. *et al.* Up-regulation of lysosomal TRPML1 channels is essential for lysosomal adaptation to nutrient starvation. *PNAS* **112**, E1373-1381 (2015).
24. Leser, C. *et al.* Chemical and pharmacological characterization of the TRPML calcium channel blockers ML-SI1 and ML-SI3. *Eur J Med Chem.* **24**, 112966 (2020).
25. Gerndt, S. *et al.* Agonist-mediated switching of ion selectivity in TPC2 differentially promotes lysosomal function. *Elife* **9**, e54712 (2020).
26. Pindur, U. & Schall, T. Proton acid-catalysed transformations of estrogen derivatives: New results and some mechanistic aspects of the Kober colour reaction. *Arch. Pharm.* **327**, 637–642 (1994).
27. Triggle, D. J., Ridley, H. F. & DeMaio, D. M. Some 3-alkoxyestra-1,3,5(10)-trien-17-beta-ols. *J. Med. Chem.* **12**, 346 (1969).
28. Tedesco, R., Thomas, J. A., Katzenellenbogen, B. S. & Katzenellenbogen, J. A. The estrogen receptor: A structure-based approach to the design of new specific hormone–receptor combinations. *Chem. Biol.* **8**, 277–287 (2001).
29. Santra, S. & Guin, J. Enhanced reactivity of aerobic diimide olefin hydrogenation with arylboronic compounds: An efficient one-pot reduction/oxidation protocol. *Eur. J. Org. Chem.* **2015**, 7253–7257 (2015).
30. Lin, X., Hou, C., Li, H. & Weng, Z. Decarboxylative trifluoromethylating reagent [Cu(O2 CCF3)(phen)] and difluorocarbene precursor [Cu(phen)2][O2 CCF2 Cl]. *Chem. Eur. J.* **22**, 2075–2084 (2016).
31. Zafrani, Y., Sod-Moriah, G. & Segall, Y. Diethyl bromodifluoromethylphosphonate: A highly efficient and environmentally benign difluorocarbene precursor. *Tetrahedron* **65**, 5278–5283 (2009).
32. Himeshima, Y., Sonoda, T. & Kobayashi, H. Fluoride-induced 1,2-elimination Ofo-trimethylsilylphenyl triflate to benzyne under mild conditions. *Chem. Lett.* **12**, 1211–1214 (1983).
33. Hostetler, E. D., Jonson, S. D., Welch, M. J. & Katzenellenbogen, J. A. Synthesis of 2-[(18)F]Fluoroestradiol, a potential diagnostic imaging agent for breast cancer: strategies to achieve nucleophilic substitution of an electron-rich aromatic ring with [(18)F]F(-). *J. Org. Chem.* **64**, 178–185 (1999).
34. Shi, Y. & Koh, J. T. Functionally orthogonal ligand-receptor pairs for the selective regulation of gene expression generated by manipulation of charged residues at the ligand-receptor interface of ER alpha and ER beta. *J. Am. Chem. Soc.* **124**, 6921–6928 (2002).
35. Zierau, O. *et al.* Estrogenic activity of the phytoestrogens naringenin, 6-(1,1-dimethylallyl)naringenin and 8-prenylnaringenin. *Planta Med.* **68**, 449–451 (2002).
36. Curcio-Morelli, C. *et al.* Macroautophagy is defective in mucolipin-1-deficient mouse neurons. *Neurobiol. Dis.* **40**, 370–377 (2010).
37. Vergarajauregui, S., Connelly, P. S., Daniels, M. P. & Puertollano, R. Autophagic dysfunction in mucolipidosis type IV patients. *Hum. Mol. Genet.* **17**, 2723–2737 (2008).
38. Ohkuma, S. *et al.* Inhibition of cell growth by bafilomycin A1, a selective inhibitor of vacuolar H(+)-ATPase. *In Vitro Cell. Dev. Biol. Anim.* **29A**, 862–866 (1993).

39. Rubinsztein, D. C., Codogno, P. & Levine, B. Autophagy modulation as a potential therapeutic target for diverse diseases. *Nat. Rev. Drug. Discov.* **11**, 709–730 (2012).
40. Perez-Hernandez, M. *et al.* Targeting autophagy for cancer treatment and tumor chemosensitization. *Cancers* **11**, 1599 (2019).
41. Urban, N. & Schaefer, M. Direct activation of TRPC3 channels by the antimalarial agent artemisinin. *Cells* **9**, 202 (2020).
42. Grimm, C., Jörs, S., Guo, Z., Obukhov, A. G. & Heller, S. Constitutive activity of TRPML2 and TRPML3 channels versus activation by low extracellular sodium and small molecules. *J. Biol. Chem.* **287**, 22701–22708 (2012).

Acknowledgements
We thank Dr. Yu-Kai Chao and Marcel Passon for technical support.

Author contributions
P.R. synthesized the compounds and performed calcium imaging experiments. A.S.R. performed autophagy experiments. N.U. and S.G. performed and analyzed screening experiments. C.A. created the CRISPR/Cas9 human MCOLN1 KO for MDA-MB-231 breast cancer lines and performed invasion and migration experiments. A.J., J.S. and R.T. performed patch-clamp experiments. C.L. synthesized ML-SI3. G.V. performed testing on the estrogen receptor. C.G. and F.B. designed the study, analyzed data, wrote the manuscript and provided funding. M.S. edited the manuscript and provided funding. All of the authors discussed the results and commented on the manuscript.

Funding
This work was supported, in part, by funding of the German Research Foundation DFG (SFB/TRR152 TP04 to C.G., GR-4315/2-1 to C.G., BR-1034/7-1 to F.B., and SFB/TRR152 TP18 to M.S.).

Competing interests
The authors declare no competing interests.

Additional information
Supplementary Information The online version contains supplementary material available at https://doi.org/10.1038/s41598-021-87817-4.

Correspondence and requests for materials should be addressed to M.S., F.B. or C.G.

Reprints and permissions information is available at www.nature.com/reprints.

Publisher's note Springer Nature remains neutral with regard to jurisdictional claims in published maps and institutional affiliations.

Supplementary Information

Estradiol analogs attenuate autophagy, cell migration and invasion by direct and selective inhibition of TRPML1, independent of estrogen receptors

Philipp Rühl[1#], Anna Scotto Rosato[2#], Nicole Urban[3#], Susanne Gerndt[1], Rachel Tang[2], Carla Abrahamian[2], Charlotte Leser[1], Jiansong Sheng[4], Archana Jha[5], Günter Vollmer[6], Michael Schaefer[3*], Franz Bracher[1*], Christian Grimm[2*]

[1]Department of Pharmacy – Center for Drug Research, Ludwig-Maximilians University, Munich, Germany
[2]Walther Straub Institute of Pharmacology and Toxicology, Faculty of Medicine, Ludwig-Maximilians University, Munich, Germany
[3]Rudolf-Boehm-Institute for Pharmacology and Toxicology, University of Leipzig, Germany
[4]CiPA LAB, LLC, Gaitherburg, MD, USA
[5]Casma Therapeutics Inc., Cambridge, MA, USA
[6]Institute of Zoology, Molecular Cell Physiology and Endocrinology, University of Dresden, Germany

Supplementary Tables: 1

Supplementary Figures: 3

Supplementary Schemes: 1

Synthetic Procedures

Table S1

Potency and selectivity of PRU compounds and estradiol.

	TRPML1	TRPML2	TRPML3	TRPML1:TRPML2	TRPML1:TRPML3
	IC_{50} (µM)	IC_{50} (µM)	IC_{50} (µM)	fold selectivity	fold selectivity
Estradiol	5.3	30.43	>50	5.77	n.c.
PRU-1 = EDME	0.6	5.85	19.5	9.14	30.47
PRU-2	13.8	37.02	>50	2.67	n.c.
PRU-4	0.5	5.23	4.78	10.25	9.37
PRU-5	0.8	3.38	14.88	4.45	19.58
PRU-6	0.41	3.57	7.87	8.71	19.2
PRU-7	0.73	2.64	15.2	3.62	20.82
PRU-8	0.72	15.32	38.65	21.28	53.68
PRU-9	0.17	2.53	5.96	14.88	35.06
PRU-10	0.41	5.4	15.83	13.17	38.61
PRU-11	0.44	2.4	32.11	5.45	72.98
PRU-12	0.28	5.28	14.08	18.86	50.29

Fig. S1

Structures of the noteworthy compounds of the high-throughput screening. (a) Structures of the four specific screening hits (b) Structures of retested and pharmacologically relevant steroids.

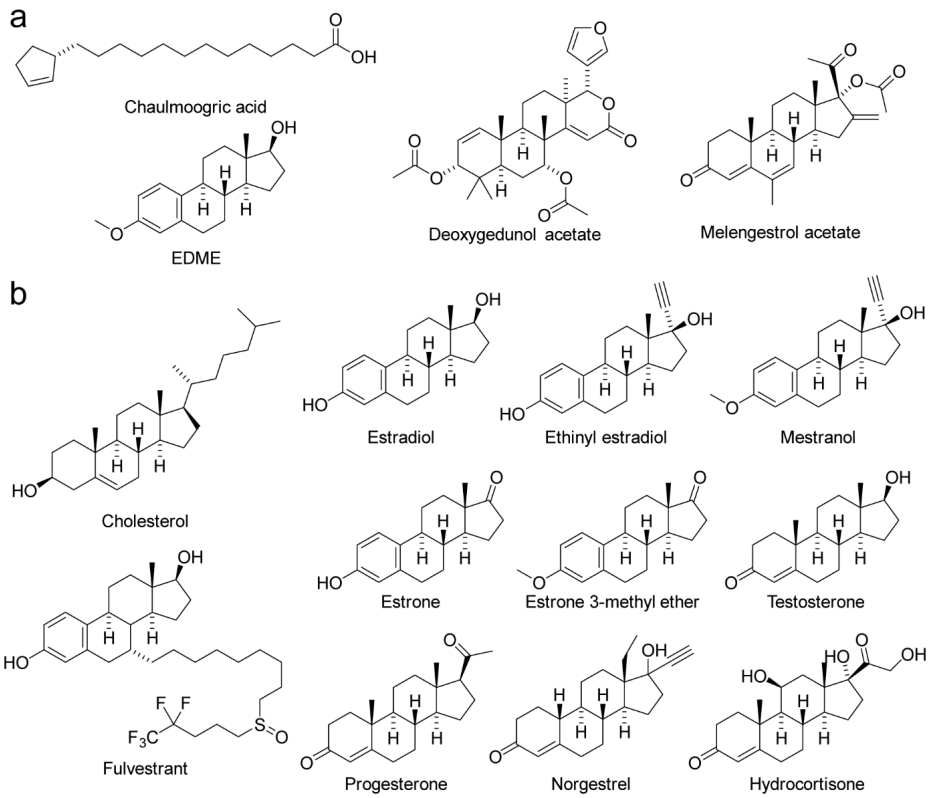

Fig. S2

Effects of PRU-10 and PRU-12 on hTPC2. Representative Fura-2 calcium signals recorded from HEK293 cells stably expressing hTPC2$^{L11A/L12A}$-RFP. Cells were either stimulated with PRU-10 or PRU-12 alone (a-b) or they were sequentially stimulated with TPC2 agonist TPC2-A1-N (10 µM) and then treated with EDME analogs (10 µM, each) (c-d). Neither an activating nor a blocking effect on TPC2 was found for PRU-10 and PRU-12.

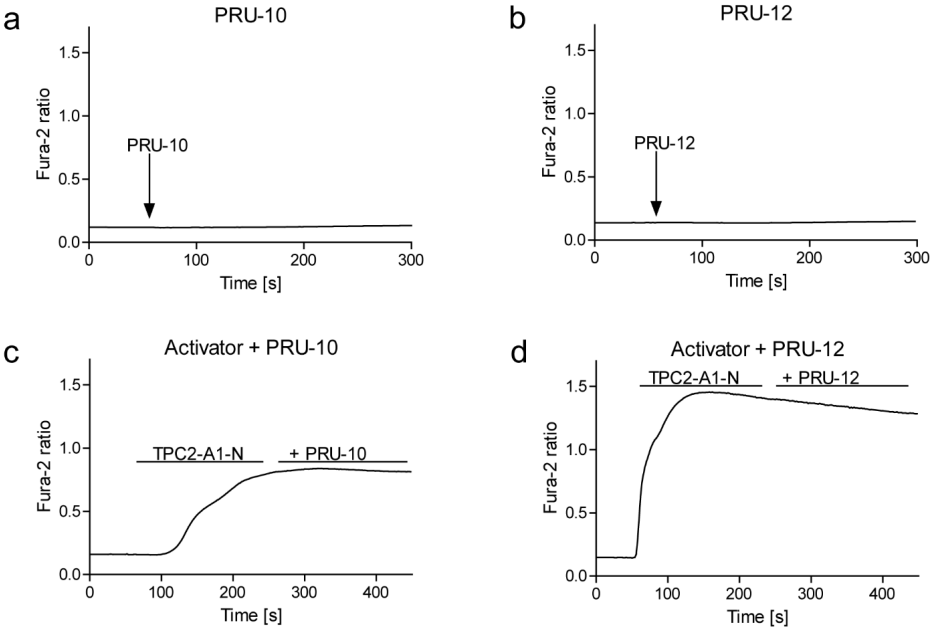

Fig. S3

Western blots uncropped. Shown are the Western blots from Fig. 6 in uncropped format.

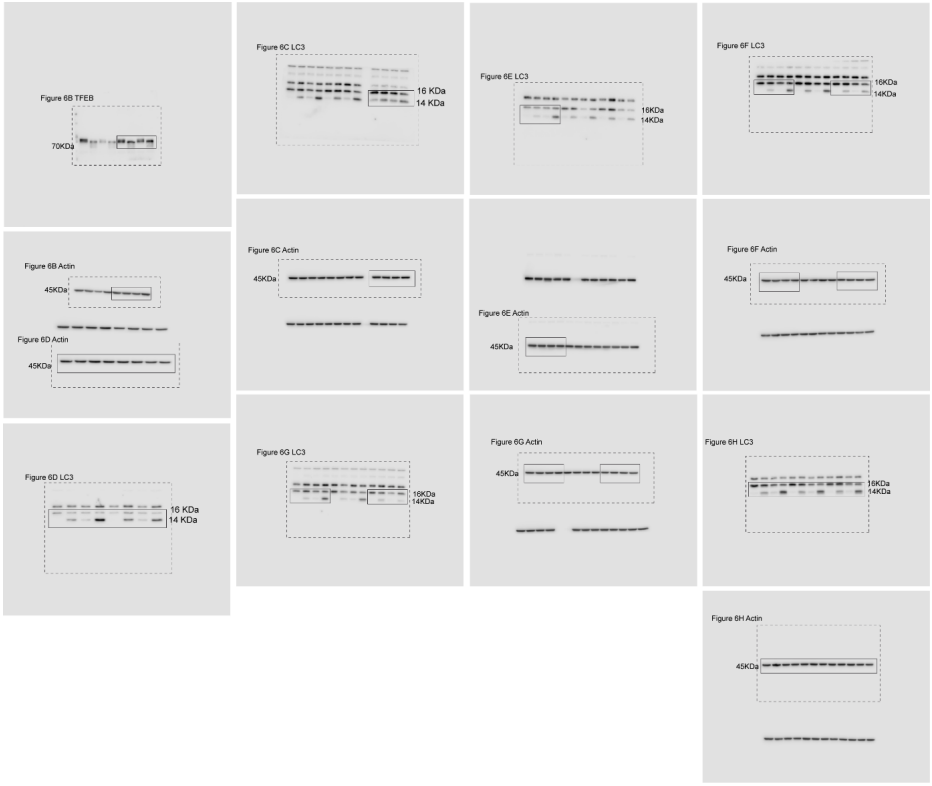

Suppl. Scheme 1

Synthesis of EDME analogs. Reaction conditions: a) for **PRU-2**: dimethyl sulfate, KOH, water/methanol, 65 °C, 1 h (51 %); b) for **PRU-4**: diethyl (bromodifluoromethyl) phosphonate, acetonitrile/water, 0 to 20 °C, 15 min (35 %); c) for **PRU-5**: bromoethane, NaOH, THF/water, reflux, 7 h (71%); d) for **PRU-6**: 2-bromopropane, NaOH, THF/water, reflux, 7 h (32 %); e) for **PRU-7**: 3-bromopropene, K_2CO_3, acetone, 50 °C, 40 h (89 %); f) for **PRU-8**: 2-(trimethylsilyl)phenyl trifluoromethanesulfonate, CsF, acetonitrile, 20 °C, 24 h (39 %); g) for **PRU-9**: 4-nitrophenyl trifluoromethanesulfonate, K_2CO_3, DMF, 20 °C, 2 h (74 %); h) for **PRU-10**: tributyl(vinyl)tin, cat. bis(triphenylphosphine)palladium(II)chloride, LiCl, 2,6-di-*tert*-butyl-4-methylphenol, DMF, N_2 atmosphere, 90 °C, 4 h (88 %); i) for **PRU-11**: phenylboronic acid, K_3PO_4, cat. $Pd(OAc)_2$, cat. SPhos, dioxane, N_2 atmosphere, 100 °C, 20 h (50 %); j) for **PRU-12**: tributyl(1-ethoxyvinyl)tin, cat. bis(triphenylphosphine) palladium(II)chloride, LiCl, DMF, N_2 atmosphere, 110 °C, 14 h, then water (54 %).

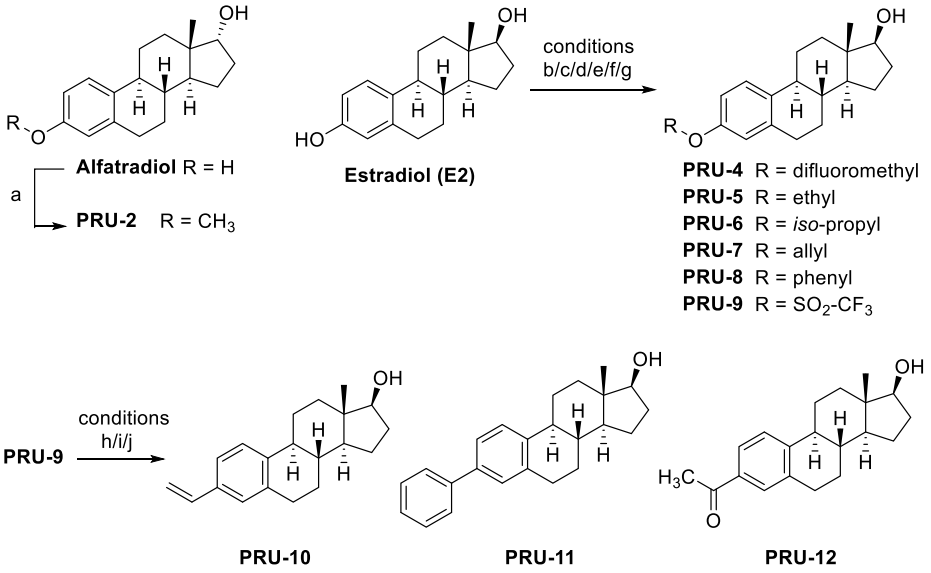

Synthetic procedures

Synthesis details and analytical data

All NMR spectra (^{1}H, ^{13}C, DEPT, H-H-COSY, HSQC, HMBC) were recorded at 23 °C on an Avance III 400 MHz Bruker BioSpin or Avance III 500 MHz Bruker BioSpin instrument unless otherwise specified. Chemical shifts δ are stated in parts per million (ppm) and are calibrated using residual protic solvents as an internal reference for proton ($CDCl_3$: δ = 7.26 ppm, DMSO: δ = 2.50 ppm) and for carbon the central carbon resonance of the solvent ($CDCl_3$: δ = 77.16 ppm, DMSO: δ = 39.52 ppm). Multiplicity is defined as s = singlet, d = doublet, t = triplet, q = quartet, m = multiplet. NMR spectra were analyzed with NMR software MestReNova, version 12.0.1-20560 (Mestrelab Research S.L.). High resolution mass spectra were performed by the LMU Mass Spectrometry Service applying a Thermo Finnigan MAT 95 or Joel MStation Sektorfeld instrument at a core temperature of 250 °C and 70 eV for EI or a Thermo Finnigan LTQ FT Ultra Fourier Transform Ion Cyclotron Resonance device at 250 °C for ESI. IR spectra were recorded on a Perkin Elmer FT-IR Paragon 1000 instrument as neat materials. Absorption bands were reported in wave number (cm^{-1}) with ATR PRO450-S. Melting points were determined by the open tube capillary method on a Büchi melting point B-540 apparatus and are uncorrected. HPLC purities were determined using an HP Agilent 1100 HPLC with a diode array detector and an Agilent Poroshell column (120 EC-C18; 3.0 × 100 mm; 2.7 micron) with acetonitrile/water as eluent (70:30 acetonitrile/water). All chemicals used were of analytical grade. 17β-Estradiol was purchased from TCI Deutschland GmbH (Eschborn, Germany), 17α-estradiol (alfatradiol, Ph. Eur. quality) from EDQM (Strasbourg, France). Isohexane, ethyl acetate and methylene chloride were purified by distillation. All reactions were monitored by thin-layer chromatography (TLC) using pre-coated plastic sheets POLYGRAM® SIL G/UV254 from Macherey-Nagel (Düren, Germany). Flash column chromatography was performed on Merck silica gel Si 60 (0.015 – 0.040 mm).

17β-Estradiol-3-methylether (EDME)

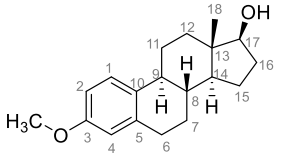

17β-Estradiol (222 mg, 0.815 mmol) was dissolved in 20 mL methanol. After addition of 5 mL of aqueous KOH (10%) and 0.50 mL (5.3 mmol) dimethyl sulfate, the solution was stirred at 65 °C for 30 min before another 0.50 mL (5.3 mmol) of dimethyl sulfate was added. After further 30 min, the solution was allowed to cool to room temperature and diluted with 20 mL of water. The precipitated solid was collected by filtration, washed with water, dried and purified by silica

gel column chromatography (isohexane/ethyl acetate 3:1) to give the methyl ether **EDME** as a colorless solid (160 mg, 0.559 mmol, 69%). m.p.: 121°C[1]: 119-120°C]. ^{1}H NMR (400 MHz, $CDCl_3$) *δ*/ppm = 7.21 (d, *J* = 8.4 Hz, 1H, 1-H), 6.71 (dd, *J* = 8.6 Hz, 2.8 Hz,1H, 2-H), 6.63 (d, *J* = 2.7 Hz, 1H, 4-H), 3.78 (s, 3H, 3-OCH_3), 3.73 (dd, *J* = 9.0 Hz, 8.0 Hz, 1H, 17α-H), 2.85 (m, 2H, 6-α-H, 6-β-H), 2.32 (m, 1H, 11-H), 2.19 (m, 1H, 9-H), 2.12 (m, 1H, 16-H), 1.95 (m, 1H, 12-H), 1.88 (m, 1H, 7-H), 1.70 (m, 1H, 15-H), 1.51 (m, 1H, 11-H), 1.46 (m, 1H, 16-H), 1.43 (m, 1H, 8-H), 1.39 (m, 1H, 15-H), 1.33 (m, 1H, 7-H), 1.29 (m, 1H, 12-H), 1.20 (m, 1H, 14-H), 0.71 (s, 3H, 18-H). ^{13}C NMR (100 MHz, $CDCl_3$) *δ*/ppm = 157.6 (C3), 138.1 (C5), 132.8 (C10), 126.5 (C1), 114.0 (C4), 111.6 (C2), 82.1 (C17), 55.4 (3-OCH_3), 50.2 (C14), 44.1 (C13), 43. (C9), 39.0 (C8), 36.9 (C12), 30.8 (C16), 30.0 (C6), 27.4 (C7), 26.5 (C11), 23.3 (C15), 11.2 (C18). IR (ATR): $\tilde{\nu}_{max}$/cm^{-1} = 3410, 2920, 2866, 1605, 1574, 1500, 1477, 1444, 1390, 1344, 1310, 1281, 1254, 1232, 1182, 1158, 1133, 1115, 1075, 1055, 964, 947, 862, 846, 818, 777, 572, 486, 442. HRMS (EI): calcd. for $C_{19}H_{26}O_2$ $(M)^{\bullet+}$: 286.1927; found: 286.1927. Purity (HPLC): >96% (λ = 210 nm), 93% (λ = 254 nm).

17α-Estradiol-3-methylether (PRU-2)

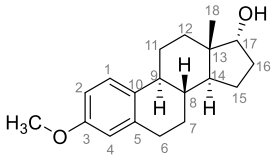

Prepared from 17α-estradiol (alfatradiol) (179 mg, 0.657 mmol) in the same manner as described above for the 17β epimer **EDME**. 17α-Estradiol-3-methylether (**PRU-2**) was obtained as a colorless solid (95.5 mg, 0.333 mmol, 51 %). m.p.: 109°C[2]: 106-107°C]. ^{1}H NMR *δ*/ppm = 7.18 (d, *J* = 8.6 Hz, 1H, 1-H), 6.67 (dd, *J* = 8.6 Hz, 2.8Hz,1H, 2-H), 6.59 (d, *J* = 2.8 Hz, 1H, 4-H), 4.34 (d, *J* = 4.2 Hz, 1H, OH) 3.68 (s, 3H, OCH_3), 3.57 (dd, J = 5.8 Hz, 4.1 Hz, 1H, 17β-H), 2.78 (m, 2H, 6α-H, 6β-H), 2.30 (m, 1H, 11-H), 2.10 (m, 1H, 9-H), 2.04 (m, 1H, 16-H), 1.83 (m, 1H, 7-H), 1.76 (m, 1H, 12-H), 1.71 (m, 1H, 15-H), 1.55 (m, 1H, 14-H), 1.44 (m, 1H, 12-H), 1.38 (m, 1H, 16-H), 1.34 (m, 1H, 11-H), 1.31 (m, 1H, 7-H), 1.27 (m, 1H, 8-H), 1.16 (m, 1H, 15-H), 0.61 (s, 3H, 18-H). ^{13}C NMR *δ*/ppm = 157.0(C3), 137.4 (C5), 132.3 (C10), 126.2 (C1), 113.4 (C4), 111.4 (C2), 78.0(C17), 54.8 (OCH_3), 47.2 (C14), 45.0(C13). 43.4 (C9), 38.8 (C8), 32.1 (C16), 31.5 (C12), 29.4 (C6), 27.8 (C7), 26.0 (C11), 23.9 (C15), 17.0 (C18). IR (ATR): $\tilde{\nu}_{max}$/cm^{-1} = 3599, 3513, 3324, 2910, 2862, 1608, 1576, 1499, 1467, 1378, 1280, 1254, 1235, 1155, 1119, 1104, 1075, 1037, 970, 941, 683, 663, 441. HRMS (EI): calcd. for $C_{19}H_{26}O_2$ $(M)^{\bullet+}$: 286.1927; found: 286.1920. Purity (HPLC): >96% (λ = 210 nm), >96% (λ = 254 nm)

The PRU numbers arise from consecutive numbering of synthesis experiments in our electronic lab book. Experiment **PRU-3** did not lead to an identifiable product. We attempted here to prepare an EDME analogue in which the metabolically labile methoxy group is replaced by a trifluoromethoxy group. Since (based on clear evidence from literature) the same stability can as well be achieved by a difluoromethoxy analogue (= PRU-4), compound PRU-3 was no longer persued.

17β-Estradiol-3-(difluoromethyl)ether (PRU-4)

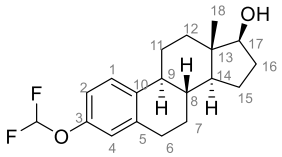

17β-Estradiol (300 mg, 1.10 mmol, 1.00 eq) and KOH (1.27 g, 22.6 mmol, 20.5 eq) were combined in a round-bottom flask following the addition of 30 mL of an acetonitrile/ water mixture (1:1). After cooling down to 0°C, diethyl (bromodifluoromethyl)phosphonate (600 mg, 2.25 mmol, 2.05 eq) was added and the biphasic mixture was allowed to reach room temperature over 15 minutes. The reaction mixture was diluted with 10 mL of diethyl ether, the layers were separated and the aqueous layer was further extracted with diethyl ether (3 × 10 mL). The combined organic layers were dried over anhydrous Na_2SO_4 and concentrated *in vacuo*. Purification was accomplished by silica gel column chromatography (isohexane/ethyl acetate 3:1) to yield **PRU-4** as a colorless oil (125 mg, 0.388 mmol, 35%). Analytical data are in accordance with literature[3]. ^{1}H NMR *δ*/ppm = 7.30 (d, *J* = 8.50 Hz, 1H, 1-H), 7.14 (t, *J* = 74.50 Hz,1H, CHF_2), 6.90 (dd, *J* = 8.5, 2.7 Hz, 1H, 2-H), 6.85 (d, *J* = 2.7 Hz,1H, 4-H), 4.50 (d, *J* = 4.8 Hz,1H, OH), 3.52 (m, 1H, 17-α-H), 2.80 (m, 2H, 6-α-H, 6-β-H), 2.28 (m, 1H, 11-H), 2.13 (m, 1H, 9-H), 1.88 (m, 1H, 16-H), 1.83 (m, 1H, 12-H), 1.79 (m, 1H, 7-H), 1.59 (m, 1H, 15-H), 1.38 (m, 1H, 16-H), 1.35 (m, 1H, 11-H), 1.32 (m, 1H, 8-H), 1.29 (m, 1H, 7-H), 1.26 (m, 1H, 15-H), 1.20 (m, 1H, 12-H), 1.14 (m, 1H, 14-H), 0.66 (s, 3H, 18-H). ^{13}C NMR *δ*/ppm= 148.7 (C3), 138.4 (C5), 137.2 (C10), 126.8 (C1), 118.7 (C4), 116.5 (t, *J* = 257 Hz, CHF_2), 116.0 (C2), 80.0 (C17), 49.5 (C14), 43.6 (C9), 42.8 (C13), 38.2 (C8), 36.5 (C12), 29.9 (C16), 29.0(C6), 26.6 (C7), 25.9 (C11), 22.8 (C15), 11.2 (C18). IR (ATR): $\tilde{\nu}_{max}$/cm^{-1} =3410, 2929, 2870, 1611, 1496, 1452, 1382, 1356, 1233, 1165, 1128, 1047, 934, 878, 821, 792, 763, 575, 449. HRMS (EI): calcd. for $C_{19}H_{24}F_2O_2$ $(M)^{\bullet+}$: 322.1739; found: 322.1749. Purity (HLPC): >96% (λ = 210 nm), >96% (λ = 254 nm).

17β-Estradiol-3-ethylether (PRU-5)

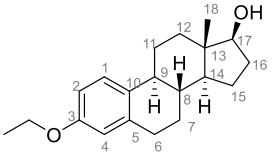

Bromoethane (118 mg, 1.08 mmol, 1.35 eq) was added to a solution of 17β-estradiol (217 mg, 0.797 mmol, 1.00 eq) and NaOH (44 mg, 1.1 mmol, 1.4 eq) in THF (20 mL) and water (5 mL). The reaction mixture was heated under reflux for 7 h and then diluted with water (10 mL). The mixture was extracted with diethyl ether (3 × 10 mL), the combined organic layers were dried over anhydrous Na_2SO_4 and concentrated *in vacuo*. The crude product was purified by column chromatography (isohexane/ethyl acetate 3:1) to yield **PRU-5** as a colorless solid (171 mg, 0.571 mmol, 71%). m.p.: 120°C[4]: 124-125°C]. ^{1}H NMR *δ*/ppm = 7.14 (d, *J* = 8.2 Hz, 1H, 1-H), 6.64 (dd, *J* = 8.6 Hz, 2.8 Hz, 1H, 2-H), 6.57 (d, *J* = 2.8 Hz, 1H, 4-H), 4.48 (d, *J* = 4.8, 1H, OH), 3.94 (q, *J* = 6.9 Hz, 2H, OCH_2), 3.51 (td, *J* = 8.5 Hz, 4.8 Hz 1H, 17-α-H), 2.75 (m, 2H, 6-α-H, 6-β-H), 2.25 (m, 1H, 11-H), 2.10 (m, 1H, 9-H), 1.86 (m, 1H, 16-H), 1.82 (m, 1H, 12-H), 1.78 (m, 1H, 7-H), 1.58 (m, 1H, 15-H), 1.37 (m, 1H, 16-H), 1.32 (m, 1H, 11-H), 1.29 (t, J = 7.0 Hz, 3H, ethyl CH_3), 1.27 (m, 1H, 8-H), 1.24 (m, 1H, 7-H), 1.21 (m, 1H, 15-H), 1.16 (m, 1H, 12-H), 1.10 (m, 1H, 14-H), 0.66 (s, 3H, 18-H). ^{13}C NMR *δ*/ppm = 156.3 (C3), 137.4 (C5), 132.1 (C10), 126.2 (C1), 114.1 (C4), 112.0(C2), 80.1 (C17), 62.7 (OCH_2), 49.6 (C14), 43.6 (C9), 42.9 (C13), 38.6 (C8), 36.6 (C12), 29.9 (C16), 29.3 (C6), 26.9 (C7), 26.1 (C11), 22.8 (C15), 14.8 (ethyl CH_3), 11.3 (C18). IR (ATR): $\tilde{\nu}_{max}$/cm^{-1} = 3410, 2920, 2866, 1605, 1500, 1477, 1390, 1344, 1310, 1254, 1232, 1182, 1157, 1133, 1054, 947, 862, 818, 777, 572. HRMS (EI): calcd. for $C_{20}H_{28}O_2$ $(M)^{\bullet+}$: 300.2089; found: 300.2082. Purity (HPLC): >96% (λ = 210 nm), >96% (λ = 254 nm).

17β-Estradiol-3-isopropylether (PRU-6)

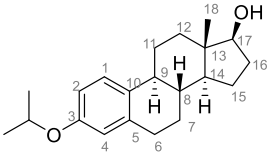

2-Bromopropane (128 mg, 1.03 mmol, 1.40 eq) was added to a solution of 17β-estradiol (200 mg, 0.734 mmol, 1.00 eq) and NaOH (41 mg, 1.10 mmol, 1.50 eq) in THF (20 mL) and water (5 mL). The solution was heated under reflux for 7 h and then diluted with water. The reaction mixture was extracted with diethyl ether (3 × 10 mL) and the combined organic layers

were dried over Na_2SO_4, filtered and concentrated *in vacuo*. Purification was accomplished by column chromatography (isohexane/ethyl acetate 3:1) to yield **PRU-6** as a colorless solid (74.9 mg 0.238 mmol, 32%). m.p.: 124°C[5]:119-122°C]. ^{1}H NMR *δ*/ppm = 7.13 (d, *J* = 8.5 Hz,1H, 1-H)), 6.63 (dd, J = 8.5 Hz, 2.7 ,1H, 2-H)), 6.56 (d, *J* = 2.7 Hz, 1H, 4-H), 4.50 (sept, *J* = 6.1 Hz, 1H, isopropyl CH), 4.48 (d, *J* = 4.8 Hz, 1H, OH), 3.51 (td, *J* = 8.5 Hz, 4.8 Hz,1H, 17-H), 2.74 (m, 2H, 6-α-H, 6-β-H), 2.24 (m, 1H, 11-H), 2.07 (m, 1H, 9-H), 1.87 (m, 1H, 16-H), 1.83 (m, 1H, 12-H), 1.77 (m, 1H, 7-H), 1.57 (m, 1H, 15-H), 1.38 (m, 1H, 16-H), 1.32 (m, 1H, 11-H), 1.29 (m, 1H, 8-H), 1.26 (m, 1H, 15-H), 1.23 (m, 1H, C7), 1.21 (2 d, *J* = 6.0 Hz, 2 x 3H, 2 isopropyl CH_3), 1.17 (m, 1H, 12-H), 1.11 (m, 1H, 14-H), 0.66 (s, 3H, 18-H). ^{13}C NMR *δ*/ppm = 155.1 (C3), 137.4 (C5), 132.0 (C10), 126.1 (C1), 115.4 (C4), 113.1 (C2), 80.0 (C17), 68.8 (isopropyl CH), 49.5 (C14), 43.5 (C9), 42.8 (C13), 38.6 (C8), 36.6 (C12), 29.9 (C16), 29.2 (C6), 26.9 (C7), 26.0 (C11), 22.8 (C15), 21.9 and 21.9 (2 isopropyl CH_3), 11.3 (C18). IR (ATR): $\tilde{\nu}_{max}$/cm^{-1} = 3478, 2914, 2863, 1610, 1494, 1378, 1333, 1279, 1252, 1109, 1052, 1008, 970, 874, 808, 774, 572. HRMS (EI): calcd. for $C_{21}H_{30}O_2$ $(M)^{\cdot+}$: 314.2240; found: 314.2241. Purity (HPLC): >96% (λ = 210 nm), >96% (λ = 254 nm).

17β-Estradiol-3-allylether (PRU-7)

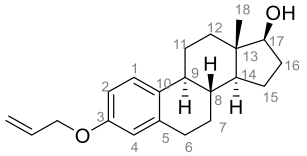

17β-Estradiol (136 mg, 0.499 mmol, 1.00 eq), 3-bromopropene (121 mg, 1.00 mmol, 86.0 µL, 2.00 eq), K_2CO_3 (248 mg, 1.50 mmol, 3.00 eq) and acetone (7.5 mL) were combined in a round bottom flask and stirred at 50 °C for 40 h. Then the mixture was diluted with water (5 mL) and extracted with CH_2Cl_2 (3 × 10 mL). The combined organic layers were dried over anhydrous Na_2SO_4 and concentrated *in vacuo*. The crude product was purified by silica gel column chromatography (isohexane/ethyl acetate 3:1) to afford **PRU-7** as a colorless solid (138 mg, 0.443 mmol, 89%). Analytical data are in accordance with literature[6]. m.p.: 64°C. ^{1}H NMR *δ*/ppm = 7.15 (d, *J* = 8.9 Hz ,1H, 1-H), 6.68 (dd, *J* = 8.6 Hz, 2.8 Hz,1H, 2-H), 6.61 (d, *J* = 2.7 Hz, 1H, 4-H), 6.01 (ddt, *J* = 17.4 Hz, 10.5 Hz, 5.2 Hz,1H, allyl CH), 5.36 (dq, *J* = 17.2 Hz, 1.8 Hz, 1H, allyl =CH_2), 5.22 (dq, *J* = 10.5 Hz, 1.6 Hz, 1H, 21-H), 4.49 (m, 3H, OH, OCH_2), 3.52 (td, *J* = 8.5 Hz, 4.9 Hz, 1H, 17-H), 2.75 (m, 2H, 6-H), 2.25 (m, 1H, 11-H), 2.09 (m, 1H, 9-H), 1.88 (m, 1H, 16-H), 1.84 (m, 1H, 12-H), 1.79 (m, 1H, 7-H), 1.58 (m, 1H, 15-H), 1.38 (m, 1H, 16-H), 1.32 (m, 1H, 11-H), 1.29 (m, 1H, 8-H), 1.26 (m, 1H, 15-H), 1.23 (m, 1H, 7-H), 1.18 (m, 1H, 12-H), 1.12 (m, 1H, 14-H), 0.66 (s, 3H, 18-H). ^{13}C NMR *δ*/ppm = 155.9 (C3), 137.4 (C5), 134.0 (allyl CH), 132.3 (C10), 126.1 (C1), 117.0 (allyl =CH_2), 114.3 (C4), 112.1 (C2), 80.0

(C17), 68.0(OCH_2), 49.5 (C14), 43.5 (C9), 42.8 (C13), 38.5 (C8), 36.6 (C12), 29.9 (C16), 29.2 (C6), 26.8 (C7), 26.0(C11), 22.8 (C15), 11.2 (C18). IR (ATR): $\tilde{\nu}_{max}/cm^{-1}$ = 3399, 2923, 2359, 1606, 1498, 1455, 1381, 1345, 1309, 1282, 1230, 1158, 1133, 1053. 1023, 917, 861, 818, 788, 569. HRMS (EI): calcd. for $C_{21}H_{28}O_2$ $(M)^{\cdot+}$: 312.2084; found: 312.2083. Purity (HPLC): >96% (λ = 210 nm), >96% (λ = 254 nm).

17β-Estradiol-3-phenylether (PRU-8)

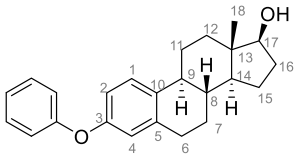

17β-Estradiol (202 mg, 0.741 mmol, 1.00 eq) and CsF (337 mg, 2.22 mmol, 3.00 eq) were suspended in acetonitrile (6.2 mL), then 2-(trimethylsilyl)phenyl trifluoromethanesulfonate (270 µL, 1.11 mmol, 1.50 eq) was added and the suspension was stirred for 24 h at room temperature. The resulting mixture was washed with brine (20 mL) and extracted with diethyl ether (3 × 10 mL). The combined ether fractions were dried over Na_2SO_4 and concentrated under reduced pressure. Purification was accomplished by column chromatography (isohexane/ethyl acetate 3:1) to yield **PRU-8** as a colorless oil (100 mg, 0.29 mmol, 39%). ^{1}H NMR *δ*/ppm = 7.36 (m, 2H), 7.27 (d, *J* = 8.5 Hz, 1H), 7.1 (m, 1H), 6.96 (m, 2H), 6.75 (dd, *J* = 8.5 Hz, 2.6 Hz, 1H, 2-H), 6.69 (d, *J* = 2.7 Hz, 1H, 4-H), 4.50 (d, *J* = 4.9Hz, 1H, OH), 3.53 (td, *J* = 8.5 Hz, 4.8 Hz, 17-H), 2.76 (m, 2H, 6-H), 2.28 (m, 1 H, 11-H), 2.15 (m, 1H, 9-H). 1.88 (m, 1H, 16-H), 1.85 (m, 1H, 12-H), 1.79 (m, 1H, 7-H), 1.59 (m, 1H, 15-H), 1.38 (m, 1H, 11-H), 1.35 (m, 1H, 16-H), 1.33 (m, 1H, 8-H), 1.29 (m, 1H, 7-H), 1.25 (m, 1H, 15-H), 1.19 (m, 1H, 12-H), 1.12 (m, 1H, 14-H), 0.68 (s, 3H, 18-H). ^{13}C NMR *δ*/ppm = 157.1, 154.1, 138.3, 135.4, 129.9, 126.8, 123.0, 118.6, 118.7, 116.1 (C2), 80.0 (C17), 49.6 (C14), 43.6 (C9), 42.8 (C13), 38.4 (C8), 36.6 (C12), 29.9 (C16), 29.1 (C6), 26.7 (C7), 25.9 (C11), 22.77 (C15), 11.2 (C18). HRMS (EI): calcd. for $C_{24}H_{28}O_2$ $(M)^{\cdot+}$: 348.2084, found: 348.2089. Purity (HPLC): >91% (λ = 210 nm), >91% (λ = 254 nm).

17β-Estradiol-3-trifluoromethanesulfonate (PRU-9)

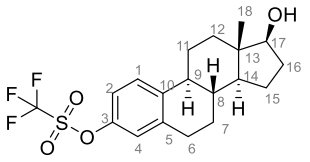

17β-Estradiol (1.00 g, 3.68 mmol, 1.00 eq) was dissolved in DMF (12 mL). K_2CO_3 (1.20 g, 7.34 mmol, 2.00 eq) was added, followed by 4-nitrophenyl trifluoromethanesulfonate (1.04 g, 3.85 mmol, 1.05 eq), and the resulting suspension was stirred for 2 h at room temperature. Then water (12 mL) and diethyl ether (5 mL) were added, the aqueous layer was separated and extracted with diethyl ether (3 × 5 mL). The combined organic layers were washed with cold 1M hydrochloric acid (10 mL), 1M NaOH solution (3 × 10 mL), water (3 × 10 mL), brine (10 mL) and 1M aqueous LiCl solution and dried over anhydrous Na_2SO_4. After evaporation the crude product was purified by column chromatography (isohexane/ethyl acetate 2:1) to yield **PRU-9** as a colorless solid (1.10 g, 2.72 mmol, 74%). m.p.: 79°C[7]: 123-125°C]. ^{1}H NMR *δ*/ppm = 7.34 (d, *J* = 8.7 Hz, 1H, 1-H), 7.02 (dd, *J* = 8.7 Hz, 2.7 Hz, 1H, 2-H), 6.97 (d, *J* = 2.7 Hz, 1H, 4-H), 3.74 (t, *J* = 8.7 Hz, 1H, 17-H), 2.89 (m, 2H, 6-H), 2.32 (m, 1H, 11-H), 2.24 (m, 1H, 9-H), 2.13 (m, 1H, 16-H), 1.98 (m, 1H, 12-H), 1.92 (m, 1H, 7-H), 1.71 (m, 1H, 15-H), 1.55 (m, 1H, 11-H), 1.49 (m, 1H, 16-H), 1.44 (m, 1H, 8-H), 1.38 (m, 1H, 15-H), 1.34 (m, 7-H), 1.30 (m, 1H, 12-H), 1.20 (m, 1H, 14-H), ^{13}C NMR *δ*/ppm = 147.6 (C3), 141.0 (C5), 139.7 (C10), 127.3 (C1), 121.3 (C4), 119.3 (q, *J* = 322.6 Hz, CF_3), 118.3 (C2), 81.9 (C17), 50.2 (C14), 44.2 (C9), 43.3 (C13), 38.4 (C8), 36.7 (C12), 30.7 (C16), 29.7 (C6), 26.9 (C7), 26.2 (C11), 23.3 (C15), 11.2 (C18). IR (ATR): $\tilde{\nu}_{max}$/cm^{-1} = 3400, 2958, 1489, 1418, 1250, 1206, 1142, 1049, 1002, 928, 976, 856, 718, 618, 499. HRMS (EI): calcd. for $C_{19}H_{23}F_3O_4S$ $(M)^{\bullet+}$: 404.1264, found: 404.1269. Purity (HPLC) >96% (λ = 210 nm), >96% (λ = 254 nm).

(8*R*,9*S*,13*S*,14*S*,17*S*)-13-Methyl-3-ethenyl-7,8,9,11,12,13,14,15,16,17-decahydro-6*H*-cyclopenta[a]phenanthren-17-ol (PRU-10)

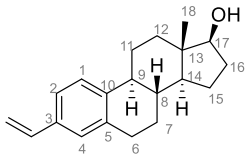

A flame-dried Schlenk flask was evacuated and backfilled with nitrogen 5 times prior to the addition of 300 mg (0.742 mmol, 1.00 eq) of 17β-estradiol-3-trifluoromethanesulfonate (**PRU-9**), 135 mg (3.15 mmol, 4.26 eq) lithium chloride, 1.6 mg of 2,6-di-*tert*-butyl-4-methylphenol and 52 mg (0.074 mmol, 0.10 eq) of bis(triphenylphosphine)palladium(II)chloride. After addition of 4.5 mL DMF, 0.28 mL (305 mg, 0.962 mmol, 1.30 eq) tributyl(vinyl)tin were added dropwise. The resulting suspension was stirred for 4 h at 90 °C under nitrogen atmosphere, then cooled to room temperature and treated with 0.3 mL of pyridine and 0.6 mL of hydrogen fluoride pyridine (Olah's reagent). The resulting mixture was stirred at room temperature overnight and then diluted with 20 mL diethyl ether, filtered and washed with 10 mL of water, 10 mL of 10% hydrochloric acid, again 10 mL of water and 10 mL of brine. The organic layer was dried over anhydrous Na_2SO_4 and concentrated under reduced pressure. The crude

product was suspended in cold isohexane and left in the fridge overnight. The precipitated solid was collected by filtration and purified by silica gel column chromatography (isohexane/ethyl acetate 4:1) to yield **PRU-10** as a colorless solid (184 mg, 0.651 mmol, 88%). Analytical data are in accordance with literature[8]. m.p.: 104°C. ^{1}H NMR *δ*/ppm = 7.24 (d, *J* = 8.2 Hz, 1H, 1-H), 7.2 (dd, *J* = 8.1 Hz, 1.8 Hz, 1H, 2-H), 7.12 (d, *J* = 1.8 Hz, 1H, 4-H), 6.64 (dd, *J* = 17.6 Hz, 10.9 Hz, 1H, vinyl CH), 5.73 (dd, *J* = 17.7 Hz, 1.2 Hz, 1H, vinyl CH_2), 5.17 (dd, *J* = 17.7 Hz, 1.2 Hz, 1H, vinyl CH_2), 4.50 (d, *J* = 4.8 Hz, 1H, 17-OH), 3.53 (td, *J* = 8.5 Hz, 4.8 Hz, 1H, 17α-H), 2.79 (dd, *J* = 8.8 Hz, 4.1 Hz, 2H, 6α-H, 6β-H), 2.29 (m, 1H, 11-H) 2.16 (m, 1H, 9-H) 1.89 (m, 1H, 16-H) 1.85 (m, 1H, 12-H) 1.81 (m, 1H, 7-H) 1.59 (m,1H, 11-H) 1.38 (m, 1H, 16-H), 1.35 (m, 1H, 11-H), 1.33 (m, 1H, 9-H), 1.28 (m, 1H, 7-H) 1.26 (m, 1H, 15-H), 1.19 (m, 1H, 12-H), 1.14 (m, 1H, 14-H), 0.67 (s, 3H, 18-H). ^{13}C NMR *δ*/ppm = 140.0 (C10), 136.6 (C19), 136.4 (C5), 134.3 (C3), 126.5 (C4), 125.4 (C1), 123.3 (C2), 113.1 (C20), 80.0 (C17), 49.6 (C8), 44.0(C14), 42.8 (C13), 38.5 (C9), 36.6 (C12), 29.9 (C16), 28.9 (C6), 26.8 (C7), 25.8 (C11), 22,8 (C15), 11.2 (C18). IR (ATR): $\tilde{\nu}_{max}$/cm^{-1} = 3410, 2930, 2864, 1629, 1562, 1496, 1445, 1385, 1335, 1250, 1134, 1074, 1052, 1021, 988, 898, 823, 787, 727, 567, 443. HRMS (EI): calcd. for $C_{20}H_{26}O$ $(M)^{\cdot+}$: 282.1978, found: 282.1984. Purity (HPLC): >96% (λ = 210 nm), >96% (λ = 254 nm).

(8*R*,9*S*,13*S*,14*S*,17*S*)-13-Methyl-3-phenyl-7,8,9,11,12,13,14,15,16,17-decahydro-6*H*-cyclopenta[a]phenanthren-17-ol (PRU-11)

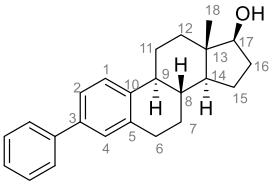

A flame dried Schlenk flask was evacuated and backfilled with nitrogen 5 times prior to the addition of 17β-estradiol-3-trifluoromethanesulfonate (**PRU-9**), 209 mg, 0.50 mmol, 1.00 eq), phenylboronic acid (122 mg, 1.00 mmol, 2.00 eq), K_3PO_4 (212 mg, 1.00 mmol, 2.00 eq), $Pd(OAc)_2$ (5.7 mg, 0.025 mmol, 0.05 eq), SPhos (20.5 mg, 0.0500 mmol, 0.100 eq) and dioxane (8 mL). The resulting suspension was heated at 100 °C for 20 h under nitrogen atmosphere and then quenched with water (15 mL) and diluted with ethyl acetate (15 mL). The organic phase was separated and the aqueous phase was extracted with ethyl acetate (3 × 10 mL). The combined organic phases were filtered, washed with brine and dried over anhydrous Na_2SO_4. The crude product was purified by column chromatography (hexane/ethyl acetate 4:1) to yield **PRU-11** as a colorless solid (174 mg, 0.501 mmol, 50%). m.p.: 172°C.^{1}H NMR *δ*/ppm = 7.58 (m, 2H), 7.42 (m, 2H), 7,39 (m, 2H, 1-H, 2-H), 7.33 (m, 2H), 3.76 (dd, *J* = 9.0 Hz, 7.9 Hz ,1H, 17α-H), 2.96 (m, 2H, 6-H), 2.40 (m, 1H, 11-H), 2.30 (m,1H, 9-H), 2.15 (m, 1H, 16-H),

1.99 (m,1H, 12-H), 1.94 (m, 1H, 7-H), 1.74 (m, 1H, 15-H), 1.58 (m, 1H, 11-H), 1.52 (m, 1H, 16-H), 1,50 (m, 1H, 8-H), 1,43 (m, 1H, 7-H), 1.40 (m, 1H, 15-H), 1.35 (m, 1H, 12-H), 1.27 (m, 1H, 14-H), 0.81 (s, 3H, 18-H). ^{13}C NMR *δ*/ppm = 141.3, 139.7 (C10), 138.7 (C3), 137.3 (C5), 128.8, 127.9 (C4), 127.2, 127.1, 126.0(C1), 124.6 (C2), 82.1 (C17), 50.3 (C14), 44.5 (C9), 43.4 (C13), 38.8 (C8), 36.9 (C12), 30.8 (C16), 29.8 (C6), 27.4 (C7), 26.3 (C11), 23.3 (C15), 11.2 (C18). IR (ATR): $\tilde{\nu}_{max}$/cm^{-1} = 3563, 2935, 2898, 1484, 1376, 1127, 1067, 1028, 1008, 889, 849, 762, 713, 698, 529. HRMS (EI): calcd. for $C_{24}H_{28}O$ $(M)^{\bullet+}$: 332.2135, found: 332.2132. Purity (HPLC): >95% (λ = 210 nm), >95% (λ = 254 nm)

1-((8*R*,9*S*,13*S*,14*S*,17*S*)-17-Hydroxy-13-methyl-7,8,9,11,12,13,14,15,16,17-decahydro-6*H*-cyclopenta[a]phenanthren-3-yl)ethan-1-one (PRU-12)

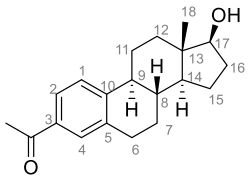

A flame dried Schlenk flask was evacuated and backfilled with nitrogen 5 times prior to the addition of 202 mg (0.50 mmol, 1.00 eq) 17β-estradiol-3-trifluoromethane-sulfonate (PRU-9), 64.2 mg (1.50 mmol, 3.00 eq) lithium chloride and 35.1 mg (0.0500 mmol, 0.100 eq) bis(triphenylphosphine)palladium(II)chloride. After addition of 3 mL of DMF, tributyl(1-ethoxyvinyl)tin (0.170 mL, 181 mg, 0.503 mmol, 1.00 eq) was added dropwise and the resulting suspension was stirred at 110 °C for 14 h under nitrogen atmosphere. After cooling, the mixture was treated with 5 mL of water and diluted with 5 mL of ethyl acetate. The organic phase was separated and washed with cold water (3 × 10 mL), brine and aqueous 1M LiCl solution, dried over anhydrous Na_2SO_4 and concentrated *in vacuo*. The crude product was purified by flash column chromatography (isohexane/ ethyl acetate 4:1) to yield PRU-12 as a colorless solid (80.2 mg, 0.27 mmol, 54%). m.p.: 180°C[8]:170-172°C]. ^{1}H NMR *δ*/ppm = 7.72 (dd, *J* = 8.1 Hz, 2.0 Hz, 1H, 2-H), 7.68 (d, *J* = 1.9 Hz, 1H, 4-H), 7.38 (d, *J* = 8.3Hz, 1H, 1-H), 3.74 (dd, 9.0 Hz, 8.0 Hz, 17α-H), 2.92 (m, 2H, 6α-H, 6β-H), 2.57 (s, 3H, acetyl CH_3), 2.37 (m, 1H, 11-H), 2.28 (m, 1H, 9-H), 2.13 (m, 1H, 16-H), 1.98 (m, 1H, 12-H), 1.93 (m, 1H, 7-H), 1.72 (m, 1H, 15-H), 1.55 (m, 1H, 11-H), 1.50 (m, 1H, 16-H), 1.46 (m, 1H, 8-H), 1.39 (m, 1H, 15-H), 1.35 (m, 1H, 7-H), 1.30 (m, 1H, 12-H), 1.22 (m, 1H, 14-H), 0.79 (s, 3H, 18-H). ^{13}C NMR *δ*/ppm = 198.4 (C=O), 146.3 (C10), 137.3 (C5), 134.8

(C3), 129.1 (C4), 125.8 (C2), 125.7 (C1), 81.9 (C17), 50.3 (C14), 44.9 (C9), 43.3 (C13), 38.5 (C8), 36.8 (C12), 30.7 (C16), 29.6 (C6), 27.1 (C7), 26.7 (acetyl CH_3), 26.1 (C11), 23.3 (C15), 11.2 (C18). IR (ATR): $\tilde{\nu}_{max}/cm^{-1}$ = 3507, 2917, 2868, 1664, 1605, 1562, 1363, 1267, 1171, 1056, 898, 834, 592. HRMS (EI): calcd. for $C_{20}H_{26}O$ $(M)^{\bullet+}$: 298.1927, found: 298.1926. Purity (HPLC): >96% (λ = 210 nm), >96% (λ = 254 nm).

Supporting Information References:

1. Muddana, S.S., Price, A.M., MacBride, M.M., and Peterson, B.R. (2004). 11beta-alkyl-Delta9-19-nortestosterone derivatives: high-affinity ligands and potent partial agonists of the androgen receptor. J Med Chem *47*, 4985-4988.
2. Pindur, U., and Schall, T. (1994). Proton Acid-Catalysed Transformations of Estrogen Derivatives: New Results and Some Mechanistic Aspects of the Kober Colour Reaction. Arch Pharm *327*, 637-642.
3. Lin, X., Hou, C., Li, H., and Weng, Z. (2016). Decarboxylative Trifluoromethylating Reagent [Cu(O2 CCF3)(phen)] and Difluorocarbene Precursor [Cu(phen)2][O2 CCF2 Cl]. Chemistry *22*, 2075-2084.
4. Triggle, D.J., Ridley, H.F., and DeMaio, D.M. (1969). Some 3-alkoxyestra-1,3,5(10)-trien-17-beta-ols. J Med Chem *12*, 346.
5. Tedesco, R., Thomas, J.A., Katzenellenbogen, B.S., and Katzenellenbogen, J.A. (2001). The estrogen receptor: a structure-based approach to the design of new specific hormone–receptor combinations. Chem Biol *8*, 277-287.
6. Santra, S., and Guin, J. (2015). Enhanced Reactivity of Aerobic Diimide Olefin Hydrogenation with Arylboronic Compounds: An Efficient One-Pot Reduction/Oxidation Protocol. Eur J Org Chem *2015*, 7253-7257.
7. Hostetler, E.D., Jonson, S.D., Welch, M.J., and Katzenellenbogen, J.A. (1999). Synthesis of 2-[(18)F]Fluoroestradiol, a Potential Diagnostic Imaging Agent for Breast Cancer: Strategies to Achieve Nucleophilic Substitution of an Electron-Rich Aromatic Ring with [(18)F]F(-). J Org Chem *64*, 178-185.
8. Shi, Y., and Koh, J.T. (2002). Functionally orthogonal ligand-receptor pairs for the selective regulation of gene expression generated by manipulation of charged residues at the ligand-receptor interface of ER alpha and ER beta. J Am Chem Soc *124*, 6921-6928.

Appendix

This appendix includes additional work from peer-reviewed publications and manuscripts, as follows:

1. **Paper V:**
   *co-first authorship

   Abrahamian, C.*, Tang, R.,* Deutsch, R.*, Ouologuem, L, Blenniger, J., Weiden, E.-M., Kudrina, V., Rilling, J., Feldmann, C., Stepanov, Y., Scotto Rosato, A., Calvo, G., Soengas, M., Fröhlich, T., Gudermann, T., Biel, M., Wahl-Schott, C., Chen, C.-C., Bartel, K.*, Grimm, C.* (2023) Rab7a is a direct effector of the intracellular Ca^{2+} channel TPC2 regulating melanoma progression through modulation of the Wnt signaling pathway. *Cell Reports. Manuscript in submission.*

2. **Paper VI:**

   Frey, N., Ouloguem, L., Siow, W. X., Stöckl, J., Blenniger, J., **Abrahamian, C.**, Grimm, C., Bartel., K. (2023). Endolysosomal TRPML1 channel regulates cancer cell-migration by facilitating the intracellular trafficking of E-cadherin and β1-integrin*. Journal of Biological Chemistry. Manuscript in submission.*

3. **Paper VII (review):**

   Abrahamian, C., & Grimm, C. (2021). Endolysosomal Cation Channels and MITF in Melanocytes and Melanoma. *Biomolecules*, *11*(7), 1021. https://doi.org/10.3390/biom11071021

4. **Paper VIII (review):**

   Spix, B.*, Chao, Y. K.*, **Abrahamian, C.***, Chen, C. C., & Grimm, C. (2020). TRPML Cation Channels in Inflammation and Immunity. *Frontiers in immunology*, *11*, 225. https://doi.org/10.3389/fimmu.2020.00225

Paper V

Rab7a is a direct effector of the intracellular Ca^{2+} channel TPC2 regulating melanoma progression through modulation of the Wnt signaling pathway

Carla Abrahamian[1#], Rachel Tang[1#], Rebecca Deutsch[1#], Lina Ouologuem[2], Julia Blenninger[2], Eva-Maria Weiden[1], Veronika Kudrina[1], Julia Rilling[2], Colin Feldmann[3], Youli Stepanov[4], Anna Scotto Rosato[1], Guadalupe Calvo[5], Marisol Soengas[5], Gudermann[1], Martin Biel[2], Christian Wahl-Schott[3], Cheng-Chang Chen[6,7], Karin Bartel[2*], Christian Grimm[1,8*]

[1]*Walther Straub Institute of Pharmacology and Toxicology, Faculty of Medicine, Ludwig-Maximilians-University, Munich, Germany.*
[2]*Department of Pharmacy, Ludwig-Maximilians-University, Munich, Germany.*
[3]*Institute of Cardiovascular Physiology and Pathophysiology, Faculty of Medicine, Ludwig-Maximilians-University, Munich, Germany.*
[4]*Laboratory for Functional Genome Analysis LAFUGA, Gene Center, Ludwig-Maximilians-University, Munich, Germany.*
[5]*Melanoma Laboratory, Molecular Pathology Programme, Centro Nacional de Investigaciones Oncológicas (Spanish National Cancer Research Centre), Madrid, Spain.*
[6]*Department of Clinical Laboratory Sciences and Medical Biotechnology, College of Medicine, National Taiwan University, Taipei, Taiwan.*
[7]*Department of Laboratory Medicine, National Taiwan University Hospital, Taipei, Taiwan.*
[8]*Immunology, Infection and Pandemic Research IIP, Fraunhofer Institute for Translational Medicine and Pharmacology ITMP*

*Corresponding authors. Email: christian.grimm@med.uni-muenchen.de or karin.bartel@cup.uni-muenchen.de

Running Title: Rab7a is a direct effector of TPC2 in melanoma

Keywords: TPC, TPC2, TPC1, Rab7, lysosome, melanoma, MITF

Highlights

Rab7a acts as an effector of the endolysosomal cation channel TPC2
Rab7a affects the Wnt signaling pathway through activation of TPC2
Rab7a acts via TPC2 on melanoma proliferation, migration and invasion

Summary

Melanoma is the deadliest form of skin cancer. It arises from pigment producing melanocytes. Extensive ultraviolet light exposure is the primary cause of melanoma and individuals with low levels of melanin are at particular risk. Humans carrying gain-of-function polymorphisms in the melanosomal/endolysosomal two-pore cation channel TPC2 present with hypopigmentation, blond hair, and albinism, and may bear a higher risk for melanoma development. Vice versa loss of TPC2 is associated with decreased cancer/melanoma proliferation, migration, invasion, tumour growth and metastasis formation, and TPC2 depleted melanoma cells show increased levels of melanin. We show here that the small GTPase Rab7a strongly enhances, through direct protein-protein interaction the activity of TPC2 and that the effects of TPC2 on melanoma hallmarks, *in vitro* and *in vivo* strongly depend on Rab7a, which controls TPC2 activity to modulate the Wnt signaling pathway, in particular GSK3β-mediated degradation of MITF, a major regulator of melanoma development and progression.

INTRODUCTION

Rab7 proteins are small GTPases, which can bind and hydrolyse guanosine triphosphate (GTP). They belong to a large protein family of more than 70 members in mammalian genomes and play fundamental roles in intracellular trafficking, vesicle formation, vesicle movement, and membrane fusion. Rabs are localized to the cytoplasmic face of organelles and vesicles and are highly selective in their subcellular localization. Two Rab7 proteins are known, Rab7a and Rab7b, which share about 50% sequence similarity. Rab7a localizes to late endosomes/lysosomes (LE/LY) and controls vesicular transport from early endosomes (EE) to LE/LY in the endocytic pathway. Rab7a plays a fundamental role not only for trafficking and degradation of many signaling receptors e.g., EGF/EGFR and adhesion molecules, but also for biogenesis, positioning, and motility of lysosomes as well as auto- and phagolysosomes[1-4]. Rab7a further plays key roles in cell survival, growth, differentiation, migration, autophagy and apoptosis. Modulation of Rab7a activity affects a number of disease pathologies including neuropathies and neurodegenerative diseases such as Charcot-Marie-Tooth type 2B, hereditary sensory neuropathy type 1, and Niemann Pick type C1 (NPC1), infectious diseases, and cancer, including melanoma[5-10]. Thus, Rab7a is e.g., associated with poor prognosis of gastric cancer and promotes proliferation, invasion, and migration of gastric cancer cells. Knockdown of Rab7a suppresses the proliferation, migration, and xenograft tumor growth of breast cancer cells and high Rab7a expression is an indicator of a higher risk of metastasis in early melanoma patients. In melanoma cells Rab7a levels are significantly elevated compared to normal skin melanocytes, impacting melanoma proliferation and invasion[5,9,11,12]. Similar to Rab7a, the Na^+ and Ca^{2+} permeable cation channel TPC2 in LE/LY and melanosomes of melanocytes has been described as an important regulator of endolysosomal trafficking, with EGF/EGFR, LDL cholesterol, or PDGF accumulating in TPC2 knockout cells[13-16]. In analogy to TPC2 inhibition, knockdown or knockout, Rab7a knockdown in NPC1 cells exacerbates cholesterol accumulation[5,17,18]. Inhibition, knockdown or knockout of TPC2 also results in reduced proliferation, migration, and invasion as well as reduced tumour growth, metastasis, tube formation and VEGF-induced angiogenesis in different types of cancer, including melanoma[16,19-23]. Besides, TPC2 affects also melanin production and pigmentation in melanocytes and melanoma

cells[19,24,25] (due to its expression in melanosomes, which are lysosome related organelles). Several human gain-of-function (GOF) polymorphisms, TPC2^{M484L}, TPC2^{G734E}, and recently TPC2^{R210C} were found to result in hypopigmentation, blond hair color and dominant albinism[26-28].

In proteomics studies Rab7a was identified as a potential interaction partner of TPC2[15,29] and direct interaction between TPC2 and Rab7a involving the N-terminus of TPC2 (residues 33-37) was proposed[29]. However, a detailed analysis of how Rab7a affects TPC2 channel activity and function, especially by direct electrophysiological means is missing and the physiological or pathophysiological consequences associated with this remain largely unexplored. By using endolysosomal patch-clamp electrophysiology and GCaMP based Ca^{2+} imaging experiments we show here that Rab7a strongly increases TPC2 activity. TPC2 is physically interacting with Rab7a, confirmed by co-immunoprecipitation and FRET experiments, suggesting a direct effect of Rab7a on TPC2 channel activity. A direct effect of Rab7a on TPC2 is further corroborated by acute application of a small molecule inhibitor of Rab7, which instantly reverts the effect on TPC2 activity. Expression of Rab7a in different cancer types strongly correlates with the expression of TPC2, with expression of both proteins being particularly high in melanoma cells. Rab7a, the major Rab7 protein in melanoma cells (Rab7b is barely expressed) is postulated here to control melanoma proliferation, growth, invasiveness, and metastasis formation through TPC2 activity regulation, specifically in melanoma cells which express high levels of MITF (microphthalmia-associated transcription factor), a known master regulator of melanocytes and melanoma development and progression. Mechanistically, TPC2 activation enhanced by Rab7a increases the endolysosomal degradation of GSK3β, contained in distinct destruction complexes[30], thus preventing proteasomal degradation of MITF. This finding provides a new mechanism, how an endolysosomal cation channel (TPC2) in direct interaction with a small GTPase (Rab7a) controls endolysosomal degradation of GSK3β, an key regulator of β-Catenin and MITF expression.

RESULTS

Expression of Rab7a correlates with TPC2 in human melanoma tissue samples and melanoma cell lines. We screened multiple human cancer cell lines including hepatocellular carcinoma (HCC; Huh7, HepG2), breast (MDA-MB-231, MCF-7, SK-BR-3), ovarian (SKOV3), cervical (HeLa), colon (Caco-2), and pancreatic (Panc-1) cancer as well as glioma (U87MG) and melanoma (SK-MEL-5, SK-MEL-2, SK-MEL-28, A375, SK-MEL-29, SK-MEL-19, SK-MEL-147, SK-MEL-103, UACC-62, UACC-257, MNT-1, CHL-1) lines for Rab7a expression and found particular high expression in the majority of melanoma lines (Figure 1A). Western blot results assessing Rab7a expression in different melanoma lines and MDA-MB-231 as control were found to correlate well with the expression levels in the qPCR dataset (Figure 1B). Compared to Rab7a expression of Rab7b was minimal in all tested cancer lines (Figure 1C). Expression of Rab7a correlated strongly with the expression of the human two-pore channel TPC2 (predominantly found in LE/LY like Rab7a), but not with the related channel TPC1 (predominantly found in EE) (Figures 1D-1E).

Rab7a physically interacts with TPC2. It has been reported previously that Rab7a interacts with TPC2[29]. We confirmed this here by an extended Two-hybrid FRET (Fluorescence Resonance Energy Transfer) and co-immunoprecipitation analysis. In FRET experiments, TPC2 coexpression with Rab7a resulted in 27% maximum FRET efficiency (Figure 1F). FRET efficiency reached 40% when pretreated with apilimod, resulting in enlarged endolysosomes. Coexpression with Rab7a^{Q67L}, a constitutively active mutant, resulted in 51% FRET efficiency after apilimod treatment while coexpression with the dominant negative Rab7a variant Rab7a^{T22N} yielded only 10% FRET efficiency under these conditions (Figures S1A). Coexpression with Rab5 (an EE marker showing less colocalization with TPC2) reached only 13% FRET efficiency (Figure S1B). As further controls we determined the FRET efficiency for TPC1 with Rab5 (= positive control, 29%) and TPC1 with Rab7a (= negative control, 6%) (Figure 1G and Figure S1C). In addition to FRET, we also performed co-immunoprecipitation experiments, which likewise confirmed interaction of TPC2 with Rab7a (Figure S1D). In

sum, these data corroborate a direct physical interaction of TPC2 but not TPC1 with Rab7a.

Rab7a functionally interacts with TPC2. To test whether Rab7a functionally interferes with TPC2, endolysosomal patch-clamp and GCaMP based Ca^{2+} imaging experiments were performed (Figure 2). $PI(3,5)P_2$, TPC2-A1-P (mimicking the effect of $PI(3,5)P_2$[31]), and TPC2-A1-N (mimicking the effect of NAADP[31]) were used as agonists to assess TPC2 activity. Patch-clamp experiments were performed using first HEK293 cells expressing either TPC2 alone or coexpressing TPC2 and $Rab7a^{WT}$, the constitutively active mutant $Rab7a^{Q67L}$, or the dominant negative mutant $Rab7a^{T22N}$ (Figures 2A-2D). These experiments revealed that $Rab7a^{WT}$ or $Rab7a^{Q67L}$ coexpression strongly enhanced TPC2 activity, independent of which agonist was applied, while coexpression with $Rab7a^{T22N}$ or TPC2 expression alone showed significantly smaller current densities when activated with the respective agonists (Figures 2A-2D). These findings were confirmed in GCaMP Ca^{2+} imaging experiments (Figure 2E). In contrast to TPC2, coexpression of $Rab7a^{WT}$ or mutants showed no effect on the activity of TRPML1, another endolysosomal Ca^{2+}/Na^{+} release channel (also highly expressed in melanoma), when stimulated with either a synthetic, TRPML1 isoform-selective small molecule agonist, ML1-SA1[32] or with the endogenous agonist $PI(3,5)P_2$ (Figures S2A-S2D). Effects were completely blocked by the TRPML1-selective blocker EDME[33]. Next, it was tested whether acute inhibition with the commercially available small molecule Rab7 inhibitor CID1067700 affects channel activity. HEK293 cells coexpressing TPC2 and $Rab7a^{WT}$ showed a dose-dependent, instant reduction of the $Rab7a^{WT}$ enhanced channel activity after application of CID1067700. Similar observations were made in cells expressing TPC2 alone (blocking endogenous Rab7) (Figures 3A-3C). In sum, these data suggest that the effect of Rab7a on TPC2 activity is a direct and acute effect and is independent of the TPC2 activation mode.

Knockout of Rab7a results in a reduction of endogenous TPC2 currents in SK-MEL-5 melanoma cells. Expression levels of Rab7a and TPC2 are particularly high in melanoma cells including SK-MEL-5 cells, which were chosen to generate knockout (KO) lines for both genes using CRISPR/Cas9 strategies (Figures 3D-3M). TPC2 KO was confirmed in three independent lines by endolysosomal patch-clamp and qPCR

experiments (Figures 3D-3G). To demonstrate that Rab7a affects the activity of TPC2 in the endogenous expression system, we next generated a Rab7a SK-MEL-5 KO line. Western blot and qPCR analyses of the Rab7a KO line (clone C1x17) demonstrated strongly reduced RNA levels and absent protein (Figures 3H-3J). The electrophysiological analysis revealed that the activity of TPC2 was absent in TPC2 KO and significantly reduced in Rab7a KO compared to WT SK-MEL-5 cells (Figures 3K-3I), corroborating the results obtained from HEK293 presented in Figures 2 and 3. By contrast, currents measured from endolysosomes isolated form Rab7a KO SK-MEL-5 cells versus WT SK-MEL-5 cells, showed no differences when activated with the synthetic, TRPML1 isoform-selective small molecule agonist ML1-SA1[26] (Figures S2E-S2G), confirming our data obtained for both TPC2 and TRPML1 in heterologous expression systems. In sum, our results suggest that Rab7a enhances endogenous TPC2 activity while loss of Rab7a reduces it. In contrast to TPC2, endogenous TRPML1 was not modulated in its activity by Rab7a and the effect on TPC2 was not due to changes in expression as expression levels of TPC2 were unchanged in WT compared to Rab7a KO cells (Figure 3M).

Migration, invasion and proliferation in TPC2 and Rab7 knockout and knockdown melanoma cells. As reported previously, knockout or knockdown of TPC2 in different cancer cell lines results in reduction of migration, invasion, and proliferation of cancer cells *in vitro*, and tumour growth and metastasis formation *in vivo*[16,19,20]. In analogy to MNT-1 melanoma cells[19], KO of TPC2 in SK-MEL-5 cells showed reduction in migration, invasion, and proliferation in all three CRISPR/Cas9 engineered TPC2 KO lines (Figures 4A-4E). Likewise, Rab7a SK-MEL-5 KO cells showed significant reduction in all three parameters: migration, invasion and proliferation (Figures 4F-4J). Rab7a protein and transcript levels were unchanged in the TPC2 KO lines (Figure 4K). We next performed TPC2 and Rab7a knockdown (KD) experiments in several other melanoma lines. Knockdown was confirmed by either qPCR (TPC2 KD) or WB (Rab7a KD) (Figures S3A-3C). In addition to SK-MEL-5, we tested 3 lines with high Rab7a expression levels (SK-MEL-29, SK-MEL-19, UACC-62) and 3 lines with medium to low Rab7a expression levels (SK-MEL-103, SK-MEL-147, A375). Results obtained after TPC2 KD for proliferation strongly correlated with Rab7a KD results with one exception, SK-MEL-29. All other lines showed comparable results after either TPC2 or Rab7a KD (Figures 5A-5B). SK-MEL-5

KD behaved like KO and was used to confirm that KD data are in accordance with KO data. SK-MEL-5, SK-MEL-19, UACC-62 and A375 showed reduced proliferation after either TPC2 or Rab7a KD while lines SK-MEL-103 and SK-MEL-147 showed no change in either KD (Figures 5A-5B). In invasion experiments, all TPC2 and Rab7a KDs showed concordant results (Figures 5C-5F). SK-MEL-5, SK-MEL-29, SK-MEL-19, and UACC-62 showed reduced invasion after either TPC2 or Rab7a KD while lines A375, SK-MEL-103 and SK-MEL-147 showed no change in both KDs. These data suggest that TPC2 and Rab7 KD are highly conserved in their effects on proliferation and invasion.

Rab7a correlates with MITF and GSK3β expression in melanoma lines.

MITF is a master regulator of melanocyte development with functions ranging from pigment production to differentiation and survival of melanocytes. MITF also plays a critical role in melanoma development and progression[34-37]. A rare functional variant of $MITF^{E318K}$ has been found to confer a 2-4-fold risk for cutaneous melanoma and may also bear risks for other cancers[38,39]. MITF, found downstream of the canonical Wnt/β-Catenin pathway contains GSK3β phosphorylation sites[30]. In the absence of Wnt signaling GSK3β phosphorylates MITF, targeting MITF for proteasomal degradation. Upon Wnt signaling, destruction complex components such as GSK3β and Axin[30] are sequestered into LE and MVBs (multivesicular bodies), which are part of the endocytic pathway, resulting in the degradation of GSK3β and stabilization of β-Catenin and MITF. While some melanoma cell lines investigated here express high MITF levels, others have low MITF expression or are considered to be MITF-independent (Figure 6A). Surprisingly, we found that melanoma lines, which showed reduced proliferation and invasion after either TPC2 or Rab7a KD express high levels of MITF. Other lines without detectable MITF expression such as SK-MEL-103 and SK-MEL-147 showed no effect after either TPC2 or Rab7a KD on both proliferation and invasion (Figure 5). TPC2 or Rab7 KD in A375 showed reduced proliferation but not reduced invasion while MITF expression was likewise not detectable. In sum, melanoma lines with high MITF dependence responded consistently with a reduction in invasion and proliferation after either TPC2 or Rab7a KD/KO.

Rab7a or TPC2 knockout and pharmacological inhibition result in decreased levels of MITF and increased GSK3β expression, enhancing MITF degradation.

Remarkably, Rab7a expression not only correlates with TPC2 but also with both MITF and GSK3β expression (Figure 6B). To confirm the hypothesis that reduced destruction complex degradation and thus increased GSK3β levels go along with enhanced degradation of MITF, we performed Western blot experiments using the SK-MEL-5 TPC2 and Rab7a KO lines. We could confirm that MITF is reduced or absent compared to controls in both Rab7 and TPC2 KOs, while GSK3β is increased (Figures 6C-6F). These data suggest that downregulation of TPC2 activity by Rab7a deletion results in reduced or absent MITF, likely due to decreased endolysosomal degradation of GSK3β, the major driver of proteasomal MITF degradation. Besides increased GSK3β and decreased MITF levels, also decreased β-Catenin levels were found in both TPC2 and Rab7a KO SK-MEL-5 lines. β-Catenin, mutations of which are associated with many types of cancer[40] including melanoma[41], is also part of the Wnt signalling pathway and its degradation is controlled by GSK3β phosphorylation[41-43], further corroborating an important regulatory role of both TPC2 and Rab7a in this pathway. In addition, we could show that a pharmacological inhibitor of TPC2, SG-094 likewise resulted in a reduction of MITF in SK-MEL-5 as well as in other melanoma lines (Figure 6G).

Rescue experiments reveal that TPC2 and Rab7a depend on each other to control proliferation and invasion of melanoma cells. Rab7a and TPC2 KO SK-MEL-5 cells were transfected with either mCherry (control), $Rab7a^{WT}$-mCherry or $Rab7a^{Q67L}$-mCherry. $Rab7a^{Q67L}$ rescued proliferation and $Rab7a^{WT}$ and $Rab7a^{Q67L}$ both rescued invasion defects in Rab7a KO SK-MEL-5 cells (Figures 7A-7L). Of note, the $TPC2^{M484L}$ GOF variant or $TPC2^{WT}$ in combination with TPC2-A1-P agonist, or TPC2-A1-P agonist alone also rescued proliferation and invasion in Rab7a KO SK-MEL-5 cells. In contrast, in TPC2 KO SK-MEL-5 cells $Rab7a^{WT}$ or $Rab7a^{Q67L}$ had no or much reduced rescue effects compared to their effects in Rab7a KO SK-MEL-5 cells, for both proliferation and invasion, suggesting that without TPC2 Rab7a cannot sufficiently rescue. TPC2 KO was rescued by $TPC2^{M484L}$, $TPC2^{WT}$, or $TPC2^{WT}$ in combination with TPC2-A1-P but not with TPC2-A1-P alone (TPC2-A1-P is expected not to work in TPC2 KO, attributing to specificity; Figures 7I-7L). In sum, these data show that Rab7a and TPC2 depend on each other. However, while loss of Rab7a can be efficiently rescued with TPC2 overexpression (OE), loss of TPC2 can either not or only marginally be rescued by Rab7a OE. In sum, these

findings corroborate the hypothesis that Rab7a acts as an effector of TPC2 but not vice versa.

Melanoma growth formation in-vivo is mediated by Rab7a as direct effector of TPC2. An ectopic tumour model with murine melanoma B16F10-luc cells was chosen for *in vivo* experiments to investigate tumour growth. After confirming expression of TPC2 and Rab7a (Figure S4A), we generated murine TPC2 and Rab7a CRISPR/Cas9 KOs in B16F10-luc cells (Figure S4B-4C). We validated these cells by qPCR and WB analysis to assess successful KO of TPC2 and Rab7a, respectively (Figures S4D-4G). C57BL/6BrdCrHsd-Tyr^{c} mice were then injected (subcutaneous injections into the flank) with either WT, TPC2 KO or Rab7a KO B16F10-luc cells. Mice injected with TPC2 KO or Rab7a KO B16F10-luc cells showed both decreased tumour growth as compared to mice injected with WT B16F10-luc cells (Figures 7N-O). Importantly, decreased melanoma growth after Rab7 KO cell injection could be significantly reverted with TPC2-A1-P agonist treatment (Figure 7O). These data corroborate our hypothesis that Rab7a KO and TPC2 KO exert similar effects and that the effect of Rab7a is mediated through TPC2, as the loss of Rab7a can be compensated with TPC2 agonist.

DISCUSSION

We show here that knockout of either Rab7a or TPC2 in melanoma lines, in particular those that express high levels of MITF result in similar phenotypes i.e., reduction of proliferation, migration, invasion, and tumour growth *in vitro* and *in vivo*. We further show that Rab7a, which directly interacts with TPC2, is a strong promoter of TPC2 activity. In endolysosomal patch-clamp and GCaMP based Ca^{2+} imaging experiments activation of TPC2 is strongly enhanced when Rab7a is present. We further indicate that KO of Rab7a reduces endogenous TPC2 activity in SK-MEL-5 melanoma cells, corroborating the findings in OE HEK293 cells. On the other hand, the lysosomal cation channel TRPML1 showed a Rab7a-independent activity since coexpression with Rab7a showed no difference in TRPML1 activation in endolysosomal patch-clamp experiments after application of either a TRPML1 synthetic small molecule agonist, ML1-SA1 or the endogenous agonist $PI(3,5)P_2$. In line with these results, activity of TRPML1 in SK-MEL-

5 melanoma cells was not affected by the KO of Rab7a. Our data imply that Rab7a acts specifically as an effector of TPC2 to regulate melanoma proliferation, migration and invasion. Effects on proliferation and invasion in Rab7a KO melanoma cells can be rescued by TPC2 OE and activation but vice versa TPC2 KO could either not be rescued by Rab7a OE (invasion) or with much reduced rescue efficacy (proliferation). In *in vivo* experiments in mice, we could show that tumour growth was reduced in mice injected with TPC2 KO or Rab7a KO B16F10-luc melanoma cells as compared to WT B16F10-luc melanoma cell injection. Importantly, tumour growth of Rab7 KO tumours could be rescued by treatment with TPC2-A1-P, confirming Rab7a as an upstream regulator of TPC2.

Effects of TPC2 or Rab7a KO or KD on proliferation, migration, and invasion were seen particularly in melanoma lines expressing high levels of MITF, and MITF levels were significantly depleted after either KO or KD of TPC2 or Rab7a. Rab7a expression correlates strongly not only with TPC2 expression but also with the expression of MITF and GSK3β. Reduced endolysosomal degradation of GSK3β promotes MITF proteasomal degradation as demonstrated previously[19,30]. Based on our data, we postulate that activation of TPC2, enhanced by Rab7a promotes degradation of GSK3β in endolysosomal compartments, thus resulting in less GSK3β being available for MITF degradation. Vice versa, loss of TPC2 or Rab7a both reduce endolysosomal degradative activity, leaving more GSK3β available for the proteasomal degradation of MITF. As further evidence for this pathway to be critically involved we found that also β-Catenin, which is directly dependent on GSK3β phosphorylation for its degradation, is reduced in Rab7a as well as TPC2 KO lines.

There are reports claiming that MITF follows a rheostat model[44] according to which MITF can result in varied cellular responses in melanoma cells based on its activity[34]. In brief, at peak MITF levels, melanoma cells express differentiation genes, promoting a pigmented phenotype and terminal differentiation. At an intermediate MITF level cells are in a reversible proliferative state, suppressing differentiation. At lower level MITF promotes invasiveness and cells exhibit more stem-cell-like properties but low proliferative and pigmentation capacities. At its lowest level MITF drives senescence and apoptosis[45,46]. This model has been discussed controversially in recent years[45-48]. That

proliferative and invasive phenotypes are mutually exclusive has been disputed by Haass et al. (2014), and Wellbrock and Arozarena (2015) point out that comparable expression of MITF can carry out opposing functions depending on a complex context-dependent set of factors[46,47]. Despite these controversies, our results clearly suggest that KO, KD, or pharmacological inhibition of Rab7a or TPC2 result in reduced proliferation, invasion and migration, most consistently in high level MITF expressing melanoma lines, which after TPC2 or Rab7 KO or KD show strongly reduced MITF levels. In accordance with our findings Alonso-Curbelo et al. (2014) showed reduced proliferation after Rab7 shRNA treatment for melanoma line UACC-62, while shRNA treatment was less efficient in reducing proliferation of SK-MEL-103 cells[9]. In addition, in their study high MITF and high Rab7 expressing lines such as SK-MEL-19 or SK-MEL-29 had shown lower basal invasiveness than lines expressing lower MITF and lower Rab7 levels such as SK-MEL-103 and SK-Mel-147. In sum, our *in vitro* KD and KO data as well as our rescue studies and *in vivo* data strongly suggest a correlation between Rab7a and TPC2 activity, with Rab7a acting as an effector of TPC2, promoting tumour hallmarks such as proliferation, migration, invasion, and tumour growth, in particular in melanoma cells expressing high levels of MITF[9]. These data provide a new concept of how a small GTPase, Rab7a affects cancer/melanoma hallmarks by directly controlling the activity of the endolysosomal cation channel TPC2 with effects on endolysosomal degradation of GSK3β and thus β-Catenin and MITF levels.

Data and materials availability

All data supporting the findings from this study are available within the manuscript and its supplementary information.

Acknowledgments.

This work was supported, in part, by funding of the German Research Foundation (SFB/TRR152 P04 to C.G., P06 to C.W.-S., P12 to M.B., and P15 to T.G., SFB1328 A21 to C.G., DFG GR4315/2-2 to C.G. and K.B., and DFG GR4315/4-1 to C.G.). C.-C.C. was supported by the Ministry of Science and Technology (MOST 110-2320-B-002-022), National Taiwan University (NTU-111L7826) and National Health Research Institutes (NHRI-EX111-11119SC).

Author contributions

C.A., R.T., R.D., L.O., E.-M.W., V.K., C.F. Y.S., A.S.R. and C.-C.C. designed experiments and collected and analyzed data. R.D. and R.T. performed endolysosomal patch-clamp experiments. R.D. performed co-immunoprecipitation experiments. L.O. and J.R. carried out animal experiments. C.F. performed FRET experiments. V.K. provided Ca^{2+} imaging experiments. M.S. and G.C. provided melanoma cell lines. T.F., T.G., M.B., C.W.-S., and K.B. provided funding and commented on the manuscript. C.G. provided funding, coordinated research, designed the study, analyzed data, designed figures, and wrote the manuscript. All of the authors discussed the results and commented on the manuscript.

Competing interests

The authors declare that they have no competing interests.

References

1. Ceresa, B.P., and Bahr, S.J. (2006). rab7 activity affects epidermal growth factor:epidermal growth factor receptor degradation by regulating endocytic trafficking from the late endosome. J Biol Chem *281*, 1099-1106. 10.1074/jbc.M504175200.
2. Shinde, S.R., and Maddika, S. (2016). PTEN modulates EGFR late endocytic trafficking and degradation by dephosphorylating Rab7. Nature Communications *7*, 10689. 10.1038/ncomms10689.
3. Guerra, F., and Bucci, C. (2016). Multiple Roles of the Small GTPase Rab7. Cells *5*. 10.3390/cells5030034.
4. Progida, C., Cogli, L., Piro, F., De Luca, A., Bakke, O., and Bucci, C. (2010). Rab7b controls trafficking from endosomes to the TGN. J Cell Sci *123*, 1480-1491. 10.1242/jcs.051474.
5. van den Boomen, D.J.H., Sienkiewicz, A., Berlin, I., Jongsma, M.L.M., van Elsland, D.M., Luzio, J.P., Neefjes, J.J.C., and Lehner, P.J. (2020). A trimeric Rab7 GEF controls NPC1-dependent lysosomal cholesterol export. Nat Commun *11*, 5559. 10.1038/s41467-020-19032-0.
6. Xie, J., Yan, Y., Liu, F., Kang, H., Xu, F., Xiao, W., Wang, H., and Wang, Y. (2019). Knockdown of Rab7a suppresses the proliferation, migration, and xenograft tumor growth of breast cancer cells. Biosci Rep *39*. 10.1042/bsr20180480.
7. Auer-Grumbach, M. (2008). Hereditary sensory neuropathy type I. Orphanet J Rare Dis *3*, 7. 10.1186/1750-1172-3-7.
8. McCray, B.A., Skordalakes, E., and Taylor, J.P. (2010). Disease mutations in Rab7 result in unregulated nucleotide exchange and inappropriate activation. Hum Mol Genet *19*, 1033-1047. 10.1093/hmg/ddp567.
9. Alonso-Curbelo, D., Riveiro-Falkenbach, E., Pérez-Guijarro, E., Cifdaloz, M., Karras, P., Osterloh, L., Megías, D., Cañón, E., Calvo, T.G., Olmeda, D., et al. (2014). RAB7 controls melanoma progression by exploiting a lineage-specific wiring of the endolysosomal pathway. Cancer Cell *26*, 61-76. 10.1016/j.ccr.2014.04.030.

10. Liu, H., Xu, J., Yao, Q., Zhang, Z., Guo, Q., and Lin, J. (2020). Rab7 Is Associated with Poor Prognosis of Gastric Cancer and Promotes Proliferation, Invasion, and Migration of Gastric Cancer Cells. Med Sci Monit *26*, e922217. 10.12659/msm.922217.
11. Cherry, S., Jin, E.J., Ozel, M.N., Lu, Z., Agi, E., Wang, D., Jung, W.H., Epstein, D., Meinertzhagen, I.A., Chan, C.C., and Hiesinger, P.R. (2013). Charcot-Marie-Tooth 2B mutations in rab7 cause dosage-dependent neurodegeneration due to partial loss of function. Elife *2*, e01064. 10.7554/eLife.01064.
12. Guadagno, N.A., and Progida, C. (2019). Rab GTPases: Switching to Human Diseases. Cells *8*. 10.3390/cells8080909.
13. Ruas, M., Galione, A., and Parrington, J. (2015). Two-Pore Channels: Lessons from Mutant Mouse Models. Messenger (Los Angel) *4*, 4-22. 10.1166/msr.2015.1041.
14. Ruas, M., Rietdorf, K., Arredouani, A., Davis, L.C., Lloyd-Evans, E., Koegel, H., Funnell, T.M., Morgan, A.J., Ward, J.A., Watanabe, K., et al. (2010). Purified TPC isoforms form NAADP receptors with distinct roles for Ca(2+) signaling and endolysosomal trafficking. Curr Biol *20*, 703-709. 10.1016/j.cub.2010.02.049.
15. Grimm, C., Holdt, L.M., Chen, C.C., Hassan, S., Müller, C., Jörs, S., Cuny, H., Kissing, S., Schröder, B., Butz, E., et al. (2014). High susceptibility to fatty liver disease in two-pore channel 2-deficient mice. Nat Commun *5*, 4699. 10.1038/ncomms5699.
16. Müller, M., Gerndt, S., Chao, Y.K., Zisis, T., Nguyen, O.N.P., Gerwien, A., Urban, N., Müller, C., Gegenfurtner, F.A., Geisslinger, F., et al. (2021). Gene editing and synthetically accessible inhibitors reveal role for TPC2 in HCC cell proliferation and tumor growth. Cell Chem Biol *28*, 1119-1131.e1127. 10.1016/j.chembiol.2021.01.023.
17. Scotto Rosato, A., Krogsaeter, E.K., Jaślan, D., Abrahamian, C., Montefusco, S., Soldati, C., Spix, B., Pizzo, M.T., Grieco, G., Böck, J., et al. (2022). TPC2 rescues lysosomal storage in mucolipidosis type IV, Niemann-Pick type C1, and Batten disease. EMBO Mol Med *14*, e15377. 10.15252/emmm.202115377.
18. Prat Castro, S., Kudrina, V., Jaślan, D., Böck, J., Scotto Rosato, A., and Grimm, C. (2022). Neurodegenerative Lysosomal Storage Disorders: TPC2 Comes to the Rescue! Cells *11*. 10.3390/cells11182807.
19. Netcharoensirisuk, P., Abrahamian, C., Tang, R., Chen, C.C., Rosato, A.S., Beyers, W., Chao, Y.K., Filippini, A., Di Pietro, S., Bartel, K., et al. (2021). Flavonoids increase melanin production and reduce proliferation, migration and invasion of melanoma cells by blocking endolysosomal/melanosomal TPC2. Sci Rep *11*, 8515. 10.1038/s41598-021-88196-6.
20. Nguyen, O.N., Grimm, C., Schneider, L.S., Chao, Y.K., Atzberger, C., Bartel, K., Watermann, A., Ulrich, M., Mayr, D., Wahl-Schott, C., et al. (2017). Two-Pore Channel Function Is Crucial for the Migration of Invasive Cancer Cells. Cancer Res *77*, 1427-1438. 10.1158/0008-5472.Can-16-0852.
21. Alharbi, A.F., and Parrington, J. (2021). TPC2 targeting evolution: Leveraging therapeutic opportunities for cancer. Cell Chem Biol *28*, 1103-1105. 10.1016/j.chembiol.2021.07.020.
22. Favia, A., Pafumi, I., Desideri, M., Padula, F., Montesano, C., Passeri, D., Nicoletti, C., Orlandi, A., Del Bufalo, D., Sergi, M., et al. (2016). NAADP-Dependent Ca(2+) Signaling Controls Melanoma Progression, Metastatic Dissemination and Neoangiogenesis. Sci Rep *6*, 18925. 10.1038/srep18925.
23. Pafumi, I., Festa, M., Papacci, F., Lagostena, L., Giunta, C., Gutla, V., Cornara, L., Favia, A., Palombi, F., Gambale, F., et al. (2017). Naringenin Impairs Two-Pore Channel 2

Activity And Inhibits VEGF-Induced Angiogenesis. Sci Rep *7*, 5121. 10.1038/s41598-017-04974-1.

24. Ambrosio, A.L., Boyle, J.A., Aradi, A.E., Christian, K.A., and Di Pietro, S.M. (2016). TPC2 controls pigmentation by regulating melanosome pH and size. Proc Natl Acad Sci U S A *113*, 5622-5627. 10.1073/pnas.1600108113.
25. Bellono, N.W., Escobar, I.E., and Oancea, E. (2016). A melanosomal two-pore sodium channel regulates pigmentation. Sci Rep *6*, 26570. 10.1038/srep26570.
26. Chao, Y.K., Schludi, V., Chen, C.C., Butz, E., Nguyen, O.N.P., Muller, M., Kruger, J., Kammerbauer, C., Ben-Johny, M., Vollmar, A.M., et al. (2017). TPC2 polymorphisms associated with a hair pigmentation phenotype in humans result in gain of channel function by independent mechanisms. Proc Natl Acad Sci U S A *114*, E8595-e8602. 10.1073/pnas.1705739114.
27. Böck, J., Krogsaeter, E., Passon, M., Chao, Y.K., Sharma, S., Grallert, H., Peters, A., and Grimm, C. (2021). Human genome diversity data reveal that L564P is the predominant TPC2 variant and a prerequisite for the blond hair associated M484L gain-of-function effect. PLoS Genet *17*, e1009236. 10.1371/journal.pgen.1009236.
28. Wang, Q., Wang, Z., Wang, Y., Qi, Z., Bai, D., Wang, C., Chen, Y., Xu, W., Zhu, X., Jeon, J., et al. (2023). A gain-of-function TPC2 variant R210C increases affinity to PI(3,5)P2 and causes lysosome acidification and hypopigmentation. Nature Communications *14*, 226. 10.1038/s41467-023-35786-9.
29. Lin-Moshier, Y., Keebler, M.V., Hooper, R., Boulware, M.J., Liu, X., Churamani, D., Abood, M.E., Walseth, T.F., Brailoiu, E., Patel, S., and Marchant, J.S. (2014). The Two-pore channel (TPC) interactome unmasks isoform-specific roles for TPCs in endolysosomal morphology and cell pigmentation. Proc Natl Acad Sci U S A *111*, 13087-13092. 10.1073/pnas.1407004111.
30. Ploper, D., Taelman, V.F., Robert, L., Perez, B.S., Titz, B., Chen, H.W., Graeber, T.G., von Euw, E., Ribas, A., and De Robertis, E.M. (2015). MITF drives endolysosomal biogenesis and potentiates Wnt signaling in melanoma cells. Proc Natl Acad Sci U S A *112*, E420-429. 10.1073/pnas.1424576112.
31. Gerndt, S., Chen, C.C., Chao, Y.K., Yuan, Y., Burgstaller, S., Scotto Rosato, A., Krogsaeter, E., Urban, N., Jacob, K., Nguyen, O.N.P., et al. (2020). Agonist-mediated switching of ion selectivity in TPC2 differentially promotes lysosomal function. Elife *9*. 10.7554/eLife.54712.
32. Spix, B., Butz, E.S., Chen, C.-C., Rosato, A.S., Tang, R., Jeridi, A., Kudrina, V., Plesch, E., Wartenberg, P., Arlt, E., et al. (2022). Lung emphysema and impaired macrophage elastase clearance in mucolipin 3 deficient mice. Nature Communications *13*, 318. 10.1038/s41467-021-27860-x.
33. Rühl, P., Rosato, A.S., Urban, N., Gerndt, S., Tang, R., Abrahamian, C., Leser, C., Sheng, J., Jha, A., Vollmer, G., et al. (2021). Estradiol analogs attenuate autophagy, cell migration and invasion by direct and selective inhibition of TRPML1, independent of estrogen receptors. Sci Rep *11*, 8313. 10.1038/s41598-021-87817-4.
34. Abrahamian, C., and Grimm, C. (2021). Endolysosomal Cation Channels and MITF in Melanocytes and Melanoma. Biomolecules *11*, 1021.
35. Goding, C.R., and Arnheiter, H. (2019). MITF-the first 25 years. Genes Dev *33*, 983-1007. 10.1101/gad.324657.119.

36. Gelmi, M.C., Houtzagers, L.E., Strub, T., Krossa, I., and Jager, M.J. (2022). MITF in Normal Melanocytes, Cutaneous and Uveal Melanoma: A Delicate Balance. Int J Mol Sci *23*. 10.3390/ijms23116001.
37. Serman, N., Vranic, S., Glibo, M., Serman, L., and Bukvic Mokos, Z. (2022). Genetic risk factors in melanoma etiopathogenesis and the role of genetic counseling: A concise review. Bosn J Basic Med Sci *22*, 673-682. 10.17305/bjbms.2021.7378.
38. Guhan, S.M., Artomov, M., McCormick, S., Njauw, C., Stratigos, A.J., Shannon, K., Ellisen, L.W., and Tsao, H. (2020). Cancer risks associated with the germline MITF(E318K) variant. Sci Rep *10*, 17051. 10.1038/s41598-020-74237-z.
39. Yokoyama, S., Woods, S.L., Boyle, G.M., Aoude, L.G., MacGregor, S., Zismann, V., Gartside, M., Cust, A.E., Haq, R., Harland, M., et al. (2011). A novel recurrent mutation in MITF predisposes to familial and sporadic melanoma. Nature *480*, 99-103. 10.1038/nature10630.
40. Zhang, Y., and Wang, X. (2020). Targeting the Wnt/β-catenin signaling pathway in cancer. J Hematol Oncol *13*, 165. 10.1186/s13045-020-00990-3.
41. Sinnberg, T., Menzel, M., Ewerth, D., Sauer, B., Schwarz, M., Schaller, M., Garbe, C., and Schittek, B. (2011). β-Catenin signaling increases during melanoma progression and promotes tumor cell survival and chemoresistance. PLoS One *6*, e23429. 10.1371/journal.pone.0023429.
42. Wu, G., Huang, H., Garcia Abreu, J., and He, X. (2009). Inhibition of GSK3 phosphorylation of beta-catenin via phosphorylated PPPSPXS motifs of Wnt coreceptor LRP6. PLoS One *4*, e4926. 10.1371/journal.pone.0004926.
43. Wu, D., and Pan, W. (2010). GSK3: a multifaceted kinase in Wnt signaling. Trends Biochem Sci *35*, 161-168. 10.1016/j.tibs.2009.10.002.
44. Carreira, S., Goodall, J., Denat, L., Rodriguez, M., Nuciforo, P., Hoek, K.S., Testori, A., Larue, L., and Goding, C.R. (2006). Mitf regulation of Dia1 controls melanoma proliferation and invasiveness. Genes Dev *20*, 3426-3439. 10.1101/gad.406406.
45. Strub, T., Giuliano, S., Ye, T., Bonet, C., Keime, C., Kobi, D., Le Gras, S., Cormont, M., Ballotti, R., Bertolotto, C., and Davidson, I. (2011). Essential role of microphthalmia transcription factor for DNA replication, mitosis and genomic stability in melanoma. Oncogene *30*, 2319-2332. 10.1038/onc.2010.612.
46. Wellbrock, C., and Arozarena, I. (2015). Microphthalmia-associated transcription factor in melanoma development and MAP-kinase pathway targeted therapy. Pigment Cell Melanoma Res *28*, 390-406. 10.1111/pcmr.12370.
47. Haass, N.K., Beaumont, K.A., Hill, D.S., Anfosso, A., Mrass, P., Munoz, M.A., Kinjyo, I., and Weninger, W. (2014). Real-time cell cycle imaging during melanoma growth, invasion, and drug response. Pigment Cell Melanoma Res *27*, 764-776. 10.1111/pcmr.12274.
48. Vachtenheim, J., and Ondrušová, L. (2015). Microphthalmia-associated transcription factor expression levels in melanoma cells contribute to cell invasion and proliferation. Exp Dermatol *24*, 481-484. 10.1111/exd.12724.
49. Yuan, Y., Jaślan, D., Rahman, T., Bolsover, S.R., Arige, V., Wagner, L.E., 2nd, Abrahamian, C., Tang, R., Keller, M., Hartmann, J., et al. (2022). Segregated cation flux by TPC2 biases Ca(2+) signaling through lysosomes. Nat Commun *13*, 4481. 10.1038/s41467-022-31959-0.

50. Feldmann, C., Schänzler, M., Ben-Johny, M., and Wahl-Schott, C. (2023). Protocol for deriving proximity, affinity, and stoichiometry of protein interactions using image-based quantitative two-hybrid FRET. STAR Protoc *4*, 102459. 10.1016/j.xpro.2023.102459.
51. Dehairs, J., Talebi, A., Cherifi, Y., and Swinnen, J.V. (2016). CRISP-ID: decoding CRISPR mediated indels by Sanger sequencing. Sci Rep *6*, 28973. 10.1038/srep28973.
52. Chen, C.C., Keller, M., Hess, M., Schiffmann, R., Urban, N., Wolfgardt, A., Schaefer, M., Bracher, F., Biel, M., Wahl-Schott, C., and Grimm, C. (2014). A small molecule restores function to TRPML1 mutant isoforms responsible for mucolipidosis type IV. Nat Commun *5*, 4681. 10.1038/ncomms5681.
53. Grimm, C., Jors, S., Saldanha, S.A., Obukhov, A.G., Pan, B., Oshima, K., Cuajungco, M.P., Chase, P., Hodder, P., and Heller, S. (2010). Small molecule activators of TRPML3. Chem Biol *17*, 135-148. 10.1016/j.chembiol.2009.12.016.
54. Yamaguchi, S., Jha, A., Li, Q., Soyombo, A.A., Dickinson, G.D., Churamani, D., Brailoiu, E., Patel, S., and Muallem, S. (2011). Transient receptor potential mucolipin 1 (TRPML1) and two-pore channels are functionally independent organellar ion channels. J Biol Chem *286*, 22934-22942. 10.1074/jbc.M110.210930.
55. Liu, L., Limsakul, P., Meng, X., Huang, Y., Harrison, R.E.S., Huang, T.-S., Shi, Y., Yu, Y., Charupanit, K., Zhong, S., et al. (2021). Integration of FRET and sequencing to engineer kinase biosensors from mammalian cell libraries. Nature Communications *12*, 5031. 10.1038/s41467-021-25323-x.
56. Müller, M., Gerndt, S., Chao, Y.K., Zisis, T., Nguyen, O.N.P., Gerwien, A., Urban, N., Müller, C., Gegenfurtner, F.A., Geisslinger, F., et al. (2021). Gene editing and synthetically accessible inhibitors reveal role for TPC2 in HCC cell proliferation and tumor growth. Cell Chem Biol. 10.1016/j.chembiol.2021.01.023.
57. Scotto Rosato, A., Montefusco, S., Soldati, C., Di Paola, S., Capuozzo, A., Monfregola, J., Polishchuk, E., Amabile, A., Grimm, C., Lombardo, A., et al. (2019). TRPML1 links lysosomal calcium to autophagosome biogenesis through the activation of the CaMKKbeta/VPS34 pathway. Nat Commun *10*, 5630. 10.1038/s41467-019-13572-w.
58. Guzmán, C., Bagga, M., Kaur, A., Westermarck, J., and Abankwa, D. (2014). ColonyArea: an ImageJ plugin to automatically quantify colony formation in clonogenic assays. PLoS One *9*, e92444. 10.1371/journal.pone.0092444.

Figure legends

Figure 1. Expression of Rab7a in melanoma versus non-melanoma cancer cells, correlation with TPC2 expression, and direct interaction of Rab7a with TPC2.
(A) Gene expression profile (qPCR) of Rab7a in human melanoma lines compared to different non-melanoma cancer lines.
(B) Protein levels corroborating mRNA expression data in melanoma lines (compared to the breast cancer line MDA-MB-231).
(C) Gene expression profile (qPCR) of Rab7b in human melanoma lines compared to different non-melanoma cancer lines.
(D) Melanoma lines showing strong expression correlation between Rab7a and TPC2 but not TPC1.
(E) Gene expression profile (qPCR) showing relative expression of TPCs in human melanoma lines compared to different non-melanoma cancer lines.

(F-G) FRET experiments showing FRET efficiencies in HEK293 cells expressing $hTPC2^{WT}$ or $hTPC1^{WT}$ with $hRab7^{WT}$.

Figure 2. Effect of Rab7a on TPC2 activity.
(A) Effect of $PI(3,5)P_2$ in endolysosomal vesicles coexpressing human TPC2 and Rab7a or mutant variants of Rab7a. Shown are representative current density-voltage relationships from -100 to +100 mV with basal currents in black, 1μM $PI(3,5)P_2$ activated currents in red and ATP (1mM) blocked currents in blue, measured from apilimod-treated, enlarged endolysosomal vesicles expressing either $hTPC2^{WT}$, $hTPC2^{WT}$ + $hRAB7a^{WT}$, $hTPC2^{WT}$ + $hRAB7a^{Q67L}$ (constitutively active Rab7a) or $hTPC2^{WT}$ + $hRAB7a^{T22N}$ (dominant negative Rab7a).
(B and C), Analogous experiments for the lipophilic small molecule agonists of TPC2 TPC2-A1-P and TPC2-A1-N (10μM, each).
(D) Statistical summary of data comprising average current densities (mean ± SEM) at -100mV measured in endolysosomal patch-clamp experiments as shown in A-C. Each dot on the bar graph represents a single value current density measured from one endolysosome. Data were tested for statistical significance with one-way ANOVA test followed by Tukey's post-test (*p<0.05, ***p<0.001, ****p<0.0001).
(E) Representative GCaMP6s traces, with mean value curves highlighted in bold (color coded), each. Bar chart: Maximal change in fluorescence after application of TPC2 agonist TPC2-A1-N (mean ± SEM). Change in GCaMP6s fluorescence (ΔF) was normalized to baseline value (ΔF/F0), each. The baseline value (F0) was acquired by averaging fluorescence from a 30 s recording before addition of compound[49]. One dot corresponds to one experiment with 3-7 transfected cells, each.

Figure 3. Effect of Rab7 inhibitor on TPC2 activity and physical interaction of Rab7a with TPC2.
(A and B) Inhibition of $PI(3,5)P_2$ evoked currents in endolysosomal vesicles expressing human TPC2 alone or coexpressed with Rab7a using the Rab7 small molecule inhibitor CID1067700. Shown are representative current density-voltage relationships of enlarged endolysosomes, treated with apilimod, expressing $hTPC2^{WT}$ + $hRab7^{WT}$ or $hTPC2^{WT}$ alone, activated with 1μM $PI(3,5)P_2$ followed by application of CID1067700 in different concentrations as indicated. All the currents were further inhibited with 1mM ATP as positive control (max. effect).
(C) Statistical summary of data comprising average current densities at -100mV measured in endolysosomal patch-clamp experiments as shown in A-B. Each dot on the bar graph represents a single value current density measured from one endolysosome. Data were tested for statistical significance with one-way ANOVA test followed by Tukey's post-test (***p<0.001, ****p<0.0001).
(D) Cartoon showing CRISPR/Cas9 strategy to knockout *TPCN2* in the SK-MEL-5 melanoma cell line.
(E) qPCR data showing relative expression of TPC2 in WT and TPC2 KO SK-MEL-5 lines.
(F) Statistical summary of data comprising average current densities at -100mV measured in endolysosomal patch-clamp experiments as shown in G elicited with 20μM of the TPC2 agonist TPC2-A1-P (WT and TPC2 KO SK-MEL-5 lines, respectively). Each dot on the bar graph represents a single value current density measured from one endolysosome.
(G) Representative current density-voltage relationships from -100 to +100 mV showing basal, TPC2-A1-P activated and ATP (1mM) blocked currents, measured from apilimod-treated, enlarged endolysosomal vesicles, in SK-MEL-5 WT and TPC2-KO cells.

(H) Cartoon showing CRISPR/Cas9 strategy to knockout Rab7a in SK-MEL-5 melanoma cell line.
I) Western blot data showing Rab7a protein levels in WT and Rab7 KO SK-MEL-5 clone (C1x17), selected for further experiments. Clone (C2x2) showed no reduction in expression and was not used further.
(J) qPCR data depicting transcript levels of Rab7 KO SK-MEL-5 clone (C1x17), compared to WT.
(K and L) Representative current density-voltage relationships from -100 to +100 mV showing basal, TPC2-A1-P activated currents, measured in SK-MEL-5 Rab KO cells from apilimod-treated, enlarged endolysosomal vesicles (K) and corresponding statistics (L).
(M) qPCR data showing relative expression of TPC2 and Rab7a in WT and Rab7 KO SK-MEL-5 cells. Electrophysiological data (C, F, and L) were tested for statistical significance using a one-way ANOVA test followed by Tukey's post-test. Statistical significance for (M) was determined using two-way ANOVA followed by Bonferroni multiple comparisons test and for (I and J) by Student's t-test. Shown are mean values ± SEM, (n = 3, each). *P <0.05, **P < 0.01, ***P < 0.001, ****P < 0.0001.

Figure 4. Proliferation, migration and invasion in WT, TPC2 KO and Rab7 KO SK-MEL-5 cells.
(A and F) Ctb assay assessing proliferation of SK-MEL-5 cells monitored over 96 h comparing WT cells to different clones for TPC2 KO (A) and Rab7a KO (F).
(B and G) Genetic ablation of either TPC2 (B) or Rab7a (G) in SK-MEL-5 melanoma line shows significantly slower invasion and migration, cells seeded on transwell chambers and monitored overnight.
(C and H) Statistical analysis for Boyden chamber migration and invasion experiments in TPC2 KO (C) and Rab7a KO (H) SK-MEL-5 cells.
(D and I) Clonogenic assay showing significant reduction in survival and growth as single colonies for both TPC2 KO (D) and Rab7a KO (I) SK-MEL-5 cells.
(E and J) Statistical analysis for SK-MEL-5 TPC2 KO (E) and Rab7a KO (J) plotted as colony area percentage, fold induction on WT cells.
(K) qPCR and Western blot analysis indicating unchanged transcript and protein levels of Rab7a in TPC2 KO clones. Statistical significance in (A and F) carried out using two-way ANOVA followed by Bonferroni multiple comparisons test, in (C and K) determined by one-way ANOVA, and in (E, H, and J) assessed by Student's t-test. Shown are mean values ± SEM, (n = 3, each). *P <0.05, **P < 0.01, ***P < 0.001, ****P < 0.0001.

Figure 5. Proliferation and invasion for different melanoma lines using knockdown siRNA.
(A and B) Proliferation monitored over 72 h using Ctb assay of the following melanoma lines: SK-MEL-5, SK-MEL-29, SK-MEL-19, UACC-62, SK-MEL-103, SK-MEL-147, and A375 in non-silencing (NS) control cells compared to TPC2 KD (A) and Rab7a KD (B).
(C and E) Statistical analysis of cell invasiveness determined in the lines mentioned above using transwell boyden chambers coated with matrigel in both Rab7 KO (C) and TPC2 (E).
(D and F) Representative images of invasion phenotype in TPC2 KD (D) and Rab7a KD (F) cells in several melanoma lines compared to NS control.
Statistical significance was determined using two-way ANOVA followed by Bonferroni multiple comparisons test (A and B) and by Student's t-test (C and E). Shown are mean values ± SEM, (n = 3, each). *P <0.05, **P < 0.01, ***P < 0.001, ****P < 0.0001.

Figure 6. Expression of MITF and GSK3β in different melanoma lines and effects of Rab7a or TPC2 KOor small molecule blockers.

(A) Representative blots for MITF, Rab7a and GSK3β protein expression in different melanoma lines, compared to control breast cancer line (MDA-MB-231). All proteins normalized to Vinculin.
(B) Melanoma lines show strong expression correlation (protein) between Rab7a and MITF (r=0.9433) and Rab7a and GSK3β (r=0.9533).
(C and E) Genetic knockout of either TPC2 or Rab7a in SK-MEL-5 cells shows reduction in the protein levels of MITF and β-Catenin but increased expression of GSK3β.
(D) Statistical analysis for expression levels for MITF, GSK3β, and β-Catenin for WT vs. Rab7a KO, significance determined by Student's t-test.
(F) Statistical analysis for expression levels for MITF, GSK3β, and β-Catenin for WT vs. TPC2 KO, significance determined by one-way ANOVA. Shown are mean values ± SEM, (n = 3, each). *P <0.05, **P < 0.01, ***P < 0.001, ****P < 0.0001.
(G) Representative blots for MITF protein expression in different melanoma lines after treatment with the TPC2 inhibitor SG-094 (7μM) or DMSO control for 24h. Statistical analysis: significance determined by one-way ANOVA. Shown are mean values ± SEM, (n = 3, each). *P <0.05, ***P < 0.001, ****P < 0.0001.

Figure 7. Rescue experiments in SK-MEL-5 TPC2 and Rab7a KO melanoma lines.
(A and B) Proliferation of Rab7 KO (A) or TPC2 KO (B) SK-MEL-5 cells expressing mCherry vector alone, $Rab7^{WT}$-mCherry or $Rab7^{Q67L}$-mCherry, assessed for 24-, 48-, and 72-hr and normalized to mCherry vector.
(C and D) Proliferation assessed for 24-, 48-, and 72-hr for Rab7 KO (C) or TPC2 KO (D) SK-MEL-5 cells expressing $TPC2^{WT}$-mCherry normalized to $TPC2^{L265P}$-mCherry, $TPC2^{M484L}$-YFP normalized to $TPC2^{WT}$-YFP, and treatment with the agonist TPC2-A1P normalized to DMSO control vehicle.
(E, F, G, H) Representative images of the invasive phenotype determined by overexpression of mCherry vector alone, $Rab7^{WT}$-mCherry or $Rab7^{Q67L}$-mCherry in Rab7a KO (F) and TPC2 KO (H), normalized to mCherry vector and statistical analysis shown in (E) and (G), respectively. Statistical significance was determined using one-way ANOVA.
(I, J, K, L) Representative images and statistical analysis of the invasive phenotype determined by overexpression of $TPC2^{WT}$-mCherry, $TPC2^{M484L}$-YFP, and/or treatment with TPC2-A1P in Rab7a KO (I, J) and TPC2 KO (K, L), normalized to respective control (grey bars with black dots). Statistical significance was determined using one-way ANOVA followed by Bonferroni multiple comparisons test. Shown are mean values ± SEM, (n = 3, each). *P <0.05, **P < 0.01, ***P < 0.001, ****P < 0.0001.
(M, N, O) *In vivo* experiments showing tumour growth after subcutaneous injection (into the flank) of either B16F10luc WT, TPC2 KO or Rab7KO cells into 5-6 week old female C57Bl/6-Tyr mice as well as after Rab7KO cell injection in combination with daily intraperitoneal TPC2-A1-P injections (0.02mg/g) starting right after implantation of the cells (M). (N) Representative bioluminescence images from day 7 after injection are shown. (O) Line chart displaying bioluminescence signal intensities of tumours over time as mean ± SEM (n=15 for WT + TPC2-A1-P, n=17 for all other groups, ROUT outlier test [Q = 5%], Two-Way ANOVA, multiple comparison.

Supplementary Figures

Figure S1. FRET and co-immunoprecipitation experiments.
(A, B, C) FRET experiments showing FRET efficiencies in HEK293 cells expressing $hTPC2^{WT}$ + $hRab7^{WT}$, $hTPC2^{WT}$ + $hRab7^{Q67L}$, or $hTPC2^{WT}$ + $hRab7^{T22N}$ in presence of apilimod. Shown in B and C are the controls $Rab5^{WT}$ + $TPC2^{WT}$ (negative) and $Rab5^{WT}$ + $TPC1^{WT}$ (positive).

(D) Representative co-immunoprecipitation experiment indicating an interaction between both hRab7a^{WT}-mCherry and hTPC2^{WT}-YFP and hRab7a^{Q67L}-mCherry with hTPC2^{WT}-YFP[50].

Figure S2. Effect of Rab7a on TRPML1 activity.
(A and C) Effect of lipophilic small molecule agonist of TRPML1 ML1-SA1 in endolysosomal vesicles coexpressing human TRPML1 and Rab7a or mutant variants of Rab7a. Shown are representative current density-voltage relationships from -100 to +100 mV with basal currents in black, 10μM ML1-SA1 activated currents in red and EDME (10μM) blocked currents in blue, measured from apilimod-treated, enlarged endolysosomal vesicles expressing either hTRPML1^{WT}, hTRPML1^{WT} + hRAB7a^{WT}, hTRPML1^{WT} + hRAB7a^{Q67L} (constitutively active Rab7a) or hTRPML1^{WT} + hRAB7a^{T22N} (dominant negative Rab7a).
(B and C) Analogous experiments for PI(3,5)P_2 (1μM).
(C and D) Statistical summary of data comprising average current densities (mean ± SEM) at -100 mV measured in endolysosomal patch-clamp experiments as shown in (A) and (B). Each dot on the bar graph represents a single value current density measured from one endolysosome. Data were tested for statistical significance with a one-way ANOVA test followed by Tukey's post-test.
(E and F) Representative current density-voltage relationships from -100 to +100 mV showing basal, ML1-SA1 activated and EDME (10μM) blocked currents, measured from apilimod-treated, enlarged endolysosomal vesicles, in SK-MEL-5 WT cells (E) and Rab7a KO (F).
(G) Statistical summary of data comprising average current densities at -100 mV measured in endolysosomal patch-clamp experiments as shown in (E) and (F) elicited with 10μM of ML1-SA1 (WT and Rab7a KO SK-MEL-5 lines, respectively). Each dot on the bar graph represents a single value current density measured from one endolysosome. Data were tested for statistical significance using Student's t-test.

Figure S3. Knockdown efficiencies for different melanoma lines.
(A) TPC2 KD in different melanoma lines determined by transcript levels using qPCR, fold induction on NS control, normalized to the house-keeping gene HPRT.
(B) Rab7 KD efficiency determined by Western blot experiments showing reduced proteins levels, fold induction on NS control, normalized to β-Actin.
(C) Representative blots for Rab7 KD experiments as shown in B.
Statistical significance was determined using one-way ANOVA followed by Bonferroni multiple comparisons test. Shown are mean values ± SEM, (n = 3, each). **P < 0.01, ***P < 0.001, ****P < 0.0001.

Figure S4. Characterization of B16F10-luc Tpc2 and Rab7a knockout lines.
(A) Gene expression profile of TPC2 and Rab7a in the B16F10-luc cell line.
(B and C) CRISPR/Cas9 gene editing strategy used for the knockout of Tpcn2 (B) and Rab7 (C) in the B16F10-luc cells.
(D) Agarose gels showing KO clone selection with primers spanning exon 2 for PCR.
(E) Potential clones were sequenced and alignments of homozygous deletion clones 1B3 and 7B9 are shown. For all clones, homogeneity within the deletion amplicons was determined with Sanger sequencing and the CRISPR-ID *in silico* tool as described by Dehairs et al., 2016[51].
(F-G) Western blot results for the Rab7a KO in B16F10-luc cells.
(H) qPCR experiments showing reduced Tpcn2 transcript levels in the Tpc2 KO B16F10-luc cell line.
(I) qPCR experiments showing reduced Rab7a transcript levels in the Rab7a KO B16F10-luc cell line.

Statistical significance was determined using Student's t-test. Shown are mean values ± SEM, (n = 3, each). **P < 0.01, ****P < 0.0001.

Methods adapted from Cell Press

LIFE SCIENCE TABLE WITH EXAMPLES FOR AUTHOR REFERENCE

REAGENT or RESOURCE	SOURCE	IDENTIFIER
Antibodies		
anti-c-myc	Santa Cruz Biotechnology	sc-40
Anti-Mouse	Cell Signaling Technology	7076
Anti-Rabbit	Cell Signaling Technology	7074
anti-RFP	Proteintech	6g6
GAPDH	Cell Signaling Technology	5174
GSK3β	Cell Signaling Technology	9832
MITF	Cell Signaling Technology	97800
Rab7	Cell Signaling Technology	2094S
Rab7	Cell Signaling Technology	9367S
β-Catenin	Cell Signaling Technology	9562
β-Actin	Santa Cruz Biotechnology	Sc-47778
Bacterial and virus strains		
DH5α Competent Cells	Thermo Fisher	EC0112
Chemicals, peptides, and recombinant proteins		
2 x NuPAGE™ LDS - sample buffer	Invitrogen	NP0007
2-Mercaptoethanol	Merck	M3148
2-Propanol	Carl Roth	CP441.1
Agar	Merck	05040
Agarose	Carl Roth	3810.3
AIM-V	Thermo Fisher	31035-025
Ampicilin	Carl Roth	K029.2
anti-Myc magnetic agarose beads	Proteintech	ytma
ApaI	Thermo Fisher	FD1414
Apilimod	Axon Medchem	1369
ATP magnesium salt	Sigma Aldrich	A9187-500MG
BamHI	Thermo Fisher	FD0054
Blasticidin S -hydrochlorid	Merck	15205-25MG
Bradford Assay	BioRad	5000006
BSA	Sigma Aldrich	A3294
$CaCl_2$	Merck	1.02382
Ca-MSA	ChemCruz	Sc-486421
CID1067700	Sigma-Aldrich	SML0545
Crystal violet	Merck	C0775
D-(+)-Glucose	Sigma-Aldrich	G7021
D-(+)-Glucose	Sigma-Aldrich	G7021

DMEM (1 g/L glucose) + glutamaxi	Thermo Fisher	21885-025
DMEM (4.5 g/L glucose) + glutamaxi	Thermo Fisher	31966-047
DMSO (Dimethyl Sulfoxide)	Corning	25-950-CQC
DNase I, recombinant, Rnase free	Roche	4716728001
EDME	Rühl et al. 2021	PMID: 33859333
EGTA	Merck	324626
Ethanol	Carl Roth	5054.4
FastDigest Bpil	Thermo Fisher	FD1014
Fetal Bovine Serum (FBS)	Thermo Fisher	10500-064
G 418 disulfate salt solution	Sigma Aldrich	G8168-10ML
GeneRuler 1kb DNA Ladder	Thermo Fisher	SM0311
Geneticin™ Selective Antibiotic (G418 Sulfate)	Thermo Fisher	10131035
HEPES	Fisher Scientific	BP310
Immobilon® Crescendo Western HRP Substrate	Merck	WBLUR0500
Isoflurane CP 1mL/mL	cp pharma	1214
Kanamycin	Carl Roth	T832.3
KCl	Carl Roth	6781.1
K-MSA	Sigma-Aldrich	83000
KOH	Merck	1.05032
Lipofectamine 2000	Thermo Fisher	11668027
Lipofectamine 3000	Thermo Fisher	L3000-015
Matrigel basement membrane matrix	Corning	354234
MEM	Thermo Fisher	10370-021
MES	Merck	M2933
Methanol	Merck	34860
$MgCl_2$	Sigma-Aldrich	M2670
ML1-SA1	Spix et al. 2022	PMID: 32184778
NaCl	Sigma-Aldrich	S5886
Na-MSA	Acros Organics	442111000
NaOH	Sigma-Aldrich	06306
NheI	Thermo Fisher	FD0974
Nitrocellulose Membrane	Millipore Merck	GE10600007
OptiMEM	Thermo Fisher	31985-070
PageRulerTM Prestained Protein Ladder	Thermo Fisher	26616
Penicillin-Streptomycin (10,000 units)	Sigma Aldrich	p4333-100ML
peqGREEN DNA/RNA Dye	VWR, peqlab	37-5010
Phosphatase Inhibitor Cocktail Tablets	Roche	04906845001
Phosphate-buffered saline	Thermo Fisher	14190169
$PI(3,5)P_2$-di8	Echelon Biosciences	P-350
Plasmid Safe Exonuclease (1000 units)	Biozym	161010
Polycarbonate membranes	Corning	3421
Poly-L-Lysine	Serva	33225.01
Poly-L-Lysine	Sigma Aldrich	P4832
Poly-L-ornithine hydrobromide	Sigma Aldrich	P3655-100MG
D-Luciferin, potassium salt	Thermo Fisher	L2916
Protease Inhibitor Cocktail Tablets	Roche	04693132001
Protein Assay Dye Reagent Con-centrate	Bio-Rad	500-0006
Puromycin	Sigma Aldrich	P8833-10MG
Puromycin -dihydrochlorid	Sigma Aldrich	P9620

PVDF membrane	Millipore Merck	IPVH00010
ROTIPHORESE ® Gel 30	Carl Roth	3029.1
Rotiphorese® Gel 30	Carl Roth	3029.1
RPMI 1640	Thermo Fisher	21875-034
SG094	Müller et al., 2021	PMID: 33626324
Sodium deodecyl sulfate	Carl Roth	2326.2
Sodium Pyruvate	Thermo Fisher	11360070
Solutol HS-15	Sigma Aldrich	42966
T4 DNA ligase	Thermo Fisher	15224090
TEMED	Carl Roth	2367.1
TPC2-A1-N	Gerndt et al., 2020	PMID: 32167471
TPC2-A1-P	Gerndt et al., 2020	PMID: 32167471
TRIS base	Sigma Aldrich	T1503
TRIS hydrochloride	Merck	PHG0002
Triton X-100	Sigma Aldrich	X100
Triton™ X-100	Merck	1.08603
Trizma Base	Sigma Aldrich	T1503
Trypsin-EDTA	Thermo Fisher	15400-054
Turbofect	Thermo Fisher	R0532
Tween 20	Carl Roth	9127.1
Critical commercial assays		
CellTiter-Blue®	Promega	G8081
GoTaq® G2 Hot Start Master Mix	Promega	M7423
High Fidelity PCR Kit	Roche	12140314001
Light Cycler® 480 SYBR Green I Master Mix	Roche	04707516001
NucleoSpin Plasmid Kit	Macherey Nagel	740588.250
PureLink™ HiPure Plasmid Filter Midiprep Kit	Thermo Fisher	K210015
Q5® High-Fidelity DNA Polymerase	NEB	M0491L
QIAprep Spin Miniprep kit	Qiagen	27104
RevertAid First Strand cDNA Syn-thesis Kit	Thermo Fisher	K1621
RNeasy Plus Mini Kit	Qiagen	74134
Site-directed mutagenesis Kit	Agilent	200518
Deposited data		
Raw and analyzed data	This paper	
Experimental models: Cell lines		
A375	ATCC	CRL-1619
B16F10-luc	ATCC	CRL-6475
Caco-2	DSMZ	ACC 169
CHL-1	ATCC	CRL-9446
HEK293	ATCC	CRL-3216
Hela	ATCC	CRM-CCL-2
HepG2	DSMZ	ACC 180
Huh-7	Japanese Collection of Research Bioresources	JCRB040
MCF-7	DSMZ	ACC 115
MDA-MB-231	DSMZ	ACC 732

MNT-1	A gift from Dr. Santiago Di Pietro at the department of Biochemistry and Molecular Biology, Colorado State University, Fort Collins, CO, USA	PMID: 33875769
Panc-1	DSMZ	ACC 783
SK-BR-3	ATCC	HTB-30
SK-MEL-103	A gift from Dr. Marisol Soengas at the Melanoma Laboratory, Molecular Pathology Programme, Centro Nacional de Investigaciones Oncológicas, Madrid, Spain	PMID: 24981740
SK-MEL-147	A gift from Dr. Marisol Soengas at the Melanoma Laboratory, Molecular Pathology Programme, Centro Nacional de Investigaciones Oncológicas, Madrid, Spain	PMID: 24981740
SK-MEL-19	A gift from Dr. Marisol Soengas at the Melanoma Laboratory, Molecular Pathology Programme, Centro Nacional de Investigaciones Oncológicas, Madrid, Spain	PMID: 24981740
SK-MEL-2	ATCC	HTB-68
SK-MEL-28	ATCC	HTB-782
SK-MEL-29	A gift from Dr. Marisol Soengas at the Melanoma Laboratory, Molecular Pathology Programme, Centro Nacional de Investigaciones Oncológicas, Madrid, Spain	PMID: 24981740
SK-MEL-5	ATCC	HTB-70
SKOV3	ATCC	HTB-77
U-87 MG	ATCC	HTB-14

UACC-62	A gift from Dr. Marisol Soengas at the Melanoma Laboratory, Molecular Pathology Programme, Centro Nacional de Investigaciones Oncológicas, Madrid, Spain	PMID: 24981740
Experimental models: Organisms/strains		
C57BL/6BrdCrHsd-Tyr^{c}	Envigo	85
Oligonucleotides		
hHPRT qPCR: fw: 5'- TGGCGTCGTGATTAGTGATG-3', rev: 5'-AACACCCTTTCCAAATCCTCA-3	This paper	
hEMC-7 qPCR: fw: 5'-AAAGGAGGTAGTCAGGCCG-3', rev: 5'-GTTGCTTCACACGGTTTTCCA-3'	This paper	
hRab7a qPCR: fw: 5'-TGACTGCCCCCAACACATTC-3', rev: 5'-TCCGTGCAATCGTCTGGAAC-3'	This paper	
hRab7b qPCR: fw: 5'-CCTCCCTCCTTCACCAATA-3', rev: 5'-CAGTGTGGTCTGGTATTCCTCA-3'	This paper	
hTPCN1 qPCR::5'-TCC CAAAGCGCTGAGATTAC-3', rev: 5'-TCTGGTTTGAGCTCCCTTTC-3'	This paper	
hTPCN2 qPCR: fw: 5'-GTACCCCTCTTGTGTGGACG-3', rev: 5'-GGCCCTGACAGTGACAACTT-3'	This paper	
mHprt qPCR: fw: 5'-GCTCGAGATGTCATGAAGGAGAT-3', rev: 5'-AAAGAACTTATAGCCCCCCTTGA-3'	This paper	
mRab7 qPCR: fw: 5'-AGCCACAATAGGAGCGGACT-3', rev: 5'-CAAGTCTGTCGTCCACCATC-3'	This paper	
mTpc2 qPCR: fw: 5'-TAAAGTACCGCTCCATCTACCA-3', rev: 5'-GCAGACGTTCGAGTAATACCAG-3'	This paper	
hRab7: Exon 2 PCR Primers: fw: 5'-TAGAAATCCCTGTGGCCTGG-3', rev: 5'- AC CCAACCTACCACAGAATC-3'	This paper	
hRab7a: sgRNA A2: 5'-TGGGTGGTGGATCAATTGAA-3'	This paper	
hRab7a: sgRNA B2: 5'-GTGCACTAAGAACGCACATC-3'	This paper	
hTPC2: Exon 3 PCR Primers: fw: 5'-CACAGCCGGCATCTTTCCTT -3', rev: 5'- TG TCCAAGAAAGTGTGCCTTGC-3'	Yuan et al., 2022	PMID: 35918320
hTPC2: sgRNA A: 5'-ACCCACCCGGGACCTAGAAT-3'	Yuan et al., 2022	PMID: 35918320
hTPC2: sgRNA F: 5'-GAGCGTGGACACTCGTGACT-3'	Yuan et al., 2022	PMID: 35918320
mRab7: Exon 2: PCR Primers: fw: 5'-TGTGCCCTCTCCCATCAATC-3', rev: 5'-TCTTGCACGGACCTTCACAC-3'	This paper	

mRab7: Exon 2: PCR Primers: fw: 5'-TGCCCTCTCCCATCAATCAC-3', rev: 5'-TTCTTGCACGGACCTTCACACC-3'	This paper	
mRab7 sgRNA A1: 5'-GCACAGGGCGCTCCTTAAAT-3'	This paper	
mRab7 sgRNA A2: 5'-CTAAAGGGTTCACAGGCCGG-3'	This paper	
mRab7 sgRNA A1: 5'-ATTTAAGGAGCGCCCTGTGC-3'	This paper	
mRab7 sgRNA B3: 5'- ATTCCTATACTCTACCCCAC-3'	This paper	
mTpc2: sgRNA pair 1 top: 5'-CACCGTCTACTAACAGGGCACGTGC-3'	Müller et al., 2021	PMID: 33626324
mTpc2: sgRNA pair 1 bottom: 5'-CACCGACAGTCTTAGCCCGTGCCAA-3'	Müller et al., 2021	PMID: 33626324
mTpc2: sgRNA pair 2 top: 5'-CACCGACAGTCTTAGCCCGTGCCAA-3'	Müller et al., 2021	PMID: 33626324
mTpc2: sgRNA pair 2 bottom: 5'-AAACTTGGCACGGGCTAAGACTGTC-3'	Müller et al., 2021	PMID: 33626324
ON-TARGETplus Human non-targeting control pool. Sequences were as follows: duplex 1: 5'-UGGUUUACAUGUCGACUAA-3', duplex 2: 5'-UGGUUUACAUGUUGUGUGA-3', duplex 3: 5'-UGGUUUACAUGUUUUCUGA-3', duplex 4: 5'-UGGUUUACAUGUUUUCCUA-3'	Dharmacon	D-00181-10-20
ON-TARGETplus Human TPCN2 siRNA -SMARTpool. Sequences were as follows: duplex 1: 5'-GGGAGAGGCUGACCUACUU-3', duplex 2: 5'-GCAAACCUGGUGUCCAUUU-3', duplex 3: 5'-GGUGGGACCUCUGCAUUGA-3', duplex 4: 5'-GGUGGUCUACUACGUAUUU-3'	Dharmacon	L-006508-00-0005
siRNA against Rab7a: 5'- CUGAACCUAUCAAACUGGA-3'	Sigma-Aldrich	SASI_Hs01_00104357
Recombinant DNA		
pSpCas9(BB)-2A-Puro plasmid	Müller et al., 2021	PMID: 33626324
eSpCas9_2A_Blasti plasmid	Müller et al., 2021	PMID: 33626324
eSpCas9(BB)_2A_GFP (PX458)	Addgene	48138
hTPC2-YFP	Chao et al., 2017	PMID: 28923947
hTPC2^{M484L}-YFP	Chao et al., 2017	PMID: 28923947
hTPC2-GCaMP6s	Gerndt et al., 2020	PMID: 32167471
hTPC2^{L265P}-GCaMP6s	Gerndt et al., 2020	PMID: 32167471
hTPC2-mCherry	Gerndt et al., 2020	PMID: 32167471
hTPC2^{L265P}-mCherry	Gerndt et al., 2020	PMID: 32167471
hTPC2-myc	A gift from Prof. Sandip Patel from the department of Cell and Developmental Biology, University College London, London, UK	
hTRPML1-YFP plasmid	Grimm et al., 2010	PMID: 20189104

hRab7a^{WT}-mCherry	This paper	
hRab7a^{T22N}-mCherry	This paper	
hRab7a^{Q67L}-mCherry	This paper	
Software and algorithms		
CRISPOR TEFOR	Haeussler et al., 2016	http://crispor.tefor.net/
ImageJ Fiji	NIH	https://imagej.nih.gov/ij/
ImageStudio software v1.0.19	ImageStudio^{TM}	https://www.licor.com/bio/image-studio/
LAS X 5.1.0 software	Leica Microsystems	https://www.leica-microsystems.com/products/microscope-software/p/leica-las-x-ls/
Light Cycler 480 software v1.5.1	Roche	https://www.roche.de/diagnostik/produkte-loesungen/systeme/lightcycler-systeme
Living Image® 4.7.4	Perkin Elmer	https://www.perkinelmer.com/de/lab-products-and-services/resources/in-vivo-imaging-software-downloads.html
MatLab function	MathWorks	https://matlab.mathworks.com/
Origin9	OriginLab	https://www.originlab.com/
Patchmaster Acquisition software	HEKA	https://www.heka.com/downloads/downloads_main.html#down_patchmaster_next
Prism 8	GraphPad	https://www.graphpad.com/

METHOD DETAILS

Plasmids

The human TPC2-YFP (C-terminally tagged) plasmid[26] and the TRPML1-YFP plasmid[52,53] were used for all patch-clamp measurements as well as human Rab7a-mCherry (N-terminally-tagged). All plasmids used for FRET measurements were generated using restriction-insertion cloning. For the construct mTq2-Rab7a, the cDNA sequence of mTurquoise was fused 5' to the sequence of human Rab7a (CCDS3052.1) and cloned into a pcDNA3.1+ expression vector. The mTq2-Rab7b (CCDS73011.1) construct and the mTq2-Rab5 (CCDS2633.1) construct were generated by replacing the Rab7a in mTq2-Rab7a. mTq2-Rab7a^{Q67L} and mTq2-Rab7A^{T22N} were generated by editing the mTq2-Rab7a via Quikchange (Agilent). Human TPC1 (CCDS31908.1) and TPC2 (CCDS8189.1) were cloned into a pcDNA3.1+ expression vector together with a C-terminal

mVenus. Single mTurquoise2 and mVenus were each cloned into pcDNA3.1+. Three tandem-constructs containing both mTurquoise2 and mVenus separated by linker sequences of different lengths were generted. For the shortest tandem-construct (Dimer-3AA) both fluorophores are separated by a GSG-linker. The second tandem-construct (Dimer-42AA) contains a 42-amino acid-long randomized sequence separating both fluorophores. The third tandem-construct (Dimer-2A) contains a 2A-peptide as a linker sequence. The original plasmid was a kind gift from Prof. Dorus Gadella (Addgene #98885). mNeongreen was exchanged with mVenus. The following plasmids were used: hTRPML1-YFP plasmid[53], the hTPC2-YFP[26] and hTPC2^{M484L}-YFP[26], hTPC2-GCaMP6s[31], hTPC2^{L265P}-GCaMP6s[31], hTPC2-mCherry[31], and hTPC2^{L265P}-mCherry[31]. The hTPC2-myc plasmid was a gift from Prof. Sandip Patel[54]. For hRab7a^{WT}-mCherry: Rab7A was amplified using High Fidelity PCR Kit (Roche). Sequences were as follows: fw: 5'- CTGTACAAGGGATCCGGAATGACCTCTAGGAAGAAAGTGTTGCTGAAG-3' and rev: 5'-GTCGGGCCCTCAGCAACTGCAGCTTTCTGCC-3' and cloned into pcDNA3.1+ using BamHI (Thermo Fisher) and ApaI (Thermo Fisher) via restriction and ligation cloning (Thermo Fisher). The following steps apply to all constructs: The plasmids are transformed into DH5-a (Thermo Fisher). Bacteria were plated on LB agar plates containing 100 µg/ml Ampicillin. Single colonies were picked and cultured overnight in 100 µg/ml Ampicillin LB liquid media at 37° C at 135 RPM. Plasmid purification was conducted with (Macherey Nagel). mCherry was amplified using High Fidelity PCR Kit (Roche). Sequences were as follows: fw: 5'-GGAGACTCGGCTAGCATGGTGAGCAAGGGCGAGG-3' and rev: 5'GGGTCCGGATCCCTTGGTACAGCTCGTCCATGCC-3' and cloned into the Rab7 containing vector N-terminally using NheI (Thermo Fisher) and BamHI (Thermo Fisher) as described above. For hRab7a^{Q67L}- mCherry: hRab7a^{WT}- mCherry was altered via Quikchange (Agilent). Sequences as follows: 5'-GGACACAGCAGGACTGGAACGGTTCCAGT-3' and rev: 5'- ACTGGAACCGTTCCAGTCCTGCTGTGTCC-3'. The entire insert (mCherry-Rab7A[Q67L]) was subcloned into pcDNA3.1 using NheI (Thermo Fisher) and ApaI (Thermo Fisher). For hRab7a^{T22N}-mCherry: hRab7a^{WT}-mCherry was altered using a site-directed mutagenesis Kit (Agilent). Sequences as follows: fw: 5'-GGAGATTCTGGAGTCGGGAAGAACTCACTCATGAACCAG-3' and rev: 5'-CTGGTTCATGAGTGAGTTCTTCCCGACTCCAGAATCTCC-3'. The entire insert (mCherry-Rab7A[T22N]) was subcloned into pcDNA3.1 using NheI (Thermo Fisher) and ApaI (Thermo Fisher).

Two-hybrid FRET experiments

For FRET experiments 17mm glass-bottom imaging dishes (Ibidi 81218-200) were treated for 2 hours with Poly-L-Lysine. Cells were seeded two days prior to measurement. Cells were transfected with Lipofectamine 2000 (Thermo Fisher) one day before measurement. Each FRET pair was transfected using 0.7µg of donor plasmid DNA (mTq2 constructs) and 1.5µg of acceptor plasmid DNA (mVenus constructs) to compensate for the lower expression rate of the channel-proteins (TPC1, TPC2, TRPML1). Images of live HEK293 cells were acquired using a Zeiss LSM980 inverted confocal microscope using a 60X oil Objective at excitation wavelengths of 445 nm and 515 nm for mTurquoise2 and mVenus, respectively. Images were acquired in three emission channels using bidirectional line-scans: mTq2DIRECT (445 nm ex; 455-526 nm em), mTq2FRET (445 nm ex; 455-526 em), mVenusDIRECT (515 ex; 526-561 em). Images were analysed using FIJI and processed with a weak Gaussian-blur. Regions of interest were drawn around mVenus-positive lysosomes. Using a FIJI macro, the mean intensity of fluorescence in

each ROI in all channels were calculated and formatted in a .csv table. Calibration constants were obtained from cells expressing single mTurquoise2, single mVenus and tandem construct, respectively. FRET Two-Hybrid curves were generated using a custom MatLab function (MathWorks). Calculation was performed according to Liu et al., 2020[55].

siRNA knockdown and compounds

Cells were silenced using small interfering RNA (siRNA) and transfection in the melanoma cell lines using lipofectamine 3000 regent (Thermo Fisher). The following siRNAs were used for experiments: hRab7a (Sigma-Aldrich), hTPC2 (Dharmacon SMARTpool) in a mixture of four oligonucleotide duplexes and non-targeting Scramble control siRNA (Dharmacon SMARTpool) was used as a control. For rescue experiments and whole-endolysosomal patch-clamp recordings, the following small-molecules/drugs were used: $PI(3,5)P_2$-di8 (Echelon Biosciences), ATP-Mg (Sigma-Aldrich), CID1067700 (Sigma-Aldrich), TPC2-A1-P and TPC2-A1-N[31], and SG094[16] .

Cell culture

Human embryonic kidney HEK293 cells were cultured in DMEM (Gibco, containing 1g/L glucose) supplemented with 100U/ml of Penicillin-streptomycin (Pen/Strep) (Sigma-Aldrich), and 10% of fetal bovine serum (FBS) (Thermo Fisher). The following cancer lines were cultured in DMEM (4.5g/L glucose, Thermo Fisher) supplemented with 100U/ml of Penicillin-streptomycin and 10% of FBS: SK-MEL-5, SK-MEL-28, A375, SK-MEL-19, SK-MEL-29, SK-MEL-103, SK-MEL-147, UACC-62, CHL-1, Huh-7, HepG2, MDA-MB-231, MCF-7, SK-BR-3, SKOV3, Hela, and Caco-2. MNT-1 cells were cultured in MEM (Thermo Fisher), 20% FBS, 10% AIM-V (Thermo Fisher), 1% sodium pyruvate (Thermo Fisher), and 1% Pen/Strep. The neuroblastoma cell line, U87MG, was cultured in MEM eagle with 10% FBS and 1% Pen/Strep. While cell lines: Panc-1, SK-MEL-2 and B16F10luc were cultured in RPMI 1640 (Thermo Fisher), 10% FBS, and 1% Pen/Strep. Cells were washed with 1x phosphate buffered saline (PBS) (Thermo Fisher) and detached from the surface of cell culture plates using Trypsin-EDTA (1x) (Thermo Fisher). Cell lines were maintained in an incubator at 37°C with 5% carbon dioxide.

CRISPR/Cas9 knockout lines

The creation of human TPC2 knockout was described in Yuan et. al 2022[47] (Figure S2). Additional confirmatory experiments are present here in Figure 3. Three SK-MEL-5 TPC2-KO clones (AF9, AF19, and AF22) were used for the experiments. Human and mouse Rab7a-KO was generated by targeting Exon 2. Guide RNAs were designed in Intron 1/2 and Intron 2/3. Murine TPC2 KO strategy in the B16F10-luc cells was adapted from Müller et al., 2021[56]. Cloning of sgRNAs was performed into eSpCas9(BB)_2A_GFP (PX458), subsequently selection and single cell sorting was performed via FACS (BD FACSAria Fusion). All KO clones were all validated using genotyping analysis by genomic PCR, genomic sequencing, and RT-qPCR. Moreover, hTPC2-KO clones were further validated using endolysosomal patch clamp experiments, measuring lysosomal currents using ATP and agonist stimulation (TPC2-A1P). While hRab7a-KO clone (C1x17) in SK-MEL-5 and mRab7 KO in B16F10-luc was validated using western blotting. The

following antibodies were used for human Rab7 protein from Cell Signaling Technology: 2094S and 9367S, binding around residues Asp193 and Glu188, respectively, corresponding to Exon 6.

Whole-endolysosome manual patch-clamp

For endolysosomal patch-clamp recordings, HEK293 and SK-MEL-5 cells were seeded into 24 well plates with poly-L-lysine (Serva) coated coverslips with a cell density of 60-70%, followed by transient transfection of the cells with proteins of interest using TurboFect Transfection Reagent (Thermofisher) in the case of HEK cells. SK-MEL-5 cells were used for endogenous assessment of endolysosomal currents. Co-transfection of TPC2 and Rab7a, and TRPML1 and Rab7a plasmids was performed in a ratio of 2:1, respectively. After 12-24 h transfection, HEK293 cells were treated overnight with 1mM Apilimod (Axon Medchem) to enlarge lysosomes and late endosomes. The compound was washed out before patch-clamp experiments were performed. Data were digitized at 49kHz and filtered at 2.8kHz. All the currents measured were recorded using an EPC-10 patch-clamp amplifier and PatchMaster acquisition software (HEKA). Recording pipettes were polished with a 4-6 MΩ resistance. Liquid junction potential was corrected. All experiments were conducted at room temperature (23-25°C). The cytoplasmic solutions were replaced after application of agonists or antagonists. Individual ramp current recordings were extracted at the -100mV current amplitudes. Unless otherwise stated, the extracellular/bath solution consisted of 140mM K-MSA, 5mM KOH, 4mM NaCl, 0.39mM $CaCl_2$, 1mM EGTA, 10mM HEPES with a 7.2 pH adjusted with KOH (300mOsm adjusted with D-(+)-glucose). The pipette/luminal solution contained 140mM Na-MSA, 5mM K-MSA, 2mM Ca-MSA, 1mM $CaCl_2$, 10mM HEPES, 10mM MES adjusted with methanesulfonic acid (310mOsm adjusted with D-(+)-glucose) to pH 4.6. In all of the experiments, 500-ms voltage ramps from -100 to +100mV were applied every 5s. All statistical analysis was done using Origin8 or GraphPadPrism software.

Ca^{2+} imaging

Ca^{2+} imaging was performed using an inverted Leica DMi8 live cell microscope. Recordings and adjustments were executed within LAS X software. At first, the DMEM was washed away from the 6-well plates with HEK293 cells, transfected with GCaMP6-tagged plasmids. Ca^{2+}-free buffer was used to carefully rinse the wells with cells before placing the glass coverslips to an imaging chamber. All GCaMP6 experiments were conducted in Ca^{2+}-free buffer comprising 138 mM NaCl, 6 mM KCl, 1 mM $MgCl_2$, 10 mM HEPES, and 5.5 mM D-glucose monohydrate (adjusted to pH = 7.4 with NaOH). To create Ca^{2+}-free environment around the cells, 450 µL of Ca^{2+}-free buffer was added to the chamber slowly, not to wash away the cells. The osmolarity of the Ca^{2+}-free buffer was also 300 mOsmol/L. GCaMP6 was excited at 470 nm (GFP excitation wavelength) and emitted fluorescence was captured with a 515 nm long-pass filter. Images were obtained every 2.671 sec with 63x objective. When the GCAMP6-tagged plasmid was co-transfected with mCherry-tagged plasmids the co-localization of GCaMP6 and mCherry signals was visually verified and these cells were chosen for measurement. mCherry was excited at 568 nm and the emitted fluorescence was captured at a 590 nm filter. For quantification of change in Ca^{2+} acquired by GCaMP6 fluorescence, regions of interest ROIs were drawn around each cell, expressing only GCaMP6 or only co-localized GCaMP6 and mCherry. The background area without cells was selected for manual background subtraction. Fluorescence was calculated using LAS X software. The baseline value (F_0) was acquired by averaging fluorescence from a 30 sec recording before

the addition of a compound. Change in GCaMP6 fluorescence (ΔF) was normalized to the baseline value ($\Delta F/F_0$) for the data presentation.

RT-qPCR

Total RNA was extracted from cell lines using RNeasy Plus Mini Kit (Qiagen) according to the manufacturer's protocol. cDNA was synthesized from total RNA with RevertAid First Strand cDNA Synthesis Kit (Thermo Scientific). Real-time quantitative Reverse Transcription PCR (qPCR) was performed using LightCycler 480 SYBR Green I Master Mix (Roche) and Light Cycler 480 Instrument (Roche, Light Cycler 480 software v1.5.1). Reactions were carried out in triplicates under conditions according to manufacturer's recommendations. The sequences for the primers used for RT-qPCR are found in the key resources table.nRelative expression of target gene levels was determined by normalization against the house-keeping genes for the appropriate species.

Western blotting (WB) and co-immunoprecipitation experiments

Buffers prepared and western blot experiments were performed as described previously[19,57]. For co-immunoprecipitation: HEK293 cells were plated on a 100 mm dish, and co-transfected at ca. 70 % confluence with the respective plasmids via TurboFect (Thermo Fisher). 48 h post-transfection, cells were washed with ice-cold 1x PBS, and lysed with ice-cold lysis buffer containing: 1x PBS, 1 % Triton X-100, supplemented with 1x protease inhibitor (Merck) and 1x phosphatase inhibitor (Roche). The cell lysate was incubated for 30 min on ice, and vortexed. To clear the cell suspension, the lysate was centrifuged for 20 min at 17,000 g, 4 °C. Protein concentration of the supernatant was quantified via a Bradford assay (BioRad). Myc-tagged TPC2 and Myc-tag only overexpressed from the "empty vector" were immunoprecipitated with anti-Myc magnetic agarose beads (Proteintech). Beads were washed with lysis buffer and incubated with 1 mg of protein, rotating overnight at 4°C. To ensure the removal of unspecific interaction partners, beads were washed three times with lysis buffer. After washing, the interaction partners were eluted from the beads by adding 2 x NuPAGE™ LDS - sample buffer (+ 10 % 2-mercaptoethanol) and incubating for 10 min at 95 °C. The "input sample" (30 µg protein sample) was treated the same way for preparation of SDS-PAGE and western blot. For analysis, the proteins were separated on a 7 % SDS-PAGE gel, transferred to a PVDF membrane (0.45 µm, Miilipore). Membranes were developed via incubation with Immobilon Crescendo Western HRP substrate (Merck) and the Odyssey FC Imaging System (LI-COR) running the ImageStudio software v1.0.19. Proteins were quantified using unsaturated images for the ImageJ 1.52a software. The following primary antibodies were used at 1:1,000 concentration in 5% Bovine Serum Albumin (BSA) diluted in tris buffered saline supplemented with 0.5% Tween-20 (TBS-T).

Cell proliferation and colony formation assays

Cells were seeded overnight in triplicates in flat-bottom 96-well microtiter plates (Sarstedt), using cells measured at 0-hrs as control blank. Proliferation was assessed using the CellTiter-Blue (Ctb) assay (Promega). Fluorescence was measured after 3 hours of adding Ctb using the FLUOstar Omega running Reader at 560Ex/600Em (BMG LAB-TECH). For the colony formation assay, cells were seeded at a low-density of 2000 cells per well in 6-well plates and grown over 3 weeks in the incubator at 37 °C with 5% CO_2. Then, cells were fixed and stained with 0.5% crystal violet

(Merck) in methanol (Carl Roth). Images were analyzed using ImageJ 1.52a software and the ImageJ plugin downloaded from and described in Guzmán et al., 2014[58].

Invasion and migration

Melanoma cells were seeded on 24-well transwell permeable supports polycarbonate membranes (Corning, 3421). The cells were pre-silenced or pre-stimulated with compounds then were additionally directly stimulated. The upper chambers contained the cells in serum-free medium and +/- compound. While the lower wells contained the chemotactic agent (10% FBS) and +/- compound. The distinction between the migration and invasion assay is the pre-coating the transwells for the latter with matrigel basement membrane matrix (Corning).

Statistical analysis

Analysis of the recordings was completed with Origin9, whilst statistics were generated with GraphPad Prism from a minimum of three repetitive, independent experiments. In addition, all the error bars depicted are ± SEM. Statistical comparison and significance were made using one-way ANOVA, two-way ANOVA followed by Bonferroni multiple comparisons test, or Student's t-test depending on the statistical analysis required in each figure, described in further detail in corresponding figure legends.

***In vivo* experiments: Ectopic tumour model**

17 C57Bl/6-Tyr mice (Envigo), female, 5-6 weeks old, were injected with either 2×10^6 B16F10luc WT, TPC2 KO or Rab7KO cells subcutaneously into the flank. Treatment of mice with vehicle control or TPC2-A1-P (0.02mg/g) was performed daily starting right after implantation of cells. Compound was dissolved in a solution containing 85% PBS, 10% Solutol-15® and 5% DMSO and injected intraperitoneally with a volume of 100µL. Bioluminescence imaging was performed on day 2, 5, 7, 9, 12 and 14 after implantation of cells following intraperitoneal injection of 6 mg/mL luciferin per mouse Previously, mice were put under anesthesia with 2.5% isoflurane in oxygen. Imaging of mice was performed in ventrodorsal position and mice were kept under narcosis with 1.5% isoflurane in oxygen. Hypothermia was prevented by a heating plate (37°C). The tumor signal per defined region of interest was calculated as photons/second/cm (total flux/area) using the Living Image 4.4 software (Perkin Elmer). All research performed complies with all relevant ethical regulations. Animals were used under animal protocols approved by the government (Regierung von Oberbayern, ROB-55.2-2532.Vet_02-22-5), and University of Munich (LMU) Institutional Animal Care Guidelines. Mice were housed in rooms maintained at constant temperature (20-24°C) and humidity (45-65%) with a 12-hour light cycle. Animals were allowed food and water ad libitum.

Figure

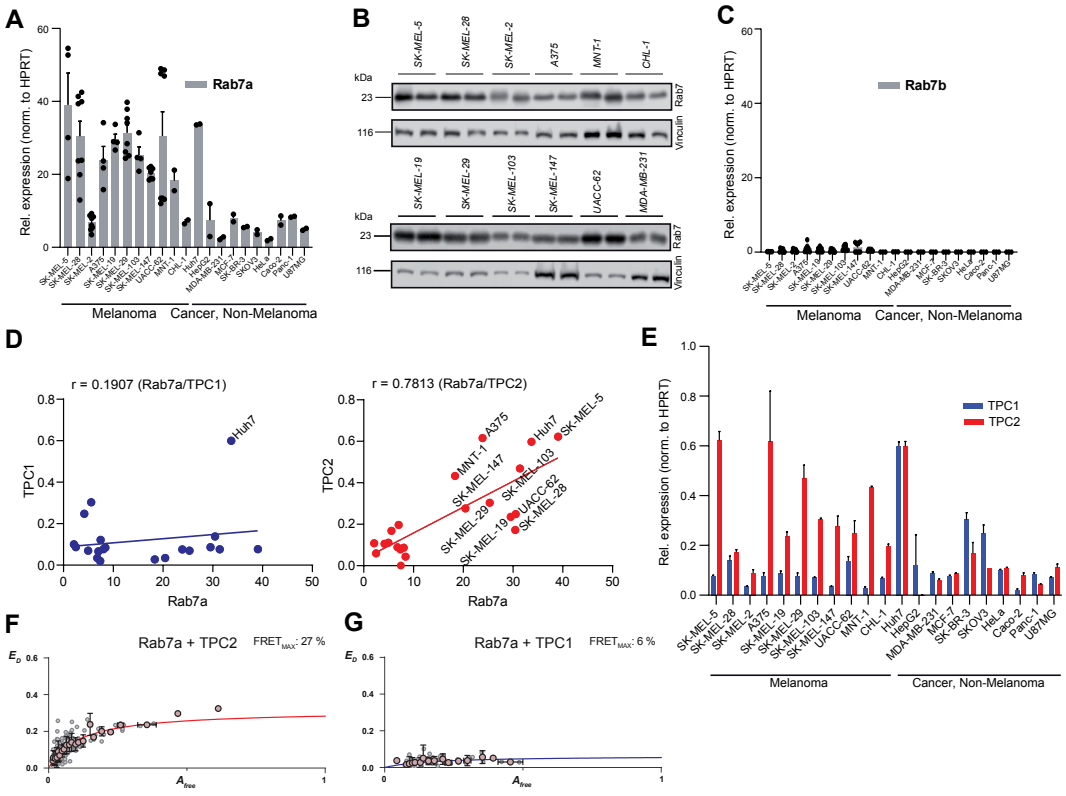
A
Rel. expression (norm. to HPRT)
Rab7a
Melanoma
Cancer, Non-Melanoma
B
kDa
Rab7
Vinculin
C
Rab7b
D
r = 0.1907 (Rab7a/TPC1)
r = 0.7813 (Rab7a/TPC2)
TPC1
TPC2
Rab7a
E
TPC1
TPC2
F
Rab7a + TPC2
FRET_MAX: 27 %
G
Rab7a + TPC1
FRET_MAX: 6 %

Figure

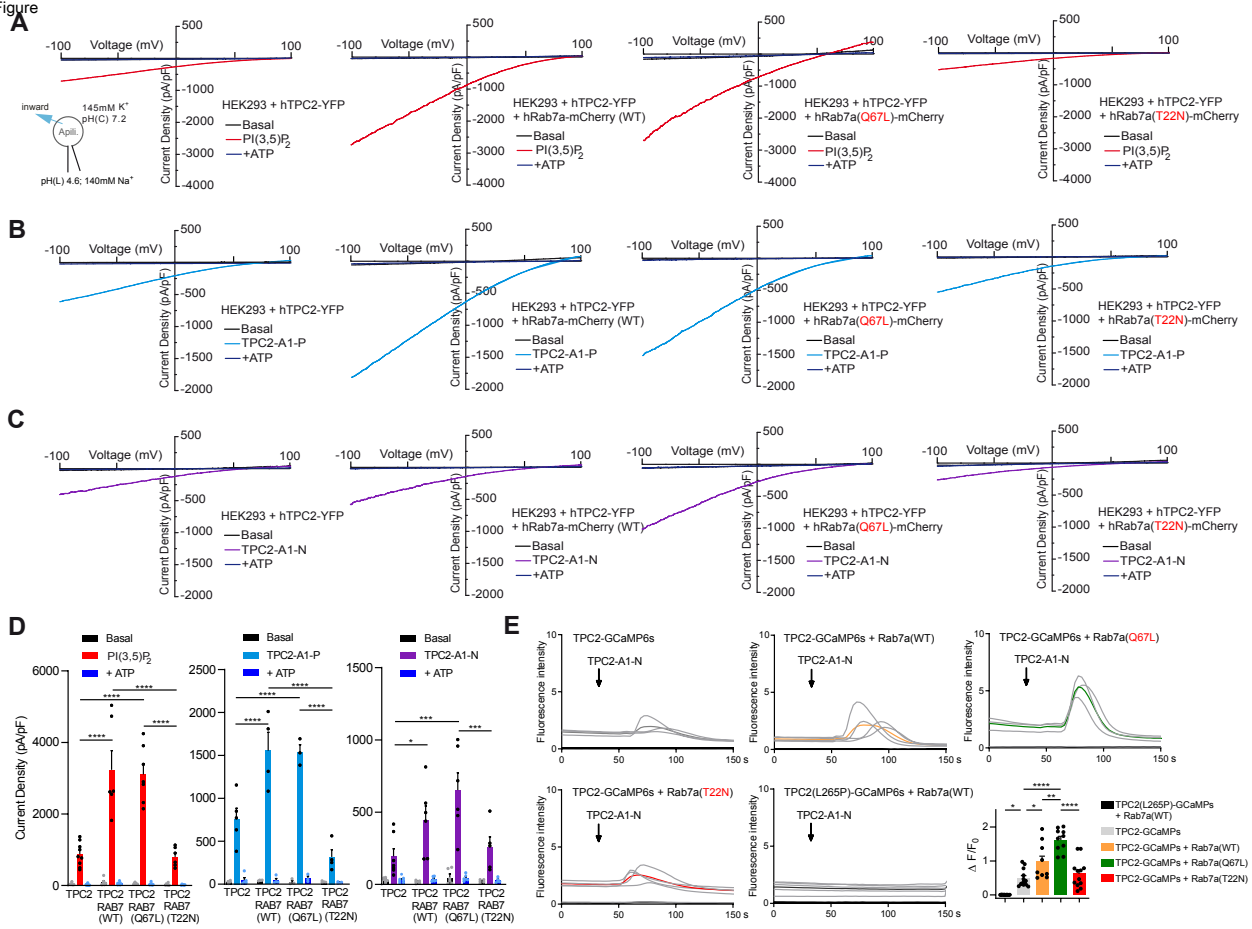
A
B
C
D
E
Voltage (mV)
Current Density (pA/pF)
HEK293 + hTPC2-YFP
HEK293 + hTPC2-YFP + hRab7a-mCherry (WT)
HEK293 + hTPC2-YFP + hRab7a(Q67L)-mCherry
HEK293 + hTPC2-YFP + hRab7a(T22N)-mCherry
Basal
PI(3,5)P2
+ATP
TPC2-A1-P
TPC2-A1-N
inward
145mM K+
pH(C) 7.2
Apili.
pH(L) 4.6; 140mM Na+
TPC2
TPC2 RAB7 (WT)
TPC2 RAB7 (Q67L)
TPC2 RAB7 (T22N)
TPC2-GCaMP6s
TPC2-GCaMP6s + Rab7a(WT)
TPC2-GCaMP6s + Rab7a(Q67L)
TPC2-GCaMP6s + Rab7a(T22N)
TPC2(L265P)-GCaMPs + Rab7a(WT)
Fluorescence intensity
Δ F/F0
TPC2-GCaMPs
TPC2-GCaMPs + Rab7a(WT)
TPC2-GCaMPs + Rab7a(Q67L)
TPC2-GCaMPs + Rab7a(T22N)

Figure

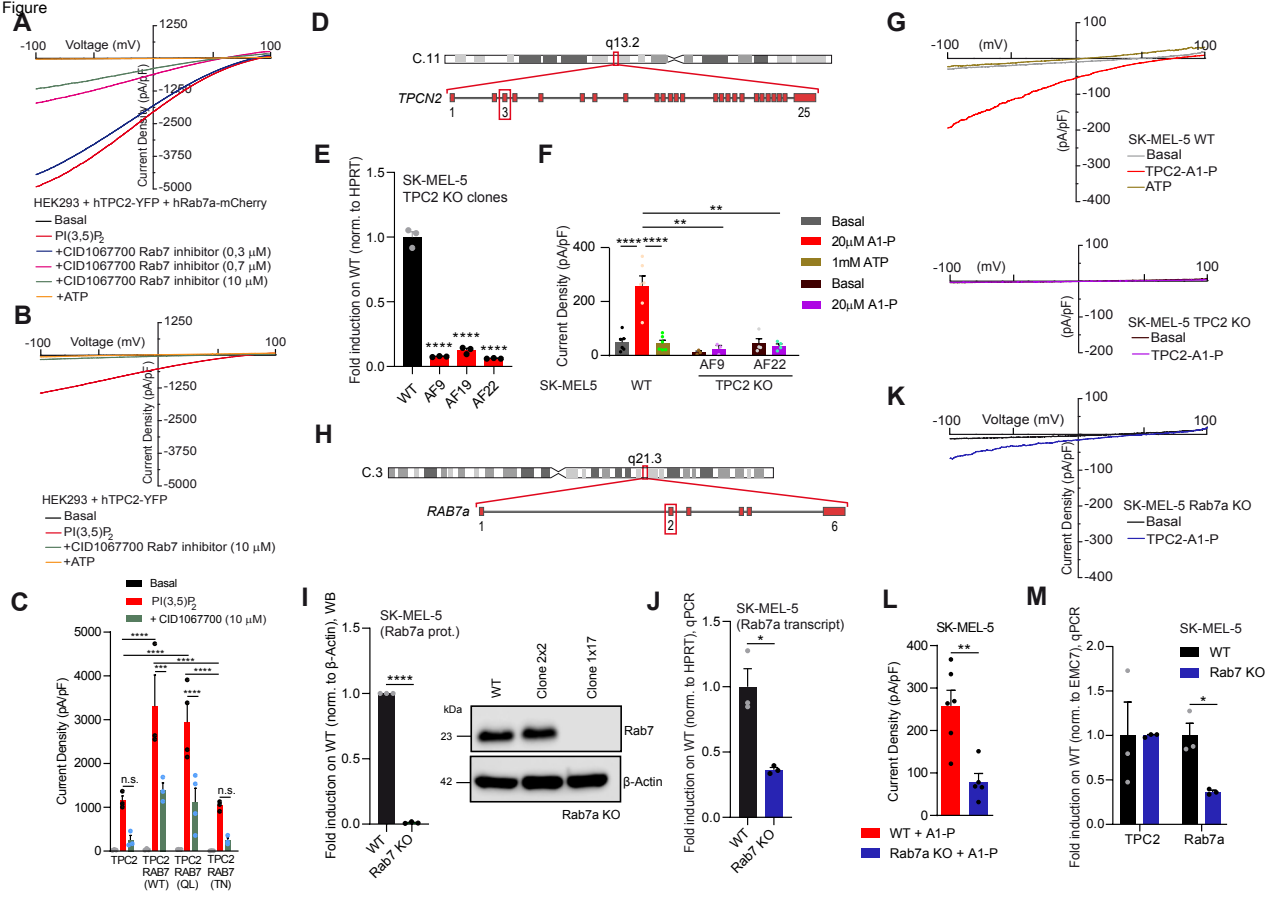
A
Voltage (mV)
Current Density (pA/pF)
HEK293 + hTPC2-YFP + hRab7a-mCherry
Basal
PI(3,5)P2
+CID1067700 Rab7 inhibitor (0,3 μM)
+CID1067700 Rab7 inhibitor (0,7 μM)
+CID1067700 Rab7 inhibitor (10 μM)
+ATP
B
HEK293 + hTPC2-YFP
Basal
PI(3,5)P2
+CID1067700 Rab7 inhibitor (10 μM)
+ATP
C
Basal
PI(3,5)P2
+ CID1067700 (10 μM)
Current Density (pA/pF)
n.s.
TPC2
TPC2 RAB7 (WT)
TPC2 RAB7 (QL)
TPC2 RAB7 (TN)
D
C.11
q13.2
TPCN2
E
SK-MEL-5
TPC2 KO clones
Fold induction on WT (norm. to HPRT)
WT
AF9
AF19
AF22
F
Current Density (pA/pF)
SK-MEL5
WT
TPC2 KO
AF9
AF22
Basal
20μM A1-P
1mM ATP
Basal
20μM A1-P
G
SK-MEL-5 WT
Basal
TPC2-A1-P
ATP
SK-MEL-5 TPC2 KO
Basal
TPC2-A1-P
H
C.3
q21.3
RAB7a
K
Voltage (mV)
SK-MEL-5 Rab7a KO
Basal
TPC2-A1-P
I
SK-MEL-5
(Rab7a prot.)
Fold induction on WT (norm. to β-Actin), WB
WT
Rab7 KO
kDa
Clone 2x2
Clone 1x17
Rab7
β-Actin
Rab7a KO
J
SK-MEL-5
(Rab7a transcript)
Fold induction on WT (norm. to HPRT), qPCR
L
SK-MEL-5
Current Density (pA/pF)
WT + A1-P
Rab7a KO + A1-P
M
SK-MEL-5
WT
Rab7 KO
Fold induction on WT (norm. to EMC7), qPCR
TPC2
Rab7a

Figure

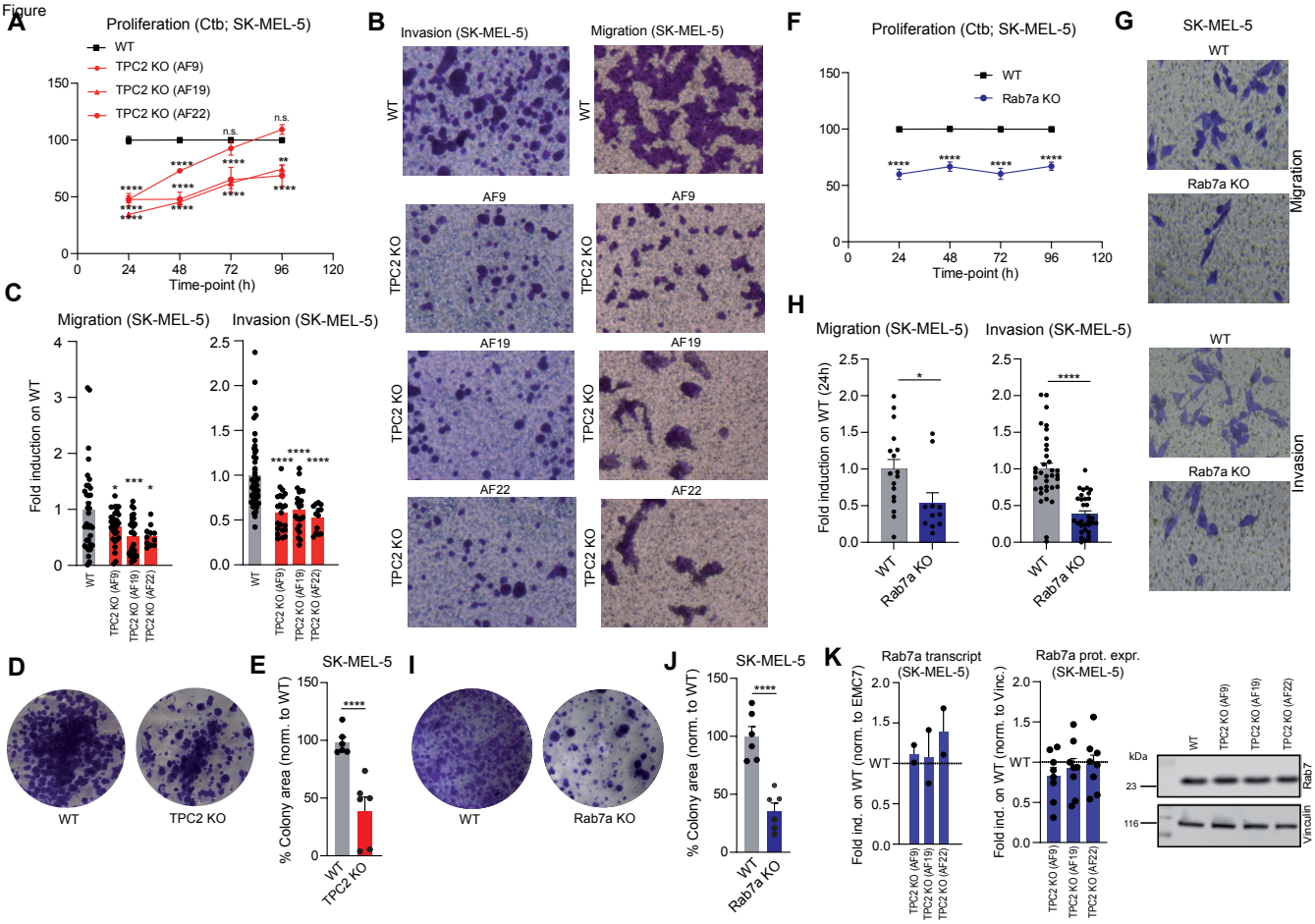
A
Proliferation (Ctb; SK-MEL-5)
WT
TPC2 KO (AF9)
TPC2 KO (AF19)
TPC2 KO (AF22)
Time-point (h)
B
Invasion (SK-MEL-5)
Migration (SK-MEL-5)
WT
AF9
AF19
AF22
TPC2 KO
C
Migration (SK-MEL-5)
Invasion (SK-MEL-5)
Fold induction on WT
D
WT
TPC2 KO
E
SK-MEL-5
% Colony area (norm. to WT)
F
Proliferation (Ctb; SK-MEL-5)
WT
Rab7a KO
Time-point (h)
G
SK-MEL-5
WT
Rab7a KO
Migration
Invasion
H
Migration (SK-MEL-5)
Invasion (SK-MEL-5)
Fold induction on WT (24h)
I
WT
Rab7a KO
J
SK-MEL-5
% Colony area (norm. to WT)
K
Rab7a transcript (SK-MEL-5)
Fold ind. on WT (norm. to EMC7)
Rab7a prot. expr. (SK-MEL-5)
Fold ind. on WT (norm. to Vinc.)
kDa
23
116
Rab7
Vinculin

Figure

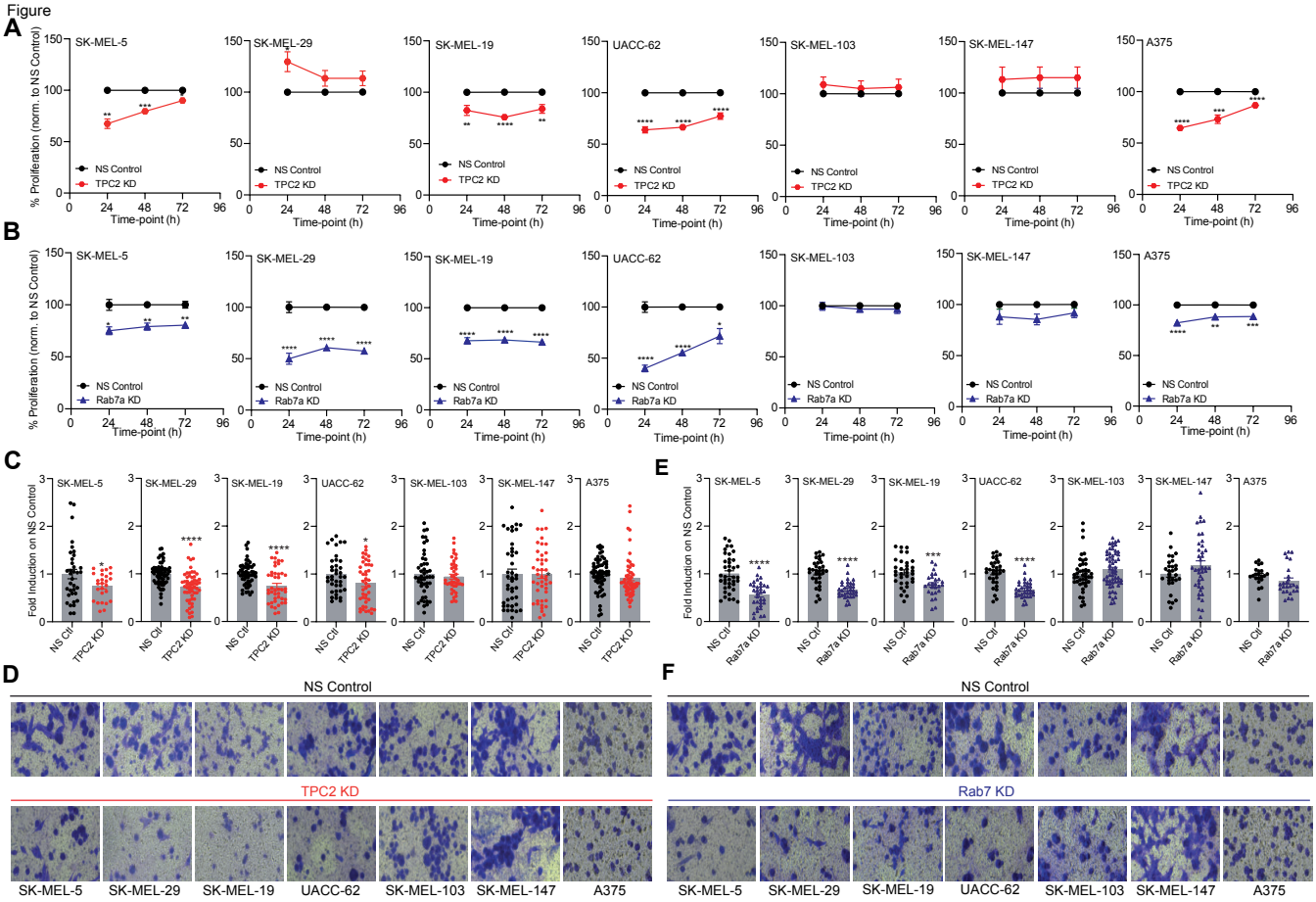
A
SK-MEL-5
SK-MEL-29
SK-MEL-19
UACC-62
SK-MEL-103
SK-MEL-147
A375
% Proliferation (norm. to NS Control)
Time-point (h)
NS Control
TPC2 KD
B
Rab7a KD
C
Fold Induction on NS Control
NS Ctrl
TPC2 KD
E
Rab7a KD
D
NS Control
TPC2 KD
F
Rab7 KD

Figure

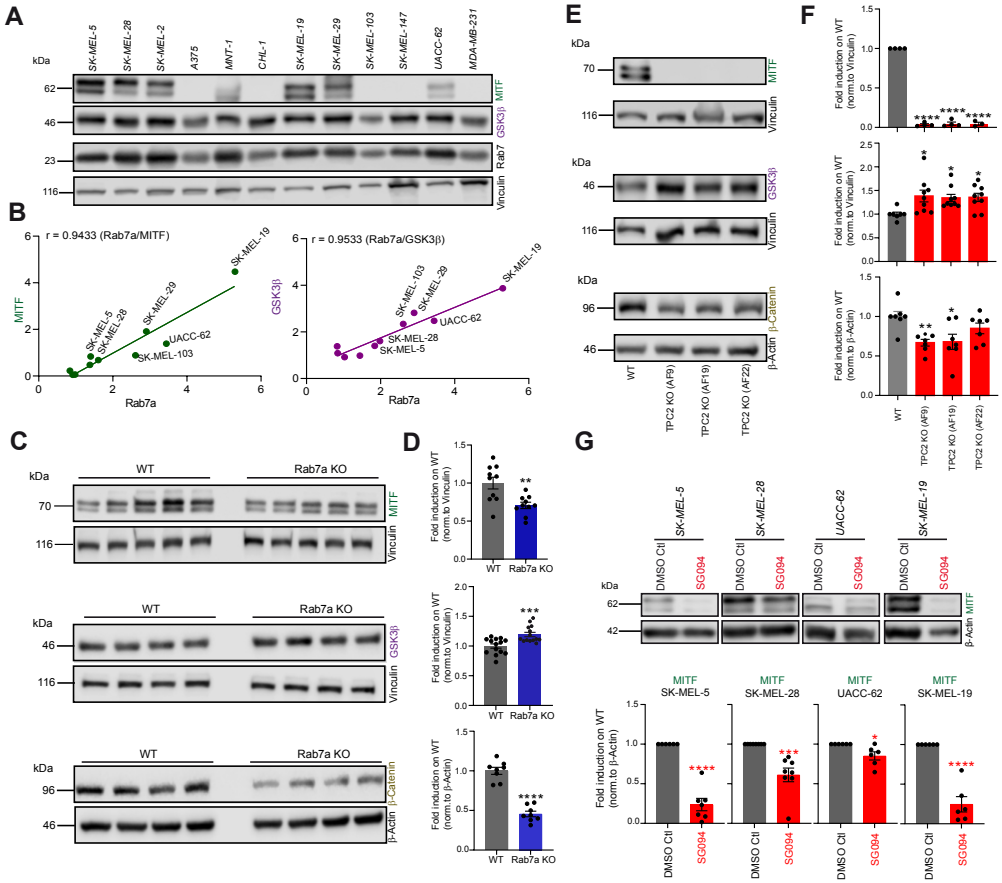
A
SK-MEL-5
SK-MEL-28
SK-MEL-2
A375
MNT-1
CHL-1
SK-MEL-19
SK-MEL-29
SK-MEL-103
SK-MEL-147
UACC-62
MDA-MB-231
kDa
62
46
23
116
MITF
GSK3β
Rab7
Vinculin
B
r = 0.9433 (Rab7a/MITF)
r = 0.9533 (Rab7a/GSK3β)
MITF
GSK3β
Rab7a
SK-MEL-19
SK-MEL-29
SK-MEL-5
SK-MEL-28
UACC-62
SK-MEL-103
C
WT
Rab7a KO
kDa
70
116
46
96
MITF
GSK3β
β-Catenin
Vinculin
β-Actin
D
Fold induction on WT (norm.to Vinculin)
Fold induction on WT (norm.to β-Actin)
E
TPC2 KO (AF9)
TPC2 KO (AF19)
TPC2 KO (AF22)
F
G
DMSO Ctl
SG094
β-Actin MITF
MITF SK-MEL-5
MITF SK-MEL-28
MITF UACC-62
MITF SK-MEL-19

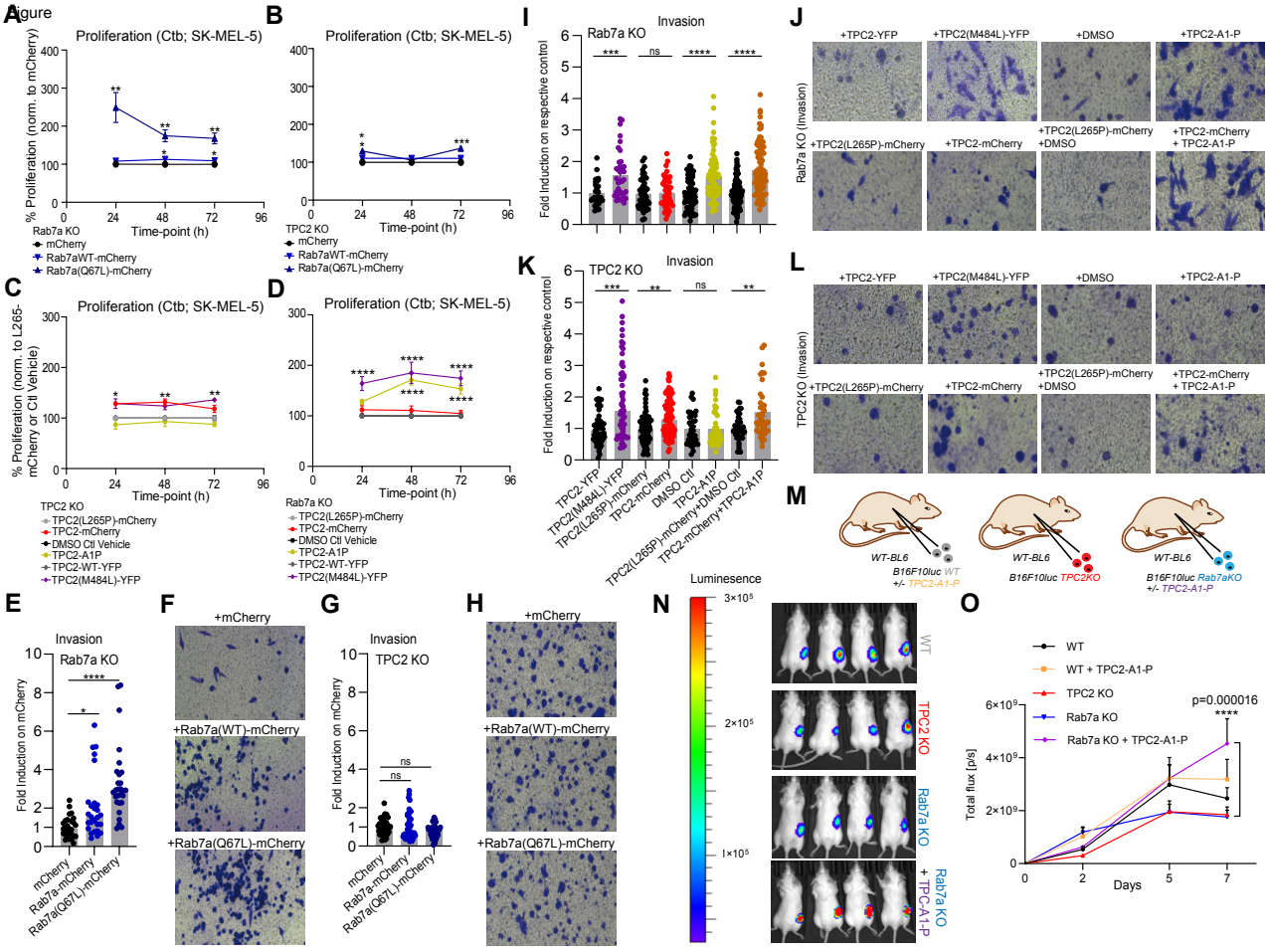
Figure
A
Proliferation (Ctb; SK-MEL-5)
% Proliferation (norm. to mCherry)
Time-point (h)
Rab7a KO
mCherry
Rab7aWT-mCherry
Rab7a(Q67L)-mCherry
B
Proliferation (Ctb; SK-MEL-5)
Time-point (h)
TPC2 KO
mCherry
Rab7aWT-mCherry
Rab7a(Q67L)-mCherry
C
Proliferation (Ctb; SK-MEL-5)
% Proliferation (norm. to L265-mCherry or Ctl Vehicle)
Time-point (h)
TPC2 KO
TPC2(L265P)-mCherry
TPC2-mCherry
DMSO Ctl Vehicle
TPC2-A1P
TPC2-WT-YFP
TPC2(M484L)-YFP
D
Proliferation (Ctb; SK-MEL-5)
Time-point (h)
Rab7a KO
TPC2(L265P)-mCherry
TPC2-mCherry
DMSO Ctl Vehicle
TPC2-A1P
TPC2-WT-YFP
TPC2(M484L)-YFP
I
Invasion
Rab7a KO
Fold Induction on respective control
J
+TPC2-YFP
+TPC2(M484L)-YFP
+DMSO
+TPC2-A1-P
+TPC2(L265P)-mCherry
+TPC2-mCherry
+TPC2(L265P)-mCherry +DMSO
+TPC2-mCherry + TPC2-A1-P
Rab7a KO (Invasion)
K
Invasion
TPC2 KO
Fold Induction on respective control
TPC2-YFP
TPC2(M484L)-YFP
TPC2(L265P)-mCherry
TPC2-mCherry
DMSO Ctl
TPC2-A1P
TPC2(L265P)-mCherry+DMSO Ctl
TPC2-mCherry+TPC2-A1P
L
+TPC2-YFP
+TPC2(M484L)-YFP
+DMSO
+TPC2-A1-P
+TPC2(L265P)-mCherry
+TPC2-mCherry
+TPC2(L265P)-mCherry +DMSO
+TPC2-mCherry + TPC2-A1-P
TPC2 KO (Invasion)
M
WT-BL6
B16F10luc WT
+/- TPC2-A1-P
WT-BL6
B16F10luc TPC2KO
WT-BL6
B16F10luc Rab7aKO
+/- TPC2-A1-P
E
Invasion
Rab7a KO
Fold Induction on mCherry
mCherry
Rab7a-mCherry
Rab7a(Q67L)-mCherry
F
+mCherry
+Rab7a(WT)-mCherry
+Rab7a(Q67L)-mCherry
G
Invasion
TPC2 KO
Fold Induction on mCherry
mCherry
Rab7a-mCherry
Rab7a(Q67L)-mCherry
H
+mCherry
+Rab7a(WT)-mCherry
+Rab7a(Q67L)-mCherry
N
Luminesence
WT
TPC2 KO
Rab7a KO
Rab7a KO + TPC2-A1-P
O
WT
WT + TPC2-A1-P
TPC2 KO
Rab7a KO
Rab7a KO + TPC2-A1-P
p=0.000016
Total flux [p/s]
Days

Figure S1

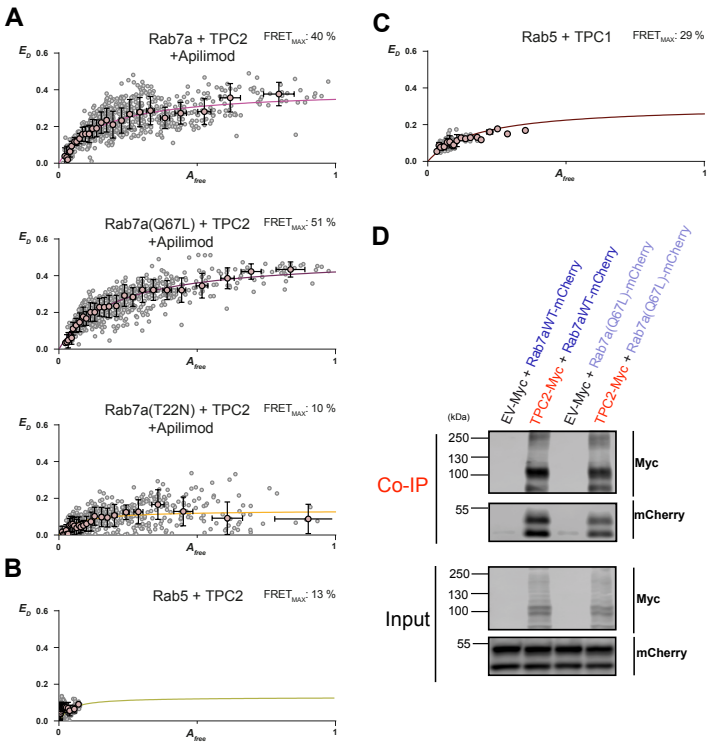
A
Rab7a + TPC2
+Apilimod
FRET_MAX: 40 %
Rab7a(Q67L) + TPC2
+Apilimod
FRET_MAX: 51 %
Rab7a(T22N) + TPC2
+Apilimod
FRET_MAX: 10 %
B
Rab5 + TPC2
FRET_MAX: 13 %
C
Rab5 + TPC1
FRET_MAX: 29 %
D
EV-Myc + Rab7aWT-mCherry
TPC2-Myc + Rab7aWT-mCherry
EV-Myc + Rab7a(Q67L)-mCherry
TPC2-Myc + Rab7a(Q67L)-mCherry
(kDa)
250
130
100
55
Co-IP
Myc
mCherry
Input
Myc
mCherry

Figure S2

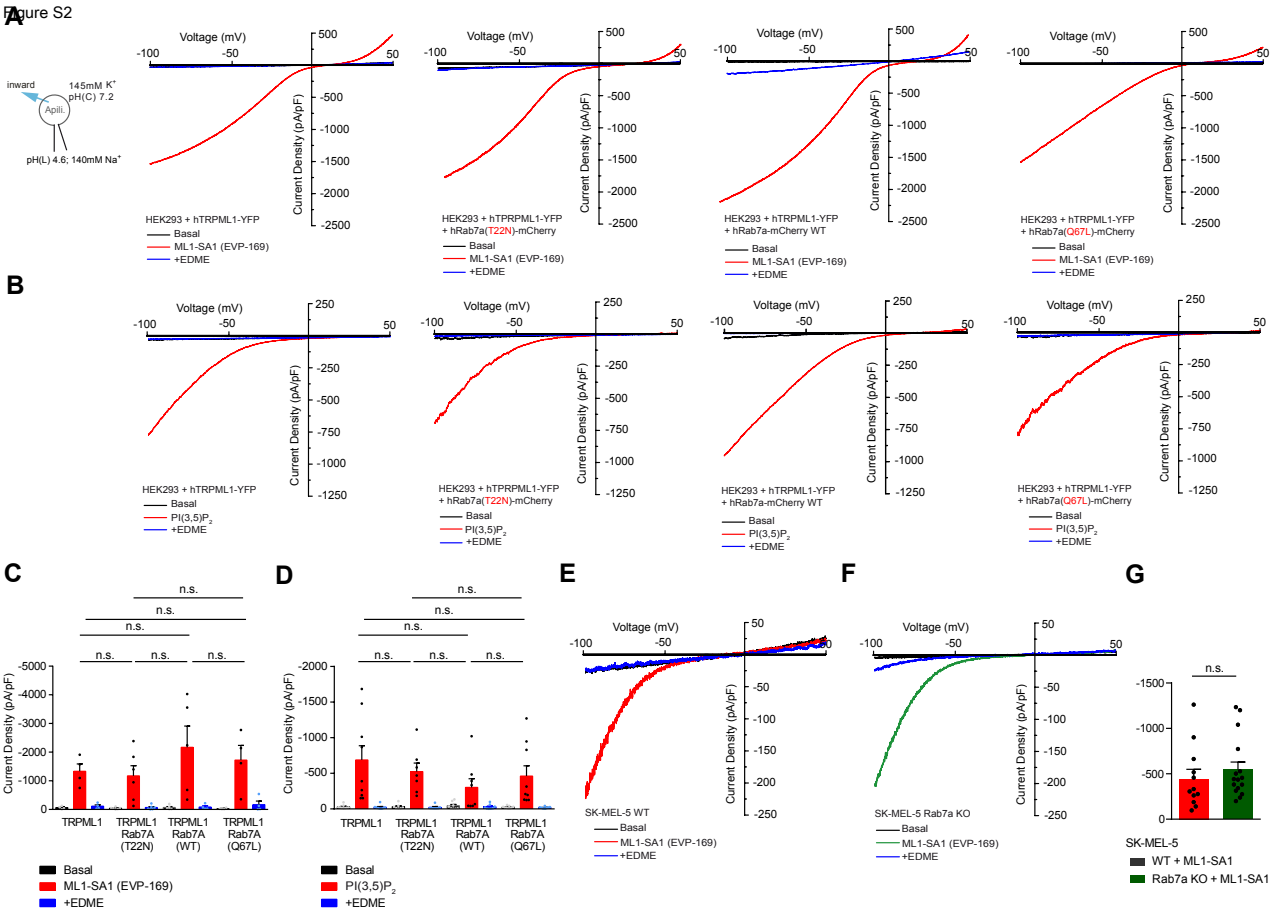
A
inward
145mM K+
pH(C) 7.2
Apili.
pH(L) 4.6; 140mM Na+
Voltage (mV)
Current Density (pA/pF)
HEK293 + hTRPML1-YFP
Basal
ML1-SA1 (EVP-169)
+EDME
HEK293 + hTPRPML1-YFP
+ hRab7a(T22N)-mCherry
HEK293 + hTRPML1-YFP
+ hRab7a-mCherry WT
HEK293 + hTRPML1-YFP
+ hRab7a(Q67L)-mCherry
B
PI(3,5)P2
C
D
n.s.
TRPML1
TRPML1 Rab7A (T22N)
TRPML1 Rab7A (WT)
TRPML1 Rab7A (Q67L)
E
SK-MEL-5 WT
F
SK-MEL-5 Rab7a KO
G
SK-MEL-5
WT + ML1-SA1
Rab7a KO + ML1-SA1

Figure S3

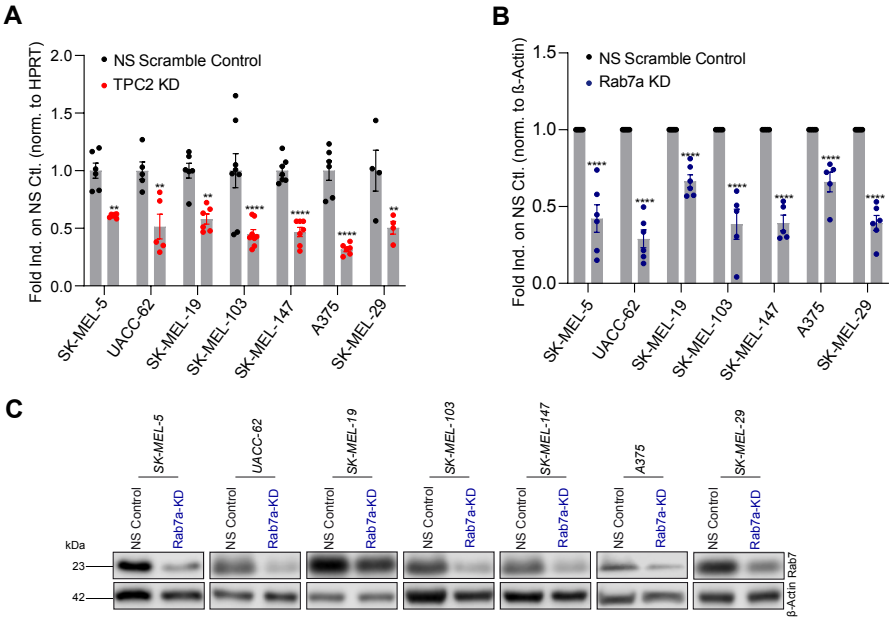
A
NS Scramble Control
TPC2 KD
Fold Ind. on NS Ctl. (norm. to HPRT)
2.0
1.5
1.0
0.5
0.0
SK-MEL-5
UACC-62
SK-MEL-19
SK-MEL-103
SK-MEL-147
A375
SK-MEL-29
B
NS Scramble Control
Rab7a KD
Fold Ind. on NS Ctl. (norm. to ß-Actin)
1.5
1.0
0.5
0.0
SK-MEL-5
UACC-62
SK-MEL-19
SK-MEL-103
SK-MEL-147
A375
SK-MEL-29
C
SK-MEL-5
UACC-62
SK-MEL-19
SK-MEL-103
SK-MEL-147
A375
SK-MEL-29
NS Control
Rab7a-KD
kDa
23
42
Rab7
β-Actin

Figure S4

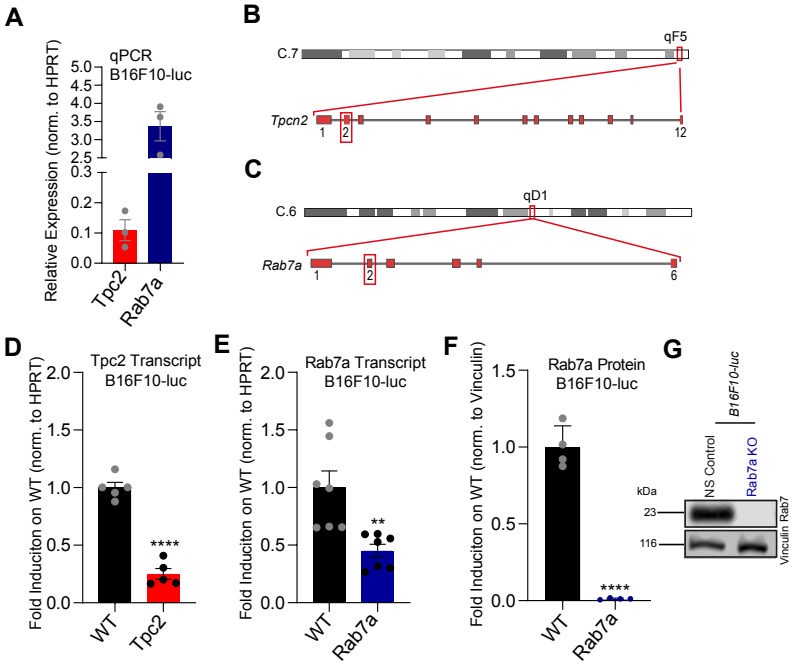

Declaration of Interests form

We declare no conflict of interest.

Paper VI

Endolysosomal TRPML1 channel regulates cancer cell-migration by facilitating the intracellular trafficking of E-cadherin and β_1-integrin

– *Manuscript* –

Nadine Frey[1], Lina Ouologuem[1], Wei-Xiong Siow[1], Jan Stöckl[2], Julia Blenninger[1], Carla Abrahamian[3], Thomas Fröhlich[2], Angelika M. Vollmar[1], Christian Grimm[3], Karin Bartel[1,*]

[1] Department of Pharmacy, Pharmaceutical Biology, Ludwig-Maximilians-University Munich, 81377 Munich, Germany

[2] Gene Center, Laboratory for Functional Genome Analysis, Ludwig Maximilians-University Munich, 81377 Munich, Germany

[3] Walther-Straub-Institute of Pharmacology and Toxicology, Ludwig-Maximilians-University Munich, 80336 Munich, Germany

*Correspondence: karin.bartel@cup.uni-muenchen.de, Twitter: @lysocancerlab

Running title: TRPML1 regulating cancer cell-migration

This article contains supporting information

Abstract

Metastasis still accounts for 90 % of all cancer related death cases. An increase of cellular mobility and invasive traits of cancer cells mark two crucial prerequisites of metastasis. Recent studies unravelled the involvement of the endolysosomal cation channel TRPML1 in cell migration. Accordingly, we identified an anti-migratory effect of channel loss-of-function in two genetic TRPML1 knockout (KO) cell lines. As mode-of-action, we established TRPML1 as a crucial regulator of intracellular trafficking of two pro-migratory proteins: E-cadherin and β_1-integrin. Interestingly, KO differentially interferes with the recycling process of E-cadherin and β_1-integrin. In MDA-MB-231 cells, KO mainly impairs endocytosis while recycling is unaffected and vice versa in RIL-175 cells. Regardless, TRPML1 loss-of-function resulted in the same phenotype of decreased migratory and adhesive capacity. In addition, we observed that TRPML1 KO negatively influences actin polymerisation and leads to insufficient polarity at the leading edge required for appropriate locomotion. Consequently, our findings establish TRPML1 as a suitable target for the inhibition of migration and invasion.

Graphical Abstract

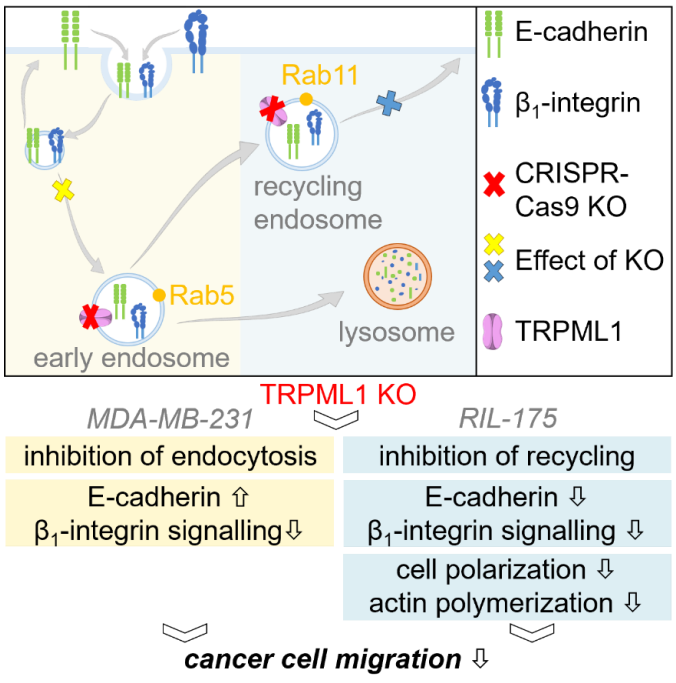

Keywords

Cancer biology, migration, adhesion, lysosome, ion channel

1. Introduction

Despite significant advances in cancer therapy [1,2], cancer remains one of the main causes of death worldwide [3]. Owing to still limited therapy options, 90 % of the cancer-related death cases are correlated to metastasizing tumorigenic cells. Tumour metastasis is initiated by increasingly invasive primary tumour cells migrating into the surrounding tissue and subsequently penetrating blood or lymphatic vessels. Upon reaching the secondary tumour site, cells extravasate and proliferate within the organ leading to the growth of the metastatic tumour [4,5]. A prerequisite for metastasis is the increase in cellular mobility [6]. Cells migrate either individually (amoeboid and mesenchymal migration) or collectively as a group of cells [7]. This movement is predominantly regulated by two classes of adhesion proteins – cadherins facilitating cell-cell adhesion and integrins mediating cell-matrix adhesion [8–11]. In this context, especially Epithelial-cadherin (E-cadherin) has become the scope of intense research. E-cadherin is a calcium-dependent single-pass transmembrane glycoprotein that mediates cell-cell adhesion through homotypic binding with neighbouring cells [12,13]. E-cadherin is stabilized at the cellular membrane by p120-catenin and linked to the actin cytoskeleton through β- and α-catenin allowing the regulation of actin-polymerization [14]. Despite its established status as tumour suppressor, the role of E-cadherin in cancer is ambivalent [14]. On the one hand, loss of E-cadherin is associated with highly invasive cancers as it allows individual dissemination from the tumour promoting individual mesenchymal migration – a process summarized as the epithelial-to-mesenchymal transition (EMT) **[15]**. On the other hand, E-cadherin can be retained in some types of cancer like colon carcinoma as a regulator of the collective cell migration. As such, it aids maintaining strong inter-cellular contacts, which mediate the mechanotransduction required for migration [16,17]. The family of integrins, heterodimeric transmembrane receptors composed of α- and β-subunits, are also indispensable for appropriate locomotion [18]. As cell-matrix adhesion proteins, they are integral for the highly coordinated cell migration cycle involving the polarization of the leading edge, adhesion to the extracellular matrix (ECM), extension and translocation of the cellular body, and lastly detachment at the cellular rear by contraction of the actin cytoskeleton [19–21]. Upon binding to the ECM, integrins however not only coordinate cell-matrix-adhesion but are also involved in the polymerization of the actin-cytoskeleton at the leading edge allowing correct cell-polarization. This is facilitated by its link to the cytoskeleton by actin-binding proteins like vinculin or by its downstream modulators, focal adhesion kinases (FAK) and Src-kinases [10,18,22,23]. Targeting the cell-ECM interface is thus of great interest for the development of new anti-metastatic therapeutics and integrin-targeting antibodies or drugs have been repeatedly investigated in clinical trials [24,25]. To fulfil their function, integrins have to be continuously recycled from and to the leading edges of migrating cells to enable a spatiotemporal restriction of focal adhesion sites

required for the extension of the cellular body [26,27]. Accordingly, E-cadherin is maintained and modulated at the plasma membrane by the internal trafficking machinery facilitating a precise regulation of cell-junctional integrity [28,29]. Taken together, this suggests the targeting of intracellular trafficking as a suitable anti-migratory and therefore anti-metastatic strategy, as it targets proteins responsible for both cell-cell and cell-matrix contacts. In this context, lysosomal membrane proteins are in the focus of intense research as crucial regulators of endocytosis, intracellular transport, and exocytosis [30]. Recently endolysosomal cation channels have emerged as an attractive anti-cancer target: namely the mucolipin subfamily of transient potential receptors (TRPMLs), which comprises three isoforms – TRPML1 (MCOLN1), TRPML2 (MCOLN2), and TRPML3 (MCOLN3) [31]. TRPML1, the most intensively researched member of the family, is ubiquitously expressed in the membranes of endosomes and lysosomes, whereas TRPML2 and TRPML3 are mainly localized in specialized cells (e. g. immune cells, hair cells of the inner ear, secretory cells, and melanocytes) [32,33]. In past research TRPML1 has been linked to ion homeostasis, vesicular trafficking, and autophagy [34,35]. Aside from these physiological functionalities, TRPML1's role in cancer is emerging. Interestingly, it has been implicated to regulate cancer cell migration as its inhibition reduces invasiveness of breast cancer cells *in vitro* [34] and *in vivo* [36]. However, the underlying mechanism is still vastly elusive. Given the apparent correlation between TRPML1 and cancer cell migration, we aimed to further elucidate its role in cancer cell migration in hepatocellular carcinoma and, most importantly, uncover the underlying mechanisms by monitoring cell-junctional and cell-adhesion proteins.

2. Methods

2.1. Cell lines and culture

RIL-175 cells were provided by Prof. Simon Rothenfußer (CIPS-M, LMU Munich, Germany) [37]. RIL-175 KO cells were generated by our group [32]. MDA-MB-231 cells were obtained from DSMZ (Braunschweig, Germany, #ACC 732). MDA-MB-231 KO cells were provided by Prof. Christian Grimm (Walter-Straub-Institute of Pharmacology and Toxicology, LMU Munich, Germany) [34]. All cell lines were cultivated in Dulbecco's modified Eagle's medium (DMEM) (Anprotec, #AC-LM-0012) supplemented with 10 % fetal calf serum (FCS) (Anprotec, #AC-SM-0027) at 37°C, 5 % CO_2. None of the cell lines used are listed in the database of commonly misidentified cell lines maintained by ICLAC. All cells are proven to be mycoplasma-free quarterly.

2.2. Migration Assays

The wound-healing assay [38], Boyden-Chamber assay [39], and the circular micropatterning [40] were performed as recently described.

For spheroid migration, 20 µL drops of a cell suspension containing $50 \cdot 10^3$ RIL-175 cells/mL and 20 % methocel stock solution (1.2 % (w/v) autoclaved methylcellulose (Sigma Aldrich, #M0152) in ECGM (PeloBiotech, #PB-MH-100-2199)) were pipetted onto the lids of a 10 cm petri-dish. The lid was placed back onto the petri-dish and incubated for 24 h allowing spheroid formation (hanging drop method).

Spheroids were embedded in TeloCol-6 collagen type I neutralized 1:10 with the supplied neutralization solution (Advanced Biomatrix, #5225, #5229) and diluted to 2.1 mg/mL in PBS. An 8-well µ-slide (ibidi) was coated with a thin base layer containing neutralized TeloCol-6:DMEM (2.125:1) on ice before incubation (30 min, 37°C, 5 % CO_2). Spheroid-containing drops were washed down using PBS, centrifuged (1000 rpm, 5 min, 25°C), and resuspended in 200 µL of FCS. EDME (50 µM) [34] was applied onto the base layer, then 125 µL of a mixture containing neutralized TeloCol-6:spheroids in FCS (2.125:1) were placed on top of the base layer. After an incubation time of 30 min (37°C, 5 % CO_2), 100 µL of DMEM were added. Spheroids were incubated for 48 h and then imaged using a Leica Dmi1 inverted microscope equipped with a MC120HD camera (Leica). Spheroid diameters and area were determined by ImageJ (NIH).

2.3. Proteome Analysis

The proteomic analysis has been published [32]. For gene set enrichment analysis (GSEA), the label-free quantification data was log2 transformed, filtered for at least 4 valid values in at least one condition, and missing values were imputed from a normal distribution (width = 0.3; down shift = 1.8). The values were de-transformed and loaded into the GSEA software [41,42]. As enrichment statistic “classic” was selected, gene names were used without collapsing, the permutation type was set to “gene_set” and as metric “t-test” was chosen. The number of permutations was 10000. All mouse gene ontologies were downloaded from MSigDB [41–43] and used as gene sets database.

2.4. Real-time quantitative PCR (RT-qPCR)

RT-qPCR was performed as described recently [44].The relative gene expression was normalized against housekeepers actin (RIL-175) or tubulin (MDA-MB-231) and calculated as a fold-change compared to the WT cells using the $\Delta\Delta C_T$ method [45]. Primers **(Tables S1 and S2)** were purchased from Metabion and validated for their efficiency prior to use.

2.5. Western Blot Analysis

For the compound stimulation, cells were grown in 6-well plates and treated as indicated (24 h) with chloroquine (Sigma Aldrich, #C6628) or EDME. For Rab11-overexpression, cells were transiently transfected with pEGFP-C1-Rab11-WT (Addgene, #12674) or pmaxGFP-plasmid (Lonza, #VCA-1001) using the Lipofectamine™ 3000 transfection reagent

(ThermoFisher, #100022057) according to manufacturer's instructions, and incubated (48 h). For Cathepsin B release, cells were grown overnight, medium was exchanged to FCS-free medium, and treated with Ionomycin (5 µM) (Sigma, #10634) for 10 min [46]. Supernatant was concentrated using Merck Amicon™ centrifugal units (Fisher Scientific, #10341782).
Western Blot analysis was performed as previously described [44] using the primary and secondary HRP-coupled antibodies listed in **Table S3**. Chemiluminescence was detected on a Chemidoc™ Touch Imaging System (Bio-Rad). Data was processed with ImageLab (Bio-Rad) and normalized to total protein (stain-free detection) [47].

2.6. Confocal Microscopy

All confocal images were collected on a Leica SP8 inverted scanning microscope (Leica). Cells were grown in collagen-coated 8-well µ-slides (ibidi) overnight. Cells were fixed (MeOH, 10 min, RT) and permeabilized (acetone, 1 min, on ice). Unspecific binding sites were blocked with 5 % BSA in PBS (1 h, RT). After incubation with primary antibodies (overnight, 4°C) and secondary antibodies (1 h, RT), cells were mounted with FluorSave™ mounting medium (Merck Millipore, #345789), covered with glass cover slips, and imaged. Antibodies are listed in **Table S4**. Nuclei were stained with Hoechst 33342 (Sigma Aldrich).

For colocalization or Rab11-OE experiments, cells were transiently transfected with a pcDNA3.1-TRPML1-HA plasmid (Addgene, #18825) or pEGFP-C1-Rab11-WT plasmid (Addgene, #12674) using the Lipofectamine™ 3000 transfection reagent (ThermoFisher) according to the manufacturer's instructions. After 48 h, cells were fixed (MeOH, 10 min, RT), permeabilized (acetone, 1 min, on ice), and stained with the antibodies listed in **Table S5**. Hoechst 33342 (Sigma Aldrich, Colocalization) or ToPo™-3 Iodide (Invitrogen, #T3605, Rab11-Overexpression) was used for the nucleus staining. For FRAP-experiments, cells were grown in collagen-coated 8-well µ-slides (ibidi) overnight and transiently transfected with pcDNA3.1-E-cadherin-GFP (Addgene, #28009) using FuGENE® HD transfection reagent (Promega Cooperation, #E2311) according to the manufacturer's instructions. After 24 h, the FRAP-experiment was performed under constant humidity provided by an objective heater (Okolab, Pazzouli, Italy). Employing the FRAP-tool on the LAS X Core Software (Leica), photobleaching of a defined region of interest was performed by nine scanning iterations with a laser intensity of 100 %. One pre-bleach and 15 post-bleach images (10 iterations, 30 s intervals / 5 iterations, 60 s intervals) at lower laser intensities were collected. Intensities were measured by the FRAP tool of the Leica LASX software. Recovery half-times were calculated after exponential curve fitting. For the adhesion assay, the protocol was adapted from [39]. A 24-well plate was coated with collagen (Matrix Bioscience, #50104, 0.4 % in PBS), fibronectin (R&D Systems, #1030-FN-01M, 10 µg/mL in PBS), or laminin (R&D Systems, #3446-005-01, 10 µg/mL in PBS) (1 h, 37°C). Unspecific binding sites were

blocked with 3 % (w/v) BSA in PBS (30 min, 37°C). Cells were seeded and allowed to adhere for 1 h. Cells were fixed (4 % paraformaldehyde (PFA) (Thermo Fisher, #38908), 20 min, RT), stained with rhodamine-phalloidin (Sigma Aldrich, Taufkirchen, Germany, #R415) and Hoechst 33342 (Sigma Aldrich) (30 min), mounted with FluorSave Reagent (Merck Millipore), and imaged. Adhered cells were counted using ImageJ.

For staining of migrating cells, a confluent cell layer was scratched. Cells were allowed to migrate (5 h) and fixed with MeOH (10 min, RT, (antibodies)) or 4 % PFA (20 min, RT, (actin)). Antibodies are listed in **Table S6**. Rhodamine-phalloidin (Sigma Aldrich) was used to stain actin, Hoechst 33342 (Sigma Aldrich) for nuclei.

For FITC-Dextran uptake, cells were grown overnight in collagen-coated 8-well µ-slides (ibidi) overnight, incubated with 200 µg/mL FITC-dextran (20 kDa) (Sigma Aldrich, #FD20S) (2 h) and Hoechst 33342 (Sigma Aldrich) (15 min). After fixation (MeOH, 10 min, RT), samples were mounted with FluorSave™ mounting medium (Merck Millipore), covered with glass cover slips and imaged.

2.7. Flow Cytometry

Cells were grown in 12-well plates overnight and incubated with 200 µg/mL FITC-dextran (20 kDa) (Sigma Aldrich) as indicated. After trypsinization, cells were collected by centrifugation, washed, and resuspended in PBS. Flow cytometry experiments were performed on a BD FACS Canto II (BD Biosciences, Franklin Lakes, NJ, USA). Fluorescence intensity of FITC-dextran was analysed using the FITC-channel. Data was evaluated using FlowJo 7.6.

2.8. β-Hexosaminidase Release

The β-Hexosaminidase assay was performed as described recently [46].

2.9. Release of FITC-dextran

Cells were seeded into 96-well plates and stimulated with 200 µg/ml FITC-dextran (20 kDa) (Sigma Aldrich). After 24 h, cells were washed and incubated with 50 mM $CaCl_2$ in phenol red free DMEM (Pan Biotech) as indicated. After diluting 1:10 in PBS, fluorescence intensity was measured using the Infinite® 200 Pro Tecan Plate reader (Tecan Trading AG) (485/535 Ex/Em).

2.10. β_1-Integrin internalization assay

β_1-integrin internalization was conducted as described recently [39].

2.11. Statistical analysis

All experiments were conducted at least three times independently unless stated otherwise. Data represents means ± SD. Unless stated otherwise, statistical significance was

determined with an unpaired t-test with Welch's correction using GraphPad Prism 9.3.0, San Diego, USA. Results were considered significant for $p < 0.0332$.

3. Results

3.1. TRPML1 loss of function reduces cancer cell migration

As model systems, we employed two different parental tumour cell lines from a preliminary screening, which displayed elevated TRPML1 levels compared to other cell lines [48]. For this study, we chose murine hepatocellular carcinoma RIL-175 and human triple-negative breast cancer MDA-MB-231 cells, as TRPML1 silencing has been linked to cell migration in these cells previously [34]. To further study the impact of loss-of-TRPML1 on migration in our model lines, we worked with TRPML1 knockout (KO) clones. For MDA-MB-231 cells, TRPML1 KO has previously been established [34]. For RIL-175 cells we performed a KO of TRPML1 using the CRISPR/Cas9 system, as previously reported [32,34].

Firstly, we analysed migration behaviour of KO cell lines compared to their parental lines in different *in vitro* migration assays. Horizontal 2D cell migration in a wound-healing assay and migration in a Boyden-Chamber was significantly reduced upon KO of TRPML1 **(Fig. 1A, B)**. Furthermore, live cell imaging data allowed us to monitor collective cell migration and exclude reduced proliferation behaviour of the RIL-175 KO cells to be responsible for reduced migration **(Video S1)**. Consistently, live cell imaging of a micropatterned platform allowing the time-controlled cell migration outside of a highly cell-adhesive fibronectin ring further revealed that the KO of TRPML1 predominantly reduced the displacement of the cells **(Fig. 1C)**.

Secondly, we used an *"in-vivo like"* 3D spheroid system to corroborate the anti-migratory effect of TRPML1 inhibition. We could show that the spheroid diameters and area in RIL-175 cells were reduced significantly upon treatment with selective TRPML1-inhibitor EDME [34] **(Fig. 1D)**. Taken together, these findings clearly depict the ability to reduce migration in 2D and 3D systems upon loss of TRPML1 function.

3.2. Impaired TRPML1 function hampers adherens junction integrity

To elucidate the underlying mechanism for the observed anti-migratory effect, we conducted an unbiased proteome analysis in RIL-175 wildtype (WT) and KO cells, as recently described by our group, in which a total of 3219 proteins were identified [32]. A functional gene set enrichment analysis (GSEA) between WT and KO cells revealed downregulated pathways required for appropriate migration, including cytoskeleton organization, cell-adhesion, and cell-matrix adhesion, as well as cell junctional integrity upon KO of TRPML1 **(Fig. 2A)**.

As loss of junctional integrity is a promoting factor of migration [14], dysregulation of cell-cell contact sites was hypothesized to be attributed to the decreased migratory capacity of the KO cell lines. We found protein expression of tight-junction associated protein ZO-1 [49] to be increased and consequently more tight-junctional contacts between neighbouring cells were observable in MDA-MB-231 KO cells. In contrast, in RIL-175 KO cells, we could neither observe an effect on protein level nor remodelling of tight junctions **(Fig. 2B, C)**. However, for the adherens junction (AJ) component E-cadherin [15], we revealed a downregulation for RIL-175 KO cells and a contrasting upregulation for MDA-MB-231 KO cells on mRNA **(Fig. 2D)** and protein level **(Fig. 2E)**. Accordingly, as shown by confocal microscopy, E-cadherin is removed from the cellular membrane of RIL-175 TPRML1 KO cells. Conversely, MDA-MB-231 TPRML1 KO cells are round and grow in clusters as opposed to the spindle-like appearance of individually growing E-cadherin negative **[50]** MDA-MB-231 WT cells **(Fig. 2G)**. In line, inhibiting the channel with EDME (50 µM) significantly decreased E-cadherin protein expression in RIL-175 cells **(Fig. 2F)**. For E-cadherin associated proteins β-catenin and p120 we observed decreased protein levels in RIL-175 KO cells and vice versa in MDA-MB-231 KO cells. Accordingly, β- and p120-catenin were condensed at the plasma membrane of MDA-MB-231 KO cells, whereas removal of those proteins was evident for RIL-175 KO **(Fig. 2H-K)**. Furthermore, co-staining of E-cadherin and β -catenin in RIL-175 cells reinforced our observations as a Colocalization at plasma membrane was observable in WT cells but not in KO cells **(Fig. S1)**. In total, the data suggests TRPML1 as a key regulator to recruit AJ complex components E-cadherin and beta-catenin to the cell membrane and therefore secure pro-migratory at cell-cell or cell-matrix contact site.

3.3. Knockout of TRPML1 impedes intracellular trafficking

E-cadherin levels can be altered by various modulators. For instance, levels can be lowered by several transcription repressors like Snail and Slug [51,52]. Furthermore, the loss of E-cadherin and consequent increase in N-cadherin is one of the hallmarks of the epithelial to mesenchymal transition (EMT), which accompanies an increase in migratory potential [9]. Additionally, endocytosis-exocytosis processes have emerged as strong E-cadherin modulators [28,29]. Of note, both KO cell lines expressed significantly more Snail, Slug, and N-cadherin on protein-level **(Fig. S2 A-C)** despite MDA-MB-231 KO cells displaying elevated E-cadherin. However, regardless of increased protein levels, nuclear translocation remains unaltered **(Fig. S2 D, E)**. Thus, we conclude that transcriptional repression of E-cadherin is not likely to be the driving factor for the observed phenotype.

Through GSEA we revealed that gene sets for endocytosis, intracellular transport, and exocytosis are downregulated in RIL-175 KO cells **(Fig. 3A)**. On the one hand, we investigated cellular uptake in RIL-175 cells with the use of FITC-dextran. Interestingly,

uptake remains unaltered upon TRPML1 KO **(Fig. 3B, C)**. On the other hand, we examined exocytosis behaviour by triggering exocytosis with Ionomycin or calcium, respectively. We observed a reduction of exocytotic activity in RIL-175 KO cells indicated by a diminished release of β-hexosaminidase **(Fig. 3D)** and FITC-dextran **(Fig. 3E)**. In contrast, for MDA-MB-231 KO cells, we noted a largely reduced endocytic uptake of FITC-dextran **(Fig. 3B, C)** whereas exocytosis remained unaltered **(Fig. 3E)**.

Supporting these observations, we observed that after triggering exocytosis with Ionomycin, MDA-MB-231 KO cells displayed significantly reduced Cathepsin B release into the medium whereas no effect was observable for RIL-175 KO cells **(Fig. 3F)**. Cancer cells often release the lysosomal protease Cathepsin B for collagen degradation in the ECM by vesicular exocytosis [53].

Vesicle tethering, i.e. the building of protein complexes that physically connect a transport vesicle to its target membrane prior to fusion [54], which is a crucial step in trafficking processes, is mediated by Rab-proteins [55]. Internalized proteins (e. g. E-cadherin) are transferred from endocytic vesicles to Rab5-positive early endosomes (EEs) and can be re-routed from recycling endosomes to the cell membrane via Rab11 [29]. In line with our previous findings, Rab5 levels remained unaffected in RIL-175 KO cells, indicating that TRPML1 has no effect on the level of Rab5-positive EEs endocytosis. **(Fig. 3G)**. This finding is opposed to the significant reduction of Rab11 in RIL-175 KO cells on mRNA level **(Fig. S3)** and protein level **(Fig. 3G)** corroborating a predominant effect on the exocytotic machinery.

In contrast, Rab5 was significantly reduced in MDA-MB-231 KO cells **(Fig. 3G)** highlighting aberrant trafficking after endocytosis. Concurrently, a TRPML1-HA-tag fusion protein colocalizes with Rab5 and Rab11 in both WT cell lines. However, in MDA-MB-231 cells we were not able to observe any significant difference in the colocalization of TRPML1 with Rab5 or Rab11 **(Fig. 3H)**. By contrast, RIL-175 cells showed a significantly larger colocalization of TRPML1 with Rab11 than with Rab5 **(Fig. 3H)**. Hence, taken together, the data strongly supports a pivotal and differential role of TRPML1 in recycling processes. While endocytic uptake is evidently hampered in MDA-MB-231 KO cells, RIL-175 KO cells display abrogated exocytosis.

3.4. Re-establishing intracellular trafficking rescues E-cadherin

Rab11, a prominent marker of recycling endosomes, has emerged as an important regulator of E-cadherin [56,57]. After transient Rab11 overexpression in RIL-175 TRPML1 KO cells, we observed an increase in E-cadherin on protein level **(Fig. 4A)**. Consistently, E-cadherin was effectively re-introduced at the plasma membrane **(Fig. 4B)**.

Proteins cannot solely be recycled via Rab11 route but also in a fast-recycling track occurring directly from early endosomes [28,29]. In RIL-175 KO cells, this pathway is unaffected, as shown by the unaltered recovery of an E-cadherin GFP-fusion protein in fluorescence recovery after photobleaching (FRAP) experiments **(Fig. 4C)**. Lastly, we observed no effect of blocking lysosomal degradation with chloroquine on E-cadherin protein expression indicating no involvement of disrupted lysosomal function in the observed mode of action **(Fig. 4D)**. Preceding data showed reduced E-cadherin mRNA-levels in RIL-175 KO cells **(Fig. 2D)**, suggesting transcriptional repression to be responsible for reduced E-cadherin levels, yet decreased levels of E-cadherin in RIL-175 KO cells can be rescued after re-establishing intracellular trafficking. In conclusion, these findings demonstrate aberrant slow recycling, and not transcriptional repression as the underlying cause for E-cadherin expression and trafficking.

3.5. Knockout of TRPML1 affects cell adhesion by abrogating β_1-integrin receptor trafficking

In addition to reduced cell-junction assembly and cytoskeleton organization, GSEA revealed reduced cell matrix-adhesion upon KO of TPRML1 **(Fig. 2A)** which is a fundamental part of the cell migration cycle [20]. Thus, we performed an adhesion assay by seeding the cells onto different coating conditions representing some of the proteins that make up the macromolecular network of the ECM, including collagen, fibronectin, and laminin [58]. Indeed, both KO cell lines displayed reduced adhesion to all employed ECM ligands, as analysed by confocal microscopy **(Fig. 5A, Fig. S4)**. Cell-matrix adhesion is predominantly mediated by the family of integrins [23]. Despite attenuated cell-matrix adhesion, β_1-integrin-activity itself remained unaltered in both KO cell lines **(Fig. 5B)**. Like E-cadherin, integrins undergo constant recycling processes at the leading edge of migrating cells allowing a spatiotemporal restriction of adhesive sites [26,27]. In this context, confocal microscopy revealed a diffusely accumulated β_1-integrin-receptor (total and active form) at the plasma membrane of MDA-MB-231 KO cells **(Fig. 5C)** contrasting the distinctive integrin-containing vesicles in the cytoplasm of the parental cell line. Disturbed endocytosis was confirmed by a receptor-internalization assay showing that only the WT cells could properly internalize the β_1-integrin receptor **(Fig. 5D)**. In contrast, unaltered β_1-integrin-internalization was detected in RIL-175 KO cells **(Fig. 5E)** indicating unaffected endocytosis. Consistently, enlarged β_1-integrin vesicles **(Fig. 5F)** implicated trapping of the receptor in endolysosomal vesicles corroborating hampered recycling processes in RIL-175 KO cells. Additionally, dysfunctional β_1-integrin trafficking is reflected in altered integrin downstream signalling. Upon clustering of integrins, autophosphorylation of FAK initiates FAK-Src-complex formation activating downstream modulators like Rac1 or RhoA to trigger actin-polymerization [18]. Loss of

TRPML1 function results in downregulated FAK-activity in both KO cell lines and reduced Src-activity in MDA-MB-231 KO cells. RIL-175 KO cells additionally displayed lowered RhoA-activity **(Fig. 5G)**. Taken together, the data suggest the downregulation of β_1-integrin signalling cascade downstream of β_1-integrin activation is a result of disturbed β_1-integrin-receptor recycling upon KO. This is reflected in the abatement of adhesive properties.

3.6. Ablation of TRPML1 function disrupts actin polymerisation and polarization of migrating cells

Recycling processes occurring directly at the leading edge of migrating cells enable spatial control of a variety of pro-migratory events like adhesion and actin-polymerization [19,59]. Indeed, we could observe altered actin polymerisation in both KO cell lines **(Fig. 6A)**. In addition, our results indicate that a colocalization of polymerised actin and E-cadherin levels secure AJ complexes at cell-cell contact site **(Fig. 6B)** and therefore adhesive traits **(Fig. 5A)**. The loss of TRPML1 function reduces E-cadherin levels at membrane site and simultaneously actin polymerisation in the whole cell **(Fig. 6B)**. Moreover, RIL-175 KO cells lack active β_1-integrin containing vesicles at the leading edge. Despite unaltered Rac1 protein levels **(Fig. 5G)**, Rac1 appears to be less condensed at the cellular front. Rac1 is indispensable for actin-polymerization at protrusion site [20,60], consequently lamellipodia formation is hampered **(Fig. 6C)**. In conclusion, due to insufficient transportation processes of Rac1 to the leading edges and disruption of actin polymerisation in KO cells, they lack distinctive pro-migratory polarization at the migration front.

4. Discussion

This study designates TRPML1 as a promising target for the treatment of invasive cancers. By abrogating the intracellular trafficking of E-cadherin and β_1-integrin, TRPML1 loss of function attenuates cancer cell migration and adhesion to the ECM. KO evidently hampered trafficking processes which is reflected in reduced endocytic activity in MDA-MB-231 and impaired recycling in RIL-175 cells **(Fig. 3)**. We observed altered β_1-integrin signalling due to aberrant β_1-integrin receptor internalization (MDA-MB-231) and recycling (RIL-175) which was manifested in lowered adhesive properties of the KO cell lines **(Fig. 5)**. Focal adhesion site formation at leading edges and in cell-cell contact site is required for efficient locomotion. It is predominantly mediated by the intracellular trafficking machinery. In our study, we observed altered β_1-integrin signalling due to aberrant β_1-integrin receptor internalization and recycling. Furthermore, AJ complex molecules E-cadherin and beta-catenin diminish from plasma membrane site upon loss of TRPML1 function (RIL-175). Altered β_1-integrin signalling and reduction of AJ complexes manifested in lowered adhesive properties of both KO cell lines [27,61].

Also, in mesenchymal MDA-MB-231 WT cells an elevation of E-cadherin levels upon loss of TRPML1 function was observed [50] **(Fig. 2)**. This elevation was associated with a re-establishment of the epithelial phenotype in KO cells. Our observations are in line with the findings of Merk et al., who have shown that impairing lysosomal function by V-ATPase inhibition resulted in impaired E-cadherin internalization and increased E-cadherin surface levels alongside reduced migration in a breast-cancer cell model [62]. Other research also highlighted the possibility of hampering cancer cell migration by increasing E-cadherin, further corroborating its status as tumour suppressor [14]. Accordingly, Chao et al. and Mbalaviele et al. observed reduced migratory capacities in MDA-MB-231 cells after stable introduction of E-cadherin both *in vitro* and *in vivo* [50,63]. Intriguingly, despite markedly reduced migration, we observed downregulation of E-cadherin in RIL-175 KO cells **(Fig. 2)**. This is at first glance counterintuitive as E-cadherin is, as aforementioned, a widely established tumour suppressor. Upon loss of E-cadherin, which is typically associated with highly invasive tumours, cells gain a mesenchymal phenotype and can individually invade the surrounding tissue due to the loss of cell-cell adhesion [15]. Interestingly, as shown by Haraguchi et al., the loss of E-cadherin impedes pro-migratory RhoA- and Rac1-signalling and thereby reduces the migratory capacity of E-cadherin KO RMG-1 cells [64]. Consistently, E-cadherin is a crucial regulator of actin dynamics and accordingly the lamellipodia and filopodia formation due to its direct link to the actin cytoskeleton via β- and α-catenin [10]. Indeed, we could not only observe hampered RhoA-activity **(Fig. 5)**, but also delocalized Rac1 at the leading edge, resulting in disrupted actin-polymerization not only at the migration front **(Fig. 6)**. Taken together, we therefore suggest that the downregulation of E-cadherin through TRPML1-mediated rerouting could be one mode of action in affecting actin-polymerization and migration. Additionally, we suggest downregulated β1-integrin signalling in KO cells to further hinder actin polymerisation.

Our findings raise the question how these are regulated by lysosomal cation channel TRPML1. In this context, one must mention that TRPML1 is suggested to be the main lysosomal Ca^{2+} cation channel, which has shown to influence not only lysosomal pH but also intracellular Ca^{2+} concentrations [65,66]. The second messenger Ca^{2+} influences i.e., vesicle fusion and fission [67–69] and Rab-proteins [70–73]. In line with literature, we could observe significant reduction of intracellular calcium upon loss of TRPML1 function in RIL-175 cells **(Fig. S5)**. Thus, TRPML1-mediated Ca^{2+}-flux will be discussed as possible mode of action for the described effects above. Previous research has highlighted the importance of TRPML1-mediated Ca^{2+}-flux in cellular trafficking, as it has shown to regulate endo-lysosomal fusion in *Drosophilia* [74] and lysosomal exocytosis [75]. Moreover, it has been implicated to interact with fusion proteins in a Ca^{2+}-dependent manner [76,77]. Of note, the inhibition of TPC2,

another endolysosomal calcium channel, has already been reported to impair cell adhesion and migration by attenuating β1-integrin recycling which is likely attributed to downregulated Ca^{2+}-signalling upon TPC2 inhibition [39]. That in mind, we propose TRPML1-mediated Ca^{2+} to be responsible for our observations of lack of active β_1-integrin at leading edges as well.
Also, KO cells displayed less condensed Rac1 at the leading edge and altered actin polymerisation, consequently hampered lamellipodia formation **(Fig. 6)**. As mentioned before, Rac1 is key regulator for cytoskeleton organisation, incl. actin polymerisation and lamellipodia formation. It has been shown that Rac1 activation and translocation is regulated by intracellular calcium levels [78]. Price et al. showed that elevated intracellular calcium concentrations induced activation of protein kinase C (PKC), which in return phosphorylates RhoGDI alpha and induce translocation of cytosolic Rac to membrane sites [78]. Furthermore, Vestre et al. linked Ca^{2+} release from TRPML1 to the activation of myosin phosphorylation, thereby triggering localized actomyosin contractility [79]. KO of TRPML1 was associated with alterations in actin distribution and therefore altered migration behaviour of DCs [79]. Taken together, we propose TRPML1-mediated Ca^{2+} flux to be another suitable mode of action for the reduction of Rac1 activation at the leading edges, alterations in actin polymerisation and consequently in altered migration behaviour as well. We propose that the opposing effects for our investigated cell lines might arise from tissue-specific functions of TRPML1. Indeed, TRPML1 is known to exhibit opposing functions in tumorigenesis as it may either be up- or downregulated in breast cancer or glioblastoma, respectively [34,80]. Additionally, TRPML1 has been implicated to have contrasting roles in autophagy regulation. While pharmacological channel activation hampers autophagy in HeLa [81], inhibition of TPRML1 with EDME in MDA-MB-231 equally attenuates autophagy [34]. In line, we have observed opposing protein expression of early-endosomes and recycling-endosomes markers Rab5 and Rab11 [28] and a stronger colocalization of TRPML1 with Rab11 than with Rab5 in RIL-175 cells, suggesting a cell-line dependent effect on intracellular trafficking processes. In summary, we demonstrate that impaired TRPML1 function reduces migration and adhesion of cancer cells in vitro resulting from disturbed trafficking of important regulators of migration i.e., E-cadherin, β1-integrin and Rac1, and cytoskeleton organisation in a cell line specific manner. Our study reveals the pivotal role for TRPML1 to fundamental processes in cancer cell migration, providing it to be an attractive target for the treatment of invasive cancers.

Acknowledgements

The authors thank Prof. Dr. Stefan Zahler for helpful discussions and Sylvia Schnegg for her excellent technical support.

Funding

Karin Bartel reports financial support was provided by German Research Foundation. Angelika Vollmar reports financial support was provided by German Research Foundation (DFG VO 376/19-1 and BA 7238/3-2).

Conflict of interest

The authors declare that they have no conflicts of interest with the contents of this article.

Materials availability

All data generated or analysed during this study is included in this published article and its supplementary information files. Any additional information might be obtained from the corresponding author upon reasonable request.

References

[1] J. Liu, P. Pandya, S. Afshar, Therapeutic Advances in Oncology, Int. J. Mol. Sci. 22 (2021). https://doi.org/10.3390/ijms22042008.

[2] C. Pucci, C. Martinelli, G. Ciofani, Innovative approaches for cancer treatment: current perspectives and new challenges, Ecancermedicalscience 13 (2019) 961. https://doi.org/10.3332/ecancer.2019.961.

[3] H. Sung, J. Ferlay, R.L. Siegel, M. Laversanne, I. Soerjomataram, A. Jemal, F. Bray, Global Cancer Statistics 2020: GLOBOCAN Estimates of Incidence and Mortality Worldwide for 36 Cancers in 185 Countries, CA Cancer J. Clin. 71 (2021) 209–249. https://doi.org/10.3322/caac.21660.

[4] M. Liu, J. Yang, B. Xu, X. Zhang, Tumor metastasis: Mechanistic insights and therapeutic interventions, MedComm (2020) 2 (2021) 587–617. https://doi.org/10.1002/mco2.100.

[5] F. Arvelo, F. Sojo, C. Cotte, Tumour progression and metastasis, Ecancermedicalscience 10 (2016) 617. https://doi.org/10.3332/ecancer.2016.617.

[6] T.D. Palmer, W.J. Ashby, J.D. Lewis, A. Zijlstra, Targeting tumor cell motility to prevent metastasis, Adv. Drug Deliv. Rev. 63 (2011) 568–581. https://doi.org/10.1016/j.addr.2011.04.008.

[7] F. van Zijl, G. Krupitza, W. Mikulits, Initial steps of metastasis: cell invasion and endothelial transmigration, Mutat. Res. 728 (2011) 23–34. https://doi.org/10.1016/j.mrrev.2011.05.002.

[8] N.A. Gloushankova, S.N. Rubtsova, I.Y. Zhitnyak, Cadherin-mediated cell-cell interactions in normal and cancer cells, Tissue Barriers 5 (2017) e1356900. https://doi.org/10.1080/21688370.2017.1356900.

[9] C.-Y. Loh, J.Y. Chai, T.F. Tang, W.F. Wong, G. Sethi, M.K. Shanmugam, P.P. Chong, C.Y. Looi, The E-Cadherin and N-Cadherin Switch in Epithelial-to-Mesenchymal Transition: Signaling, Therapeutic Implications, and Challenges, Cells 8 (2019). https://doi.org/10.3390/cells8101118.

[10] M. Canel, A. Serrels, M.C. Frame, V.G. Brunton, E-cadherin-integrin crosstalk in cancer invasion and metastasis, J. Cell Sci. 126 (2013) 393–401. https://doi.org/10.1242/jcs.100115.

[11] H. Hamidi, J. Ivaska, Every step of the way: integrins in cancer progression and metastasis, Nat. Rev. Cancer 18 (2018) 533–548. https://doi.org/10.1038/s41568-018-0038-z.

[12] T.P. Schmidt, C. Goetz, M. Huemer, G. Schneider, S. Wessler, Calcium binding protects E-cadherin from cleavage by Helicobacter pylori HtrA, Gut Pathog. 8 (2016) 29. https://doi.org/10.1186/s13099-016-0112-6.
[13] X. Liu, K.-M. Chu, E-cadherin and gastric cancer: cause, consequence, and applications, Biomed Res. Int. 2014 (2014) 637308. https://doi.org/10.1155/2014/637308.
[14] J.-H. Venhuizen, F.J.C. Jacobs, P.N. Span, M.M. Zegers, P120 and E-cadherin: Double-edged swords in tumor metastasis, Semin. Cancer Biol. 60 (2020) 107–120. https://doi.org/10.1016/j.semcancer.2019.07.020.
[15] A.M. Mendonsa, T.-Y. Na, B.M. Gumbiner, E-cadherin in contact inhibition and cancer, Oncogene 37 (2018) 4769–4780. https://doi.org/10.1038/s41388-018-0304-2.
[16] Y. Yang, H. Zheng, Y. Zhan, S. Fan, An emerging tumor invasion mechanism about the collective cell migration, Am. J. Transl. Res. 11 (2019) 5301–5312.
[17] V. Padmanaban, I. Krol, Y. Suhail, B.M. Szczerba, N. Aceto, J.S. Bader, A.J. Ewald, E-cadherin is required for metastasis in multiple models of breast cancer, Nature 573 (2019) 439–444. https://doi.org/10.1038/s41586-019-1526-3.
[18] M. Cheah, M.R. Andrews, Integrin Activation: Implications for Axon Regeneration, Cells 7 (2018). https://doi.org/10.3390/cells7030020.
[19] R. Horwitz, D. Webb, Cell migration, Curr. Biol. 13 (2003) R756-9. https://doi.org/10.1016/j.cub.2003.09.014.
[20] M.P. Sheetz, D. Felsenfeld, C.G. Galbraith, D. Choquet, Cell migration as a five-step cycle, Biochem. Soc. Symp. 65 (1999) 233–243.
[21] A.R. Horwitz, J.T. Parsons, Cell migration--movin' on, Science 286 (1999) 1102–1103. https://doi.org/10.1126/science.286.5442.1102.
[22] D. Subramani, S.K. Alahari, Integrin-mediated function of Rab GTPases in cancer progression, Mol. Cancer 9 (2010) 312. https://doi.org/10.1186/1476-4598-9-312.
[23] J.D. Hood, D.A. Cheresh, Role of integrins in cell invasion and migration, Nat. Rev. Cancer 2 (2002) 91–100. https://doi.org/10.1038/nrc727.
[24] J.S. Desgrosellier, D.A. Cheresh, Integrins in cancer: biological implications and therapeutic opportunities, Nat. Rev. Cancer 10 (2010) 9–22. https://doi.org/10.1038/nrc2748.
[25] S.M. Arias-Mejias, K.Y. Warda, E. Quattrocchi, H. Alonso-Quinones, S. Sominidi-Damodaran, A. Meves, The role of integrins in melanoma: a review, Int. J. Dermatol. 59 (2020) 525–534. https://doi.org/10.1111/ijd.14850.
[26] R.E. Bridgewater, J.C. Norman, P.T. Caswell, Integrin trafficking at a glance, J. Cell Sci. 125 (2012) 3695–3701. https://doi.org/10.1242/jcs.095810.
[27] P.T. Caswell, S. Vadrevu, J.C. Norman, Integrins: masters and slaves of endocytic transport, Nat. Rev. Mol. Cell Biol. 10 (2009) 843–853. https://doi.org/10.1038/nrm2799.
[28] L. Brüser, S. Bogdan, Adherens Junctions on the Move-Membrane Trafficking of E-Cadherin, Cold Spring Harb. Perspect. Biol. 9 (2017). https://doi.org/10.1101/cshperspect.a029140.
[29] E. Delva, A.P. Kowalczyk, Regulation of cadherin trafficking, Traffic 10 (2009) 259–267. https://doi.org/10.1111/j.1600-0854.2008.00862.x.
[30] S. Piao, R.K. Amaravadi, Targeting the lysosome in cancer, Ann. N. Y. Acad. Sci. 1371 (2016) 45–54. https://doi.org/10.1111/nyas.12953.
[31] M.P. Cuajungco, J. Silva, A. Habibi, J.A. Valadez, The mucolipin-2 (TRPML2) ion channel: a tissue-specific protein crucial to normal cell function, Pflugers Arch. 468 (2016) 177–192. https://doi.org/10.1007/s00424-015-1732-2.
[32] W.X. Siow, Y. Kabiri, R. Tang, Y.-K. Chao, E. Plesch, C. Eberhagen, F. Flenkenthaler, T. Fröhlich, F. Bracher, C. Grimm, M. Biel, H. Zischka, A.M. Vollmar, K. Bartel, Lysosomal TRPML1 regulates mitochondrial function in hepatocellular carcinoma cells, J. Cell Sci. 135 (2022). https://doi.org/10.1242/jcs.259455.

[33] C. Grimm, E. Butz, C.-C. Chen, C. Wahl-Schott, M. Biel, From mucolipidosis type IV to Ebola: TRPML and two-pore channels at the crossroads of endo-lysosomal trafficking and disease, Cell Calcium 67 (2017) 148–155. https://doi.org/10.1016/j.ceca.2017.04.003.

[34] P. Rühl, A.S. Rosato, N. Urban, S. Gerndt, R. Tang, C. Abrahamian, C. Leser, J. Sheng, A. Jha, G. Vollmer, M. Schaefer, F. Bracher, C. Grimm, Estradiol analogs attenuate autophagy, cell migration and invasion by direct and selective inhibition of TRPML1, independent of estrogen receptors, Sci. Rep. 11 (2021) 8313. https://doi.org/10.1038/s41598-021-87817-4.

[35] A. Scotto Rosato, S. Montefusco, C. Soldati, S. Di Paola, A. Capuozzo, J. Monfregola, E. Polishchuk, A. Amabile, C. Grimm, A. Lombardo, M.A. de Matteis, A. Ballabio, D.L. Medina, TRPML1 links lysosomal calcium to autophagosome biogenesis through the activation of the CaMKKβ/VPS34 pathway, Nat. Commun. 10 (2019) 5630. https://doi.org/10.1038/s41467-019-13572-w.

[36] M. Xu, S. Almasi, Y. Yang, C. Yan, A.M. Sterea, A.K. Rizvi Syeda, B. Shen, C. Richard Derek, P. Huang, S. Gujar, J. Wang, W.-X. Zong, M. Trebak, Y. El Hiani, X.-P. Dong, The lysosomal TRPML1 channel regulates triple negative breast cancer development by promoting mTORC1 and purinergic signaling pathways, Cell Calcium 79 (2019) 80–88. https://doi.org/10.1016/j.ceca.2019.02.010.

[37] L.A. Orci, S. Lacotte, V. Delaune, F. Slits, G. Oldani, V. Lazarevic, C. Rossetti, L. Rubbia-Brandt, P. Morel, C. Toso, Effects of the gut-liver axis on ischaemia-mediated hepatocellular carcinoma recurrence in the mouse liver, J. Hepatol. 68 (2018) 978–985. https://doi.org/10.1016/j.jhep.2017.12.025.

[38] M. Müller, S. Gerndt, Y.-K. Chao, T. Zisis, O.N.P. Nguyen, A. Gerwien, N. Urban, C. Müller, F.A. Gegenfurtner, F. Geisslinger, C. Ortler, C.-C. Chen, S. Zahler, M. Biel, M. Schaefer, C. Grimm, F. Bracher, A.M. Vollmar, K. Bartel, Gene editing and synthetically accessible inhibitors reveal role for TPC2 in HCC cell proliferation and tumor growth, Cell Chem. Biol. 28 (2021) 1119-1131.e27. https://doi.org/10.1016/j.chembiol.2021.01.023.

[39] O.N.P. Nguyen, C. Grimm, L.S. Schneider, Y.-K. Chao, C. Atzberger, K. Bartel, A. Watermann, M. Ulrich, D. Mayr, C. Wahl-Schott, M. Biel, A.M. Vollmar, Two-Pore Channel Function Is Crucial for the Migration of Invasive Cancer Cells, Cancer Res. 77 (2017) 1427–1438. https://doi.org/10.1158/0008-5472.CAN-16-0852.

[40] T. Zisis, D.B. Brückner, T. Brandstätter, W.X. Siow, J. d'Alessandro, A.M. Vollmar, C.P. Broedersz, S. Zahler, Disentangling cadherin-mediated cell-cell interactions in collective cancer cell migration, Biophys. J. 121 (2022) 44–60. https://doi.org/10.1016/j.bpj.2021.12.006.

[41] A. Subramanian, P. Tamayo, V.K. Mootha, S. Mukherjee, B.L. Ebert, M.A. Gillette, A. Paulovich, S.L. Pomeroy, T.R. Golub, E.S. Lander, J.P. Mesirov, Gene set enrichment analysis: a knowledge-based approach for interpreting genome-wide expression profiles, Proc. Natl. Acad. Sci. U. S. A. 102 (2005) 15545–15550. https://doi.org/10.1073/pnas.0506580102.

[42] Y. Ye, J.D. Tellez, M. Durazo, M. Belcher, K. Yearsley, S.H. Barsky, E-cadherin accumulation within the lymphovascular embolus of inflammatory breast cancer is due to altered trafficking, Anticancer Res. 30 (2010) 3903–3910.

[43] A. Liberzon, A. Subramanian, R. Pinchback, H. Thorvaldsdóttir, P. Tamayo, J.P. Mesirov, Molecular signatures database (MSigDB) 3.0, Bioinformatics 27 (2011) 1739–1740. https://doi.org/10.1093/bioinformatics/btr260.

[44] F. Geisslinger, M. Müller, Y.-K. Chao, C. Grimm, A.M. Vollmar, K. Bartel, Targeting TPC2 sensitizes acute lymphoblastic leukemia cells to chemotherapeutics by impairing lysosomal function, Cell Death Dis 13 (2022) 668. https://doi.org/10.1038/s41419-022-05105-z.

[45] S. Fleige, V. Walf, S. Huch, C. Prgomet, J. Sehm, M.W. Pfaffl, Comparison of relative mRNA quantification models and the impact of RNA integrity in quantitative real-time RT-PCR, Biotechnol. Lett. 28 (2006) 1601–1613. https://doi.org/10.1007/s10529-006-9127-2.
[46] E. Plesch, C.-C. Chen, E. Butz, A. Scotto Rosato, E.K. Krogsaeter, H. Yinan, K. Bartel, M. Keller, D. Robaa, D. Teupser, L.M. Holdt, A.M. Vollmar, W. Sippl, R. Puertollano, D. Medina, M. Biel, C. Wahl-Schott, F. Bracher, C. Grimm, Selective agonist of TRPML2 reveals direct role in chemokine release from innate immune cells, Elife 7 (2018). https://doi.org/10.7554/eLife.39720.
[47] A.D. Colella, N. Chegenii, M.N. Tea, I.L. Gibbins, K.A. Williams, T.K. Chataway, Comparison of Stain-Free gels with traditional immunoblot loading control methodology, Anal. Biochem. 430 (2012) 108–110. https://doi.org/10.1016/j.ab.2012.08.015.
[48] C. Abrahamian, C. Grimm, Endolysosomal Cation Channels and MITF in Melanocytes and Melanoma, Biomolecules 11 (2021) 1021. https://doi.org/10.3390/biom11071021.
[49] H. Bao, S. Yang, H. Li, H. Yao, Y. Zhang, J. Zhang, G. Xu, H. Jin, F. Wang, The Interplay Between E-Cadherin, Connexin 43, and Zona Occludens 1 in Retinal Pigment Epithelial Cells, Invest. Ophthalmol. Vis. Sci. 60 (2019) 5104–5111. https://doi.org/10.1167/iovs.19-27768.
[50] Y.L. Chao, C.R. Shepard, A. Wells, Breast carcinoma cells re-express E-cadherin during mesenchymal to epithelial reverting transition, Mol. Cancer 9 (2010) 179. https://doi.org/10.1186/1476-4598-9-179.
[51] X.Q. Wang, W. Zhang, E.L.H. Lui, Y. Zhu, P. Lu, X. Yu, J. Sun, S. Yang, R.T.P. Poon, S.T. Fan, Notch1-Snail1-E-cadherin pathway in metastatic hepatocellular carcinoma, Int. J. Cancer 131 (2012) E163-72. https://doi.org/10.1002/ijc.27336.
[52] E. Sterneck, D.K. Poria, K. Balamurugan, Slug and E-Cadherin: Stealth Accomplices?, Front. Mol. Biosci. 7 (2020) 138. https://doi.org/10.3389/fmolb.2020.00138.
[53] N.P. Withana, G. Blum, M. Sameni, C. Slaney, A. Anbalagan, M.B. Olive, B.N. Bidwell, L. Edgington, L. Wang, K. Moin, B.F. Sloane, R.L. Anderson, M.S. Bogyo, B.S. Parker, Cathepsin B inhibition limits bone metastasis in breast cancer, Cancer Res. 72 (2012) 1199–1209. https://doi.org/10.1158/0008-5472.CAN-11-2759.
[54] S.J. An, F. Rivera-Molina, A. Anneken, Z. Xi, B. McNellis, V.I. Polejaev, D. Toomre, An active tethering mechanism controls the fate of vesicles, Nat Commun 12 (2021) 5434. https://doi.org/10.1038/s41467-021-25465-y.
[55] A.L.E. Hutagalung, Role of Rab GTPases in membrane traffic and cell physiology, Physiol. Rev. 91 (2011) 119–149. https://doi.org/10.1152/physrev.00059.2009.
[56] J.G. Lock, J.L. Stow, Rab11 in recycling endosomes regulates the sorting and basolateral transport of E-cadherin, Mol. Biol. Cell 16 (2005) 1744–1755. https://doi.org/10.1091/mbc.E04-10-0867.
[57] Y.-C. Chung, W.-C. Wei, S.-H. Huang, C.-M. Shih, C.-P. Hsu, K.-J. Chang, W.-T. Chao, Rab11 regulates E-cadherin expression and induces cell transformation in colorectal carcinoma, BMC Cancer 14 (2014) 587. https://doi.org/10.1186/1471-2407-14-587.
[58] A.D. Theocharis, S.S. Skandalis, C. Gialeli, N.K. Karamanos, Extracellular matrix structure, Adv. Drug Deliv. Rev. 97 (2016) 4–27. https://doi.org/10.1016/j.addr.2015.11.001.
[59] M.C. Jones, P.T. Caswell, J.C. Norman, Endocytic recycling pathways: emerging regulators of cell migration, Curr. Opin. Cell Biol. 18 (2006) 549–557. https://doi.org/10.1016/j.ceb.2006.08.003.
[60] C.Y. Chung, S. Lee, C. Briscoe, C. Ellsworth, R.A. Firtel, Role of Rac in controlling the actin cytoskeleton and chemotaxis in motile cells, Proc. Natl. Acad. Sci. U. S. A. 97 (2000) 5225–5230. https://doi.org/10.1073/pnas.97.10.5225.

[61] T. Maritzen, H. Schachtner, D.F. Legler, On the move: endocytic trafficking in cell migration, Cell. Mol. Life Sci. 72 (2015) 2119–2134. https://doi.org/10.1007/s00018-015-1855-9.
[62] H. Merk, P. Messer, M.A. Ardelt, D.C. Lamb, S. Zahler, R. Müller, A.M. Vollmar, J. Pachmayr, Inhibition of the V-ATPase by Archazolid A: A New Strategy to Inhibit EMT, Mol. Cancer Ther. 16 (2017) 2329–2339. https://doi.org/10.1158/1535-7163.MCT-17-0129.
[63] G. Mbalaviele, C.R. Dunstan, A. Sasaki, P.J. Williams, G.R. Mundy, T. Yoneda, E-cadherin expression in human breast cancer cells suppresses the development of osteolytic bone metastases in an experimental metastasis model, Cancer Res. 56 (1996) 4063–4070.
[64] M. Haraguchi, T. Fukushige, T. Kanekura, M. Ozawa, E-cadherin loss in RMG-1 cells inhibits cell migration and its regulation by Rho GTPases, Biochem. Biophys. Rep. 18 (2019) 100650. https://doi.org/10.1016/j.bbrep.2019.100650.
[65] W. Wang, X. Zhang, Q. Gao, H. Xu, TRPML1: an ion channel in the lysosome, Handb. Exp. Pharmacol. 222 (2014) 631–645. https://doi.org/10.1007/978-3-642-54215-2_24.
[66] B.S. Kilpatrick, E.R. Eden, A.H. Schapira, C.E. Futter, S. Patel, Direct mobilisation of lysosomal Ca2+ triggers complex Ca2+ signals, J. Cell Sci. 126 (2013) 60–66. https://doi.org/10.1242/jcs.118836.
[67] J.P. Luzio, P.R. Pryor, N.A. Bright, Lysosomes: fusion and function, Nat. Rev. Mol. Cell Biol. 8 (2007) 622–632. https://doi.org/10.1038/nrm2217.
[68] A. Reddy, E.V. Caler, N.W. Andrews, Plasma membrane repair is mediated by Ca(2+)-regulated exocytosis of lysosomes, Cell 106 (2001) 157–169. https://doi.org/10.1016/s0092-8674(01)00421-4.
[69] J. Sargeant, J.C. Hay, Ca2+ regulation of constitutive vesicle trafficking, Fac. Rev. 11 (2022) 6. https://doi.org/10.12703/r/11-6.
[70] B.L. Grosshans, D. Ortiz, P. Novick, Rabs and their effectors: achieving specificity in membrane traffic, Proc. Natl. Acad. Sci. U. S. A. 103 (2006) 11821–11827. https://doi.org/10.1073/pnas.0601617103.
[71] J. Jing, R. Prekeris, Polarized endocytic transport: the roles of Rab11 and Rab11-FIPs in regulating cell polarity, Histol. Histopathol. 24 (2009) 1171–1180. https://doi.org/10.14670/HH-24.1171.
[72] K. Parkinson, A.E. Baines, T. Keller, N. Gruenheit, L. Bragg, R.A. North, C.R.L. Thompson, Calcium-dependent regulation of Rab activation and vesicle fusion by an intracellular P2X ion channel, Nat. Cell Biol. 16 (2014) 87–98. https://doi.org/10.1038/ncb2887.
[73] J.-B. Park, J.-S. Kim, J.-Y. Lee, J. Kim, J.-Y. Seo, A.-R. Kim, GTP binds to Rab3A in a complex with Ca2+/calmodulin, Biochem. J. 362 (2002) 651–657. https://doi.org/10.1042/0264-6021:3620651.
[74] C.-O. Wong, R. Li, C. Montell, K. Venkatachalam, Drosophila TRPML is required for TORC1 activation, Curr. Biol. 22 (2012) 1616–1621. https://doi.org/10.1016/j.cub.2012.06.055.
[75] M.A. Samie, H. Xu, Lysosomal exocytosis and lipid storage disorders, J. Lipid Res. 55 (2014) 995–1009. https://doi.org/10.1194/jlr.R046896.
[76] S. Vergarajauregui, J.A. Martina, R. Puertollano, Identification of the penta-EF-hand protein ALG-2 as a Ca2+-dependent interactor of mucolipin-1, J. Biol. Chem. 284 (2009) 36357–36366. https://doi.org/10.1074/jbc.M109.047241.
[77] X. Li, N. Rydzewski, A. Hider, X. Zhang, J. Yang, W. Wang, Q. Gao, X. Cheng, H. Xu, A molecular mechanism to regulate lysosome motility for lysosome positioning and tubulation, Nat. Cell Biol. 18 (2016) 404–417. https://doi.org/10.1038/ncb3324.

[78] L.S. Price, M. Langeslag, J.P. ten Klooster, P.L. Hordijk, K. Jalink, J.G. Collard, Calcium signaling regulates translocation and activation of Rac, Journal of Biological Chemistry 278 (2003) 39413–39421. https://doi.org/10.1074/jbc.M302083200.
[79] K. Vestre, I. Persiconi, M. Borg Distefano, N. Mensali, N.A. Guadagno, M. Bretou, S. Wälchli, C. Arnold-Schrauf, O. Bakke, M. Dalod, A.-M. Lennon-Dumenil, C. Progida, Rab7b regulates dendritic cell migration by linking lysosomes to the actomyosin cytoskeleton, J. Cell Sci. 134 (2021). https://doi.org/10.1242/jcs.259221.
[80] M.B. Morelli, C. Amantini, D. Tomassoni, M. Nabissi, A. Arcella, G. Santoni, Transient Receptor Potential Mucolipin-1 Channels in Glioblastoma: Role in Patient's Survival, Cancers (Basel) 11 (2019). https://doi.org/10.3390/cancers11040525.
[81] J. Qi, Y. Xing, Y. Liu, M.-M. Wang, X. Wei, Z. Sui, L. Ding, Y. Zhang, C. Lu, Y.-H. Fei, N. Liu, R. Chen, M. Wu, L. Wang, Z. Zhong, T. Wang, Y. Liu, Y. Wang, J. Liu, H. Xu, F. Guo, W. Wang, MCOLN1/TRPML1 finely controls oncogenic autophagy in cancer by mediating zinc influx, Autophagy 17 (2021) 4401–4422. https://doi.org/10.1080/15548627.2021.1917132.

Figure 1: TRPML1 loss of function reduces cancer cell migration.

(A-D) Images are representative. **(A, B)** Wound healing (A) and Boyden-Chamber experiments along FCS gradient (B) show fixed and crystal-violet stained cells after migration for 24 h (A, B (MDA-MB-231)) or 6 h (B, RIL-175). Significantly decreased migration for KO cells is depicted by quantification. **(C)** Speed and displacement analysis of micropatterning experiments. **(D)** Spheroids of RIL-175 cells with or without EDME-stimulation (50 µM, 48 h). Analysis of longitudinal and transverse diameter and spheroid area by ImageJ suggests decreased migration upon TRPML1-inhibition. Scale bars 100 µm. Statistical significance was assessed by unpaired student's t-test. * $p < 0.0332$, ** $p < 0.0021$, *** $p < 0.0002$, **** $p < 0.001$, ns = not significant.

Figure 2: Impaired TRPML1 function hampers adherens junction integrity.

(A) Gene set enrichment analysis (GSEA) revealed significantly enriched gene sets for KO cells in comparison to RIL-175 WT cells with an FDR q-value ≤ 0.05. Proteomic analysis was performed by LC-MS/MS. The x-axis represents the enrichment significance in –log10 (FDR *q*-value). **(B, E, F, H, J)** Relative protein levels of ZO-1 (B), E-cadherin (E), β-catenin (H), and p120 (J). (F) Relative protein level of E-cadherin after 24 h EDME-treatment (50 µM) in RIL-175 cells. One representative Western Blot is shown. **(D)** Relative E-cadherin mRNA levels acquired by RT-qPCR. **(C, G, I, K)** Representative confocal images showing ZO-1 (C), E-cadherin (G), β-catenin (I), and p120 (K) (green) and the nucleus (Hoechst). Scale bar 20 µm. Statistical significance was assessed by unpaired student's t-test. * $p < 0.0332$, *** $p < 0.0002$, ns = not significant.

Figure 3: TRPML1 knockout impedes intracellular trafficking.

(A) Gene set enrichment analysis (GSEA) revealed significantly enriched gene sets for KO cells in comparison to RIL-175 WT cells with an FDR q-value ≤ 0.05. Proteomic analysis was performed by LC-MS/MS. The x-axis represents the enrichment significance in –log10 (FDR *q*-value). **(B)** Internalized FITC-dextran (200 µg/mL, incubated for 2 h) (green) and the nucleus (Hoechst). Fluorescence intensities were measured by ImageJ and normalized to the number of cells per image. **(C)** Flow cytometry analysis of endocytosed FITC-dextran (200 µg/mL) after an incubation time of 1 or 2 h. **(D)** Lysosomal exocytosis assay showing decreased relative β-hexosaminidase release upon Ionomycin treatment (5 µM, 10 min). **(E)** Lysosomal exocytosis assay of released FITC-dextran (200 µg/mL, incubated for 24 h) upon calcium treatment (50 mM). The results were normalized to the WT level. **(F, G)** Relative protein levels of released Cathepsin B after Ionomycin treatment (5 µM, 10 min) (F) or Rab5

and Rab11 (G). **(H)** Colocalization of TRPML1 (magenta) with Rab5 or Rab11 (cyan). The nucleus is shown in blue (Hoechst). Quantification of the colocalization as analyzed by ImageJ. Images/Blots are representative. Scale bars 20 µm. Statistical significance was assessed by unpaired student's t-test. * $p < 0.0332$, ** $p < 0.0021$, *** $p < 0.0002$, ns = not significant.

Figure 4: Re-establishing intracellular trafficking rescues E-cadherin.

(A) RIL-175 WT, KO, and Rab11-OE KO cells stained for E-cadherin (green), Rab11 (magenta), and the nucleus (blue). **(B)** Representative confocal images of three FRAP-steps taken for RIL-175 WT and KO cells expressing E-cadherin-GFP (green). The boxes indicate the bleaching areas. E-cadherin recovery is blotted over time (left panel) and quantified as the recovery half-time (right panel). Images/Blots are representative. Scale bars 20µm. **(C)** Relative protein levels of E-cadherin in RIL-175 KO and MDA-MB-231 KO cells after 24 h stimulation with chloroquine (25 µM (RIL-175) or 12.5 µM (MDA-MB-231)). Statistical significance was assessed by unpaired t-test **(C)**, or unpaired t-test with Welch's correction **(B)**. ns = not significant

Figure 5: The knockout of TRPML1 affects cell adhesion by abrogating β_1-integrin receptor trafficking.

(A) Quantification of adhesion of WT and KO cells seeded onto substrates as indicated. **(B, G)** Relative protein levels of β_1-integrin and active β_1-integrin (B), FAK and pFAK, Src and pSrc, RhoA and pRhoA, Rac1 and pRac1 (G). **(C, F)** MDA-MB-231 (C) and RIL-175 (F) WT and KO cells stained for β_1-integrin and active β_1-integrin (green) and the nucleus (Hoechst). (F) The vesicle size was quantified by ImageJ and normalized to the WT level. **(D, E)** Internalized β_1-integrin (green) and the nucleus (Hoechst). As quantified by ImageJ, no significant increase in the vesicle size was observable (E). Images/Blots are representative. Scale bars 20 µm or 2 µm (zoom-ins). Statistical significance was assessed by unpaired student's t-test. * $p < 0.0332$, ** $p < 0.0021$, ns = not significant.

Figure 6: The ablation of TRPML1 function disrupts actin polymerization and polarization of migrating cells.

(A) MDA-MD-231 and RIL-175 WT and KO cells stained for actin and nuclei. Representative images shown. Experiment was performed n=3 (RIL-175) and n=2 (MDA-MD-231). **(B)** RIL-175 WT and KO cells co-stained for E-cadherin, actin and nuclei. **(C)** After 5 h of migration time, cells were stained for active β_1-integrin (left panel, green), Rac1 (middle panel, green), actin (right panel, red), and the nucleus (Hoechst). Scale bar 20 µm.

Abbreviations

AJ adherens junction

ECM extracellular matrix

EE early endosome

EMT epithelial-to-mesenchymal transition

FAK focal adhesion kinases

GSEA gene set enrichment analysis

KO knockout

WT wildtype

Figure 1: TRPML1 loss of function reduces cancer cell migration.

(A) Representative images obtained from wound healing experiments show fixed and crystal-violet stained WT and TRPML1 KO RIL-175 (upper panel) and MDA-MB-231 (lower panel) cells after a migration time of 14 hours. Scale bar 100 µm. Quantification of the wound closure by ImageJ implicates a significant decrease in migration for TRPML1 KO cells. **(B)** Representative images obtained from Boyden chamber experiments show fixed and crystal-violet stained WT and TRPML1 KO RIL-175 (upper panel) and MDA-MB-231 (lower panel) cells after a migration time of 6 hours (RIL-175) and 24 hours (MDA-MB-231) along an FCS gradient. Scale bar 100 µm. Quantification of migration shows a significant decrease in migration for TRPML1 KO cells. **(C)** Representative images obtained by micropatterning experiments for RIL-175 (upper panel) and MDA-MB-231 (lower panels) WT and TRPML1 KO cells. Scale bar 100 µm. Speed and displacement analysis was performed by ImageJ. **(D)** Representative images taken for spheroids of RIL-175 WT cells with and without EDME-stimulation (50 µM) after an incubation time of 48 hours following the spheroid embedding. Scale bar 100 µm. Quantitative analysis of both the longitudinal and transverse diameter and the area of spheroids by ImageJ suggests a significant decrease in the migratory capacity of the treated cells. Shown are mean values ± SD obtained from at least three independent experiments. * $p < 0.0332$, ** $p < 0.0021$, *** $p < 0.0002$, **** $p < 0.001$, ns = not significant, unpaired t-test with Welch's correction.

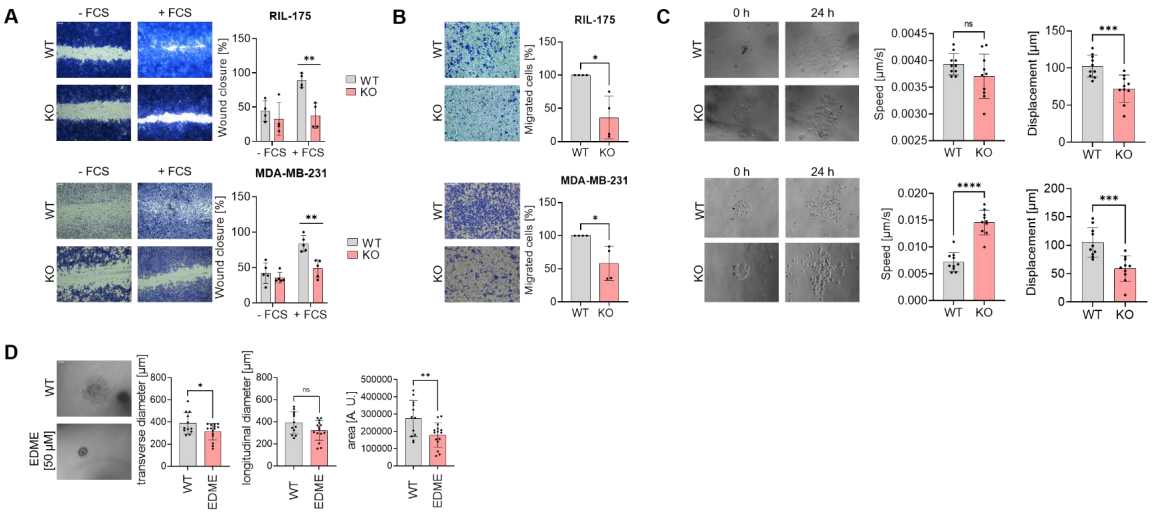

Figure 2: Impaired TRPML1 function hampers adherens junction integrity.

(A) Proteomic analysis performed by liquid chromatography tandem mass spectrometry (LC-MS/MS). Gene set enrichment analysis (GSEA) revealed significantly enriched gene sets for TRPML1 KO cells in comparison to RIL-175 WT cells with an FDR q-value ≤ 0.05. The x-axis represents the enrichment significance in –log10 (FDR *q*-value). **(B, E, G, I)** Western blot analysis and quantification of ZO-1 (B), E-cadherin (E), β-catenin (G), and p120 (I) in whole cell lysates of RIL-175, MDA-MB-231 WT and TRPML1 KO cells. The results were normalized to the protein loading and subsequently to the WT level. **(D)** mRNA levels of E-cadherin acquired by RT-qPCR experiments. The mRNA levels were normalized by actin (RIL-175) or tubulin (MDA-MB-231) and calculated as a fold-change compared to the respective WT cells. **(C, F, H, J)** Representative confocal images showing ZO-1 (C), E-cadherin (F), β-catenin (H), and p120 (J) (green) and the nucleus (Hoechst). Scale bar 20 µm. **(K)** Western Blot analysis and quantification of E-cadherin in whole cell lysates of WT and stimulated (EDME, 50 µM, 24 h incubation time) RIL-175 cells. The results were normalized to the protein loading and subsequently to the WT level (untreated). Shown are mean values ± SD obtained from at least three independent experiments. * $p < 0.0332$, *** $p < 0.0002$, ns = not significant, unpaired t-test with Welch's correction.

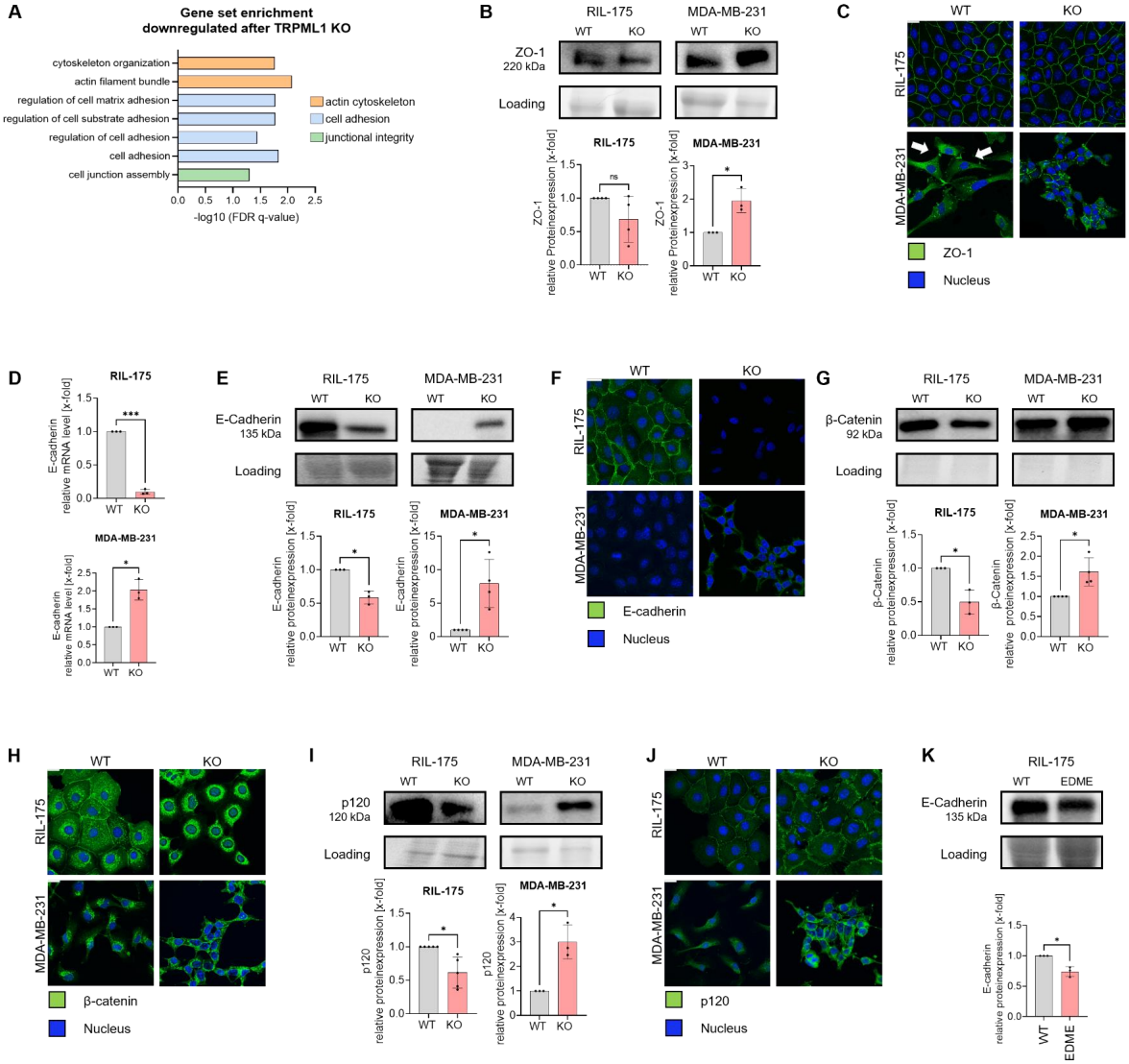

Figure 3: TRPML1 knockout impedes with intracellular trafficking.

(A) Proteomic analysis performed by liquid chromatography tandem mass spectrometry (LC-MS/MS). Gene set enrichment analysis (GSEA) revealed significantly enriched gene sets for TRPML1 KO cells in comparison to RIL-175 WT cells with an FDR q-value ≤ 0.05. The x-axis represents the enrichment significance in –log10 (FDR *q*-value). **(B)** Representative confocal images showing FITC-dextran (200 µg/mL incubated for 2 h) (green) and the nucleus (Hoechst). Scale bar 20 µm. Quantification of fluorescence intensity was conducted by ImageJ. The fluorescence intensities were normalized to the number of cells per image. **(C)** Flow cytometry analysis of the taken up FITC-dextran (200 µg/mL) after an incubation time of 1 or 2 hours. **(D)** Lysosomal exocytosis assay showing a decrease in β-hexosaminidase release upon Ionomycin treatment (5 µM, 10 min). The results were normalized to the untreated WT level. **(E)** Lysosomal exocytosis assay of released FITC-dextran (200 µg/mL, incubated for 24 h) upon calcium treatment (50 mM). **(F)** Western blot analysis and quantification of released MMP-2 and Cathepsin B in medium of RIL-175 and MDA-MB-231 WT and TRPML1 KO cells after treatment with ionomycin (5 µM, 10 min). The results were normalized to the protein loading and subsequently to the WT level. **(G)** Western blot analysis and quantification of Rab5 and Rab11 in whole cell lysates of RIL-175 and MDA-MB-231 WT and TRPML1 KO cells. The results were normalized to the protein loading and subsequently to the WT level. **(H)** Representative confocal images showing the colocalization of TRPML1 (red) with Rab5 or Rab11 (green). The nucleus is shown in blue (Hoechst). Scale bar 20 µm. Quantification of the colocalization as analyzed by ImageJ. Shown are mean values ± SD obtained from at least three independent experiments. * $p < 0.0332$, ** $p < 0.0021$, *** $p < 0.0002$, ns = not significant, unpaired t-test with Welch's correction.

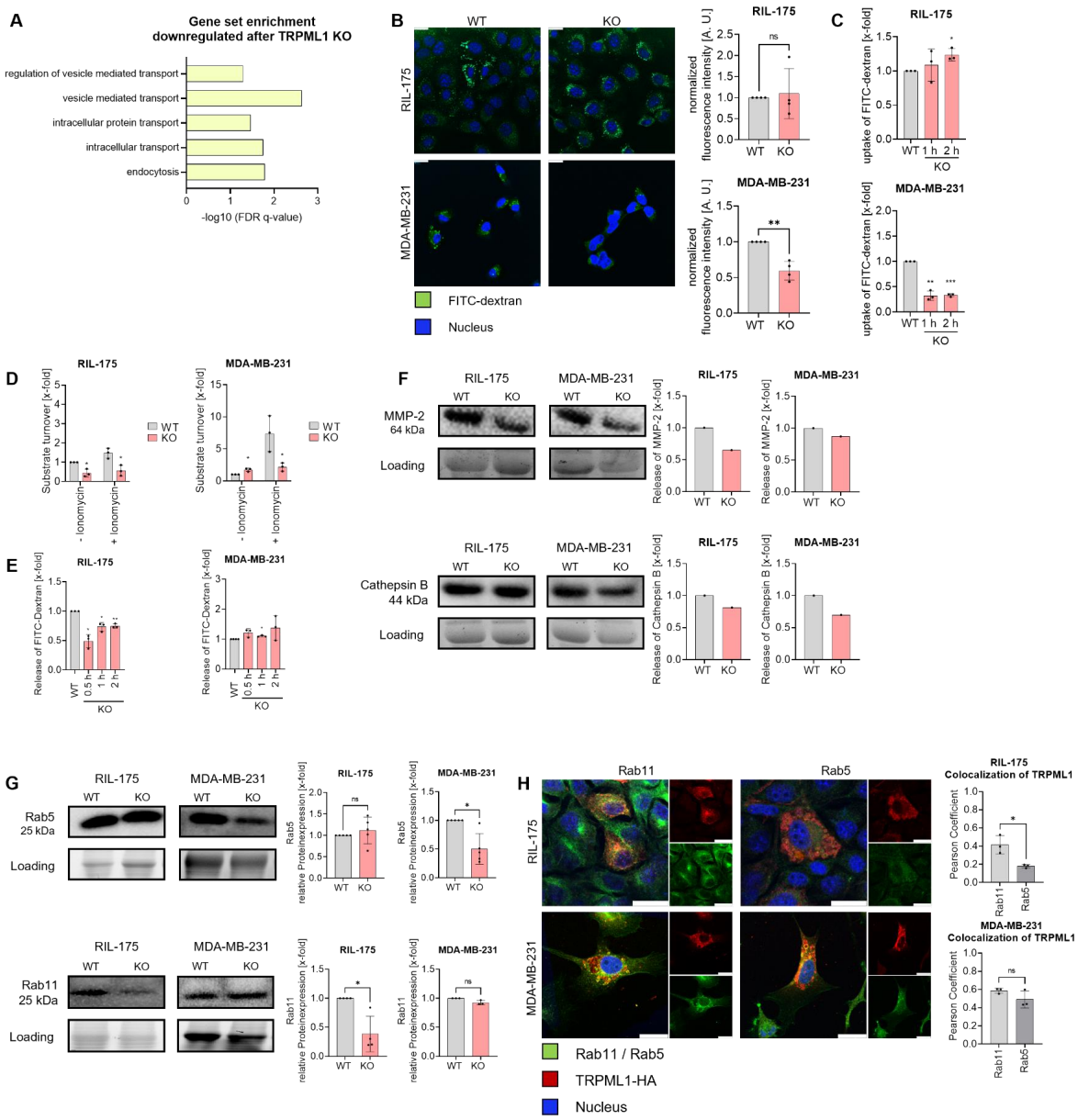
A
Gene set enrichment
downregulated after TRPML1 KO
regulation of vesicle mediated transport
vesicle mediated transport
intracellular protein transport
intracellular transport
endocytosis
-log10 (FDR q-value)
B
WT
KO
RIL-175
MDA-MB-231
FITC-dextran
Nucleus
normalized fluorescence intensity [A. U.]
ns
**
C
uptake of FITC-dextran [x-fold]
WT 1 h 2 h
KO
D
Substrate turnover [x-fold]
- Ionomycin
+ Ionomycin
E
Release of FITC-Dextran [x-fold]
0.5 h
1 h
2 h
F
MMP-2
64 kDa
Loading
Release of MMP-2 [x-fold]
Cathepsin B
44 kDa
Release of Cathepsin B [x-fold]
G
Rab5
25 kDa
Rab11
25 kDa
Rab5 relative Proteinexpression [x-fold]
Rab11 relative Proteinexpression [x-fold]
H
Rab11
Rab5
Colocalization of TRPML1
Pearson Coefficient
Rab11 / Rab5
TRPML1-HA
Nucleus

Figure 4: Re-establishing intracellular trafficking rescues E-cadherin.

(A) Western blot analysis and quantification of E-cadherin, Rab11-GFP, and endogenous Rab11 in whole cell lysates of transiently transfected, Rab11-overexpressing (OE) RIL-175 WT and TRPML1 KO cells. An EGFP-plasmid served as the negative control (mock). The results were normalized to the protein loading and subsequently to the WT level. **(B)** Representative confocal images of RIL-175 WT, TRPML1 KO, and Rab11-overexpressing TRPML1 KO cells stained for E-cadherin (blue), Rab11 (green), and the nucleus (red). Scale bar 20 µm. **(C)** Representative confocal images of three FRAP-steps taken for RIL-175 WT and TRPML1 KO cells expressing E-cadherin-GFP (green). The boxes indicate the bleaching areas. Scale bar 20 µm. E-cadherin recovery is blotted over time (left panels) and quantified as the recovery half-time (right panels). **(D)** Western blot analysis and quantification of E-cadherin in whole cell lysates of RIL-175 and MDA-MB-231 WT and TRPML1 KO cells after stimulation with chloroquine (25 µM (RIL-175) or 12.5 µM (MDA-MB-231), 24 h). Shown are mean values ± SD obtained from at least three independent experiments. * $p < 0.0332$, ** $p < 0.0021$, **** $p < 0.001$, ns = not significant, two-way ANOVA followed by Tukey's multiple comparison test **(A)**, unpaired t-test **(C)**, or unpaired t-test with Welch's correction **(D)**.

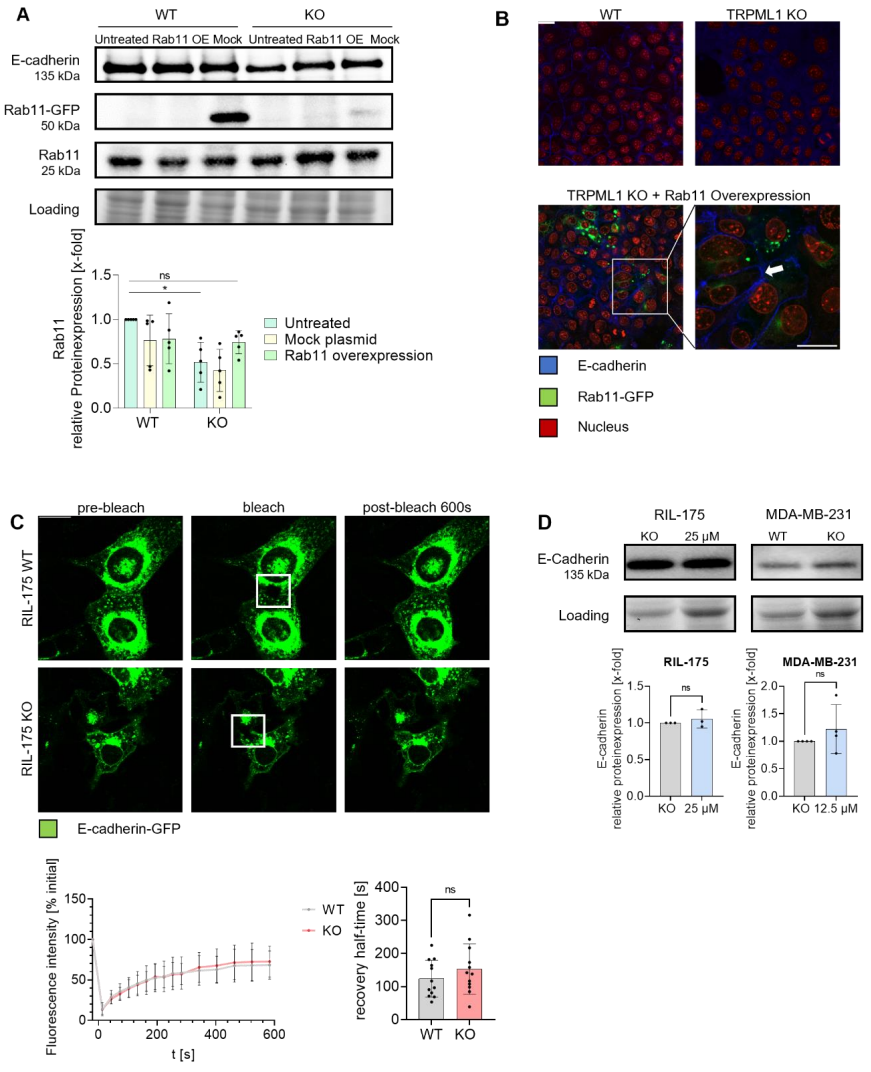

Figure 5: The knockout of TRPML1 affects cell adhesion.

(A) Adhesion assay of RIL-175 (left panel) and MDA-MB-231 (right panel) WT and TRPML1 KO cells which were seeded onto plastic, collagen G (0.4 % in PBS), fibronectin (10 µg/mL in PBS), and laminin (10 µg/mL in PBS) and allowed to adhere for 1 h. After confocal imaging, adherent cells were counted with Image J and the results for the TRPML1 KO cells were normalized to the respective WT level. **(B, G)** Western blot analysis and quantification of β_1-integrin and active β_1-integrin (B), FAK and pFAK, Src and pSrc, RhoA and pRhoA, Rac1 and pRac1 (G) in whole cell lysates of RIL-175 (left panels) and MDA-MB-231 (right panels) WT and TRPML1 KO cells. The results were normalized to the protein loading and subsequently to the WT level. Thereafter, the results for the phosphorylated/active protein were normalized to the unphosphorylated/total protein level. **(C, F)** Representative confocal images taken for MDA-MB-231 (C) and RIL-175 (F) WT and TRPML1 KO cells stained for β_1-integrin and active β_1-integrin (green) and the nucleus (Hoechst). (F) The vesicle size was quantified by ImageJ and the results for the RIL-175 TRPML1 KO cells were normalized to those of the WT cells. Scale bar 20 µm or 2 µm (zoom-ins). **(D, E)** After starving the cells for 90 minutes, the β_1-integrin antibody in DMEM was incubated for 45 min at 4°C. Following the incubation time of 1 h in the incubator, the cells were treated with PMA (30 min, 37°C). After antibody staining, taken up β_1-integrin (green) and the nucleus (Hoechst) were visualized by confocal microscopy. As quantified by ImageJ, no significant increase in the vesicle size was observable (E). Scale bar 20 µm or 2 µm (zoom-ins). Shown are mean values ± SD obtained from at least three independent experiments. * $p < 0.0332$, ** $p < 0.0021$, ns = not significant, unpaired t-test with Welch's correction.

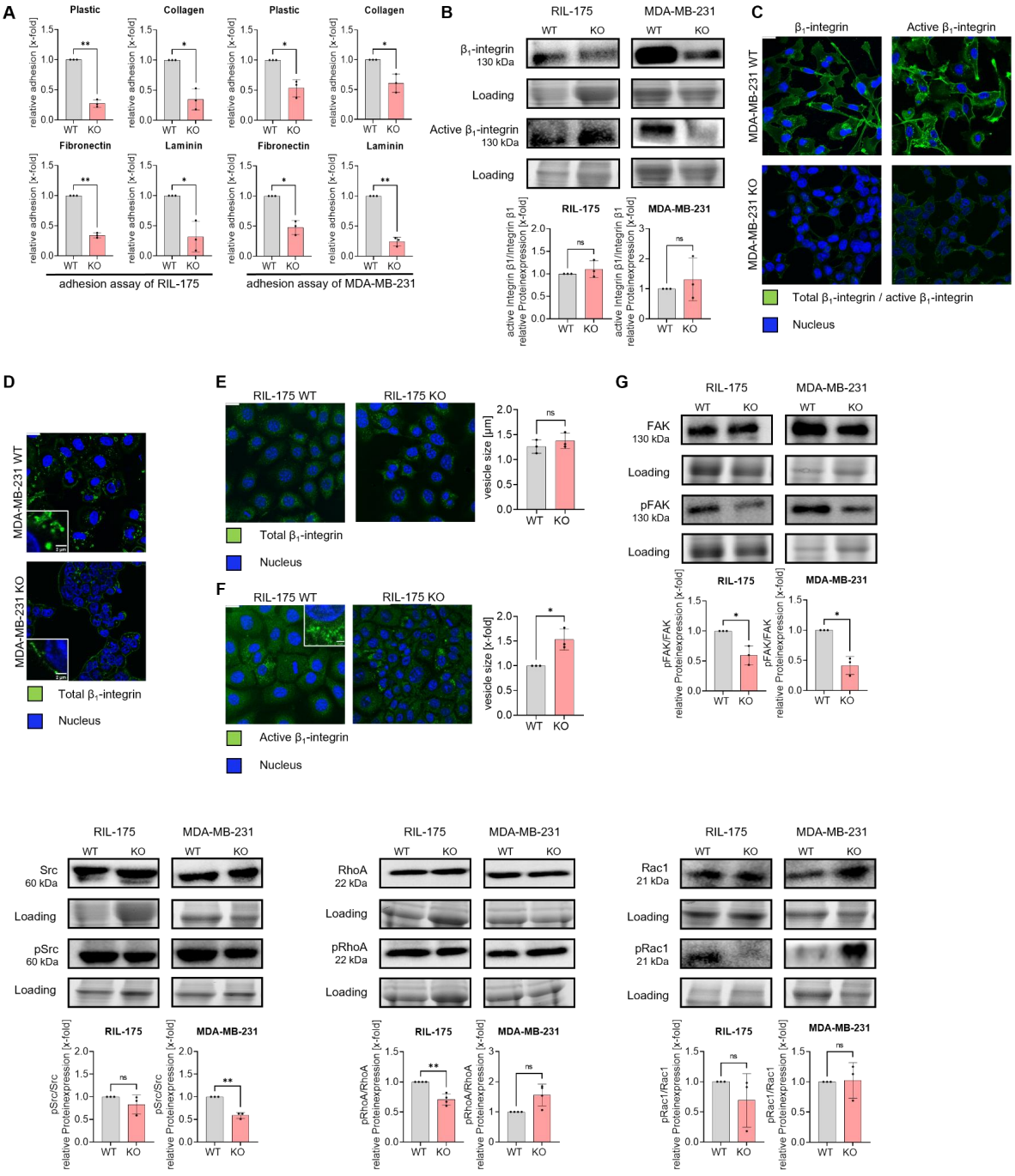
A
Plastic
Collagen
Plastic
Collagen
Fibronectin
Laminin
Fibronectin
Laminin
relative adhesion [x-fold]
WT KO
adhesion assay of RIL-175
adhesion assay of MDA-MB-231
B
RIL-175
MDA-MB-231
WT KO
β1-integrin
130 kDa
Loading
Active β1-integrin
130 kDa
Loading
active Integrin β1/Integrin β1
relative Proteinexpression [x-fold]
ns
C
β1-integrin
Active β1-integrin
MDA-MB-231 WT
MDA-MB-231 KO
Total β1-integrin / active β1-integrin
Nucleus
D
MDA-MB-231 WT
MDA-MB-231 KO
Total β1-integrin
Nucleus
E
RIL-175 WT
RIL-175 KO
vesicle size [µm]
ns
Total β1-integrin
Nucleus
F
RIL-175 WT
RIL-175 KO
vesicle size [x-fold]
Active β1-integrin
Nucleus
G
RIL-175
MDA-MB-231
FAK
130 kDa
Loading
pFAK
130 kDa
Loading
pFAK/FAK
relative Proteinexpression [x-fold]
Src
60 kDa
Loading
pSrc
60 kDa
Loading
pSrc/Src
RhoA
22 kDa
Loading
pRhoA
22 kDa
Loading
pRhoA/RhoA
Rac1
21 kDa
Loading
pRac1
21 kDa
Loading
pRac1/Rac1

Figure 6: The ablation of TRPML1 function disrupts optimal polarization of migrating cells.

After allowing migration for five hours after wounding a confluent cell layer, RIL-175 WT and TRPML1 KO were stained for active β_1-integrin (left panel, green), Rac1 (middle panel, green), actin (right panel, red), and the nucleus (Hoechst). Scale bar 20 µm. All experiments were conducted three times.

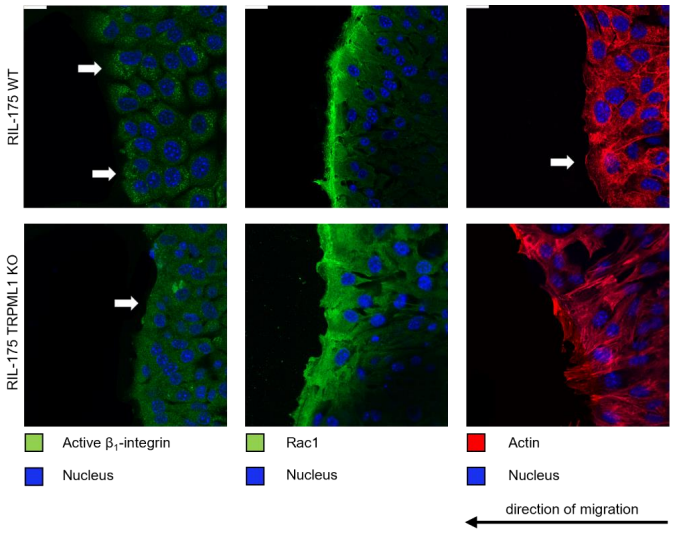

Supplementary

Supplementary Figure 1: Expression of EMT-markers in TRPML1 KO cells.

Western Blot analysis and quantification of N-cadherin **(A)**, Snail **(B)**, and Slug **(C)** in whole cell lysates of RIL-175 and MDA-MB-231 WT and TRPML1 KO cells. The results were normalized to the protein loading and subsequently to the wildtype level. Shown are mean values ± SD obtained from at least three independent experiments. * $p < 0.0332$, ** $p < 0.0021$, *** $p < 0.0002$, unpaired t-test with Welch's correction.

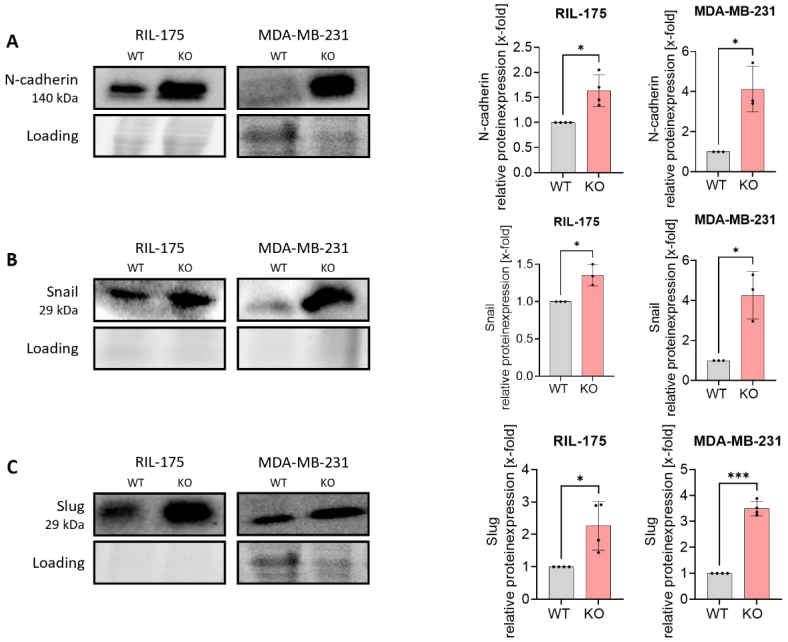

Supplementary Figure 2: mRNA levels of Rab11A and B in RIL-175 TRPML1 KO cells.

mRNA levels of Rab11A **(A)** and Rab11B **(B)** in RIL-175 WT and TRPML1 KO cells acquired by RT-qPCR experiments. The mRNA levels were normalized by actin and calculated as a fold-change compared to the respective wildtype cells. Shown are mean values ± SD obtained from at least three independent experiments. * $p < 0.0332$, ** $p < 0.0021$, ns = not significant, unpaired t-test with Welch's correction.

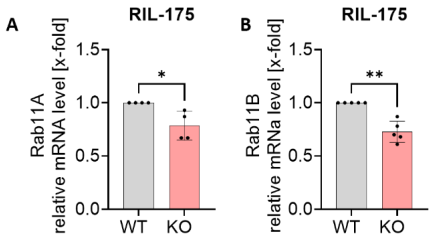

Paper VII

biomolecules

MDPI

Review

Endolysosomal Cation Channels and MITF in Melanocytes and Melanoma

Carla Abrahamian and Christian Grimm *

Walther Straub Institute of Pharmacology and Toxicology, Faculty of Medicine, Ludwig-Maximilians-University, 80336 Munich, Germany; carla.abrahamian@lrz.uni-muenchen.de
* Correspondence: christian.grimm@med.uni-muenchen.de

Abstract: Microphthalmia-associated transcription factor (MITF) is the principal transcription factor regulating pivotal processes in melanoma cell development, growth, survival, proliferation, differentiation and invasion. In recent years, convincing evidence has been provided attesting key roles of endolysosomal cation channels, specifically TPCs and TRPMLs, in cancer, including breast cancer, glioblastoma, bladder cancer, hepatocellular carcinoma and melanoma. In this review, we provide a gene expression profile of these channels in different types of cancers and decipher their roles, in particular the roles of two-pore channel 2 (TPC2) and TRPML1 in melanocytes and melanoma. We specifically discuss the signaling cascades regulating MITF and the relationship between endolysosomal cation channels, MAPK, canonical Wnt/GSK3 pathways and MITF.

Keywords: TPC; two-pore; lysosome; TPC1; TPC2; TRPML; mucolipin; MCOLN; TRPML1; MITF; melanocytes; melanoma; mTOR; TFEB; calcium

Citation: Abrahamian, C.; Grimm, C. Endolysosomal Cation Channels and MITF in Melanocytes and Melanoma. *Biomolecules* **2021**, *11*, 1021. https://doi.org/10.3390/biom11071021

Academic Editor: Maria Beatrice Morelli

Received: 16 June 2021
Accepted: 12 July 2021
Published: 13 July 2021

1. Introduction

Melanocytes are neural-crest derived cells that produce melanin, the primary determinant of skin color. Melanin is also found in hair, in the iris of the eye, and in the stria vascularis of the inner ear and, to a lesser degree, in a broad range of other tissues throughout the body [1]. There are two major types of melanin called eumelanin (dark, brown, black) and pheomelanin (yellow, red, light brown). Melanin is produced and stored in melanosomes, lysosome-related organelles that can be divided into four stages depending on their degree of maturation [2]. Stage I pre-melanosomes lack pigment but develop distinct fibrillar structures in a Pmel17-dependent process during stage II. Tyrosinase and other enzymes of melanogenesis reach stage II melanosomes via endosomal intermediates and initiate the production of melanin; these melanosomes are deposited on the fibers, resulting in their thickening and blackening with maturation to stage III. Melanin synthesis and deposition continue until all of the internal structure is masked in stage IV [3,4]. Modulators of melanin production include proteins involved in melanosome structure (i.e., Pmel17, MART-1), proteins involved in melanin synthesis and melanosome pH regulation (i.e., tyrosinase, TYRP1, TPC2), and proteins required for melanosome transport and distribution (e.g., Rab27a, myosin Va, melanophilin) [3,4]. Melanosomal pH is regulated by the vacuolar proton ATPase, Na^+/H^+ exchangers, SLC24A5 ($Na^+/K^+/Ca^{2+}$ exchanger 5), and two-pore channel 2 (TPC2) [4–8]. TPC2, a cation channel permeable for sodium and calcium, expressed in late endosomes (LE), lysosomes and melanosomes, regulates pigmentation through two fundamental determinants of melanosome function: pH and size [7]. Different steps of melanogenesis are regulated by pH. First, the activity of tyrosinase, the rate-limiting enzyme for the production of melanin the optimal pH of which is 6.8 [9] with greatly reduced activities at a more acidic pH [5], while differences between monophenol oxidase and diphenol oxidase activities of tyrosinase in their pH dependence should be noted. Second, the activation of metatyrosinase (reduction of Cu II),

the initial step of melanogenesis, is also highly pH-dependent. Third, the non-enzymatic DOPA-producing reaction, the redox exchange, is also strongly dependent on pH [10–12].

Two human TPC2 gain-of-function (GOF) variations were identified as associated with blond hair color: rs35264875 (encoding M484L), which results in an increased sensitivity to the endogenous TPC2 ligand PI(3,5)P_2, while rs3829241 (encoding G734E) results in reduced channel inhibition by ATP [8,10,13]. Both variations are mainly found in Europeans, particularly in blond-haired Northern Europeans [14]. On the contrary, knockout of TPC2 results in a strong increase in melanin production in both primary human melanocytes and in pigmented melanoma cells (i.e., MNT-1) [7].

It is well-established that melanin is one of the major protective factors against UV radiation mediated DNA damage that results in melanoma development [15]. Besides, individuals with a higher ratio of pheomelanin to eumelanin in their skin and hair, that is, blond- and red-haired individuals, have a greater risk for melanoma than black- or brown-haired individuals (by a factor of 2–4) [16,17].

In addition to melanosomes, TPC2 is also expressed in LEs/lysosomes, while expression of its relative TPC1 appears to dominate in endosomes. A role of TPCs in cancer cell migration, invasion and proliferation has been convincingly established in the last couple of years, attributed to its function in endolysosomes [18–26]. While common consensus suggests that knockout, knockdown, or pharmacological inhibition of TPCs, and in particular TPC2, reduces cancer cell migration, invasion and proliferation, including melanoma cells, some report otherwise.

2. Role of MITF in Melanoma and Pathways Implicated

2.1. MITF

Microphthalmia-associated transcription factor (MITF) is a central player of melanocyte survival, function and development [27–29]. It belongs to the MiT/TFE family of transcription factors in vertebrates, consisting of four distinct but closely related and evolutionary conserved members, including MITF, transcription factor EB (TFEB), TFE3 and TFEC. Structurally, MITF encodes a basic–helix–loop–helix leucine zipper (bHLH-ZIP) transcription factor, thereby exerting its function by regulating genes involved in cell cycle progression and differentiation, a role sustained throughout the process of melanogenesis and in melanoma [30–32]. Mutations in MITF are associated with Tietz albinism-deafness syndrome and Waardenburg syndrome type 2A [33,34], and amplification of MITF is found in 15–20% of human metastatic melanomas and has been linked to poor survival. The M-MITF isoform is the predominant isoform in 80% of human melanomas [28,29,35].

2.2. Rheostat Model of MITF

MITF is regulated by numerous factors that exercise tight control on both its transcriptional and post-translational levels (i.e., ubiquitination, acetylation and sumoylation), given that it is downstream of several pathways [36,37], as illustrated in Figure 1. A rheostat model of MITF in melanoma has been proposed by Carreira et al. (2006), where MITF yields three phenotypes, hence varied cellular responses in melanoma based on its activity. At the highest state where c-AMP induction leads to peak MITF activity, melanoma cells express differentiation target genes (i.e., Tyrosinase and MART1), giving rise to a pigmented phenotype and undergoing terminal differentiation. In contrast, the cells at the intermediate activity level are at a reversible proliferative state where enough MITF is expressed to activate MITF genes linked to survival (i.e., BCL2 and CDK2), concomitantly suppressing p27Kip1 expression through the regulation of Dia1, preventing differentiation. While MITF at its lowest activity brings about highly invasive cells exhibiting stem cell-like properties and low proliferative and pigmentation capacities that undergo p27Kip1-mediated G1 arrest [38,39]. Nonetheless, the rheostat model is controversial for many reasons. First, MITF is a downstream target of numerous signaling pathways and is subject to diverse post-translational modifications, which can direct MITF to different sets of target genes that regulate different functions in melanoma, dependent on physiological context [31,33].

is subject to diverse post-translational modifications, which can direct MITF to different sets of target genes that regulate different functions in melanoma, dependent on physiological context [31,33]. Furthermore, findings that proliferative and invasive phenotypes are mutually exclusive has been disputed by Haass et al. (2014) [40]. Wellbrock et al. (2015) describe how the comparable expression of MITF can carry out opposing functions depending on the setting [38,41]. Finally, Carreira et al. (2006) themselves specify that the roles assigned to "MITF activity" are in fact limited to expression levels using overexpression and depletion models, and most data have been established [36] in the pro-

Furthermore, findings that proliferative and invasive phenotypes are mutually exclusive has been disputed by Haass et al. (2014) [40]. Wellbrock et al. (2015) describe how the comparable expression of MITF can carry out opposing functions depending on the setting [38,41]. Finally, Carreira et al. (2006) themselves specify that the roles assigned to "MITF activity" are in fact limited to expression levels using overexpression and depletion models, and most data have been established [36] in the pro-

[38]. For the purpose of this review, we will be discussing two prominent pathways involved in the regulation of MITF: MAPK and Wnt.

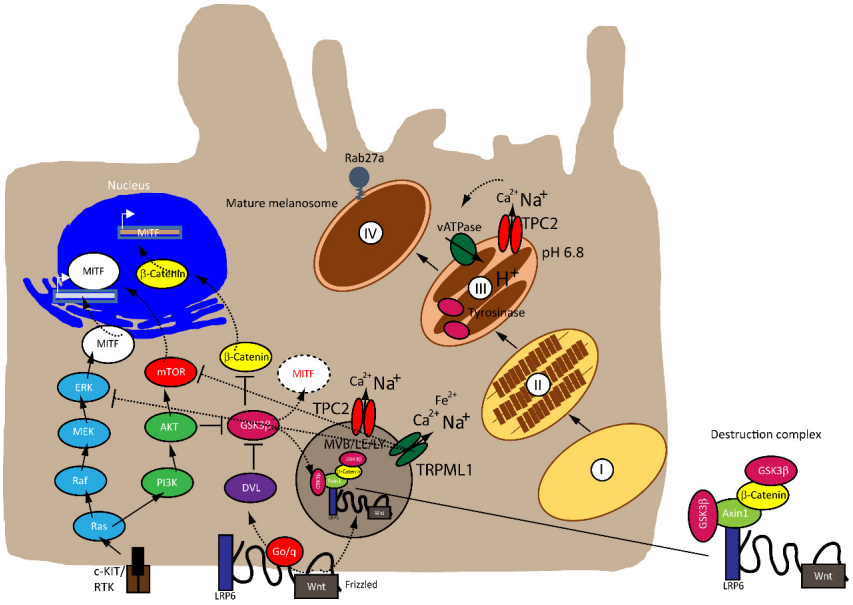

Figure 1. Signaling pathways in melanoma cells involved in MITF regulation and subcellular localization of TRPML1 and TPC2. (**a**) Several pathways regulate MITF expression: RAS/RAF/MEK/ERK, PI3K/AKT, and Wnt/GSK3β/β-Catenin. GSK3β is a negative regulator of MITF expression and promotes proteasomal degradation of MITF. GSK3β degradation in endolysosomes is enhanced by Wnt signaling. Tyrosinase activity depends on melanosomal pH and is regulated by TPC2 activity in melanosomes. Loss-of-function of TPC2 in endolysosomes and melanosomes results in increased GSK3β and decreased MITF protein levels as well as increased tyrosinase activity and melanin content.

Figure 1. Signaling pathways in melanoma cells involved in MITF regulation and subcellular localization of TRPML1 and TPC2. (**a**) Several pathways regulate MITF expression: RAS/RAF/MEK/ERK, PI3K/AKT, and Wnt/GSK3β/β-Catenin. GSK3β is a negative regulator of MITF expression and promotes proteasomal degradation of MITF. GSK3β degradation in endolysosomes is enhanced by Wnt signaling. Tyrosinase activity depends on melanosomal pH and is regulated by TPC2 activity in melanosomes. Loss-of-function of TPC2 in endolysosomes and melanosomes results in increased GSK3β and decreased MITF protein levels as well as increased tyrosinase activity and melanin content.

2.3. MITF and MAPK

The mitogen-activated protein kinase (MAPK) pathway is dysregulated in 90% of melanoma with 50% of patients harboring activating mutations in B-RAF, most commonly the $BRAF^{V600E}$ mutation—an amino acid substitution from valine (V) to glutamic acid (E)—while 28% of patients carry mutations in N-RAS, leading to constitutively hyperactivated MAPK signaling and increased melanoma cell survival, proliferation, migration, invasion, metastasis and angiogenesis. Consequently, the targeted therapies that are currently available have focused on developing specific small molecule tyrosine kinase inhibitors (TKI) for BRAF (BRAFi) and MEK (MEKi), which have shown improved survival rates [42–46]. The relationship between MITF and the MAPK signaling hub is largely relevant through p-ERK phosphorylation and the mutational status of B-RAF. Garraway et al. (2006) have observed that MITF gene amplification in metastatic melanoma coincides with $BRAF^{V600E}$ mutation and p16 inactivation, promoting tumor growth and survival, while MITF reduction exposes melanoma to conventional chemotherapeutic sensitization [29]. Van Allen et al. (2014) have shown that patients relapsed on BRAF/MEK inhibitor therapy

The mitogen-activated protein kinase (MAPK) pathway is dysregulated in 90% of melanoma with 50% of patients harboring activating mutations in B-RAF, most commonly the $BRAF^{V600E}$ mutation—an amino acid substitution from valine (V) to glutamic acid (E)—while 28% of patients carry mutations in N-RAS, leading to constitutively hyperactivated MAPK signaling and increased melanoma cell survival, proliferation, migration, invasion, metastasis and angiogenesis. Consequently, the targeted therapies that are currently available have focused on developing specific small molecule tyrosine kinase inhibitors (TKI) for BRAF (BRAFi) and MEK (MEKi), which have shown improved survival rates [42–46]. The relationship between MITF and the MAPK signaling hub is largely relevant through p-ERK phosphorylation and the mutational status of B-RAF. Garraway et al. (2006) have observed that MITF gene amplification in metastatic melanoma coincides with $BRAF^{V600E}$ mutation and p16 inactivation, promoting tumor growth and survival, while MITF reduction exposes melanoma to conventional chemotherapeutic sensitization [29]. Van Allen et al. (2014) have shown that patients relapsed on BRAF/MEK inhibitor therapy

exhibit increased gene dosage of MITF [47]. These results have been reproduced in vivo by Lister et al. (2014), where reduced expression levels of MITF in $BRAF^{V600E}$ mutated melanoma in a zebrafish model have led to tumor regression [48]. To date, two closely linked ERK-mediated phosphorylation sites on MITF have been found: S73 and S409, which target MITF for proteasomal degradation, shortening its half-life [49,50]. While single mutations on these sites, S73A and S409A, have been found to reduce the transcriptional activity of MITF, the S73A/S409A double mutation, although stable, demonstrated a complete inhibition of the transcription and transactivation of MITF [50,51]. In contrast to the S73 phosphorylation site of MITF, which could exclusively serve as an MAPK pathway target, phosphorylation events in downstream pathways, other than the MAPK, such as protein kinase A (PKA) and GSK3 take place at S409, in turn being responsible for MITF activation/degradation and serving as a focal point for the divergent pathways controlling it [50,52].

2.4. MITF and Canonical Wnt Pathway

The Wnt signaling pathway is divided into canonical β-catenin dependent and non-canonical β-catenin independent branches and is involved in regulating cellular homeostasis and development. Mutations of components of this pathway contribute to a number of pathologies, including familial exudative vitreoretinopathy, tooth development defects, Robinow syndrome, bone density defects, Alzheimer's disease, and different types of cancers, such as melanoma, hepatocellular carcinoma (HCC), ovarian cancer, breast cancer and prostate cancer [53–56]. In melanoma, aberrations of the canonical Wnt pathway are directly linked to MITF and the rheostat model described above. The key player is β-catenin, which regulates genes of the melanocyte lineages and facilitates early-stage melanocyte transformation by blocking cellular senescence and increased proliferation. In melanoma cells, β-catenin activates proteins involved in melanogenesis and pigmentation such Melan-A, dopachrome tautomerase (DCT) and tyrosinase, all through MITF [55,57–59].

Recently, Ploper et al. (2015) have established a clear link between the endolysosomal machinery, MITF and the canonical Wnt signaling pathway in melanoma. Analyzing RNA microarray databases followed by gene set enrichment analysis of numerous melanoma cell lines, the authors found a positive correlation between expression levels of MITF and lysosomal genes, independent of TFEB levels, claiming that MITF, via direct activation of the CLEAR element in lysosomal genes, induces their transcription. Moreover, MITF expression expanded multivesicular bodies (MVBs) and LE, without affecting the number of lysosomes in the C32 melanoma line, enhancing Wnt signaling and the proliferation of these cells. While the S409 phosphorylation site has been described above, Ploper et al. (2015) have discovered three novel phosphorylation sites on the C-terminus of MITF: S397, S401 and S405, which promotes the proteasomal degradation of MITF by GSK3β. The authors have proposed the following mechanism of action: during the inactive state of the Wnt pathway, GSK3β would phosphorylate MITF on the sites uncovered above, rendering MITF unstable for undergoing proteasomal degradation. Upon activation of the pathway, GSK3β would be inhibited, stabilizing MITF, which in turn would induce the translocation of the destruction complex components (i.e., Axin1, p-β-catenin, GSK3β) to $CD63^+$ MVBs and LE. MITF would then accumulate in the nucleus, activating the lysosomal genes and contributing to endolysosomal biogenesis. In turn, this generates a positive feedback loop by inducing and increasing the number of MVBs and LE that sequester the destruction complex further, without undergoing proteolysis [52].

3. Endolysosomal Cation Channels in Melanoma

An analysis of the expression of different endolysosomal cation channels in a number of cancer cell lines using real-time quantitative reverse transcription PCR (qRT-PCR), including melanoma, hepatocellular carcinoma, breast cancer, colon adenocarcinoma, ovarian cancer, cervical adenocarcinoma, pancreatic ductal adenocarcinoma, glioblastoma and lung adenocarcinoma, is shown in Figure 2. The cell lines expressing particularly

3. Endolysosomal Cation Channels in Melanoma

An analysis of the expression of different endolysosomal cation channels in a number of cancer cell lines using real-time quantitative reverse transcription PCR (qRT-PCR), including melanoma, hepatocellular carcinoma, breast cancer, colon adenocarcinoma, ovarian cancer, cervical adenocarcinoma, pancreatic ductal adenocarcinoma, glioblastoma and lung adenocarcinoma, is shown in Figure 2. The cell lines expressing particularly high levels of TPC2 are HCC and melanoma lines. Likewise, very high levels are found in melanoma lines for TRPML1. In the following, we will focus on these two channels.

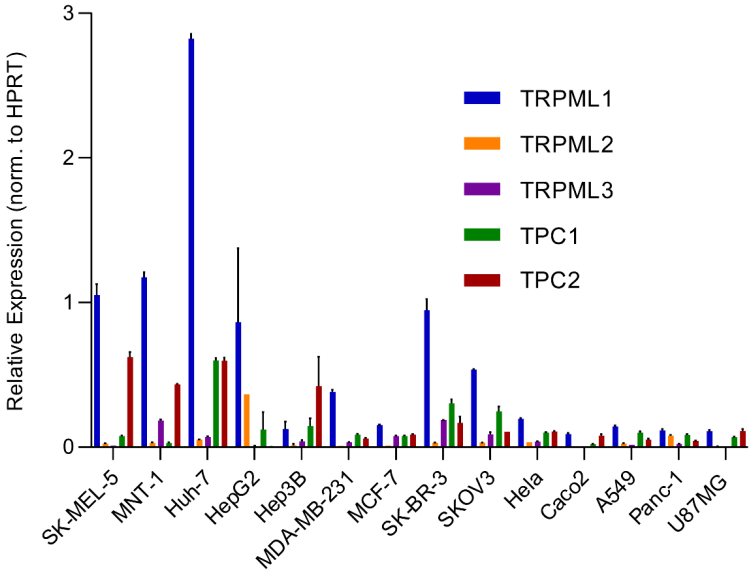

Figure 2. Gene expression profile of endolysosomal cation channels in different cancer cell lines. The expression levels of endolysosomal cation channels TRPML1, TRPML2, TRPML3, TPC1 and TPC2 were assessed in different cancer cell lines using real-time quantitative Reverse Transcription PCR (qRT-PCR): melanoma (SK-MEL-5 and MNT-1); hepatocellular carcinoma (HUH-7, HebG2, and Hep3B); breast cancer (MDA-MB-231, MCF-7, and SK-BR-3); colon adenocarcinoma (Caco-2); ovarian cancer (SKOV-3), cervical adenocarcinoma (Hela); pancreatic ductal adenocarcinoma (Panc-1); glioblastoma (U87MG); lung adenocarcinoma (A-549). Melanoma and HCC lines consistently showed the highest expression levels of TRPML1 and TPC2. Primer sequences and qRT-PCR were performed as discussed previously [60].

3.1. TPC2

Two recent works have examined the role of TPC2 in melanoma cells in more detail [24,26]. D'Amore et al. (2020) used human CHL-1 amelanotic melanoma cells (derived from a metastatic site: pleural effusion) while Netcharoensirisuk et al. (2021) used the highly pigmented human MNT-1 melanoma cell line (likewise derived from a metastatic site: lymph node). The latter study used TPC2 knockout MNT-1 melanoma cells previously published by Ambrosio et al. (2016), confirming that TPC2 knockout results in a strong increase in melanin content. It was further shown that knockout of TPC2 in MNT-1 cells results in a significant decrease in cell proliferation, migration and invasion [7,19,25]. In addition, an increase in the activity and expression of tyrosinase was found while transcript levels were unchanged. Expression levels of other proteins involved in melanogenesis or regulated by MITF, such as dopachrome tautomerase (Dct, TYRP2), Ras-related protein Rab-27A (Rab27a) or premelanosome protein (PMEL), were normal. This increase in tyrosinase activity and expression is surprising but even more surprising is the finding that protein levels of MITF were decreased in TPC2$^{-/-}$ versus WT cells.

Besides the involvement of MAPK and Wnt/GSK3β/β-Catenin pathways described above, melanin formation is also triggered by melanocyte-stimulating hormone (MSH), a peptide hormone encoded by the proopiomelancortin gene (POMC). MSH binding to MC1R results in the induction of MITF via the cAMP response element-binding protein (CREB).

In the TPC2$^{-/-}$ MNT-1 cells, the expression levels of ERK, AKT, and CREB were found to be unchanged while the expression of GSK3β was increased [20]. It was thus concluded that the increased level of GSK3β results in reduced degradation of the GSK3β containing destruction complexes in endolysosomes, leading to increased GSK3β-dependent MITF degradation. These findings were recapitulated in MNT-1 cells treated with blockers for TPC2 [26] and it was found that flavonoid blockers of TPC2, such as naringenin [61], pratensein or duartin [26] like genetic loss of TPC2, increases melanin content and decreases proliferation, migration and invasion in a TPC2 dependent manner. In TPC2$^{-/-}$ cells, no significant effects of the compounds were seen. In sum, Netcharoensirisuk et al. (2021) concluded that melanoma cell proliferation, migration and invasion are inversely correlated with TPC2-dependent melanin production in MNT-1 cells as the reduction of TPC2 expression increases melanin content but decreases proliferation, migration and invasion. It was suggested that this is the consequence of independent mechanisms: the regulation of MITF protein levels through interference with the endolysosomal activity of TPC2 and endolysosomal GSK3β degradation on the one hand and, on the other hand, the regulation of tyrosinase activity in melanosomes, independent of MITF by indirect interference with the melanosomal proton pump activity (decreased driving force for the pump due to absent or reduced TPC2 activity, resulting in reduced proton uptake by melanosomes, leading to less acidic melanosomal pH, increased tyrosinase activity, and eventually increased melanin production).

Clearly, this dual activity of TPC2 in melanosomes and endolysosomes is a special feature for TPC2 in melanoma cells, which requires further attention to understand its full potential as a possible drug target to treat melanoma.

In the work by d'Amore et al. (2020), amelanotic cells were used. The dual expression of TPC2 in melanosomes and endolysosomes was not discussed. The authors generated a CHL-1 TPC2 knockout line and found that the knockout cells were more invasive and the expression of MITF was increased in the TPC2$^{-/-}$ KO cells as compared to the WT, in contrast to the study by Netcharoensirisuk et al. (2021). A link was shown to the Hippo signaling pathway, which regulates several biological processes including cellular proliferation and survival, and differentiation was postulated. Dysregulation of this pathway, resulting in an increase in YAP/TAZ activity, is associated with cancer, promoting, for example, hyper-proliferation, cellular invasion and metastasis. While YAP/TAZ expression was unchanged in the TPC2 knockout line, some YAP/TAZ target genes were found to be increased, including ANKRD1, CYR61 and CTGF. The drastic differences between these two studies may be due to the amelanotic versus highly pigmented nature of the used melanoma lines, the status of the B-RAF mutation, MITF or other upstream pathways controlling MITF [24,26].

3.2. TRPML1

TPCs are functionally related to another group of non-selective, endolysosomal cation channels—the TRPMLs or mucolipins—with three members in the mammalian genome: TRPML1, 2 and 3. Roles in cancer for all three channels have been proposed, excellently summarized in a number of recent reviews [20,62–64].

Kasitinon and colleagues (2019) have recently screened ion channels and transporters throughout the genome to identify those required by human melanoma cells but not by normal melanocytes, and found that TRPML1 deficient melanoma cells exhibit decreased proliferation, tumor growth and survival [65]. The growth of healthy human melanocytes was unaffected by the loss of TRPML1. They further found TRPML1 to be required in melanoma cells to negatively regulate the MAPK pathway and mTORC1 signaling. mTORC1 promotes cellular proliferation by activating anabolic pathways and by inactivating catabolic pathways such as autophagy, and the MAPK pathway regulates MITF, introduced above as a major regulator of melanoma proliferation and progression. While Kasitinon et al. (2019) found that the deletion of TRPML1 in melanoma increases p-ERK and mTORC1 signaling, they did not discuss their findings in the context of MITF. TRPML1

has been postulated before to promote mTORC1 activity [66–68]. According to the concept by Kasitinon et al. (2019) of the augmentation of MEK-ERK signaling in TRPML1 deficient cells, knockout of TRPML1 would promote MITF transcription and expression [65].

4. Summary and Conclusions

The studies discussed here lack information about the role of the endolysosomal cation channels in melanoma development. More melanoma cell lines should be tested in the future as contradictory findings in MNT-1 (highly pigmented) versus CHL-1 (amelanotic) cell lines need further attention. In particular, a clear mechanistic overview of the different signaling pathways involved upstream of MITF—the key player in melanoma—would be of utmost importance.

Funding: This work was supported, in part, by funding from the German Research Foundation (SFB/TRR152 project P04 to C.G. and GR4315/2–1 to C.G.).

Conflicts of Interest: The authors declare no conflict of interest.

References

1. Shain, A.H.; Bastian, B.C. From melanocytes to melanomas. *Nat. Rev. Cancer* **2016**, *16*, 345–358. [CrossRef]
2. Yamaguchi, Y.; Hearing, V.J. Melanocytes and their diseases. *Cold Spring Harb. Perspect. Med.* **2014**, *4*, a017046. [CrossRef]
3. Raposo, G.; Marks, M.S. Melanosomes–dark organelles enlighten endosomal membrane transport. *Nat. Rev. Mol. Cell Biol.* **2007**, *8*, 786–797. [CrossRef]
4. Wasmeier, C.; Hume, A.N.; Bolasco, G.; Seabra, M.C. Melanosomes at a glance. *J. Cell Sci.* **2008**, *121*, 3995–3999. [CrossRef]
5. Ito, S.; Wakamatsu, K. Human hair melanins: What we have learned and have not learned from mouse coat color pigmentation. *Pigment Cell Melanoma Res.* **2011**, *24*, 63–74. [CrossRef]
6. Bellono, N.W.; Escobar, I.E.; Oancea, E. A melanosomal two-pore sodium channel regulates pigmentation. *Sci. Rep.* **2016**, *6*, 26570. [CrossRef]
7. Ambrosio, A.L.; Boyle, J.A.; Aradi, A.E.; Christian, K.A.; Di Pietro, S.M. TPC2 controls pigmentation by regulating melanosome pH and size. *Proc. Natl. Acad. Sci. USA* **2016**, *113*, 5622–5627. [CrossRef]
8. Chao, Y.K.; Schludi, V.; Chen, C.C.; Butz, E.; Nguyen, O.N.P.; Muller, M.; Kruger, J.; Kammerbauer, C.; Ben-Johny, M.; Vollmar, A.M.; et al. TPC2 polymorphisms associated with a hair pigmentation phenotype in humans result in gain of channel function by independent mechanisms. *Proc. Natl. Acad. Sci. USA* **2017**, *114*, E8595–E8602. [CrossRef]
9. Lerner, A.B.; Fitzpatrick, T.B.; Calkins, E.; Summerson, W.H. Mammalian tyrosinase; preparation and properties. *J. Biol. Chem.* **1949**, *178*, 185–195. [CrossRef]
10. Slominski, A.; Tobin, D.J.; Shibahara, S.; Wortsman, J. Melanin pigmentation in mammalian skin and its hormonal regulation. *Physiol. Rev.* **2004**, *84*, 1155–1228. [CrossRef]
11. Schallreuter, K.U.; Kothari, S.; Chavan, B.; Spencer, J.D. Regulation of melanogenesis–controversies and new concepts. *Exp. Dermatol.* **2008**, *17*, 395–404. [CrossRef]
12. Land, E.J.; Ramsden, C.A.; Riley, P.A. Quinone chemistry and melanogenesis. *Methods Enzymol.* **2004**, *378*, 88–109.
13. Sulem, P.; Gudbjartsson, D.F.; Stacey, S.N.; Helgason, A.; Rafnar, T.; Jakobsdottir, M.; Steinberg, S.; Gudjonsson, S.A.; Palsson, A.; Thorleifsson, G.; et al. Two newly identified genetic determinants of pigmentation in Europeans. *Nat. Genet.* **2008**, *40*, 835–837. [CrossRef]
14. Böck, J.; Krogsaeter, E.; Passon, M.; Chao, Y.K.; Sharma, S.; Grallert, H.; Peters, A.; Grimm, C. Human genome diversity data reveal that L564P is the predominant TPC2 variant and a prerequisite for the blond hair associated M484L gain-of-function effect. *PLoS Genet.* **2021**, *17*, e1009236. [CrossRef]
15. Sample, A.; He, Y.Y. Mechanisms and prevention of UV-induced melanoma. *Photodermatol. Photoimmunol. Photomed.* **2018**, *34*, 13–24. [CrossRef]
16. Premi, S.; Wallisch, S.; Mano, C.M.; Weiner, A.B.; Bacchiocchi, A.; Wakamatsu, K.; Bechara, E.J.; Halaban, R.; Douki, T.; Brash, D.E. Photochemistry. Chemiexcitation of melanin derivatives induces DNA photoproducts long after UV exposure. *Science* **2015**, *347*, 842–847. [CrossRef]
17. Williams, P.F.; Olsen, C.M.; Hayward, N.K.; Whiteman, D.C. Melanocortin 1 receptor and risk of cutaneous melanoma: A meta-analysis and estimates of population burden. *Int. J. Cancer* **2011**, *129*, 1730–1740. [CrossRef]
18. Favia, A.; Desideri, M.; Gambara, G.; D'Alessio, A.; Ruas, M.; Esposito, B.; Del Bufalo, D.; Parrington, J.; Ziparo, E.; Palombi, F.; et al. VEGF-induced neoangiogenesis is mediated by NAADP and two-pore channel-2-dependent Ca2+ signaling. *Proc. Natl. Acad. Sci. USA* **2014**, *111*, E4706–E4715. [CrossRef]
19. Nguyen, O.N.; Grimm, C.; Schneider, L.S.; Chao, Y.K.; Atzberger, C.; Bartel, K.; Watermann, A.; Ulrich, M.; Mayr, D.; Wahl-Schott, C.; et al. Two-Pore Channel Function Is Crucial for the Migration of Invasive Cancer Cells. *Cancer Res.* **2017**, *77*, 1427–1438. [CrossRef]

20. Grimm, C.; Bartel, K.; Vollmar, A.M.; Biel, M. Endolysosomal Cation Channels and Cancer-A Link with Great Potential. *Pharmaceuticals* **2018**, *11*, 4. [CrossRef]
21. Sun, W.; Yue, J. TPC2 mediates autophagy progression and extracellular vesicle secretion in cancer cells. *Exp. Cell. Res.* **2018**, *370*, 478–489. [CrossRef]
22. Alharbi, A.F.; Parrington, J. Endolysosomal Ca(2+) Signaling in Cancer: The Role of TPC2, From Tumorigenesis to Metastasis. *Front. Cell Dev. Biol.* **2019**, *7*, 302. [CrossRef] [PubMed]
23. Faris, P.; Pellavio, G.; Ferulli, F.; Di Nezza, F.; Shekha, M.; Lim, D.; Maestri, M.; Guerra, G.; Ambrosone, L.; Pedrazzoli, P.; et al. Nicotinic Acid Adenine Dinucleotide Phosphate (NAADP) Induces Intracellular Ca(2+) Release through the Two-Pore Channel TPC1 in Metastatic Colorectal Cancer Cells. *Cancers* **2019**, *11*, 542. [CrossRef] [PubMed]
24. D'Amore, A.; Hanbashi, A.A.; Di Agostino, S.; Palombi, F.; Sacconi, A.; Voruganti, A.; Taggi, M.; Canipari, R.; Blandino, G.; Parrington, J.; et al. Loss of Two-Pore Channel 2 (TPC2) Expression Increases the Metastatic Traits of Melanoma Cells by a Mechanism Involving the Hippo Signalling Pathway and Store-Operated Calcium Entry. *Cancers* **2020**, *12*, 2391. [CrossRef] [PubMed]
25. Müller, M.; Gerndt, S.; Chao, Y.K.; Zisis, T.; Nguyen, O.N.P.; Gerwien, A.; Urban, N.; Müller, C.; Gegenfurtner, F.A.; Geisslinger, F.; et al. Gene editing and synthetically accessible inhibitors reveal role for TPC2 in HCC cell proliferation and tumor growth. *Cell Chem. Biol.* **2021**. [CrossRef]
26. Netcharoensirisuk, P.; Abrahamian, C.; Tang, R.; Chen, C.C.; Rosato, A.S.; Beyers, W.; Chao, Y.K.; Filippini, A.; Di Pietro, S.; Bartel, K.; et al. Flavonoids increase melanin production and reduce proliferation, migration and invasion of melanoma cells by blocking endolysosomal/melanosomal TPC2. *Sci. Rep.* **2021**, *11*, 8515. [CrossRef] [PubMed]
27. Vachtenheim, J.; Borovanský, J. "Transcription physiology" of pigment formation in melanocytes: Central role of MITF. *Exp. Dermatol.* **2010**, *19*, 617–627. [CrossRef] [PubMed]
28. Levy, C.; Khaled, M.; Fisher, D.E. MITF: Master regulator of melanocyte development and melanoma oncogene. *Trends Mol. Med.* **2006**, *12*, 406–414. [CrossRef]
29. Garraway, L.A.; Widlund, H.R.; Rubin, M.A.; Getz, G.; Berger, A.J.; Ramaswamy, S.; Beroukhim, R.; Milner, D.A.; Granter, S.R.; Du, J.; et al. Integrative genomic analyses identify MITF as a lineage survival oncogene amplified in malignant melanoma. *Nature* **2005**, *436*, 117–122. [CrossRef] [PubMed]
30. Steingrímsson, E.; Copeland, N.G.; Jenkins, N.A. Melanocytes and the microphthalmia transcription factor network. *Annu. Rev. Genet.* **2004**, *38*, 365–411. [CrossRef]
31. Slade, L.; Pulinilkunnil, T. The MiTF/TFE Family of Transcription Factors: Master Regulators of Organelle Signaling, Metabolism, and Stress Adaptation. *Mol. Cancer Res.* **2017**, *15*, 1637–1643. [CrossRef] [PubMed]
32. La Spina, M.; Contreras, P.S.; Rissone, A.; Meena, N.K.; Jeong, E.; Martina, J.A. MiT/TFE Family of Transcription Factors: An Evolutionary Perspective. *Front. Cell Dev. Biol.* **2021**, *8*, 1580. [CrossRef] [PubMed]
33. Ni, C.; Zhang, D.; Beyer, L.A.; Halsey, K.E.; Fukui, H.; Raphael, Y.; Dolan, D.F.; Hornyak, T.J. Hearing dysfunction in heterozygous Mitf(Mi-wh)/+ mice, a model for Waardenburg syndrome type 2 and Tietz syndrome. *Pigment Cell Melanoma Res.* **2013**, *26*, 78–87. [CrossRef] [PubMed]
34. Rauschendorf, M.A.; Zimmer, A.D.; Laut, A.; Demmer, P.; Rösler, B.; Happle, R.; Sartori, S.; Fischer, J. Homozygous intronic MITF mutation causes severe Waardenburg syndrome type 2A. *Pigment Cell Melanoma Res.* **2019**, *32*, 85–91. [CrossRef] [PubMed]
35. Wiedemann, G.M.; Aithal, C.; Kraechan, A.; Heise, C.; Cadilha, B.L.; Zhang, J.; Duewell, P.; Ballotti, R.; Endres, S.; Bertolotto, C.; et al. Microphthalmia-Associated Transcription Factor (MITF) Regulates Immune Cell Migration into Melanoma. *Transl. Oncol.* **2019**, *12*, 350–360. [CrossRef]
36. Cheli, Y.; Ohanna, M.; Ballotti, R.; Bertolotto, C. Fifteen-year quest for microphthalmia-associated transcription factor target genes. *Pigment Cell Melanoma Res.* **2010**, *23*, 27–40. [CrossRef]
37. Wellbrock, C.; Arozarena, I. Microphthalmia-associated transcription factor in melanoma development and MAP-kinase pathway targeted therapy. *Pigment Cell Melanoma Res.* **2015**, *28*, 390–406. [CrossRef]
38. Carreira, S.; Goodall, J.; Denat, L.; Rodriguez, M.; Nuciforo, P.; Hoek, K.S.; Testori, A.; Larue, L.; Goding, C.R. Mitf regulation of Dia1 controls melanoma proliferation and invasiveness. *Genes. Dev.* **2006**, *20*, 3426–3439. [CrossRef]
39. Hoek, K.S.; Goding, C.R. Cancer stem cells versus phenotype-switching in melanoma. *Pigment Cell Melanoma Res.* **2010**, *23*, 746–759. [CrossRef]
40. Miller, A.J.; Levy, C.; Davis, I.J.; Razin, E.; Fisher, D.E. Sumoylation of MITF and its related family members TFE3 and TFEB. *J. Biol. Chem.* **2005**, *280*, 146–155. [CrossRef]
41. Haass, N.K.; Beaumont, K.A.; Hill, D.S.; Anfosso, A.; Mrass, P.; Munoz, M.A.; Kinjyo, I.; Weninger, W. Real-time cell cycle imaging during melanoma growth, invasion, and drug response. *Pigment Cell Melanoma Res.* **2014**, *27*, 764–776. [CrossRef]
42. Barysch, M.J.; Mangana, J.; Dummer, R. A new B-Raf inhibitor combo for advanced melanoma. *Oncotarget* **2018**, *9*, 34457–34458. [CrossRef]
43. Greaves, W.O.; Verma, S.; Patel, K.P.; Davies, M.A.; Barkoh, B.A.; Galbincea, J.M.; Yao, H.; Lazar, A.J.; Aldape, K.D.; Medeiros, L.J.; et al. Frequency and spectrum of BRAF mutations in a retrospective, single-institution study of 1112 cases of melanoma. *J. Mol. Diagn.* **2013**, *15*, 220–226. [CrossRef]

44. Heppt, M.V.; Siepmann, T.; Engel, J.; Schubert-Fritschle, G.; Eckel, R.; Mirlach, L.; Kirchner, T.; Jung, A.; Gesierich, A.; Ruzicka, T.; et al. Prognostic significance of BRAF and NRAS mutations in melanoma: A German study from routine care. *BMC Cancer* **2017**, *17*, 536. [CrossRef]
45. Zhou, A.Y.; Johnson, D.B. Combinatorial Therapies in Melanoma: MAPK Inhibitors and Beyond. *Am. J. Clin. Dermatol.* **2018**, *19*, 181–193. [CrossRef]
46. Inamdar, G.S.; Madhunapantula, S.V.; Robertson, G.P. Targeting the MAPK pathway in melanoma: Why some approaches succeed and other fail. *Biochem. Pharmacol.* **2010**, *80*, 624–637. [CrossRef]
47. Van Allen, E.M.; Wagle, N.; Sucker, A.; Treacy, D.J.; Johannessen, C.M.; Goetz, E.M.; Place, C.S.; Taylor-Weiner, A.; Whittaker, S.; Kryukov, G.V.; et al. The genetic landscape of clinical resistance to RAF inhibition in metastatic melanoma. *Cancer Discov.* **2014**, *4*, 94–109. [CrossRef]
48. Lister, J.A.; Capper, A.; Zeng, Z.; Mathers, M.E.; Richardson, J.; Paranthaman, K.; Jackson, I.J.; Elizabeth Patton, E. A conditional zebrafish MITF mutation reveals MITF levels are critical for melanoma promotion vs. regression in vivo. *J. Investig. Dermatol.* **2014**, *134*, 133–140. [CrossRef] [PubMed]
49. Hemesath, T.J.; Price, E.R.; Takemoto, C.; Badalian, T.; Fisher, D.E. MAP kinase links the transcription factor Microphthalmia to c-Kit signalling in melanocytes. *Nature* **1998**, *391*, 298–301. [CrossRef] [PubMed]
50. Wu, M.; Hemesath, T.J.; Takemoto, C.M.; Horstmann, M.A.; Wells, A.G.; Price, E.R.; Fisher, D.Z.; Fisher, D.E. c-Kit triggers dual phosphorylations, which couple activation and degradation of the essential melanocyte factor Mi. *Genes. Dev.* **2000**, *14*, 301–312. [PubMed]
51. Price, E.R.; Horstmann, M.A.; Wells, A.G.; Weilbaecher, K.N.; Takemoto, C.M.; Landis, M.W.; Fisher, D.E. alpha-Melanocyte-stimulating hormone signaling regulates expression of microphthalmia, a gene deficient in Waardenburg syndrome. *J. Biol. Chem.* **1998**, *273*, 33042–33047. [CrossRef]
52. Ploper, D.; Taelman, V.F.; Robert, L.; Perez, B.S.; Titz, B.; Chen, H.W.; Graeber, T.G.; von Euw, E.; Ribas, A.; De Robertis, E.M. MITF drives endolysosomal biogenesis and potentiates Wnt signaling in melanoma cells. *Proc. Natl. Acad. Sci. USA* **2015**, *112*, E420–E429. [CrossRef]
53. Nusse, R.; Clevers, H. Wnt/β-Catenin Signaling, Disease, and Emerging Therapeutic Modalities. *Cell* **2017**, *169*, 985–999. [CrossRef]
54. Gajos-Michniewicz, A.; Czyz, M. WNT Signaling in Melanoma. *Int. J. Mol. Sci.* **2020**, *21*, 4852. [CrossRef]
55. Johnson, M.L.; Rajamannan, N. Diseases of Wnt signaling. *Rev. Endocr. Metab. Disord.* **2006**, *7*, 41–49. [CrossRef]
56. De Ferrari, G.V.; Inestrosa, N.C. Wnt signaling function in Alzheimer's disease. *Brain Res. Brain Res. Rev.* **2000**, *33*, 1–12. [CrossRef]
57. Larue, L.; Beermann, F. Cutaneous melanoma in genetically modified animals. *Pigment Cell Res.* **2007**, *20*, 485–497. [CrossRef]
58. Larue, L.; Luciani, F.; Kumasaka, M.; Champeval, D.; Demirkan, N.; Bonaventure, J.; Delmas, V. Bypassing melanocyte senescence by beta-catenin: A novel way to promote melanoma. *Pathol. Biol.* **2009**, *57*, 543–547. [CrossRef] [PubMed]
59. Delmas, V.; Beermann, F.; Martinozzi, S.; Carreira, S.; Ackermann, J.; Kumasaka, M.; Denat, L.; Goodall, J.; Luciani, F.; Viros, A.; et al. Beta-catenin induces immortalization of melanocytes by suppressing p16INK4a expression and cooperates with N-Ras in melanoma development. *Genes. Dev.* **2007**, *21*, 2923–2935. [CrossRef]
60. Pafumi, I.; Festa, M.; Papacci, F.; Lagostena, L.; Giunta, C.; Gutla, V.; Cornara, L.; Favia, A.; Palombi, F.; Gambale, F.; et al. Naringenin Impairs Two-Pore Channel 2 Activity And Inhibits VEGF-Induced Angiogenesis. *Sci. Rep.* **2017**, *7*, 5121. [CrossRef] [PubMed]
61. Sterea, A.M.; Almasi, S.; El Hiani, Y. The hidden potential of lysosomal ion channels: A new era of oncogenes. *Cell Calcium* **2018**, *72*, 91–103. [CrossRef]
62. Santoni, G.; Santoni, M.; Maggi, F.; Marinelli, O.; Morelli, M.B. Emerging Role of Mucolipins TRPML Channels in Cancer. *Front. Oncol.* **2020**, *10*, 659. [CrossRef] [PubMed]
63. Xu, M.; Dong, X.P. Endolysosomal TRPMLs in Cancer. *Biomolecules* **2021**, *11*, 65. [CrossRef] [PubMed]
64. Kasitinon, S.Y.; Eskiocak, U.; Martin, M.; Bezwada, D.; Khivansara, V.; Tasdogan, A.; Zhao, Z.; Mathews, T.; Aurora, A.B.; Morrison, S.J. TRPML1 Promotes Protein Homeostasis in Melanoma Cells by Negatively Regulating MAPK and mTORC1 Signaling. *Cell Rep.* **2019**, *28*, 2293–2305.e9. [CrossRef] [PubMed]
65. Li, R.J.; Xu, J.; Fu, C.; Zhang, J.; Zheng, Y.G.; Jia, H.; Liu, J.O. Regulation of mTORC1 by lysosomal calcium and calmodulin. *eLife* **2016**, *5*, e19360. [CrossRef] [PubMed]
66. Li, X.; Rydzewski, N.; Hider, A.; Zhang, X.; Yang, J.; Wang, W.; Gao, Q.; Cheng, X.; Xu, H. A molecular mechanism to regulate lysosome motility for lysosome positioning and tubulation. *Nat. Cell Biol.* **2016**, *18*, 404–417. [CrossRef]
67. Wang, W.; Gao, Q.; Yang, M.; Zhang, X.; Yu, L.; Lawas, M.; Li, X.; Bryant-Genevier, M.; Southall, N.T.; Marugan, J.; et al. Up-regulation of lysosomal TRPML1 channels is essential for lysosomal adaptation to nutrient starvation. *Proc. Natl. Acad. Sci. USA* **2015**, *112*, E1373–E1381. [CrossRef] [PubMed]
68. Rühl, P.; Rosato, A.S.; Urban, N.; Gerndt, S.; Tang, R.; Abrahamian, C.; Leser, C.; Sheng, J.; Jha, A.; Vollmer, G.; et al. Estradiol analogs attenuate autophagy, cell migration and invasion by direct and selective inhibition of TRPML1, independent of estrogen receptors. *Sci. Rep.* **2021**, *11*, 8313. [CrossRef] [PubMed]

Paper VIII

frontiers in Immunology

REVIEW
published: 28 February 2020
doi: 10.3389/fimmu.2020.00225

TRPML Cation Channels in Inflammation and Immunity

Barbara Spix[1†], *Yu-Kai Chao*[1†], *Carla Abrahamian*[1†], *Cheng-Chang Chen*[2] *and Christian Grimm*[1*]

[1] *Faculty of Medicine, Walther Straub Institute of Pharmacology and Toxicology, Ludwig-Maximilians-Universität, Munich, Germany,* [2] *Department of Pharmacy, Center for Drug Research, Ludwig-Maximilians-Universität, Munich, Germany*

Background: In 1883, Ilya Mechnikov discovered phagocytes and established the concept of phagocytosis by macrophages. In 1908, he was awarded the Nobel Prize in Physiology/Medicine for his findings, which laid the foundations for today's understanding of the innate immune response. Only in the 1960s, Max Cooper and Robert Good significantly advanced our understanding of the immune system by demonstrating that B- and T-cells cooperate to regulate the adaptive immune response. Both, innate and adaptive immune response are essential to effectively protect the individual against infectious agents, such as viruses, bacterial or insect toxins, or allergens. Innate immune responses occur rapidly upon exposure to noxious or infectious agents or organisms, in contrast to the adaptive immune system that needs days rather than hours to develop and acts primarily on the basis of antigen-specific receptors expressed on the surface of B- and T-lymphocytes. In recent years, it has become evident that endosomes and lysosomes are involved in many aspects of immune cell function, such as phagocytosis, antigen presentation and processing by antigen-presenting cells, release of proinflammatory mediators, e.g., by mast cells, or secretion of the pore-forming protein perforin by cytotoxic T lymphocytes. Several lysosomal storage disorders (LSDs) have been associated with defects in immune system function or immune system hyperactivity, such as Gaucher, Fabry, or Niemann-Pick type C1 disease, mucopolysaccharidoses (MPS), gangliosidosis, or juvenile neuronal ceroid lipofuscinosis (JNCL). Beside accumulating evidence on the importance of endolysosomes in immune cell function, recent results suggest direct roles of endolysosomal ion channels, such as the TRPML channels (mucolipins), which are members of the transient receptor potential (TRP) superfamily of non-selective cation channels, for different aspects of immune cell function. The aim of this review is to discuss the current knowledge about the roles of TRPML channels in inflammation and immunity, and to assess their potential as drug targets to influence immune cell functions.

Advances: Examples of recently established roles of TRPML channels in immune system function and immune response include the TRPML1-mediated modulation of secretory lysosomes, granzyme B content, and tuning of effector function in NK cells, TRPML1-dependent directional dendritic cell (DC) migration and DC chemotaxis, and the role of TRPML2 in chemokine release from LPS-stimulated macrophages.

OPEN ACCESS

Edited by:
Albrecht Schwab,
University of Münster, Germany

Reviewed by:
Shmuel Muallem,
National Institutes of Health (NIH), United States
Kartik Venkatachalam,
University of Texas Health Science Center at Houston, United States

***Correspondence:**
Christian Grimm
christian.grimm@med.uni-muenchen.de

[†] *These authors have contributed equally to this work*

Specialty section:
This article was submitted to Molecular Innate Immunity, a section of the journal Frontiers in Immunology

Received: *28 November 2019*
Accepted: *28 January 2020*
Published: *28 February 2020*

Citation:
Spix B, Chao Y-K, Abrahamian C, Chen C-C and Grimm C (2020) TRPML Cation Channels in Inflammation and Immunity. Front. Immunol. 11:225. doi: 10.3389/fimmu.2020.00225

Outlook: Although our understanding of the functional roles of TRPML channels in inflammation and immunity is still in its infancy, a few interesting findings have been made in the past years, encouraging further and more detailed work on the role of TRPMLs, e.g., in intracellular trafficking and release of chemokines, cytokines, or granzyme B, or in phagocytosis and bacterial toxin and virus trafficking through the endolysosomal machinery.

Keywords: immune system, immune cells, TRPML cation channels, mucolipin, lysosome

INTRODUCTION

TRP channels are a very diverse and heterogenous group of cation channels. With few exceptions, the majority of them are expressed at the plasma membrane. One subfamily of the TRP channels, the mucolipin or TRPML/MCOLN subfamily comprises three members in mammalian genomes, TRPML1, 2, and 3 which are all found to be expressed in the endolysosomal system, i.e., in early and late endosomes, in recycling endosomes and in lysosomes to various degrees. All three channels are regulated by the phosphoinositide $PI(3,5)P_2$, a major component of endolysosomal membranes and by luminal pH (1, 3–5). Thus, TRPML1 is most active at highly acidic pH as found in lysosomes while TRPML2 and TRPML3 are more active at higher pH as it occurs in early and recycling endosomes (1, 3–5). TRPML1 activity already decreases under mild acidic conditions (pH 5.5; **Figure 1**) and is lowest at neutral conditions (4). A recent hypothesis suggested that elevated lysosomal pH may hyperactivate the TRPML1 calcium channel (2), is not supported by endolysosomal patch-clamp evidence (**Figure 1**).

Several functional roles have been proposed for TRPML1, e.g., in gastric acid secretion by parietal cells (6, 7), as a ROS sensor in lysosomes to regulate autophagy (8, 9), as an autophagy regulator through calcineurin and TFEB (10), or in membrane repair, e.g., repair of the sarcolemma to prevent muscular dystrophy (11). Loss or dysfunction of TRPML1 causes the rare lysosomal storage disorder mucolipidosis type IV, major hallmarks of which are severe neuro- and retinal degeneration, mental and psychomotor retardation, hypotonia, achlorhydria, and premature death. The observation that macromolecules, e.g., certain lipids (sphingolipids, phospholipids) and mucopolysaccharides as well as metals like iron or zinc accumulate in patient cells suggested roles for TRPML1 in metal cation release, in addition to the release of calcium and other cations from lysosomes as well as a critical function for the overall integrity of lysosomes including their roles in intracellular trafficking, fission/fusion and autophagy. While most research has focused on TRPML1, due to its clear association with human disease, function and pathophysiological relevance of the related channels TRPML2 and TRPML3 are less well-understood, with no links to human (genetic) disease so far. In mice, gain-of-function variants of TRPML3 have been shown to cause deafness, circling behavior, and coat color dilution due to the loss of inner ear hair cells and melanocytes following intracellular calcium overload. (12–16). $TRPML2^{-/-}$ and $TRPML3^{-/-}$ mice are viable and according to genomic databases, human TRPML2 and TRPML3 knockouts do also exist. Nothing however is known about health issues they may have. In contrast to the ubiquitously expressed TRPML1, the expression of TRPML2 and TRPML3 is restricted to certain cell types including a number of immune cells. Recently, several roles of immune cell function could be linked to TRPML channels, e.g., a role of TRPML1 for the phagocytosis of large particles (17), the migration of dendritic cells (18), or for the tuning of the functional potential in self-KIR+ natural killer (NK) cells (19) while TRPML2 was found to play a role in chemokine and cytokine secretion by macrophages (5, 20). In the following, the current state of knowledge on TRPML channel expression and function in different immune cells shall be discussed (**Figure 2**).

CHAPTER I: INNATE IMMUNE SYSTEM

Macrophages

Macrophages are phagocytic cells. They express receptors on their surface called pattern recognition receptors (PRRs), which are able to detect varying molecular structures of microbes, referred to as pathogen-associated molecular pattern (PAMP). One example for a PRR are the toll-like receptors (TLRs). Sun et al. (20) have recently discovered that activation of these receptors leads to a strong increase of both mRNA and protein levels of the TRPML2 channel. They tested different TLR activators, including LPS (a component of bacteria that activates TLR4), zymosan A (a component of fungi that activates TLR2), loxoribine which activates TLR7, and resiquimod (R848) which activates TLR7/8. The latter two are involved in recognizing viruses. In all cases and both in primary (murine microglia) and cultured cells (RAW 264.7) an upregulation of TRPML2 was found, suggesting that the TRPML2 channel is involved in the host defense against different pathogens like bacteria, viruses and fungi.

The binding of such particles to the PRRs or the binding of IgG-opsonized particles to the FCγ-receptor trigger an important process in the innate immune response: phagocytosis. During this process the particle is surrounded by the macrophage with the help of extensions of the cytoplasm (i.e., pseudopods) and is completely enclosed with membrane in structures called phagosomes. These phagosomes mature by fusing with lysosomes into phagolysosomes, which have an acidic luminal pH and contain hydrolytic enzymes to break down the engulfed particles. Samie et al. (17) have first shown that TRPML1 regulates the ingestion of large particles by providing the membrane for the cell surface, necessary for phagosome formation. They suggested the following cascade of events and signaling pathways: after

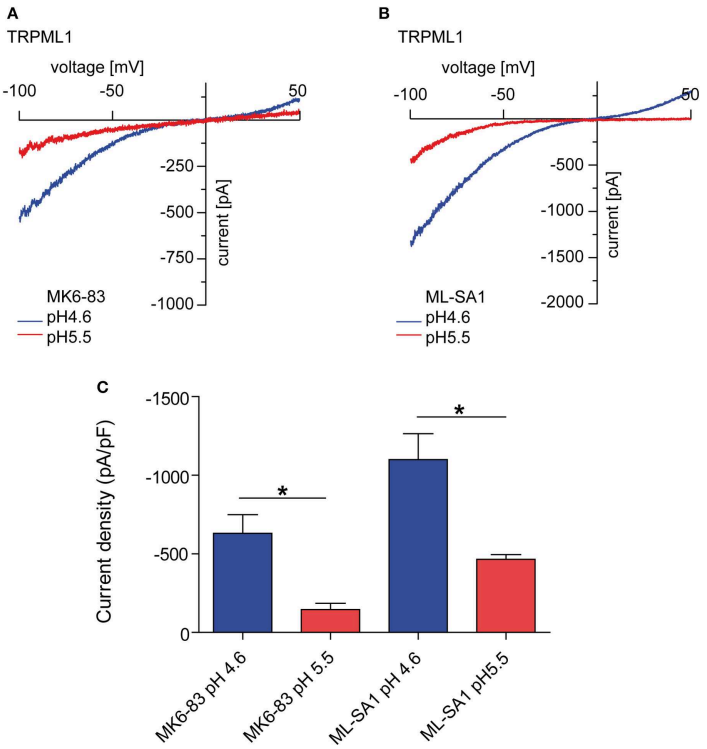

FIGURE 1 | Endolysosomal patch-clamp experiments showing TRPML1 currents induced by MK6-83 and ML-SA1 (10 μM, each) at different luminal pH. **(A)** Representative MK6-83 elicited currents from TRPML1 expressing HEK293 cells at pH 4.6 or pH 5.5. **(B)** Representative ML-SA1 elicited currents from TRPML1 expressing HEK293 cells at pH 4.6 or 5.5. **(C)** Statistical summary of data as shown in **(A,B)**. Shown are average current densities at −100 mV (mean ± SEM). In all statistical analyses, the mean values of independent experiments ($n > 4$, each) are shown as indicated. *$p < 0.05$, Student's *t*-test, unpaired.

particle binding of the phagocytic cell the endolysosomal PI-5 kinase, PIKfyve is stimulated and phosphorylates PI(3)P to form $PI(3,5)P_2$, which is then present in sufficient amounts to activate the TRPML1 channel in lysosomes. The resulting Ca^{2+} release induces lysosomal exocytosis at the site of the formation of the phagocytic cup. Such fusion events with the plasma membrane increase the surface area of the phagocytosing macrophage which is essential for the engulfment of large particles. Thus, TRPML1 plays a crucial role in the initial steps of phagocytosis and enables the innate immune system to eliminate large particles quickly (17). However, the TRPML1 channel does not only seem to be involved in phagosome formation but also in phagosome maturation, i.e., the fusion process of phagosomes with lysosomes. This was proposed by Dayam et al. (21) who analyzed phagocytosis in TRPML1-silenced or PIKfyve-inhibited cells in which the phagolysosomal biogenesis was impaired, because the phagosomes and lysosomes were not able to fuse after docking. The phagolysosome maturation could be rescued by Ca^{2+} ionophores like ionomycin. This suggested that both PIKfyve and TRPML1, more specifically the TRPML1-mediated Ca^{2+} release from lysosomes, were key mediators in phagosome maturation. PIKfyve would presumably act upstream of TRPML1, since it produces the endogenous TRPML1 activator $PI(3,5)P_2$ (21). Impaired ability to eliminate the ingested bacteria was also observed in PIKfyve and TRPML1 deficient macrophages. This is in line with previous findings showing reduced levels of cathepsin D, a common lysosomal enzyme, in phagosomes of PIKfyve inhibited cells (22). Mycobacteria for example, interfere with the PI(3)P metabolism and thereby induce an impaired phagosome maturation, enabling them to prevent degradation through fusion with lysosomes (23).

Furthermore, TRPML1 has been found to enhance the degradative function of lysosomes during phagocytosis through TFEB (24). Gray et al. speculated that the protein phosphatase calcineurin, activated by the Ca^{2+} release through TRPML1, dephosphorylates TFEB to induce its translocation to the nucleus.

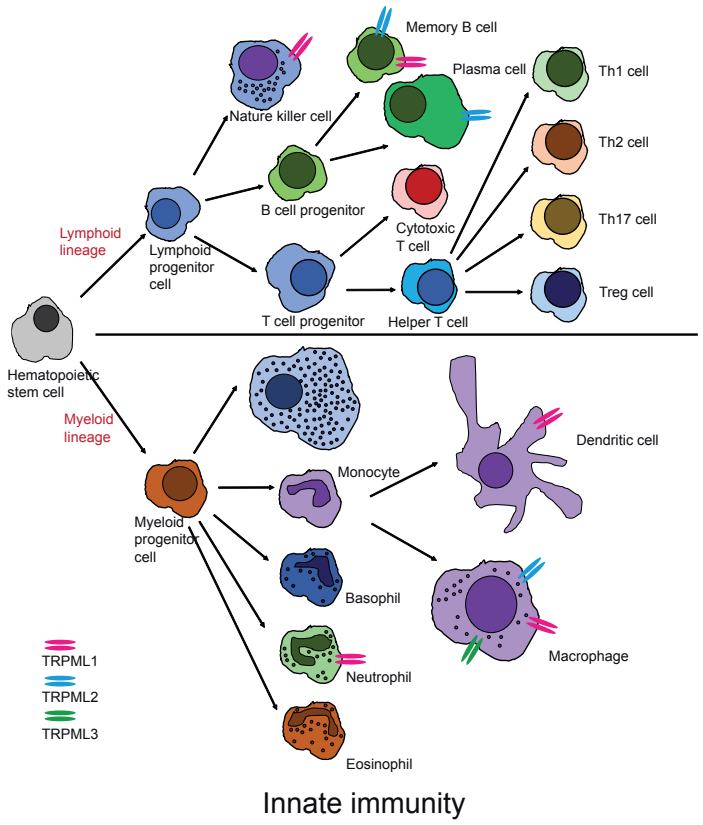

FIGURE 2 | Cartoon showing expression of TRPML channels in different cells of the innate and adaptive immune system. Expression has either been confirmed by direct patch-clamp experimentation of endo-lysosomes isolated from these cells or by other published experimental evidence as outlined in chapter I and II.

There, it acts as a transcription factor for the lysosomal enzyme cathepsin D and the H subunit of the V-ATPase, which regulates the acidic and hydrolytic environment in the phagolysosomes. This enhances the degradation ability of the existing lysosomes, so that bacteria are eliminated more efficiently in the phagolysosomes. They showed this for opsonic phagocytosis mediated by the FCγ-receptor and for non-opsonic phagocytosis as well. Hence, the TRPML1 channel may not only be necessary for the initial steps of phagocytosis but also for later steps in the phagocytosis process like phagosome maturation and efficient degradation of engulfed particles. This is important, in particular when large numbers of bacteria are present.

Cathepsins and their proteolytic functions are essential for the degradation of bacteria captured in lysosomes during phagocytosis. The role of different cathepsins has been studied in great detail. Cathepsin D, besides its degradative capacity, may also induce bacterial killing by activating apoptosis in alveolar macrophages after take-up of pneumococci by phagosomes (25). Mice lacking cathepsin E are more sensitive to infections by Staphylococcus aureus and Porphyromonas gingivalis (26). Qi et al. (27) detected a role of cathepsin B in the defense of macrophages against Francisella novicida. Thus, bone marrow-derived macrophages (BMDM) from cathepsin B deficient mice were able to clear bacteria more efficiently and these mice were protected from lethality (27) which may be due to the down-regulation of mTOR activity and prevention of TRPML1 degradation (28). Decreased mTOR activity means that TFEB is no longer kept in the cytosol by phosphorylation but tanslocates

into the nucleus (29), where it promotes the transcription of genes encoding lysosomal proteins and the kinase ULK1 as inducer of autophagy. In addition, TRPML1 contributes to the regulation of TFEB through the protein phosphatase calcineurin. Both, enhanced lysosomal biogenesis and induction of autophagy promote the ability of cathepsin B deficient macrophages to get rid of ingested bacteria. TRPML3 has also been shown by several groups to be involved in autophagy (30–32), suggesting that as described above for TRPML1 it may play similar roles in certain cell types. Evidence for an evolutionary conserved role of TRPMLs in bacterial clearance by macrophages comes from drosophila work. Thus, Wong et al. (33) found that flies lacking trpml in macrophages exhibited compromised clearance of *E. coli*, a phenotype similar to the one observed in macrophages deficient of ClC-b, the drosophila homolog of the mammalian late-endosomal/lysosomal Cl^-/H^+ transporter CLCN7. Wong et al. further showed that ClC-b-mediated Cl^- transport into endolysosomes was necessary for the accumulation of luminal Ca^{2+}, which, when released through TRPML, drives the delivery of phagocytic cargo to lysosomes for degradation. Beside phagocytosis, macrophages play another important role within the innate immune system as they produce and secrete a variety of cytokines and chemokines after stimulation. Inflammatory cytokines and chemokines are signaling molecules that attract other immune cells to the inflammation herd. Apart from this, cytokines may also determine the polarization state of macrophages, where classically activated macrophages (M1) are stimulated by interferon-γ, TLR ligands, or microbial substrates like LPS. This is connected with an increased production of proinflammatory cytokines, such as TNF-α, IL-6, IL-1, IL-23 and reactive oxygen/nitrogen species. These macrophages have a high pro-inflammatory and microbicidal activity. Alternatively, activated macrophages (M2) are stimulated by IL-4 and IL-13 and are involved in tissue repair, suppression of inflammation and tumor progression by secreting the anti-inflammatory cytokines IL-10 and TGF-β. A third class of macrophages are regarded as tumor-associated macrophages. They differentiate from circulating monocytes after migrating into tumor tissue upon stimulation with IL-4, IL-10, or IL-13 and exhibit pro-tumorigenic functions (34, 35).

The release of cytokines by macrophages is a highly regulated process. Time, volume and site of release must be controlled, but first cytokines need to be transported to the plasma membrane. To this end, they make use of the cell's trafficking machinery including the trans-Golgi network (TGN) and the endolysosomal system, especially recycling endosomes (36). In the latter ones high levels of TRPML2 are found (37, 38). Sun et al. demonstrated that lack of TRPML2 in BMDM leads to an intracellular accumulation and decreased secretion of CCL2 [chemokine (C-C motif) ligand 2, also called monocyte chemoattractant protein 1 (MCP1)] (20). They also found reduced macrophage recruitment in TRPML2$^{-/-}$ mice after LPS stimulation which is in accordance with the role of CCL2 as chemoattractant recruiting additional immune cells to the site of inflammation (39). The link between TRPML2 and CCL2 was further investigated by Plesch et al. who developed ML2-SA1, a selective agonist for TRPML2, and found that activation of the channel directly stimulates the secretion of CCL2 from BMDM. The release is most likely mediated via the early/recycling endosomal pathway, since activation of TRPML2 by ML2-SA1 promotes trafficking through this pathway. In addition, Plesch et al. found that direct activation of TRPML2 leads to enhanced recruitment of macrophages (5). These findings by Sun et al. and Plesch et al. strongly suggest that TRPML2 plays a crucial role in the release of CCL2 and likely other chemokines as well as in the stimulation of macrophage migration.

Neutrophils

Neutrophils are another essential cell type in the innate immune system. They are the first cells to arrive at the site of inflammation or infection as they have a high chemotactic ability (40). They carry out numerous functions: First, they express and secrete cytokines that recruit more immune cells like macrophages to amplify the inflammatory response (41). Second, they perform phagocytosis of pathogens resulting in phagosome formation and fusion with lysosomes to kill engulfed bacteria (41, 42). Third, they release a variety of antimicrobial proteins (cathepsins, neutrophil elastase, lysozyme, NADPH oxidase) that help eliminate the pathogens (41).

In 2017, Dayam et al. showed the lipid kinase PIKfyve to play an essential role in coordinating various neutrophil functions. As mentioned above, PIKfyve is responsible for the synthesis of $PI(3,5)P_2$, an endogenous activator of TRPML channels that results in lysosomal Ca^{2+} release also in neutrophils. The authors further found that the PIKfyve-TRPML1-Ca^{2+} axis regulates phagosome maturation, i.e., the fusion of phagosomes and lysosomes. They also found that inhibition of this axis blocks phagosome maturation (43). These findings are in line with their previous works and other works by Kim et al. (22), reporting on the same PIKfyve-TRPML1-Ca^{2+} pathway to trigger phagosome-lysosome-fusion in macrophages (21, 22). Furthermore, Dayam et al. found that PIKfyve activity is essential for ROS generation and chemotaxis mediated through the stimulation of Rac GTPases. Taken together these data suggest that PIKfyve and TRPML1 are important regulators of several neutrophil functions that are critical for the rapid response of the innate immune system (43).

Dendritic Cells

Dendritic cells (DCs) are antigen-presenting cells (APCs) which play key roles in the adaptive immune response (44, 45). After capturing pathogenic antigens via macropinocytosis, immature DCs turn into mature DCs. They start to process and express high level of antigens, stimulatory molecules, and cytokines that are able to induce the T-cell response after migrating to lymph nodes, where they present the antigens to activate T-cells (46–48). Intracellular Ca^{2+} signaling from endolysosomal TRPML1 channel is involved in DC functions, such as regulating TLRs for nucleic acid sensing and DC migration (18). TLRs can recognize structurally conserved molecules from pathogens. Membrane lipids from pathogens can be recognized by cell surface located TLR1, TLR2, TLR4, and TLR6 while nucleic acids from pathogens can be recognized by intracellular located TLR3, TLR7, TLR8, and TLR9 (49–51). TRPML1 has been

reported to be involved in the TLR7 response to single strand RNA (ssRNA). Li et al. demonstrated that loss of TRPML1 function or inhibition of PI(3,5)P_2 generating PIKfyve blocks the transportation of ssRNA into lysosomes while activation of TRPML1 by the TRPML channel agonist ML-SA1 enhances this process. Impaired transportation of ssRNA leads to an impaired TLR7 response, demonstrating that the P(3,5)P_2-TRPML1 axis plays an important role in this process (52).

Regarding the role of TRPML1 in DC migration, Bretou et al. (18) found that after the down regulation of macropinocytosis in DCs upon sensing the pathogens, lysosomal calcium signaling through TRPML1 regulates DC chemotaxis and migration to lymph nodes by controlling the motor protein myosin II retrograde flow at the cell rear to induce fast and directional migration. TRPML1 mediated calcium signaling further initiates TFEB translocation from cytoplasm to nucleus which will further maintain TRPML1 expression forming a positive feedback loop mediated by the TFEB-TRPML1 axis. Therefore, activation of the TFEB-TRPML1 axis via the inhibition of macropinocytosis is a critical step to switch DCs from patrolling mode to fast migration mode and homing into lymph nodes (18).

Natural Killer Cells

Natural killer (NK) cells differentiate from the same lymphoid progenitor as T- and B-cells but are classified as innate immunity lymphocytes because of their rapid response to pathogens, especially viruses and fungi. NK cells are also functionally active against tumor cells (53, 54). Killing of target cells is mediated by cytotoxic factors, such as perforin and granzymes which are secreted from lysosome related organelles called lytic granules in NK cells (55, 56). Besides killing target cells directly through cytotoxicity, NK cells can indirectly contribute to immune defense via secretion of cytokines, such as interferon-γ (IFN-γ) or tumor necrosis factor–α (TNF-α) to regulate antigen-presenting cell function and T cell responses (57). NK cell activity is regulated by the dynamic balance between activating and inhibitory signals generated from a combination of germ-line encoded receptors which recognize the ligands expressed on the target cell surface. These determine whether or not the NK cell will kill the target cell (58, 59). Major histocompatibility complex (MHC) class I molecules are antigen-presenting molecules and critical for adaptive immune responses, which can be recognized by inhibitory receptors, such as killer cell Ig-like receptors (KIR), Ly49, and CD94/NKG2A on NK cells (60, 61). Decrease of MHC class I expression occurs when cells are infected by virus or under cellular transformation. This situation is called "missing-self" and can be detected by NK cells and promote NK cell cytotoxicity and cytokine production to selectively kill the target cell (57, 62). A process called NK cell education is the interaction between self-MHC and inhibitory receptors on NK cells to calibrate NK cell effector capacities (63). Goodridge et al. have recently reported that TRPML1 is involved in this process by modulating secretory lysosomes, granzyme B content, and by regulating effector function in NK cells (19). Goodridge et al. found that silencing of TRPML1 or pharmacological interference with PIKfyve resulted in enlarged lysosomes with increased granzyme B content and higher effector function, representing the educated state of NK cells. Therefore, these findings establish a link between NK cell education and remodeling of the lysosomal compartment. They also suggest a potential way to increase NK cell function via manipulating calcium homeostasis within lysosome related organelles (19).

CHAPTER II: ADAPTIVE IMMUNE SYSTEM

B Cells

B cells form a vital part of the adaptive immune system. They cooperate with other immune cells, such as T-cells, macrophages, and dendritic cells to eliminate foreign antigens. B-cells operate by producing and secreting millions of different antibody

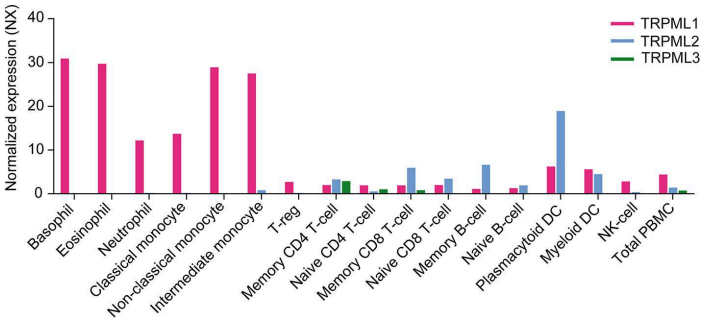

FIGURE 3 | Gene expression level in various human immune cells showing the RNA sequencing data averaged from three different sources (Internally generated Human Protein Atlas (HPA) as well as data generated by Monaco et al. and Schmiedel et al.) Data are shown as normalized expression (NX) (71, 72), resulting from an internal normalization pipeline for the different cell types and total peripheral blood mononuclear cells (PBMC). The NX value for each gene represents the maximum NX value in the three data sources (Based on data from Human Protein Atlas: Blood Cell Type Expression (RNA) of MCOLN1/MCOLN2/MCOLN3 available from: https://www.proteinatlas.org).

molecules, which in turn recognize and respond to a pathogen or foreign antigen. This response is partially mediated by an integral membrane protein called the B-cell receptor (BCR) (64, 65). BCRs are specialized receptors, structurally composed of two Ig light chains, two Ig heavy chains, and two heterodimers Igα and Igβ (65). B-cells have a specialized lysosomal compartment in which antigens deriving from endocytosed BCRs are loaded onto MHC class II. Upon BCR engagement, this compartment undergoes a regulated transformation linked to the *de-novo* formation of multi-vesicular bodies (MVBs) which mature from tubulo-vacuolar early endosomes by a process of remodeling (66, 67). Although these processes are thought to be crucial for the role of B-lymphocytes in immune-modulatory and antigen processing, the molecular pathways underlying the regulation and formation of the specialized lysosomal compartment within B-cells are still poorly understood (66). Specifically, the distribution of MHC class II products over endolysosomal compartments including MVBs in response to BCR engagement remains a matter of debate (68).

Song et al. (66) have verified the expression of TRPML1 and TRPML2 in B-lymphocytes. Their results however indicate that TPRML1 deficient B-lymphocytes are not linked to gross changes in the lysosomal compartment. This is in accordance with the finding that MLIV patients do not exhibit any obvious abnormalities in lymphocyte function, nor do they have obvious immune function defects, arguing for compensatory mechanisms. The authors suggested that normal lysosomal compartments seen in lymphocytes with TRPML1 deficiency may be due to a role of TRPML2 in compensating for the loss of TRPML1 function, and therefore postulated overlapping functions of TRPML1 and TRPML2 in B-lymphocytes. In contrast, expression of TRPML3 had not been demonstrated for B cells (66).

Normal immune response is dependent on an intact development of B-lymphocytes and mutations of genes involved in B-cell differentiation distort this process. Bruton's tyrosine kinase (Btk) gene, that is part of the Tec family of cytoplasmic non-receptor protein-tyrosine kinases, encodes for one of these crucial molecules. Mutations in this gene lead to a partial blockage between the pre- and pro-B-lymphocyte stage, and a complete blockage between the pre- and mature B-lymphocyte stage, leading to X-linked immunodeficiency pathologies in mice and to X-linked agammaglobulinemia in humans. A more severe phenotype is observed in humans as compared to mice because only a partial blockage is established between the pre- and mature B-cell stage in the latter (69).

The phosphorylation and activation of Btk is dependent on plasma membrane (PM) localization. BCR engagement by an antigen results in the activation of PI3K, generating the phosphoinositide phosphatidylinositol-3,4,5-trisphosphate (PIP3). Btk, along with other signaling proteins, are then recruited, as a result of PIP3 accumulation to the PM. Subsequent binding of the pleckstrin homology (PH) domain to PIP3 is a pre-requisite for Btk activation. Even though the molecular mechanisms which target Btk to the cell surface remain largely unclear, the PH domain seems to play an important role. As Btk is a cytoplasmic tyrosinase kinase, loss of Btk leads to dysregulation in downstream signaling pathways, impacting several effector molecules (70).

Lindvall et al. have shown that TRPML2 is expressed in T-, B-, myeloma, and mastocytoma cell lines, in addition to whole primary splenocytes. TRPML2 was also shown to be expressed at pre-B cell, mature B-cell, and plasma cell stages, and in splenic T1 B-lymphocyte cell populations. TRPML2 was up-regulated in both Btk-defective and wild-type splenic primary mouse B-cells post-stimulation with either phorbol-12-myristate-13-acetate (PMA) plus ionomycin or anti-IgM while it was downregulated by a factor of four in unstimulated Btk-defective splenic primary mouse B-cells. The authors further proposed a role of Btk in B-cells in suppressing the activation of TRPML2. However, these results await further confirmation.

CONCLUSIONS AND OUTLOOK

Functional expression of TRPML channels has been demonstrated for a number of cells belonging to both the innate and the adaptive immune system, in particular macrophages, dendritic cells, neutrophils, NK cells, and B lymphocytes as outlined above. Based on gene expression data from different sources (**Figure 3**), TRPML channels may however be functionally active in many more cells of the immune system, such as basophils, eosinophils, monocytes as well as CD4+ and CD8+ T cells. Which functional roles they have in these very diverse immune cell types remains to be elucidated as well as potential functional differences between the different TRPML channels which may act as homomers or heteromers in some of these cells.

AUTHOR CONTRIBUTIONS

All authors wrote and discussed the manuscript. Y-KC and C-CC provided the patch-clamp data in **Figure 1**.

FUNDING

This work was supported, in part, by funding from the German Research Foundation, DFG (project number 239283807, SFB/TRR152 project P04 to CG).

REFERENCES

1. Chen CC, Butz ES, Chao YK, Grishchuk Y, Becker L, Heller S, et al. Small molecules for early endosome-specific patch clamping. *Cell Chem Biol*. (2017) 24:907–16.e904. doi: 10.1016/j.chembiol.2017.05.025

2. Lee JH, McBrayer MK, Wolfe DM, Haslett LJ, Kumar A, Sato Y, et al. Presenilin 1 Maintains lysosomal Ca(2+) homeostasis via TRPML1 by regulating vATPase-mediated lysosome acidification. *Cell Rep*. (2015) 12:1430–44. doi: 10.1016/j.celrep.2015.07.050

3. Dong XP, Cheng X, Mills E, Delling M, Wang F, Kurz T, et al. The type IV mucolipidosis-associated protein TRPML1 is an endolysosomal iron release channel. *Nature*. (2008) 455:992–6. doi: 10.1038/nature07311
4. Chen CC, Keller M, Hess M, Schiffmann R, Urban N, Wolfgardt A, et al. A small molecule restores function to TRPML1 mutant isoforms responsible for mucolipidosis type IV. *Nat Commun*. (2014) 5:4681. doi: 10.1038/ncomms5681
5. Plesch E, Chen CC, Butz E, Scotto Rosato A, Krogsaeter EK, Yinan H, et al. Selective agonist of TRPML2 reveals direct role in chemokine release from innate immune cells. *Elife*. (2018) 7:e39720. doi: 10.7554/eLife.39720
6. Chandra M, Zhou H, Li Q, Muallem S, Hofmann SL, Soyombo AA. A role for the Ca2+ channel TRPML1 in gastric acid secretion, based on analysis of knockout mice. *Gastroenterology*. (2011) 140:857–67. doi: 10.1053/j.gastro.2010.11.040
7. Sahoo N, Gu M, Zhang X, Raval N, Yang J, Bekier M, et al. Gastric acid secretion from parietal cells is mediated by a Ca(2+) efflux channel in the tubulovesicle. *Dev Cell*. (2017) 41:262–273.e266. doi: 10.1016/j.devcel.2017.04.003
8. Coblentz J, St Croix C, Kiselyov K. Loss of TRPML1 promotes production of reactive oxygen species: is oxidative damage a factor in mucolipidosis type IV? *Biochem J*. (2014) 457:361–8. doi: 10.1042/BJ20130647
9. Zhang X, Cheng X, Yu L, Yang J, Calvo R, Patnaik S, et al. MCOLN1 is a ROS sensor in lysosomes that regulates autophagy. *Nat Commun*. (2016) 7:12109. doi: 10.1038/ncomms12109
10. Medina DL, Di Paola S, Peluso I, Armani A, De Stefani D, Venditti R, et al. Lysosomal calcium signalling regulates autophagy through calcineurin and TFEB. *Nat Cell Biol*. (2015) 17:288–99. doi: 10.1038/ncb3114
11. Cheng X, Zhang X, Gao Q, Ali Samie M, Azar M, Tsang WL, et al. The intracellular Ca(2)(+) channel MCOLN1 is required for sarcolemma repair to prevent muscular dystrophy. *Nat Med*. (2014) 20:1187–92. doi: 10.1038/nm.3611
12. Di Palma F, Belyantseva IA, Kim HJ, Vogt TF, Kachar B, Noben-Trauth K. Mutations in Mcoln3 associated with deafness and pigmentation defects in varitint-waddler (Va) mice. *Proc Natl Acad Sci USA*. (2002) 99:14994–9. doi: 10.1073/pnas.222425399
13. Grimm C, Cuajungco MP, van Aken AF, Schnee M, Jors S, Kros CJ, et al. A helix-breaking mutation in TRPML3 leads to constitutive activity underlying deafness in the varitint-waddler mouse. *Proc Natl Acad Sci USA*. (2007) 104:19583–8. doi: 10.1073/pnas.0709846104
14. Xu H, Delling M, Li L, Dong X, Clapham DE. Activating mutation in a mucolipin transient receptor potential channel leads to melanocyte loss in varitint-waddler mice. *Proc Natl Acad Sci USA*. (2007) 104:18321–6. doi: 10.1073/pnas.0709096104
15. Nagata K, Zheng L, Madathany T, Castiglioni AJ, Bartles JR, Garcia-Anoveros J. The varitint-waddler (Va) deafness mutation in TRPML3 generates constitutive, inward rectifying currents and causes cell degeneration. *Proc Natl Acad Sci USA*. (2008) 105:353–8. doi: 10.1073/pnas.0707963105
16. Kim HJ, Li QS Tjon-Kon-Sang, So I, Kiselyov K, Muallem S. Gain-of-function mutation in TRPML3 causes the mouse Varitint-Waddler phenotype. *J Biol Chem*. (2007) 282:36138–42. doi: 10.1074/jbc.C700190200
17. Samie M, Wang X, Zhang X, Goschka A, Li X, Cheng X, et al. A TRP channel in the lysosome regulates large particle phagocytosis via focal exocytosis. *Dev Cell*. (2013) 26:511–24. doi: 10.1016/j.devcel.2013.08.003
18. Bretou M, Saez PJ, Sanseau D, Maurin M, Lankar D, Chabaud M, et al. Lysosome signaling controls the migration of dendritic cells. *Sci Immunol*. (2017) 2:eaak9573. doi: 10.1126/sciimmunol.aak9573
19. Goodridge JP, Jacobs B, Saetersmoen ML, Clement D, Hammer Q, Clancy T, et al. Remodeling of secretory lysosomes during education tunes functional potential in NK cells. *Nat Commun*. (2019) 10:514. doi: 10.1038/s41467-019-08384-x
20. Sun L, Hua Y, Vergarajauregui S, Diab HI, Puertollano R. Novel Role of TRPML2 in the Regulation of the Innate Immune Response. *J Immunol*. (2015) 195:4922–32. doi: 10.4049/jimmunol.1500163
21. Dayam RM, Saric A, Shilliday RE, Botelho RJ. The phosphoinositide-gated lysosomal Ca(2+) channel, TRPML1, is required for phagosome maturation. *Traffic*. (2015) 16:1010–26. doi: 10.1111/tra.12303
22. Kim GH, Dayam RM, Prashar A, Terebiznik M, Botelho RJ. PIKfyve inhibition interferes with phagosome and endosome maturation in macrophages. *Traffic*. (2014) 15:1143–63. doi: 10.1111/tra.12199
23. Vergne I, Chua J, Deretic V. Tuberculosis toxin blocking phagosome maturation inhibits a novel Ca2+/calmodulin-PI3K hVPS34 cascade. *J Exp Med*. (2003) 198:653–9. doi: 10.1084/jem.20030527
24. Gray MA, Choy CH, Dayam RM, Ospina-Escobar E, Somerville A, Xiao X, et al. Phagocytosis enhances lysosomal and bactericidal properties by activating the transcription factor TFEB. *Curr Biol*. (2016) 26:1955–64. doi: 10.1016/j.cub.2016.05.070
25. Bewley MA, Marriott HM, Tulone C, Francis SE, Mitchell TJ, Read RC, et al. A cardinal role for cathepsin d in co-ordinating the host-mediated apoptosis of macrophages and killing of pneumococci. *PLoS Pathog*. (2011) 7:e1001262. doi: 10.1371/journal.ppat.1001262
26. Tsukuba T, Yamamoto S, Yanagawa M, Okamoto K, Okamoto Y, Nakayama KI, et al. Cathepsin E-deficient mice show increased susceptibility to bacterial infection associated with the decreased expression of multiple cell surface Toll-like receptors. *J Biochem*. (2006) 140:57–66. doi: 10.1093/jb/mvj132
27. Qi X, Man SM, Malireddi RK, Karki R, Lupfer C, Gurung P, et al. Cathepsin B modulates lysosomal biogenesis and host defense against Francisella novicida infection. *J Exp Med*. (2016) 213:2081–97. doi: 10.1084/jem.20151938
28. Kiselyov K, Chen J, Rbaibi Y, Oberdick DS, Tjon-Kon-Sang, Shcheynikov N, et al. TRP-ML1 is a lysosomal monovalent cation channel that undergoes proteolytic cleavage. *J Biol Chem*. (2005) 280:43218–23. doi: 10.1074/jbc.M508210200
29. Settembre C, Fraldi A, Medina DL, Ballabio A. Signals from the lysosome: a control centre for cellular clearance and energy metabolism. *Nat Rev Mol Cell Biol*. (2013) 14:283–96. doi: 10.1038/nrm3565
30. Kim HJ, Soyombo AAS, Tjon-Kon-Sang, So I, Muallem S. The Ca(2+) channel TRPML3 regulates membrane trafficking and autophagy. *Traffic*. (2009) 10:1157–67. doi: 10.1111/j.1600-0854.2009.00924.x
31. Kim SW, Kim DH, Park KS, Kim MK, Park YM, Muallem S, et al. Palmitoylation controls trafficking of the intracellular Ca2+ channel MCOLN3/TRPML3 to regulate autophagy. *Autophagy*. (2019) 15:327–40. doi: 10.1080/15548627.2018.1518671
32. Scotto Rosato A, Montefusco S, Soldati C, Di Paola S, Capuozzo A, Monfregola J, et al. TRPML1 links lysosomal calcium to autophagosome biogenesis through the activation of the CaMKKβ/VPS34 pathway. *Nat Commun*. (2019) 10:5630. doi: 10.1038/s41467-019-13572-w
33. Wong CO, Gregory S, Hu H, Chao Y, Sepúlveda VE, He Y, et al. Lysosomal degradation is required for sustained phagocytosis of bacteria by macrophages. *Cell Host Microbe*. (2017) 21:719–30.e6. doi: 10.1016/j.chom.2017.05.002
34. Gordon S, Taylor PR. Monocyte and macrophage heterogeneity. *Nat Rev Immunol*. (2005) 5:953–64. doi: 10.1038/nri1733
35. Aras S, Zaidi MR. TAMeless traitors: macrophages in cancer progression and metastasis. *Br J Cancer*. (2017) 117:1583–91. doi: 10.1038/bjc.2017.356
36. Manderson AP, Kay JG, Hammond LA, Brown DL, Stow JL. Subcompartments of the macrophage recycling endosome direct the differential secretion of IL-6 and TNFalpha. *J Cell Biol*. (2007) 178:57–69. doi: 10.1083/jcb.200612131
37. Lelouvier B, Puertollano R. Mucolipin-3 regulates luminal calcium, acidification, and membrane fusion in the endosomal pathway. *J Biol Chem*. (2011) 286:9826–32. doi: 10.1074/jbc.M110.169185
38. Venkatachalam K, Wong CO, Zhu MX. The role of TRPMLs in endolysosomal trafficking and function. *Cell Calcium*. (2015) 58:48–56. doi: 10.1016/j.ceca.2014.10.008
39. Ajuebor MN, Flower RJ, Hannon R, Christie M, Bowers K, Verity A, et al. Endogenous monocyte chemoattractant protein-1 recruits monocytes in the zymosan peritonitis model. *J Leukoc Biol*. (1998) 63:108–16. doi: 10.1002/jlb.63.1.108
40. Mayadas TN, Cullere X, Lowell CA. The multifaceted functions of neutrophils. *Annu Rev Pathol*. (2014) 9:181–218. doi: 10.1146/annurev-pathol-020712-164023
41. Nauseef WM, Borregaard N. Neutrophils at work. *Nat Immunol*. (2014) 15:602–11. doi: 10.1038/ni.2921
42. Lee WL, Harrison RE, Grinstein S. Phagocytosis by neutrophils. *Microbes Infect*. (2003) 5:1299–306. doi: 10.1016/j.micinf.2003.09.014

43. Dayam RM, Sun CX, Choy CH, Mancuso G, Glogauer M, Botelho RJ. The lipid kinase PIKfyve coordinates the neutrophil immune response through the activation of the rac GTPase. *J Immunol.* (2017) 199:2096–105. doi: 10.4049/jimmunol.1601466
44. Banchereau J, Steinman RM. Dendritic cells and the control of immunity. *Nature.* (1998) 392:245–52. doi: 10.1038/32588
45. Lipscomb MF, Masten BJ. Dendritic cells: immune regulators in health and disease. *Physiol Rev.* (2002) 82:97–130. doi: 10.1152/physrev.00023.2001
46. Sallusto F, Cella M, Danieli C, Lanzavecchia A. Dendritic cells use macropinocytosis and the mannose receptor to concentrate macromolecules in the major histocompatibility complex class II compartment: downregulation by cytokines and bacterial products. *J Exp Med.* (1995) 182:389–400. doi: 10.1084/jem.182.2.389
47. Martin-Fontecha A, Sebastiani S, Hopken UE, Uguccioni M, Lipp M, Lanzavecchia A, et al. Regulation of dendritic cell migration to the draining lymph node: impact on T lymphocyte traffic and priming. *J Exp Med.* (2003) 198:615–21. doi: 10.1084/jem.20030448
48. Mellman I. Dendritic cells: master regulators of the immune response. *Cancer Immunol Res.* (2013) 1:145–9. doi: 10.1158/2326-6066.CIR-13-0102
49. Beutler B, Jiang Z, Georgel P, Crozat K, Croker B, Rutschmann S, et al. Genetic analysis of host resistance: Toll-like receptor signaling and immunity at large. *Annu Rev Immunol.* (2006) 24:353–89. doi: 10.1146/annurev.immunol.24.021605.090552
50. Kaisho T, Akira S. Toll-like receptor function and signaling. *J Allergy Clin Immunol.* (2006) 117:979–87; quiz 988. doi: 10.1016/j.jaci.2006.02.023
51. Kawai T, Akira S. The role of pattern-recognition receptors in innate immunity: update on Toll-like receptors. *Nat Immunol.* (2010) 11:373–84. doi: 10.1038/ni.1863
52. Li X, Saitoh S, Shibata T, Tanimura N, Fukui R, Miyake K. Mucolipin 1 positively regulates TLR7 responses in dendritic cells by facilitating RNA transportation to lysosomes. *Int Immunol.* (2015) 27:83–94. doi: 10.1093/intimm/dxu086
53. Smyth MJ, Hayakawa Y, Takeda K, Yagita H. New aspects of natural-killer-cell surveillance and therapy of cancer. *Nat Rev Cancer.* (2002) 2:850–61. doi: 10.1038/nrc928
54. Lee SH, Miyagi T, Biron CA. Keeping NK cells in highly regulated antiviral warfare. *Trends Immunol.* (2007) 28:252–9. doi: 10.1016/j.it.2007.04.001
55. Orange JS. Formation and function of the lytic NK-cell immunological synapse. *Nat Rev Immunol.* (2008) 8:713–25. doi: 10.1038/nri2381
56. Galandrini R, Capuano C, Santoni, A. Activation of lymphocyte cytolytic machinery: where are we? *Front Immunol.* (2013) 4:390. doi: 10.3389/fimmu.2013.00390
57. Vivier E, Raulet DH, Moretta A, Caligiuri MA, Zitvogel L, Lanier LL, et al. Innate or adaptive immunity? The example of natural killer cells. *Science.* (2011) 331:44–9. doi: 10.1126/science.1198687
58. Vivier E, Nunes JA, Vely F. Natural killer cell signaling pathways. *Science.* (2004) 306:1517–9. doi: 10.1126/science.1103478
59. Lanier LL. Up on the tightrope: natural killer cell activation and inhibition. *Nat Immunol.* (2008) 9:495–502. doi: 10.1038/ni1581
60. Raulet DH, Vance RE, McMahon CW. Regulation of the natural killer cell receptor repertoire. *Annu Rev Immunol.* (2001) 19:291–330. doi: 10.1146/annurev.immunol.19.1.291
61. Parham P. MHC class I molecules and KIRs in human history, health and survival. *Nat Rev Immunol.* (2005) 5:201–14. doi: 10.1038/nri1570
62. Raulet DH, Guerra N. Oncogenic stress sensed by the immune system: role of natural killer cell receptors. *Nat Rev Immunol.* (2009) 9:568–80. doi: 10.1038/nri2604
63. Anfossi N, Andre P, Guia S, Falk CS, Roetynck S, Stewart CA, et al. Human NK cell education by inhibitory receptors for MHC class I. *Immunity.* (2006) 25:331–42. doi: 10.1016/j.immuni.2006.06.013
64. Pleiman CM, D'Ambrosio D, Cambier JC. The B-cell antigen receptor complex: structure and signal transduction. *Immunol Today.* (1994) 15:393–9. doi: 10.1016/0167-5699(94)90267-4
65. Ollila J, Vihinen M. B cells. *Int J Biochem Cell Biol.* (2005) 37:518–23. doi: 10.1016/j.biocel.2004.09.007
66. Song Y, Dayalu R, Matthews SA, Scharenberg AM. TRPML cation channels regulate the specialized lysosomal compartment of vertebrate B-lymphocytes. *Eur J Cell Biol.* (2006) 85:1253–64. doi: 10.1016/j.ejcb.2006.08.004
67. Clague MJ, Urbe S. Multivesicular bodies. *Curr Biol.* (2008) 18:R402–4. doi: 10.1016/j.cub.2008.02.068
68. Avalos AM, Ploegh HL. Early BCR events and antigen capture, processing, and loading on MHC class II on B Cells. *Front Immunol.* (2014) 5:92. doi: 10.3389/fimmu.2014.00092
69. Lindvall JM, Blomberg KE, Wennborg A, Smith CI. Differential expression and molecular characterisation of Lmo7, Myo1e, Sash1, and Mcoln2 genes in Btk-defective B-cells. *Cell Immunol.* (2005) 235:46–55. doi: 10.1016/j.cellimm.2005.07.001
70. Mohamed AJ, Yu L, Backesjo CM, Vargas L, Faryal R, Aints A, et al. Bruton's tyrosine kinase *(Btk):* function, regulation, and transformation with special emphasis on the PH domain. *Immunol Rev.* (2009) 228:58–73. doi: 10.1111/j.1600-065X.2008.00741.x
71. Schmiedel BJ, Singh D, Madrigal A, Valdovino-Gonzalez AG, White BM, Zapardiel-Gonzalo J, et al. Impact of genetic polymorphisms on human immune cell gene expression. *Cell.* (2018) 175:1701–15.e1716. doi: 10.1016/j.cell.2018.10.022
72. Monaco G, Lee B, Xu W, Mustafah S, Hwang YY, Carre C, et al. RNA-Seq signatures normalized by mRNA abundance allow absolute deconvolution of human immune cell types. *Cell Rep.* (2019) 26:1627–40.e1627. doi: 10.1016/j.celrep.2019.01.041

Conflict of Interest: The authors declare that the research was conducted in the absence of any commercial or financial relationships that could be construed as a potential conflict of interest.

Bibliography

1. Neefjes J, Jongsma MML, Berlin I. Stop or Go? Endosome Positioning in the Establishment of Compartment Architecture, Dynamics, and Function. Trends Cell Biol. 2017;27(8):580-94.
2. Takenouchi T, Sekiyama K, Tsukimoto M, Iwamaru Y, Fujita M, Sugama S, et al. Chapter 14 - Role of Autophagy in P2X7 Receptor-Mediated Maturation and Unconventional Secretion of IL-1β in Microglia. In: Hayat MA, editor. Autophagy: Cancer, Other Pathologies, Inflammation, Immunity, Infection, and Aging. Amsterdam: Academic Press; 2015. p. 211-22.
3. Chen C-C, Krogsaeter E, Grimm C. Two-pore and TRP cation channels in endolysosomal osmo-/mechanosensation and volume regulation. Biochimica et Biophysica Acta (BBA) - Molecular Cell Research. 2021;1868(2):118921.
4. Grimm C, Bartel K, Vollmar AM, Biel M. Endolysosomal Cation Channels and Cancer-A Link with Great Potential. Pharmaceuticals (Basel). 2018;11(1).
5. Bach G, Zeevi DA, Frumkin A, Kogot-Levin A. Mucolipidosis type IV and the mucolipins. Biochem Soc Trans. 2010;38(6):1432-5.
6. Bargal R, Avidan N, Ben-Asher E, Olender Z, Zeigler M, Frumkin A, et al. Identification of the gene causing mucolipidosis type IV. Nat Genet. 2000;26(1):118-23.
7. Rosato AS, Tang R, Grimm C. Two-pore and TRPML cation channels: Regulators of phagocytosis, autophagy and lysosomal exocytosis. Pharmacol Ther. 2021;220:107713.
8. Scotto Rosato A, Krogsaeter EK, Jaślan D, Abrahamian C, Montefusco S, Soldati C, et al. TPC2 rescues lysosomal storage in mucolipidosis type IV, Niemann-Pick type C1, and Batten disease. EMBO Mol Med. 2022;14(9):e15377.
9. Xu M, Almasi S, Yang Y, Yan C, Sterea AM, Rizvi Syeda AK, et al. The lysosomal TRPML1 channel regulates triple negative breast cancer development by promoting mTORC1 and purinergic signaling pathways. Cell Calcium. 2019;79:80-8.
10. Ensenyat-Mendez M, Llinàs-Arias P, Orozco JIJ, Íñiguez-Muñoz S, Salomon MP, Sesé B, et al. Current Triple-Negative Breast Cancer Subtypes: Dissecting the Most Aggressive Form of Breast Cancer. Front Oncol. 2021;11:681476.
11. Rühl P, Rosato AS, Urban N, Gerndt S, Tang R, Abrahamian C, et al. Estradiol analogs attenuate autophagy, cell migration and invasion by direct and selective inhibition of TRPML1, independent of estrogen receptors. Sci Rep. 2021;11(1):8313.
12. Gerndt S, Chen CC, Chao YK, Yuan Y, Burgstaller S, Scotto Rosato A, et al. Agonist-mediated switching of ion selectivity in TPC2 differentially promotes lysosomal function. Elife. 2020;9.
13. Yuan Y, Jaślan D, Rahman T, Bolsover SR, Arige V, Wagner LE, 2nd, et al. Segregated cation flux by TPC2 biases Ca(2+) signaling through lysosomes. Nat Commun. 2022;13(1):4481.
14. Heistein JB, Acharya U, Mukkamalla SKR. Malignant Melanoma. StatPearls. Treasure Island (FL): StatPearls Publishing

Copyright © 2023, StatPearls Publishing LLC.; 2023.
15. Bellono NW, Oancea EV. Ion transport in pigmentation. Arch Biochem Biophys. 2014;563:35-41.
16. Chao YK, Schludi V, Chen CC, Butz E, Nguyen ONP, Muller M, et al. TPC2 polymorphisms associated with a hair pigmentation phenotype in humans result in gain of channel function by independent mechanisms. Proc Natl Acad Sci U S A. 2017;114(41):E8595-e602.
17. Netcharoensirisuk P, Abrahamian C, Tang R, Chen CC, Rosato AS, Beyers W, et al. Flavonoids increase melanin production and reduce proliferation, migration and invasion of melanoma cells by blocking endolysosomal/melanosomal TPC2. Sci Rep. 2021;11(1):8515.
18. Lin-Moshier Y, Keebler MV, Hooper R, Boulware MJ, Liu X, Churamani D, et al. The Two-pore channel (TPC) interactome unmasks isoform-specific roles for TPCs in endolysosomal morphology and cell pigmentation. Proc Natl Acad Sci U S A. 2014;111(36):13087-92.

19. Guerra F, Bucci C. Multiple Roles of the Small GTPase Rab7. Cells. 2016;5(3).
20. Ploper D, Taelman VF, Robert L, Perez BS, Titz B, Chen HW, et al. MITF drives endolysosomal biogenesis and potentiates Wnt signaling in melanoma cells. Proc Natl Acad Sci U S A. 2015;112(5):E420-9.
21. Scotto Rosato A, Krogsaeter EK, Jaślan D, Abrahamian C, Montefusco S, Soldati C, et al. TPC2 rescues lysosomal storage in mucolipidosis type IV, Niemann-Pick type C1, and Batten disease. EMBO Mol Med. 2022:e15377.
22. Li RJ, Xu J, Fu C, Zhang J, Zheng YG, Jia H, et al. Regulation of mTORC1 by lysosomal calcium and calmodulin. Elife. 2016;5.
23. Chao YK, Schludi V, Chen CC, Butz E, Nguyen ONP, Müller M, et al. TPC2 polymorphisms associated with a hair pigmentation phenotype in humans result in gain of channel function by independent mechanisms. Proc Natl Acad Sci U S A. 2017;114(41):E8595-e602.
24. Winckler B, Faundez V, Maday S, Cai Q, Guimas Almeida C, Zhang H. The Endolysosomal System and Proteostasis: From Development to Degeneration. J Neurosci. 2018;38(44):9364-74.
25. Hu Y-B, Dammer EB, Ren R-J, Wang G. The endosomal-lysosomal system: from acidification and cargo sorting to neurodegeneration. Translational Neurodegeneration. 2015;4(1):18.
26. Scott CC, Vacca F, Gruenberg J. Endosome maturation, transport and functions. Semin Cell Dev Biol. 2014;31:2-10.
27. Dammai V. Endosomal Compartments. In: Schwab M, editor. Encyclopedia of Cancer. Berlin, Heidelberg: Springer Berlin Heidelberg; 2011. p. 1244-8.
28. Cullen PJ, Steinberg F. To degrade or not to degrade: mechanisms and significance of endocytic recycling. Nature Reviews Molecular Cell Biology. 2018;19(11):679-96.
29. Homma Y, Hiragi S, Fukuda M. Rab family of small GTPases: an updated view on their regulation and functions. Febs j. 2021;288(1):36-55.
30. Jovic M, Sharma M, Rahajeng J, Caplan S. The early endosome: a busy sorting station for proteins at the crossroads. Histol Histopathol. 2010;25(1):99-112.
31. O'Sullivan MJ, Lindsay AJ. The Endosomal Recycling Pathway-At the Crossroads of the Cell. Int J Mol Sci. 2020;21(17).
32. Li X, DiFiglia M. The recycling endosome and its role in neurological disorders. Prog Neurobiol. 2012;97(2):127-41.
33. Ma L, Ouyang Q, Werthmann GC, Thompson HM, Morrow EM. Live-cell Microscopy and Fluorescence-based Measurement of Luminal pH in Intracellular Organelles. Front Cell Dev Biol. 2017;5:71.
34. Goldenring JR. Recycling endosomes. Curr Opin Cell Biol. 2015;35:117-22.
35. Rozés-Salvador V, González-Billault C, Conde C. The Recycling Endosome in Nerve Cell Development: One Rab to Rule Them All? Front Cell Dev Biol. 2020;8:603794.
36. Li H, Li HF, Felder RA, Periasamy A, Jose PA. Rab4 and Rab11 coordinately regulate the recycling of angiotensin II type I receptor as demonstrated by fluorescence resonance energy transfer microscopy. J Biomed Opt. 2008;13(3):031206.
37. Bastin G, Heximer SP. Rab family proteins regulate the endosomal trafficking and function of RGS4. J Biol Chem. 2013;288(30):21836-49.
38. Huotari J, Helenius A. Endosome maturation. Embo j. 2011;30(17):3481-500.
39. Piper RC, Luzio JP. Late endosomes: sorting and partitioning in multivesicular bodies. Traffic. 2001;2(9):612-21.
40. Bright NA, Davis LJ, Luzio JP. Endolysosomes Are the Principal Intracellular Sites of Acid Hydrolase Activity. Curr Biol. 2016;26(17):2233-45.
41. Harata NC, Aravanis AM, Tsien RW. Kiss-and-run and full-collapse fusion as modes of exo-endocytosis in neurosecretion. J Neurochem. 2006;97(6):1546-70.
42. Johannes L, Popoff V. Tracing the retrograde route in protein trafficking. Cell. 2008;135(7):1175-87.
43. Lu L, Hong W. From endosomes to the trans-Golgi network. Semin Cell Dev Biol. 2014;31:30-9.

44. Forgac M. Vacuolar ATPases: rotary proton pumps in physiology and pathophysiology. Nature Reviews Molecular Cell Biology. 2007;8(11):917-29.
45. Xu H, Ren D. Lysosomal physiology. Annu Rev Physiol. 2015;77:57-80.
46. Young R, Francis S. Chapter 23 - Form and Function of the Animal Cell. In: Badal S, Delgoda R, editors. Pharmacognosy. Boston: Academic Press; 2017. p. 459-75.
47. De Duve C, Pressman BC, Gianetto R, Wattiaux R, Appelmans F. Tissue fractionation studies. 6. Intracellular distribution patterns of enzymes in rat-liver tissue. Biochem J. 1955;60(4):604-17.
48. Opperdoes F. A Feeling for the Cell: Christian de Duve (1917–2013): PLoS Biol. 2013 Oct 1;11(10):e1001671. doi: 10.1371/journal.pbio.1001671. eCollection 2013 Oct.
49. Jeger JL. Endosomes, lysosomes, and the role of endosomal and lysosomal biogenesis in cancer development. Mol Biol Rep. 2020;47(12):9801-10.
50. Barral DC, Staiano L, Guimas Almeida C, Cutler DF, Eden ER, Futter CE, et al. Current methods to analyze lysosome morphology, positioning, motility and function. Traffic. 2022;23(5):238-69.
51. Saftig P. Physiology of the lysosome. In: Mehta A, Beck M, Sunder-Plassmann G, editors. Fabry Disease: Perspectives from 5 Years of FOS. Oxford: Oxford PharmaGenesis

Copyright © 2006, Oxford PharmaGenesis™. 2006.
52. de Araujo MEG, Liebscher G, Hess MW, Huber LA. Lysosomal size matters. Traffic. 2020;21(1):60-75.
53. Hess MW, Huber LA. Chapter 5 - Measuring lysosomal size and frequency by electron microscopy. In: Kepp O, Galluzzi L, editors. Methods in Cell Biology. 164: Academic Press; 2021. p. 47-61.
54. Saftig P, Klumperman J. Lysosome biogenesis and lysosomal membrane proteins: trafficking meets function. Nat Rev Mol Cell Biol. 2009;10(9):623-35.
55. Lübke T, Lobel P, Sleat DE. Proteomics of the lysosome. Biochim Biophys Acta. 2009;1793(4):625-35.
56. Keohane EM. 3 - Cellular structure and function. In: Keohane EM, Otto CN, Walenga JM, editors. Rodak's Hematology (Sixth Edition). St. Louis (MO): Elsevier; 2020. p. 31-42.
57. Settembre C, Fraldi A, Medina DL, Ballabio A. Signals from the lysosome: a control centre for cellular clearance and energy metabolism. Nat Rev Mol Cell Biol. 2013;14(5):283-96.
58. Ballabio A. The awesome lysosome. EMBO Mol Med. 2016;8(2):73-6.
59. Trybus W, Trybus E, Król T. Lysosomes as a Target of Anticancer Therapy. Int J Mol Sci. 2023;24(3).
60. Spix B, Chao YK, Abrahamian C, Chen CC, Grimm C. TRPML Cation Channels in Inflammation and Immunity. Front Immunol. 2020;11:225.
61. Parenti G, Andria G, Ballabio A. Lysosomal storage diseases: from pathophysiology to therapy. Annu Rev Med. 2015;66:471-86.
62. Parenti G, Medina DL, Ballabio A. The rapidly evolving view of lysosomal storage diseases. EMBO Mol Med. 2021;13(2):e12836.
63. Udayar V, Chen Y, Sidransky E, Jagasia R. Lysosomal dysfunction in neurodegeneration: emerging concepts and methods. Trends Neurosci. 2022;45(3):184-99.
64. Almeida MF, Bahr BA, Kinsey ST. Endosomal-lysosomal dysfunction in metabolic diseases and Alzheimer's disease. Int Rev Neurobiol. 2020;154:303-24.
65. Spix B, Butz ES, Chen C-C, Rosato AS, Tang R, Jeridi A, et al. Lung emphysema and impaired macrophage elastase clearance in mucolipin 3 deficient mice. Nature Communications. 2022;13(1):318.
66. Bonam SR, Wang F, Muller S. Lysosomes as a therapeutic target. Nat Rev Drug Discov. 2019;18(12):923-48.
67. Gros F, Muller S. The role of lysosomes in metabolic and autoimmune diseases. Nat Rev Nephrol. 2023.

68. Nguyen ON, Grimm C, Schneider LS, Chao YK, Atzberger C, Bartel K, et al. Two-Pore Channel Function Is Crucial for the Migration of Invasive Cancer Cells. Cancer Res. 2017;77(6):1427-38.
69. Müller M, Gerndt S, Chao YK, Zisis T, Nguyen ONP, Gerwien A, et al. Gene editing and synthetically accessible inhibitors reveal role for TPC2 in HCC cell proliferation and tumor growth. Cell Chem Biol. 2021;28(8):1119-31.e27.
70. Geisslinger F, Müller M, Chao YK, Grimm C, Vollmar AM, Bartel K. Targeting TPC2 sensitizes acute lymphoblastic leukemia cells to chemotherapeutics by impairing lysosomal function. Cell Death Dis. 2022;13(8):668.
71. Sterea AM, Almasi S, El Hiani Y. The hidden potential of lysosomal ion channels: A new era of oncogenes. Cell Calcium. 2018;72:91-103.
72. Mindell JA. Lysosomal acidification mechanisms. Annu Rev Physiol. 2012;74:69-86.
73. Xiong J, Zhu MX. Regulation of lysosomal ion homeostasis by channels and transporters. Sci China Life Sci. 2016;59(8):777-91.
74. Murrell-Lagnado RD. A role for P2X(4) receptors in lysosome function. J Gen Physiol. 2018;150(2):185-7.
75. Tedeschi V, Petrozziello T, Secondo A. Calcium Dyshomeostasis and Lysosomal Ca(2+) Dysfunction in Amyotrophic Lateral Sclerosis. Cells. 2019;8(10).
76. Nilius B, Owsianik G. The transient receptor potential family of ion channels. Genome Biol. 2011;12(3):218.
77. Latorre R, Díaz-Franulic I. Profile of David Julius and Ardem Patapoutian: 2021 Nobel Laureates in Physiology or Medicine. Proc Natl Acad Sci U S A. 2022;119(1).
78. Puertollano R, Kiselyov K. TRPMLs: in sickness and in health. Am J Physiol Renal Physiol. 2009;296(6):F1245-54.
79. Schmiege P, Fine M, Li X. The regulatory mechanism of mammalian TRPMLs revealed by cryo-EM. Febs j. 2018;285(14):2579-85.
80. Grimm C, Hassan S, Wahl-Schott C, Biel M. Role of TRPML and two-pore channels in endolysosomal cation homeostasis. J Pharmacol Exp Ther. 2012;342(2):236-44.
81. Di Paola S, Scotto-Rosato A, Medina DL. TRPML1: The Ca(2+)retaker of the lysosome. Cell Calcium. 2018;69:112-21.
82. Venkatachalam K, Hofmann T, Montell C. Lysosomal localization of TRPML3 depends on TRPML2 and the mucolipidosis-associated protein TRPML1. J Biol Chem. 2006;281(25):17517-27.
83. Dong XP, Shen D, Wang X, Dawson T, Li X, Zhang Q, et al. PI(3,5)P(2) controls membrane trafficking by direct activation of mucolipin Ca(2+) release channels in the endolysosome. Nat Commun. 2010;1(4):38.
84. Cheng X, Shen D, Samie M, Xu H. Mucolipins: Intracellular TRPML1-3 channels. FEBS Lett. 2010;584(10):2013-21.
85. Thakore P, Pritchard HAT, Griffin CS, Yamasaki E, Drumm BT, Lane C, et al. TRPML1 channels initiate Ca(2+) sparks in vascular smooth muscle cells. Sci Signal. 2020;13(637).
86. Li M, Zhang WK, Benvin NM, Zhou X, Su D, Li H, et al. Structural basis of dual Ca2+/pH regulation of the endolysosomal TRPML1 channel. Nature Structural & Molecular Biology. 2017;24(3):205-13.
87. Zhang X, Cheng X, Yu L, Yang J, Calvo R, Patnaik S, et al. MCOLN1 is a ROS sensor in lysosomes that regulates autophagy. Nat Commun. 2016;7:12109.
88. Schmiege P, Fine M, Blobel G, Li X. Human TRPML1 channel structures in open and closed conformations. Nature. 2017;550(7676):366-70.
89. Siow WX, Kabiri Y, Tang R, Chao YK, Plesch E, Eberhagen C, et al. Lysosomal TRPML1 regulates mitochondrial function in hepatocellular carcinoma cells. J Cell Sci. 2022;135(6).
90. Chen CC, Keller M, Hess M, Schiffmann R, Urban N, Wolfgardt A, et al. A small molecule restores function to TRPML1 mutant isoforms responsible for mucolipidosis type IV. Nat Commun. 2014;5:4681.

91. Leser C, Keller M, Gerndt S, Urban N, Chen C-C, Schaefer M, et al. Chemical and pharmacological characterization of the TRPML calcium channel blockers ML-SI1 and ML-SI3. European Journal of Medicinal Chemistry. 2021;210:112966.
92. King JS. Autophagy across the eukaryotes: is S. cerevisiae the odd one out? Autophagy. 2012;8(7):1159-62.
93. Settembre C, Di Malta C, Polito VA, Garcia Arencibia M, Vetrini F, Erdin S, et al. TFEB links autophagy to lysosomal biogenesis. Science. 2011;332(6036):1429-33.
94. Chun Y, Kim J. Autophagy: An Essential Degradation Program for Cellular Homeostasis and Life. Cells. 2018;7(12).
95. Kohli L, Roth KA. Autophagy: cerebral home cooking. Am J Pathol. 2010;176(3):1065-71.
96. Yun CW, Lee SH. The Roles of Autophagy in Cancer. Int J Mol Sci. 2018;19(11).
97. Bhutia SK, Mukhopadhyay S, Sinha N, Das DN, Panda PK, Patra SK, et al. Autophagy: cancer's friend or foe? Adv Cancer Res. 2013;118:61-95.
98. Medina DL, Di Paola S, Peluso I, Armani A, De Stefani D, Venditti R, et al. Lysosomal calcium signalling regulates autophagy through calcineurin and TFEB. Nat Cell Biol. 2015;17(3):288-99.
99. Medina DL, Fraldi A, Bouche V, Annunziata F, Mansueto G, Spampanato C, et al. Transcriptional activation of lysosomal exocytosis promotes cellular clearance. Dev Cell. 2011;21(3):421-30.
100. LaPlante JM, Sun M, Falardeau J, Dai D, Brown EM, Slaugenhaupt SA, et al. Lysosomal exocytosis is impaired in mucolipidosis type IV. Mol Genet Metab. 2006;89(4):339-48.
101. Dong XP, Wang X, Shen D, Chen S, Liu M, Wang Y, et al. Activating mutations of the TRPML1 channel revealed by proline-scanning mutagenesis. J Biol Chem. 2009;284(46):32040-52.
102. Patel S, Kilpatrick BS. Two-pore channels and disease. Biochim Biophys Acta Mol Cell Res. 2018;1865(11 Pt B):1678-86.
103. Patel S. Two-pore channels open up. Nature. 2018;556(7699):38-40.
104. Guo J, Zeng W, Jiang Y. Tuning the ion selectivity of two-pore channels. Proc Natl Acad Sci U S A. 2017;114(5):1009-14.
105. Ruas M, Galione A, Parrington J. Two-Pore Channels: Lessons from Mutant Mouse Models. Messenger (Los Angel). 2015;4(1):4-22.
106. Krogsaeter EK, Biel M, Wahl-Schott C, Grimm C. The protein interaction networks of mucolipins and two-pore channels. Biochim Biophys Acta Mol Cell Res. 2019;1866(7):1111-23.
107. Grimm C, Chen CC, Wahl-Schott C, Biel M. Two-Pore Channels: Catalyzers of Endolysosomal Transport and Function. Front Pharmacol. 2017;8:45.
108. Jha A, Ahuja M, Patel S, Brailoiu E, Muallem S. Convergent regulation of the lysosomal two-pore channel-2 by Mg^{2+}, NAADP, $PI(3,5)P_2$ and multiple protein kinases. Embo j. 2014;33(5):501-11.
109. Pafumi I, Festa M, Papacci F, Lagostena L, Giunta C, Gutla V, et al. Naringenin Impairs Two-Pore Channel 2 Activity And Inhibits VEGF-Induced Angiogenesis. Sci Rep. 2017;7(1):5121.
110. Lu Y, Hao BX, Graeff R, Wong CW, Wu WT, Yue J. Two pore channel 2 (TPC2) inhibits autophagosomal-lysosomal fusion by alkalinizing lysosomal pH. J Biol Chem. 2013;288(33):24247-63.
111. Müller M, Gerndt S, Chao YK, Zisis T, Nguyen ONP, Gerwien A, et al. Gene editing and synthetically accessible inhibitors reveal role for TPC2 in HCC cell proliferation and tumor growth. Cell Chem Biol. 2021.
112. Abrahamian C, Grimm C. Endolysosomal Cation Channels and MITF in Melanocytes and Melanoma. Biomolecules. 2021;11(7):1021.
113. Ambrosio AL, Boyle JA, Aradi AE, Christian KA, Di Pietro SM. TPC2 controls pigmentation by regulating melanosome pH and size. Proc Natl Acad Sci U S A. 2016;113(20):5622-7.

114. Yamaguchi Y, Hearing VJ. Melanocytes and their diseases. Cold Spring Harb Perspect Med. 2014;4(5).
115. Sulem P, Gudbjartsson DF, Stacey SN, Helgason A, Rafnar T, Jakobsdottir M, et al. Two newly identified genetic determinants of pigmentation in Europeans. Nat Genet. 2008;40(7):835-7.
116. Böck J, Krogsaeter E, Passon M, Chao YK, Sharma S, Grallert H, et al. Human genome diversity data reveal that L564P is the predominant TPC2 variant and a prerequisite for the blond hair associated M484L gain-of-function effect. PLoS Genet. 2021;17(1):e1009236.
117. Wang Q, Wang Z, Wang Y, Qi Z, Bai D, Wang C, et al. A gain-of-function TPC2 variant R210C increases affinity to PI(3,5)P2 and causes lysosome acidification and hypopigmentation. Nature Communications. 2023;14(1):226.
118. Bellono NW, Escobar IE, Oancea E. A melanosomal two-pore sodium channel regulates pigmentation. Sci Rep. 2016;6:26570.
119. Jaślan D, Ferro IF, Kudrina V, Yuan Y, Patel S, Grimm C. PI(3,5)P(2) and NAADP: Team players or lone warriors? - New insights into TPC activation modes. Cell Calcium. 2023;109:102675.
120. Wang X, Zhang X, Dong XP, Samie M, Li X, Cheng X, et al. TPC proteins are phosphoinositide- activated sodium-selective ion channels in endosomes and lysosomes. Cell. 2012;151(2):372-83.
121. Roggenkamp HG, Khansahib I, Hernandez CL, Zhang Y, Lodygin D, Krüger A, et al. HN1L/JPT2: A signaling protein that connects NAADP generation to Ca(2+) microdomain formation. Sci Signal. 2021;14(675).
122. Gunaratne GS, Brailoiu E, He S, Unterwald EM, Patel S, Slama JT, et al. Essential requirement for JPT2 in NAADP-evoked Ca(2+) signaling. Sci Signal. 2021;14(675).
123. Zhang J, Guan X, Shah K, Yan J. Lsm12 is an NAADP receptor and a two-pore channel regulatory protein required for calcium mobilization from acidic organelles. Nat Commun. 2021;12(1):4739.
124. Krogsaeter E, Tang R, Grimm C. JPT2: The missing link between intracellular Ca(2+) release channels and NAADP? Cell Calcium. 2021;97:102405.
125. Parmar N, Tamanoi F. Chapter 3 - Rheb G-Proteins and the Activation of mTORC1. The Enzymes. 27: Academic Press; 2010. p. 39-56.
126. Chenette EJ, Der CJ. 5 - Lipid Modification of Ras Superfamily GTPases: Not Just Membrane Glue. In: Tamanoi F, Hrycyna CA, Bergo MO, editors. The Enzymes. 29: Academic Press; 2011. p. 59-95.
127. Pereira-Leal JB, Seabra MC. Evolution of the rab family of small GTP-binding proteins11Edited by J. Thornton. Journal of Molecular Biology. 2001;313(4):889-901.
128. Grosshans BL, Ortiz D, Novick P. Rabs and their effectors: Achieving specificity in membrane traffic. Proceedings of the National Academy of Sciences. 2006;103(32):11821-7.
129. Ohbayashi N, Fukuda M. Role of Rab family GTPases and their effectors in melanosomal logistics. J Biochem. 2012;151(4):343-51.
130. Diekmann Y, Seixas E, Gouw M, Tavares-Cadete F, Seabra MC, Pereira-Leal JB. Thousands of rab GTPases for the cell biologist. PLoS Comput Biol. 2011;7(10):e1002217.
131. Progida C, Cogli L, Piro F, De Luca A, Bakke O, Bucci C. Rab7b controls trafficking from endosomes to the TGN. J Cell Sci. 2010;123(Pt 9):1480-91.
132. Stenmark H. Rab GTPases as coordinators of vesicle traffic. Nature Reviews Molecular Cell Biology. 2009;10(8):513-25.
133. Zhang B, Zhang Y, Shacter E, Zheng Y. Mechanism of the guanine nucleotide exchange reaction of Ras GTPase--evidence for a GTP/GDP displacement model. Biochemistry. 2005;44(7):2566-76.
134. Peurois F, Peyroche G, Cherfils J. Small GTPase peripheral binding to membranes: molecular determinants and supramolecular organization. Biochem Soc Trans. 2019;47(1):13-22.
135. Vanlandingham PA, Ceresa BP. Rab7 regulates late endocytic trafficking downstream of multivesicular body biogenesis and cargo sequestration. J Biol Chem. 2009;284(18):12110-24.

136. Rivera-Molina FE, Novick PJ. A Rab GAP cascade defines the boundary between two Rab GTPases on the secretory pathway. Proc Natl Acad Sci U S A. 2009;106(34):14408-13.
137. Markgraf DF, Peplowska K, Ungermann C. Rab cascades and tethering factors in the endomembrane system. FEBS Letters. 2007;581(11):2125-30.
138. Borchers AC, Langemeyer L, Ungermann C. Who's in control? Principles of Rab GTPase activation in endolysosomal membrane trafficking and beyond. J Cell Biol. 2021;220(9).
139. Ortiz D, Medkova M, Walch-Solimena C, Novick P. Ypt32 recruits the Sec4p guanine nucleotide exchange factor, Sec2p, to secretory vesicles; evidence for a Rab cascade in yeast. J Cell Biol. 2002;157(6):1005-15.
140. Mottola G. The complexity of Rab5 to Rab7 transition guarantees specificity of pathogen subversion mechanisms. Front Cell Infect Microbiol. 2014;4:180.
141. Rink J, Ghigo E, Kalaidzidis Y, Zerial M. Rab Conversion as a Mechanism of Progression from Early to Late Endosomes. Cell. 2005;122(5):735-49.
142. Poteryaev D, Datta S, Ackema K, Zerial M, Spang A. Identification of the switch in early-to-late endosome transition. Cell. 2010;141(3):497-508.
143. Langemeyer L, Borchers A-C, Herrmann E, Füllbrunn N, Han Y, Perz A, et al. A conserved and regulated mechanism drives endosomal Rab transition. eLife. 2020;9:e56090.
144. Stroupe C. This Is the End: Regulation of Rab7 Nucleotide Binding in Endolysosomal Trafficking and Autophagy. Front Cell Dev Biol. 2018;6:129.
145. Hyttinen JMT, Niittykoski M, Salminen A, Kaarniranta K. Maturation of autophagosomes and endosomes: A key role for Rab7. Biochimica et Biophysica Acta (BBA) - Molecular Cell Research. 2013;1833(3):503-10.
146. Bucci C, Thomsen P, Nicoziani P, McCarthy J, van Deurs B. Rab7: a key to lysosome biogenesis. Mol Biol Cell. 2000;11(2):467-80.
147. Yap CC, Digilio L, McMahon LP, Wang T, Winckler B. Dynein Is Required for Rab7-Dependent Endosome Maturation, Retrograde Dendritic Transport, and Degradation. J Neurosci. 2022;42(22):4415-34.
148. Jordens I, Fernandez-Borja M, Marsman M, Dusseljee S, Janssen L, Calafat J, et al. The Rab7 effector protein RILP controls lysosomal transport by inducing the recruitment of dynein-dynactin motors. Curr Biol. 2001;11(21):1680-5.
149. Umehara K, Nemoto K, Matsushita A, Terada E, Monthakantirat O, De-Eknamkul W, et al. Flavonoids from the heartwood of the Thai medicinal plant Dalbergia parviflora and their effects on estrogenic-responsive human breast cancer cells. J Nat Prod. 2009;72(12):2163-8.
150. Frasa MA, Maximiano FC, Smolarczyk K, Francis RE, Betson ME, Lozano E, et al. Armus is a Rac1 effector that inactivates Rab7 and regulates E-cadherin degradation. Curr Biol. 2010;20(3):198-208.
151. Carroll B, Mohd-Naim N, Maximiano F, Frasa MA, McCormack J, Finelli M, et al. The TBC/RabGAP Armus coordinates Rac1 and Rab7 functions during autophagy. Dev Cell. 2013;25(1):15-28.
152. Pankiv S, Alemu EA, Brech A, Bruun JA, Lamark T, Overvatn A, et al. FYCO1 is a Rab7 effector that binds to LC3 and PI3P to mediate microtubule plus end-directed vesicle transport. J Cell Biol. 2010;188(2):253-69.
153. Pereira-Leal JB, Seabra MC. The mammalian Rab family of small GTPases: definition of family and subfamily sequence motifs suggests a mechanism for functional specificity in the Ras superfamily. J Mol Biol. 2000;301(4):1077-87.
154. Progida C, Nielsen MS, Koster G, Bucci C, Bakke O. Dynamics of Rab7b-dependent transport of sorting receptors. Traffic. 2012;13(9):1273-85.
155. Ceresa BP, Bahr SJ. rab7 activity affects epidermal growth factor:epidermal growth factor receptor degradation by regulating endocytic trafficking from the late endosome. J Biol Chem. 2006;281(2):1099-106.
156. Alonso-Curbelo D, Osterloh L, Cañón E, Calvo TG, Martínez-Herranz R, Karras P, et al. RAB7 counteracts PI3K-driven macropinocytosis activated at early stages of melanoma development. Oncotarget. 2015;6(14):11848-62.

157. Alonso-Curbelo D, Riveiro-Falkenbach E, Pérez-Guijarro E, Cifdaloz M, Karras P, Osterloh L, et al. RAB7 controls melanoma progression by exploiting a lineage-specific wiring of the endolysosomal pathway. Cancer Cell. 2014;26(1):61-76.
158. Cherry S, Jin EJ, Ozel MN, Lu Z, Agi E, Wang D, et al. Charcot-Marie-Tooth 2B mutations in rab7 cause dosage-dependent neurodegeneration due to partial loss of function. Elife. 2013;2:e01064.
159. De Luca A, Progida C, Spinosa MR, Alifano P, Bucci C. Characterization of the Rab7K157N mutant protein associated with Charcot-Marie-Tooth type 2B. Biochem Biophys Res Commun. 2008;372(2):283-7.
160. Spinosa MR, Progida C, De Luca A, Colucci AM, Alifano P, Bucci C. Functional characterization of Rab7 mutant proteins associated with Charcot-Marie-Tooth type 2B disease. J Neurosci. 2008;28(7):1640-8.
161. Agola JO, Hong L, Surviladze Z, Ursu O, Waller A, Strouse JJ, et al. A competitive nucleotide binding inhibitor: in vitro characterization of Rab7 GTPase inhibition. ACS Chem Biol. 2012;7(6):1095-108.
162. Qin Y, He Y, Zhu YM, Li M, Ni Y, Liu J, et al. CID1067700, a late endosome GTPase Rab7 receptor antagonist, attenuates brain atrophy, improves neurologic deficits and inhibits reactive astrogliosis in rat ischemic stroke. Acta Pharmacol Sin. 2019;40(6):724-36.
163. Lin JZ, Long JY, Wang AQ, Zheng Y, Zhao HT. Precision medicine: In need of guidance and surveillance. World J Gastroenterol. 2017;23(28):5045-50.
164. Akhoon N. Precision Medicine: A New Paradigm in Therapeutics. Int J Prev Med. 2021;12:12.
165. Piao S, Amaravadi RK. Targeting the lysosome in cancer. Ann N Y Acad Sci. 2016;1371(1):45-54.
166. Inpanathan S, Botelho RJ. The Lysosome Signaling Platform: Adapting With the Times. Front Cell Dev Biol. 2019;7:113.
167. Samie MA, Xu H. Lysosomal exocytosis and lipid storage disorders. Journal of Lipid Research. 2014;55(6):995-1009.
168. Garrity AG, Wang W, Collier CM, Levey SA, Gao Q, Xu H. The endoplasmic reticulum, not the pH gradient, drives calcium refilling of lysosomes. Elife. 2016;5.
169. Faris P, Shekha M, Montagna D, Guerra G, Moccia F. Endolysosomal Ca(2+) Signalling and Cancer Hallmarks: Two-Pore Channels on the Move, TRPML1 Lags Behind! Cancers (Basel). 2018;11(1).
170. Santoni G, Maggi F, Amantini C, Marinelli O, Nabissi M, Morelli MB. Pathophysiological Role of Transient Receptor Potential Mucolipin Channel 1 in Calcium-Mediated Stress-Induced Neurodegenerative Diseases. Front Physiol. 2020;11:251.
171. Santoni G, Santoni M, Maggi F, Marinelli O, Morelli MB. Emerging Role of Mucolipins TRPML Channels in Cancer. Front Oncol. 2020;10:659.
172. Prat Castro S, Kudrina V, Jaślan D, Boϋc J, Scotto Rosato A, Grimm C. Neurodegenerative Lysosomal Storage Disorders: TPC2 Comes to the Rescue! Cells. 2022;11(18).
173. Brenner M, Hearing VJ. The protective role of melanin against UV damage in human skin. Photochem Photobiol. 2008;84(3):539-49.
174. Davis LE, Shalin SC, Tackett AJ. Current state of melanoma diagnosis and treatment. Cancer Biol Ther. 2019;20(11):1366-79.
175. Sturm RA, Teasdale RD, Box NF. Human pigmentation genes: identification, structure and consequences of polymorphic variation. Gene. 2001;277(1-2):49-62.
176. Guyonneau L, Murisier F, Rossier A, Moulin A, Beermann F. Melanocytes and pigmentation are affected in dopachrome tautomerase knockout mice. Mol Cell Biol. 2004;24(8):3396-403.
177. Sharma N, Sharma A, Motiani RK. A novel gain of function mutation in TPC2 reiterates pH-pigmentation interplay: Emerging role of ionic homeostasis as a master pigmentation regulator. Cell Calcium. 2023;111:102705.
178. Cichorek M, Wachulska M, Stasiewicz A, Tymińska A. Skin melanocytes: biology and development. Postepy Dermatol Alergol. 2013;30(1):30-41.

179. Sitaram A, Marks MS. Mechanisms of protein delivery to melanosomes in pigment cells. Physiology (Bethesda). 2012;27(2):85-99.
180. Raposo G, Marks MS. Melanosomes — dark organelles enlighten endosomal membrane transport. Nature Reviews Molecular Cell Biology. 2007;8(10):786-97.
181. Jordens I, Westbroek W, Marsman M, Rocha N, Mommaas M, Huizing M, et al. Rab7 and Rab27a control two motor protein activities involved in melanosomal transport. Pigment Cell Res. 2006;19(5):412-23.
182. Alonso-Curbelo D, Soengas MS. Hyperactivated endolysosomal trafficking in melanoma. Oncotarget. 2015;6(5):2583-4.
183. Kasitinon SY, Eskiocak U, Martin M, Bezwada D, Khivansara V, Tasdogan A, et al. TRPML1 Promotes Protein Homeostasis in Melanoma Cells by Negatively Regulating MAPK and mTORC1 Signaling. Cell Rep. 2019;28(9):2293-305.e9.
184. Favia A, Desideri M, Gambara G, D'Alessio A, Ruas M, Esposito B, et al. VEGF-induced neoangiogenesis is mediated by NAADP and two-pore channel-2-dependent Ca2+ signaling. Proc Natl Acad Sci U S A. 2014;111(44):E4706-15.
185. Levy C, Khaled M, Fisher DE. MITF: master regulator of melanocyte development and melanoma oncogene. Trends Mol Med. 2006;12(9):406-14.
186. Garraway LA, Widlund HR, Rubin MA, Getz G, Berger AJ, Ramaswamy S, et al. Integrative genomic analyses identify MITF as a lineage survival oncogene amplified in malignant melanoma. Nature. 2005;436(7047):117-22.
187. Hartman ML, Czyz M. MITF in melanoma: mechanisms behind its expression and activity. Cell Mol Life Sci. 2015;72(7):1249-60.
188. Du W, Gu M, Hu M, Pinchi P, Chen W, Ryan M, et al. Lysosomal Zn(2+) release triggers rapid, mitochondria-mediated, non-apoptotic cell death in metastatic melanoma. Cell Rep. 2021;37(3):109848.
189. Favia A, Pafumi I, Desideri M, Padula F, Montesano C, Passeri D, et al. NAADP-Dependent Ca(2+) Signaling Controls Melanoma Progression, Metastatic Dissemination and Neoangiogenesis. Sci Rep. 2016;6:18925.
190. Katalinic A, Eisemann N, Kraywinkel K, Noftz MR, Hübner J. Breast cancer incidence and mortality before and after implementation of the German mammography screening program. Int J Cancer. 2020;147(3):709-18.
191. Hübner J, Katalinic A, Waldmann A, Kraywinkel K. Long-term Incidence and Mortality Trends for Breast Cancer in Germany. Geburtshilfe Frauenheilkd. 2020;80(6):611-8.
192. Yalaza M, İnan A, Bozer M. Male Breast Cancer. J Breast Health. 2016;12(1):1-8.
193. Dorak MT, Karpuzoglu E. Gender differences in cancer susceptibility: an inadequately addressed issue. Front Genet. 2012;3:268.
194. Alkabban FM, Ferguson T. Breast Cancer. StatPearls. Treasure Island (FL): StatPearls Publishing

Copyright © 2023, StatPearls Publishing LLC.; 2023.
195. Petrucelli N, Daly MB, Pal T. BRCA1- and BRCA2-Associated Hereditary Breast and Ovarian Cancer: University of Washington, Seattle, Seattle (WA); 1993 1993.
196. Anders C, Carey LA. Understanding and treating triple-negative breast cancer. Oncology (Williston Park). 2008;22(11):1233-9; discussion 9-40, 43.
197. Zeichner SB, Terawaki H, Gogineni K. A Review of Systemic Treatment in Metastatic Triple-Negative Breast Cancer. Breast Cancer (Auckl). 2016;10:25-36.
198. Sun W, Yue J. TPC2 mediates autophagy progression and extracellular vesicle secretion in cancer cells. Exp Cell Res. 2018;370(2):478-89.
199. Jahidin AH, Stewart TA, Thompson EW, Roberts-Thomson SJ, Monteith GR. Differential effects of two-pore channel protein 1 and 2 silencing in MDA-MB-468 breast cancer cells. Biochem Biophys Res Commun. 2016;477(4):731-6.
200. Watts C. Lysosomes and lysosome-related organelles in immune responses. FEBS Open Bio. 2022;12(4):678-93.
201. Rajkumar V, Dumpa V. Lysosomal Storage Disease. StatPearls. Treasure Island (FL): StatPearls Publishing

Copyright © 2023, StatPearls Publishing LLC.; 2023.
202. Platt FM, d'Azzo A, Davidson BL, Neufeld EF, Tifft CJ. Lysosomal storage diseases. Nature Reviews Disease Primers. 2018;4(1):27.
203. Sun A. Lysosomal storage disease overview. Ann Transl Med. 2018;6(24):476.
204. Wakabayashi K, Gustafson AM, Sidransky E, Goldin E. Mucolipidosis type IV: an update. Mol Genet Metab. 2011;104(3):206-13.
205. Bargal R, Avidan N, Olender T, Ben Asher E, Zeigler M, Raas-Rothschild A, et al. Mucolipidosis type IV: novel MCOLN1 mutations in Jewish and non-Jewish patients and the frequency of the disease in the Ashkenazi Jewish population. Hum Mutat. 2001;17(5):397-402.
206. Alroy J, García-Moliner ML, Lee RE. The Pathology of the Skeleton in Lysosomal Storage Diseases. In: McManus LM, Mitchell RN, editors. Pathobiology of Human Disease. San Diego: Academic Press; 2014. p. 874-92.
207. Edelmann L, Dong J, Desnick RJ, Kornreich R. Carrier screening for mucolipidosis type IV in the American Ashkenazi Jewish population. Am J Hum Genet. 2002;70(4):1023-7.
208. Negri S, Faris P, Moccia F. Chapter Six - Endolysosomal Ca2+ signaling in cardiovascular health and disease. In: Marchi S, Galluzzi L, editors. International Review of Cell and Molecular Biology. 363: Academic Press; 2021. p. 203-69.
209. Schiffmann R, Dwyer NK, Lubensky IA, Tsokos M, Sutliff VE, Latimer JS, et al. Constitutive achlorhydria in mucolipidosis type IV. Proc Natl Acad Sci U S A. 1998;95(3):1207-12.
210. Yu C. Chapter 9 - Lysosomal storage disorders: Mucopolysaccharidoses. In: Garg U, Smith LD, editors. Biomarkers in Inborn Errors of Metabolism. San Diego: Elsevier; 2017. p. 191-209.
211. Misko AL, Wood LB, DeBono M, Oberman R, Raas-Rothschild A, Grishchuk Y, et al. Cross-sectional Observations on the Natural History of Mucolipidosis Type IV. Neurol Genet. 2022;8(2):e662.
212. Boudewyn LC, Walkley SU. Current concepts in the neuropathogenesis of mucolipidosis type IV. J Neurochem. 2019;148(5):669-89.
213. Rivero-Ríos P, Fernández B, Madero-Pérez J, Lozano MR, Hilfiker S. Two-Pore Channels and Parkinson's Disease: Where's the Link? Messenger (Los Angel). 2016;5(1-2):67-75.
214. Szegö EM, Van den Haute C, Höfs L, Baekelandt V, Van der Perren A, Falkenburger BH. Rab7 reduces α-synuclein toxicity in rats and primary neurons. Exp Neurol. 2022;347:113900.
215. Bose A, Petsko GA, Eliezer D. Parkinson's Disease and Melanoma: Co-Occurrence and Mechanisms. J Parkinsons Dis. 2018;8(3):385-98.
216. Ye Q, Wen Y, Al-Kuwari N, Chen X. Association Between Parkinson's Disease and Melanoma: Putting the Pieces Together. Front Aging Neurosci. 2020;12:60.
217. Dong XP, Cheng X, Mills E, Delling M, Wang F, Kurz T, et al. The type IV mucolipidosis-associated protein TRPML1 is an endolysosomal iron release channel. Nature. 2008;455(7215):992-6.
218. Ruas M, Davis LC, Chen CC, Morgan AJ, Chuang KT, Walseth TF, et al. Expression of Ca^{2+}-permeable two-pore channels rescues NAADP signalling in TPC-deficient cells. Embo j. 2015;34(13):1743-58.
219. Cang C, Zhou Y, Navarro B, Seo YJ, Aranda K, Shi L, et al. mTOR regulates lysosomal ATP-sensitive two-pore Na(+) channels to adapt to metabolic state. Cell. 2013;152(4):778-90.
220. Patel S, Yuan Y, Chen CC, Jaślan D, Gunaratne G, Grimm C, et al. Electrophysiology of Endolysosomal Two-Pore Channels: A Current Account. Cells. 2022;11(15).
221. Pereira GJ, Antonioli M, Hirata H, Ureshino RP, Nascimento AR, Bincoletto C, et al. Glutamate induces autophagy via the two-pore channels in neural cells. Oncotarget. 2017;8(8):12730-40.
222. Pereira GJS, Hirata H, Fimia GM, do Carmo LG, Bincoletto C, Han SW, et al. Nicotinic Acid Adenine Dinucleotide Phosphate (NAADP) Regulates Autophagy in Cultured Astrocytes*. Journal of Biological Chemistry. 2011;286(32):27875-81.

223. Fernández B, Fdez E, Gómez-Suaga P, Gil F, Molina-Villalba I, Ferrer I, et al. Iron overload causes endolysosomal deficits modulated by NAADP-regulated 2-pore channels and RAB7A. Autophagy. 2016;12(9):1487-506.
224. Lin P-H, Duann P, Komazaki S, Park KH, Li H, Sun M, et al. Lysosomal Two-pore Channel Subtype 2 (TPC2) Regulates Skeletal Muscle Autophagic Signaling*. Journal of Biological Chemistry. 2015;290(6):3377-89.
225. Morgan AJ, Martucci LL, Davis LC, Galione A. Two-pore channels: going with the flows. Biochem Soc Trans. 2022;50(4):1143-55.
226. McCray BA, Skordalakes E, Taylor JP. Disease mutations in Rab7 result in unregulated nucleotide exchange and inappropriate activation. Hum Mol Genet. 2010;19(6):1033-47.
227. Spooner E, McLaughlin BM, Lepow T, Durns TA, Randall J, Upchurch C, et al. Systematic screens for proteins that interact with the mucolipidosis type IV protein TRPML1. PLoS One. 2013;8(2):e56780.
228. Vassileva K, Marsh M, Patel S. Two-pore channels as master regulators of membrane trafficking and endocytic well-being. Curr Opin Physiol. 2020;17:163-8.
229. Venkatachalam K, Wong CO, Zhu MX. The role of TRPMLs in endolysosomal trafficking and function. Cell Calcium. 2015;58(1):48-56.
230. Zhang M, Chen L, Wang S, Wang T. Rab7: roles in membrane trafficking and disease. Biosci Rep. 2009;29(3):193-209.
231. Shen D, Wang X, Li X, Zhang X, Yao Z, Dibble S, et al. Lipid storage disorders block lysosomal trafficking by inhibiting a TRP channel and lysosomal calcium release. Nat Commun. 2012;3:731.
232. van den Boomen DJH, Sienkiewicz A, Berlin I, Jongsma MLM, van Elsland DM, Luzio JP, et al. A trimeric Rab7 GEF controls NPC1-dependent lysosomal cholesterol export. Nat Commun. 2020;11(1):5559.
233. Yu T, Chung C, Shen D, Xu H, Lieberman AP. Ryanodine receptor antagonists adapt NPC1 proteostasis to ameliorate lipid storage in Niemann-Pick type C disease fibroblasts. Hum Mol Genet. 2012;21(14):3205-14.
234. Tiscione SA, Vivas O, Ginsburg KS, Bers DM, Ory DS, Santana LF, et al. Disease-associated mutations in Niemann-Pick type C1 alter ER calcium signaling and neuronal plasticity. J Cell Biol. 2019;218(12):4141-56.
235. Zong X, Schieder M, Cuny H, Fenske S, Gruner C, Rötzer K, et al. The two-pore channel TPCN2 mediates NAADP-dependent Ca(2+)-release from lysosomal stores. Pflugers Arch. 2009;458(5):891-9.
236. Yang Y, Zhai X, El Hiani Y. TRPML1-Emerging Roles in Cancer. Cells. 2020;9(12).
237. Sun X, Yang Y, Zhong XZ, Cao Q, Zhu XH, Zhu X, et al. A negative feedback regulation of MTORC1 activity by the lysosomal Ca(2+) channel MCOLN1 (mucolipin 1) using a CALM (calmodulin)-dependent mechanism. Autophagy. 2018;14(1):38-52.

Acknowledgments

I would like to express my sincere gratitude to all the individuals who have supported me throughout the completion of this PhD thesis. I have been fortunate to be surrounded by a remarkable group of people, making it challenging to fairly limit the extent of their contribution during this PhD in just a few sentences.

First and foremost, I would like to extend my appreciation to **Prof. Dr. Dr. Christian Grimm** for providing me with the opportunity to pursue my PhD at his group at the Walther-Straub Institute. Thank you for trusting me with different projects and granting me the freedom to explore my ideas. Your hard-working attitude and dedication to pushing projects forward has taught me a lot.

I would also like to thank **Prof. Dr. Thomas Gudermann**, **Prof. Dr. Alexander Dietrich**, **Jutta Schreier**, and the staff members of the **LMU gateway**. Your assistance with bureaucratic matters and your efforts in ensuring my job security at the institute, particularly during the challenges of issuing and prolonging my residence permit are deeply appreciated.

I would like to extend my thanks to our DFG cancer project collaborators at the Pharmaceutical Biology department of LMU: **Prof. Dr. Angelika Vollmar** and **Dr. Karin Bartel**. Thank you for the great collaborative work over the past few years. Your guidance for the projects and provision of key reagents for my experiments have been invaluable. Within this group, I'd like to give thanks to **Dr. Martin Müller** for your advice during the early stages of my work at the WSI and to **Lina Ouologuem** for performing the animal experiments for the final stages of our mansucript.

Moreover, I would like to express my gratitude to our big network of collaborators: **Prof. Dr. Martin Biel** for grating us access to work at the mouse facility, **Prof. Dr. Chen Cheng-Chang (Maxo)** for sharing your expertise for all the electrophysiology experiments, **Prof. Dr. Franz Bracher** and your group for your continuous support in providing chemical compounds for our experiments, **Prof. Wanchai De-Eknamkul** and **Dr. Ponsawan Netcharoensirisuk** for your support for the flavonoids project and smooth collaborative work, **Prof. Dr. Christian Wahl-Schott** and your group for your invaluable FRET measurements for our manuscript, **Dr. Thomas Fröhlich** and **Youli Stepanov** for the proteomics collaboration.

Scientifically, I owe a great debt of gratitude to **Dr. Anna Scotto Rosato** and **Dr. Einar Krogsaeter**. You have served as inspiring role models. Your kindness, patience, and expertise have been instrumental in my development as a scientist. Furthermore, I would like to thank **Rachel Tang** for your contributions to the electrophysiology experiments and your readiness to patch my CRISPR clones for several projects. Cordial thanks to **Rebecca Deutsch** for completing the electrophysiology experiments on the Rab7 project and for your unwavering kindness.

I am truly grateful to the amazing colleagues who have made the lab and the institute a fun and productive place to work. In specific, I'd like to thank **Dr. Julia Dorfmeister** for introducing me to German and Bavarian culture and your spontaneity to travel adventures**. Dr. Yu-Kai Chao** for your support and motivation, **Dr. Barbara Spix** for always being very warm-hearted, **Eva-Maria Weiden** for engaging in intriguing conversation and being a wonderful friend and desk mate, **Irene Ferro** for always being there to lend an ear and providing me with great Italian food, **Veronika Kudrina** for your enthusiastic sing-alongs to my loud music in the lab, **Francesca Dona** for your vibrant spirit, **Gonxhe Lokaj** for the elaborate discussions during the weekends, **Pranav Kumar Shadmarshan Rengasayee** and **Philipp Alt** for your willingness to help whenever in need.

Moreover, I would like to extend thanks to **Fabienne Geiger** for being my best friend, it wouldn't have been the same without you. Thank you for all the fun times at the institute, concerts, trips, and

most importantly for the karaoke sessions at the licor. Cordial thanks to **Antonio Ramírez-Fernández** for all the after-work pizza/beer session and for being the Mediterranean presence I needed during socially isolated and workaholic Covid-19 pandemic times. A huge thank you to **Anna Durner (Krauti)** for all those late-night Friday sessions, for extending help during difficult times, and for constituting, along with **Dr. Ellis Durner**, my German family.

I am truly grateful to the amazing colleagues who have made the lab and the institute a joyful and productive place to work, including **Dr. Robin Kopp**, **Suhasini Rajan**, **Dr. Yvonne Klingl**, **Keyne Talbot**, **Sandra Prat-Castro**, **Zagorka Bekjarova**, **Pattara Pounghcho**, **Marcel Passon**, **Alina Nakhabina**, **Mane Mkhitaryan**, **Marco Müller**, **Lena Schaller**, **Isabel Müller**, **Heinz Janser**, **Dr. Larissa Bendiks**, and **Dr. Juan David Sierra**. Further thanks to **Dr. Alexander Haupt** and **Dr. Simon Mayr** for their help in the final structuring of the thesis.

I would like to thank my friends in and outside of Germany for your immeasurable support and for (most) 10+ years of friendship: **Vicken Margossian, Bashar Salloum**, **Fawaz Al Hosh**, **Dr. Nourhan El Ahmar**, **Dr. Reem Alwan**, **Gassia Telvizian**, **Marcelino Al Ghafari**, **Dr. Silvia Fanti**, **Angelica Ayvazian**, and **Jean-Paul Dishoyan**.

With the utmost gratitude, I dedicate this thesis to my family. To **my parents**, thank you for all your sacrifices and support throughout my upbringing, education, and move to different countries. Your unwavering support has been the cornerstone of my journey. To **my grandma and aunts**, thank you for always believing in me and constituting a driving force, I am inspired by your strength and kindness. To **my siblings**, thank you for all the teasing and your never-ending requests that kept me grounded, I wouldn't have chosen it any other way. Additional thanks to my extended family spread across the United States, Lebanon, Syria, and Armenia, your enduring presence and support have transcended borders.

Amidst the Covid-19 global pandemic, the Beirut Blast, conflicts in Armenia, and the war in Syria, unfolding during this PhD, I have been constantly reminded of my privilege to carry out this research work in Munich. In light of this, I am immensely grateful to colleagues at the **Foundation for Armenian Science and Technology** for their impactful work and to all my labmates at the WSI who have generously contributed to numerous cherished causes and who have served as an invaluable support system throughout these times, I thank you.